CRONUS

Controlled Reentry Orbiting NUclear System

MARTIN

RTG/RB CIR AGE

Study for 250-Watt Controlled Reentry Orbiting NUclear System

MND-2050-F. 2

VOLUME II

APPENDICES

DISCLAIMER

C-92A Distribution
M-3679 (48th Ed.)

AEC Research and
Development Report

CRONUS

Controlled Reentry Orbiting NUclear System

Study for 250-Watt Controlled Reentry Orbiting NUclear System

VOLUME II
APPENDICES

RTG/RB CIR AGE

November 2, 1966

MND-2050-F-2 (Vol 2 APP.)

MARTIN COMPANY
BALTIMORE, MARYLAND 21203

LEGAL NOTICE

This report was prepared as an account of Government sponsored work. Neither the United States, nor the Commission, nor any person acting on behalf of the Commission:

A. Makes any warranty or representation, expressed or implied, with respect to the accuracy, completeness, or usefulness of the information contained in this report, or that the use of any information, apparatus, method, or process disclosed in this report may not infringe privately owned rights; or

B. Assumes any liabilities with respect to the use of, or for damages resulting from the use of any information, apparatus, method, or process disclosed in this report.

As used in the above, "person acting on behalf of the Commission" includes any employee or contractor of the Commission, or employee of such contractor, to the extent that such employee or contractor of the Commission, or employee of such contractor prepares, disseminates, or provides access to, any information pursuant to his employment or contract with the Commission, or his employment with such contractor.

FOREWORD

The United States Atomic Energy Commission awarded the Martin Company Contract AT(29-2)-2050 for a six-month study, effective May 2, 1966, to develop and evaluate a feasible concept(s) for a 250-watt(e) radioisotopic thermoelectric generator providing controlled intact reentry of the fuel from earth orbit. A concept(s) for handling and fueling the RTG at a Titan III launch site was also to be developed and evaluated. Based upon the selected system concept, a development program plan was to be prepared, including estimated costs, for the design, development, flight test and delivery of operationally flight qualified hardware systems.

The flight and ground systems have been integrated by Martin into a single system concept designated CRONUS, an abbreviation for Controlled Reentry Orbiting NUclear System. Major CRONUS systems include the 250-watt(e) generator/reentry body (RTG/RB), the controlled intact reentry (CIR), and required ground support (AGE) systems which include fuel loading (GHE).

The following is a complete list of the documents prepared and submitted in accordance with Contract AT(29-2)-2050.

Volume I--Summary

Volume II--Technical

Volume II--Appendices

Volume III--Development Program Plan

Volume IV--Specifications and Data Management

Volume V--Budgetary Estimate

Volume VI--Quality Assurance Plan

BLANK

CONTENTS

CONTENTS (continued)

CONTENTS (continued)

BLANK

APPENDIX A

BARE HEAT SOURCE TEMPERATURE CALCULATION

An analysis was performed to predict average heat source surface temperature in air with natural convection and radiation. This condition will approximate that existent on the launch pad prior to fueling but after removal of the heat source from the shipping cask.

Also, this heat source surface temperature can be used later as an initial condition for predicting transient generator behavior on the pad following insertion of the heat source into the RTG.

The heat source average surface temperature with natural convection and radiation is described by the following equation:

$$q = \sigma \epsilon A (T^4 - \theta^4) + h_c A (T - \theta)$$

$$h_c = \frac{0.59\ k_f}{L} (Gr\ Pr)_f^{1/4}$$

where

q = beginning-of-life fuel inventory = 23,500 Btu/hr

σ = Stefan-Boltzmann constant

A = lateral area of heat source = 6.15 ft^2

θ = ambient temperature = 100° F

T = average surface temperature of heat source

h_c = natural convection heat transfer coefficient (laminar flow in this case) (Btu/ft^2-hr-°F)

k_f = air thermal conductivity at film temperature (i.e., average between T and θ) (Btu/ft-hr-°F)

ϵ = heat source emissivity = a variable

Gr = Grashof number

Pr = Prandtl number

L = fuel capsule height = 1.05 feet

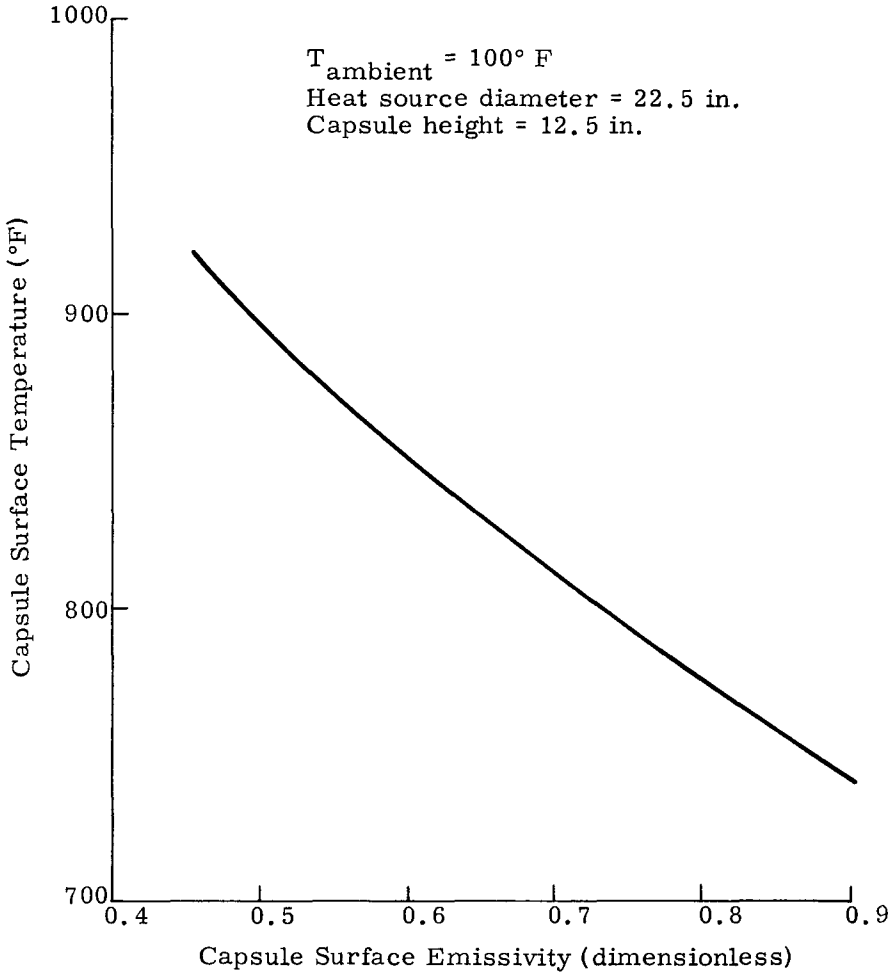

Fig. A-1. Capsule Surface Temperature Versus Emissivity in Air

The solution, obtained by the Newton-Raphson technique, is presented in Fig. A-1 as a function of emissivity.

A heat source emissivity of 0.80 is expected. From Fig. A-1, for combined radiation and natural convection, the resultant average steady-state temperature in air will be approximately 775° F.

BLANK

APPENDIX B

STEADY STATE FUEL CAPSULE TEMPERATURE

For steady state conditions, capsule temperature can be computed by a hand calculation at both beginning and end of life. At end of life, capsule temperature was computed for normal operation only. At beginning of life, capsule temperatures were computed for both normal operation and open circuit conditions.

A. CASE I: BEGINNING OF LIFE--NORMAL OPERATION

At the beginning of life, the hot junction temperature is 1590°F (Chapter III). Since the ΔT through the hot shoe will be 50°F, the maximum hot shoe temperature will be 1640°F. The resultant capsule surface temperature due to radiative heat transfer is given by:

$$T_{cap} = \left[\frac{q_{BOL} \left(\frac{1}{F_{12}} + \frac{\rho_1}{\epsilon_1} + \frac{A_1}{A_2} \frac{\rho_2}{\epsilon_2} \right)}{\sigma A_1} + T_{shoe}^4 \right]^{1/4}$$

where

q_{BOL} = beginning-of-life fuel inventory = 21,850 Btu/hr

F_{12} = view factor from capsule to shoe = 1

ρ_1 = capsule reflectivity = 0.2

ρ_2 = shoe reflectivity = 0.2

ϵ_1 = capsule emissivity = 0.8

ϵ_2 = shoe emissivity = 0.8

A_1 = heat source lateral area = 6.15 ft^2

A_2 = hot shoe area = 7.0 ft^2

σ = Stefan-Boltzmann constant

T_{shoe} = shoe temperature = 1640° F = 2100° R

The result is

$$T_{cap} = 2180° R = 1720° F.$$

This capsule temperature applies to the surface exposed to the hot shoes.

With the present heat source configuration, a temperature gradient exists circumferentially around the capsule wall to the hot spot at the midline on the back wall. This ΔT can be approximated by a hand calculation for Phase 0. In Phase I, recourse should be taken to the digital computer for this thermal analysis.

The following assumptions are made for the hand calculation:

(1) The front surface of the capsule as "seen" by the hot shoes is isothermal.

(2) All the heat is transferred uniformly from the fuel into the capsule wall. The heat on the back surface of the capsule is then conducted to the front surface. This assumption effectively allows no contribution from heat flow through the fuel. This model is somewhat conservative as the conductance of the capsule is about an order of magnitude higher than the conductance of the fuel.

With these assumptions

$$\Delta T = \frac{SL^2}{2K} = 67° F$$

where

$$S = \frac{q}{V}$$

ΔT = delta temperature between isothermal front surface of capsule and back midline

q = beginning-of-life fuel inventory per capsule = 178 watts

V = fuel capsule side wall volume = 6 $in.^3$ (corresponds to a wall thickness of ~90 mils on a 1.75-inch OD; capsule length is 12.5 inches)

L = path length for heat flow (quarter arc of capsule inches = 1.3 inches)

K = Haynes-25 conductivity at 1700° F = 15.9 Btu/ft-hr-°F

Thus, the maximum back wall temperature is 1787° F.

B. CASE II: BEGINNING OF LIFE--OPEN CIRCUIT

In the event of an open circuit in the RTG electrical circuit (such as could occur when the reentry vehicle is separated from the spacecraft prior to reentry), higher hot junction and capsule temperatures occur because of the loss of Peltier cooling (a current dependent effect) in the thermoelements. On open circuit, the resultant steady-state hot junction temperature can be determined from the following heat balance on the thermoelements:

$$q_{BOL} = K_{par}\,(T_H - T_C) + N\left(\frac{\bar{K}_N A_N}{\ell_N} + \frac{\bar{K}_P A_P}{\ell_P}\right)\quad (T_H - T_C)$$

where

K_{par} = parasitic conductance $\approx \frac{q_{par}}{\Delta T} = \frac{610 \text{ watts}}{1450\text{-}550^\circ \text{ F}} =$ 2.3 Btu/hr.-$^\circ$F

$\frac{NA_N}{\ell_N}$ = $\frac{\text{number of couples x N-element area}}{\text{N-element length}}$ = 4.00 feet

$\frac{NA_P}{\ell_P}$ = $\frac{\text{number of couples x P-element area}}{\text{P-element length}}$ = 2.45 feet

q_{BOL} = beginning-of-life fuel inventory of 6420 watts = 21,850 Btu/hr

T_C = open circuit cold junction temperature at beginning of life = 590° F

$\bar{K}_P$, $\bar{K}_N$ = integrated average thermal conductivity on the P and N thermoelements = 2.68 Btu/ft-hr-°F, 2.26 Btu/ft-hr-°F, respectively

T_H = hot junction open circuit temperature at beginning of life

The steady-state solution is T_H = 1795° F.

As in the previous case, the ΔT through the hot shoe is 50° F so that T_{shoe} = 1845° F = 2305° R.

The resultant capsule temperature is given by

$$T_{cap} = \left[\frac{q_{BOL} \left(\frac{1}{F_{12}} + \frac{\rho_1}{\epsilon_1} + \frac{A_1 \rho_2}{A_2 \epsilon_2} \right)}{\sigma A_1} + T_{shoe}^4 \right]^{1/4} = 2370^\circ R = 1910^\circ F$$

Since the circumferential ΔT from the front wall to the back wall on the capsule is 67° F, the maximum back wall capsule temperature under open circuit conditions is 1977° F.

C. CASE III: END OF LIFE--NORMAL OPERATION

At end of life (design point), capsule temperature is given by

$$T_{cap} = \left[\frac{q_{BOL} \left(\frac{1}{F_{12}} + \frac{\rho_1}{\epsilon_1} + \frac{A_1 \rho_2}{A_2 \epsilon_2} \right)}{\sigma A_1} + T_{shoe}^4 \right]^{1/4} = 2040^\circ R = 1580^\circ F$$

where

q_{EOL} = end-of-life fuel inventory = 5660 watts = 19,300 Btu/hr

T_{shoe} = 1495° F

At the end of life, the circumferential ΔT to the back wall is ~60° F so that the maximum back wall temperature is 1640° F.

APPENDIX C

RTG/RB THERMAL ANALYSIS

A. INTRODUCTION AND SUMMARY

Transient and steady-state thermal analyses were performed on the generator system with an IBM 1130 digital computer. In particular, the following conditions were examined to establish feasibility and/or aid in the radiator design:

Investigation	Purpose
Steady state in orbit; end of life; normal operation of the thermoelectric module	To establish radiator characteristics
Steady state in orbit; beginning of life; open circuit operation of the thermoelectric module	Resultant temperature profile serves as worst case initial conditions for the reentry
Reentry (descent) using flight path angles of -8, -0.1 and -2 degrees coupled with separate heating rates on the forward, middle and aft sectors of the radiator	Feasibility (of particular concern are the maximum temperatures that result on the radiator and the fuel capsule)
Fireball (entire generator system and individual fuel capsule)	Examine capsule integrity

These studies are presented in the following. The conclusions of these numerical analyses are:

(1) The reference generator system will survive the intense reentry heating even when the descent is initiated from the worst case initial condition in orbit--that of an open-circuited

generator at beginning of life. For the selected system, the most severe flight path angle was the -0.1 degree. In this particular case, the hot spot on the capsule (i.e., the back wall) reached a maximum of 2050° F at time of impact, 2100 seconds, while the extremities of the conical shell radiator (beryllium) reached a maximum of 1424° F at 1700 seconds.

As a general conclusion, capsule temperature rose 12°, 30° and 70° F for flight path angles of -8, -2 and -0.1 degrees, respectively.

(2) Both an entire generator system and an individual fuel capsule will survive the expected 16-second Titan fireball.

B. THERMAL MODEL

All transient and steady-state thermal analyses on the generator system were performed with the IBM 1130 digital computer using the sampled perturbation theory (Appendix M). Figure C-1 is a schematic of the 15-node thermal model used in these studies. Also shown in the figure are the dimensions finally selected for the system.

Node 1 in the figure is the ablator section of the spacecraft. Nodes 2, 3, 4, 5 and 6 are those which comprise the radiator section of the system with Node 4 as the center section of the radiator and attached directly to the thermoelectric elements in the system. Nodes 2, 3, 5 and 6 are considered as truncated conical shells of equal length. Node 4 is in conductive contact with Node 13 (thermoelectric elements), Node 11 (insulation between the hot shoes and radiator) and Nodes 3 and 5.

The forward section of the model (cross hatched area in Fig. C-1) is insulated sufficiently that heat transfer between the ablator (Node 1) and other nodes in the generator system is negligible.

Internal radiative interchange is provided in the aft section from Nodes 5 and 6 to Nodes 7 and 14 as well as between Nodes 7 and 14.

The isotope is represented by Node 8 which is conductively coupled with the capsule, Node 9. The hot shoes are represented by Node 10 which is coupled to the capsule by radiative heat transfer only. Nodes 9 and 10 are approximated by concentric cylinders, each radiating with an emissivity of 0.8. Although the hot shoe node is taken as one node, there are many hot shoes in the system that are lumped into this single node. This approach does not affect the thermal balance to an appreciable extent as long as the true area of all hot shoes is encompassed in

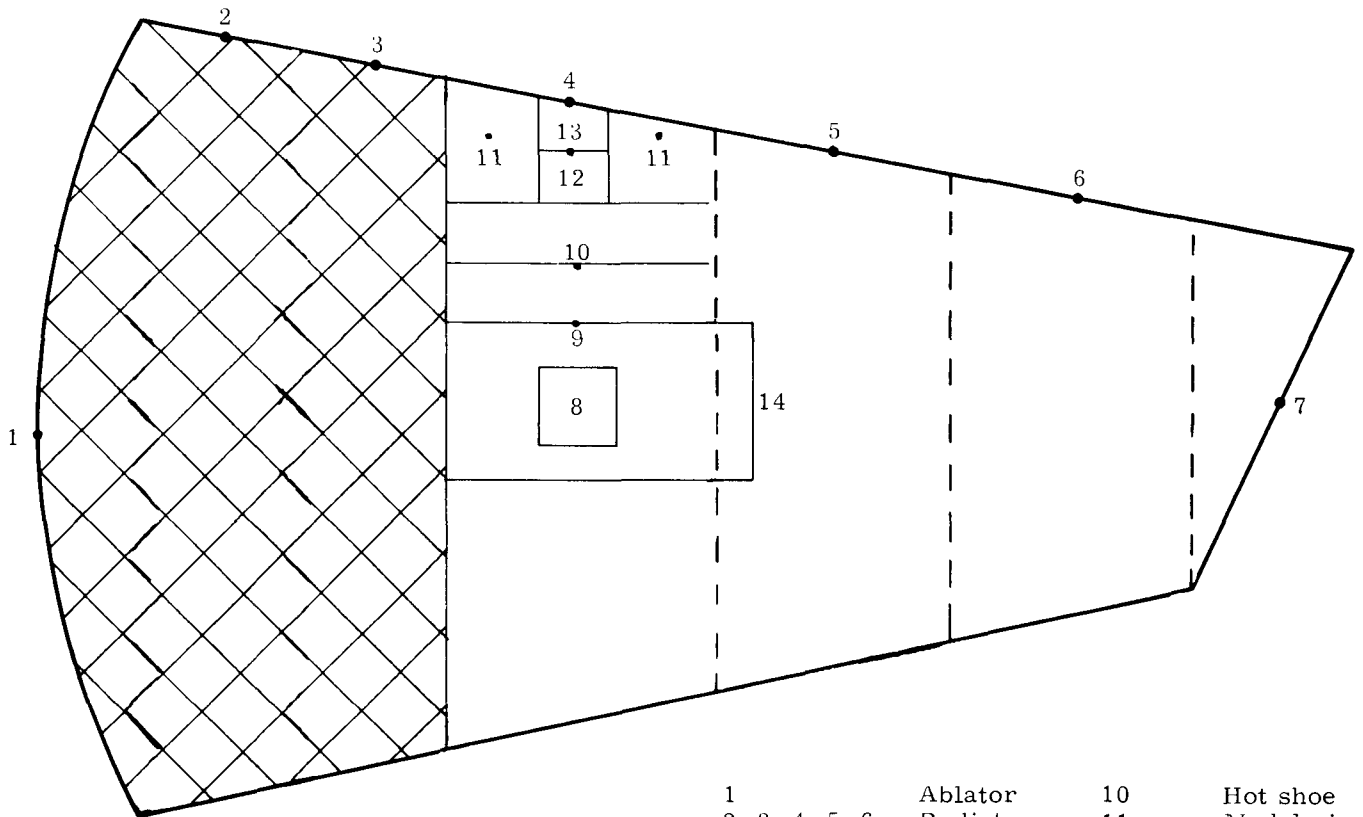

1	Ablator	10	Hot shoe
2, 3, 4, 5, 6	Radiator	11	Module insulation
7	Aft cap	12, 13	Thermoelements
8	Fuel	14	Heat source insulation
9	Capsule	15	Space

Fig. C-1. Thermal Model Under Consideration

this lumped node system. Nodes 12 and 13 are the thermoelectric elements within the system and are conductively attached to the hot shoes (Node 10) on one end and the radiator (Node 4) on the other end and surrounded by insulation (Node 11). Once again, Nodes 12 and 13 are a lumped representation of all the thermoelectric elements within the system. Two nodes were used to allow for property variations through the elements. Node 14 is the heat source insulation. Node 15 is the environment node whether it is in space or the atmosphere.

Table C-1 shows the thermal properties associated with the nodes for both beginning- and end-of-life conditions. Note that the thermal conductivity on the radiator nodes varies according to the approximate steady-state temperatures found for the respective node when in orbit conditions. The thermal conductivity of Node 7 (the back section of the generator) was minimized in order that heat transport by conduction between Nodes 7 and 6 would be small and that the main mode of heat transfer would be by radiation. All exterior nodes in the system were assumed to have an emissivity of 0.85 by virtue of a coating.

C. BEGINNING-OF-LIFE

The beginning-of-life steady-state condition under open circuit is of importance in that it is used as the worst case initial condition for the transient reentry heating of the system.

This steady-state orbit condition was investigated on the 1130 IBM computer with the generator system thermal model. For this analysis solar, solar reflected and terrestrial heat inputs were not considered since it is a reasonable first approximation to neglect them due to the high temperature operation of a SiGe system (provided a low optical-wavelength coating is used on the beryllium radiator).

The beginning-of-life temperature profile serves as the initial temperature condition for the descent. In addition, it was conservatively assumed that at the time of separation, the nature of the separation was such that an open circuit* was produced on the module. (If it had been necessary, a shorting plug could have been introduced into the generator design so that, with a certain reliability, open circuit would not be possible.)

*By definition, an open circuit involves zero current and, therefore, zero Peltier cooling. The net result is that hot junction and capsule temperatures are 200° F higher than with a module under normal load.

TABLE C-1

Properties of Nodes

Node	Thermal Conductivity (Btu/hr/ft-°F)	Internal Heat (Btu/hr)	Specific Heat (Btu/lb-°R)	Emissivity
1	0.1728	0.	0.40	0.85
2	85.0	0.	0.68	0.85
3	82.0	0.	0.68	0.85
4	75.0	0.	0.68	0.85
5	82.0	0.	0.68	0.85
6	85.0	0.	0.68	0.85
7	0.0001	0.	0.68	0.85
8	1.0	***	0.17	0.85
9	15.0	0.	0.10	0.80
10	15.4	0.	0.18	0.80
11	0.0125	0.	0.26	0.85
12	**	0.	0.15	0.85
13	**	0.	0.15	0.85
14	0.015	0.	0.26	0.85
15	--	--	--	1.00

*See Fig. C-5 for various tapers
**For EOL Node 12 = 3.39; Node 13 = 3.39
For BOL Node 12 = 2.50; Node 13 = 2.55
***For EOL Q = 19,300 Btu/hr
For BOL Q = 21,850 Btu/hr

Figures C-2, C-3 and C-4 show the results of the steady-state beginning-of-life conditions as a function of the tapers considered. Figure C-2 graphs Nodes 2, 3, 5 and 6 on the radiator, showing a general decrease in the temperatures of Nodes 3 and 5 as the taper diminishes, whereas Nodes 2 and 6 show a rise as the taper diminishes. Figure C-3 is a graph of Node 4 as a function of temperature, showing a decreasing temperature as taper diminishes. The least affected nodes, 8 and 9 (fuel and capsule) are shown in Fig. C-4 and show, as expected, a slight drop in temperature as the taper diminishes.

In tabular form, the results for the entire 15-node problem are presented in Table C-2.

Again, it is noted that there is only one design set of temperatures, and the differences that are apparent in Figs. C-2, C-3 and C-4 result from the different tapers studied. Thus, all temperatures in Figs. C-2, C-3 and C-4 are nominal and should definitely be adjusted to a common base (the design point). The effect on capsule temperature (Fig. C-4) and on the results obtained later in the descent study is not important, however, and therefore this adjustment was not made. For accurate capsule temperature at beginning of life (and for other conditions) reference is made to Appendix B. The results do agree favorably.

D. FIREBALL

In a launch pad accident fireball environment, the fuel containment structure must survive the accident criteria established in Appendix Z. In the 1130 digital computer analyses that follow, a conservative heat flux of 86 Btu/ft^2-sec was assumed to impinge on all external nodes of the system.

Two conditions were examined for fireball exposure. In the first case the entire generator assembly was subjected to the fireball. In the second analysis, an individual capsule was immersed in the fireball.

For both conditions, the duration of the fireball was taken as 16 seconds following the empirical expression presented in Appendix Z, viz:

$$T = 0.23\ W^{1/3} = 16 \text{ seconds}$$

where

T = time (sec)

W = propellant mass $\approx$ 350,000 pounds.

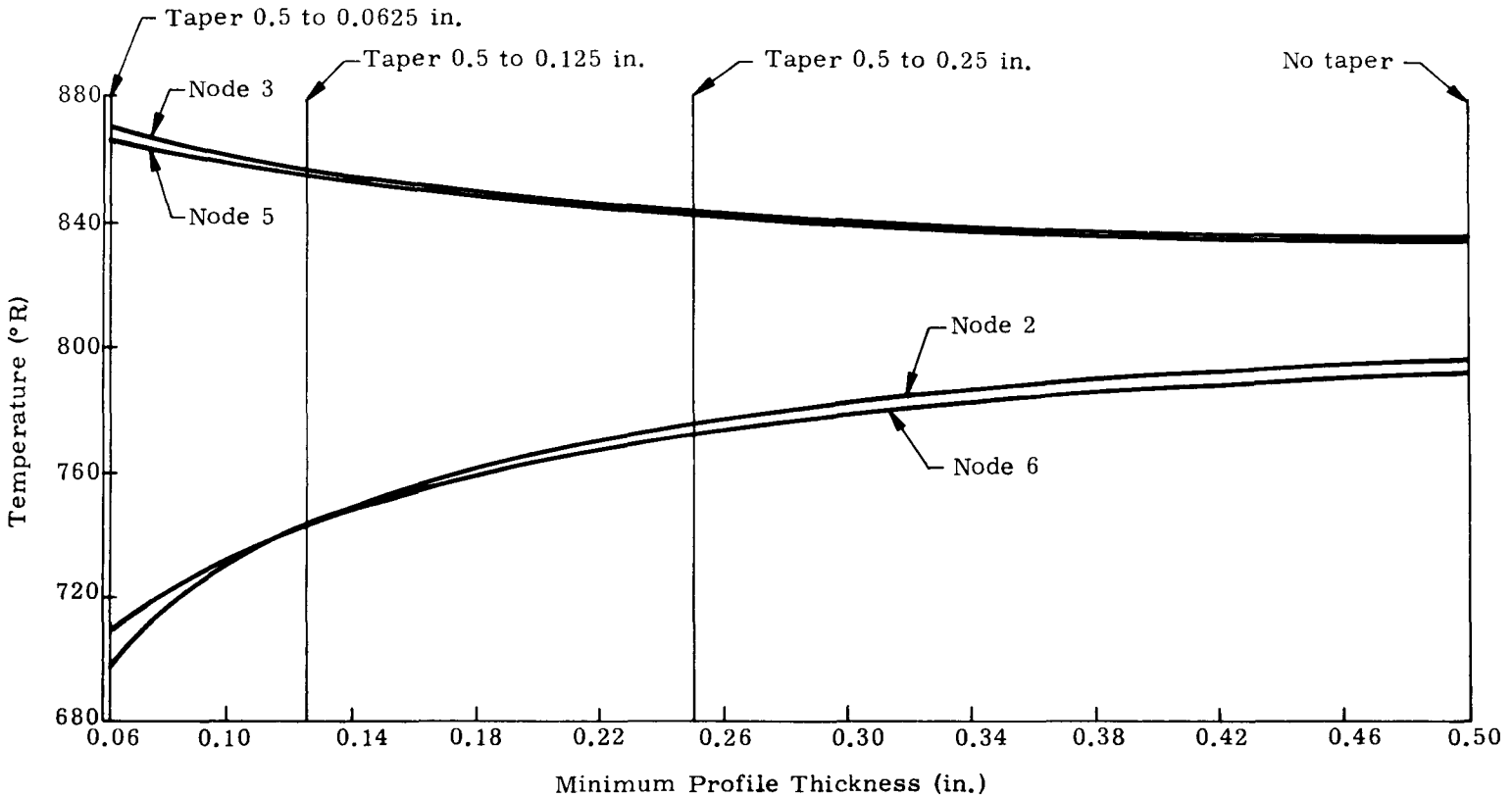

Fig. C-2. Radiator Temperature Versus Minimum Profile Thickness in Steady-State Orbit at Beginning of Life for Triangularized Profile

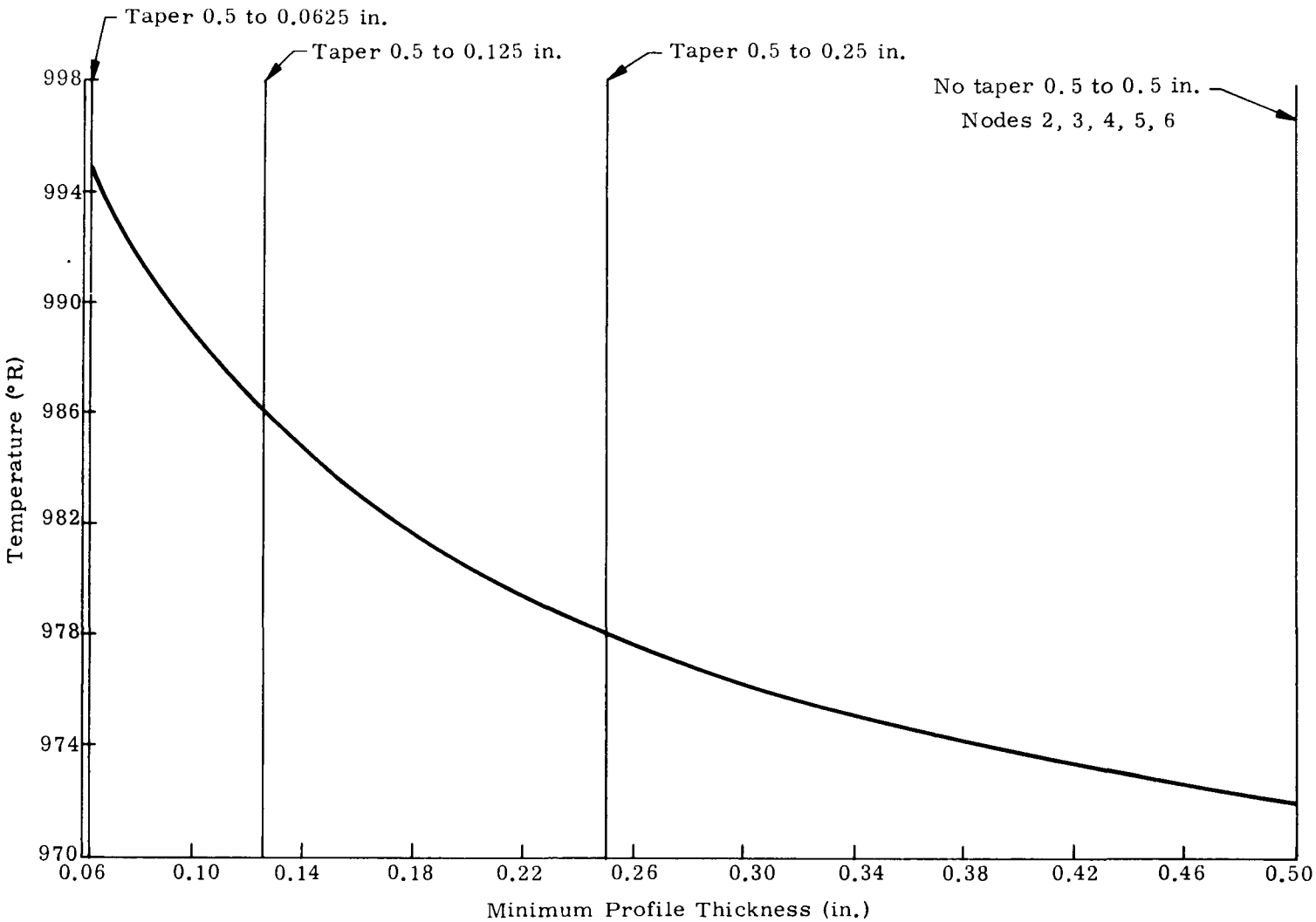

Fig. C-3. Radiator Temperature Versus Minimum Profile Thickness in Steady-State Orbit at Beginning of Life for Triangularized Profile (Node 4)

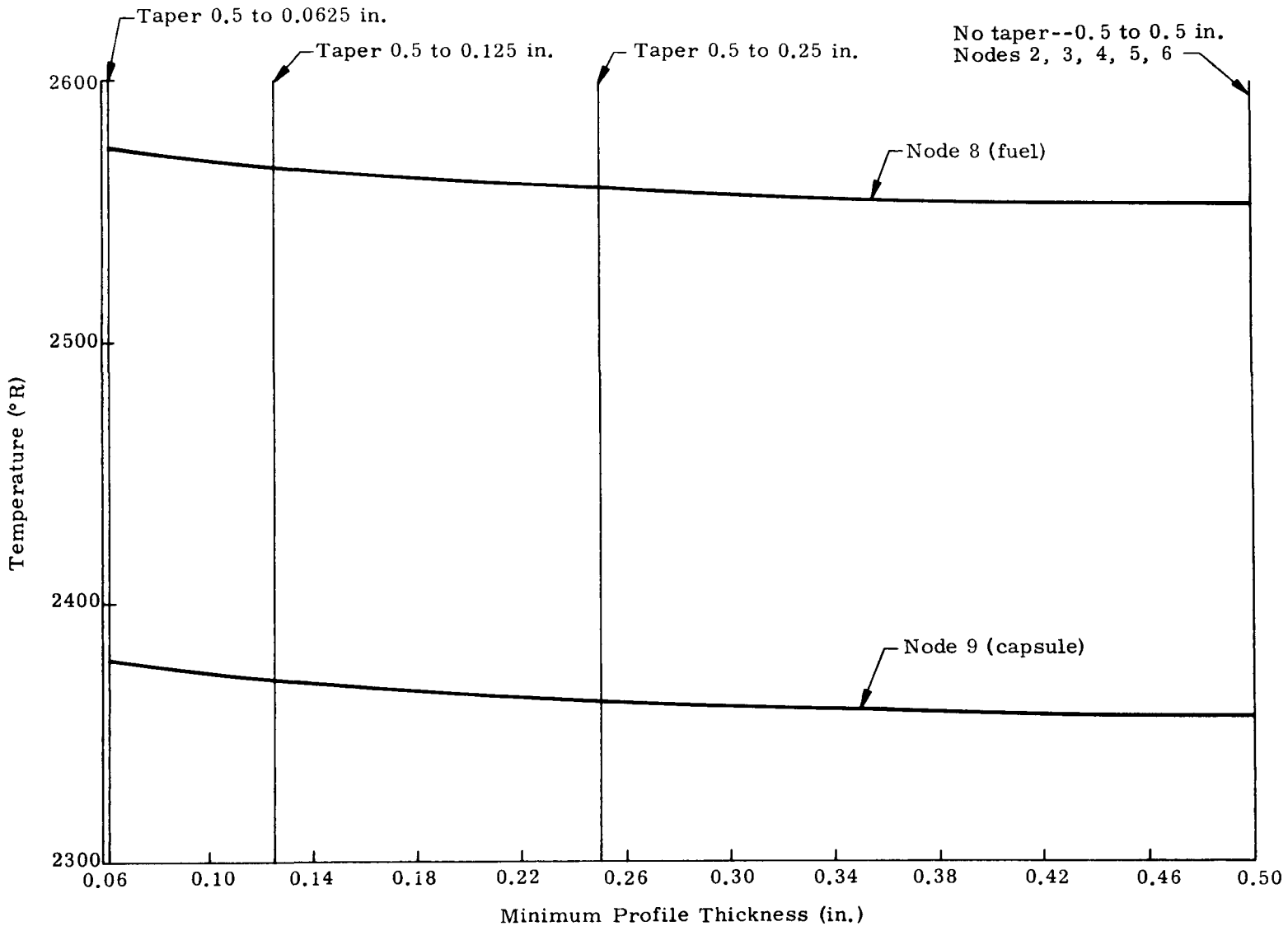

Fig. C-4. Fuel and Capsule Temperatures Versus Minimum Profile Thickness in Steady-State Orbit at Beginning of Life for Triangularized Profile

TABLE C-2

Steady-State Temperatures for Various Radiator Tapers at Beginning of Life with an Open Circuit

Node	No Taper 0.5 to 0.5 in.	Taper 0.5 to 0.25 in.	Taper 0.5 to 0.125 in.	Taper 0.5 to 0.0625 in.
1 Ablator	706° R / 246° F	706° R / 246° F	706° R / 246° F	706° R / 246° F
2 Radiator	797° R / 337° F	776° R / 316° F	743° R / 283° F	696° R / 236° F
3 Radiator	835° R / 375° F	844° R / 384° F	857° R / 397° F	872° R / 412° F
4 Radiator	972° R / 512° F	978° R / 518° F	986° R / 526° F	995° R / 535° F
5 Radiator	834° R / 374° F	843° R / 383° F	855° R / 395° F	867° R / 407° F
6 Radiator	792° R / 332° F	772° R / 312° F	743° R / 283° F	709° R / 249° F
7 Back section	673° R / 213° F	667° R / 207° F	659° R / 199° F	652° R / 192° F
8 Fuel	2553° R / 2093° F	2558° R / 2098° F	2566° R / 2106° F	2573° R / 2113° F
9 Capsule	2357° R / 1897° F	2363° R / 1903° F	2370° R / 1910° F	2378° R / 1918° F
10 Hot Shoe	2298° R / 1838° F	2304° R / 1844° F	2312° R / 1852° F	2320° R / 1860° F
11 Insulation	1635° R / 1175° F	1641° R / 1181° F	1649° R / 1189° F	1657° R / 1197° F
12 T/E element	1641° R / 1181° F	1647° R / 1187° F	1655° R / 1195° F	1663° R / 1203° F
13 T/E element	1014° R / 554° F	1020° R / 560° F	1628° R / 568° F	1037° R / 577° F
14 Insulation	805° R / 345° F	804° R / 344° F	802° R / 342° F	801° R / 341° F
15 Space	0° R / -460° F	0° R / -460° F	0° R / -460° F	0° R / -460° F

1. Generator System Study

This transient thermal analysis was performed parametrically using the thermal model of the generator assembly established for Phase 0 (see Fig. C-1). Initial conditions assumed to exist on the launch pad prior to the fireball are presented in Table C-3. These initial temperatures are only estimates but are reasonable values, and expected changes should not change the conclusions.

By the sampled perturbation theory (see Appendix M), the temperature-time history of each node was ascertained. For conservatism, the entire generator was isolated in the sense that it was not allowed to reradiate or convect to the surroundings. The problem was run for 60 seconds although the fireball lasts for only 16 seconds.

From Figs. C-5 to C-9, it is seen that Nodes 2 and 6 (radiator tips) melt during the fireball for the most severe taper configuration (0.5 inch on Node 4 to 0.0625 inch on Nodes 2 and 6). On the other three tapers, radiator melting does not occur over the 16-second period.

From Fig. C-10, it may be seen that the capsule is nearly unchanged from its initial value of ~1600° F because of the large thermal inertia of the radiator. This response lag of the capsule accounts for its non-dependency on the configuration of the radiator (i.e., the taper) and furthermore is the basis for the previous comment that an error in the initial conditions would not affect the result that the capsule does not melt.

2. Capsule Study

As a more severe case, the heat flux of 86 Btu/ft^2-sec was assumed to impinge directly on the fuel capsule. In this case, the initial temperature was taken as 1500° F and the capsule emissivity was assumed to be 0.85. The resultant transient behavior is presented in Fig. C-11. Capsule melting did not occur over the 16-second fireball.

It is unlikely that an individual capsule would ever be exposed directly to the fireball since the CRONUS is able to withstand the shock overpressures and remain intact. The condition is theoretically possible, however, and thus is of some interest.

TABLE C-3

Assumed Generator Assembly Initial Conditions for Fireball Analyses

Node*	Initial Temperature (°F)
1 Ablator	150
2 Radiator	90
3 Radiator	250
4 Radiator	350
5 Radiator	250
6 Radiator	100
7 Aft cap	75
8 Fuel	1775
9 Capsule	1600
10 Hot shoe	1500
11 Module insulation	925
12 T/E	925
13 T/E	400
14 Heat source insulation	90

*Refer to Fig. C-1 for nodal locations.

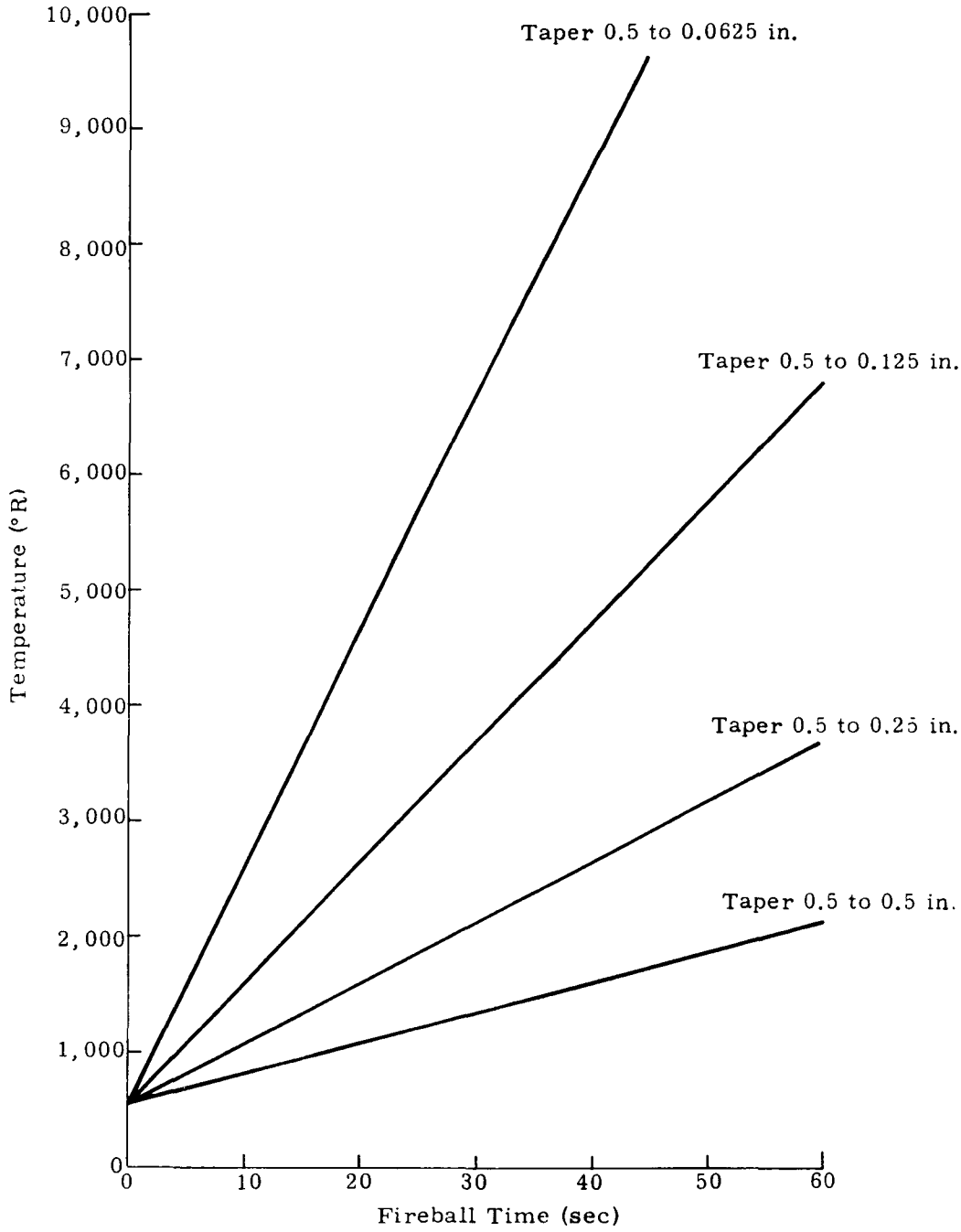

Fig. C-5. Temperature Versus Fireball Time for Node 2 at Radiator Tip

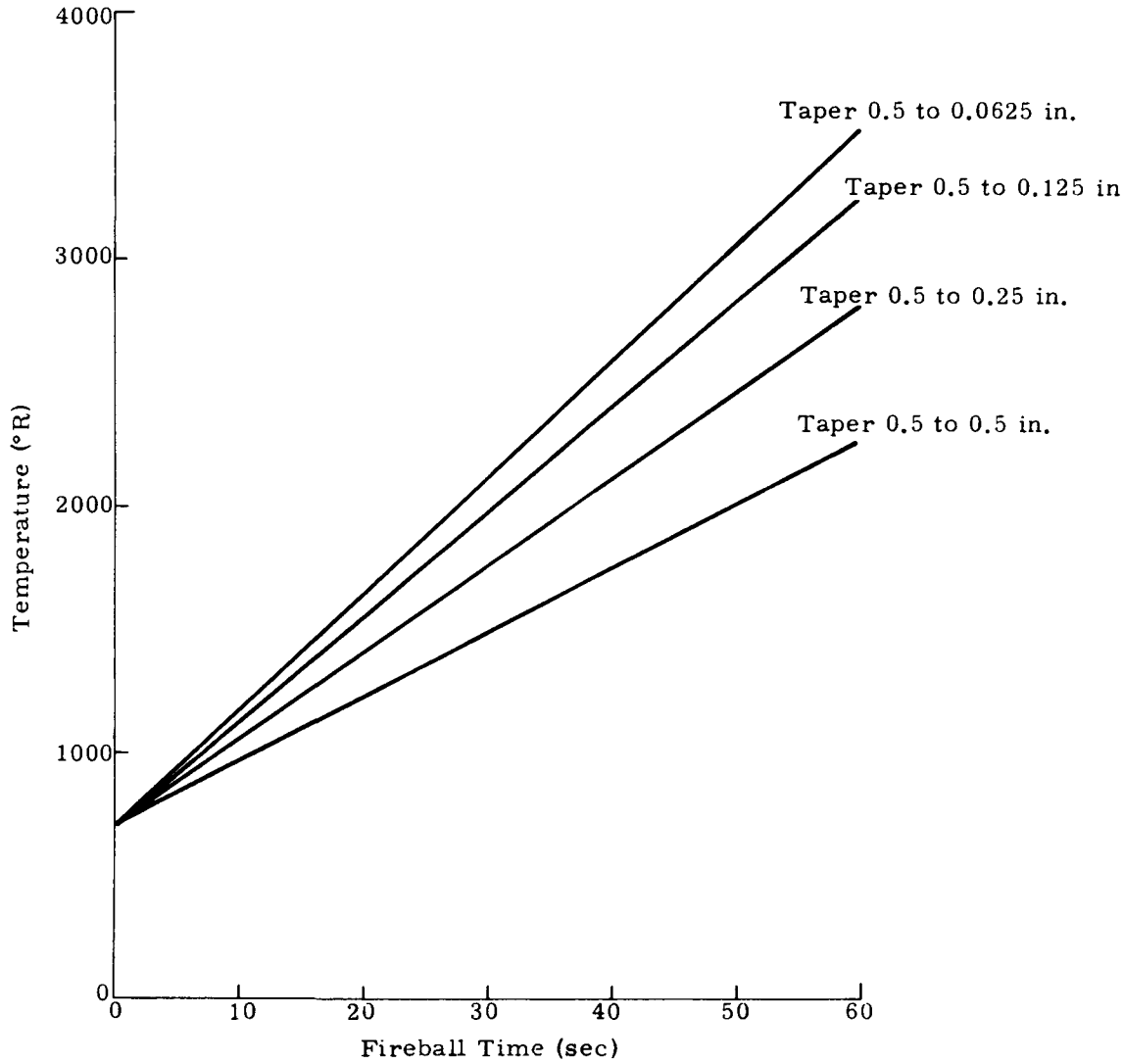

Fig. C-6. Temperature Versus Fireball Time for Node 3 at Radiator

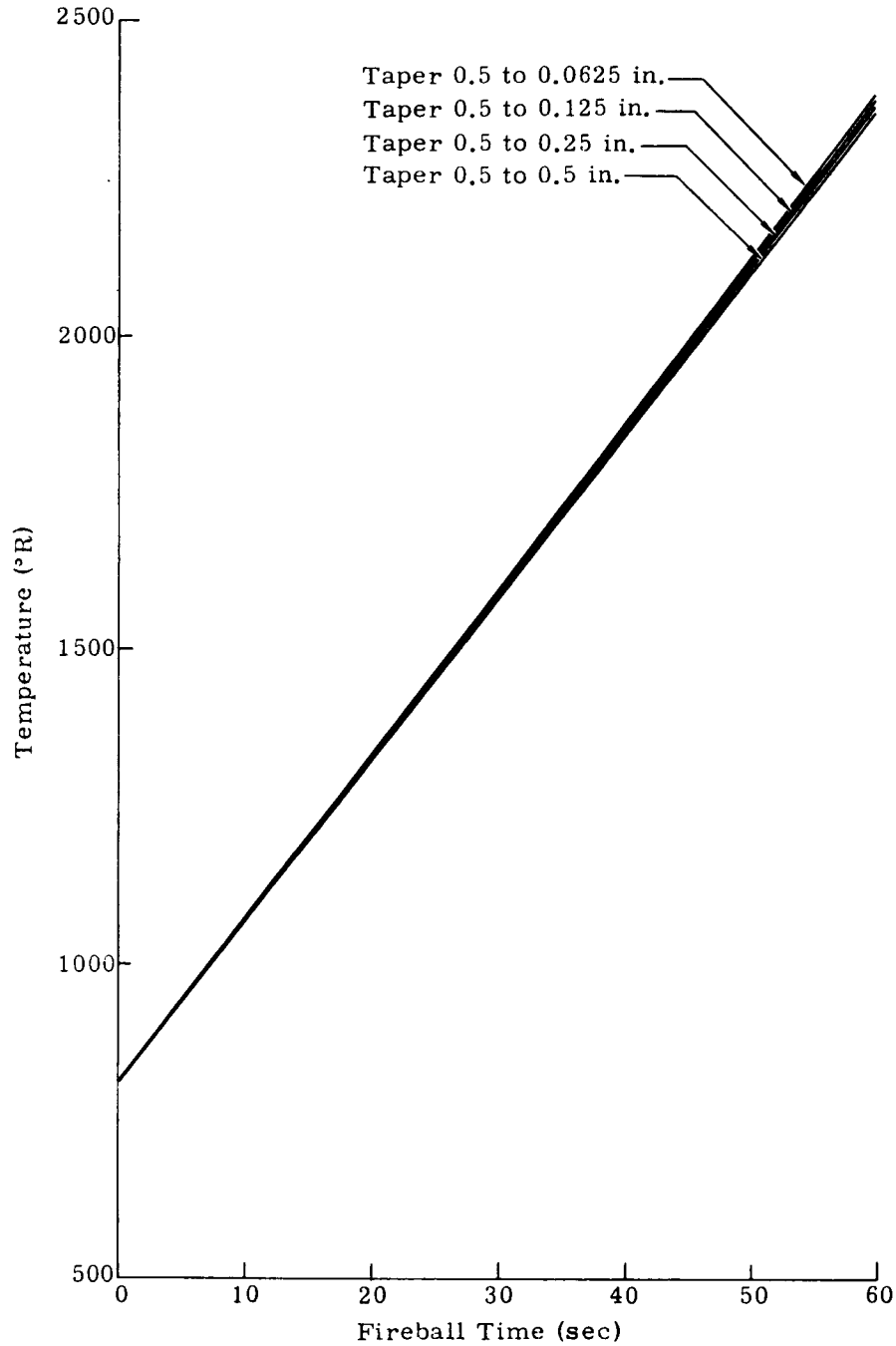

Fig. C-7. Temperature Versus Fireball Time for Node 4 at Radiator Root

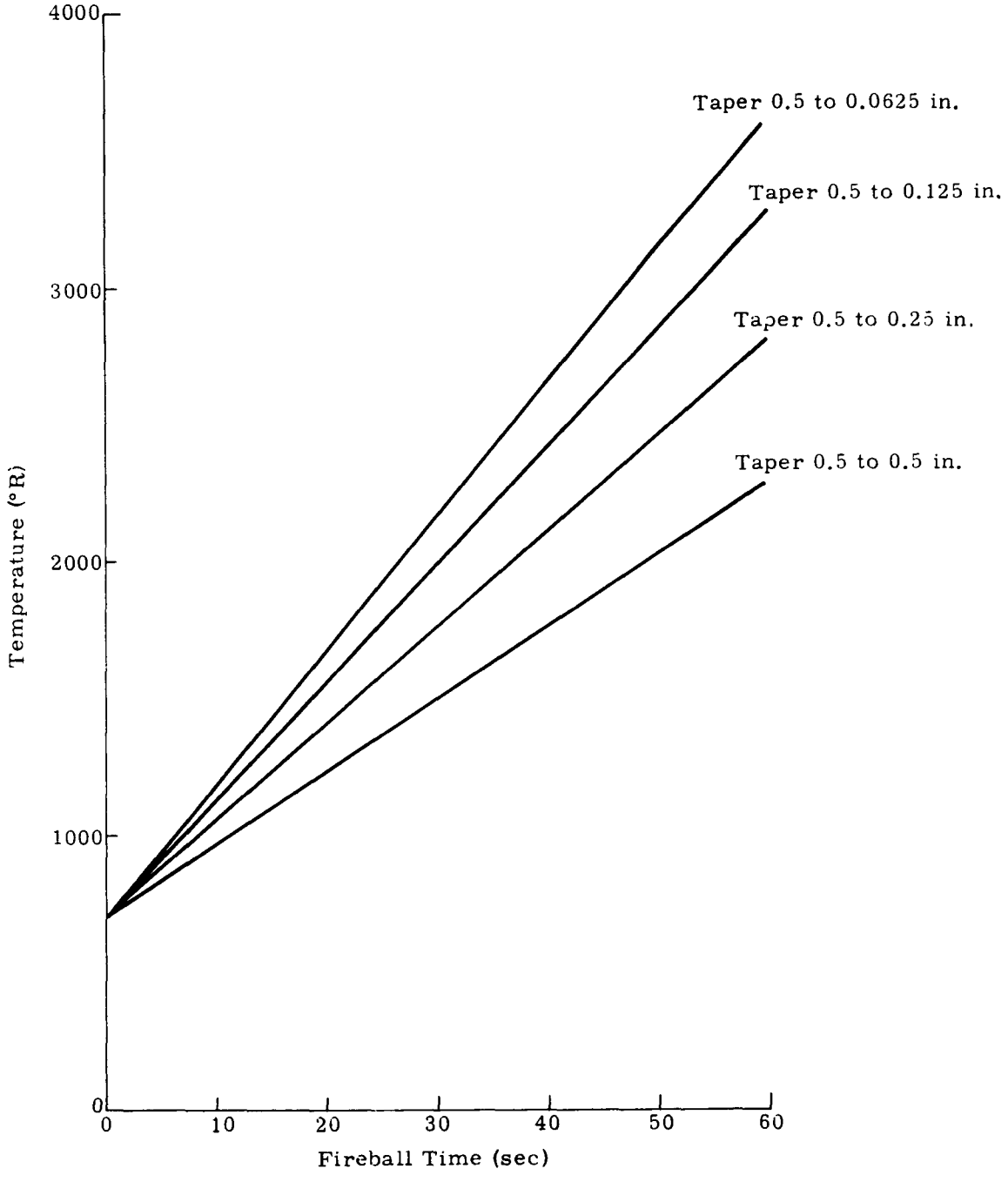

Fig. C-8. Temperature Versus Fireball Time for Node 5 at Radiator

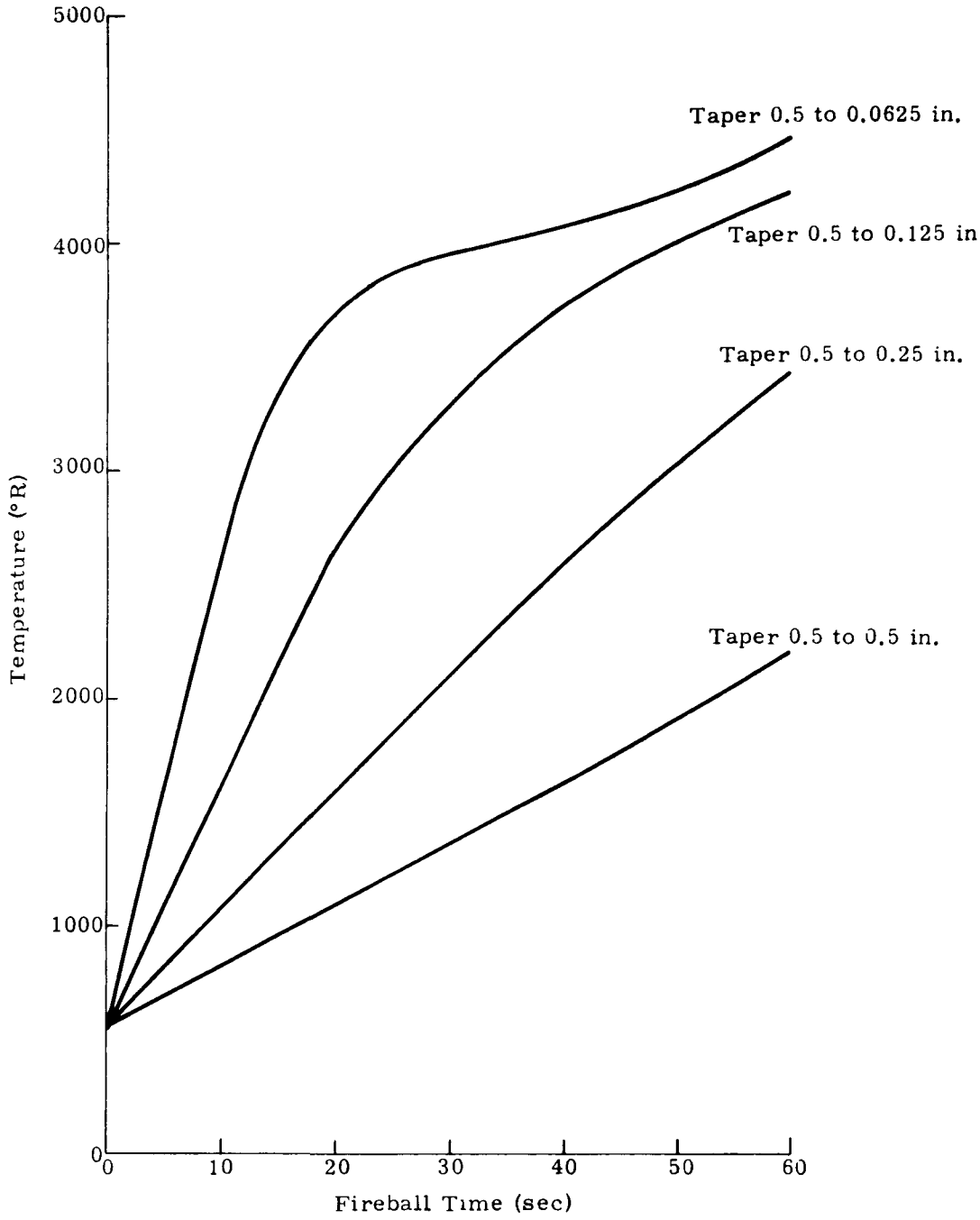

Fig. C-9. Temperature Versus Fireball Time for Node 6 at Radiator Tip

E. DESCENT ANALYSIS

Descent of the generator system is one of the more severe thermal environments because of the high heating loads applied for relatively long periods of time. To determine the thermal effects on the system, a transient thermal analysis was performed using the 15-node thermal model previously presented. The entire reentry phase from deorbit to impact was examined for flight path angles of -8, -2 and -0.1 degrees.

Heating rates associated with these angles are present in Figs. C-12, C-13 and C-14 from the 400,000-foot level. On each curve, the stagnation heat rate is applied to Node 4 on the thermal model. K_q (aft) is a correction factor to the stagnation heating rate to be used for Nodes 5 and 6 while K_q (forward) applied to Nodes 2, 3, and 4.

As the most severe case, open circuit beginning-of-life initial temperatures were used as the input to the analysis.

The results are presented for Nodes 2, 3, 4, 5, 6, 8 and 9 in Figs. C-15 to C-21. ($\gamma = -8°$), Figs. C-22 to C-28 ($\gamma = -0.1°$) and Figs. C-29 to C-35 ($\gamma = -2°$). Tables C-4, C-5 and C-6 are summaries of the maximum temperatures reached for the three flight path angles, whereas the other figures are complete temperature-time plots.

The major conclusions reached are:

(1) Capsule temperature rose 12°, 30° and 70° F for flight path angles of -8, -2 and -0.1 degrees, respectively, essentially independent of the radiator profile taper considered. In the worst case, the capsule temperature on the back walls reached 2050° F. In all cases, the maximum capsule temperature was reached at time of impact.

(2) For the selected design (taper to 0.125 inch), the extremities of the beryllium conical shell radiator reached a maximum of 1424° F at 1700 seconds into the 2100-second reentry for the -0.1 degree case.

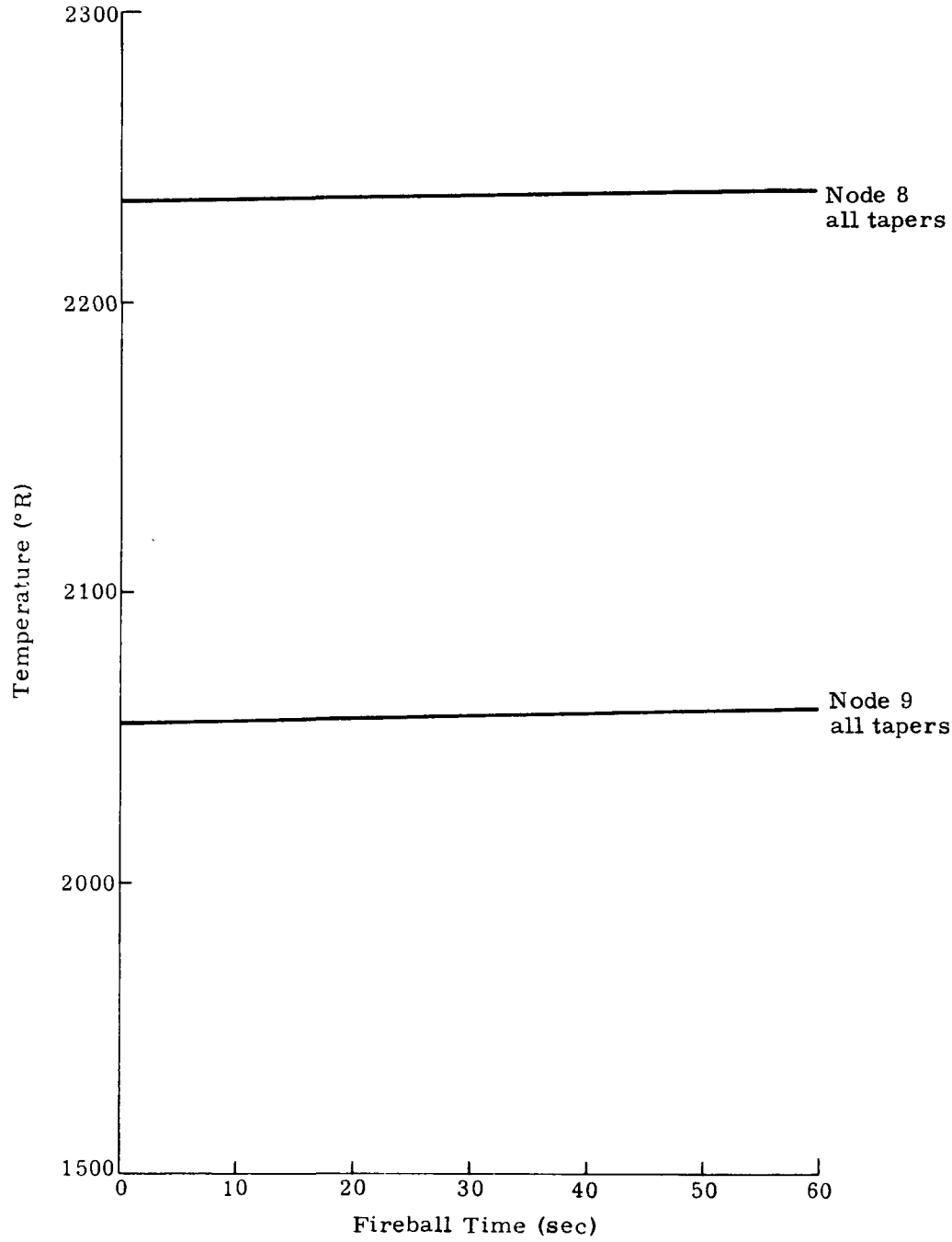

Fig. C-10. Temperature Versus Fireball Time for Nodes 8 and 9 at Fuel and Capsule - Capsule within RTG.

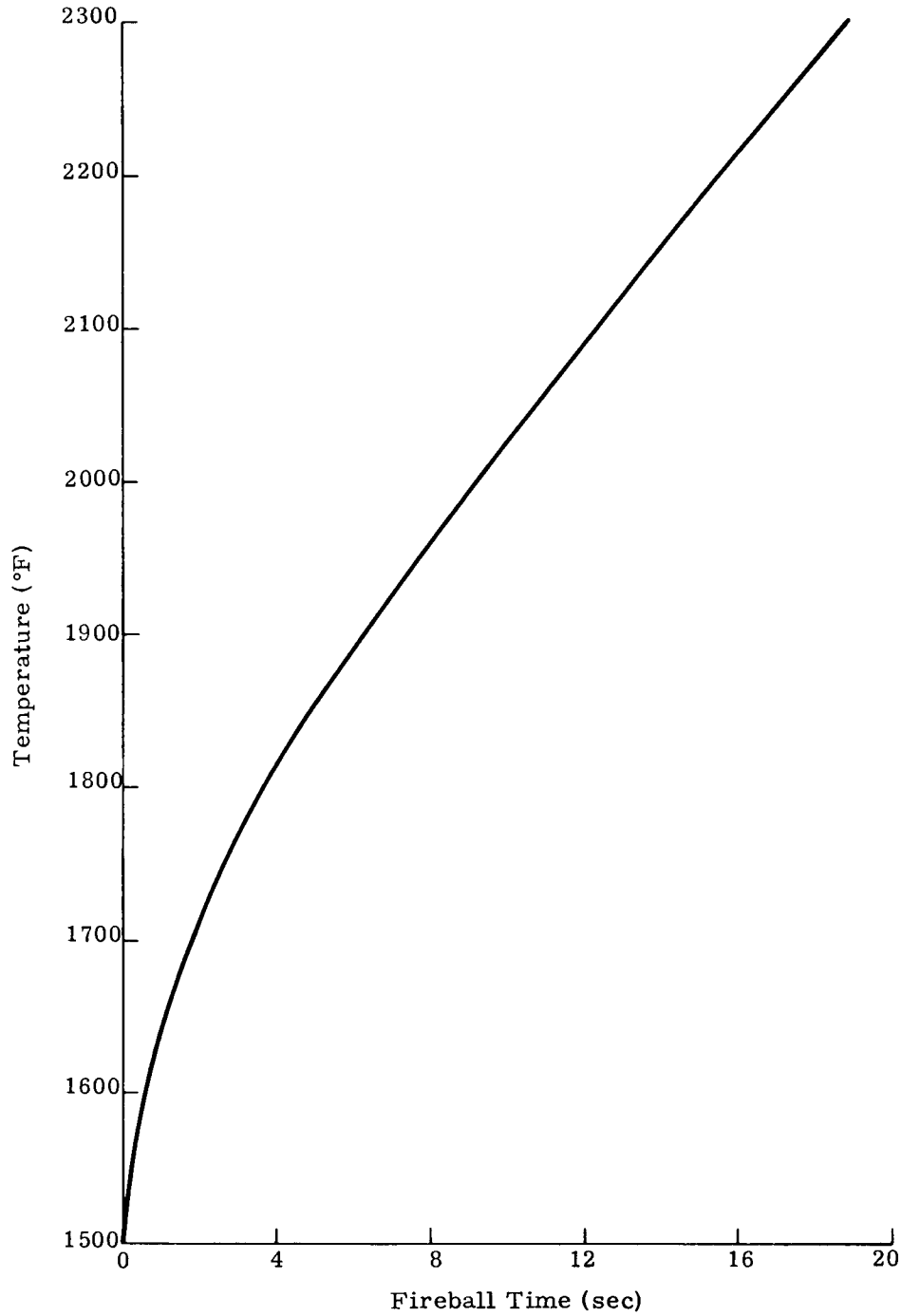

Fig. C-11. Capsule Surface Temperature Versus Exposure Time to Fireball - Bare Capsule

TABLE C-4

Maximum Temperature of Nodes for Various Tapers at Flight Path Angle, γ_E = 8.0 at 400,000 Feet, τ_{max} = 420 Seconds

Nodes	No Taper 0.5 to 0.5 in.	Taper 0.5 to 0.25 in.	Taper 0.5 to 0.125 in.	Taper 0.5 to 0.0625 in.
1 Ablator	3113° R / 2653° F	3113° R / 2653° F	3113° R / 2653° F	3113° R / 2653° F
2 Radiator	961° R / 501° F	1095° R / 635° F	1345° R / 885° F	1746° F / 1286° F
3 Radiator	998° R / 538° F	1061° R / 601° F	1117° R / 657° F	1158° R / 698° F
4 Radiator	1130° R / 670° F	1138° R / 678° F	1149° R / 689° F	1160° R / 700° F
5 Radiator	1085° R / 625° F	1176° R / 716° F	1253° R / 793° F	1310° R / 850° F
6 Radiator	1046° R / 586° F	1253° R / 793° F	1592° R / 1132° F	2054° R / 1594° F
7 Back section	709° R / 249° F	730° R / 270° F	753° R / 293° F	767° R / 307° F
8 Fuel	2558° R / 2098° F	2563° R / 2103° F	2571° R / 2111° F	2579° R / 2119° F
9 Capsule	2370° R / 1910° F	2376° R / 1916° F	2384° R / 1924° F	2392° R / 1932° F
10 Hot shoe	2316° R / 1856° F	2323° R / 1863° F	2332° R / 1872° F	2341° R / 1881° F
11 Insulation	1648° R / 1188° F	1655° R / 1195° F	1663° R / 1203° F	1672° R / 1212° F
12 T/E element	1710° R / 1250° F	1719° R / 1259° F	1731° R / 1271° F	1741° R / 1281° F
13 T/E element	1166° R / 706° F	1174° R / 714° F	1186° R / 726° F	1197° R / 737° F
14 Insulation	850° R / 390° F	875° R / 415° F	901° R / 441° F	918° R / 458° F
15 Space	0° R / -460° F	0° R / -460° F	0° R / -460° F	0° R / -460° F

TABLE C-5

Maximum Temperature of Nodes for Various Tapers at Flight Path Angle, γ_E = -0.1 at 400,000 Feet, τ_{max} = 2100 Seconds

Nodes	No Taper 0.5 to 0.5 in.	Taper 0.5 to 0.25 in.	Taper 0.5 to 0.125 in.	Taper 0.5 to 0.0625 in.
1 Ablator	3181° R / 2721° F	3181° R / 2721° F	3181° R / 2721° F	3181° R / 2721° F
2 Radiator	1389° R / 929° F	1669° R / 1209° F	1884° R / 1424° F	1981° R / 1521° F
3 Radiator	1414° R / 954° F	1559° R / 1099° F	1640° R / 1180° F	1675° R / 1215° F
4 Radiator	1497° R / 1037° F	1528° R / 1068° F	1550° R / 1090° F	1563° R / 1103° F
5 Radiator	1508° R / 1048° F	1642° R / 1182° F	1720° R / 1260° F	1756° R / 1296° F
6 Radiator	1481° R / 1021° F	1722° R / 1262° F	1859° R / 1399° F	1926° R / 1466° F
7 Back section	927° R / 467° F	1009° R / 549° F	1048° R / 588° F	1068° R / 608° F
8 Fuel	2593° R / 2133° F	2601° R / 2141° F	2610° R / 2150° F	2618° R / 2158° F
9 Capsule	2424° R / 1964° F	2433° R / 1973° F	2443° R / 1983° F	2451° R / 1991° F
10 Hot shoe	2381° R / 1921° F	2392° R / 1932° F	2402° R / 1942° F	2410° R / 1950° F
11 Insulation	1714° R / 1254° F	1725° R / 1265° F	1735° R / 1275° F	1744° R / 1284° F
12 T/E element	1917° R / 1457° F	1938° R / 1478° F	1953° R / 1493° F	1964° R / 1504° F
13 T/E element	1522° R / 1062° F	1553° R / 1093° F	1574° R / 1114° F	1587° R / 1127° F
14 Insulation	1106° R / 646° F	1192° R / 732° F	1236° R / 776° F	1258° R / 798° F
15 Space	0° R / -460° F	0° R / -460° F	0° R / -460° F	0° R / -460° F

TABLE C-6

Maximum Temperature of Nodes for Various Tapers at Flight Path Angle, γ_E = -2.0 at 400,000 Feet, τ_{max} = 630 Seconds

Nodes	No Taper 0.5 to 0.5 in.	Taper 0.5 to 0.25 in.	Taper 0.5 to 0.125 in.	Taper 0.5 to 0.0625 in.
1 Ablator	3289° R / 2829° F	3289° R / 2829° F	3289° R / 2829° F	3289° R / 2829° F
2 Radiator	1147° R / 687° F	1416° R / 956° F	1786° R / 1326° F	2085° R / 1625° F
3 Radiator	1182° R / 722° F	1302° R / 842° F	1396° R / 936° F	1451° R / 991° F
4 Radiator	1301° R / 841° F	1315° R / 855° F	1331° R / 871° F	1343° R / 883° F
5 Radiator	1272° R / 812° F	1411° R / 951° F	1516° R / 1056° F	1576° R / 1116° F
6 Radiator	1236° R / 776° F	1531° R / 1071° F	1852° R / 1392° F	2012° R / 1552° F
7 Back section	770° R / 310° F	825° R / 365° F	865° R / 405° F	880° R / 420° F
8 Fuel	2566° R / 2106° F	2572° R / 2112° F	2580° R / 2120° F	2588° R / 2128° F
9 Capsule	2387° R / 1927° F	2394° R / 1934° F	2402° R / 1942° F	2411° R / 1951° F
10 Hot shoe	2339° R / 1879° F	2347° R / 1887° F	2356° R / 1896° F	2365° R / 1905° F
11 Insulation	1667° R / 1207° F	1675° R / 1215° F	1684° R / 1224° F	1692° R / 1232° F
12 T/E element	1800° R / 1340° F	1812° R / 1352° F	1825° R / 1365° F	1836° R / 1376° F
13 T/E element	1331° R / 871° F	1347° R / 887° F	1362° R / 902° F	1374° R / 914° F
14 Insulation	923° R / 463° F	984° R / 524° F	1027° R / 567° F	1046° R / 586° F
15 Space	0° R / -460° F	0° R / -460° F	0° R / -460° F	0° R / -460° F

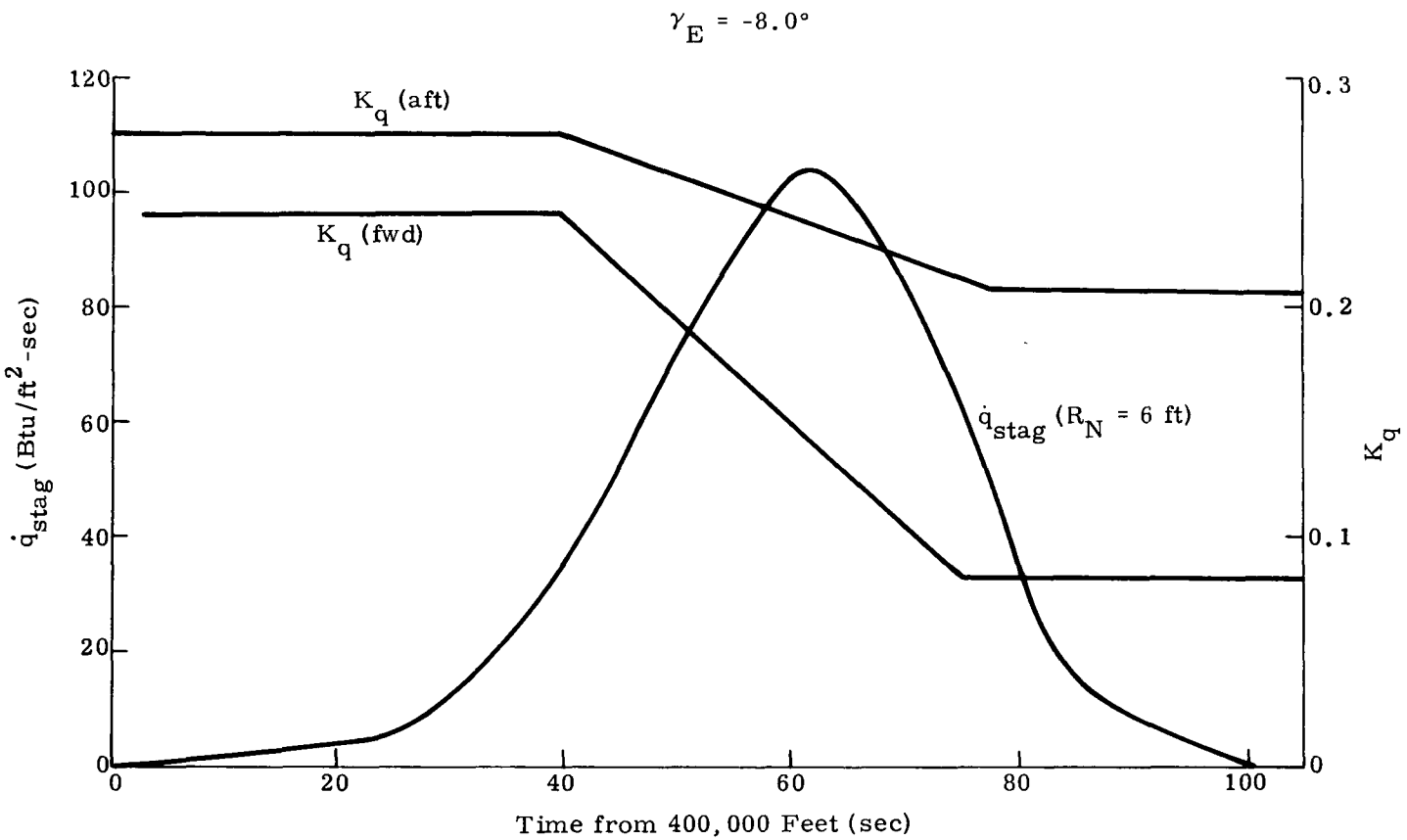

Fig. C-12. Heating Rates for Ablator and Radiator--$\dot{q}_{rad} = K_q\ (\dot{q}_{stag})$

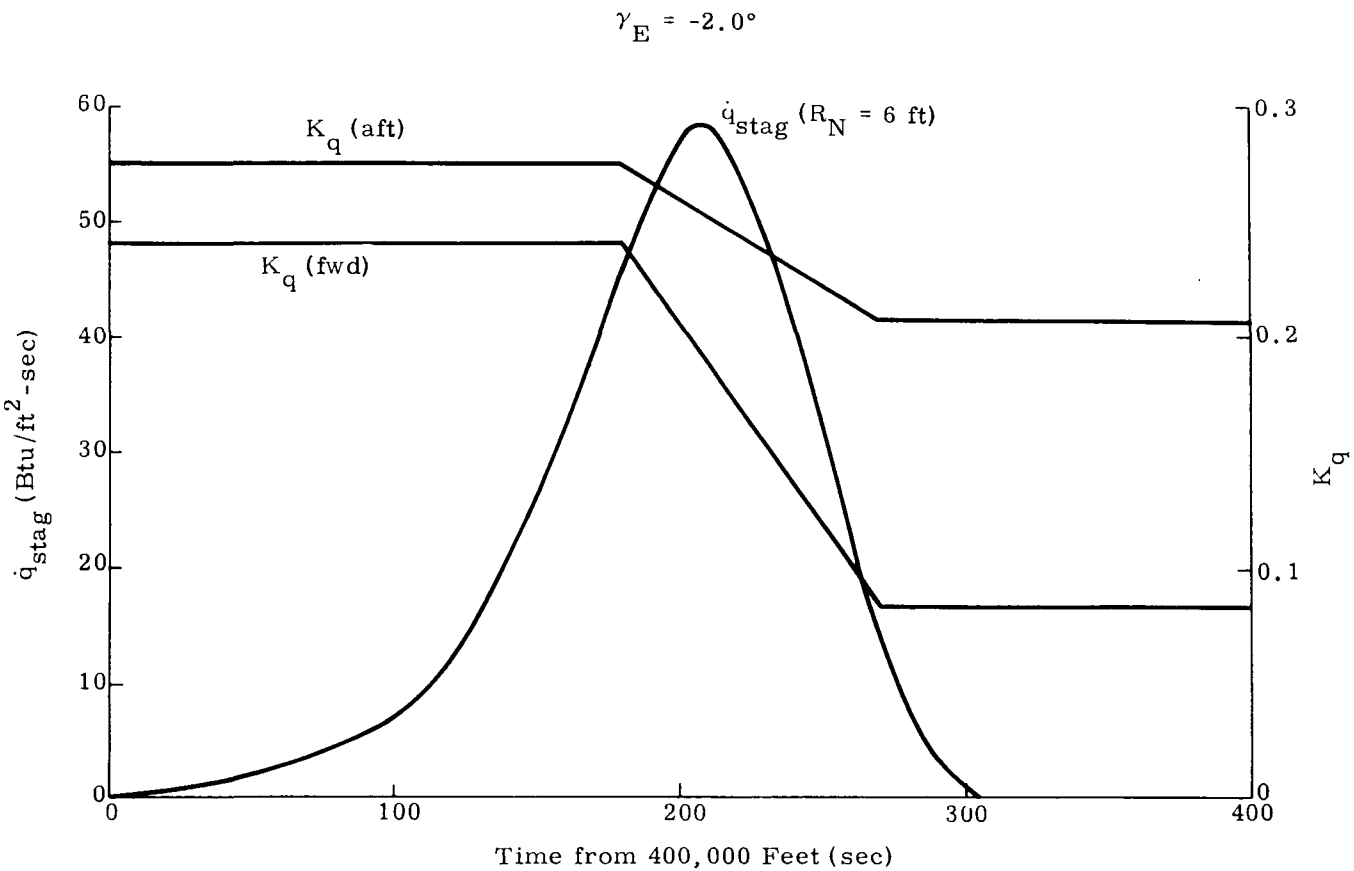

Fig. C-13. Heating Rates for Ablator and Radiator--$\dot{q}_{rad} = K_q\ (\dot{q}_{stag})$

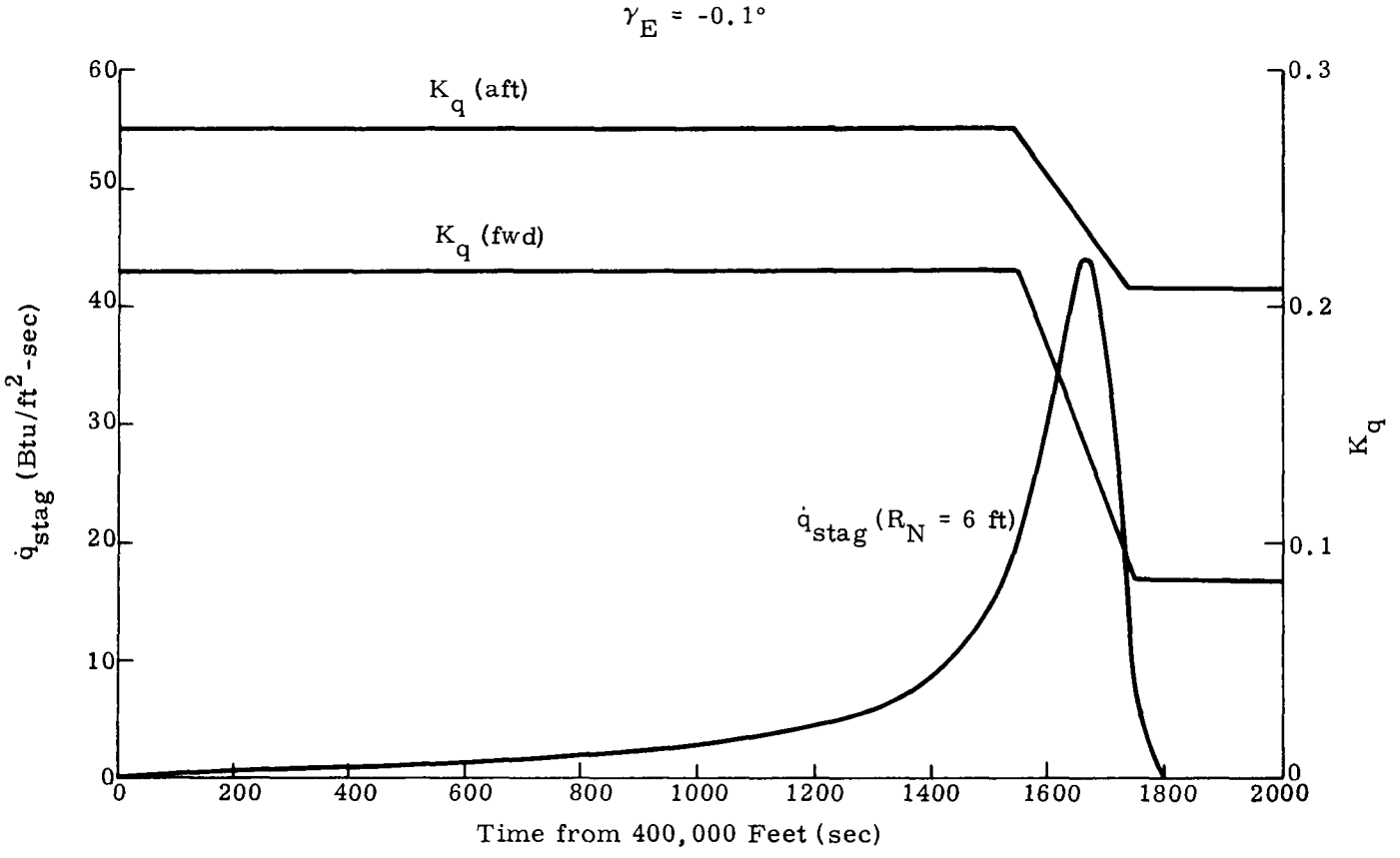

Fig. C-14. Heating Rates for Ablator and Radiator--$\dot{q}_{rad} = K_q\ (\dot{q}_{stag})$

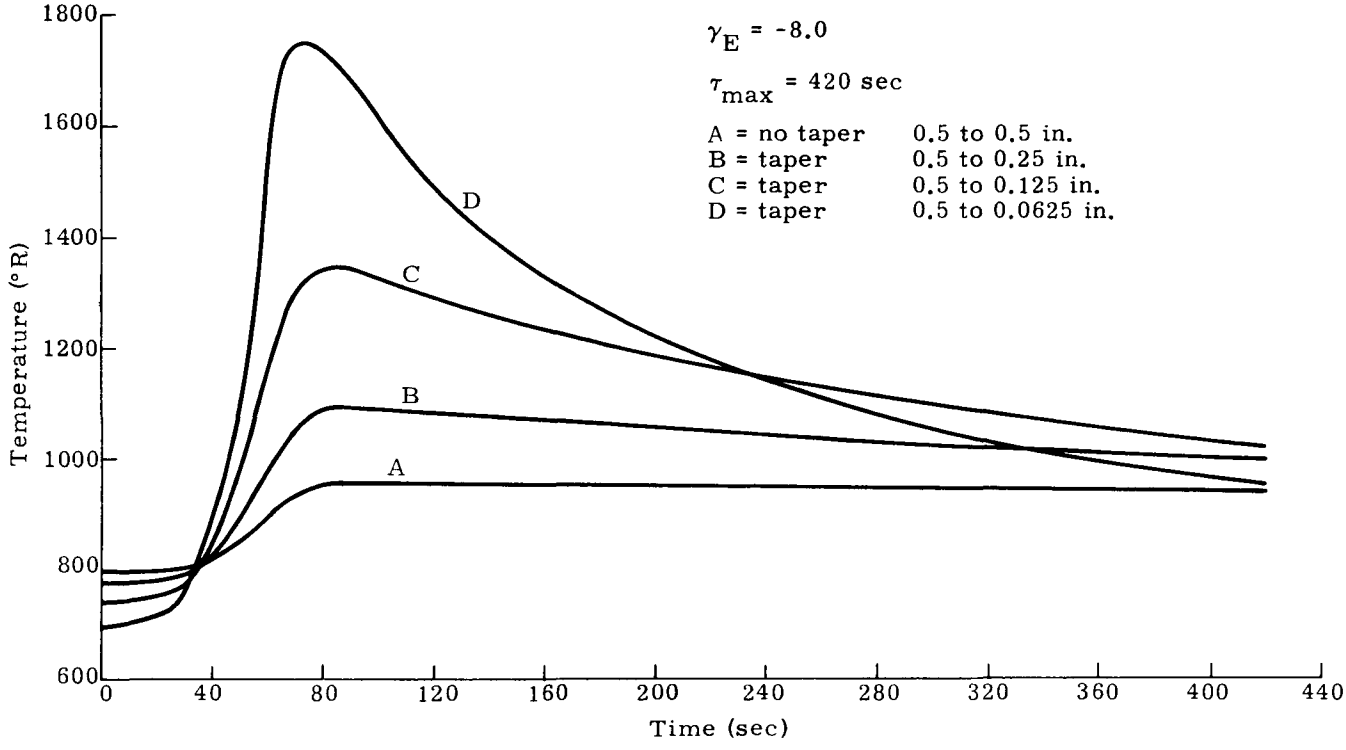

Fig. C-15. Temperature Versus Time for Node 2 at Radiator Tip

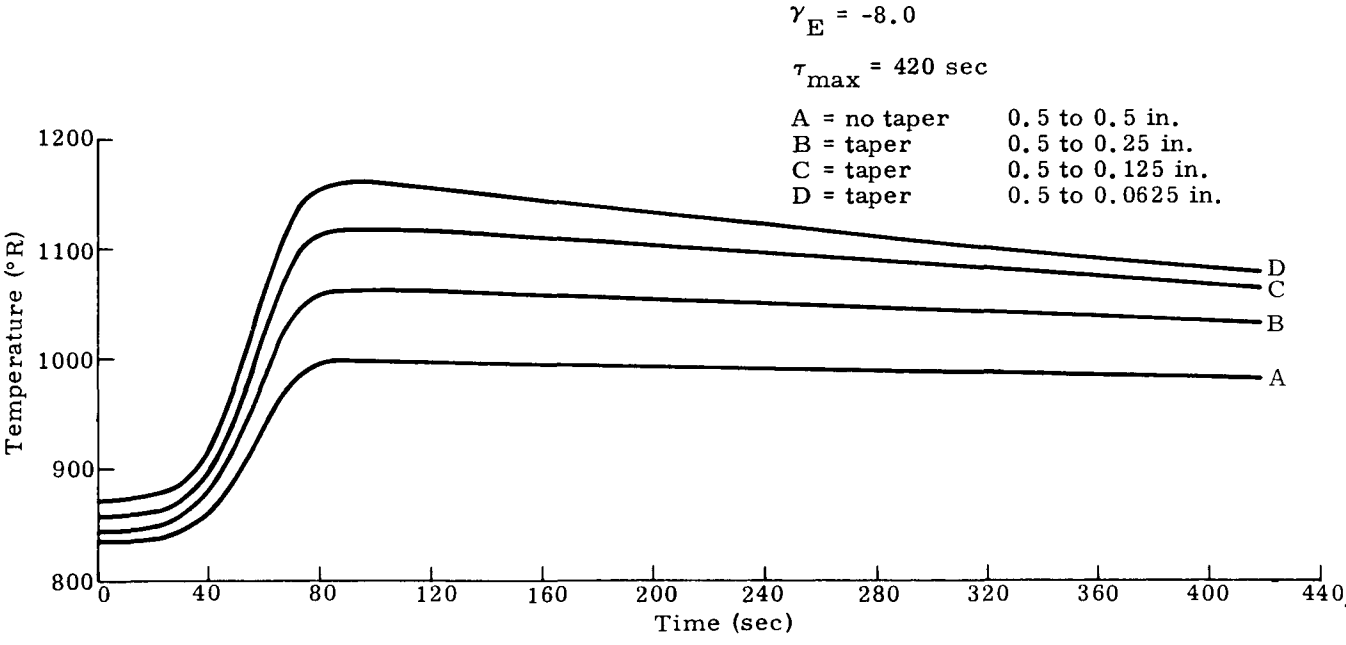

Fig. C-16. Temperature Versus Time for Node 3 at Radiator

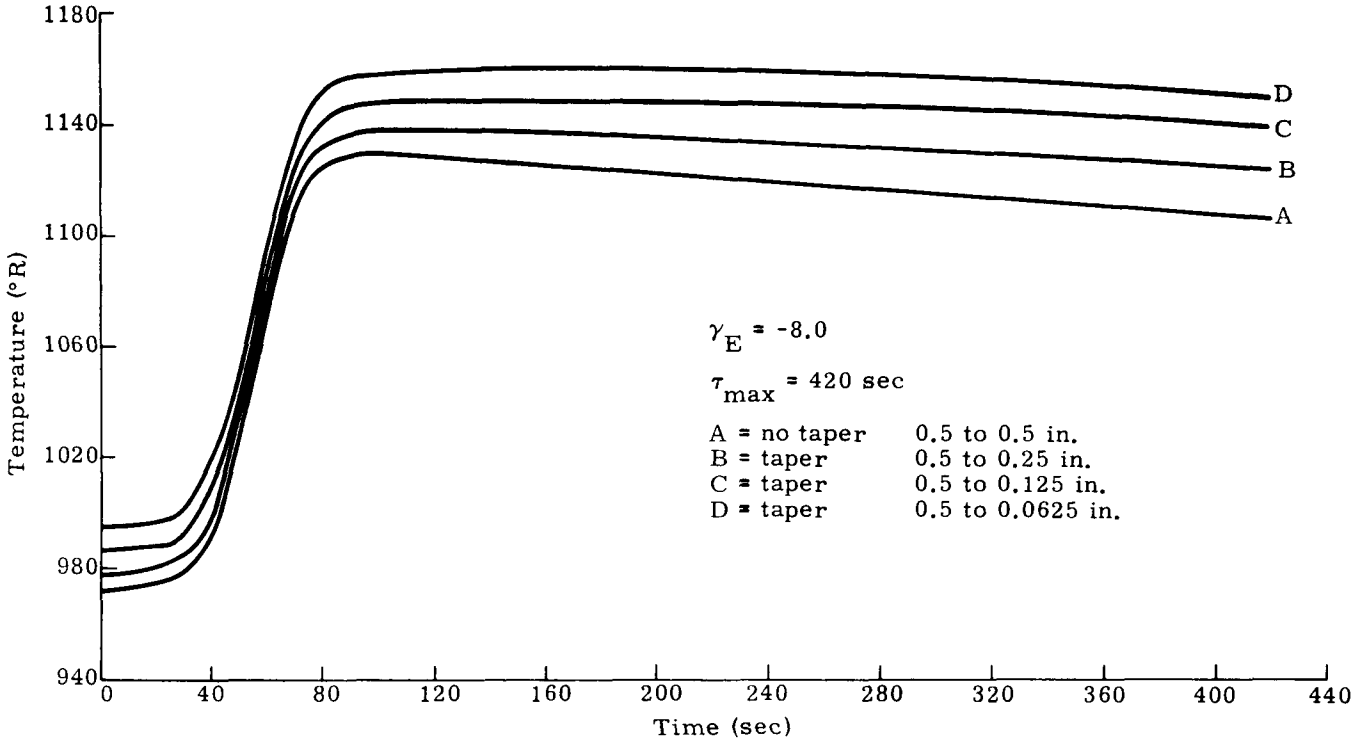

Fig. C-17. Temperature Versus Time for Node 4 at Radiator Root

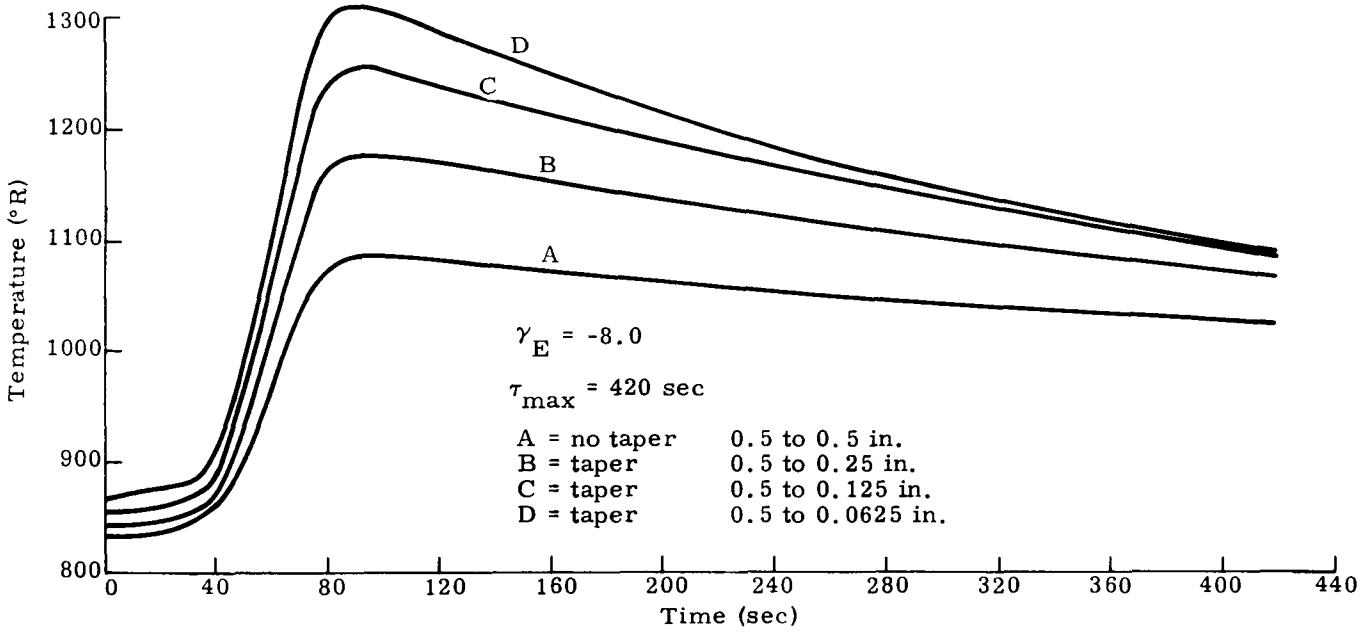

Fig. C-18. Temperature Versus Time for Node 5 at Radiator

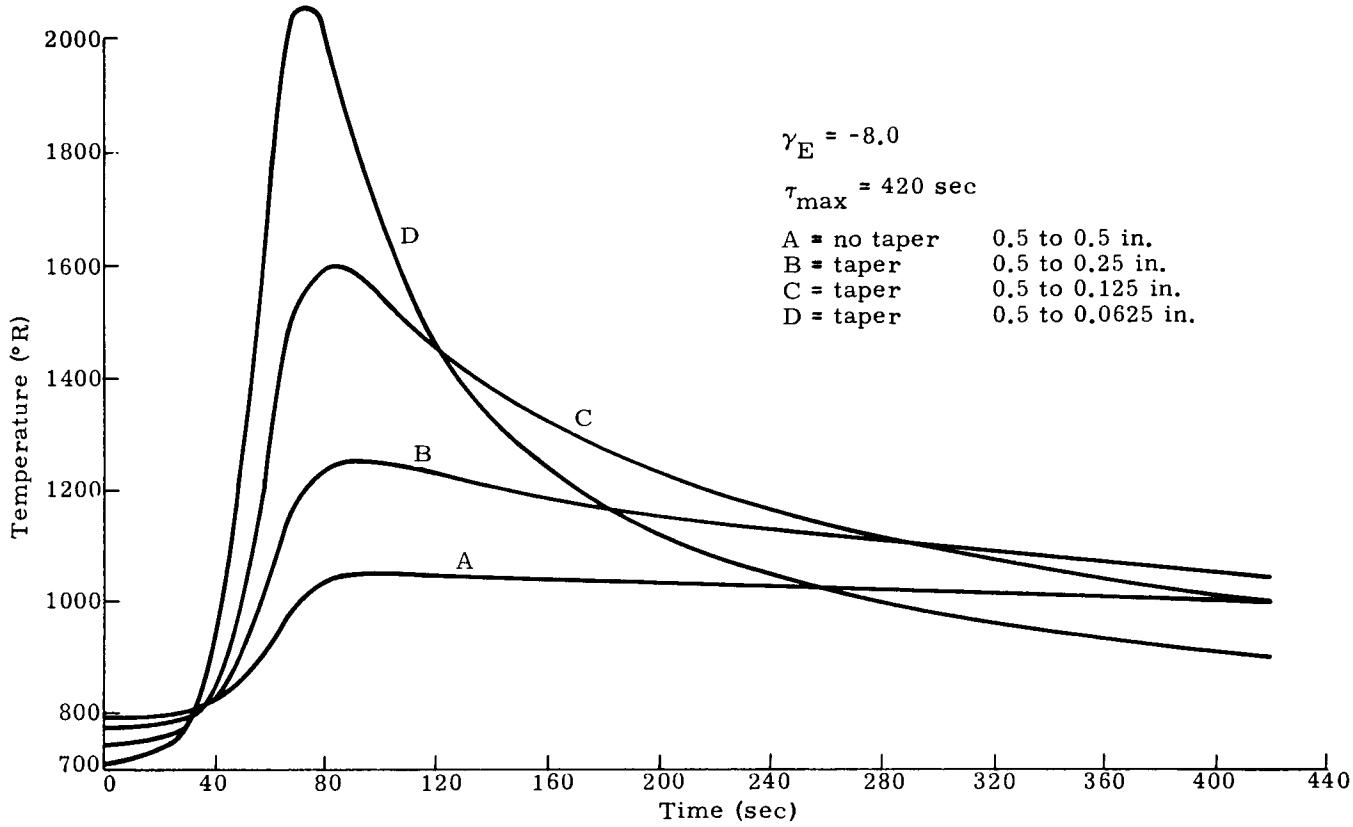

Fig. C-19. Temperature Versus Time for Node 6 at Radiator Tip

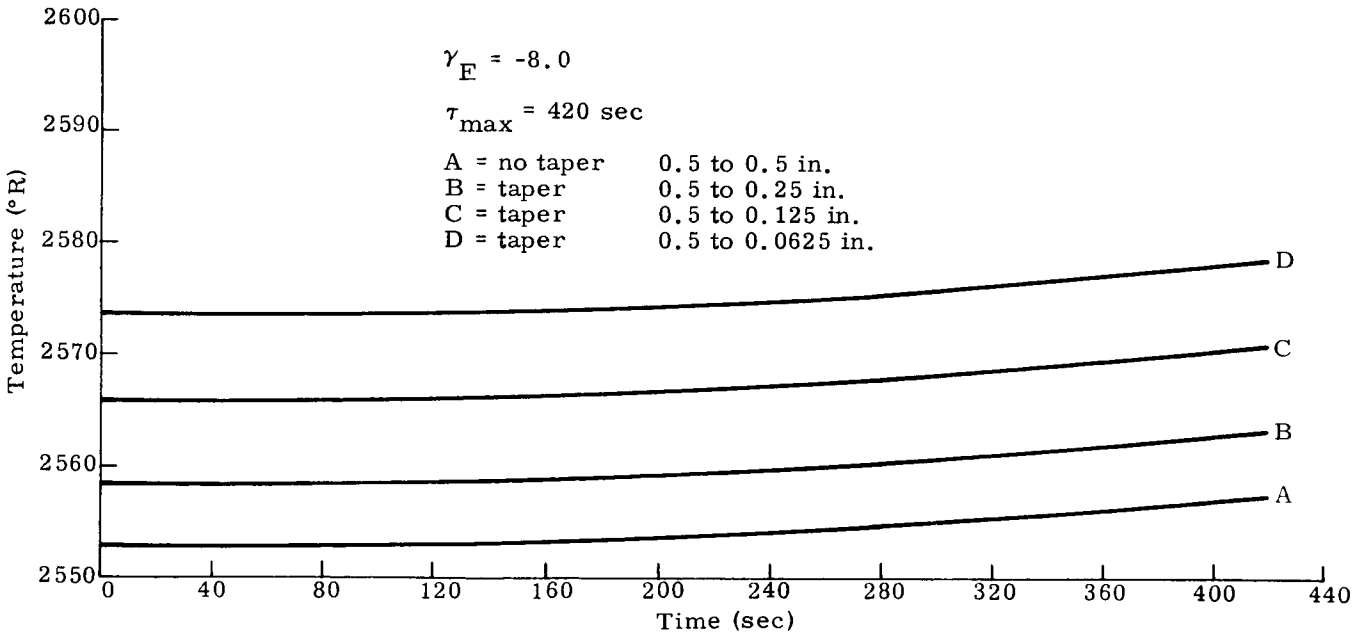

Fig. C-20. Temperature Versus Time for Node 8 at Fuel

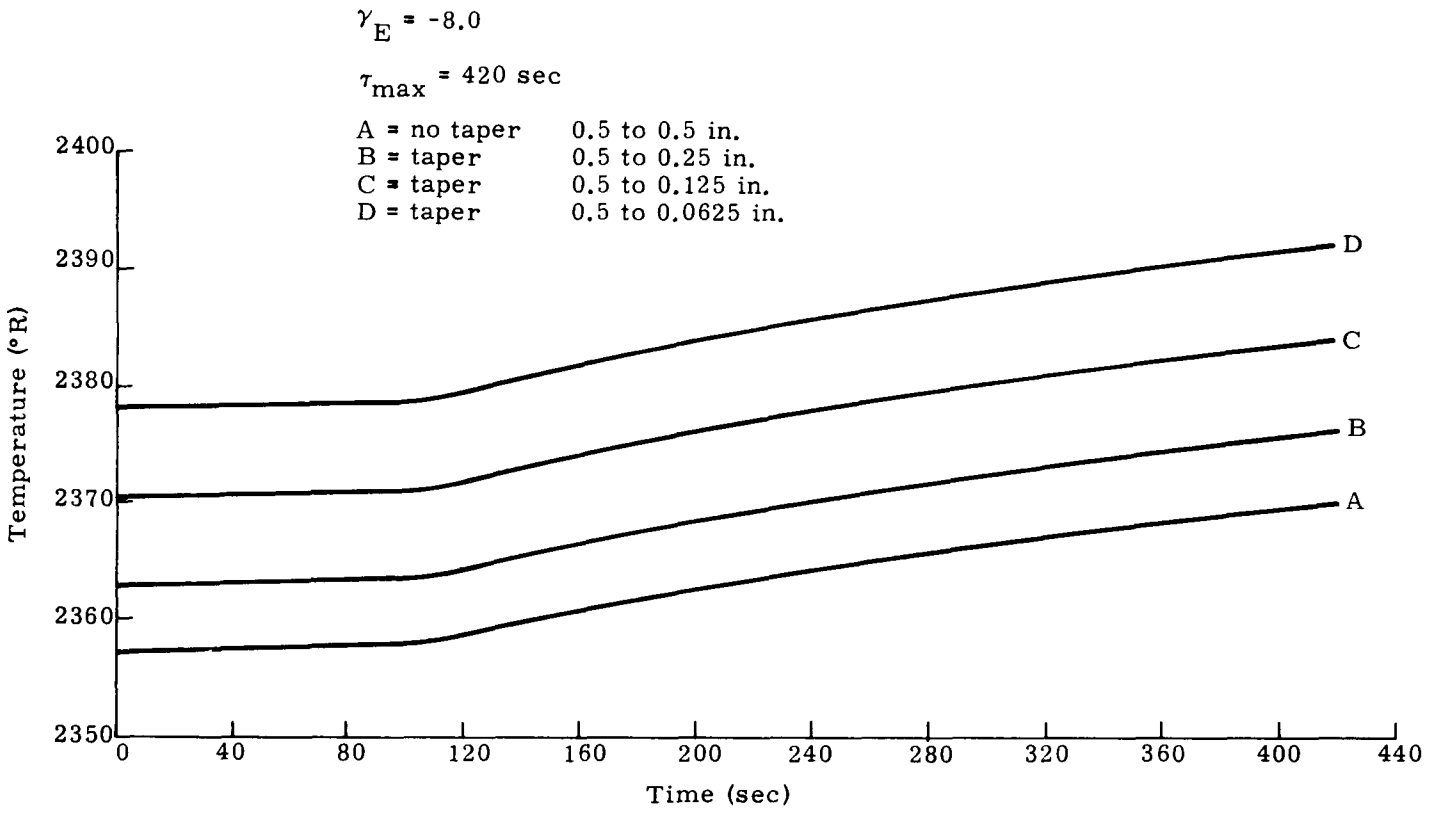

Fig. C-21. Temperature Versus Time for Node 9 at Capsule

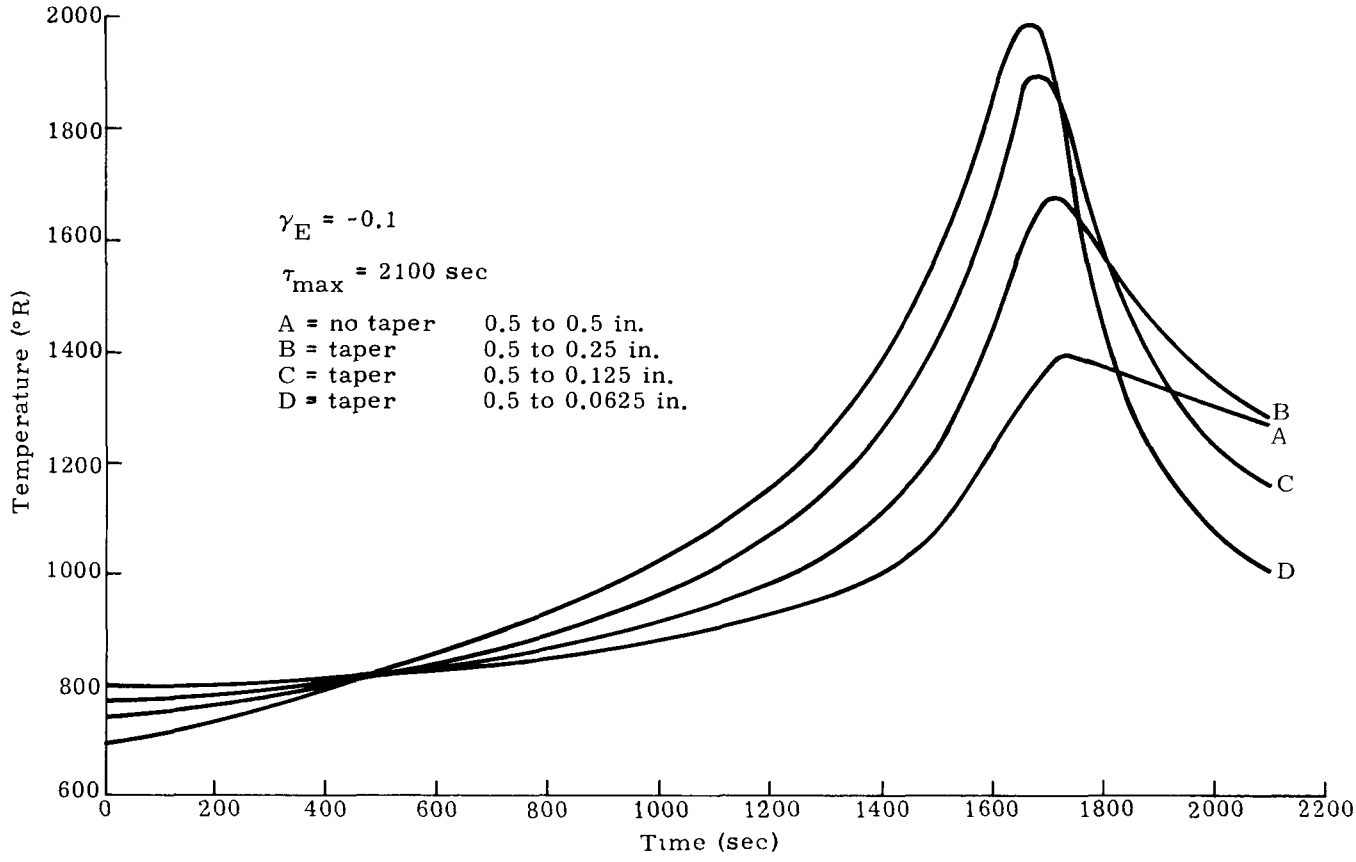

Fig. C-22. Temperature Versus Time for Node 2 at Radiator Tip

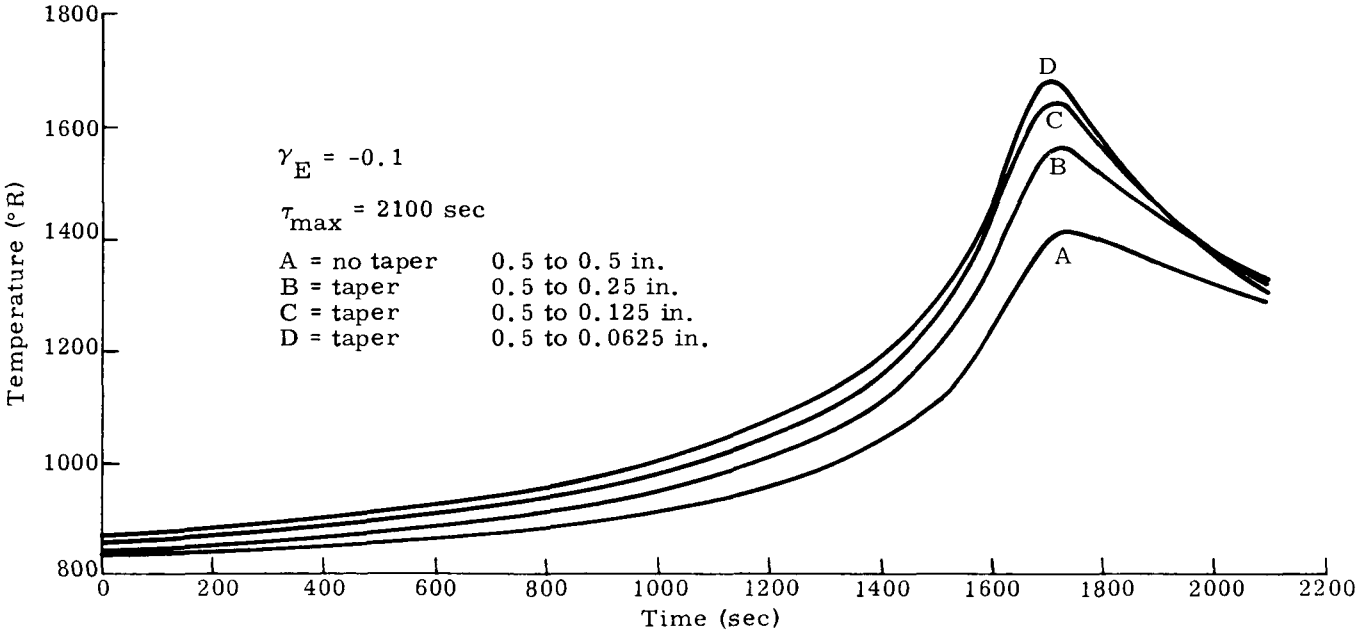

Fig. C-23. Temperature Versus Time for Node 3 at Radiator

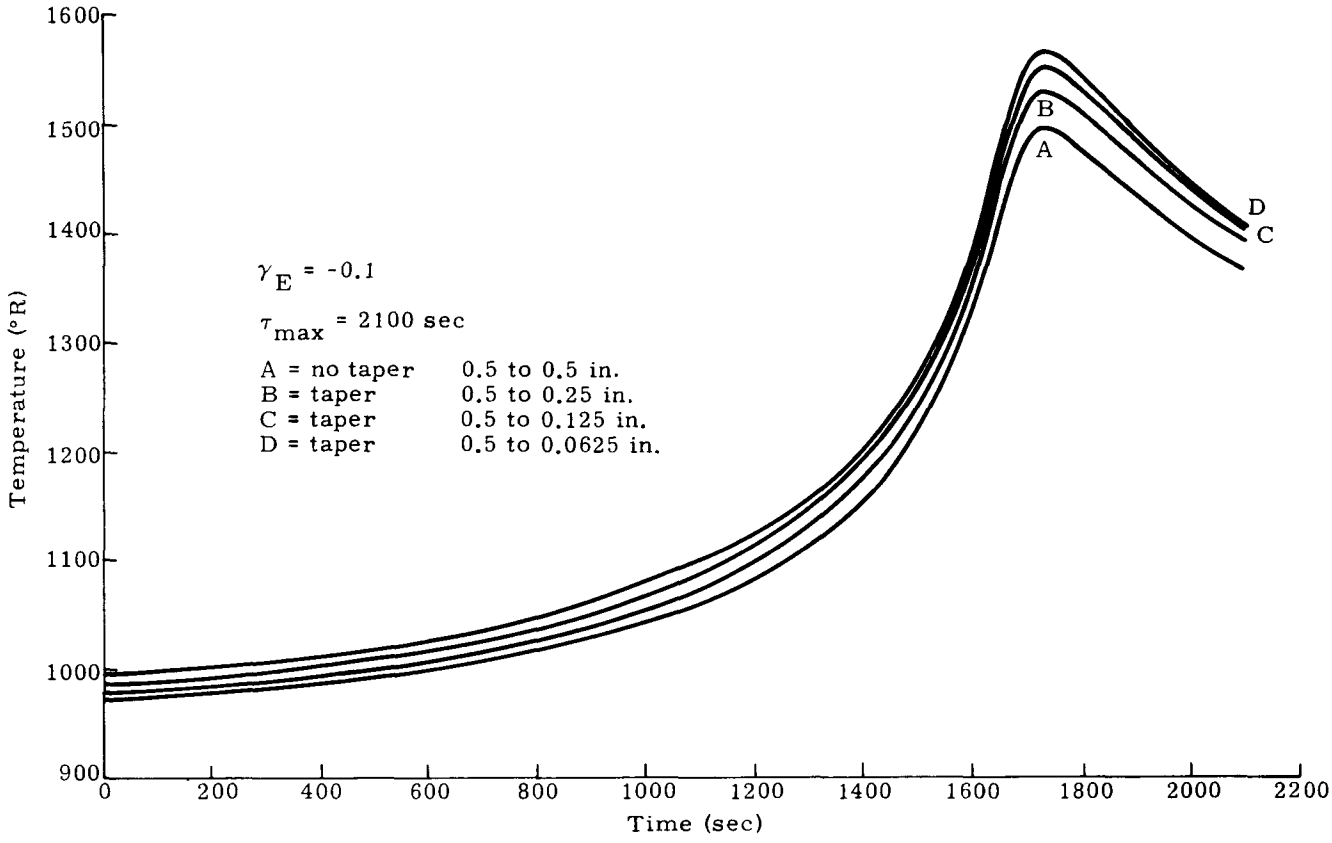

Fig. C-24. Temperature Versus Time for Node 4 at Radiator Root

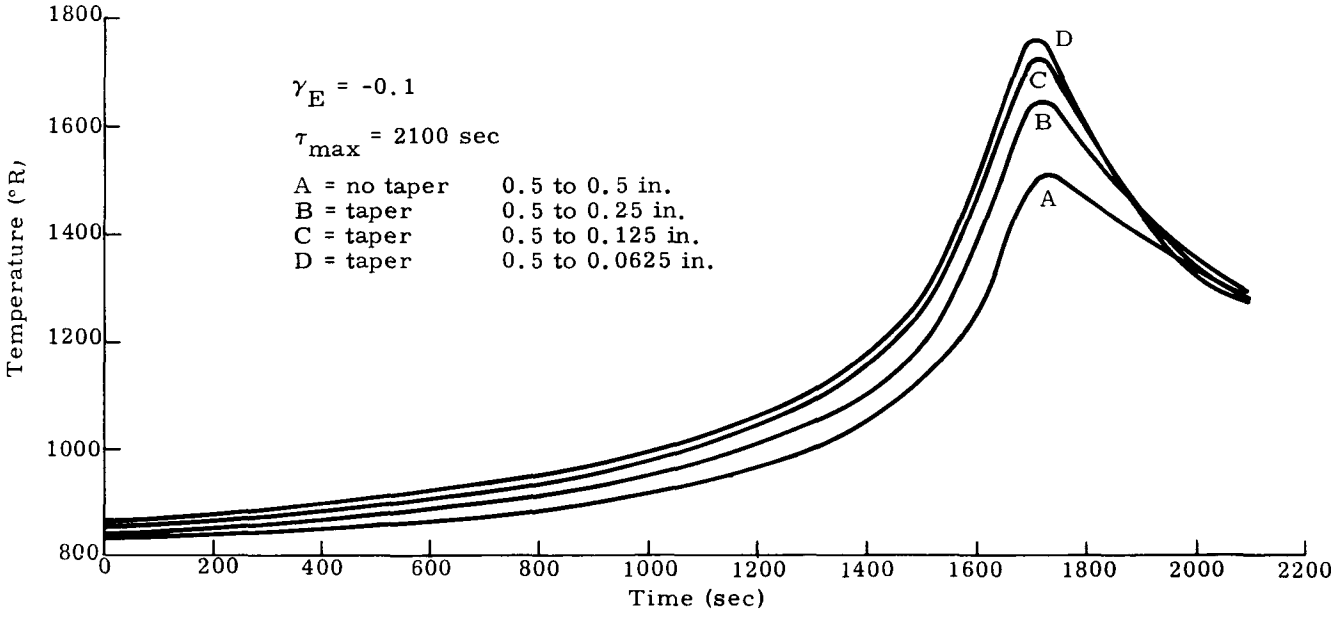

Fig. C-25. Temperature Versus Time for Node 5 at Radiator

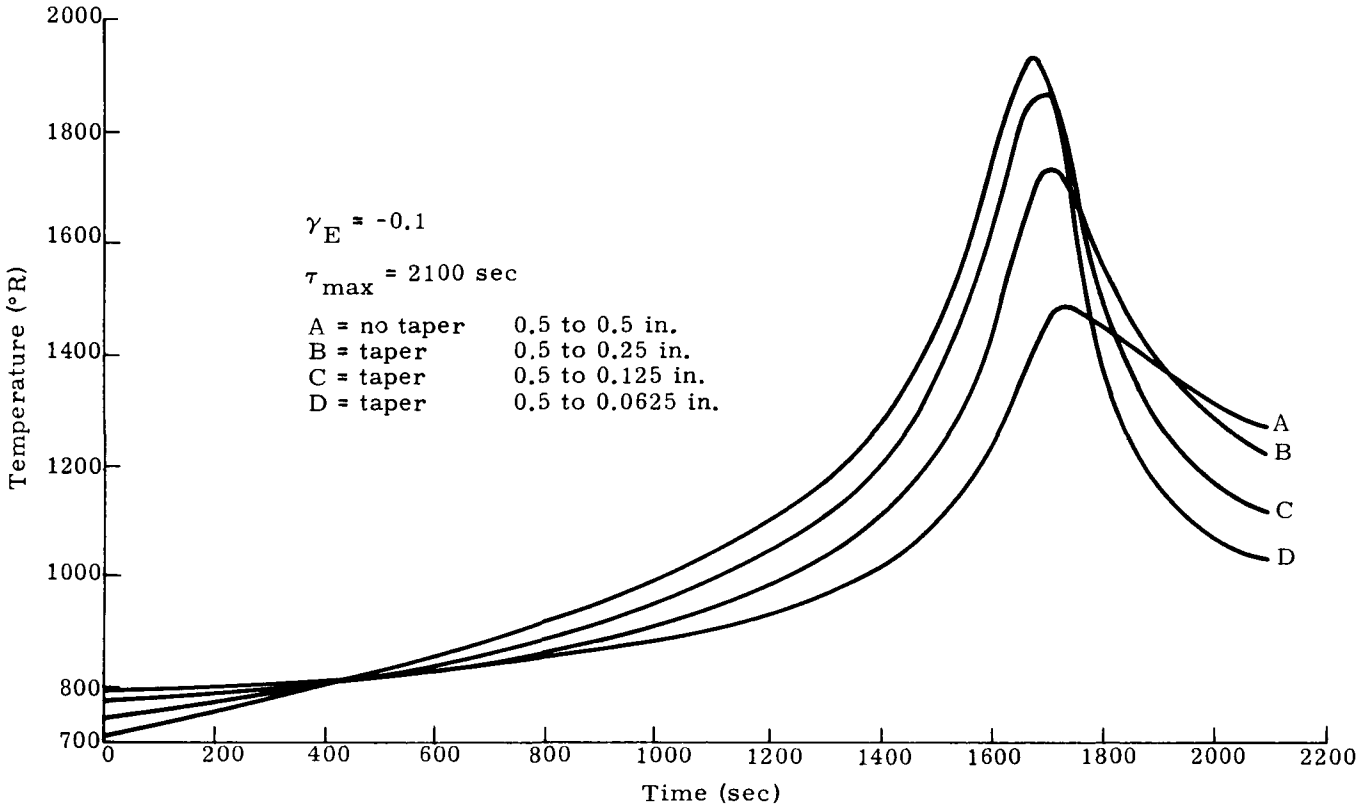

Fig. C-26. Temperature Versus Time for Node 6 at Radiator Tip

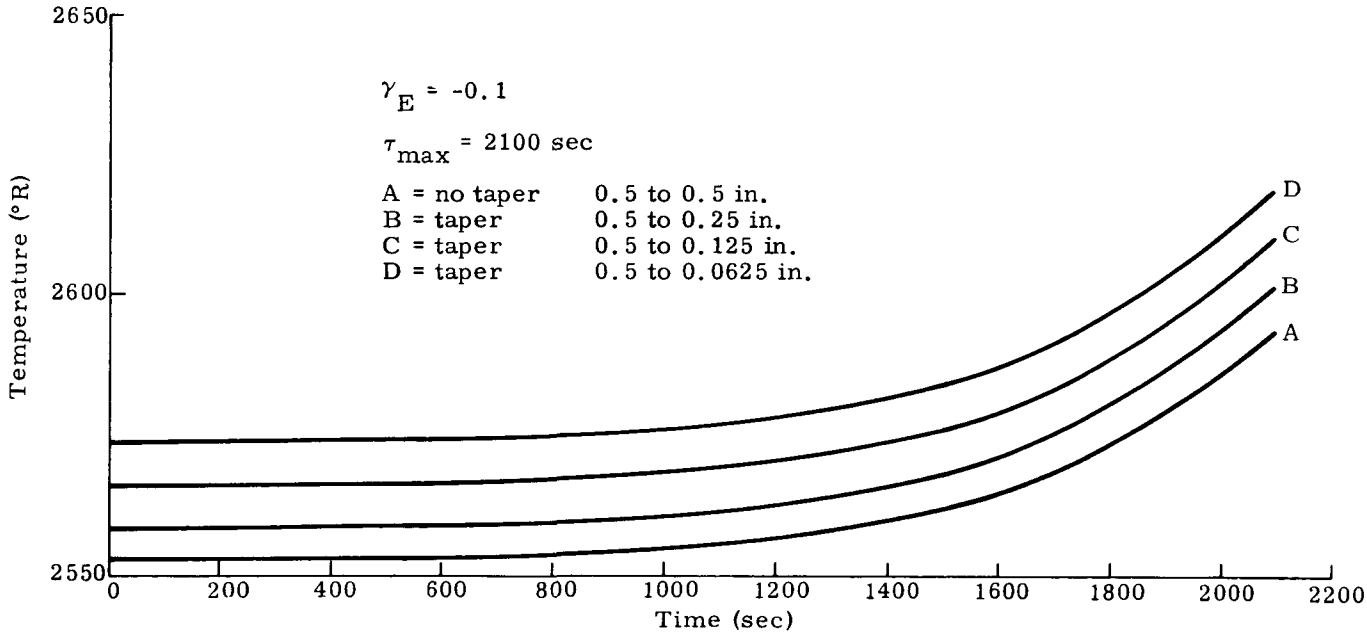

Fig. C-27. Temperature Versus Time for Node 8 at Fuel

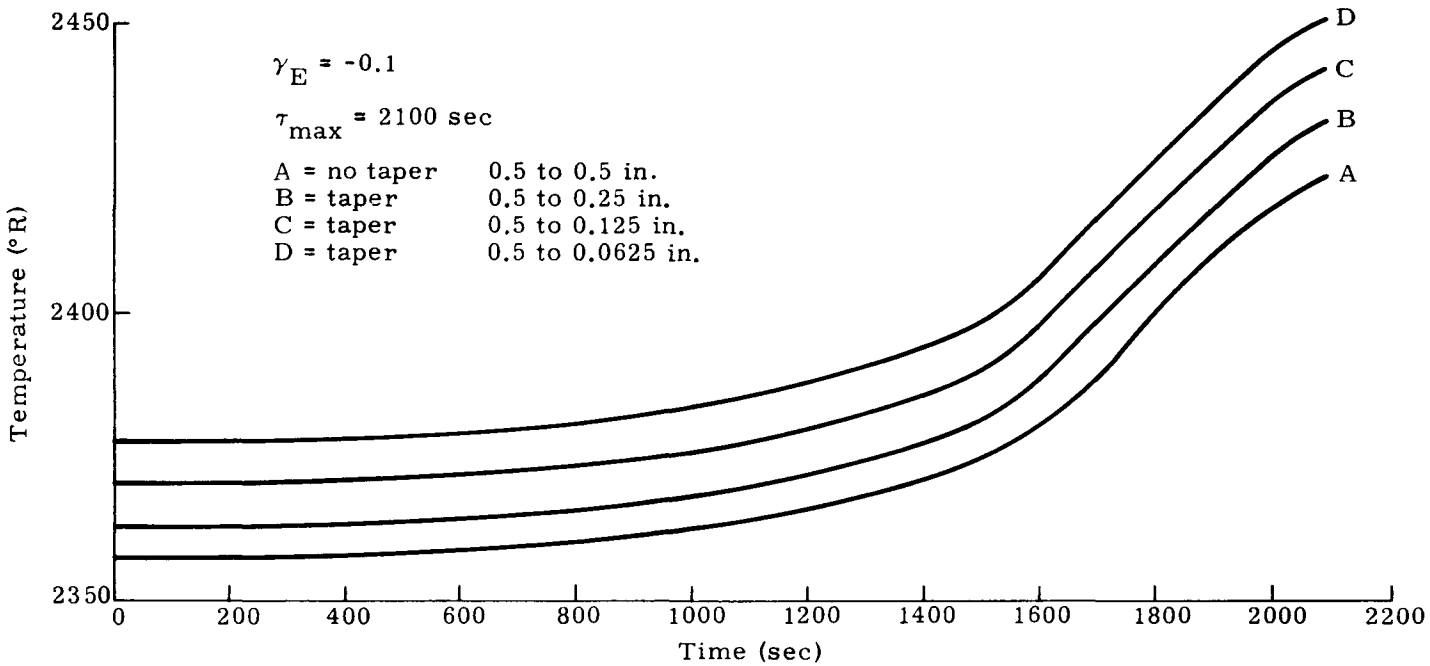

Fig. C-28. Temperature Versus Time for Node 9 at Capsule

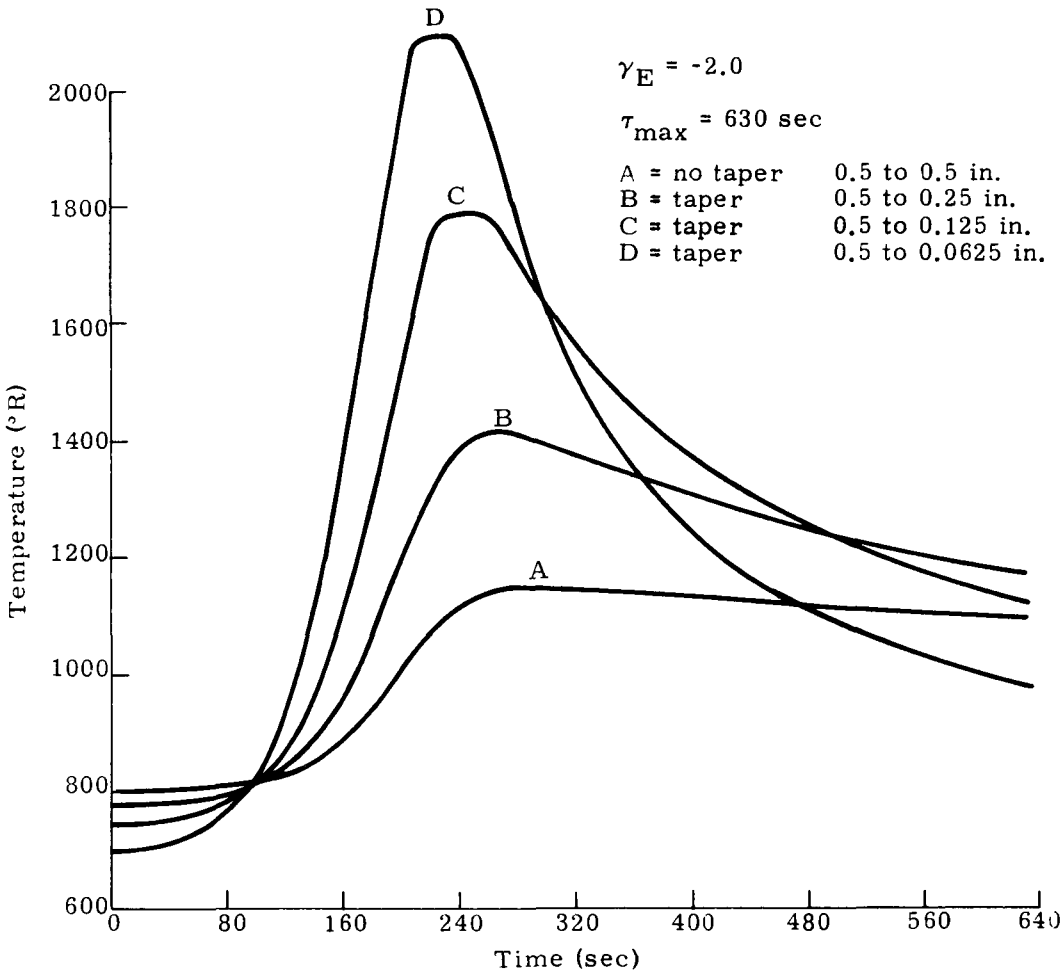

Fig. C-29. Temperature Versus Time for Node 2 at Radiator Tip

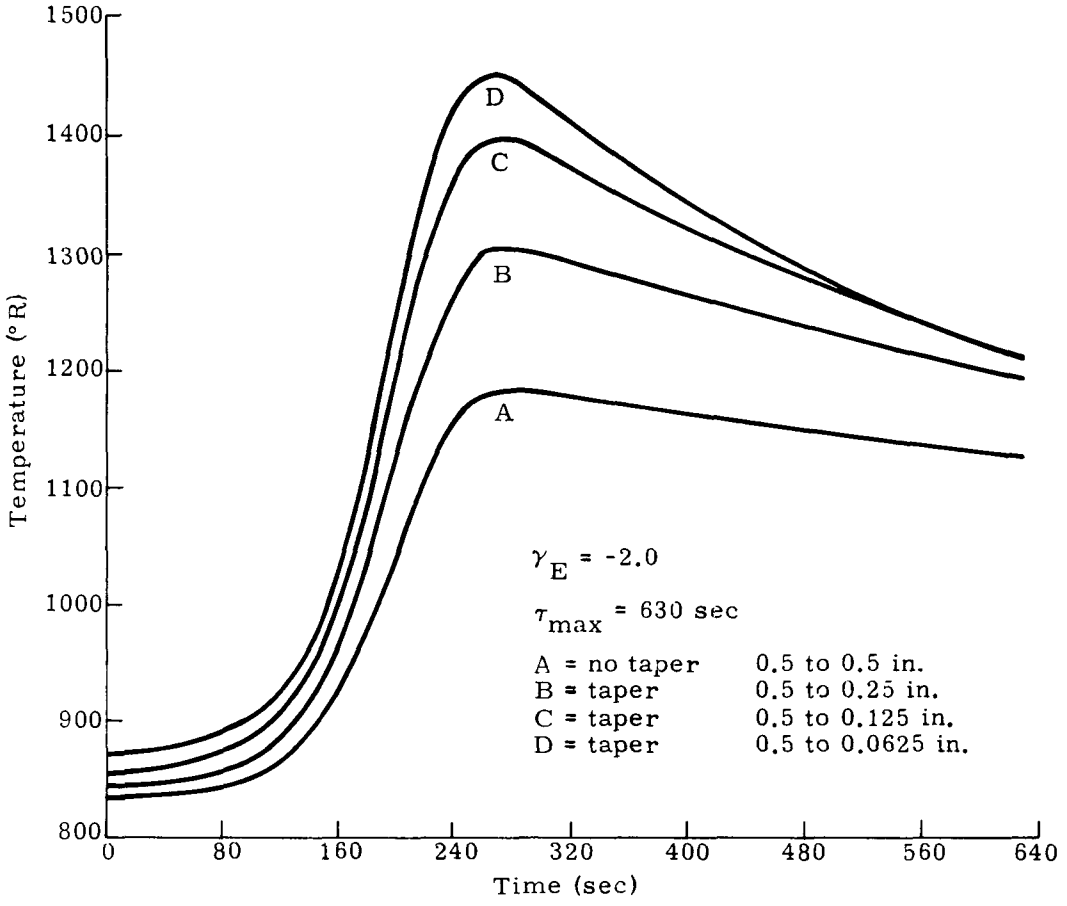

Fig. C-30. Temperature Versus Time for Node 3 at Radiator

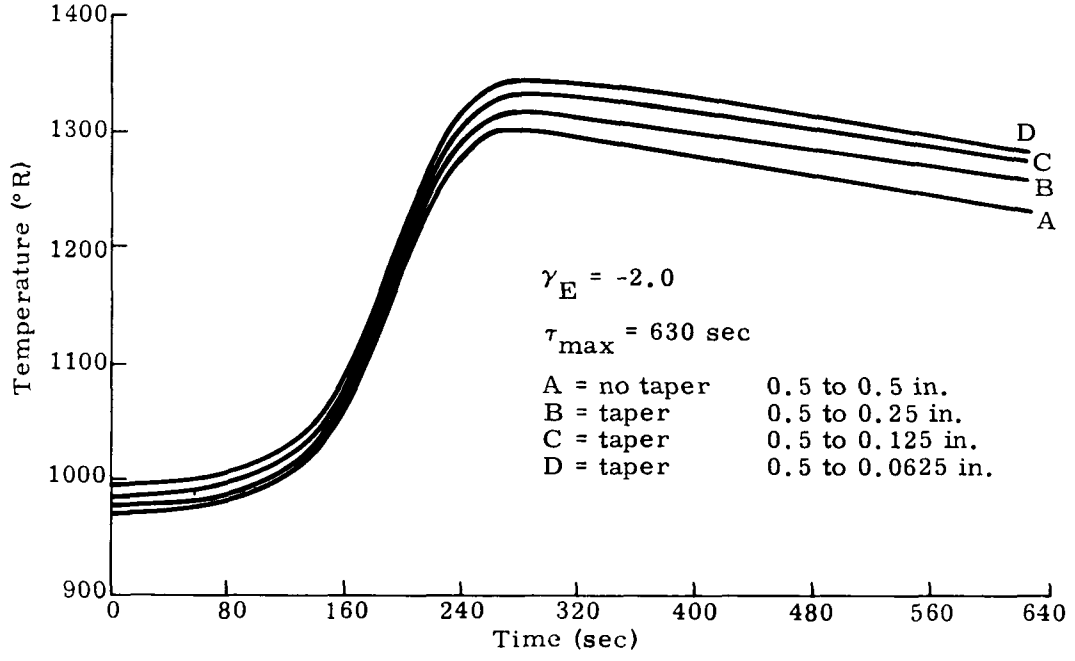

Fig. C-31. Temperature Versus Time for Node 4 at Radiator Root

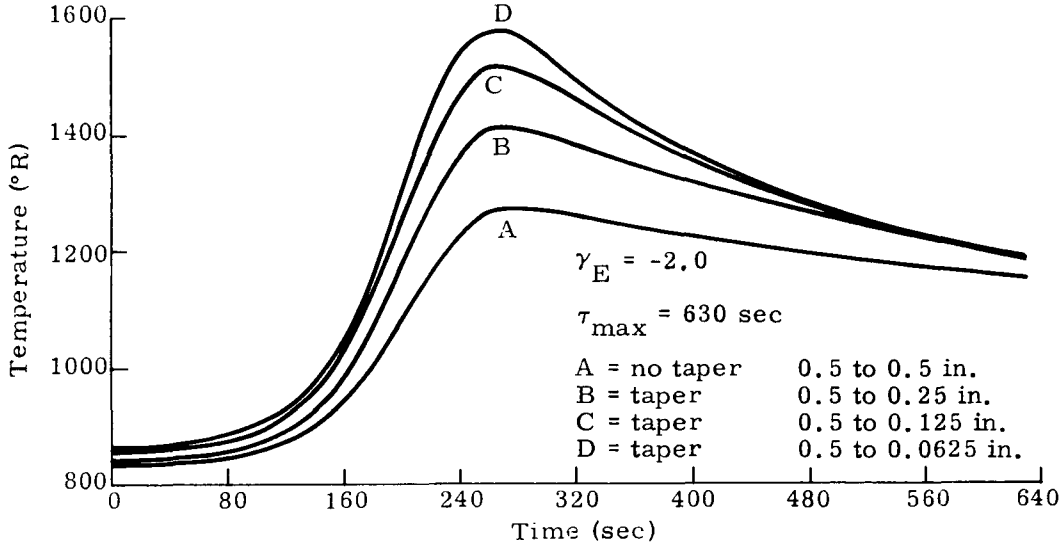

Fig. C-32. Temperature Versus Time for Node 5 at Radiator

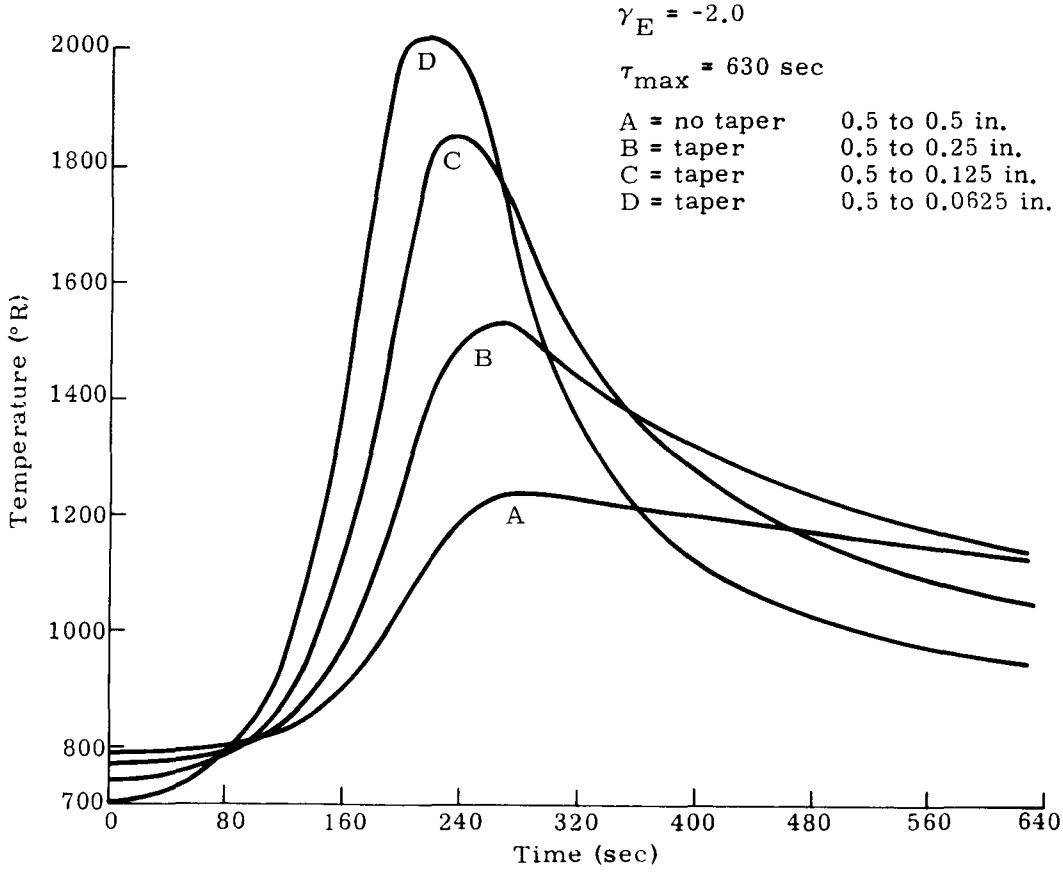

Fig. C-33. Temperature Versus Time for Node 6 at Radiator Tip

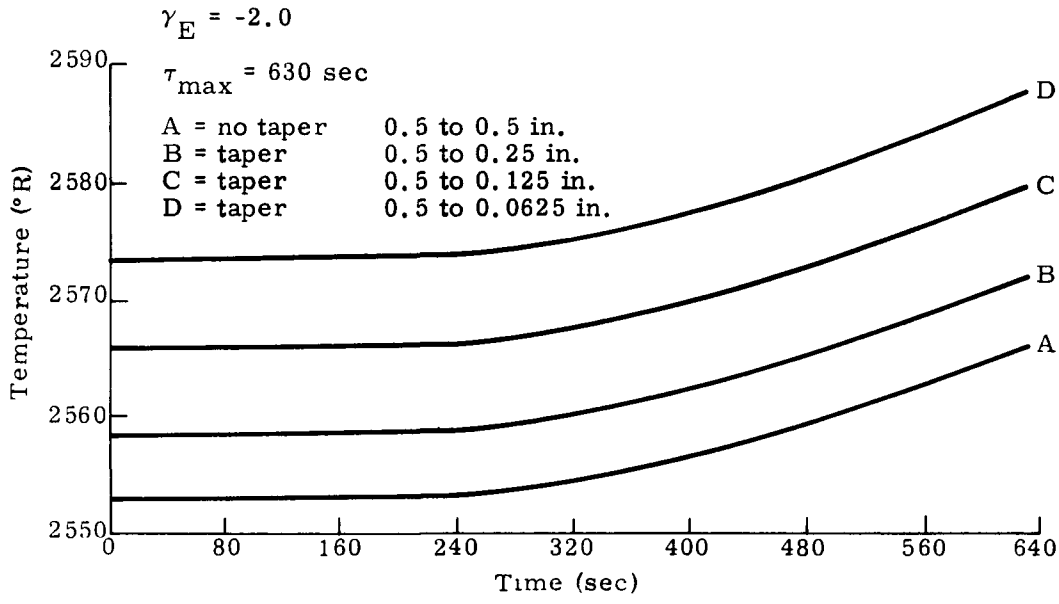

Fig. C-34. Temperature Versus Time for Node 8 at Fuel

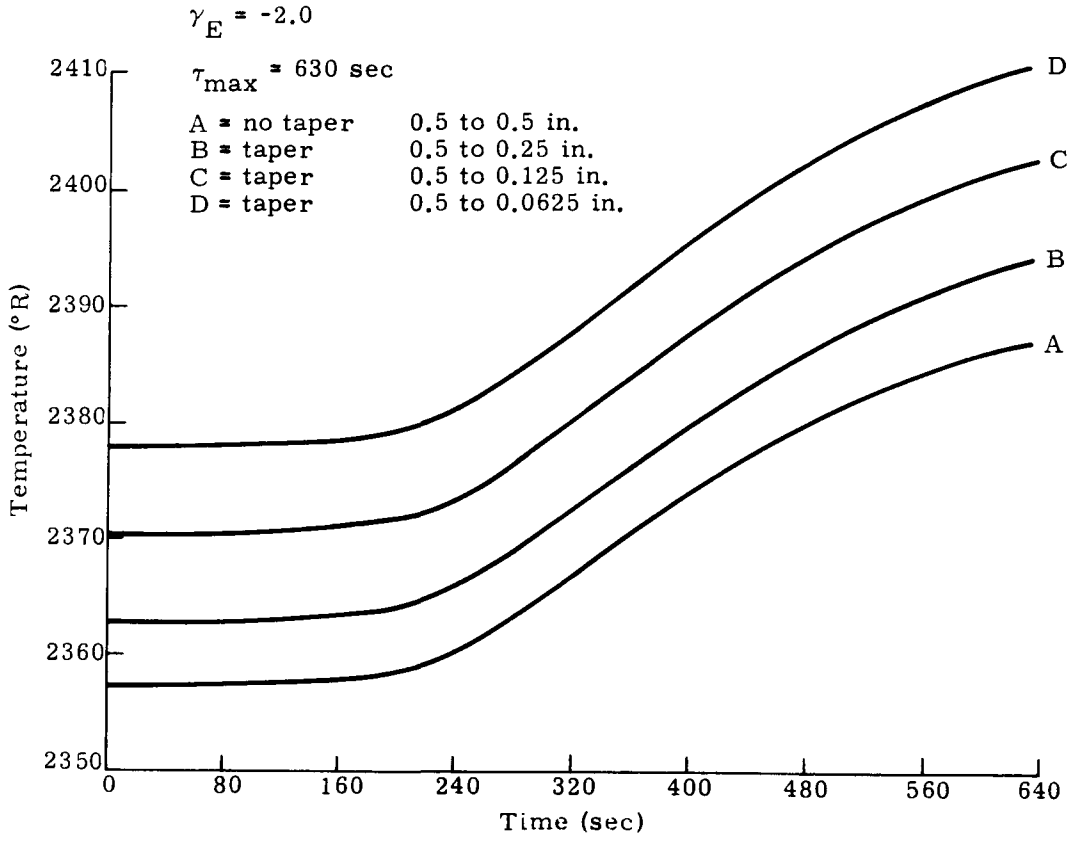

Fig. C-35. Temperature Versus Time for Node 9 at Capsule

Pages 47 thru 57 have been deleted.

Blank

Blank

Blank

Blank

Blank

Blank

Blank

Blank

Blank

Blank

BLANK

APPENDIX D

FUEL CAPSULE THERMAL SHOCK ANALYSIS

From "Approximate Solution to Thermal Shock Problems in Plates, etc., with Heat Transfer at Two Surfaces," by Mendelson and Manson, the dimensionless stress σ^* as a result of thermal shock is given as:

$$\sigma^* = \frac{\sigma}{E\,\alpha\,(1 - \nu)\,\Delta T}$$

where σ represents the circumferential stress in the capsule wall. The consideration of thermal shock is based upon a fuel capsule at 2000° F during descent and suddenly immersed in sea water. Therefore, the ΔT is approximately 1930° F.

The dimensionless stress is some value $0 < \sigma^* < 1$ and is a function of the Biot modulus at the inside and outside surfaces of the capsule.

Thus, the actual stress is some fraction of $E\,\alpha\,(1 - \nu)\,\Delta T$. At 70° F and 2000° F, $E\,\alpha$ is 224 and 193, respectively. Therefore,

$$\sigma < \left(\frac{224 + 193}{2}\right)(1 - 0.3)\,(1930)$$

or

$$\sigma < 282,000 \text{ psi.}$$

It should be noted that thermal shock may promote a catastrophic failure in very brittle materials. However, Haynes-25 is ductile and has a large plastic strain capability. This is shown by the fact that to solution heat treat Haynes-25, the material is water quenched from about 2275° F in the sheet, plate and bar forms.

BLANK

APPENDIX E

FUEL CAPSULE STRUCTURAL ANALYSIS--EXTERNAL PRESSURE CAPABILITY

From a shock overpressure due to a potential booster vehicle explosion during the launch phase ($T \cong 1600°$ F) and submergence in seawater after descent and water impact, the capsule must have the structural capability to withstand buckling modes as a result of these environments.

For design flexibility, the critical buckling pressures and/or yield pressures were considered as a function of capsule wall thickness, t, from 0.040 to 0.160 inch. The inside shell diameter, d, is held constant at 1.286 inches and the length of the shell, L, is taken as 3.88 inches. This length is considered as the constant thickness span between reinforced sections. The analysis is conservative since the foundation support provided by the liner and fuel is not considered.

On the basis of various geometric parameters such as r/t and L^2/rt, the shell falls within the category of either a "long" or "very long" cylinder. On this basis, the critical buckling pressure is obtained by

$$P_{cr} = 0.93\ E\ (\frac{t}{r})^{5/2}\ (\frac{r}{L})$$

where for the fuel capsule

$$r = 0.643 + \frac{t}{2}$$

Ref.: Gerard and Becker, Handbook of Structural Stability, Part III. NASA TN 3783, 1957.

The pressure necessary for a yield condition in the circumferential direction (maximum principal stress) is simply

$$P_y = \frac{\sigma_y t}{r}$$

For the wall thickness range considered, the critical buckling pressure and yielding pressure are presented in Table E-1. The latter is also presented as a function of wall thickness and depth in seawater by Fig. E-1. In all cases, the pressure necessary to provide yielding becomes the critical value for design comparisons since yielding would initiate buckling.

TABLE E-1

Critical Buckling Pressure and Yielding Pressure
(maximum principal stress)

Case 1: T = 70° F $\sigma_y = 67,000$ psi, $E = 33.5 \times 10^6$ psi

t	r	P_{cr}	P_y
0.160	0.723	133,760	14,825
0.140	0.713	97,780	13,160
0.120	0.703	67,970	11,440
0.100	0.693	44,020	9,670
0.080	0.683	25,750	7,850
0.060	0.673	12,820	5,980
0.040	0.663	4,493	4,042

Case 2: T = 1600° F $\sigma_y = 32,000$ psi, $E = 23.1 \times 10^6$ psi

t	r	P_{cr}	P_y
0.160	0.723	127,770	7082
0.140	0.713	67,430	6285
0.120	0.703	46,870	5460
0.100	0.693	30,350	4620
0.080	0.683	17,760	3750
0.060	0.673	8,840	2860
0.040	0.663	4,292	1931

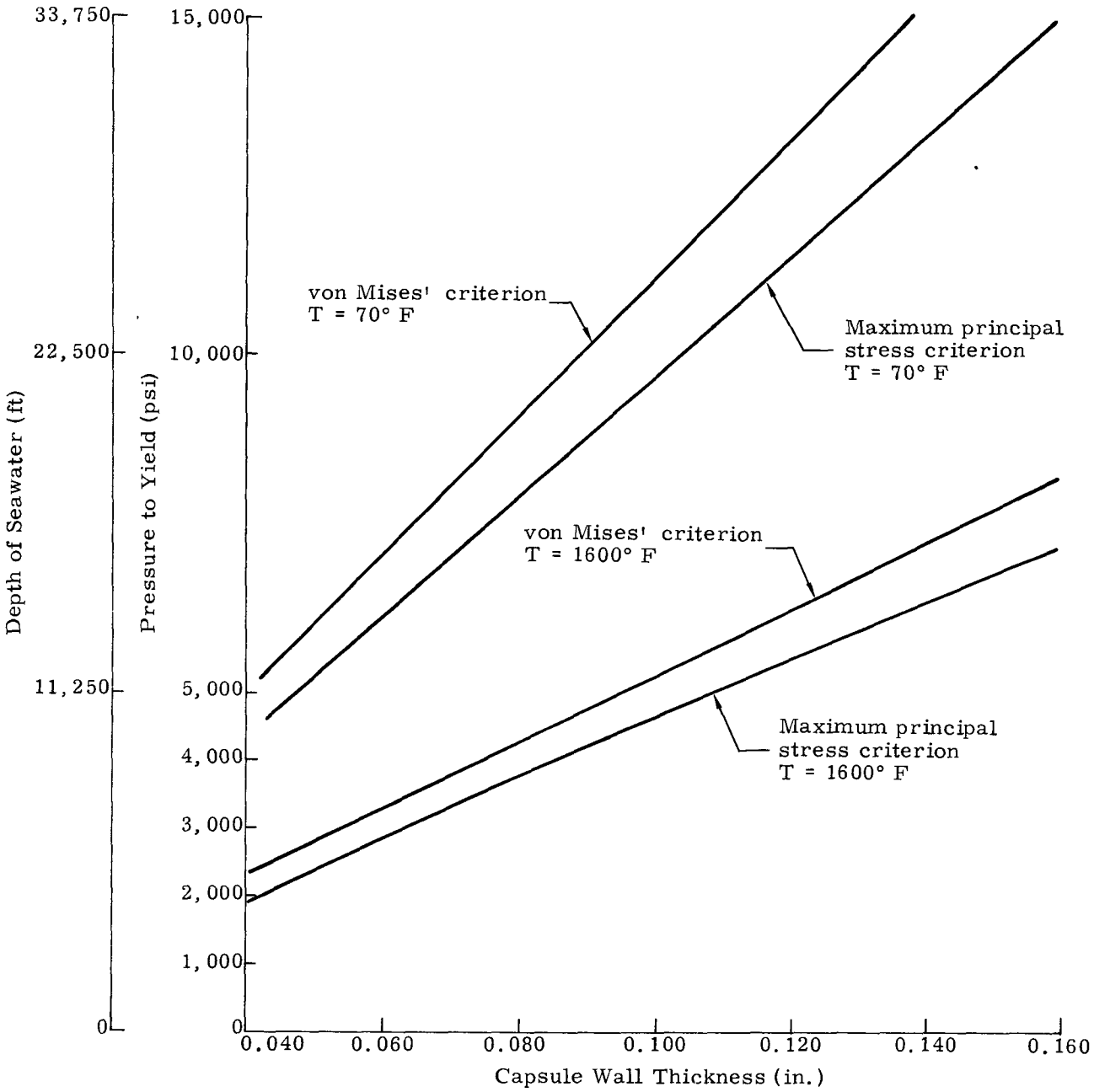

Fig. E-1. Pressure to Yield and Seawater Depth Versus Capsule Wall Thickness

The seawater depth capability is defined by

$$h = \frac{144}{64} p = 2.25 p$$

where p is pressure (psi) and h is the depth potential (ft).

To inject greater accuracy in predicting the pressure necessary to yield, the von Mises criterion is employed where

$$\sigma_y = \sqrt{\sigma_1^2 - \sigma_1 \sigma_2 + \sigma_2^2}$$

where σ_i are the principal stresses.

Therefore,

$$\sigma_1 = \sigma_\theta = p \frac{r}{t}$$

$$\sigma_2 = \sigma_x = \frac{pr}{2t} = \frac{\sigma_1}{2}$$

Substituting,

$$\sigma_y = \frac{1}{2}\sqrt{3\sigma_\theta^2}$$

or

$$P_y = \frac{\sigma_y t}{0.866 r}$$

This pressure is also included in Fig. E-1.

In consideration of the potential blast loading, a 100-psi side on overpressure, P_s, is assumed. The reflected pressure, P_r, may be obtained from the following equation (Ref.: "Structural Effects of Impact," by M. Kornhauser),

$$P_r = 2 P_s \left[\frac{7 P_o + 4 P_s}{7 P_o + P_s}\right]$$

$$P_r = 2 (100) \left[\frac{7 (14.7) + 4 (100)}{7 (14.7) + 100}\right] = 495 \text{ psi}$$

The reflected shock waves during diffraction are the predominant cause of damage for a high frequency structure. Assuming a sinusoidal shock pulse, an amplification factor of 1.8 could be realized. Thus the effective pressure may correspond to 1.8 (495) or 891 psi. It should be noted that from experimental evidence the peak pressure on a cylindrical body is significantly lower than the theoretical results. However, for this investigation, this factor may be dismissed in favor of conservatism.

From Table E-1 illustrating the structural capability versus an external pressure, a reflected pressure, including amplification, of 891 psi should provide no concern for structural integrity.

A. ANALYSIS OF DISCONTINUITY STRESSES AT CAPSULE END CLOSURES DUE TO EXTERNAL PRESSURE

Considering the geometry at the wall end closure as shown in Fig. E-2, the wall thickness is 0.141 inch. With a thick end closure reinforced by the cylindrical continuation as shown at the ends, the cylinder approaches the case where the ends are fixed from rotation.

From the deflection and slope equations (Ref.: "Theory of Plates and Shells", by Timoshenko and Woinowski-Krieger),

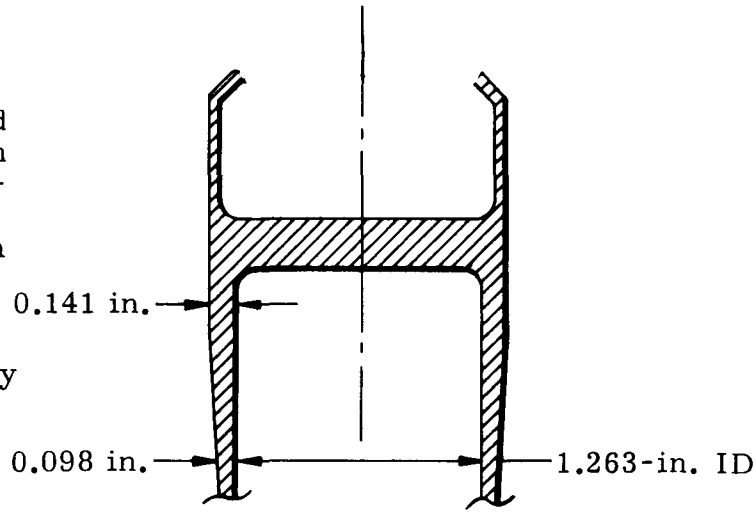

Fig. E-2. Capsule End Configuration

$$W\Big|_{x=o} = -\frac{1}{2\beta^3 D}(\beta M_o + Q_o) = \delta$$

and

$$\frac{dw}{dx}\Big|_{x=o} = \frac{1}{2\beta^2 D}(2\beta M_o + Q_o) = 0$$

where M_o and Q_o are the discontinuity moment and shear, respectively, and

$$\beta = \left(\frac{3(1-\nu^2)}{R^2 t^2} \right)^{1/4}$$

$$\delta = \frac{PR^2}{Et}$$

Solving for M_o and Q_o:

$$-2\beta M_o = Q_o$$

$$\therefore \delta = -\frac{1}{2\beta^3 D} (\beta M_o - 2\beta M_o)$$

$$= \frac{M_o}{2\beta^2 D}$$

$$M_o = \frac{PR^2}{Et} (2\beta^2 D)$$

where

$$D = \frac{Et^3}{12(1-\gamma^2)}$$

Let $R = \frac{1.263 + 0.141}{2} = 0.702$, $t = 0.141$, $E = 33.5 \times 10^6$ at ambient temperature, $\gamma = 0.3$ and assume for an illustrative example that $P = 4450$ psi which is equivalent to a depth of 10,000 feet in seawater.

$$\beta = \left(\frac{3(0.91)}{(0.702)^2 (0.141)^2} \right)^{1/4} = 4.086$$

$$D = \frac{33.5 \times 10^6 (0.141)^3}{12(0.91)} = 8600$$

Therefore,

$$M_o = \frac{4450 (0.702)^2 (2) (4.086)^2 (8600)}{33.5 \times 10^6 (0.141)}$$

$= 133.3$ in. -lb/in.

$$Q_o = \frac{-4450}{4.086} = -1089.2 \text{ lb/in.}$$

From NASA TR-103, the meridional and circumferential stresses at the shell closure interface are given as

$$\sigma_x = \frac{6 M_o}{t^2} + \frac{PR}{2t}$$

$$\sigma_\theta = \frac{PR}{t} + \frac{2\beta^2 R}{t} + \frac{6\gamma}{t^2} M_o + 2 \frac{\beta R Q_o}{t}$$

Therefore,

$$\sigma_x = \frac{6(133.3)}{(0.141)^2} + \frac{4450(0.712)}{2(0.141)} = 51,306 \text{ psi (max)}$$

and $$\sigma_\theta = \frac{4450(0.702)}{0.141} + \left[\frac{2(4.086)^2 (0.702)}{0.141} \pm \frac{6(0.3)}{(0.141)^2}\right] 133.3$$

$$- \frac{2(4.086)(0.702)(1089.2)}{0.141}$$

$= -12,070$ psi (max).

Since the material yield strength is in excess of 60,000 psi, the design is more than adequate.

The majority of the magnitudes of the above stresses are of a discontinuity in nature. Thus, yielding may take place and the result is a redistribution of stresses (decrease of stress magnitude) which in no way should signify a catastrophic failure.

~~CONFIDENTIAL~~

BLANK

~~CONFIDENTIAL~~

APPENDIX F

FUEL CAPSULE IMPACT ANALYSIS

For impending rupture, the following expression holds true.

$$U_k = U_a \qquad \text{(F-1)}$$

where

U_k = kinetic energy of the fuel capsule prior to impact (ft-lb)

$= \frac{1}{2} \frac{W}{g} V^2$

U_a = energy absorbed by the capsule prior to rupture (ft-lb)

$= K (U_{a_e} + U_{a_p})$

U_{a_e} = energy absorbed in elastic deformation of the encapsulant material (ft-lb). As an approximation,

$$U_{a_e} = \frac{1}{12} \frac{W_c}{\rho_c} \frac{\sigma_y \epsilon_y}{2}$$

U_{a_p} = energy absorbed in plastic deformation of the encapsulant material (ft-lb). As an approximation,

$$U_{a_p} = \frac{1}{12} \frac{W_c}{\rho_c} \frac{(\sigma_y + \sigma_u) \epsilon_u}{2}$$

W = total capsule weight (lb)

$= W_c + W_f + W_s$

W_c = encapsulant weight (lb)

W_f = fuel weight (lb)

W_s = liner, separator and spacer weight (lb)

g = acceleration due to gravity = 32.2 ft/sec^2

V = capsule velocity prior to impact (fps)

K = absorption efficiency factor (configuration-dependent)

ρ_c = density of encapsulant material (lb/in.^{3})

σ_y = yield stress in tension (lb/in.^{2})

σ_u = ultimate stress in tension (lb/in.^{2})

ϵ_y = yield strain (in./in.)

ϵ_u = ultimate elongation (in./in.)

Substituting into Eq (1),

$$\frac{1}{2}\frac{W}{g}V^2 = \frac{K W_c}{12\,\rho_c}\left(\frac{\sigma_y\,\epsilon_y}{2} + \frac{(\sigma_y + \sigma_u)\,\epsilon_u}{2}\right)$$

Rearranging,

$$w_c = \frac{W_c}{W} = \frac{V^2}{2g\,K\,u_a} \qquad \text{(F-2)}$$

where

w_c = encapsulant weight fraction (lb, encapsulant/lb total capsule) $(0 < w_c < 1)$

u_a = specific energy absorption (ft-lb/lb of encapsulant)

$$= \frac{1}{12\,\rho_c}\left(\frac{\sigma_y\,\epsilon_y}{2} + \frac{(\sigma_y + \sigma_u)\,\epsilon_u}{2}\right)$$

APPENDIX G

RADIATOR STRUCTURAL ANALYSIS WITH RESPECT TO BLAST OVERPRESSURE

Critical external pressure of a conical shell can be determined by a modification presented in STL Report No. TR-59-0000-09959, "Semi-Annual Report on Development of Design Criteria for Elastic Stability of Thin Shell Structures," P. Seide, December 1959. The equation in this reference was reduced by 20% to include all the test points shown in Fig. 8 of the reference. The resulting equation yields:

$$P_{cr} = \frac{0.736\, E\, t^{2.5}}{\ell\, \rho^{1.5}}$$

where

E = Young's modulus = 38.2×10^6 psi at 550° F

t = skin thickness

ℓ = slant height

ρ = average slant radius.

Considering the unsupported section at the wide end of the cone between the ablator mounting ring and the heat source support structure, and conservatively assuming the minimum thickness of 0.125 inch to apply over this entire section, the following dimensions are obtained:

$t = 0.125$ inch

$\ell = 8.0$ inches

$$\rho = \frac{43 + 38.4}{4 \cos 18^\circ} = 21.4 \text{ inches}$$

Substituting,

$$P_{cr} = \frac{0.736 \times 38.2 \times 10^6 (0.125)^{2.5}}{8.0(21.4)^{1.5}} = 197 \text{ psi}$$

~~CONFIDENTIAL~~

BLANK

~~CONFIDENTIAL~~

APPENDIX H

THERMAL EFFICIENCY ANALYSIS

The heat losses in the system occur through the module and the heat source support insulation. At end of life these losses are given by:

$$q_1 = \frac{\bar{k}_1 \left[\bar{A}_1 - A_{elements}\right] \left[T_H - T_C\right]}{\ell_1} = 370 \text{ watts}$$

$$q_2 = \frac{2\,\bar{k}_2\, A_2 \left[T_2 - T_3\right]}{\ell_2} = 250 \text{ watts}$$

where

q_1 = module insulation heat loss

q_2 = insulation support heat loss

$\bar{k}_1$ = average insulation conductivity of Min-K 2000 between 1450° and 550° F = 0.012 Btu/ft-hr-°F

$\bar{A}_1$ = mean module area = 7.5 ft^2

$A_{elements}$ = total element cross-sectional area = 0.40 ft^2

T_H = hot junction temperature = 1450° F

T_C = cold junction temperature = 550° F

ℓ_1 = module insulation thickness = 0.75 inch

$\bar{k}_2$ = average insulation conductivity of Min-K 2000 between 1700° and 500° F = 0.015 Btu/ft-hr-°F

A_2 = end cap area $\approx$ 6 ft^2

ℓ_2 = heat source and insulation thickness = 3 inches

T_2 = approximate hot side insulation temperature at end of life = 1700° F

T_3 = approximate cold side insulation temperature at end of life = 500° F

With Dyna-Quartz in the module, the module heat loss would become 630 watts

$$\left(\bar{k}_{\text{Dyna-Quartz}} = 0.021 \text{ Btu/ft-hr-°F}\right).$$

The heat losses for the two schemes are:

	System 1 (watts)	System 2 (watts)
Module insulation	370 (Min-K 2000)	630 (Dyna-Quartz)
Support insulation	250	250
Total	620	880

For System 1, the thermal efficiency is

$$\eta_{\text{therm}} = \frac{q_{\text{elem}}}{q_{\text{tot}}} = \frac{5040}{5040 + 620} = 0.89$$

For System 2, the thermal efficiency is

$$\eta_{\text{therm}} = \frac{5040}{5040 + 880} = 0.85$$

APPENDIX I

THERMAL INSULATION CONDUCTIVITY DATA

The thermal conductivity data from Johns-Manville on Dyna-Quartz, Micro-Quartz and Min-K 2000 are presented in Figs. I-1 through I-7. The data should be considered preliminary since differences among the three sources on Dyna-Quartz data are apparent and since some of the Min-K 2000 data in vacuum were constructed from air data by correction factors.

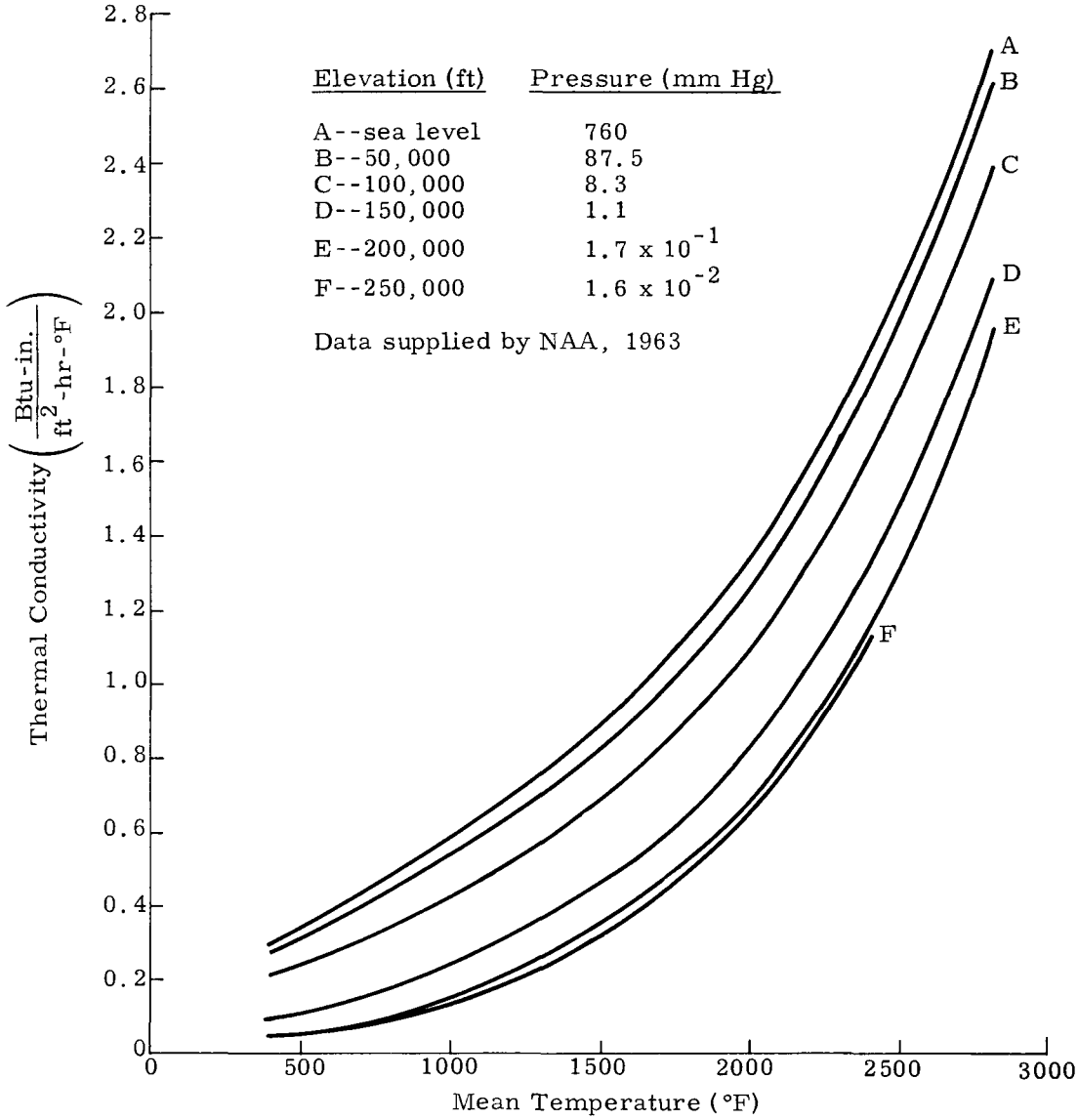

Fig. I-1. Micro-Quartz--6 pcf

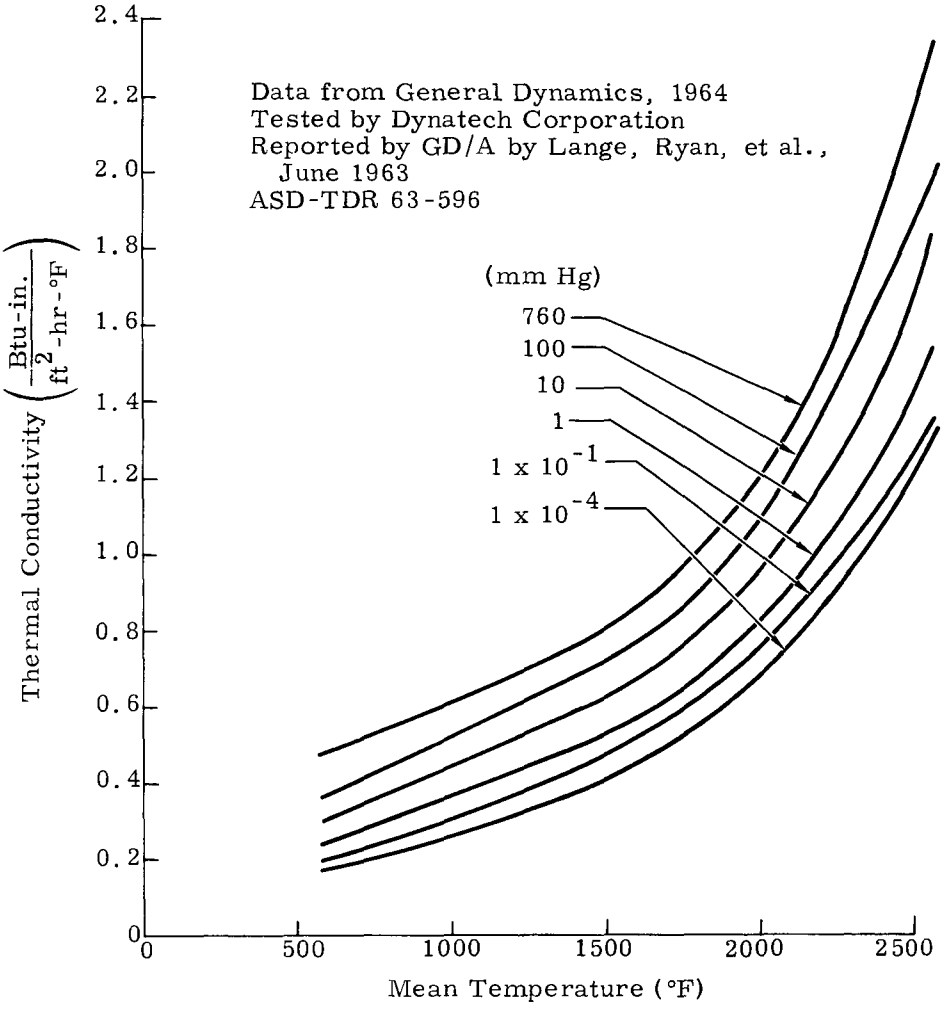

Fig. I-2. Dyna-Quartz--4.5 pcf in Air

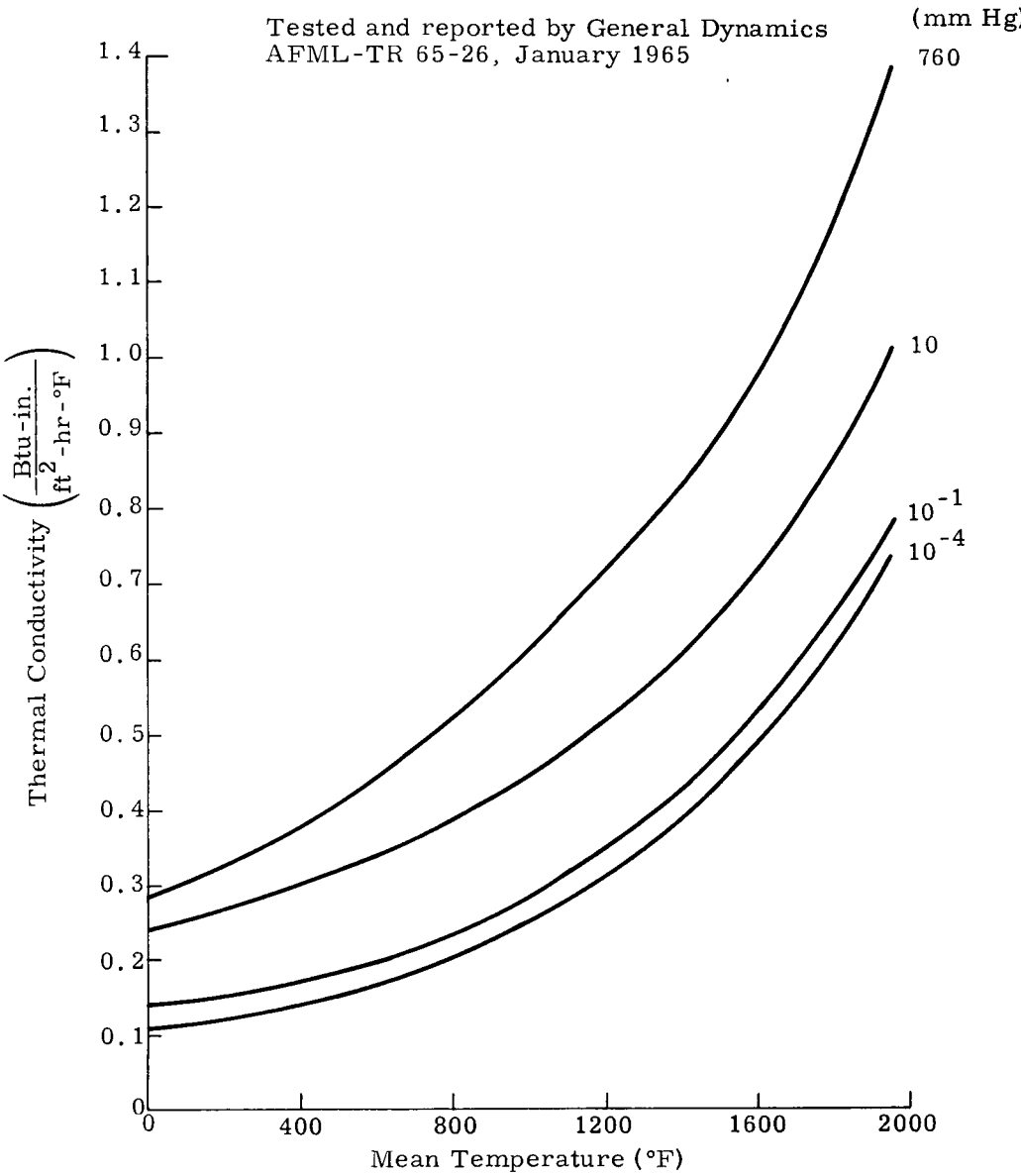

Fig. I-3. Dyna-Quartz--6.2 pcf

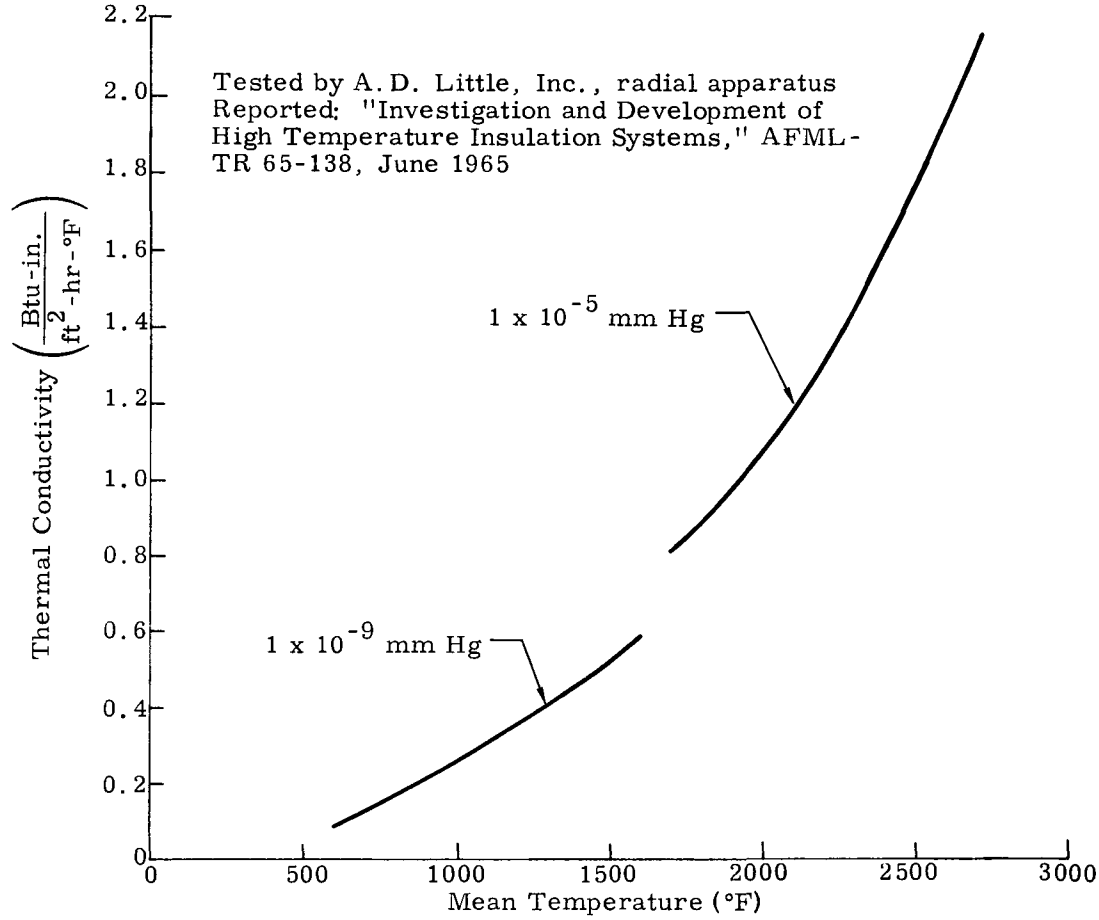

Fig. I-4. Dyna-Quartz--6.2 pcf

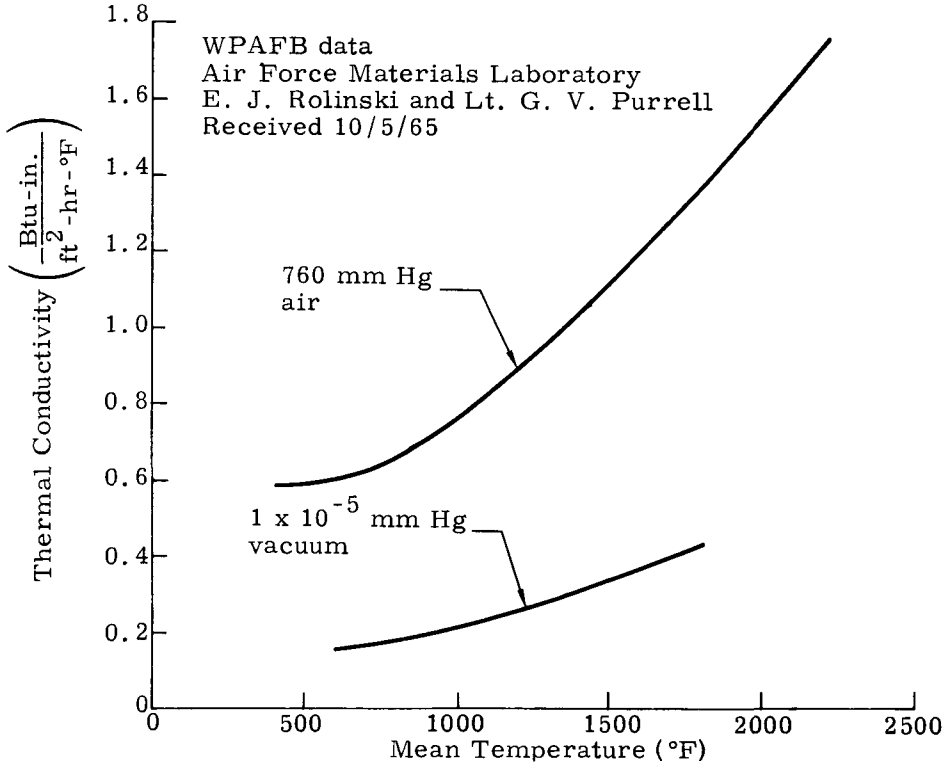

Fig. I-5. Dyna-Quartz--6.2 pcf in Air and Vacuum

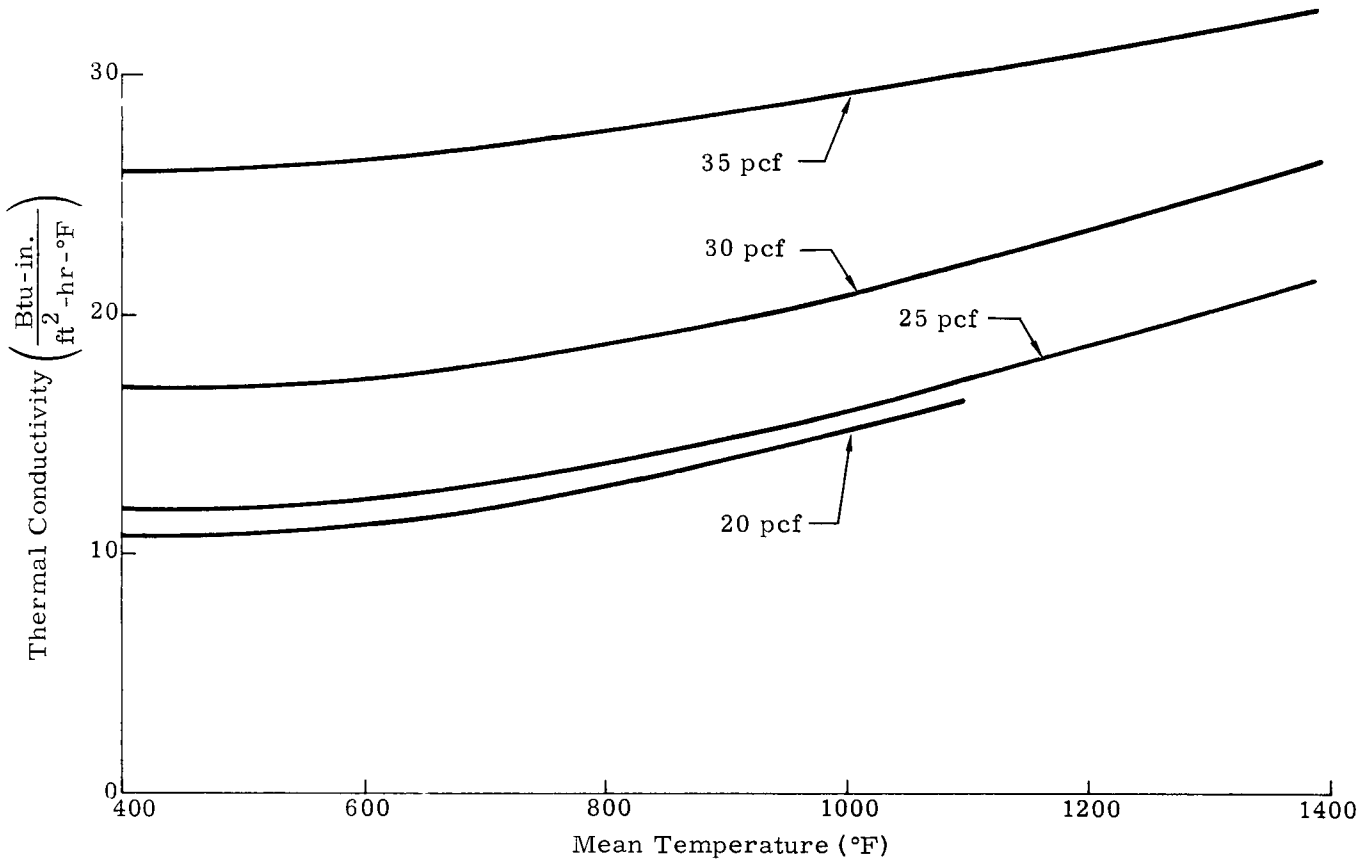

Fig. I-6. Thermal Conductivity of Min-K 2000 in Vacuum

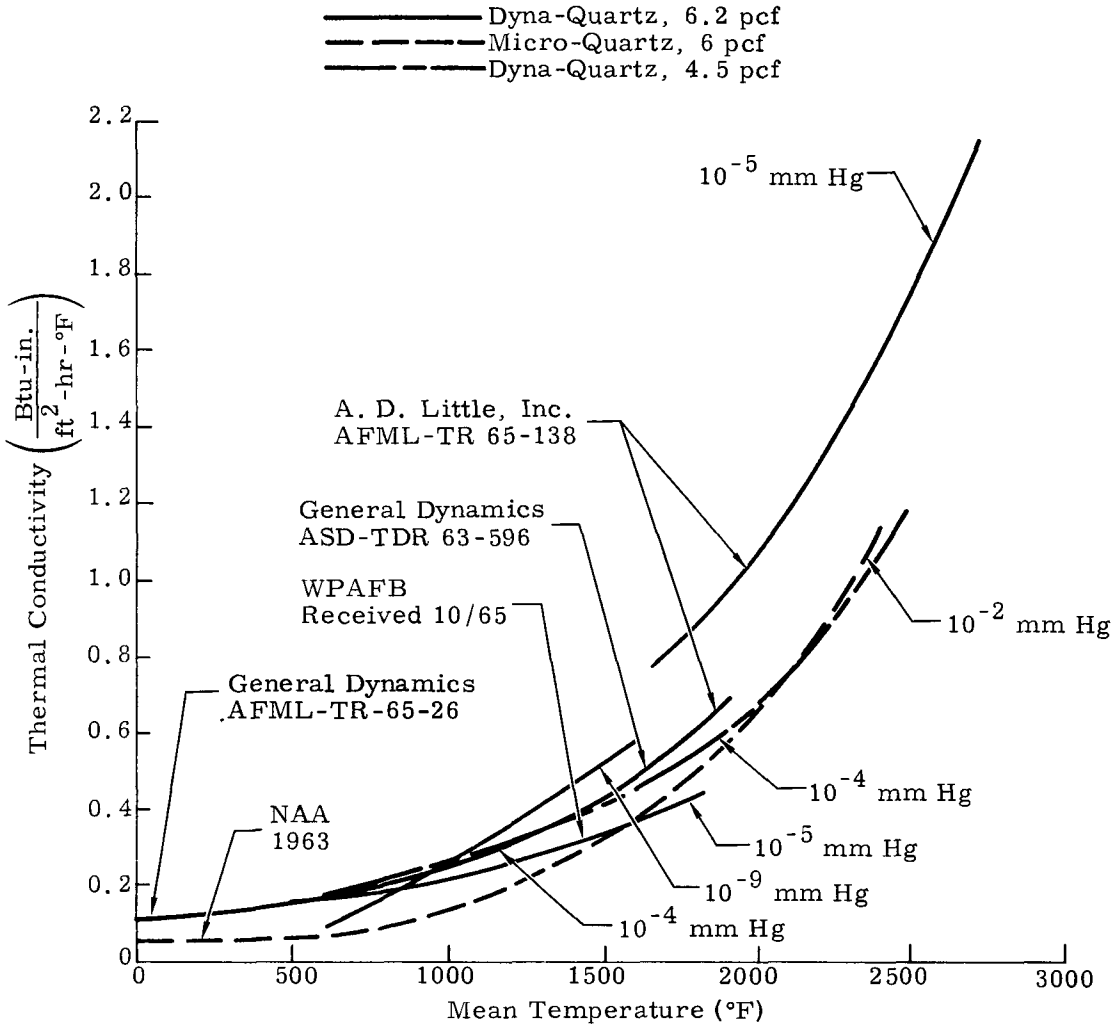

Fig. I-7. Thermal Conductivity Versus Temperature

BLANK

APPENDIX J

THERMOELECTRIC DATA AND INTEGRATED AVERAGES

In Figs. J-1 through J-6 the 1500-hour data, as supplied by RCA, on Seebeck coefficient, electrical resistivity, and thermal conductivity on both N-type and P-type SiGe are presented.

Figures J-7 through J-12 are integrated averages of these properties for cold junctions from 400° to 700° F and hot junctions from 1200° to 1700° F. Integrated averages are useful in hand calculations for various thermoelectric analyses.

In Figs. J-13 and J-14 the thermal resistivity and electrical resistivity data, respectively, on the silicon-molybdenum alloy used for the hot shoe are given.

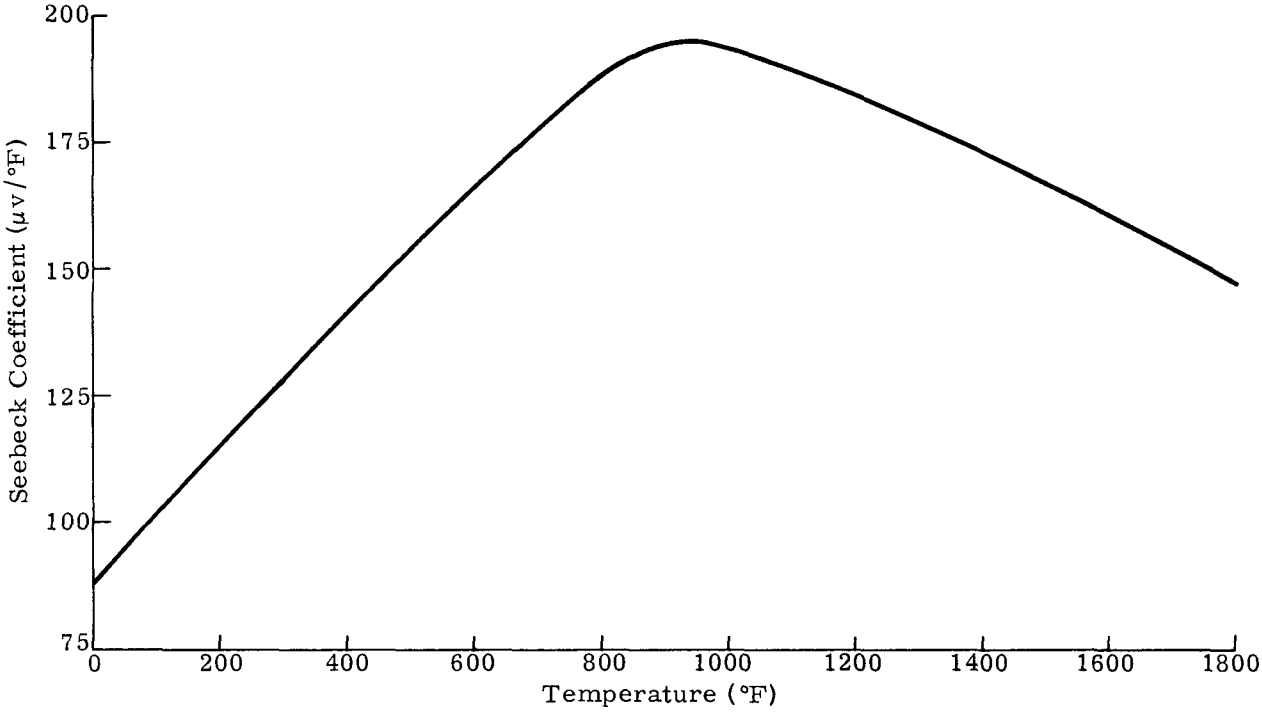

Fig. J-1. Absolute Seebeck Coefficient for SiGe, N Element. Data Compiled 11/65

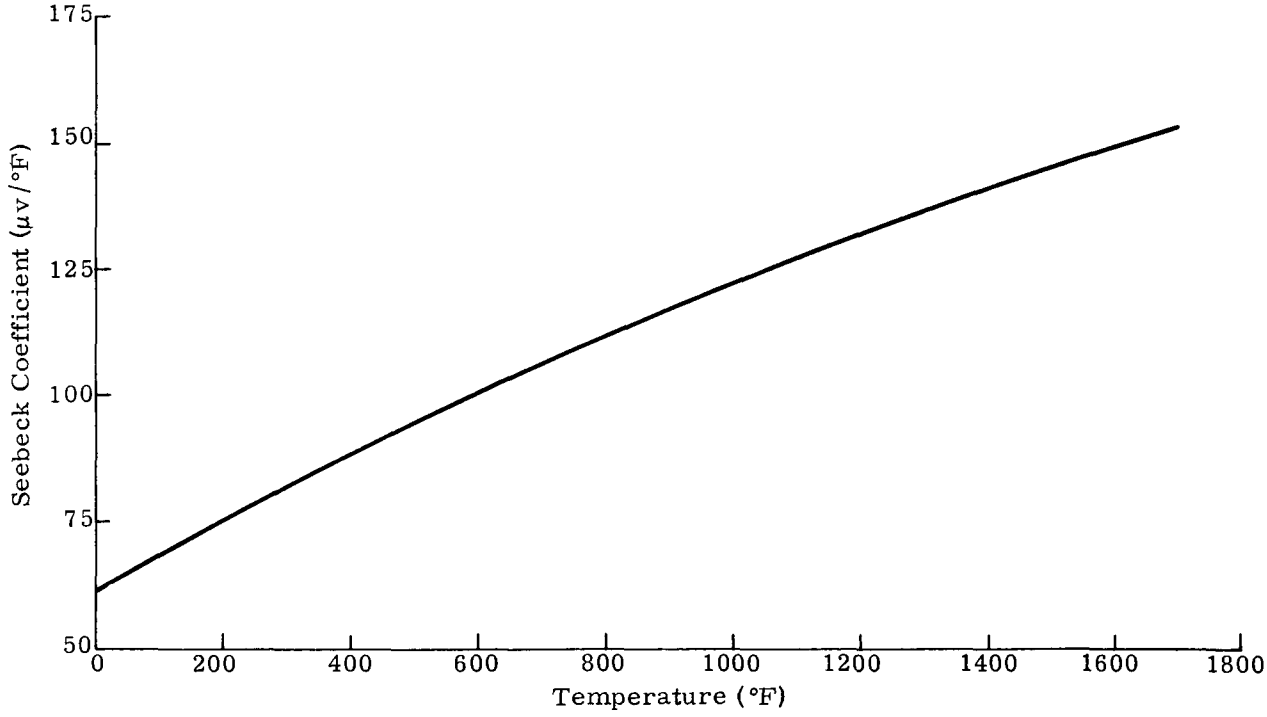

Fig. J-2. Seebeck Coefficient for SiGe, P Element. Data Compiled 11/65

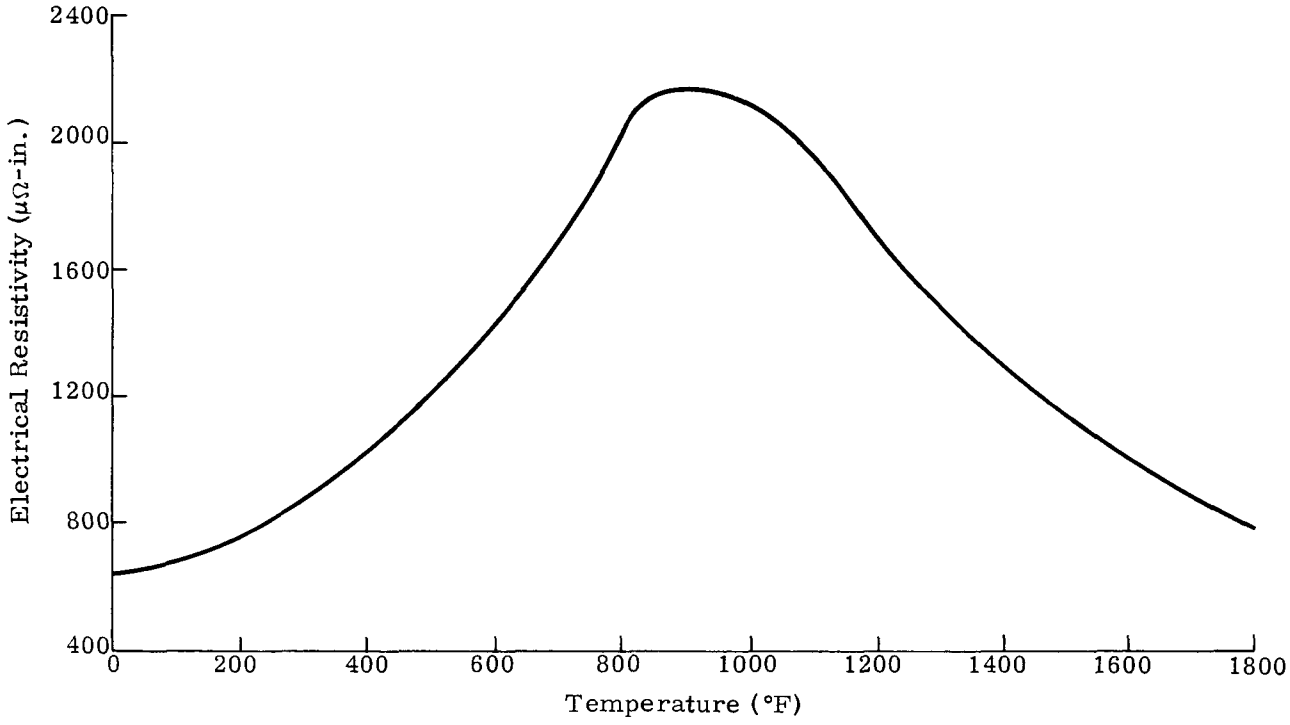

Fig. J-3. Electrical Resistivity for SiGe, N Element. Data Compiled 11/65

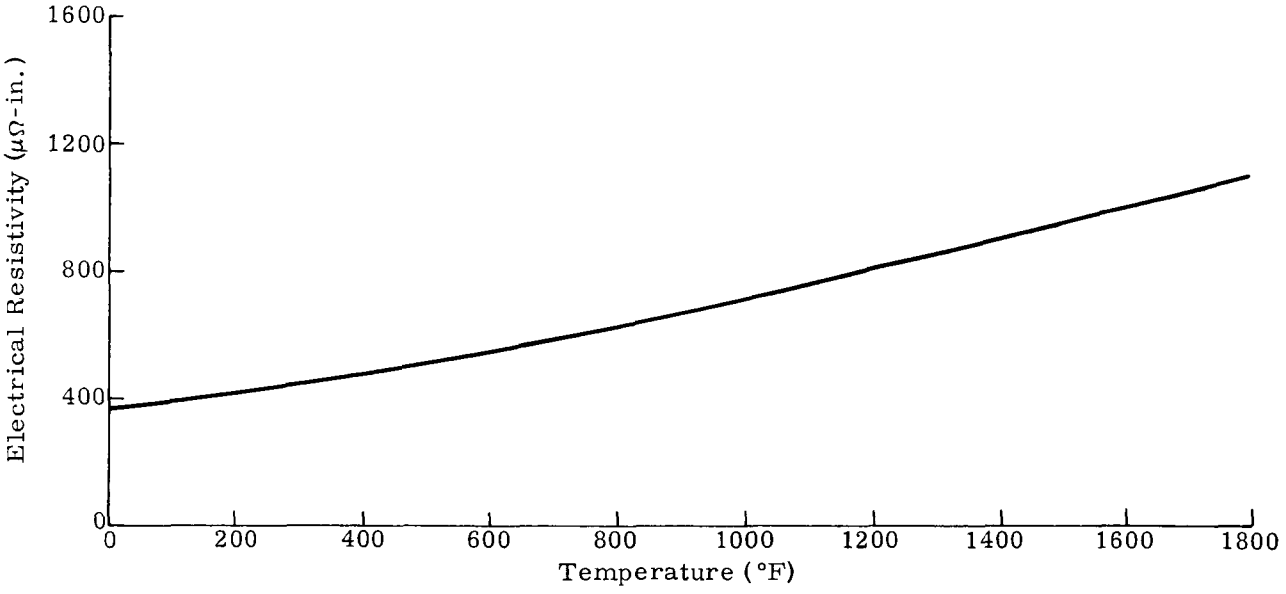

Fig. J-4. Electrical Resistivity for SiGe, P Element. Data Compiled 11/65

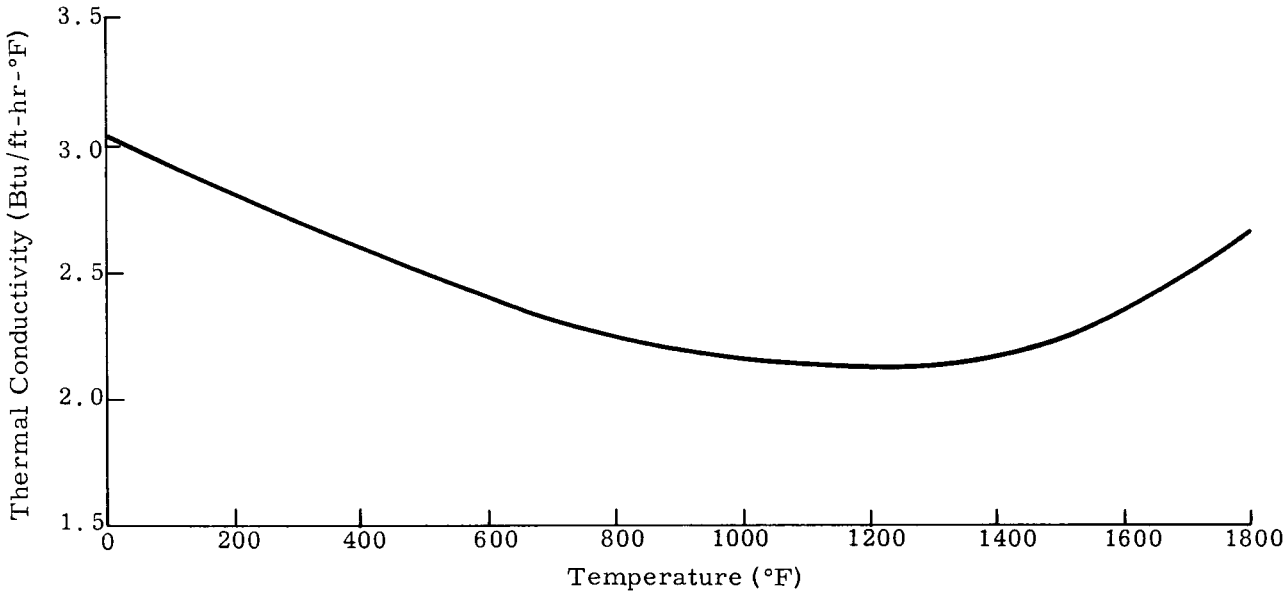

Fig. J-5. Thermal Conductivity for SiGe, N Element. Data Compiled 11/65

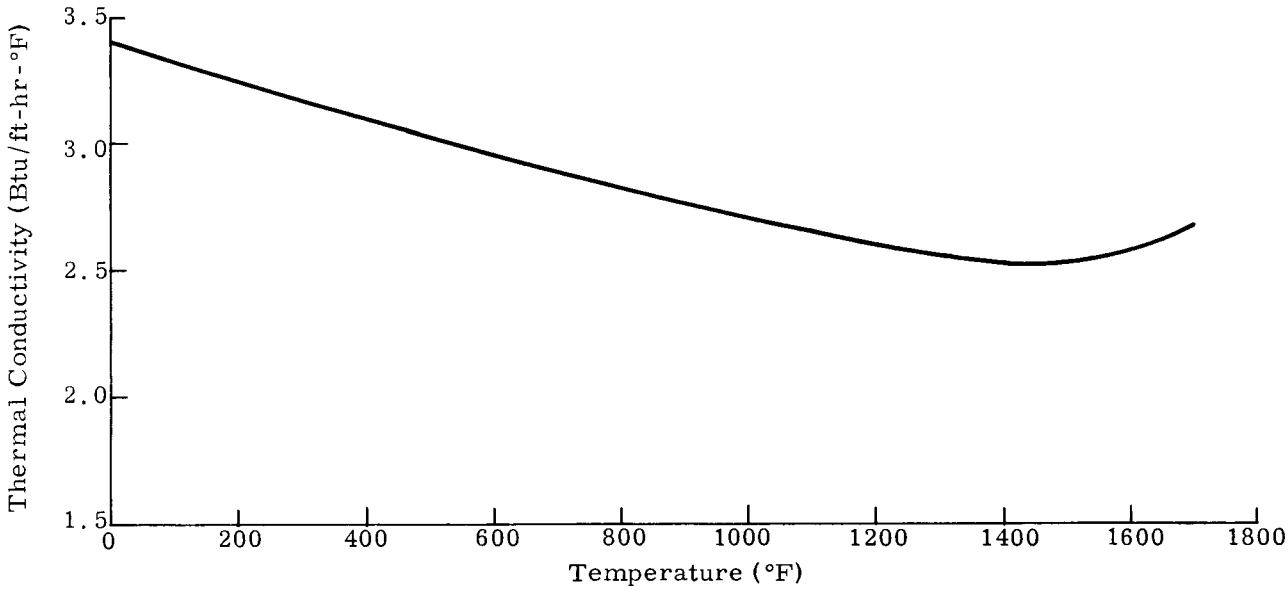

Fig. J-6. Thermal Conductivity for SiGe, P Element. Data Compiled 11/65

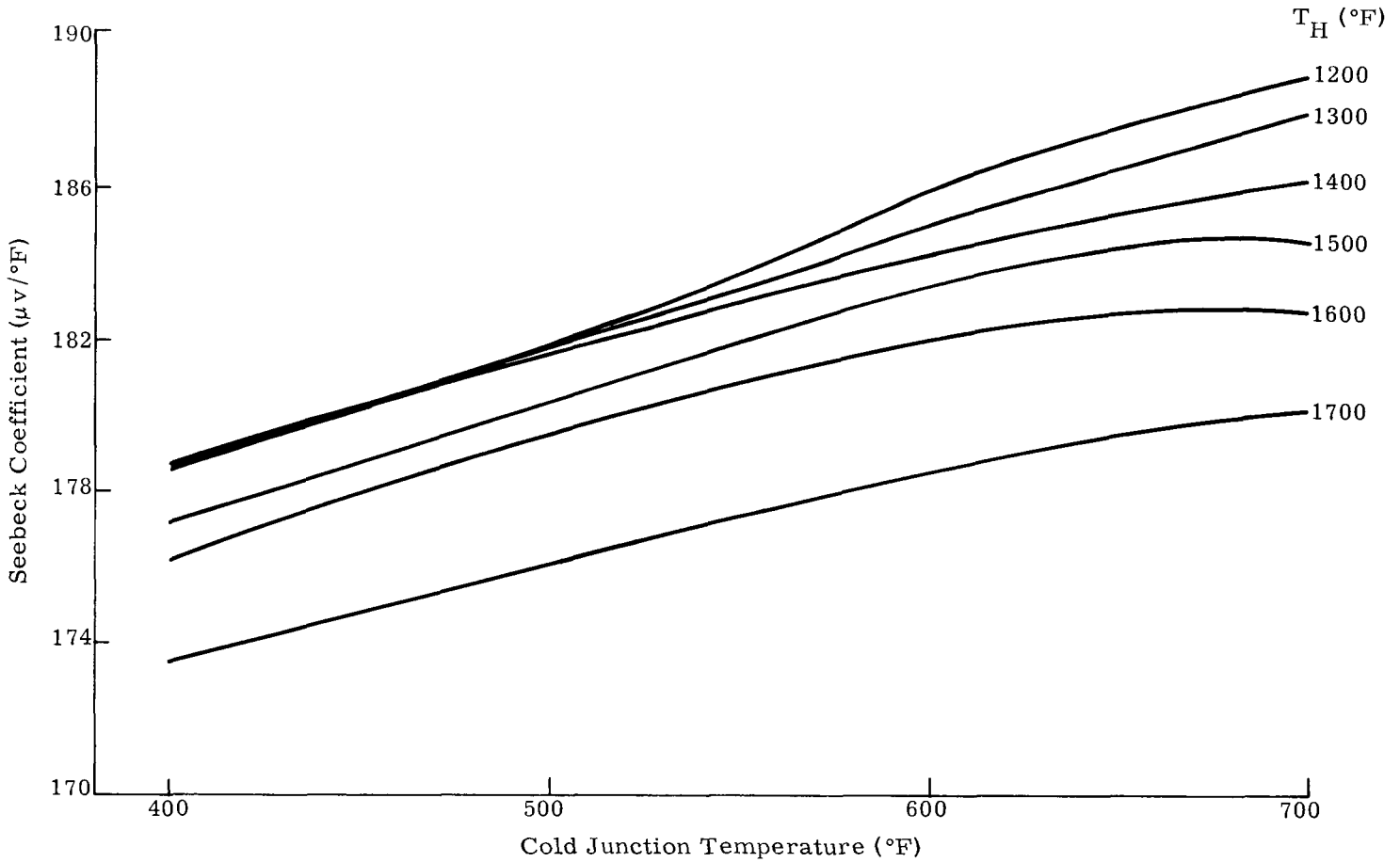

Fig. J-7. Integrated Average Seebeck Coefficient for SiGe, N Element. Data Compiled 11/65

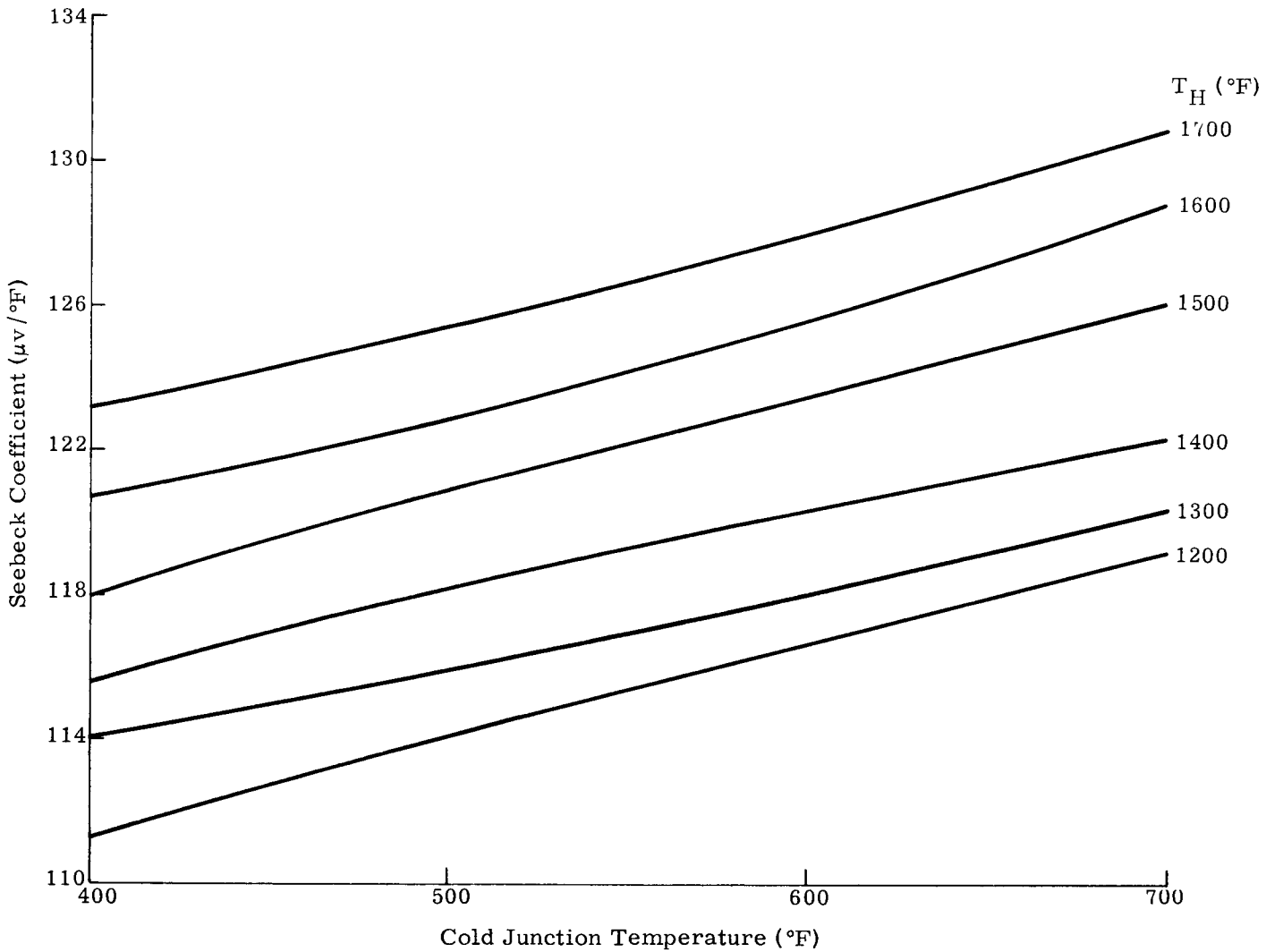

Fig. J-8. Integrated Average Seebeck Coefficient for SiGe, P Element. Data Compiled 11/65

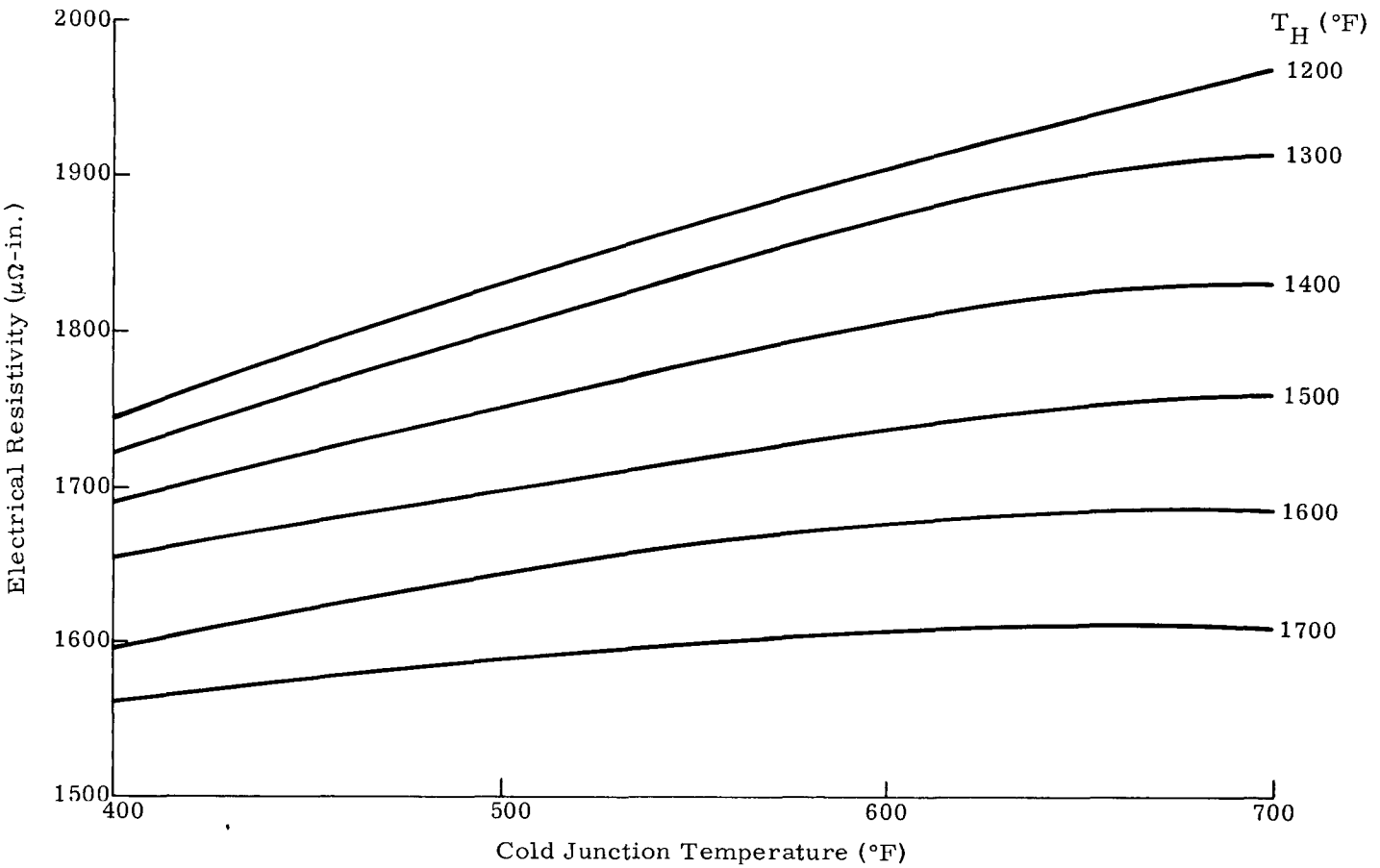

Fig. J-9. Integrated Average Electrical Resistivity for SiGe, N Element. Data Compiled 11/65

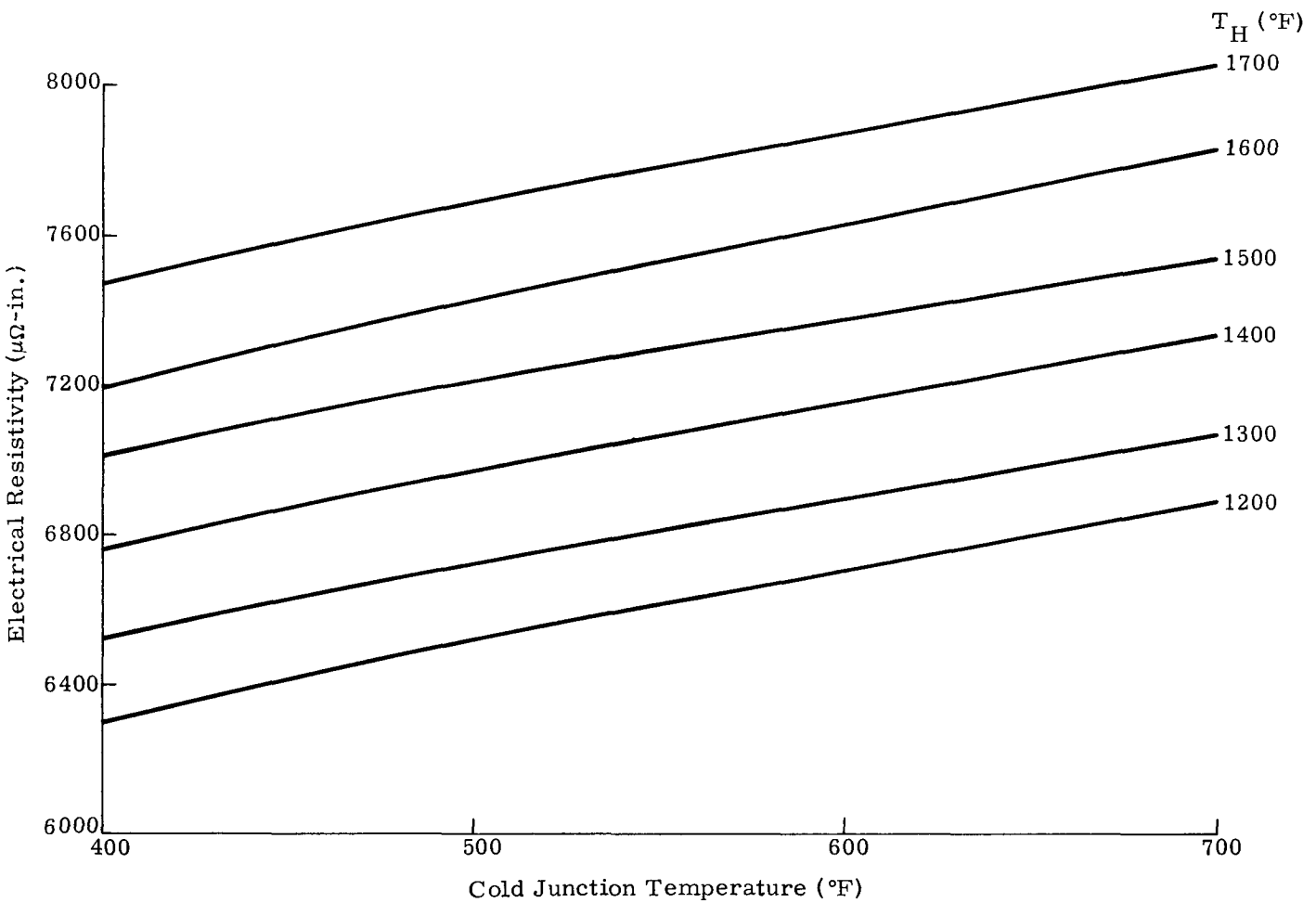

Fig. J-10. Integrated Average Electrical Resistivity for SiGe, P Element. Data Compiled 11/65

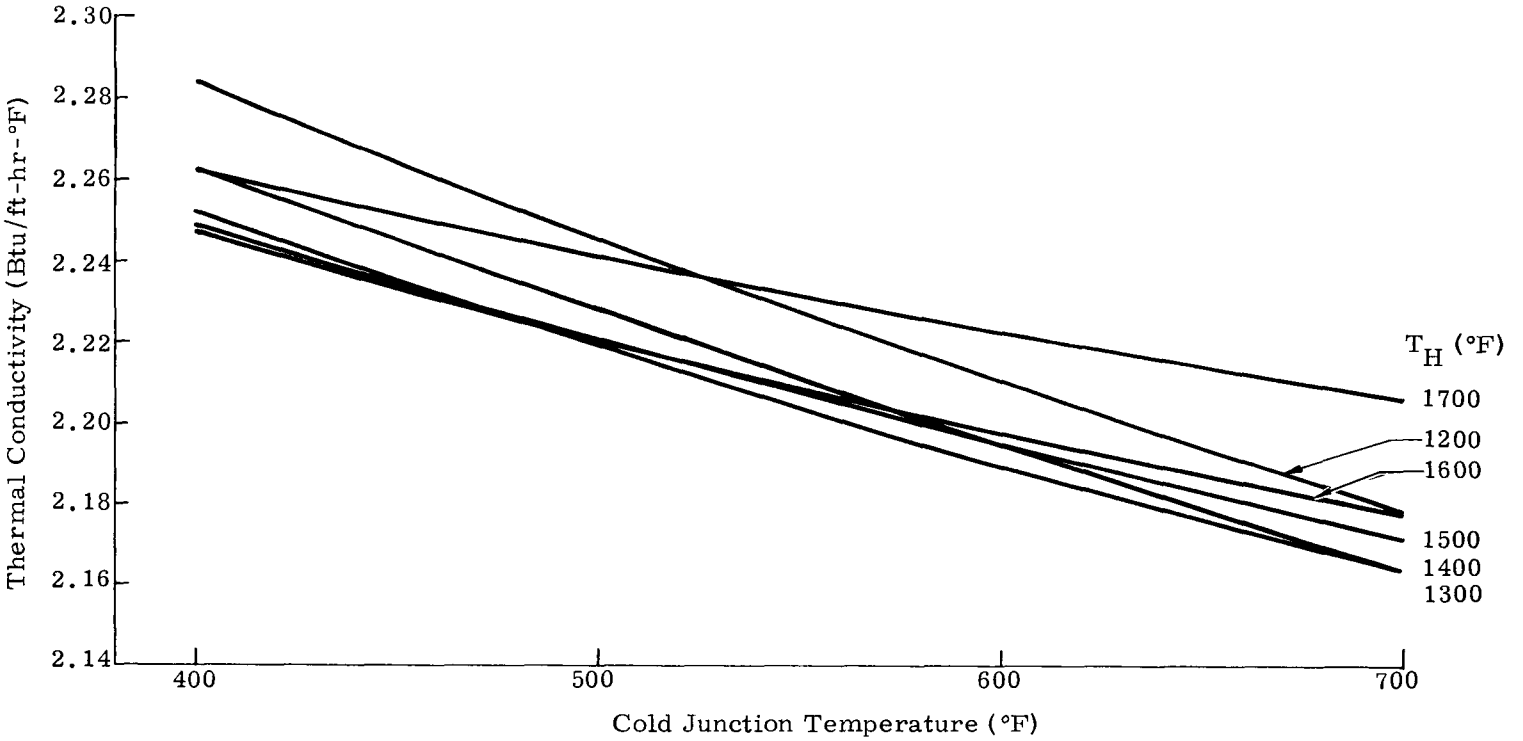

Fig. J-11. Integrated Average Thermal Conductivity for SiGe, N Element. Data Compiled 11/65

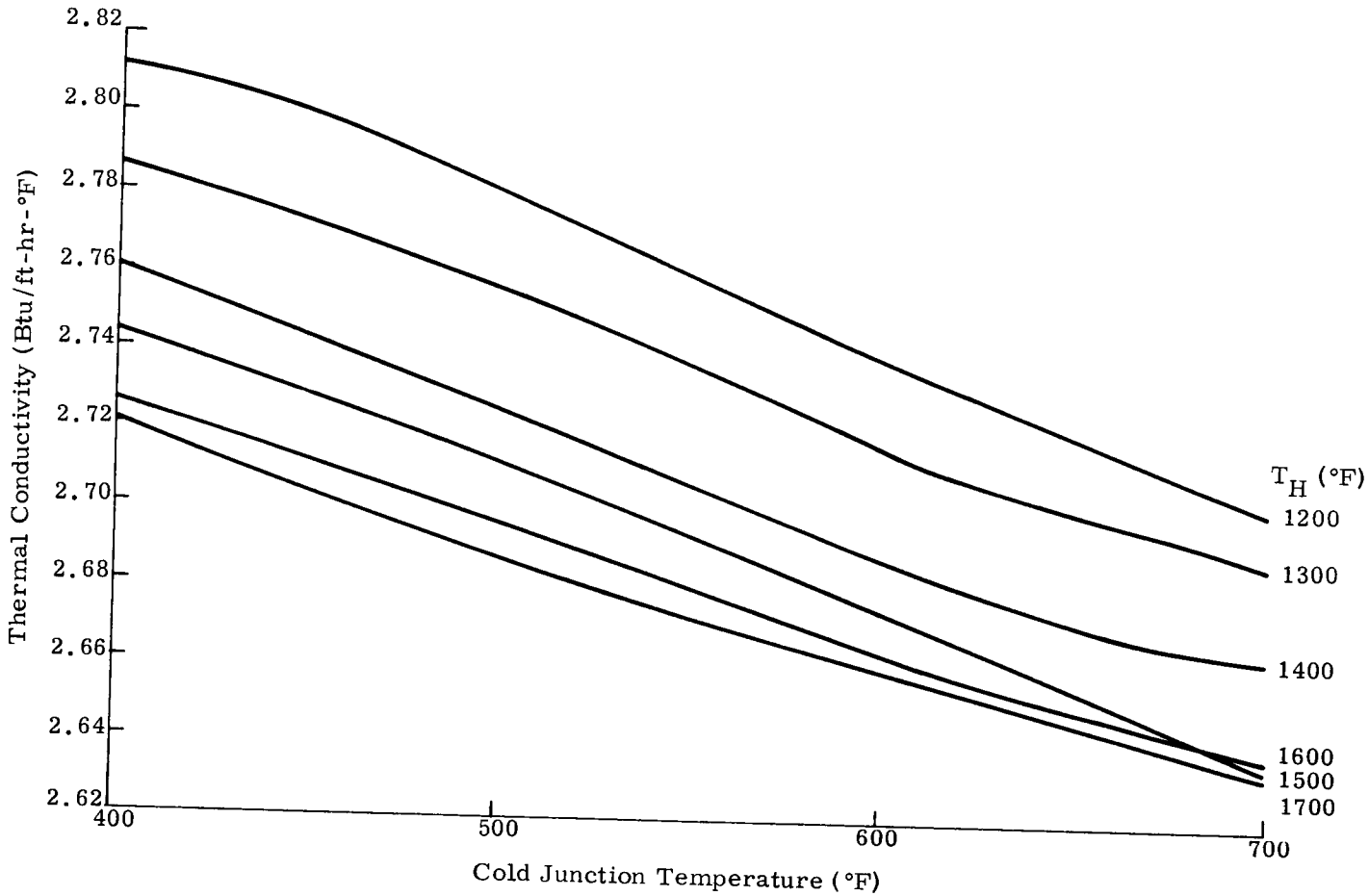

Fig. J-12. Integrated Average Thermal Conductivity for SiGe, P Element. Data Compiled 11/65

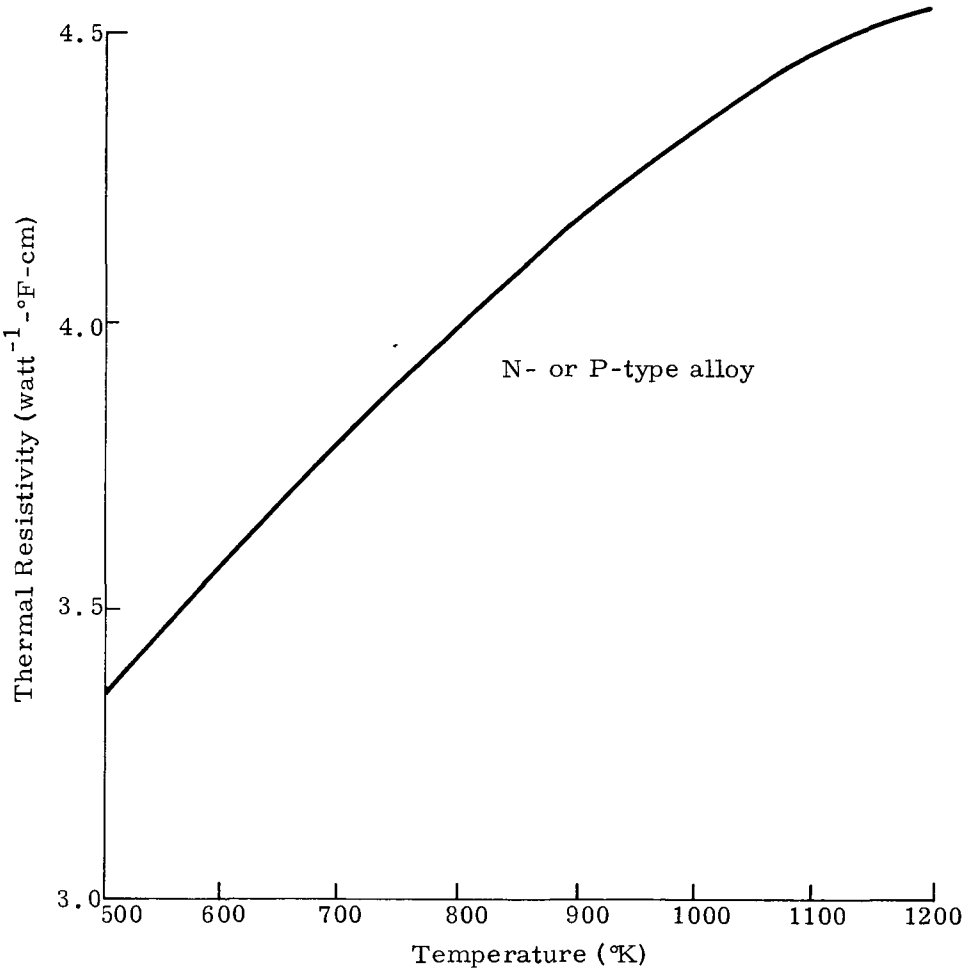

Fig. J-13. Thermal Resistivity of Silicon-Molybdenum Alloy

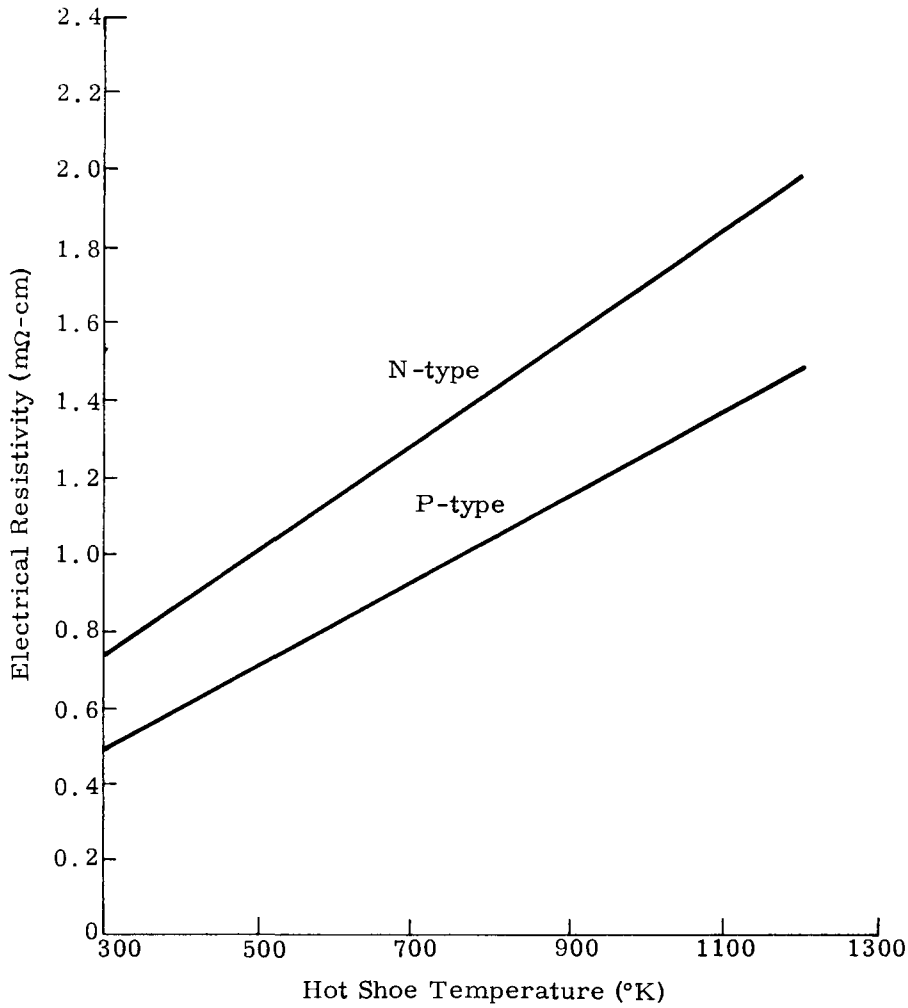

Fig. J-14. Electrical Resistivity of N-Type and P-Type Silicon-Molybdenum Alloy

APPENDIX K

CAPSULE SURFACE TEMPERATURE PARAMETRIC STUDY

During the program, a parametric analysis was developed to assist in readily determining capsule surface temperature for various configurations as a function of hot shoe temperature, heat source envelope area, capsule emissivity and hot shoe emissivity. The analysis is applicable to an RTG employing radiation heat transfer between the capsules and the module.

A. ANALYSIS AND RESULTS

1. Thermal Analysis

The equation describing radiant heat transfer between the heat source and the module is:

$$T_{cap} = \left(T_s^4 + \frac{q}{\sigma \bar{\epsilon} A_{env}} \right)^{1/4}$$

where

T_{cap} = capsule surface temperature, an unknown (°R)

q = heat transferred from capsules to hot shoes, a variable (Btu/hr)

σ = Stefan-Boltzmann constant = 0.171×10^{-8} Btu/sq ft-hr-°R^4

A_{env} = enveloped heat source area adjacent to hot shoes, a variable (sq ft)

$\bar{\epsilon}$ = effective emissivity between capsules and hot shoes, a variable

T_s = hot shoe surface temperature, a variable (°R)

This equation has been solved for capsule temperature as a function of heat flux, q/A_{env}, parametric in hot shoe (module) temperature (Fig. K-1).

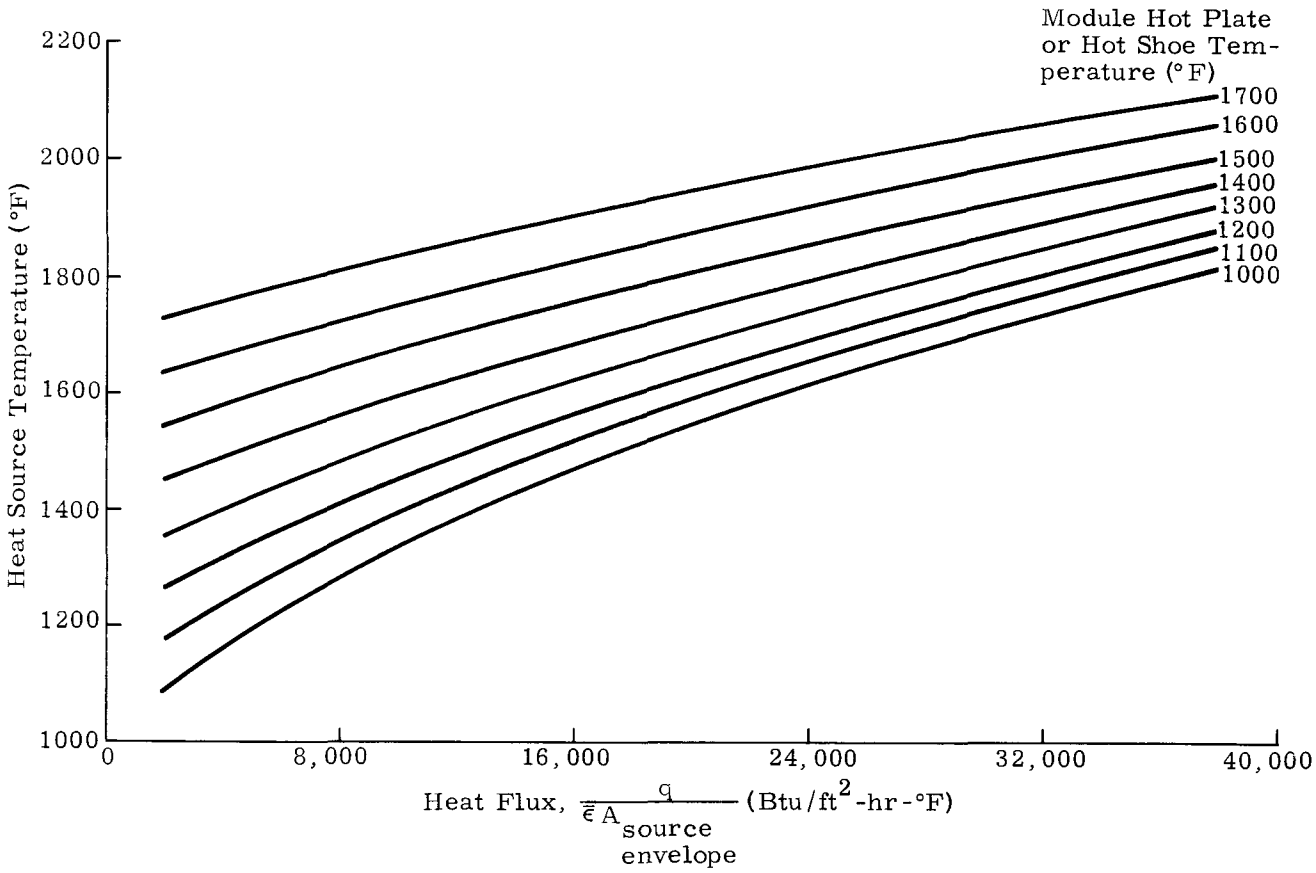

Fig. K-1. Heat Source Temperature Versus Impinging Heat Flux

2. Emissivity Analysis

The effective emissivity, $\bar{\epsilon}$, can be related to individual material emisivities by the expression

$$\bar{\epsilon} = \frac{1}{\frac{1}{\epsilon_{cap}} + \frac{1}{\epsilon_{s}} - 1}$$

where

ϵ_{cap} = capsule emissivity

ϵ_{s} = hot shoe or module hot plate emissivity

This equation was solved parametrically in ϵ_{cap} and ϵ_{s}, and the results are presented in Fig. K-2.

A likely material for the capsules will be Haynes-25. Variously measured emissivity data are given in Fig. K-3.

For the case of a SiGe generator, the SiMo hot shoes would be directly exposed to the fuel capsules. The emissivity of this material is presented in Fig. K-4 as a function of temperature.

3. Envelope Area Analysis for Cylindrical Heat Source

This is an analysis of the envelope area of a cylindrical heat source consisting of m bays of n capsules per bay. Defining the m x n matrix in this way provides a parametric tool for the analysis of several heat source configurations. The total number of capsules in the heat source is given by N = mn. A 12-capsule heat source having a 2 by 6 matrix (2 bays of 6 capsules per bay) has been illustrated in Fig. K-5. Heat transfer is assumed to occur radially from the perimeter of the bay, p, over the length of two bays (2 L_c).

Envelope area is therefore given by

$$A_{env} = mpL_c$$

Calculation of the heat transfer area depends on the type and quantity of fuel, number of capsules, fuel capsule configuration, and heat source configuration or matrix. Constraints have been made on these parameters to simplify the study and permit meaningful results to be obtained. These constraints are further described in the following paragraphs.

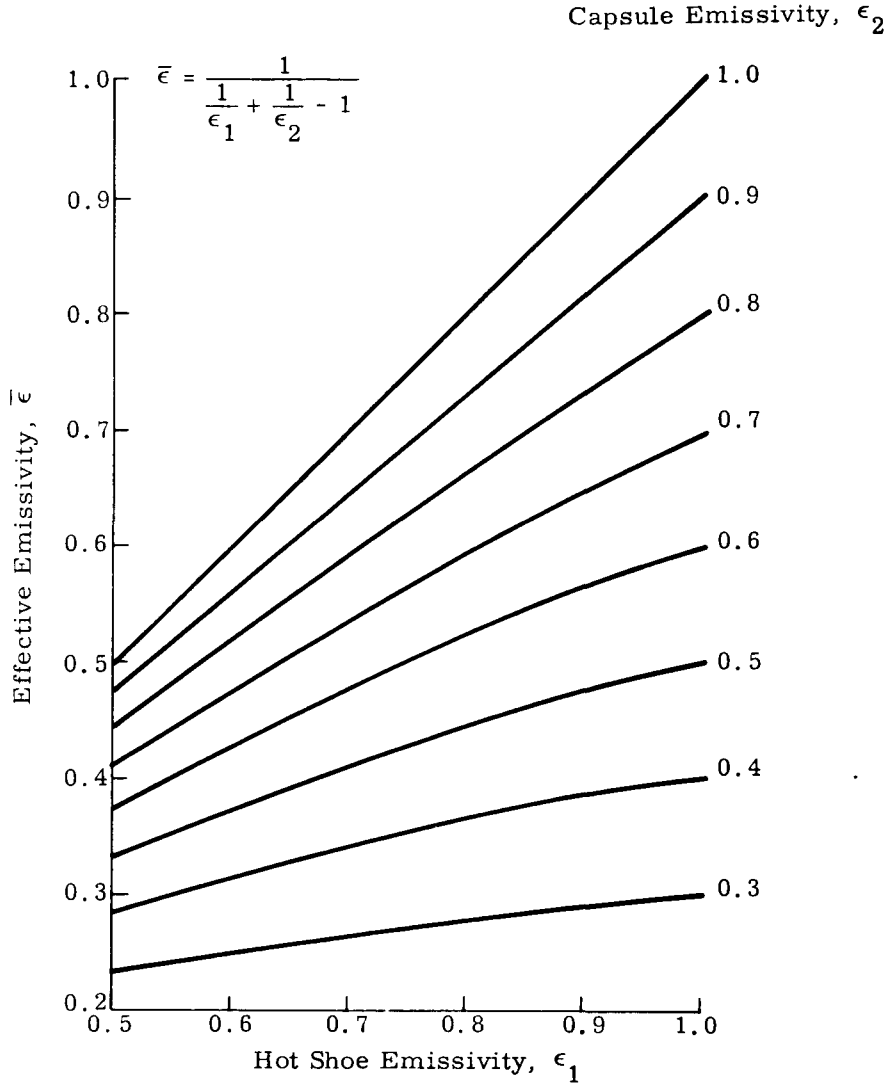

Fig. K-2. Effective Emissivity Versus Emissivity

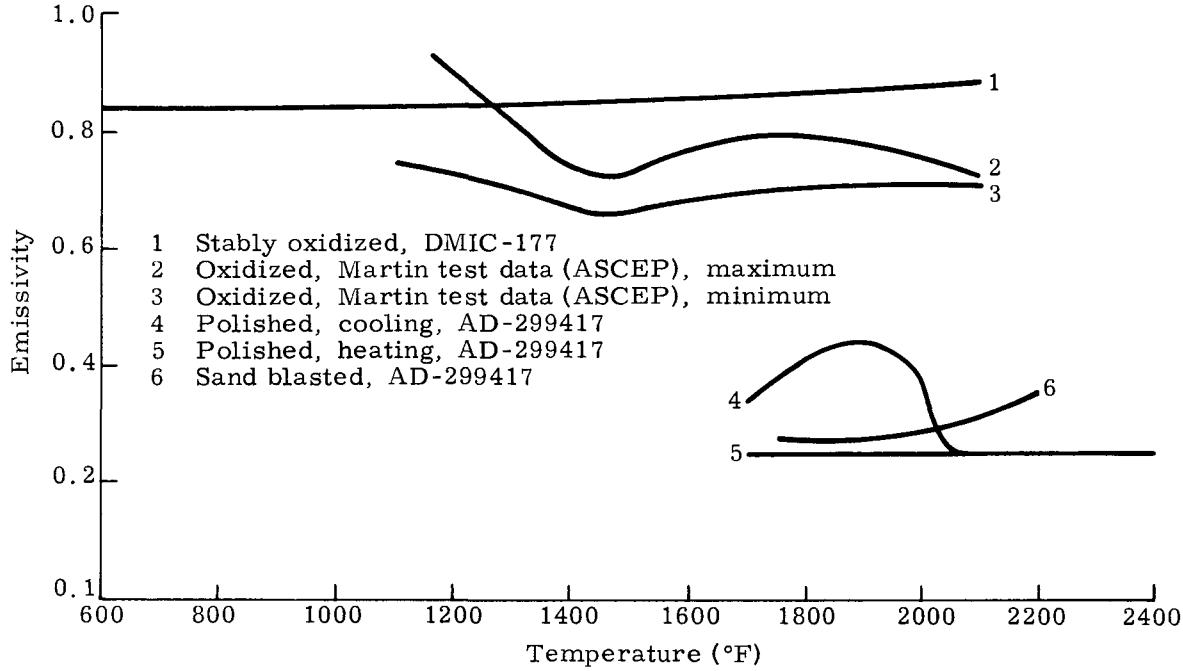

Fig. K-3. Emissivity Versus Temperature for Haynes-25

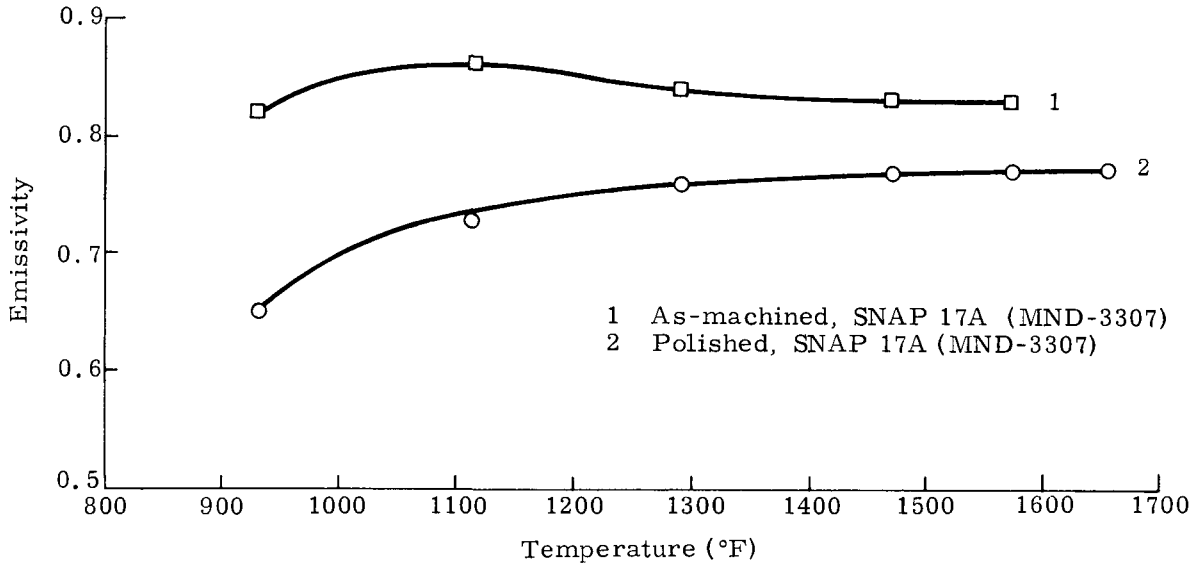

Fig. K-4. Emissivity Versus Temperature for SiMo

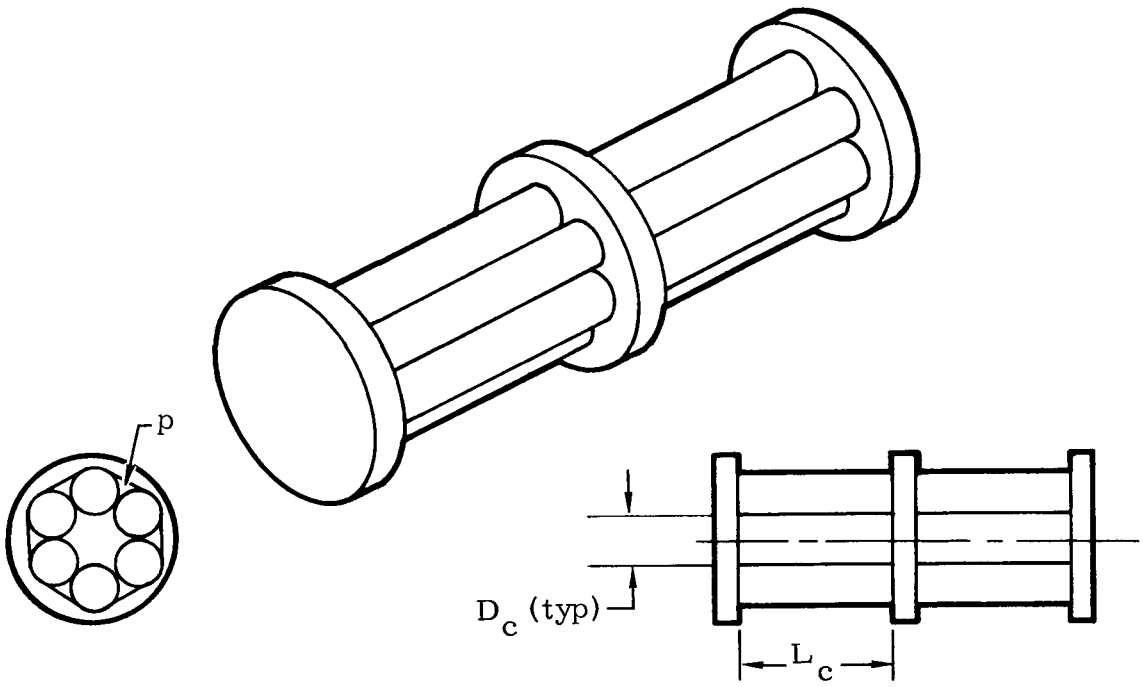

Fig. K-5. Cylindrical Heat Source Having 2 x 6 Matrix

It was first assumed that the fuel capsule is a right circular cylinder having an internal fuel volume defined by the fuel length, L_f, and diameter, D_f, and external dimensions, L_c and D_c. Actually, capsule wall thickness and end cap dimensions will depend largely on its required impact resistance, which is the subject of another study. As a simplification, it was assumed that $D_c = 1.30\ D_f$ and that $L_c = L_f + 0.75\ D_f$. This neglects minor area differences which arise from different impact requirements, and it gives all capsules under consideration nearly equal impact resistance.

In considering various heat source configurations, it will be assumed that the type of fuel and its required thermal output, q, at beginning of life are known. Two charts have been prepared to relate the number of capsules, N, the fuel volume, V_f, per capsule, the ratio L_f/D_f, and the fuel diameter, D_f. These charts are shown as Figs. K-6 and K-7, and their use is self-explanatory. The selection of L_f/D_f, D_f and N is somewhat discretionary at early stages of the heat source design and is based largely on past SNAP experience.

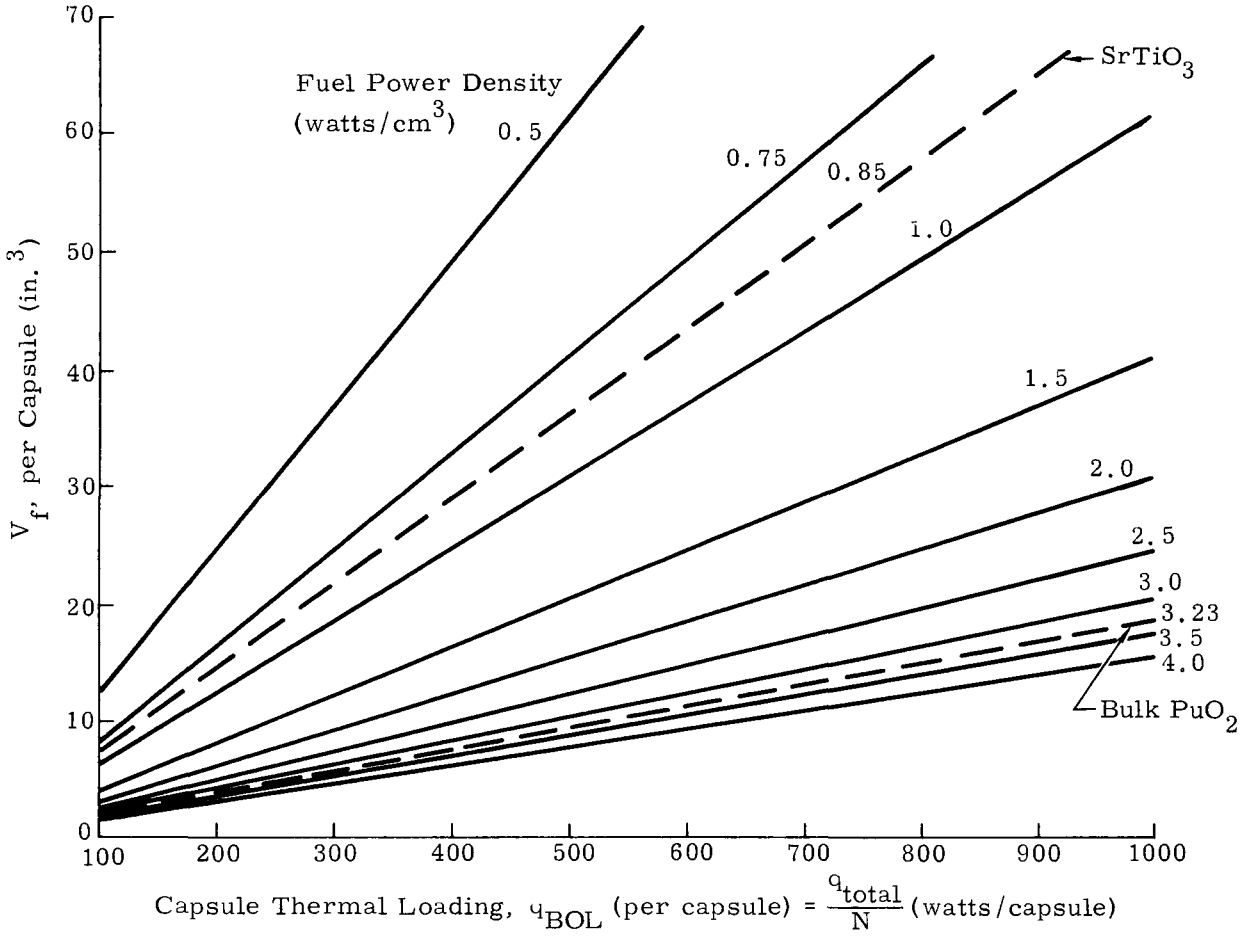

Fig. K-6. Fuel Volume Versus Capsule Thermal Loading

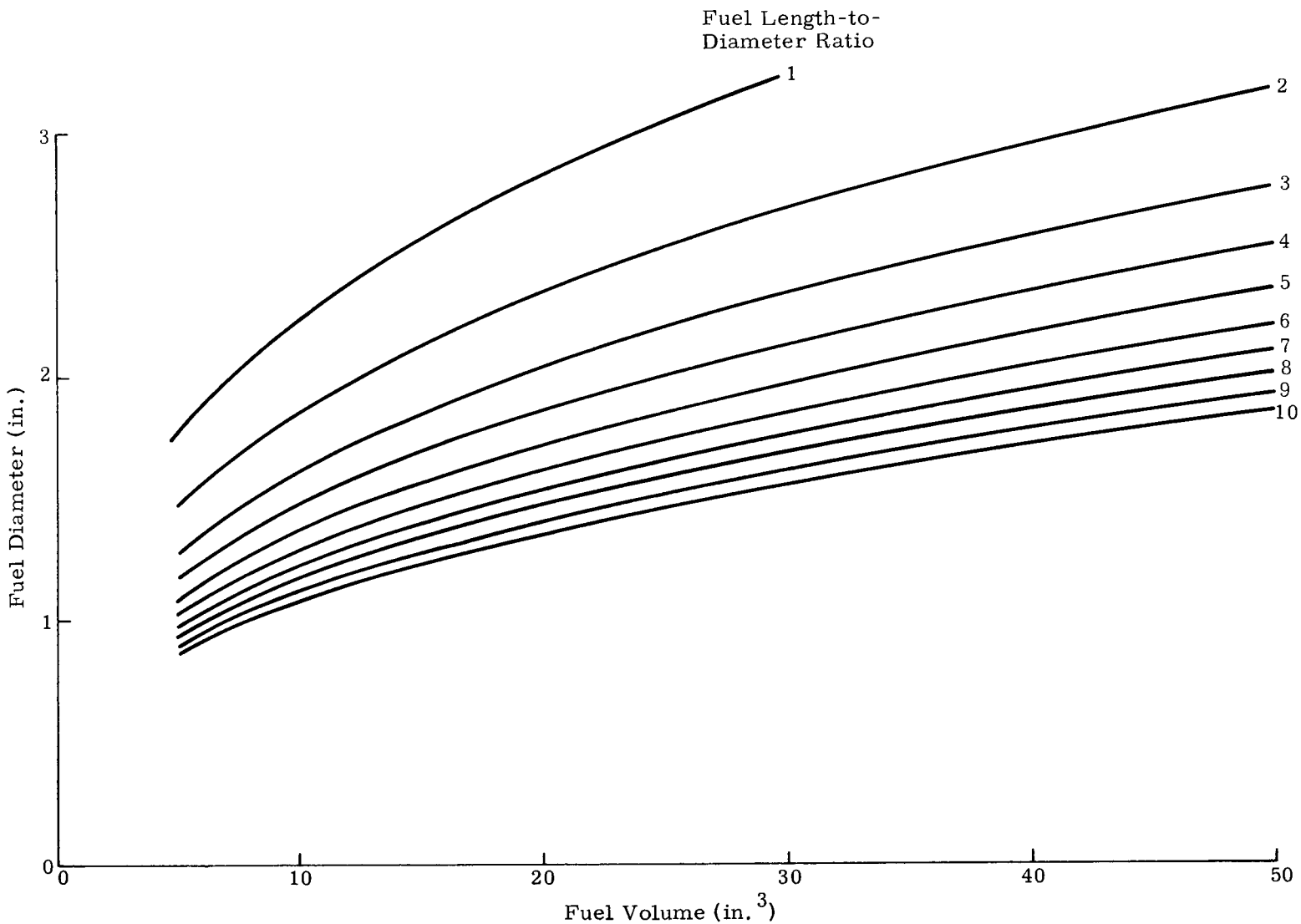

Fig. K-7. Fuel Diameter Versus Fuel Volume per Capsule

The envelope area of a single capsule is shown in Fig. K-8 as a function of L_f/D_f and V_f per capsule. The lateral area only has been plotted since no heat transfer is expected from the capsule end caps.

If the heat source consisted of a single row of N capsules, an N by 1 matrix would result; the total envelope area then would be N times the cylindrical area per capsule. However, if the heat source contains more than one capsule per bay, as was illustrated in Fig. K-5, the effective heat transfer area per capsule is reduced due to shielding by the adjacent capsules. A reduction factor, R, has been defined by the relationship

$$R = \frac{A_{effective}\ (\text{per capsule})}{A_{cylindrical}\ (\text{per capsule})}$$

which was found to be proportional to the perimeter, p, of a bay of n capsules divided by n times the perimeter of a single capsule. This yields the expression

$$R = \frac{1 + \pi/n}{\pi} \quad (\text{for } n \neq 1)$$

This expression holds true as long as the capsules are arranged in a close-packed circle; the factor R is independent of the capsule dimensions.

The reduction factor, R, has been plotted as a function of the number of capsules per bay in Fig. K-9, and the effective heat transfer, A_{eff}, per capsule has been plotted as a function of R and A_{cyl} in Fig. K-10. The total envelope area is given by A_{env} = N (capsules) x A_{eff} (per capsule) and is charted in Fig. K-11.

4. Envelope Area Analysis for Rectangular Heat Source

The fuel capsules may be arranged side by side in a rectangular matrix to form any of several rectangular heat source configurations. One configuration having a 2 by 6 matrix is illustrated in Fig. K-12. Here, heat transfer occurs from one or both of the large rectangular faces toward the thermoelectric module(s).

In considering the heat transfer area, it will be assumed that the capsules are close-packed and that all sides not facing a thermoelectric module are well insulated. The heat transfer area in the case wherein one side of the capsule is exposed is given by

$$A_{env} = ND_cL_c$$

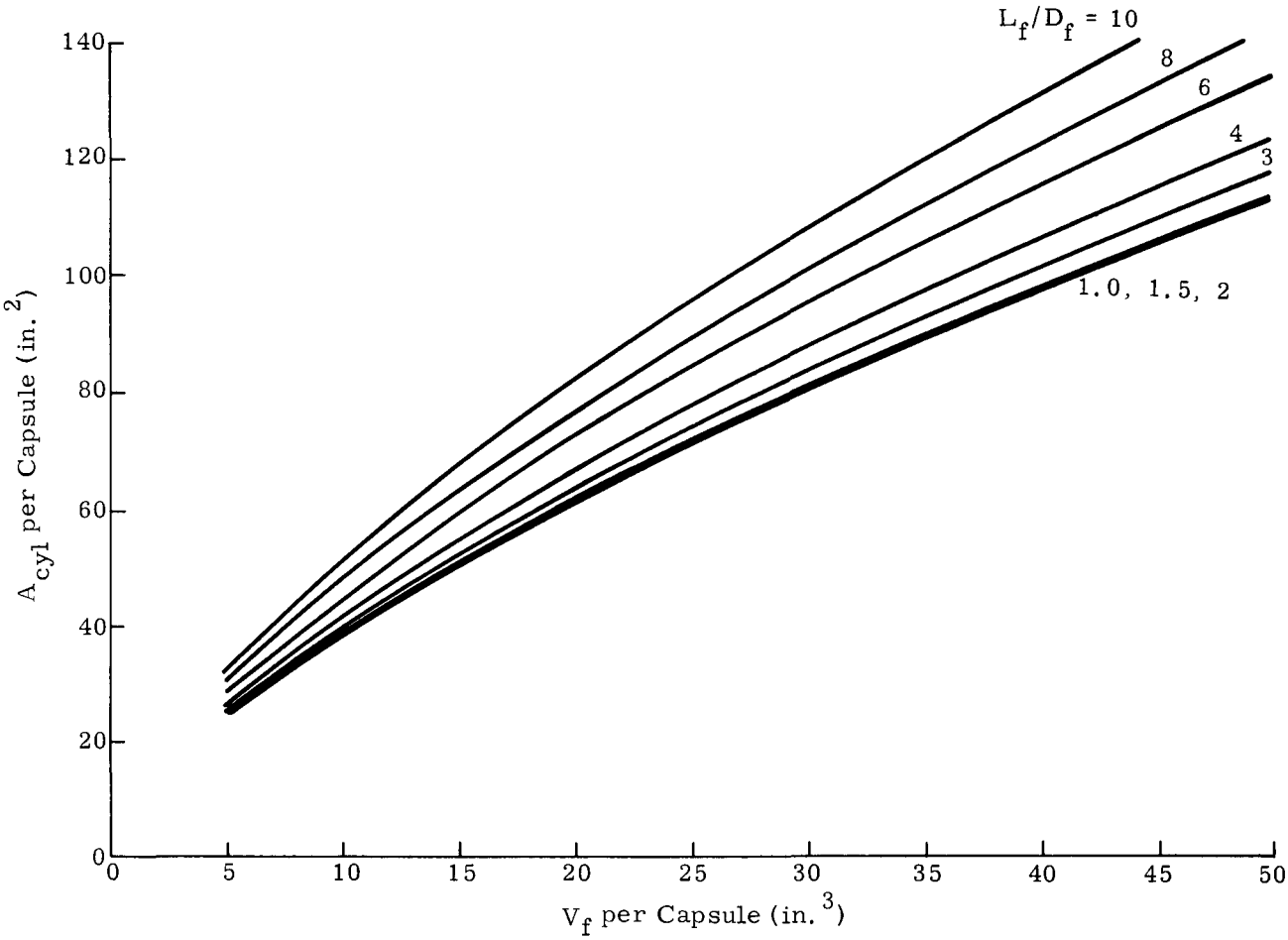

Fig. K-8. Capsule Cylindrical Area Versus Fuel Volume

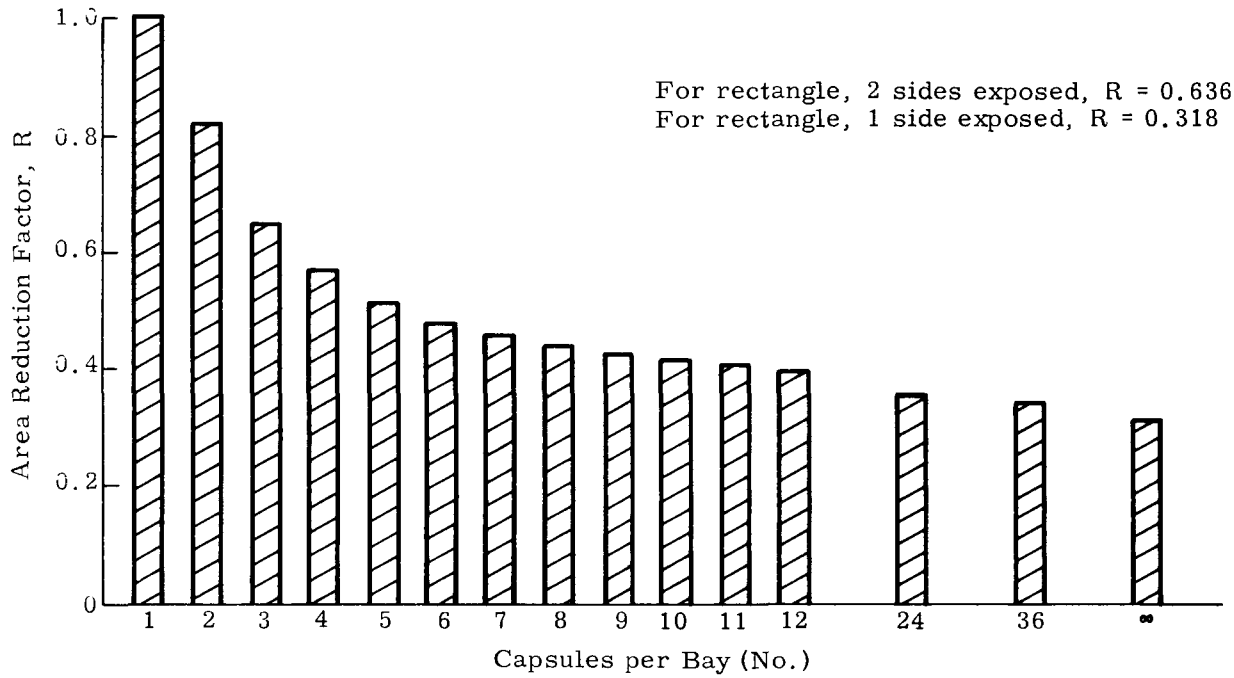

Fig. K-9. Area Reduction Factor for Cylinders Versus Number of Capsules per Bay

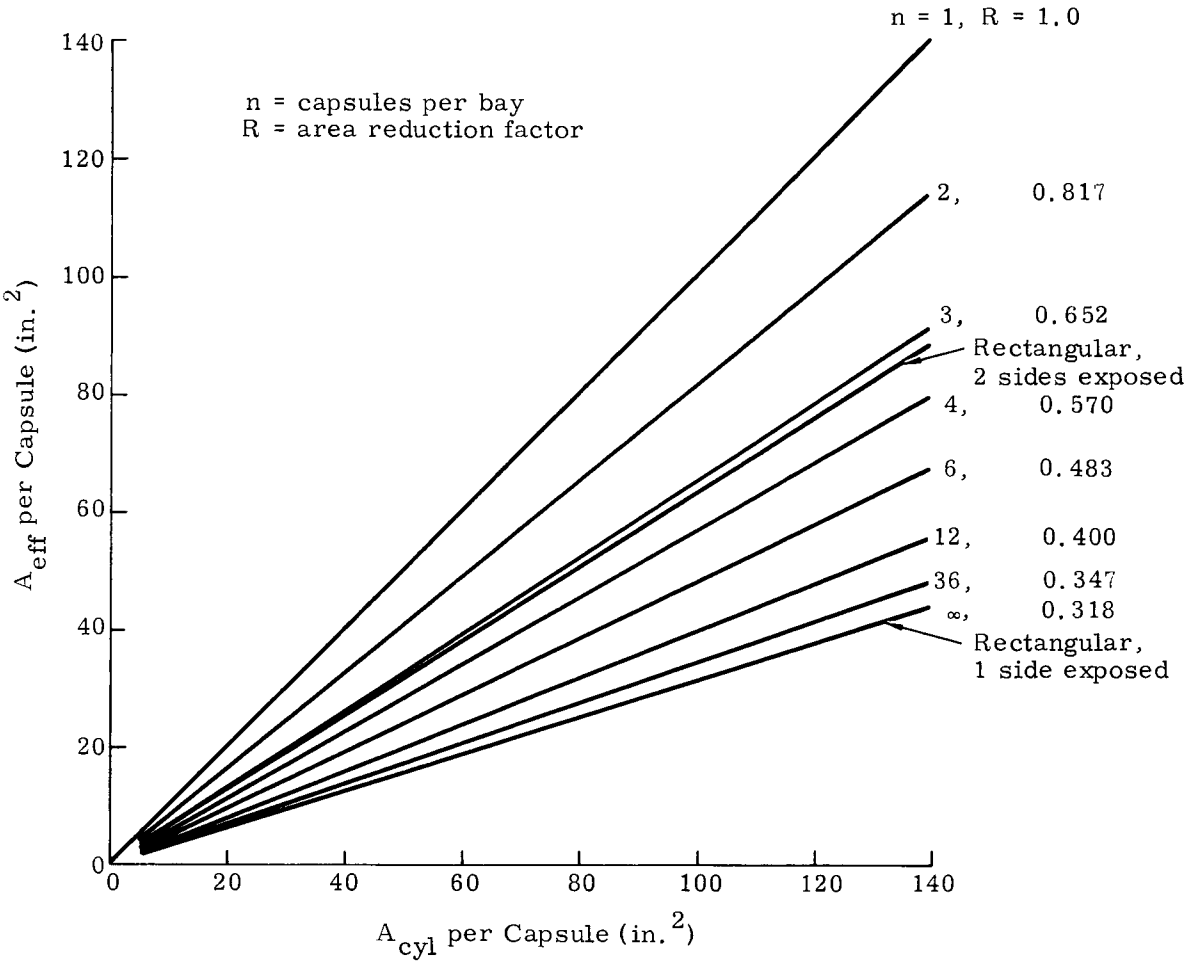

Fig. K-10. Effective Heat Transfer Area per Capsule

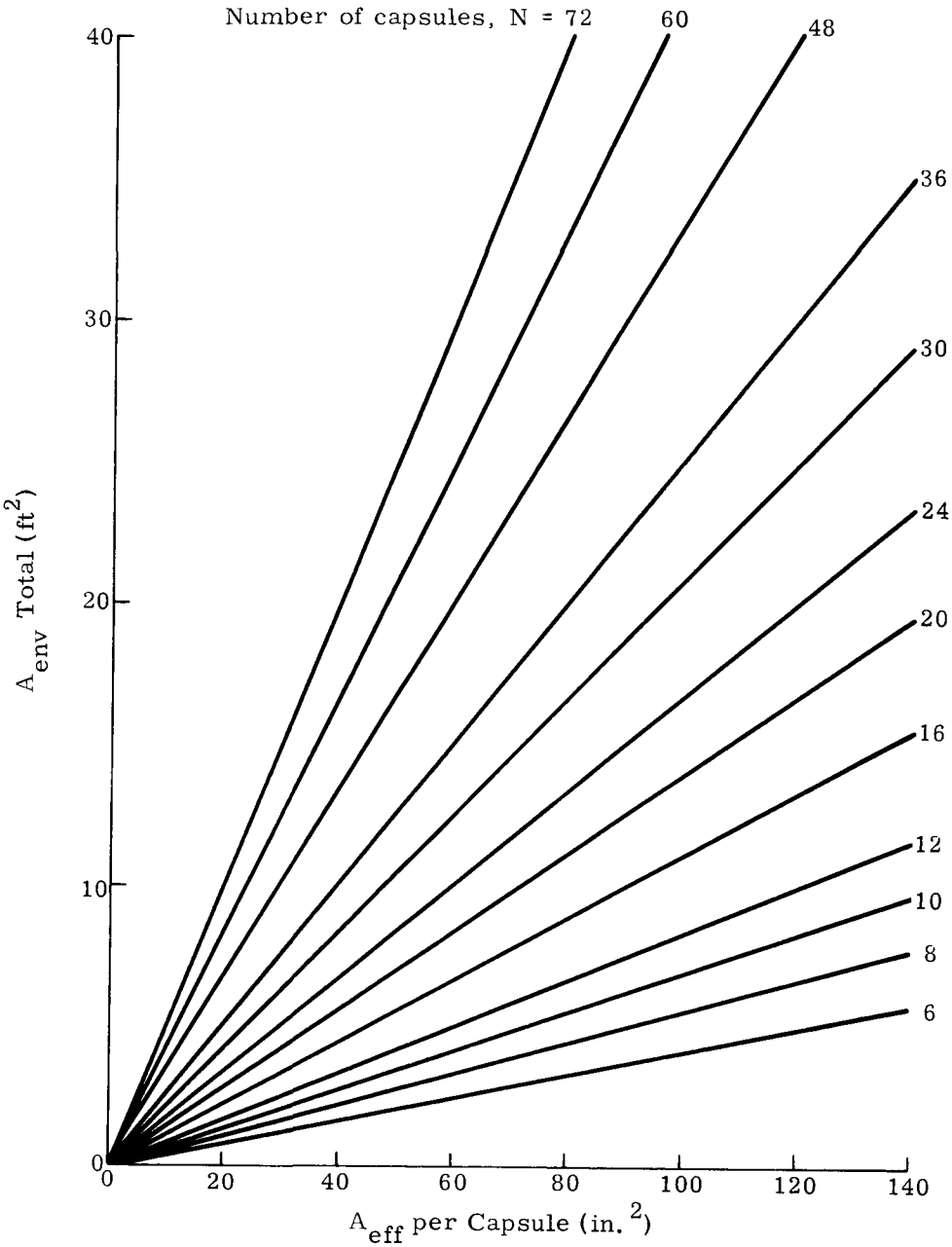

Fig. K-11. Heat Source Envelope Area

In the case with two sides exposed,

$$A_{env} = 2ND_cL_c$$

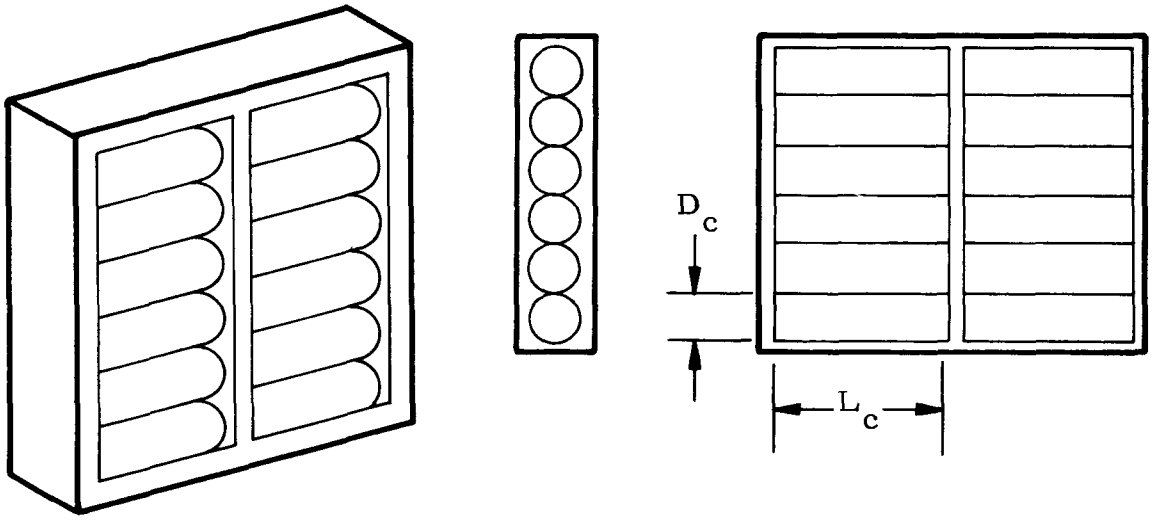

Fig. K-12. A Rectangular Heat Source Having 2 x 6 Matrix

The envelope area may be calculated from these equations, or it may be derived from Figs. K-10 and K-11 which were developed for the cylindrical heat source by considering

$$R = \frac{A_{eff}\text{ (per capsule)}}{A_{cyl}\text{ (per capsule)}} = \frac{D_cL_c}{\pi D_cL_c} = \frac{1}{\pi} \quad \text{(for one side exposed)}$$

or

$$R = \frac{2}{\pi} \quad \text{(for two sides exposed)}$$

These values of R have been tabulated in Fig. K-9.

B. USE OF RESULTS

From the analyses developed in the previous subsections, capsule temperature can be computed for various emissivities, heat fluxes and envelope areas.

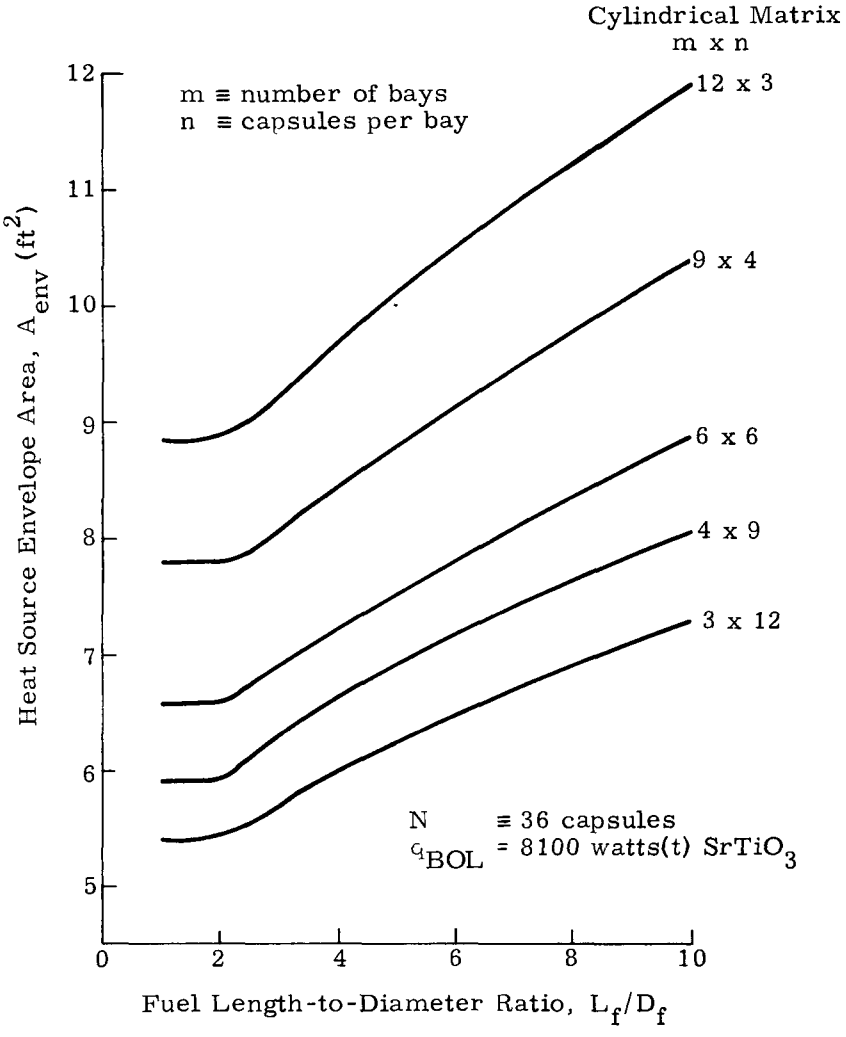

Fig. K-13. Heat Source Envelope Area

As an example, consider the case for a 250-watt(e) SiGe cylindrical generator requiring 8100 watts(t) of $SrTiO_3$ at beginning of life. Assume 24 capsules will be used, hot shoe temperature will be 1600° F, hot shoe emissivity will be 0.80 and capsule emissivity will be 0.60.

From these data, $\frac{q_{bol}}{N}$ = 337 watts/capsule. From Fig. K-6, fuel volume is 24.5 in.^{3}/capsule. From Fig. K-7, for $\left(\frac{L}{D}\right)_{fuel}$ = 6, fuel diameter is 1.73 inches and fuel length becomes 10.4 inches. With the assumption (mentioned previously that $D_c = 1.30\ D_f$ and $L_c = L_f + 0.75\ D_f$, capsule diameter and length are 2.25 and 11.7 inches, respectively.

From Fig. K-8, the cylindrical (lateral) area per capsule is 77 in.^{2}. With an array of 4 bays of 6 capsules each, Fig. K-9 shows that the area reduction factor is 0.483 (i.e., only 48.3% of each capsule lateral area will be directly viewed by hot shoes because of adjacent capsule blockage). From Fig. K-10, for n = 6 capsules per bay, the effective area per capsule is 37.2 in.^{2}. For all 24 capsules, Fig. K-11 indicates the total envelope area is 6.3 ft^2.

From Fig. K-2, for individual emissivities of 0.8, the effective emissivity, $\bar{\epsilon}$, is 0.665. Therefore, $\frac{q_{bol}}{A_{env}\bar{\epsilon}} = \frac{8100}{(6.3)(0.665)}$ = 1935 watts/ft^2 = 6600 Btu/ft^2-hr. From Fig. K-1, for a hot shoe temperature of 1600° F, the resulting capsule surface temperature is 1700° F.

A considerable variation in effective heat source envelope area can be obtained by simply permuting the arrangement of a fixed number of capsules. As an example, Fig. K-13 was developed for the case of N = 36 capsules initially containing 8100 watts of $SrTiO_3$ (0.85 watt/cc). Thus for an $\left(\frac{L}{D}\right)_{fuel}$ = 6, a 9 by 4 matrix gives an envelope area of 9.15 ft^2 while a 6 by 6 matrix yields 7.8 ft^2. The effect of these area changes on capsule temperature can be determined directly from Fig. K-1.

BLANK

APPENDIX L

SiGe VERSUS PbTe RTG COMPARISON

A. ANALYSIS

1. SiGe System

By use of the thermoelectric (T/E) analysis reported in Appendix Q and the hot junction temperature, cold junction temperature, RCA reported contact resistivity and element length chosen for this study (Table L-1), the following T/E performance figures hold for SiGe:

$$\eta_{T/E} = 5.43\%$$

$$\frac{A_N}{\text{element}} = 0.091 \text{ in.}^2 \text{ (series-parallel)}$$

$$\frac{A_P}{\text{element}} = 0.056 \text{ in.}^2 \text{ (series-parallel).}$$

The system overall efficiency (see Table L-1) is

$$*\eta_{o/a} = \eta_{T/E}\,\eta_{therm}\,\eta_i{}^2{}_R\,\eta_{reg} = (.0543)\,(0.83)\,(0.92)\,(0.995) = .0412 \text{ or } 4.12\%$$

The end-of-life fuel inventory is

$$q_{EOL} = \frac{P_{o,\,net}}{\eta_{o/a}} = \frac{250 \text{ watts}}{0.0412} = 6080 \text{ watts.}$$

The fuel volume ($SrTiO_3$) is given by (5-yr life)

$$V_{fuel} = \frac{q_{EOL}\, e^{\lambda t}}{\beta} = \frac{6080\,(1.132)}{0.85} = 8100 \text{ cm}^3 = 495 \text{ in.}^3.$$

The fuel weight is

$$W_{fuel} = \rho V_{fuel} = 3.83 \text{ gm/cm}^3 \times 8100 \text{ cm}^3 = 31,000 \text{ grams} = 68.5 \text{ pounds of fuel.}$$

*This value applies only to the cylindrical RTG and does not equal that of the selected reference configuration presented elsewhere.

TABLE L-1

SiGe Input Parameter Logic

Parameter	Value	Reason for Choice
Temperatures (°F)		
Hot junction (end of life)	1450	At beginning of 5-yr life with $SrTiO_3$, hot junction temperature will be ~1590° F, resulting in capsule surface temperature of ~1700° F. Maximum steady state capsule temperature cannot exceed ~1800° F; maximum hot junction temperature cannot exceed ~1650° F. Appears 1450° F end-of-life hot junction temperature is reasonable choice.
Cold junction	550	Higher cold junction would add to system weight because of decreasing efficiency; lower cold junction would create larger radiator areas. Final design of SiGe generator may use a different cold junction than 550° F but was reasonable choice for this study.
Radiator	505	Experimental data from RCA indicate 45° F temperature difference exists between the cold junction and radiator with Flexi-Mod concept.
Contact resistivity--end of life ($\mu\Omega$-cm^2)	1800	Extrapolation of RCA SNAP 17A data.
Efficiency (%)		
Thermal	83	Detailed thermal analysis of cylindrical layout on 250-watt program.
Joule	92	Calculation of typical I^2R losses in 250-watt generator.
Regulator	99.5	Experience with similar regulators.
Element length (in.)	0.75	Length is recommended by RCA for ease of fabrication; results in cross-sectional areas compatible with PuO_2 or $SrTiO_3$ fueled system. Also was length used for SNAP 17A.
Capsule weight	Equal to weight of fuel plus liner	SNAP 17A impact test data.

The fuel liner is assumed to be 10% of the fuel weight; i.e.,

$$W_{fuel} + W_{liner} = (1.1)\,(68.5) = 75.3 \text{ pounds.}$$

Based on data from the SNAP 17A impact test program, the required capsule weight will be that of the fuel plus liner. Therefore

$$W_{heat\ source} = W_{capsule} + W_{liner} + W_{fuel} = 150.6 \text{ pounds.}$$

It is arbitrarily assumed that the structure required to hold the fuel capsules together weighs 10% of the heat source weight or 15.1 pounds.

The thermoelectric module, including associated thermal insulation, was weighted in detail (see Table L-5 for breakdown) and totals 32.5 pounds.

The heat rejected by the radiator is

$$q_{rej} = q_{EOL} - P_o = 6080 - 250 = 5830 \text{ watts(t).}$$

For a casing diameter of 10 inches, a fin root thickness of 0.1 inch, six fins, a fin width of 6 inches, an emissivity of 0.85 and a radiator temperature of 505°F, the heat rejected per unit length of generator is

$$q/L = 141.8 \text{ watts/in.}$$

The required generator length is

$$L = \frac{q_{rej}}{(q/L)} = \frac{5830}{141.8} = 41 \text{ inches.}$$

For an aluminum radiator, a housing thickness of 0.125 inch is assumed. With a fin tip thickness of 0.030 inch, the total radiator weight (housing and six fins) is 28.2 pounds.

With a beryllium radiator, where a housing thickness of 0.080 inch was assumed, the total radiator weight is 16.9 pounds.

The beginning-of-life hot junction temperature will be about 1590° F. Since the increase through the hot shoe will be about 50° F, the corresponding capsule temperature (on the outer surface) is

$$T_{CAP} = \left(\frac{q_{BOL}}{\sigma \bar{\epsilon} A_{ENV}} + T^4_{hot\ shoe,\ BOL} \right)^{1/4} =$$

$$\left(\frac{6900 \times 3.41}{1710 \times 10^{-12}\ 0.65 \times 6.8} + 2100^4 \right)^{1/4} = 2180° \text{ R} = 1720° \text{ F.}$$

2. PbTe System

The PbTe (2N-3P) analysis is similar to the SiGe analysis. A summary discussion of the input parameter selection is given in Table L-2. Figures L-1 through L-3 are plots of thermoelectric efficiency, element diameters, and number of couples as a function of hot and cold junction temperatures for 2N-3P type material.

As mentioned in Table L-2, both a cold junction of 500° F and one of 400° F were investigated to determine the tradeoffs in weight, efficiency and size.

B. SUMMARY OF RESULTS

A performance summary of the SiGe and two PbTe systems is given in Table L-3 and a weight summary is given in Table L-4. For the SiGe system, a detailed weight breakdown of the module is given in Table L-5.

C. CONCLUSIONS

On a weight basis, the SiGe generator at 239 pounds is ~100 pounds lighter than the 400° F cold junction PbTe generator (System B) and ~150 pounds lighter than the 500° F cold junction PbTe generator (System A).

On an overall efficiency basis, the SiGe system is essentially equal to System B and 1/2% better (absolute) than System A.

On a size basis (all diameters are the same), the SiGe generator is superior with its length of 41 inches as compared to lengths of 58 and 77 inches on PbTe Systems A and B, respectively.

D. NOMENCLATURE

General		Subscripts	
A	area	BOL	beginning of life
L	generator length	ENV	envelope (of heat source)
N	number of couples	EOL	end of life
P	power	i^2R	joule
q	heat rate	N	N element

TABLE L-2

PbTe Input Parameter Logic

Parameter	Value	Reason for Choice
Temperatures (°F)		
Hot junction--end of life	970	At beginning of 5-yr life with $SrTiO_3$, hot junction temperature will be ~1050° F.
Cold junction	400 500	The 400° F cold junction results in high efficiency but large area and volume; 500° F cold junction results in smaller area and volume and lower efficiency.
Radiator	350 450	For cold end hardware similar to SNAP 19, radiator-to-cold junction temperature difference of 50° F is reasonable.
Contact resistivity--end of life ($\mu\Omega$-cm^2)	3000	Extrapolation of SNAP 11 module data.
Efficiency (%)		
Thermal	90	Carnot efficiency ratio using 83% value for SiGe generator.
Joule	92	Calculation of typical I^2R losses in 250-watt generator.
Regulator	99.5	Experience with similar regulators.
Element length (in.)	0.50	Previous SNAP experience shows half-inch elements are logical choice for space generator based on efficiency and weight tradeoffs.
Capsule weight	Equal to 80% of weight of fuel plus liner	Based on SNAP 19 impact test data.

CONFIDENTIAL

TABLE L-3

RTG Performance Summary ($SrTiO_3$)

	SiGe	PbTe	PbTe
Temperatures (°F)			
Cold junction	550	500	400
Hot junction			
End of life	1450	970	97
Beginning of life	1585	1050	1050
Capsule--beginning of life	1685	1300	1265
Efficiency (%)			
Thermoelectric	5.43	4.40	5.10
System	4.12	3.62	4.20
Element length (in.)	0.75	0.50	0.50
Contact resistivity--end of life ($\mu\Omega$-cm^2)	1800	3000	3000
Number of couples Series parallel	396	930	810
D_N--series parallel (in.)	0.340*	0.462	0.410
D_P--series parallel (in.)	0.267*	0.463	0.415
Fuel inventory--BOL (watts)	6900	7820	6750
Diameters (in.)			
Housing	10	10	10
Fin tip-to-tip	22	22	22
Generator length (in.)	41	58	77

*Assumed to be circular; in practice D-shaped elements will be used for close spacing.

TABLE L-4

RTG Weight Summary ($SrTiO_3$)

		System A*	System B**
	SiGe (lb)	PbTe (lb)	
Heat source	150.6	157.4	128.1
Heat source cage	15.1	15.7	12.8
Module	32.5	122.1	84.3
Inner housing seal	--	35.0	46.4
Insulation (outside of modules)	3.0	2.0	2.0
Housing plus fins			
Aluminum	28.2	39.1	49.0
Beryllium	16.9	23.0	30.0
Miscellaneous (4%)	9.6	15.7	13.4
Total--radiator			
Aluminum	239	387	336
Beryllium	228	371	317
Specific power--radiator (watts/lb)			
Aluminum	1.04	0.65	0.74
Beryllium	1.1	0.67	0.79

*System A--500° F cold junction.
**System B--400° F cold junction.

TABLE L-5

SiGe Module Weight Breakdown

Component	Weight (lb)
Hot shoe	6.44
Two tungsten shoes	4.55
Two copper wafers	1.32
Copper strap	1.28
Ceramic wafer	0.24
Stainless steel wafer	0.67
Steel cone	1.29
Aluminum cone	1.80
Insulation (Min-K 2000 + Dyna-Quartz)	9.39
Elements	5.56
Total	32.5

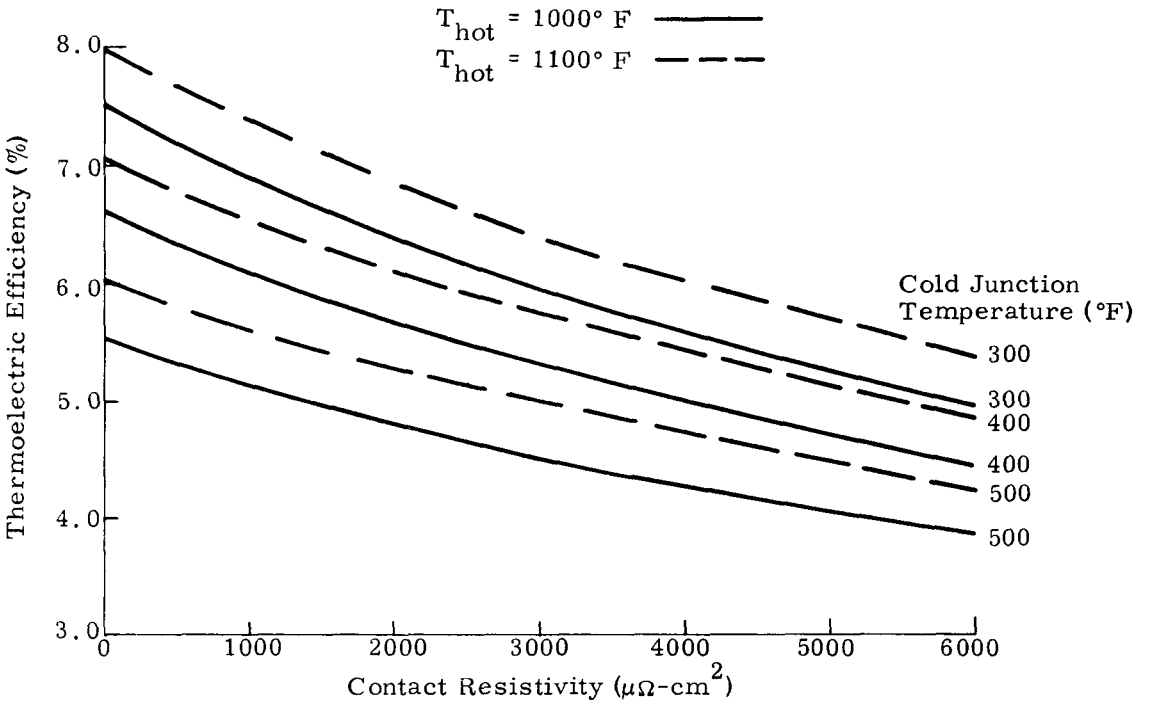

Fig. L-1. Thermoelectric Efficiency Versus Contact Resistivity for PbTe, 2N and 3P

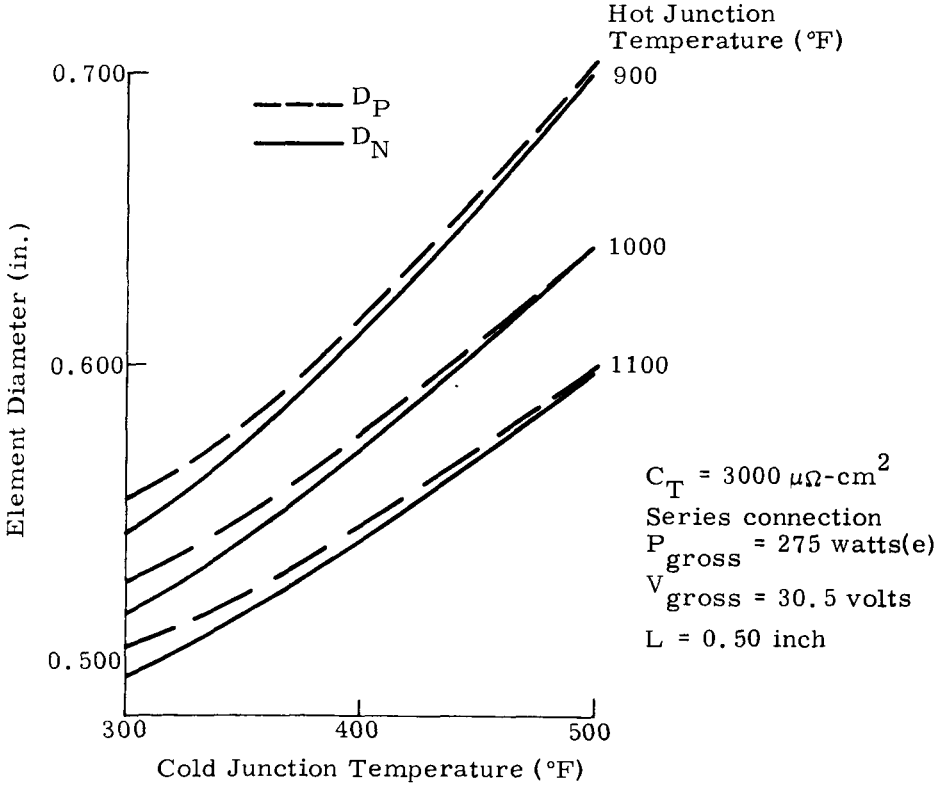

Fig. L-2. Element Diameter Versus Cold Junction Temperature for PbTe, 2N and 3P

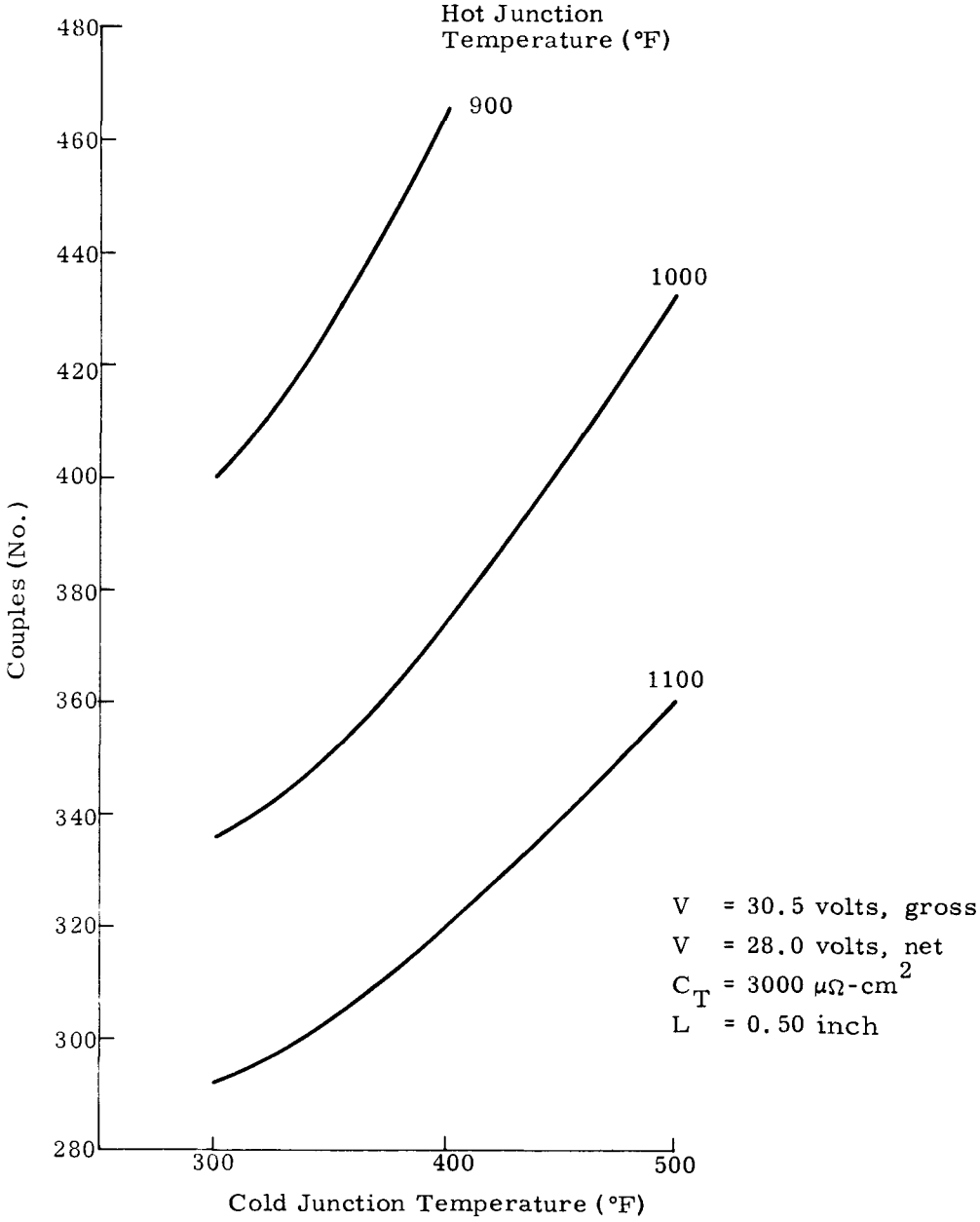

Fig. L-3. Number of Couples (series) Versus Cold Junction Temperature for PbTe, 2N and 3P

General

T	temperature
t	time
V	volume, voltage
W	weight

Subscripts

O	output
o/a	overall
P	P element
reg	regulator
rej	reject
T/E	thermoelectric
therm	thermal

Greek

β	fuel power density
$\bar{\epsilon}$	effective emissivity between capsule and hot shoe
η	efficiency
ρ	density
λ	fuel decay constant
σ	Stefan-Boltzmann constant

BLANK

APPENDIX M

SAMPLED PERTURBATION THEORY*

Exact solutions to the generalized heat transfer problem are practically confined to linear problems on boundaries of various simple shapes. A great deal of attention has therefore been given to the development of numerical methods for the solution of the heat transfer problem, particularly with the advent of the analog and digital computers.

The method of sampled perturbations as applied to the generalized heat flow problem, including absorption factor theory for enclosed gray body surfaces, is a combination of sampled-data theory and perturbation theory. This combination is used to obtain a digital computer solution to the problem.

Sampled perturbation theory has definite advantages over the two popularly used techniques, the backward difference scheme and the forward difference scheme. The forward difference scheme allows the user to save computer time by solving the heat flow equations explicitly. Unfortunately, this method becomes unstable when the sampling time is too large. The backward difference scheme is inherently stable, but unfortunately all the equations must be solved simultaneously. For complex problems, this means that the computing time will be a maximum, and very often the cost of the solution will become prohibitive.

The thermal model for sampled-perturbation theory is idealized with discrete thermal nodes. For each node a heat balance equation is constructed. Using perturbation theory, this equation is linearized. Once the differential equation is linearized, it can be easily operated on with LaPlace transforms thereby transforming the differential equation into an algebraic one. Application of the sampled-data theory to the equation for each node allows the user to derive a set of difference equations which are solved individually for each discrete time interval.

Until now most work has been done under the assumption that only the first emission of radiating nodes is considered. With the addition of absorption factor theory to the problem, the solution is generalized to include infinite numbers of emissions to radiating gray body enclosures. This relaxation of constraints to the problem has been found to be very important in doing transient analyses, especially when the view factors between various nodes are large.

---

* Rosenberg, Morton Jacob, "Sampled Perturbation Theory as Applied to Gray Body Enclosures for Numerical Solution of the Generalized Heat Transfer Problem," Presented at AIAA Unmanned Spacecraft Conference, March 1965.

A. RADIATION HEAT TRANSFER

Assume that N nodes are radiating with respect to each other. The following analysis will assume that all bodies are gray and that the total of N nodes makes up an enclosure. The latter assumption does not put a major restriction on the problem because space itself may be thought of as the all encompassing node. Therefore, in essence, an enclosure is always present in the problem.

A radiation thermal balance on the ith node gives:

$$Q_{net} = Q_{rad_{in}} - Q_{rad_{out}} \tag{M-1}$$

The rate of heat loss ($Q_{rad_{out}}$) will be equal to the amount of heat emission given by Node i.

The Stefan-Boltzmann law for blackbody radiation is

$$E_b = \sigma T^4 \tag{M-2}$$

If the radiant emission from a black surface were broken into its spectrum, it would be found that the emission is not equally distributed over all the wavelengths. Monochromatic emittance may be defined as the rate of energy emitted per unit area of emitting surface at a particular wavelength, λ ; then E_b may be shown to be:

$$E_b = \int_0^\infty E_{b,\lambda}\, d\lambda \tag{M-3}$$

The monochromatic blackbody emittance, E_b, is then some function of the wavelength λ. The Stefan-Boltzmann law applies only to blackbodies.

For a particular wavelength, the ratio of the monochromatic emittance of a nonblackbody to that of a blackbody is known as the monochromatic emissivity of the nonblackbody.

$$\epsilon_\lambda = E_\lambda / E_{b,\lambda} \tag{M-4}$$

A gray body is a special type of nonblackbody and is defined as one for which the monochromatic emissivity is independent of the wavelength of the emitted radiation. From this definition ϵ_λ in Eq (M-4) is a constant value for the entire wavelength under consideration. To solve for

E of the gray body substitution of Eq (M-3) into Eq (M-4) yields:

$$E \Big/ \int_0^\infty E_{b,\lambda} d\lambda = \epsilon \tag{M-5}$$

and from Eq (M-5) it is seen that

$$E = \epsilon E_b = \epsilon \sigma T^4 \tag{M-6}$$

which is the emittance of a gray surface.

To calculate the rate of heat loss from Node i, Eq (M-6) must be multiplied by the radiating area of Node i. This, therefore, gives:

$$Q_{rad_{out_i}} = \sigma \epsilon_i A_i T_i^4 \tag{M-7}$$

The heat entering Node i must now be considered. Heat transfer rates that consider first emissions only may induce large errors in temperature, particularly if nodes in the system are rather close to each other.

To solve the problem, an absorption factor, B_{ji}, must be defined. The absorption factor is the total fraction of the emission of the jth node which is absorbed by the ith node. The thermal balance equation for radiation then becomes:

$$Q_{net_i} = \sigma \sum_{j=1}^{N} \epsilon_j A_j B_{ji} T_j^4 - \epsilon_i A_i \sigma T_i^4 \tag{M-8}$$

It should be noted that this factor is only applicable to gray surfaces.

As derived in Appendix N,

$$B_{Ki} = \sum_{\ell=1}^{N} F_{KL} \rho_L B_{Li} + F_{Ki} \epsilon_i \tag{M-9}$$

Equation (M-9) now gives a total of n equations for K = 1, 2, 3, 4, . . . , n. It should now be noted that these equations are linear and that a determinant may be set up to solve each B_{Ki}. These equations take the form:

$$
\begin{aligned}
&(F_{11}\rho_1 - 1)B_{1i} + F_{12}\rho_2 B_{2i} + \ldots + F_{1i}\epsilon_i = 0 \\
&\quad\vdots \qquad\qquad \vdots \qquad\qquad \vdots \\
&F_{n1}\rho_1 B_{1i} + \ldots + (F_{nn}\rho_n - 1)B_{ni} + F_{ni}\epsilon_i = 0
\end{aligned}
\tag{M-10}
$$

This set of n linear equations can now be solved for the n unknowns B_{1i}, $B_{2i}, \ldots B_{ni}$.

Since an enclosure is assumed, all emission of a Node i must be absorbed by all other nodes. Therefore,

$$\sum_{j=1}^{N} B_{ij} = 1 \tag{M-11}$$

Putting this in a more useful form:

$$(1 - B_{ii}) = \sum_{\substack{j=1 \\ j\neq i}}^{N} B_{ij} \tag{M-12}$$

It can also be shown that the following relation must hold:

$$B_{Kj}\epsilon_K A_K = B_{jK}\epsilon_i A_K \tag{M-13}$$

Combining Eqs (M-12) and (M-13) with Eq (M-8) now allows the writing of the radiation heat balance equation in a more convenient form:

$$Q_{net_i} \equiv q_{R_i} = \sigma \sum_{\substack{j=1 \\ j\neq i}}^{N} B_{ji}\epsilon_j A_j T_j^4 - \sigma\epsilon_i A_i T_i^4 + B_{ii}\epsilon_i A_i T_i^4 \tag{M-14}$$

Substituting Eq (M-12) into Eq (M-13) gives:

$$q_{R_i} = \sigma \sum_{\substack{j=1 \\ j\neq i}}^{N} B_{ji}\epsilon_j A_j T_j^4 - \sigma\epsilon_i A_i T_i^4 + \epsilon_i A_i T_i^4 \left(1 - \sum_{\substack{j=1 \\ j\neq i}}^{N} B_{ij}\right) \tag{M-15}$$

Equation (M-15) becomes:

$$q_{R_i} = \sigma \sum_{\substack{j=1 \\ j \neq i}}^{N} B_{ji} \epsilon_j A_j T_j^4 - \sigma \sum_{\substack{j=1 \\ j \neq i}}^{N} B_{ij} \epsilon_i A_i T_i^4 \qquad \text{(M-16)}$$

Combining the two terms on the right side of the equation and applying Eq (M-13), it is seen:

$$q_{R_i} = \sigma \sum_{j=1}^{N} \epsilon_i A_i B_{ij} (T_j^4 - T_i^4) \qquad \text{(M-17)}$$

Equation (M-17) now becomes the heat transfer by radiation term to be considered in the following heat transfer balance equations.

B. CONDUCTION HEAT TRANSFER

The theory of heat flow by conduction has been developed from the fundamental equation:

$$q_c = - K A \frac{dT}{d\eta} \qquad \text{(M-18)}$$

When considering the numerical approximation nodal technique to a problem, the heat flow due to conduction between Nodes i and j becomes:

$$q_{c_{ij}} = K_{ij} A_{c_{ij}} (T_j - T_i) \qquad \text{(M-19)}$$

$$K_{ij} = \frac{1}{\frac{1}{K_c} + \frac{L_{ij} k_j + L_{ji} k_i}{k_i k_j}} \qquad \text{(M-20)}$$

where K_c is a contact coefficient and the $k_i k_j$ are thermal conductivities. Equation (M-19) may now be summed over j to account for all nodes in the system.

Substitution of Eq (M-20) into Eq (M-19) gives

$$q_{c_{ij}} = \frac{A_{c_{ij}} (T_j - T_i)}{\frac{1}{K_c} + \frac{L_{ij} k_j + L_{ji} k_i}{k_i k_j}} \qquad \text{(M-21)}$$

Once again, to denote conduction of the ith node with more than one other node, a summation over j is in order on the right side of Eq (M-21).

C. COMBINED HEAT TRANSFER

Assume a node of cubical dimensions, and write the heat balance equation for this node.

$$q_{in} - q_{out} + q_{int} = q_{stored} \tag{M-22}$$

The heat stored term may be written as:

$$q_{s_i} = W_i C_{P_i} \frac{dT_i}{d\tau} \tag{M-23}$$

Assuming that n nodes exist in the thermal model, the heat balance equation for the ith node may be written:

$$\sum_{j=1}^{n} A_{c_{ij}} K_{ij}(T_j - T_i) + \sum_{j=1}^{n} A_{co_{ij}} h_{ij}(T_j - T_i)$$

$$+ \sigma \sum_{j=1}^{n} A_{R_{ij}} B_{ij} \epsilon_i (T_j^4 - T_i^4) + q_i = W_i C_{P_i} \frac{dT_i}{d\tau} \tag{M-24}$$

the first term being conduction, the second being convection, and the third being radiation. Combining terms in Eq (M-24) gives:

$$\sum_{j=1}^{n} (A_{c_{ij}} K_{ij} + A_{co_{ij}} h_{ij}) (T_j - T_i) + \sigma \sum_{j=1}^{n} A_{R_{ij}} B_{ij} \epsilon_i (T_j^4 - T_i^4)$$

$$+ q_i = W_i C_{P_i} \frac{dT_i}{d\tau} \tag{M-25}$$

Now consider small changes or perturbations in the heat balance, Eq (M-25). These small changes will appear in the heat balance equation as an addition to each of the various terms of the equation considered as variables. Perturbations of a function g(X) that varies with X can be written as:

$$g(X) = \sum_{n=0}^{\infty} \epsilon^n g_n(X) \tag{M-26}$$

It should further be noted that $g_i(X)$ is a sufficiently smooth quantity such that:

$$\lim_{i \to \infty} \epsilon^i g_i(X) = 0 \tag{M-27}$$

In order not to diverge from standard nomenclature, the notation Δ will be used instead of $\Delta\epsilon$. The following perturbations may now be introduced into the heat balance, Eq (M-25). These perturbations may be considered as quite small and, therefore, the infinite series of Eq (M-26) may be truncated after the linear terms involved. Therefore, the terms to be added will appear as:

$$\left.A_{c_{ij}} K_{ij}\right\}_{t_i + \Delta t} = \left.A_{c_{ij}} K_{ij}\right\}_{t_i} + \Delta A_{c_{ij}} K_{ij}$$

$$\left.A_{co_{ij}} h_{ij}\right\}_{t_i + \Delta t} = \left.A_{co_{ij}} h_{ij}\right\}_{t_i} + \Delta A_{co_{ij}} h_{ij} \tag{M-28}$$

$$\left.T_i\right\}_{t_i + \Delta t} = \left.T_i\right\}_{t_i} + \Delta T_i$$

$$\left.B_{ij}\right\}_{t_i + \Delta t} = \left.B_{ij}\right\}_{t_i} + \Delta B_{ij}$$

Putting the perturbations into Eq (M-25) gives the following results:

$$\sum_{j=1}^{n} \left\{A_{c_{ij}} (K_{ij} + \Delta K_{ij}) + A_{co_{ij}} (h_{ij} + \Delta h_{ij})\right\}$$

$$(T_j + \Delta T_j - T_i - \Delta T_i) + \sigma \sum_{j=1}^{n} \left\{A_{R_{ij}} (B_{ij} + \Delta B_{ij}) (\epsilon_i + \Delta\epsilon_i)\right. \tag{M-29}$$

$$\left.\left[(T_j + \Delta T_j)^4 - (T_i + \Delta T_i)^4\right]\right\} + q_i + \Delta q_i = W_i C_{P_i} \frac{dT_i}{d\tau}$$

The magnitudes of T_i will now be considered as constants and the change in these values will come about by the change in ΔT_i. Therefore, although T_i is considered a constant, ΔT_i is not, and, therefore, T_i will take on new values as a result of ΔT_i. The perturbations in the thermal properties, namely, ΔK_{ij}, Δh_{ij}, ΔB_{ij}, $\Delta \epsilon_i$ and Δq_i may now be considered to be functions of the temperature of the specific nodes, or, if it is appropriate, to be functions of time.

With this fact in mind, Eq (M-29) may now be algebraically simplified:

$$W_i C_{P_i} \frac{d\Delta T_i}{d\tau} + \left\{ \sum_{j=1}^{n} \left(A_{c_{ij}} K_{ij} + A_{co_{ij}} h_{ij} + 4 B_{ij} \sigma A_{R_{ij}} \epsilon_i T_i^3 \right) \Delta T_i \right\} =$$

$$\left\{ \sum_{j=1}^{n} \left[A_{c_{ij}} (K_{ij} + \Delta K_{ij}) (T_j - T_i) + A_{c_{ij}} K_{ij} \Delta T_j \right.\right.$$

$$+ A_{co_{ij}} (h_{ij} + \Delta h_{ij}) (T_j - T_i) + A_{co_{ij}} h_{ij} \Delta T_j \qquad \text{(M-30)}$$

$$+ \sigma A_{R_{ij}} B_{ij} \epsilon_i (T_j^4 - T_i^4) + \sigma A_{R_{ij}} B_{ij} \Delta \epsilon_i (T_j^4 - T_i^4)$$

$$\left.\left. + \sigma A_{R_{ij}} \epsilon_i \Delta B_{ij} (T_j^4 - T_i^4) + 4 \sigma A_{R_{ij}} B_{ij} \epsilon_i T_j^3 \Delta T_j \right] \right\} + q_i + \Delta q_i$$

Allow:

$$\alpha_i = W_i C_{P_i}$$

$$\beta_i = \sum_{j=1}^{n} \left(A_{c_{ij}} K_{ij} + A_{co_{ij}} h_{ij} + 4 B_{ij} \sigma A_{R_{ij}} \epsilon_i T_i^3 \right)$$

$$f_i(t) = \sum_{j=1}^{n} \Big\{ A_{c_{ij}} (K_{ij} + \Delta K_{ij}) (T_j - T_i) + A_{c_{ij}} K_{ij} \Delta T_j$$

$$+ A_{co_{ij}} (h_{ij} + \Delta h_{ij}) (T_j - T_i) + A_{co_{ij}} h_{ij} \Delta T_j$$

$$+ \sigma A_{R_{ij}} (B_{ij} \epsilon_i + B_{ij} \Delta \epsilon_i + \epsilon_i \Delta B_{ij}) (T_j^4 - T_i^4)$$

$$+ 4 \sigma A_{R_{ij}} B_{ij} \epsilon_i T_j^3 \Delta T_j \Big\} + q_i + \Delta q_i$$

Then Eq (M-30) becomes:

$$\alpha_i \frac{d \Delta T_i}{d\tau} + \beta_i \Delta T_i = f_i(t) \qquad \text{(M-31)}$$

where it must be noted for the purposes of this analysis that

α_i = constant

β_i = constant

$f_i(t)$ = a function of time.

By noting the form of Eq (M-31), it becomes quite obvious that Eq (M-31) is linear in form. Since it is linear, it can be transformed by means of the LaPlace transform.

$$\mathcal{L} \left\{ \alpha_i \frac{d \Delta T_i}{dt} + \beta_i \Delta T_i \right\} = \mathcal{L} \left\{ f_i(t) \right\} \qquad \text{(M-32)}$$

Taking the LaPlacian of the left side of Eq (M-32) gives:

$$\mathcal{L} \left\{ \alpha_i \frac{d \Delta T_i}{dt} + \beta_i \Delta T_i \right\} = \mathcal{L} \left\{ \alpha_i S + \beta_i \right\} \mathcal{L} (\Delta T_i) \qquad \text{(M-33)}$$

Therefore, Eq (M-32) becomes:

$$\mathcal{L} \left\{ \alpha_i S + \beta_i \right\} \cdot (\Delta T_i) = \mathcal{L} \left\{ f_i(t) \right\} \qquad \text{(M-34)}$$

The LaPlace transformation of ΔT_i is then seen to be:

$$\mathcal{L}(\Delta T_i) = \mathcal{L}\{f_i(t)\} \cdot \left\{\frac{1}{\alpha_i S + \beta_i}\right\} \qquad \text{(M-35)}$$

Equation (M-35) is very important in the solution of the problem and may be represented pictorially from the standpoint of control system theory:

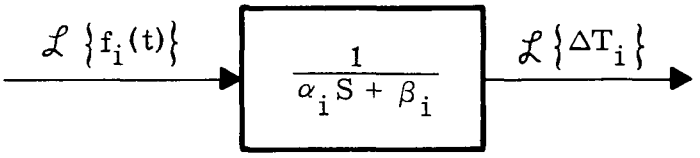

Fig. M-1

In Fig. M-1, $\mathcal{L}\{f_i(t)\}$ may be considered to be the input, $\frac{1}{\alpha_i S + \beta_i}$ may be thought of as the transfer function, and $\mathcal{L}\{\Delta T_i\}$ is to be considered as the output of the control system. The quantities T_i for $i = 1, 2, \ldots, n$ will change as a result of the perturbations ΔT_i for $i = 1, 2, \ldots, n$ during transient conditions. This leads to the point where sampled data theory must be introduced.

Pictorially, the introduction of sampling technique to the problem may be seen in Fig. M-2. In this figure, samplers are shown operating on the input $\mathcal{L}\{f_i(t)\}$ before it reaches the transfer function, and operating on the output, $\mathcal{L}\{\Delta T_i\}$. Note that the sampled properties are labeled with an asterisk, such as $\mathcal{L}\{f_i^*(t)\}$ and $\mathcal{L}\{\Delta T_i^*\}$.

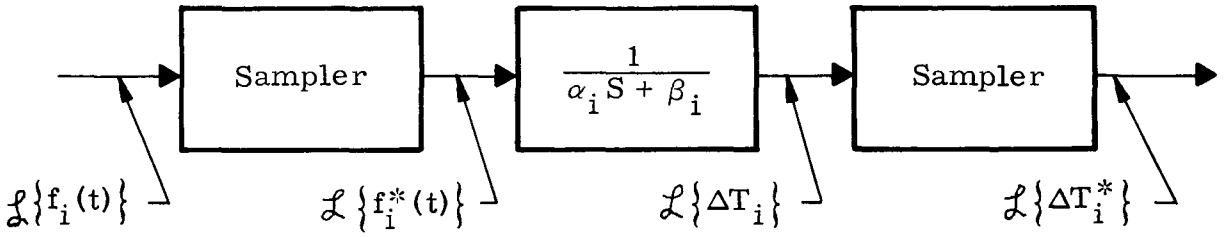

Fig. M-2

The short period of time during which perturbations occur is defined by P. The sampled function $f_i^*(t)$ can then be represented by:

$$f_i^*(t) = \delta_P(t)\, f_i(t) \tag{M-36}$$

where

$$\delta_P(t) = \sum_{n=0}^{\infty} \delta(t - nP) \tag{M-37}$$

Note that Eq (M-37) is defined as the unit impulse function occurring at nP times.

In order for $\frac{1}{\alpha_i S + \beta_i}$ (a continuous function) to operate on $\mathcal{L}\{f_i^*(t)\}$ (a sampled quantity), the latter must be smoothed out into a function which is defined at all points in the time domain, not only those points that are sampled. To accomplish the smoothing out of the pulsed data, $f_i^*(t)$, supplied to the transfer function, a zero order holding function is introduced. The zero holding function approximates the time function between two consecutive sampling instants ((j - 1) P and jP) by a zero order polynomial or a constant equal to the value of the function at the beginning of the interval in question. Higher order holding devices may be utilized, but the mathematical representations become more involved than those of the zero order hold. The holding device must now be inserted into the control circuit. The LaPlace transformation of a zero order holding function may be written

$$\overline{G(S)} = \frac{1 - e^{-PS}}{S} \tag{M-38}$$

With the insertion of this holding device, Fig. M-3 now represents the complete sampled data control system needed to complete the solution of this general heat transfer problem.

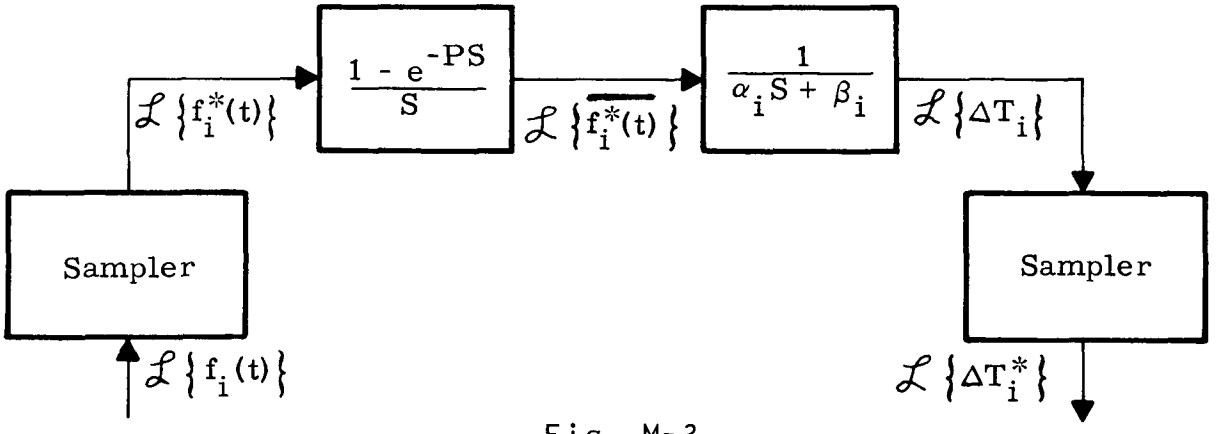

Fig. M-3

Using Eq (M-38), the equation for $\mathcal{L}(\Delta T_i)$ can be obtained:

$$\mathcal{L}(\Delta T_i) = \mathcal{L}\left\{f_i^*(t)\right\} \cdot \left(\frac{1 - e^{-PS}}{S}\right) \cdot \left(\frac{1}{\alpha_i S + \beta_i}\right) \tag{M-39}$$

The problem now centers itself in finding the LaPlace transformation of $f_i^*(t)$. It has been shown that

$$f_i^*(t) = \delta_P(t)\, f_i(t) \tag{M-40}$$

$$\delta_P(t) = \sum_{j=0}^{\infty} \delta(t - jP) \tag{M-41}$$

Then

$$f_i^*(t) = \sum_{j=0}^{\infty} f_i(jP)\, \delta(t - jP) \tag{M-42}$$

Now take the LaPlace transform of Eq (M-42) to give:

$$\mathcal{L}\left\{f_i^*(t)\right\} = \mathcal{L}\left\{\sum_{j=0}^{\infty} f_i(jP)\, \delta(t - jP)\right\} \tag{M-43}$$

$$\mathcal{L}\left\{f_i^*(t)\right\} = \sum_{j=0}^{\infty} f_i(jP)\, \mathcal{L}\left\{\delta(t - jP)\right\} \tag{M-43a}$$

This LaPlacian can easily be derived and leads to:

$$\mathcal{L}\left\{f_i^*(t)\right\} = \sum_{j=0}^{\infty} f_i(jP)\, e^{-jPS} \tag{M-44}$$

By taking the Z-transform, Eq (M-44) leads directly to a difference equation with respect to time. Taking the real part of the equation leads to an expression of the final form:

$$\Delta T_i(K) = \left[\frac{1 - e^{\left(-\frac{\beta_i P}{\alpha_i}\right)}}{\beta_i}\right] f_i(K - 1) + e^{\left(-\frac{\beta_i P}{\alpha_i}\right)} \cdot \Delta T_i(K - 1) \tag{M-45}$$

or

$$\Delta T_i(K) = \left[\Delta T_i(K-1) - \frac{f_i(K-1)}{\beta_i}\right] e^{\left(-\frac{\beta_i P}{\alpha_i}\right)} + \frac{f_i(K-1)}{\beta_i} \qquad \text{(M-46)}$$

allowing

$$\gamma_i(K-1) \equiv \frac{f_i(K-1)}{\beta_i} \qquad \text{(M-47)}$$

The final equation becomes:

$$\Delta T_i(K) = \left[\Delta T_i(K-1) - \gamma_i(K-1)\right] e^{\left(-\frac{\beta_i P}{\alpha_i}\right)} + \gamma_i(K-1) \qquad \text{(M-48)}$$

Equation (M-48) now represents the change in temperature for the second node in the thermal system within the K time interval. Adding this calculated value to the temperature of the second node in the last interval yields the new temperature considerations for this node. As is seen, the calculation of temperatures becomes one of explicit solutions with large time savings over implicit solutions; furthermore, this solution is inherently a stable one.

~~CONFIDENTIAL~~

BLANK

~~CONFIDENTIAL~~

APPENDIX N

ABSORPTION FACTORS

View factor determination for solving the generalized radiation heat transfer problem is also necessary for the solution of space vehicle temperatures. Direct use of the view factors in the radiation heat transfer problem was sufficient for close approximations for the simple early types of spacecraft. However, as spacecraft design becomes more complex, the accurate solution of the radiation portion of the heat transfer equation becomes more and more dependent on reflections within the system. Use of view factors only in the equations yields only initial impingement and absorption from one node of the thermal system to another and disregards the energy which is reflected from the impinging node to other portions of the thermal system. For accurate solution, a method for determining the infinite reflections within the system becomes very important. This method is that of absorption factor determination and is directly applicable to the nodal radiation heat transfer equations in use today.

Assume a thermal system exists which consists of N nodes forming an enclosure. Each node in the system is to be considered at a constant temperature, although all nodes in the system are not at the same temperature, and the properties of all nodes are totally diffuse. The total emissive power of a Node i in the system is represented by the value E_i.

According to the conservation of energy law, all energy leaving this node must be absorbed by the other nodes in the system. (It should be remembered that the system is an enclosure, and all energy remains within the system.) Therefore, B_{ij} is defined as the percent of energy emitted by i which is absorbed by the j node; this is known as the diffuse absorption factor. From this, it is seen that the sum of the emitted energy from the i node, taken over the entire system enclosure, must equal unity.

Therefore:

$$\sum_{j=1}^{N} B_{ij} = 1.0 \qquad (N-1)$$

The total energy emitted by the i node and absorbed by some other j node may be written as $E_i B_{ij}$. The energy emitted and absorbed by the j node is made up of two distinct quantities:

(1) That which goes directly to the j node and is absorbed

(2) That which is reflected from other nodes in the system and is eventually absorbed at the j node.

This may be written:

$$\begin{array}{l}\text{Energy emitted}\\ \text{from i being}\\ \text{absorbed at j}\end{array} = \begin{array}{l}\text{Direct energy}\\ \text{from i being}\\ \text{absorbed at j}\end{array} + \begin{array}{l}\text{Reflected energy}\\ \text{from i being}\\ \text{absorbed at j}\end{array} \qquad \text{(N-2)}$$

This equation simply states that the sum of the parts is equal to the total.

The direct energy emitted from i and absorbed at j is simply the percent of energy from i which impinges on j (shown, for the diffuse case, to be simply a geometric factor labeled the view factor, F_{ij}), multiplied by the percent of energy that the j node absorbed (α_{ji}). The absorptivity is constant with respect to all nodes.

Therefore:

$$\alpha_{ji} = \alpha_{j1} = \alpha_{j2} = \cdots = \alpha_{jN} = \alpha_j \qquad \text{(N-3)}$$

and, as shown by Kirchhoff's law:

$$\epsilon_j = \alpha_j \qquad \text{(N-4)}$$

where ϵ_j is the emissivity of the j node. The direct energy being absorbed at the j node may then be written:

$$\begin{array}{l}\text{Direct energy}\\ \text{from i being}\\ \text{absorbed at j}\end{array} = E_i F_{ij} \alpha_j = E_i F_{ij} \epsilon_j . \qquad \text{(N-5)}$$

Assume that a portion of the total energy emitted from the i node arrives and is absorbed by the j node after reflecting from other nodes in the system. Assume a general L node exists in the system from which a portion of the emitted energy reflects. The amount of energy from the i node which impinges on the L node is:

$$E_{iL} = E_i F_{iL} \qquad \text{(N-6)}$$

where E_{iL} is the amount of energy from the i node impinging on the L node.

The total amount of energy reflected from the L surface is:

$$E_L = \rho_L E_{iL} \tag{N-7}$$

or, simply:

$$E_L = \rho_L E_i F_{iL} \tag{N-8}$$

A certain percent of this energy will be absorbed by the j node, and by definition of the absorption factor, it is seen that this is equal to B_{Lj}. An important point is that the reflected energy from the L node may be treated as an emitted energy since the reflectance is constant in all directions (because it is a diffuse node). Therefore, the E_L shown in Eq (N-8) may be treated as an emittance from Node L, and the amount of energy which is absorbed by the j node from this node is $E_L B_{Lj}$.

Therefore:

$$\text{Reflected energy from the i node which is reflected from an L node and absorbed by j node} = E_i F_{iL} \rho_L B_{Lj} \tag{N-9}$$

Since this L node was a general node in the system, the total energy reflected which is absorbed by the j node from a simple summation over the entire system is as follows:

$$\text{Total reflected energy absorbed by the j node} = \sum_{L=1}^{N} E_i F_{iL} \rho_L B_{Lj} \tag{N-10}$$

Substituting all values solved for into Eq (N-2):

$$E_i B_{ij} = E_i F_{ij} \epsilon_j + \sum_{L=1}^{N} E_i F_{iL} \rho_L B_{Lj} \tag{N-11}$$

Since the summation is over the L and not i, it may be divided through by E_i, yielding:

$$B_{ij} = F_{ij} \epsilon_j + \sum_{L=1}^{N} F_{iL} \rho_L B_{Lj} \tag{N-12}$$

Equation (N-12) may be solved using standard matrix solutions and yields a closed form solution for the absorption factors within a system. The solution of all absorption factors within the system now allows the user to write the general radiation heat transfer equation for radiation in the general Node i, as:

$$C_{P_i} W_i \frac{dT_i}{d\tau} = q_i + \sigma \sum_{J=1}^{N} A_i \epsilon_i B_{ij} (T_j^4 - T_i^4) \qquad \text{(N-13)}$$

Where:

C_{P_i} = specific heat of Node i

W_i = weight of Node i

T_i = temperature of Node i

τ = time

q_i = internal heat of Node i

σ = Stefan-Boltzmann constant

A_i = area of radiation of Node i

ϵ_i = emissivity of Node i

B_{ij} = absorption factor from Node i to Node j

APPENDIX O

DESCRIPTION OF MARTIN T-CAP-III THERMO-CHEMICAL ABLATION PROGRAM

The T-CAP-III digital analysis program considers the ablative layer to consist of a char layer, pyrolysis zone, and virgin ablator material, each of which is characterized by a density profile. Where applicable, a melt layer is superimposed on the char. For general application, the capability of handling an arbitrary composite arrangement of ablator, insulator and internal structure is included. The surface boundary conditions include arbitrary heating functions versus time based on convection and radiant heating histories, heat input due to char combustion, heat blocked by mass addition to the boundary layer, radiative cooling from the hot char surface, and heat absorbed due to vaporization in the melt layer. A program option is also available to describe the surface boundary condition as a temperature-time history. Surface recession resulting from char oxidation or melt layer flow and/or vaporization is computed with a special option available to read in the surface recession rate as a function of heat input rate or surface temperature. The nonablator material properties input data are considered either in the equation form as power series functions of temperature or in curve form as arbitrary functions of temperature. The ablator thermal properties input data are considered in curve form as functions of both temperature and density. The rate of change of the ablative layer density profile and the resulting pyrolysis products mass flow are calculated utilizing reaction kinetics of the ablator with nth order reaction data based on thermogravimetric analysis. A summary of applicable equations and required material property inputs is contained in Tables O-1 and O-2.

TABLE O-1

Summary of Ablation Equations in T-CAP III

Purpose	General Equations
Surface heat balance Section 1	$k \left(\frac{\partial T}{\partial x}\right)_{surface} = h_{bl} (H_S - H_W) + \dot{q}_r - \dot{m}_v M (H_S - H_W) \pm r_c \rho_c \Delta H_r - \sigma \epsilon T_W^4$
Ablative layer heat balance Section 2	$\rho C_p \frac{\partial T}{\partial t} = \frac{\partial}{\partial x}\left(k \frac{\partial T}{\partial x}\right) - \dot{m}_v (x, t)\, C_{p_g} \frac{\partial T}{\partial x} + f \rho_p L_p \frac{\partial \lambda}{\partial t}$
Ablator degradation Section 3	$\frac{\partial \lambda}{\partial t} = - k_r \lambda^n$ where $= \frac{\rho - \rho_c}{\rho_p - \rho_c}$, $k_r \quad A e^{-E/RT}$, n = reaction order $\rho(x, t)\, \lambda = \lambda (x, t)(\rho_p - \rho_c) + \rho_c$ $\dot{m}_v (x, t) = - f \rho_p \int_0^x \frac{\partial \lambda}{\partial t}\, dx$ where $f = \frac{\rho_p - \rho_c}{\rho_p}$
Surface recession Section 4	Burning rate limited $r_c = \frac{\left[P_e C_{O_2}\right]^n}{\rho_c} k_1 e^{-k_2/T}$ where k_1 and k_2 are burning rate constants Oxygen diffusion limited $r_c = \frac{h_{net} L_e \left[C_{O_2}\right]_o \left[W_o / W_{O_2}\right]}{\rho_c}$ Flow $r_{flow} = \int_0^y \frac{1}{R} \frac{d}{dx} (u R)\, dy$ where $u = \tau \int_0^y \frac{dy}{\mu} + \frac{dp}{dx} \int_0^y \frac{y}{\mu}\, dy$ τ = aerodynamic shear stress μ = melt viscosity dp/dx = local pressure gradient R = body radius Vaporization $r_{vap} = \frac{h_{net}}{\rho_{melt}} \frac{1}{M\left(\frac{p_\ell}{p_v}\right) - 1}$ where $M = \frac{\text{Molecular weight of air}}{\text{Molecular weight of vapor}}$ p_ℓ = local ambient pressure p_v = vapor pressure at ablating surface
Internal structure and insulation heat balance Section 5	$\rho C_p \frac{\partial T}{\partial t} = \frac{\partial}{\partial x}\left(k \frac{\partial T}{\partial x}\right) + \frac{\partial}{\partial y}\left(k \frac{\partial T}{\partial y}\right)$

TABLE O-2

Material Properties

Material	Property
Ablator	
Virgin material	Density Specific heat Thermal conductivity
Pyrolysis zone	Activation energy Rate constant Reaction order Mass fraction (total pyrolysis) Molecular weight of gas Enthalpy of gas Heat of pyrolysis
Char layer	Density Specific heat Thermal conductivity
Surface	Emissivity Combustion rate constant Combustion activation energy Heat of combustion Heat of vaporization or sublimation Heat of melting Melt viscosity Molecular weight of vapor
Insulation and Structure	Density Specific heat Thermal conductivity Emissivity Coolant enthalpy

~~CONFIDENTIAL~~

BLANK

~~CONFIDENTIAL~~

APPENDIX P

DISPERSION ANALYSIS

Chapter VII has discussed the importance of restricting dispersions to a tolerable level measured in plus or minus a few hundred miles. However, the burden of proof in actually achieving such restrictions can only be expressed in terms of the confidence level placed on the dispersion itself. To this end, statistical theory lends itself quite readily by actually assigning confidence levels to impact patterns. It is the purpose of this appendix to present an outline of the basic theory and analytic suppositions that have been used in the generation of dispersion contours.

A. THEORETICAL BACKGROUND

Assuming that linear theory holds, the covariance matrix of errors can be obtained at any time, t_j, provided that the covariance matrix at some earlier time, t_i, is known. The equation relating these errors is

$$\phi(t_j, t_i)\, CV_{t_i}\, \phi^T(t_j, t_i) = CV_{t_j} \qquad \text{(P-1)}$$

where $\phi(t_j, t_i)$ is the sensitivity or state transition matrix from time t_i to time t_j, $\phi^T(t_j, t_i)$ is the transpose of this matrix, and CV_{t_i} is the covariance matrix at time t_i. In Eq (P-1) and subsequent discussion it should be understood that the reference of time can be interchanged to a reference of constant altitude as well. The following discussion, however, will refer to the time reference.

The covariance matrix, CV_{t_j}, represents the state error at some time t_j that can be associated with a nominal trajectory.

A sightly different form of Eq (P-1) is obtained when tracking data are factored into the system. In this case a "best estimate" of the nominal trajectory can be obtained via weighted least squares methods by using these tracking data. Filtering techniques have been developed, where linear theory holds, to predict the covariance matrix that is associated with the predicted nominal trajectory. Thus, if tracking data are taken until some time t_i there will exist a nominal trajectory

and a tracking covariance matrix, $TRCV_{t_i}$, based on these data. If no further data are recorded and one is interested in knowing what the covariance matrix of errors is at some later time t_j, this can be obtained by using (P-1) to obtain

$$\phi(t_j, t_i)\,(TRCV_{t_i})\,\phi^T(t_j, t_i) = CV_{t_j}. \qquad \text{(P-2)}$$

If no other errors are introduced into the system, Eq (P-2) is sufficient to determine the errors at any time t. Unfortunately, when a velocity impulse is added to the velocity of the nominal trajectory at some time t_o, new errors are introduced into the system. Some of the questions that naturally arise from such a stituation are:

(1) What type of errors are actually introduced into the system?

(2) What type of a covariance matrix representation would these errors have?

(3) What is the total error at time t_o? (That is, how is this new covariance matrix added to the tracking or state covariance matrix?)

(4) How is the total error obtained at some later time?

The following analysis is designed to answer these questions.

B. ANALYTIC ANALYSIS

1. Shutoff Error

Due to the uncertainty in the burn time, there exists an error in the magnitude of the velocity impulse vector. This error is in the same direction as the ΔV vector, and the magnitude of the error can be represented by taking a percentage of the magnitude of the ΔV vector. Assume CA represents the appropriate percent.

The ΔV vector is defined as

$$\underline{\Delta V} = \Delta\dot{x}\,\underline{i} + \Delta\dot{y}\,\underline{j} + \Delta\dot{z}\,\underline{k} \qquad \text{(P-3)}$$

where i, j, k are orthogonal unit vectors in the base or reference system. $\Delta\dot{x}$, $\Delta\dot{y}$, and $\Delta\dot{z}$ are the components of the ΔV vector in this reference system. Another orthogonal unit vector (called prime) is

$$i' = \frac{\vec{\Delta V}}{|\Delta V|} = a_1 \underset{\rightarrow}{i} + a_2 \underset{\rightarrow}{j} + a_3 \underset{\rightarrow}{k}$$

$$\underset{\rightarrow}{j'} = b_1 \underset{\rightarrow}{i} + b_2 \underset{\rightarrow}{j} + b_3 \underset{\rightarrow}{k} \qquad \text{(P-4)}$$

$$\underset{\rightarrow}{k'} = \underset{\rightarrow}{i'} \times \underset{\rightarrow}{j'} = c_1 \underset{\rightarrow}{i} + c_2 \underset{\rightarrow}{j} + c_3 \underset{\rightarrow}{k}$$

where i' is a unit vector in the ΔV direction and x denotes the vector product. The magnitude of the shutoff error is

$$\sigma_A = CA \quad |\underset{\rightarrow}{\Delta V}| \qquad \text{(P-5)}$$

and is in the direction of the ΔV or i' vector. The convenience matrix for shutoff errors is

$$\left[CV'\right] = \begin{bmatrix} \sigma_A^2 & 0 & 0 \\ 0 & 0 & 0 \\ 0 & 0 & 0 \end{bmatrix} \qquad \text{(P-6)}$$

This matrix is defined in the i', j', k' unit vector system. By the following steps the covariance matrix for shutoff error is transformed back to the reference system ($\underset{\rightarrow}{i}$, $\underset{\rightarrow}{j}$, $\underset{\rightarrow}{k}$). In matrix form

$$\begin{bmatrix} \underset{\rightarrow}{i'} \\ \underset{\rightarrow}{j'} \\ \underset{\rightarrow}{k'} \end{bmatrix} = \begin{bmatrix} a_1 & a_2 & a_3 \\ b_1 & b_2 & b_3 \\ c_1 & c_2 & c_3 \end{bmatrix} \begin{bmatrix} \underset{\rightarrow}{i} \\ \underset{\rightarrow}{j} \\ \underset{\rightarrow}{k} \end{bmatrix} \qquad \text{(P-7)}$$

and since both vector systems are orthogonal

$$\begin{bmatrix} \underset{\rightarrow}{i} \\ \underset{\rightarrow}{j} \\ \underset{\rightarrow}{k} \end{bmatrix} = \begin{bmatrix} a_1 & b_1 & c_1 \\ a_2 & b_2 & c_2 \\ a_3 & b_3 & c_3 \end{bmatrix} \begin{bmatrix} \underset{\rightarrow}{i'} \\ \underset{\rightarrow}{j'} \\ \underset{\rightarrow}{k'} \end{bmatrix} \qquad \text{(P-8)}$$

where the transformation matrix is

$$\left[Q\right] = \begin{bmatrix} a_1 & a_2 & a_3 \\ b_1 & b_2 & b_3 \\ c_1 & c_2 & c_3 \end{bmatrix} \qquad \text{(P-9)}$$

then

$$\left[Q^{-1}\right] = \left[Q^{T}\right] \tag{P-10}$$

where Q^{-1} and Q^{T} are the inverse and the transpose of the matrix Q. For an arbitrary vector, A, the following is true

$$\underrightarrow{A} = X\underrightarrow{i} + Y\underrightarrow{j} + Z\underrightarrow{k} = X'\underrightarrow{i'} + Y'\underrightarrow{j'} + Z'\underrightarrow{k'} \tag{P-11}$$

Therefore, the origins of these two coordinates coincide. In matrix form

$$\underrightarrow{R} = \begin{bmatrix} X \\ Y \\ Z \end{bmatrix} \left[\underrightarrow{i}, \underrightarrow{j}, \underrightarrow{k}\right] = \begin{bmatrix} X' \\ Y' \\ Z' \end{bmatrix} \left[\underrightarrow{i'}, \underrightarrow{j'}, \underrightarrow{k'}\right] \tag{P-12}$$

$$= \begin{bmatrix} a_1 & b_1 & c_1 \\ a_2 & b_2 & c_2 \\ a_3 & b_3 & c_3 \end{bmatrix} \begin{bmatrix} X' \\ Y' \\ Z' \end{bmatrix} \left[\underrightarrow{i}, \underrightarrow{j}, \underrightarrow{k}\right]$$

In matrix form

$$\left[R\right] = \begin{bmatrix} X \\ Y \\ Z \end{bmatrix} = \begin{bmatrix} a_1 & b_1 & c_1 \\ a_2 & b_2 & c_2 \\ a_3 & b_3 & c_3 \end{bmatrix} \begin{bmatrix} X' \\ Y' \\ Z' \end{bmatrix} \tag{P-13}$$

Then the covariance vector in the i, j, k unit vector system is

$$\left[CV_1\right] \begin{bmatrix} \underrightarrow{i} \\ \underrightarrow{j} \\ \underrightarrow{k} \end{bmatrix} = \left[Q^{T}\right]\left[CV'\right] \begin{bmatrix} \underrightarrow{i'} \\ \underrightarrow{j'} \\ \underrightarrow{k'} \end{bmatrix} = \left[Q^{T}\right]\left[CV'\right]\left[Q\right] \begin{bmatrix} \underrightarrow{i} \\ \underrightarrow{j} \\ \underrightarrow{k} \end{bmatrix} \tag{P-14}$$

and in matrix form

$$\left[CV_1\right] = \left[Q^{T}\right]\left[CV'\right]\left[Q\right] = \sigma_A^{\,2} \begin{bmatrix} a_1^2 & (a_1\,a_2) & (a_1\,a_3) \\ (a_1\,a_2) & a_2^2 & (a_2\,a_3) \\ (a_1\,a_3) & (a_2\,a_3) & a_3^2 \end{bmatrix} \tag{P-15}$$

Note: The elements of this covariance matrix for shutoff errors depend completely on the components of the unit vector $\underrightarrow{i'}$.

2. Coning Error

Another error that arises when injecting a ΔV impulse into the system is the attitude control error, called the coning error. This error is dependent on the magnitude of the ΔV vector and the ability to control the direction of this thrust vector as is illustrated in the diagram.

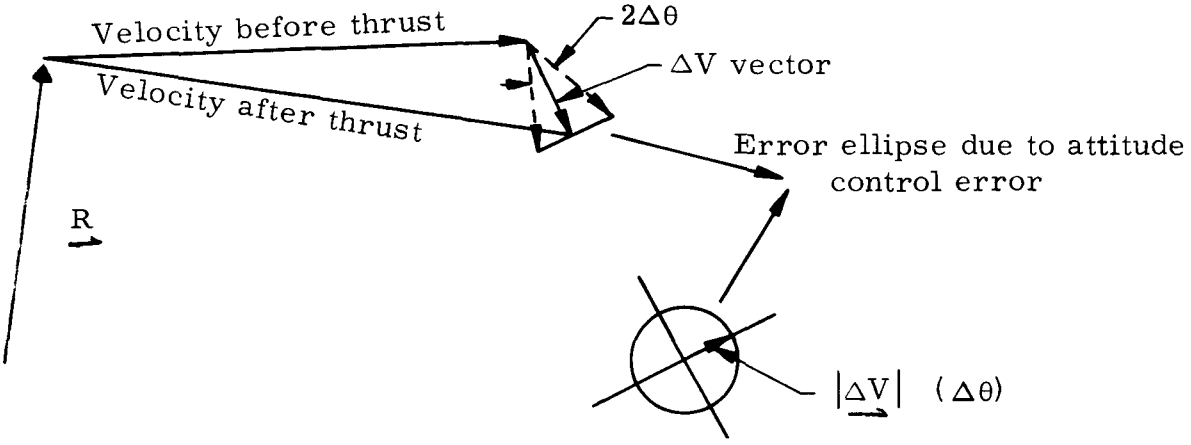

The treatment of this error will depend on the following assumptions.

(1) For a small angle $\Delta\theta$, the base of the cone can be considered a circle in a plane perpendicular to the ΔV vector.

(2) For small $\Delta\theta$, the radius of the cone is approximately $|\Delta V|\ (\Delta\theta)$.

Define a new unit vector system (called double prime) whose unit vectors are

$$\underrightarrow{k''} = \frac{\underrightarrow{\Delta V}}{\underrightarrow{\Delta V}} = f_1 \underrightarrow{i} + f_2 \underrightarrow{j} + f_3 \underrightarrow{k}$$

$$\underrightarrow{i''} = \frac{\underrightarrow{k''} \times \underrightarrow{k}}{\underrightarrow{k''} \times \underrightarrow{k}} = d_1 \underrightarrow{i} + d_2 \underrightarrow{j} \qquad \text{(P-16)}$$

$$\underrightarrow{j''} = \underrightarrow{k''} \times \underrightarrow{i''} = e_1 \underrightarrow{i} + e_2 \underrightarrow{j} + e_3 \underrightarrow{k}$$

where i, j, k are the same reference unit vectors in the shutoff error section. There is no component of the i'' unit vector in the $\underrightarrow{k}$ direction since $\underrightarrow{i''}$ is perpendicular to it.

The magnitude of the coning error is

$$\sigma_r = |\underrightarrow{\Delta V}| \quad \Delta\theta \tag{P-17}$$

The coning error will be described only in the pitch and yaw planes and therefore, the covariance matrix for the coning error in the i'', j'', k'' system is

$$CV'' = \begin{bmatrix} \sigma_r^2 & 0 & 0 \\ 0 & \sigma_r^2 & 0 \\ 0 & 0 & 0 \end{bmatrix} \tag{P-18}$$

Again for an arbitrary vector, A, the following is true

$$A = X\,i + Y\,j + Z\,k = X''\,i'' + Y''\,j'' + Z''\,k'' \tag{P-19}$$

Using the same matrix technique described in the shutoff error section, the covariance matrix for the coning error in the i, j, k system is

$$CV_{11} = \begin{bmatrix} d_1 & e_1 & f_1 \\ d_2 & e_2 & f_2 \\ 0 & e_3 & f_3 \end{bmatrix} \begin{bmatrix} \sigma_r^2 & 0 & 0 \\ 0 & \sigma_r^2 & 0 \\ 0 & 0 & 0 \end{bmatrix} \begin{bmatrix} d_1 & d_2 & 0 \\ e_1 & e_2 & e_3 \\ f_1 & f_2 & f_3 \end{bmatrix} \tag{P-20}$$

or

$$CV = \sigma_r^2 \begin{bmatrix} (d_1^2 + e_1^2) & (d_1 d_2 + e_1 e_2) & e_1 e_3 \\ (d_1 d_2 + e_1 e_2) & (d_2^2 + e_2^2) & e_2 e_3 \\ e_1 e_3 & e_2 e_3 & e_3^2 \end{bmatrix} \tag{P-21}$$

3. Total Covariance Matrix

Since the shutdown and coning errors are independent of each other, the covariance matrices, CV_1 and CV_2, can be added in the normal matrix fashion to yield

$$CV_3 = CV_1 + CV_2 \tag{P-22}$$

This covariance matrix, CV_3, represents errors due to both shutdown and coning. It should be noted that CV_3 is a 3 by 3 matrix and represents an error in velocity only. The following 6 by 6 covariance matrix is completely representative of the mentioned errors

$$CV_3^* = \left[\begin{array}{c|c} 0 & 0 \\ \hline 0 & CV_3 \end{array}\right] \qquad \text{(P-23)}$$

The total error at time t_o must be a function of CV_3^*, TRCV and/or CV_{t_i} and since the associated errors are independent, the total error can again be obtained by normal matrix addition. Thus,

$$CV_{tot} = TRCV + CV_3^* \qquad \text{(P-24)}$$

and now that CV_{tot} has been obtained, it is just a matter of formality to propagate this error from time t_o to t_i by means of Eq (P-1). Thus,

$$CV(t_i) = \theta(t_i, t_o)\, CV_{tot}\, \theta^T(t_i, t_o) \qquad \text{(P-25)}$$

where $CV(t_i)$ is the covariance matrix at time t_i in the i, j, k coordinate system.

It is often desirable to obtain the covariance matrix in a downrange, crossrange, altitude coordinate system and this can be obtained by considering the following transformation. Let $\underrightarrow{i}^1$ denote the downrange direction, $\underrightarrow{j}$ the crossrange direction, and k^1 the altitude direction. If $\vec{R}$ and $\vec{V}$ denote the position and velocity of a particle in the nominal orbit at time t_i, then

It is often desirable to obtain the covariance matrix in a downrange, crossrange, altitude coordinate system and this can be obtained by considering the following transformation. Let $\underrightarrow{i'''}$ denote the downrange direction, $\underrightarrow{j'''}$ the crossrange direction, and $\underrightarrow{k'''}$ the altitude direction. If $\underrightarrow{R}$ and $\underrightarrow{V}$ denote the position and velotiy of a particle in the nominal orbit at time t_i, then

$$\underrightarrow{k'''} = \frac{\underrightarrow{R}}{\underrightarrow{R}} = n_1 \underrightarrow{i} + n_2 \underrightarrow{j} + n_3 \underrightarrow{k}$$

$$\underrightarrow{j'''} = \frac{\underrightarrow{R} \times \underrightarrow{V}}{\underrightarrow{R} \times \underrightarrow{V}} = m_1 \underrightarrow{i} + m_2 \underrightarrow{j} + m_3 \underrightarrow{k} \qquad \text{(P-26)}$$

$$\underrightarrow{i'''} = \underrightarrow{j'''} \times \underrightarrow{k'''} = l_1 \underrightarrow{i} + l_2 \underrightarrow{j} + l_3 \underrightarrow{k}$$

where i, j, k are the same unit vector system defined previously. Using an arbitrary vector, A,

$$A = X\,i + Y\,j + Z\,k = X'''\,i''' + Y'''\,j''' + Z'''\,k''' \qquad \text{(P-27)}$$

This implies that the transformation matrix is

$$s = \left[\begin{array}{ccc|ccc} l_1 & l_2 & l_3 & & & \\ m_1 & m_2 & m_3 & & & \\ n_1 & n_2 & n_3 & & & \\ \hline & & & l_1 & l_2 & l_3 \\ & & & m_1 & m_2 & m_3 \\ & & & n_1 & n_2 & n_3 \end{array}\right] \qquad \text{(P-28)}$$

then the covariance matrix in the i''', j''', k''' coordinates at time t_i is

$$CV'''(t_i) = s\,CV\,(t_i)\,S^T \qquad \text{(P-29)}$$

C. NUMERICAL ANALYSIS

This technique, carried out numerically, now enables one to interpret the covariance matrix $CV^i\,(t_i)$ to obtain the dispersion pattern to any degree of confidence. For example, if all covariance matrices are represented in their 3σ form rather than in the standard 1σ form, then the resulting dispersion ellipse will represent a 3σ impact boundary.

It is most important to realize that this analysis and the following numerical analysis do not attempt to account for double failures. For instance, the probability of a malfunction in the abort system is not considered; the system is presumed to carry out its function within prescribed limits.

1. Ascent Phase

During the boost or ascent phase it is assumed that the error in the launch vehicle's state vector is self-generated; i. e., no outside influence such as tracking can improve the vehicle's state. The state covariance matrix, CV_{t_i}, can be expressed thusly:

$$CV_{t_i} = \begin{bmatrix} (3\sigma_x)^2 & & & & & \\ & (3\sigma_y)^2 & & & \bigcirc & \\ & & (3\sigma_z)^2 & & & \\ & & & (3\sigma_{\dot{x}})^2 & & \\ & \bigcirc & & & (3\sigma_{\dot{y}})^2 & \\ & & & & & (3\sigma_{\dot{z}})^2 \end{bmatrix}$$

where $3\sigma_x$, $3\sigma_{\dot{x}}$ - three sigma variation in position and velocity, respectively, along the x - axis;

$3\sigma_y$, $3\sigma_{\dot{y}}$ - three sigma variation in the position and velocity, respectively, along the y - axis;

and $3\sigma_z$, $3\sigma_{\dot{z}}$ - three sigma variation in the position and velocity, respectively, along the z - axis.

The variances were obtained by means of simulating the boost flight in the presence of propulsion and guidance system errors. For arbitrarily selected times during ascent, the following table is compiled showing the numerical $(3\sigma)^2$ used in the analysis.

TABLE P-1

$(3\sigma)^2$ Variances--ETR Launch Trajectory for Titan IIIC

Time from Liftoff (sec)	$(3\sigma_x)^2$ (km^2)	$(3\sigma_y)^2$ (km^2)	$(3\sigma_z)^2$ (km^2)	$(3\sigma_{\dot{x}})^2$ (km^2/sec^2)	$(3\sigma_{\dot{y}})^2$ (km^2/sec^2)	$(3\sigma_{\dot{z}})^2$ (km^2/sec^2)
160	129.25	17.78	51.21	0.0146	0.0016	0.0005
260	1046.78	77.41	32.29	0.1146	0.0028	0.0011
360	4537.37	204.08	28.90	0.1480	0.0032	0.0024
460	11459.7	411.81	0.60	0.1884	0.0040	0.0015
660	49729	561.22	0.28	0.0412	0.0040	0.0003
Injection	104976	719.37	0.10	0.00001	0.0040	1×10^{-8}

The injection covariance matrix was then propagated to various range angles (various altitudes) along the transfer trajectory. Here again it was assumed that the abort would have to be preprogrammed or timed either before flight or at some time near injection, and hence no improvement in state vector knowledge exists. The propagated covariance matrix now takes on the following form:

$$CV_L = \begin{bmatrix} (3\sigma_v)^2 & & & & & \\ (9\sigma_v\sigma_\gamma) & (3\sigma_\gamma)^2 & & \text{symmetrical} & & \\ (9\rho\sigma_v\sigma_{R_D}) & (9\rho\sigma_\gamma\sigma_{R_D}) & (3\sigma_{R_D})^2 & & & \\ (9\rho\sigma_v\sigma_{R_C}) & (9\rho\sigma_\gamma\sigma_{R_C}) & (9\rho\sigma_{R_D}\sigma_{R_C}) & (3\sigma_{R_C})^2 & & \\ (9\rho\sigma_v\sigma_t) & (9\rho\sigma_\gamma\sigma_t) & (9\rho\sigma_{R_D}\sigma_t) & (9\rho\sigma_{R_C}\sigma_t) & (3\sigma_t)^2 & \end{bmatrix}$$

where ρ is a correlation coefficient and the three sigma subscripts are:

v - inertial velocity
γ - inertial flight path angle
R_D - downrange
R_C - cross range
t - time

Table P-2 records the values for the range angles of 30, 60, 90, 120 and 180 degrees.

After orbit is attained, it is assumed that tracking information will be available for the updating of the primary vehicle's ephemeris and that the preliminary vehicle's (e.g., Nimbus) attitude system would be at the RB disposal. For this situation the uncertainty in state is the uncertainty in tracking. The tracking covariance matrix is CVTR and is equivalent in form to CV_{t_i}. The 3σ variances used are:

$$(3\sigma_x)^2 = (3\sigma_y)^2 = (3\sigma_z)^2 = 0.003716 \text{ km}^2$$

$$(3\sigma_{\dot{x}})^2 = (3\sigma_{\dot{y}})^2 = (3\sigma_{\dot{z}})^2 = 0.9029\ 10^{-9} \text{ km}^2/\text{sec}^2$$

TABLE P-2

Propagated Covariance Matrix Transfer Orbit

Range Angle	$(3\sigma_v)^2$	$(3\sigma_\gamma)^2$	$(3\sigma_{R_D})^2$	$(3\sigma_{R_C})^2$	$q_{\rho\sigma_v\sigma_\gamma}$	$q_{\rho\sigma_{R_D}\sigma_v}$	$q_{\rho\sigma_{R_D}\sigma_\gamma}$	$q_{\rho\sigma_t\sigma_v}$	$q_{\rho\sigma_t\sigma_\gamma}$	$q_{\rho\sigma_t\sigma_{R_D}}$	$(3\sigma_t)^2$
	$\times 10^{-4}$	$\times 10^{-7}$	$\times 10^{-2}$	$\times 10^{-4}$	$\times 10^{-6}$	$\times 10^{-4}$	$\times 10^{-6}$	$\times 10^{-1}$	$\times 10^{-3}$		
(deg)	$(km/sec)^2$	$(deg)^2$	$(rad)^2$	$(rad)^2$	(ft/sec-deg)	(rad-ft/sec)	(rad-deg)	(ft)	(sec-deg)	(sec-rad)	(sec)
30	0.1405	0.5981	0.2457	0.2916	-0.8434	0.1635	-0.8500	0.1418	-0.7465	0.01801	15.522
60	0.1468	2.657	0.2512	0.5179	-1.964	0.3325	-4.422	0.2932	3.903	0.06656	58.663
90	0.1565	8.560	0.2652	0.6177	-3.658	0.5811	-13.57	0.5251	-12.27	0.1950	176.194
120	0.1675	28.04	0.3077	0.4886	-6.851	1.036	-42.38	0.9714	-39.75	0.6007	563.533
180	0.1792	1015.	2.340	0.1795	-42.64	6.128	-1459	6.309	-1502	21.58	22223.9

There remains now only to specify the thrust (ΔV) cutoff and alignment error before the propagation to impact can be carried through. For 3σ thrust cutoff error, CA = 1% (see Eq (P-5)) and for the 3σ coning error, $\Delta\theta = 5°$. Minor contributions to the coning error are incurred during the ascent phase.

Table P-3 catalogs the results of the error propagation for aborts from each of the specified points using a ΔV = 1500 fps. Three sigma dispersions in downrange and crossrange yield impact areas contained by elliptical boundaries. For the two random variables of downrange and crossrange, the boundaries represent a 99% confidence level that impact will occur in the enclosed area.

TABLE P-3

3σ Dispersions in Impact Position

0 and 1500 fps Deorbit Velocity

Launch Phase

Deorbit Velocity ΔV (fps)	Phase Time (sec)	Downrange Dispersion ΔR_D (naut mi)	Crossrange Dispersion ΔR_C (naut mi)	Reentry Time t_R (min)
0	160	16	4	2.7
0	260	78	8	4.3
0	360	119	12	4.5
0	460	454	18	7.8
0	660	504	21	9.0
1500	160	18	8	2.3
1500	260	32	7	3.5
1500	360	94	14	3.7
1500	460	239	17	5.7
1500	660	225	19	6.7
1500	Injection 832	384	31	15.3

Transfer Orbit and 600-Nautical Mile Circular Orbit

Range Angle (deg)	Downrange Dispersion ΔR_D (naut mi)	Crossrange Dispersion ΔR_C (naut mi)	Reentry Time t_R (min)
30	314	34	17.0
30 spin stabilized	208	34	12.0
60	237	34	19.6
60 spin stabilized			
90	218	36	22.2
120	217	37	23.5
150	285	39	23.6
180	526	38	23.0
Circular orbit	50	19	30.0

APPENDIX Q

THERMOELECTRIC ANALYSIS

First, a brief description of factors that influence generator design parameters (number of couples, thermoelectric efficiency, output power, couple junction resistivity, etc.), will be presented and then the analysis will follow.

Most basic is the fact that at the end of life, fuel decay causes operating temperatures to be at their lowest values and thus the generator must be designed to produce the 250 watts(e) at this time to ensure producing this minimum at all other times. During the life of the system, fuel decay is a large contributor to power degradation with Sr-90, amounting to 13.2% change in thermal inventory based on the end-of-life value. The corresponding change in output power is greater than 13.2% at beginning of life due to increased operating temperatures. This effect has been shown in Fig. Q-1 along with several other effects that will be discussed. The power axis shown in this figure is not meant to be accurate but merely indicates the qualitative aspects involved.

The second largest contributor to power reduction is degradation of the thermoelectric couples with time. The selected configuration has been sized to accommodate couple degradation using degradation rates based on the two-year operation of five AirVac modules at RCA.

A further allowance must be made for variations in degradation to ensure that the 250-watt power is met within the reliability specified (e.g., 0.95 reliability after five years). It is possible, by extensive testing, to determine the statistical distribution of the degradation and to select a design value at end of life several standard deviations above the norm in order to guarantee minimum power.

With statistical data on catastrophic couple failures, generally believed to occur primarily during launch but possible to occur at any time during mission life, allowance can be made for discrete couple failures (usually open circuits). The reliability analysis discussed in Chapter VI shows that with an assumed couple failure rate of 0.0035% per 1000 hours (based on SNAP 10A SiGe data), up to five discrete couple failures must be allowed during the five-year mission to meet the reliability goals of 0.95 after five years and 0.99 after one year. With five allowed failures, 10 extra couples will be required since loss of one couple in a two-string parallel arrangement will deregulate the adjacent couple so as to cause almost total loss of power in both couples. In the design presented, no allowance was made for this catastrophic failure since the statistical SNAP 10A data (used as the only estimate available) were not available

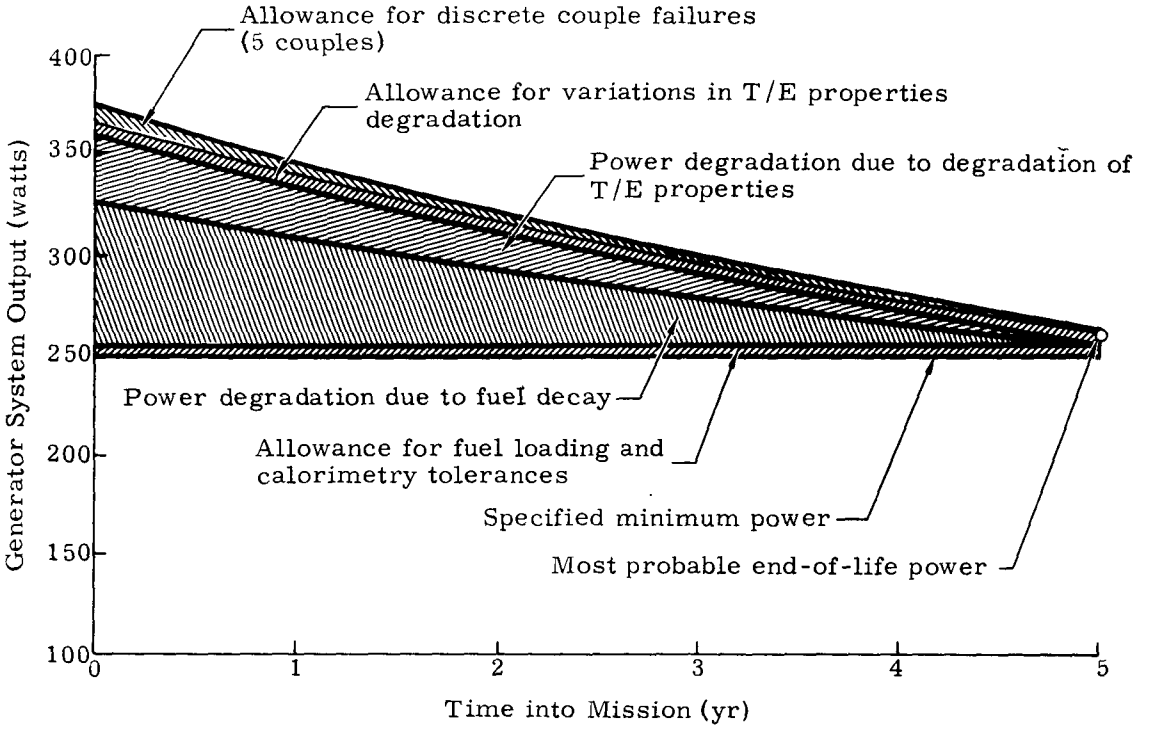

Fig. Q-1. Output Power Reduction with Time

until after the design was frozen. It is estimated that the system would weigh another 1 to 2% due to the addition of the extra couples, extra fuel, extra radiator, etc.

A small allowance must be made for fuel loading and calorimetry tolerances, presently ±3% for Quehanna Laboratories, to ensure that EOL power does not fall below 250 watts. This information was available early enough to be factored into the design.

It is also of importance to mention that tolerances of several percent exist in BOL thermoelectric properties but with initial electrical testing the departure, if any, can be determined and compensated for by an adjustment in fuel inventory (to the ±3% fueling accuracy).

With these considerations in mind, the thermoelectric analysis will now be presented based on the thermoelectric property data supplied by RCA (Appendix J) as measured in a partially aged condition (1500 hours).

This analysis was performed on the Martin digital computer code. Since the results apply to a generator at the end-of-life condition (5 yr) the first computation was to correct α_N, the N element Seebeck coefficient (as presented in Appendix J) by increasing all values 4.2%. The reasons for this correction, as well as the basis for this particular value, will be described here.

On the N element of SiGe, an increase in electrical resistivity and Seebeck coefficient occurs with time. The changes are caused by the precipitation of excess dopant from solid solution with a resulting modification of the carrier concentration. The N-type SiGe alloys are doped to the solid solubility limit at very high temperatures. Since the solid solubility decreases with decreasing temperature, excess dopant develops and is precipitated when the alloy is operated at lower temperatures, i.e., an equilibrium is established for each temperature level. The loss is not retrievable when returning to a higher temperature. The deterioration of the carrier concentration is therefore permanent but small if the couples have not been operated for any length of time at the lower temperature levels. Due to the inverse dependence of the resistivity and the Seebeck effect upon the carrier concentration, their values will increase somewhat with time in the normal use of the couples (the N-type component). The thermal conductivity, chiefly a lattice effect, is little affected. The P-type material does not generally undergo any changes in its normal use.

The net result is that these changes must be factored into the end-of-life design point analysis since T/E data from RCA is taken at the 1500-hour point. The resistivity increase is handled by extrapolating the total internal resistance of experimental module data (e.g., SNAP 17A)

to the mission time desired (a straight line on a log time plot) and then using the attendant contact resistivity.

The Seebeck effect increase on the N element is most appropriately handled by use of the SNAP 17A averaged (over seven SNAP 17A modules containing 50 couples) Seebeck data observed, for which the relation

$E(t) = 275.113 + 8.734 \log_{10} t$ holds, where E = open circuit voltage and t = time (hr.)

Again, this relation is a straight line on an E versus log t plot. Since data exist in excess of 10,000 hours, this line may easily be extended another decade.

Thus, for a five-year mission (43,800 hours), the percentage increase in α_N would be computed as

$$\left(\frac{E_{43,800} - E_{1500}}{E_{1500}}\right) \times 100\% = \frac{8.734\,[\log (43,800 - \log (1500)]}{275.113 + 8.734 \log (1500)}$$

$\times 100\% = 4.23\%$.

The next computation was to determine an appropriate junction electrical resistivity that would be applicable to the 250-watt generator after five years of operation. SNAP 17A test data provide a most meaningful basis for this prediction since the modules tested under that program were consistent in their behavior (reproducible) and since this couple construction will be similar to SNAP 17A. As shown in the statistical analysis (Ref. Q-1 of SNAP 17A data, average couple resistance on those modules is described by RCA as a straight line on a plot of total resistance versus the $\log_{10}$ of time, viz.

$$R(t) = 38.512 + 7.467 \log_{10} t$$

where

R = total couple internal resistance ($\mu\Omega$)

t = time (hr).

Data exist for two years of operation and because of the linearity of this relationship, on a log-time plot, extrapolation for five years of operation has been made.

From this five years of couple resistance data, junction resistivity can be directly determined by subtracting the resistances of the elements, hot shoes and cold stack members. The result is that after

five years, the junction (contact)resistivity per couple will be 1800 $\mu\Omega$-cm^2, based on the RCA equation.

The equation used by RCA essentially presents an average value of resistance describing SNAP 17A modules. Rigorously, one should use the 3σ value of resistance to assure that 99^+% of the modules will produce at least the required power. This rigorous statistical approach was justifiably not used in Phase 0 since there was very little scatter in the data and the net result would not have been substantially different. In Phase I, provided additional life data are available, the 3σ approach will be used.

The thermoelectric analysis itself was performed by a digital computer code developed by Martin several years ago. The technique used is described in detail in Ref. Q-2 and will not be repeated here.

The thermoelectric computer analysis was performed for junction resistivities of 1200, 1800 and 2400 $\mu\Omega$-cm^2 to determine the effect of a variation in this resistivity.

Hot junction temperatures of 1300°, 1400° and 1500° F were used in conjunction with cold junction temperatures of 400°, 500° and 600° F. All computations were performed for 3/4-inch length elements and a gross electrical power of 275 watts (net power of 250 watts).

The results are presented in Figs. Q-2 through Q-5.

The nominal operating point at end of life for the 250-watt RTG is 1450° F on the hot junction and 550° F on the cold junction. From Fig. Q-2, the thermoelectric efficiency is 5.43% for a resistivity of 1800 $\mu\Omega$-cm^2. Figure Q-4 shows that for 28 volts net and a simple series connection, 198 couples are required. For a series parallel connection, 396 couples are necessary. From Fig. Q-5, for the series-parallel connection, it can be determined that the required N- and P-element cross-sectional areas are 0.091 and 0.056 in.^{2}, respectively.

REFERENCES

Q-1. "High Temperature Cascaded Thermoelectric Module Development Program and Module Testing," NYO-3484-42 for the period April 1, 1965 to June 30, 1965, Second Quarterly Report, "Power Level Analysis of SNAP 17A Developmental Modules as a Function of Operational Life."

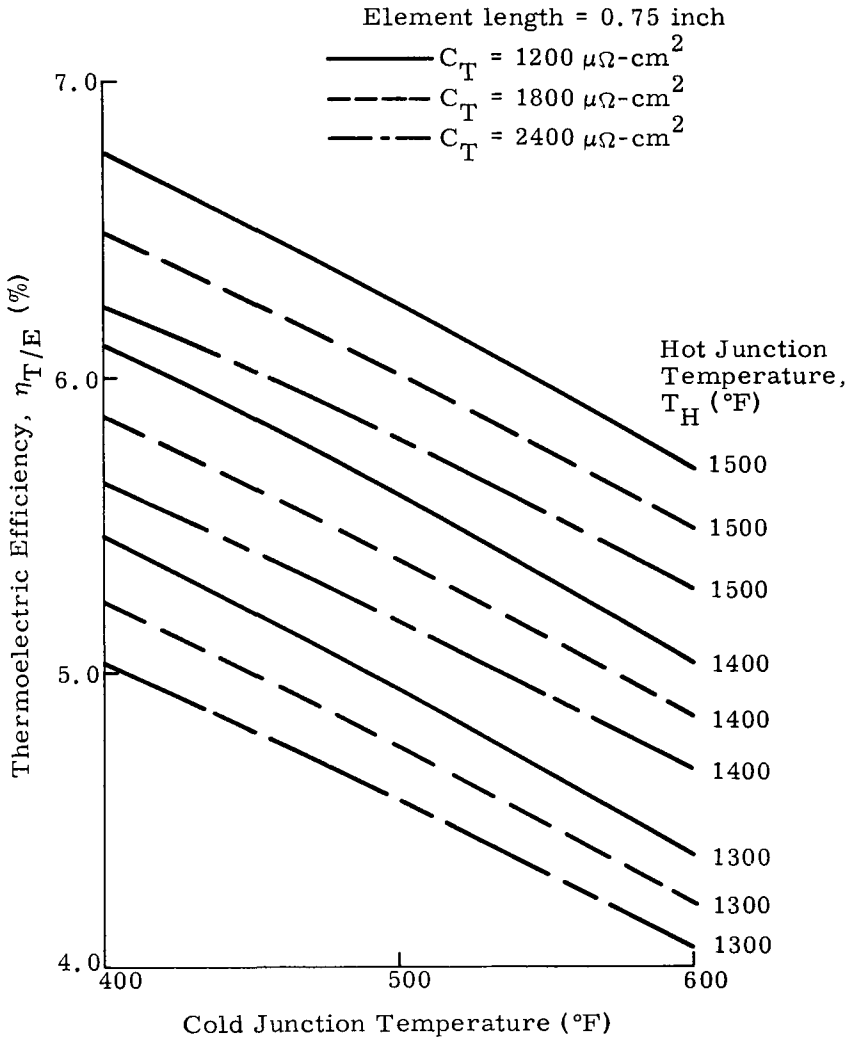

Fig. Q-2. Thermoelectric Efficiency Versus Cold Junction Temperature for SiGe

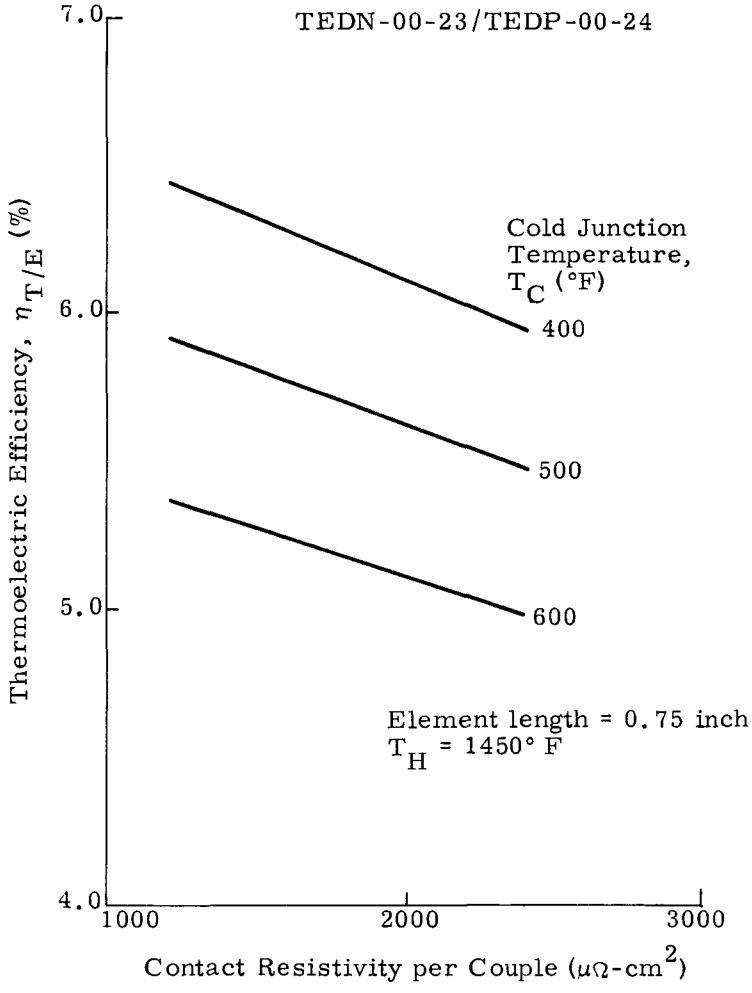

Fig. Q-3. Thermoelectric Efficiency Versus Contact Resistivity for SiGe

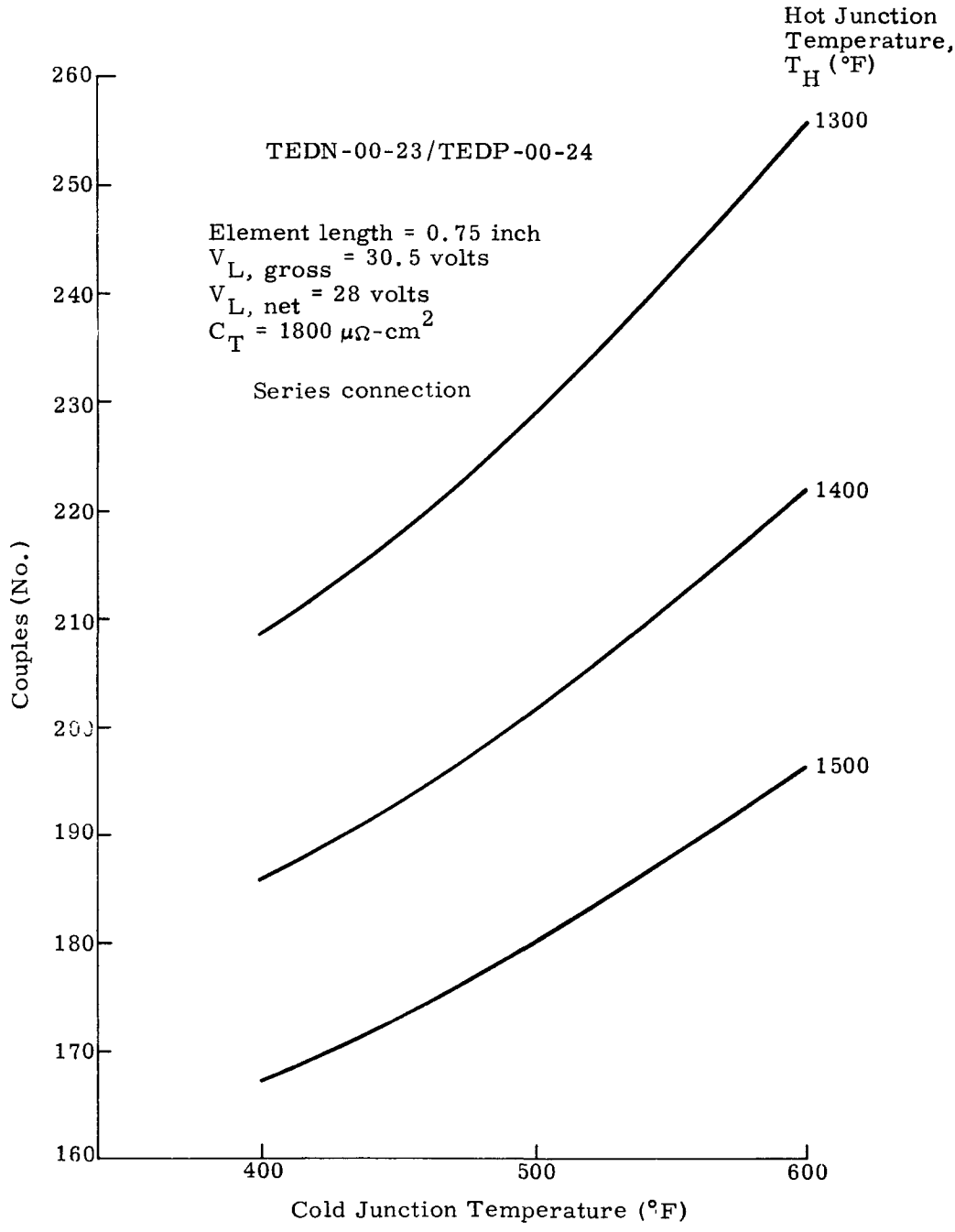

Fig. Q-4. Number of Couples Versus Cold Junction Temperature for SiGe

TEDN-00-23/TEDP-00-24

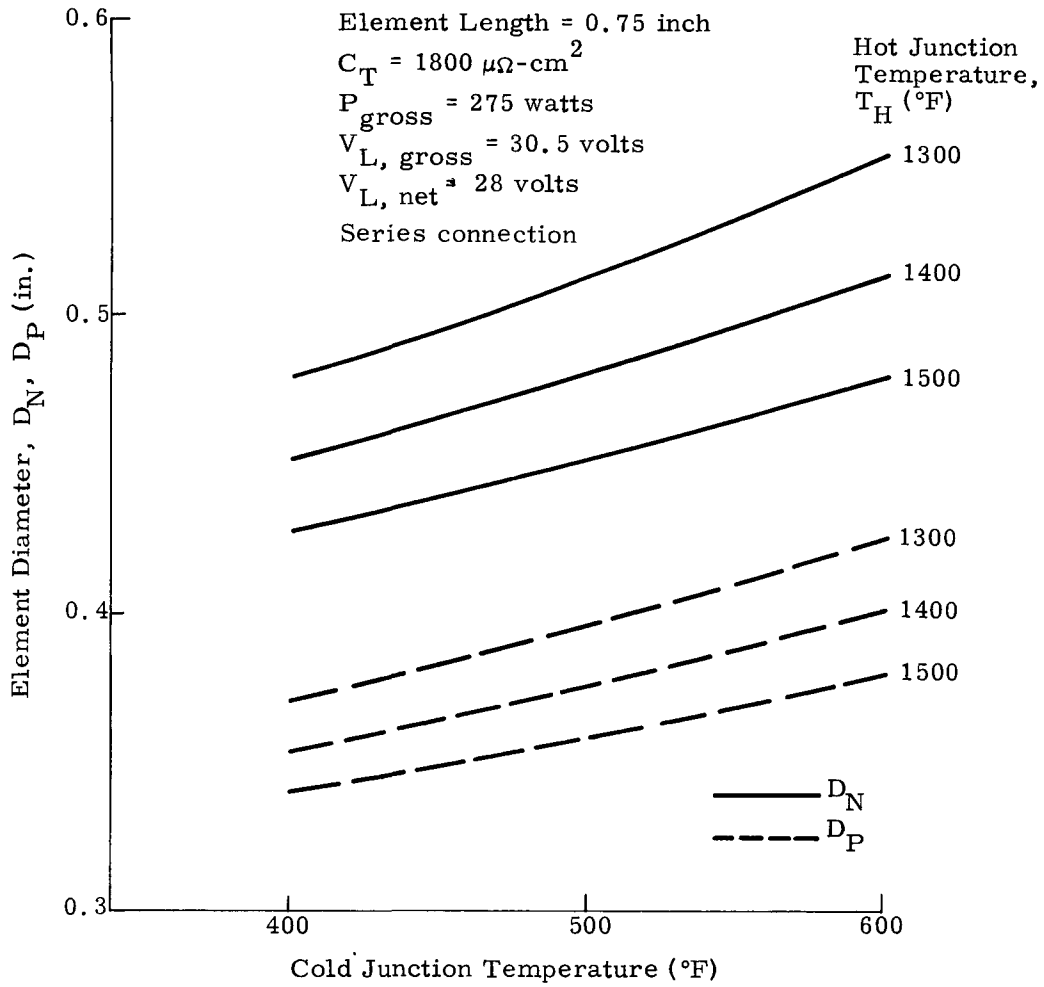

Fig. Q-5. Element Diameter Versus Cold Junction Temperature for SiGe

Q-2. "Engineering Study Proposal--Radioisotope Thermoelectric Generator for Nimbus and OAO Satellites," Appendix A, Martin Company MND-5139, October 1965.

APPENDIX R

BEGINNING-OF-LIFE ELECTRICAL CHARACTERISTICS

A. ANALYSIS

The equations that describe the RTG during its life once an end-of-life design has been selected* are

$$E_{oc} = N\bar{\alpha}(T_H - T_C) \tag{R-1}$$

$$\bar{\alpha} = \left|\bar{\alpha}_N\right| + \bar{\alpha}_P \tag{R-2}$$

$$R_i = \left[\frac{\bar{\rho}_P \ell_P}{A_P} + \frac{\bar{\rho}_N \ell_N}{A_N}\right] N \tag{R-3}$$

$$R_I = R_i + R_c \tag{R-4}$$

$$R_c = \left[\frac{C_{N,H} + C_{N,C}}{A_N} + \frac{C_{P,H} + C_{P,C}}{A_P}\right] N \tag{R-5}$$

$$I = \frac{E_{oc}}{R_I + R_L}** \tag{R-6}$$

$$V_L = IR_L** \tag{R-7}$$

$$P = I^2 R_L \tag{R-8}$$

$$q = \left(\frac{\bar{k}_N A_N}{\ell_N} + \frac{\bar{k}_P A_P}{\ell_P}\right) N (T_H - T_C) + \alpha_H I T_H N + K_{PAR}(T_H - T_C) - I^2 R_{CH} N - 1/2 I^2 R_i \tag{R-9}$$

$$q = q_{EOL} e^{\lambda t} \tag{R-10}$$

* Nomenclature at end of IDC.

** R_L includes R_{MISC} (straps, shoes, wiring, etc.).

These equations can be solved at any time in life to determine the corresponding electrical performance or temperature history.

The procedure for solution is to select a hot junction temperature and solve Eqs (R-1) through (R-10). All properties in the equations are temperature dependent. The reference end-of-life conditions used for a 250-watt(net) SiGe RTG were:

q_{EOL} = 5660 watts

N = 198 (series)

A_N = 0.181 in.^{2} (series)

A_P = 0.112 in.^{2} (series)

ℓ_P = 0.75 inch

K_{PAR} = 1.12 watts/°F

T_H = 1450° F

T_C = 550° F

V_L = 30.5 volts (gross)

V_L = 29.2 volts (net).

The results are presented in Fig. R-1 for a net end-of-life voltage of 29.2 volts. The contract, however, defines the allowable voltage range to be 28 ± 10%, or from 25.2 to 30.8 volts. The results show that it is possible to be within this range without voltage regulation during the entire five-year mission if the end-of-life voltage is changed to 25.2 (rather than 29.2). This can be done by simply changing the number of couples and area per couple to:

N = 346 couples (series-parallel)

A_N/couple = 0.1040 in.^{2} (series-parallel)

A_P/couple = 0.0642 in.^{2} (series-parallel).

The resultant voltage and current during the five years are presented in Fig. R-2. The hot junction temperatures and net powers presented in Fig. R-1 are still applicable.

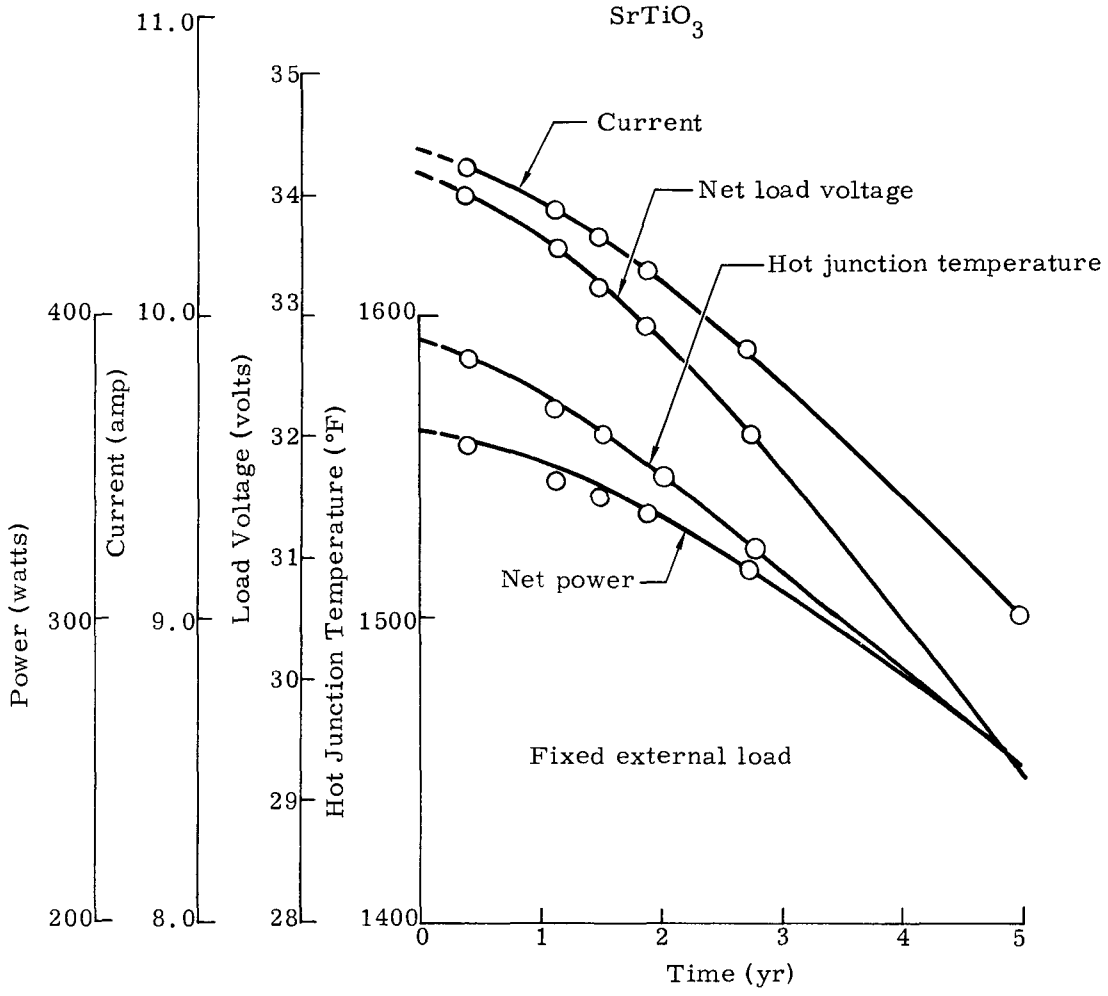

Fig. R-1. RTG Characteristics Versus Time for SiGe

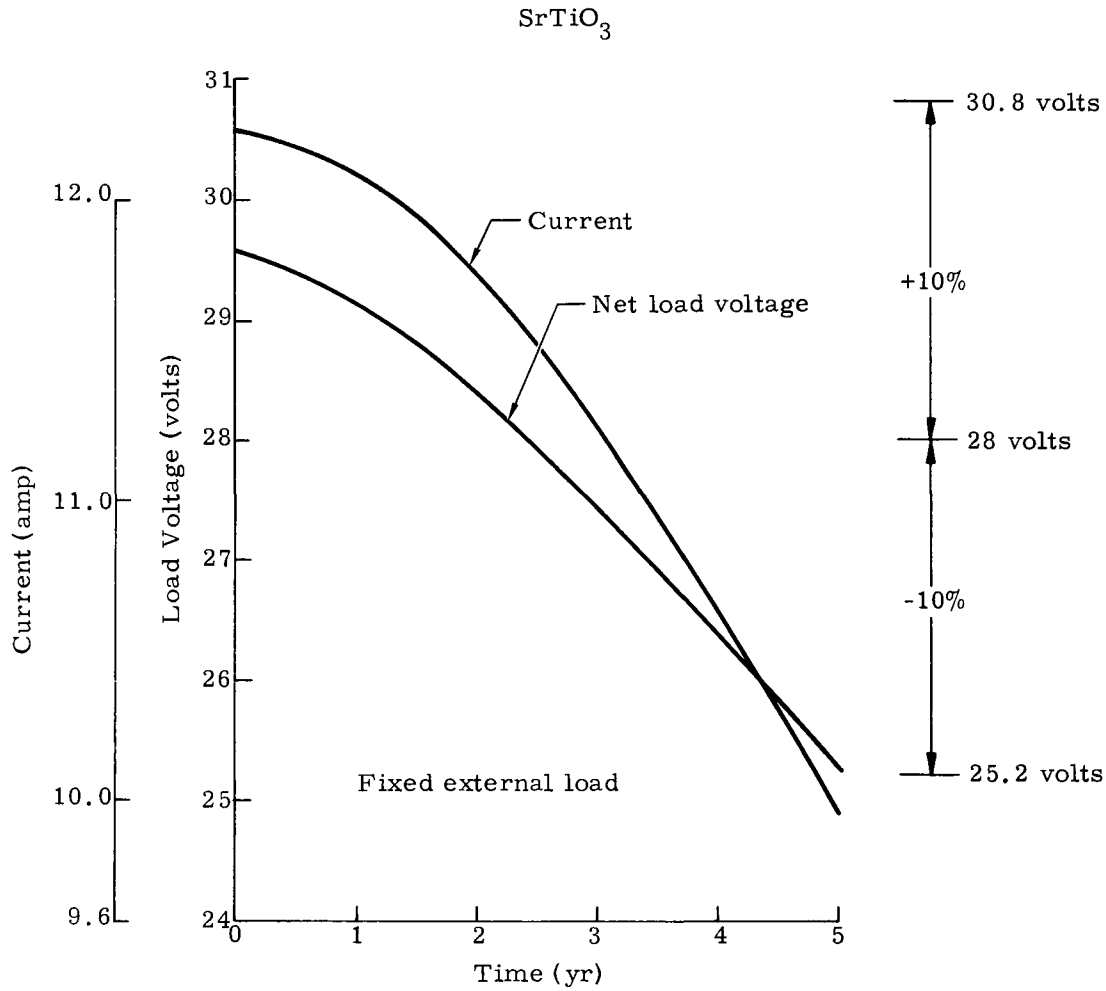

Fig. R-2. RTG Revised Current and Voltage Versus Time for SiGe

If voltage regulation is used (because of spacecraft requirements), a different power-temperature characteristic would have resulted during the life of the RTG. The key to understanding this is the E-I and P-I curves at end of life and beginning of life (Ref. Fig. R-3). Four conditions can theoretically be applied to the generator during its life:

(1) Constant total load (impedance)

(2) Constant current drawn

(3) Constant voltage

(4) Constant power to the usable load.

Each of these conditions is shown in Fig. R-3. Note that each of the dotted lines crosses the beginning-of-life E-I curve at a different voltage and different current. Also, a different beginning-of-life power results. The difference in current (which accounts for different Peltier cooling) at beginning of life is responsible for different hot junction temperatures initially. (The greater the current, the lower the initial hot junction temperature.)

With a plutonium generator, the excess fuel at beginning of life is only 4% and thus the changes in power, temperature, etc., are much less severe than with Sr-90. Specific values of these parameters were not computed for a Pu-238 system but can be in Phase I. The lower decay rate of Pu-238 may also permit increasing the end-of-life design point for the Pu-238 system.

B. NOMENCLATURE

A	Area
C	Contact resistivity
E	Voltage (open circuit)
I	Current
k	Thermal conductivity
ℓ	Element length
N	Number of couples
P	Power

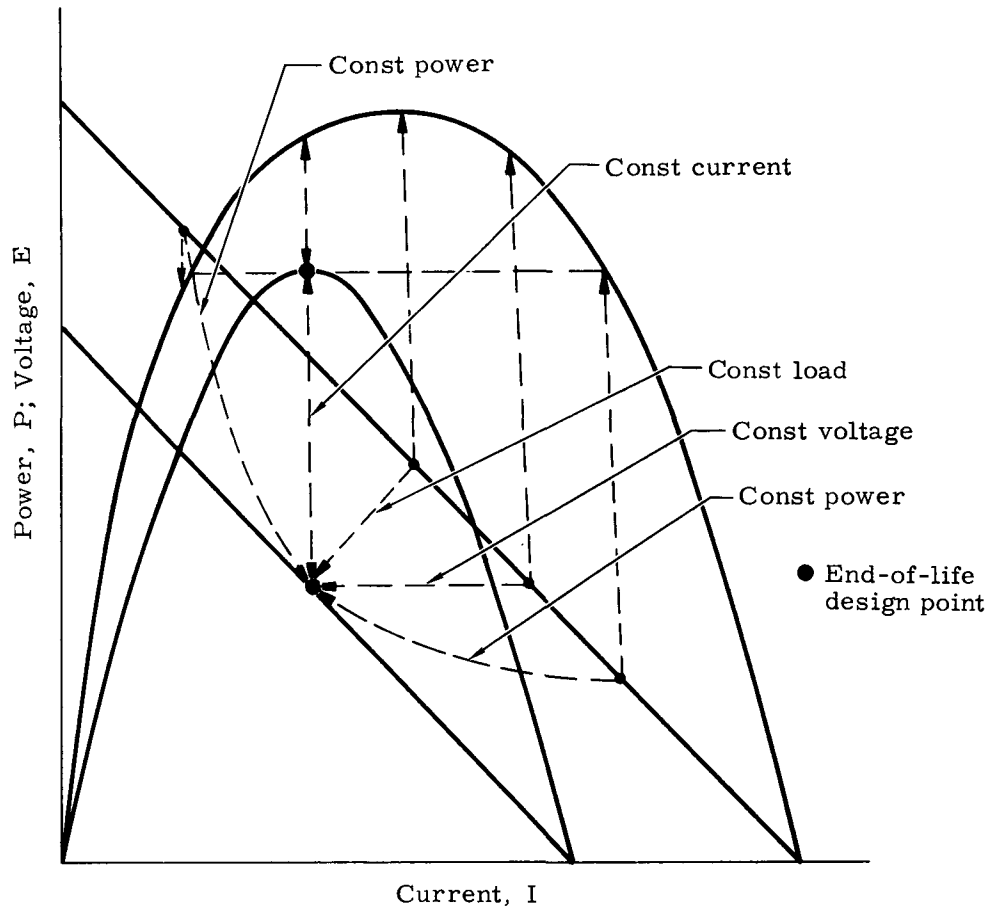

Fig. R-3. End-of-Life and Beginning-of-Life Voltage and Power Curves for Fixed Heat Input

q	Heat rate
R	Electrical resistance
T	Temperature
V	Voltage (load)
α	Seebeck coefficient
ρ	Electrical resistivity
λ	Isotope decay constant

Subscripts

C	Contact resistance
C	Cold junction
H	Hot junction
I	(Total) internal (resistance)
i	(Element) internal (resistance)
K	Thermal conductance
L	Refers to load
ℓ	Element length
N	Refers to N element
oc	Open circuit
P	Refers to P element
t	Time

~~CONFIDENTIAL~~

BLANK

~~CONFIDENTIAL~~

APPENDIX S

SEGMENTED THERMOELECTRIC SUBSYSTEM

The development of couples of higher efficiency than SiGe can be accomplished by the use of III-V compound alloys in segmented structures. RCA is currently under contract to the Atomic Energy Commission to investigate the III-V compound thermoelectric materials for use in advanced nuclear power systems (Contract AT(30-1)-3500).

This program was started in early 1965 although basic research at RCA on the III-V compounds had been performed prior to this. Task I, covering the effort between March 1, 1965 and August 31, 1965, is reported in Ref. S-1. At the beginning of Task I, the reported status of the program was as follows:

(1) An N-type III-V alloy, InAs-GaAs, was developed with a Z (figure of merit) approximately 30% better than SiGe up to 550° C (1022° F). This temperature is the maximum practical limit of the material.

(2) Exploratory literature and laboratory investigation showed practical bonds to InAs-GaAs could be achieved with low thermal and electrical losses.

At the conclusion of Task I, the reported status of the development was as follows:

(1) A practical demonstration couple with a segmented N leg was developed using N-type InAs-GaAs segmented to N-SiGe.

(2) A SiGe-InAs-GaAs segment joint was developed using a tungsten-gold-molybdenum interface.

(3) The upper temperature limit on InAs-GaAs based on weight loss in sealed tubes and joint stability tests was defined as 500° (932° F) to 550° C (1022° F).

(4) Preliminary data indicated that the resistivity of InAs-GaAs was stable with life.

(5) Work was initiated on a backup segmenting joint using graphite.

(6) An experimental technique was developed that gives a direct comparison between a segmented couple and an all-SiGe couple under the same experimental conditions.

Task II, covering the effort between September 1, 1965 to February 28, 1966, is reported in Ref. S-2. At the conclusion of this task, the reported status was as follows:

(1) Segmented couples utilizing N-type InAs-GaAs and P-type SiGe were prepared for test and evaluation. Thermal diffusivity measurements (to determine conductivity) confirmed the high figure of merit of the InAs-GaAs.

(2) Development of the interface segmenting bond continued in order to develop a stable joint with respect to mechanical properties.

(3) Advanced technology efforts were initiated. These are aimed at the development of a P-III-V compound alloy of better performance than P-type SiGe, the development of an improved N-III-V compound alloy, consideration of other thermoelectric materials for segmenting such as tellurides, and the development of couple designs to increase segment interface temperatures.

A. APPLICATION TO 250-WATT PROGRAM

To date, RCA has not developed a P-type material that is better than SiGe. On the N leg, InAs-GaAs shows improvement over N-SiGe for use below 550° C (1022° F). Very recently, some thermoelectric property data have shown that N-type GaSb-InSb is even better than InAs-GaAs (Ref. Fig. S-1) although the work on this material is in its infancy.

RCA reports efficiency gains on the order of 14% and higher with the use of InAs-GaAs. However, these high increases are compared to SiGe operating at only 700° C (1292° F) on the hot junction. Furthermore, much of their data is generated at the maximum allowable interface temperature of 550° C. With a Sr-90 system designed for five-year operation where the isotope decays 13% in thermal inventory, the end-of-life allowable interface temperature would only be about 500° C. RCA reports one theoretical efficiency gain curve along with experimental data obtained with comparison modules at temperatures of

T_{hot} = 800° C = 1472° F

T_{int} = 500° C = 932° F

T_{cold} = 300° C = 572° F.

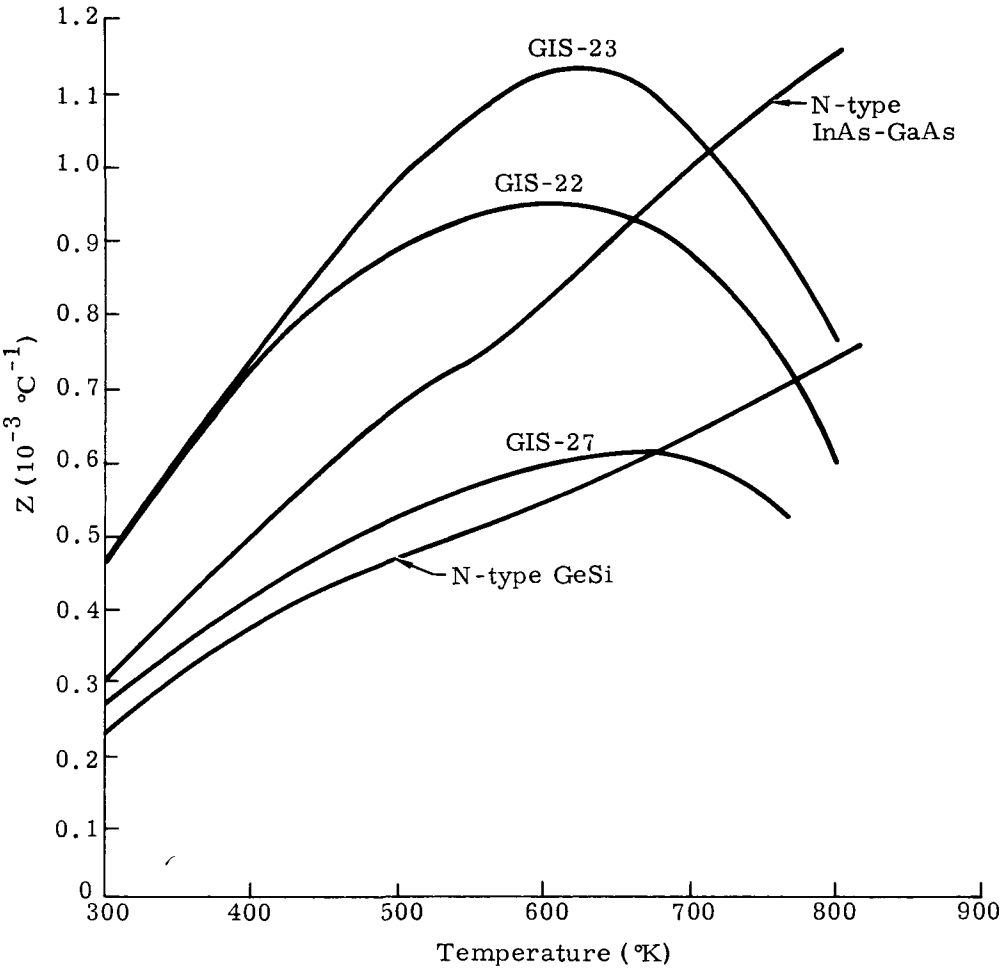

Fig. S-1. Temperature Dependence of Figure of Merit for N-Type GaSb-InSb Alloys (Ref. S-2)

These temperature points are close to the SiGe system design point and thus give a very good estimate of the gain that can be realized from a segmented system. The data are presented in Fig. S-2. From this figure, it appears that an efficiency gain of about 4% is possible with InAs-GaAs.

Reference back to Fig. S-1 leads one to hypothesize that with GaSb-InSb on the N leg, an efficiency gain of about 7 to 8% over SiGe might be possible. At this point, however, it is not clear that the use of the material in a practical couple or device is possible. Further work will have to be done by RCA.

B. CONCLUSIONS

From the RCA work on segmented couples reported in Refs. S-1 and S-2, it appears that with suitable development (several years work), an efficiency gain of 4 to 8% over the present unsegmented couple can be realized by using N-type InAs-GaAs or N-type GaSb-InSb. Improvements beyond this will occur only if new improved P-type segments can be found (a development that has not yet come to fruition despite work in the area) or if the segment temperature on the N leg can be increased. The gain from an increased segment temperature would probably not be very large.

From these conclusions, it appears that only a nominal increase will be realized by segmenting in this design. Further breakthroughs are needed to make segmenting attractive for the CRONUS system.

REFERENCES

S-1. "Final Report for Preliminary Investigation of III-V Compound Directed Toward Segmented Thermoelectric Materials Advanced Nuclear Power Systems," NYO 3500-8, for the period March 1, 1965 to August 31, 1965.

S-2. "Topical Report for Preliminary Investigation III-V Compound Thermoelectric Materials Directed Toward Segmented Silicon-Germanium III-V Compound Advanced Nuclear Power Systems," NYO 3500-11, for the period September 1, 1965 to February 28, 1966.

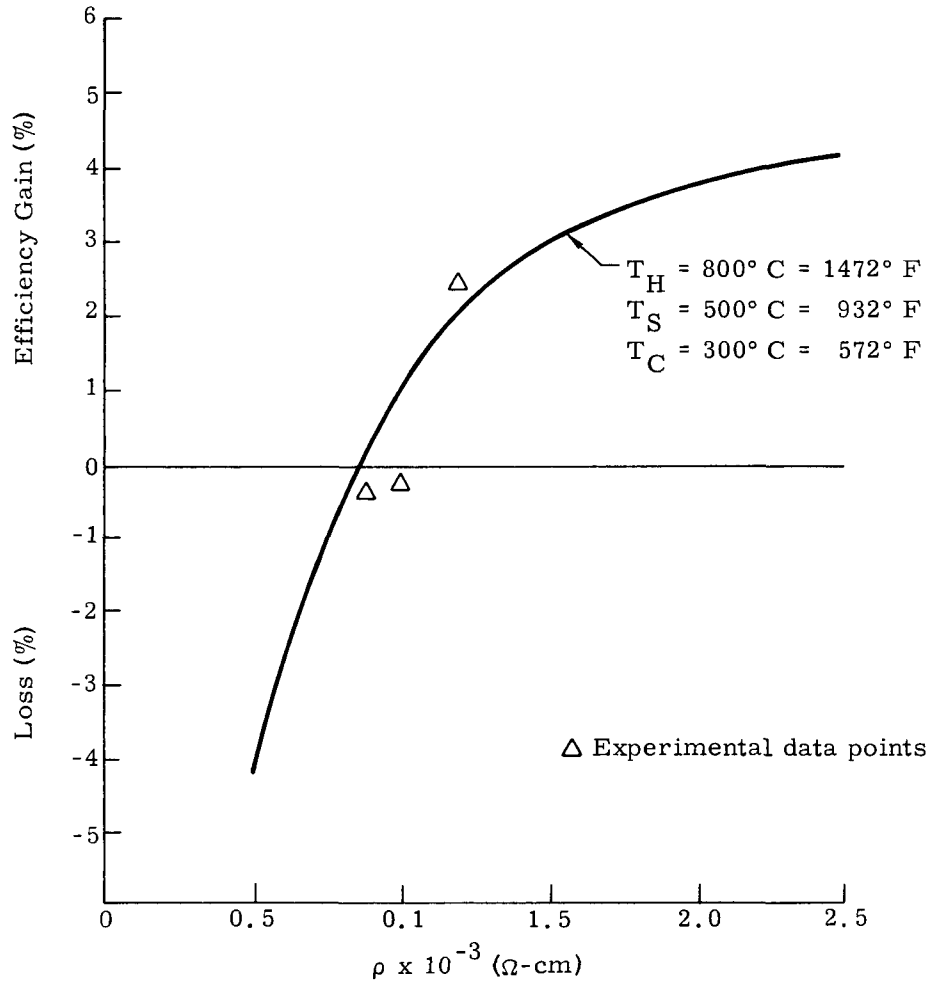

Fig. S-2. Predicted Theoretical Efficiency Gain Realized by Using Segmented N Leg Couple as Function of InAs-GaAs Resistivity. Experimental Data Obtained on Comparison Modules also Shown (Ref. S-1)

BLANK

APPENDIX T

INTERNAL CAPSULE PRESSURE BUILDUP ANALYSIS

A general expression for the liberation of helium gas from plutonium decay is illustrated in Fig. T-1. The PV/MT parameter is plotted as a function of time based on a half life of 86.4 years for the plutonium. Figure T-2 represents a typical capsule open circuit temperature profile as a function of time for the plutonium-fueled 250-watt generator system (see Appendix X for derivation). These temperatures were used to reduce the pressure parameter to PV/M as shown in Table T-1.

TABLE T-1

Time (yr)	PV/MT	Temperature (°R)	PV/M
5	2.75	2355	6,470
10	5.50	2305	12,650
15	8.20	2260	18,500
20	10.80	2215	23,950
25	13.30	2190	29,100

Internal capsule pressures were then calculated parametrically for various void volumes as a function of time as shown in Fig. T-3. The void volume is defined with respect to the total internal capsule volume. Therefore, the fuel volume is 1 - void volume. An effective plutonium density of 0.324 lb/in.^{3} (9.7 gm/cm^3 PuO_2) was used to establish unit values of M/V as shown in Table T-2. The data displayed in Fig. T-3 are independent of capsule geometry, but not the temperature profile of Fig. T-2. Normal temperature for the 250-watt system is approximately 1800° F.

The power ratio of plutonium to strontium fuel is about 5.3 (4.51 watts/cm^3 vs 0.85 watts/cm^3). Therefore a void volume of 80% can theoretically be achieved for plutonium loaded in a capsule originally designed for strontium. A liner would most likely be used to create a central void with the plutonium fuel filling an outer annulus. Fully packed plutonium fuel yields a void volume around 25%.

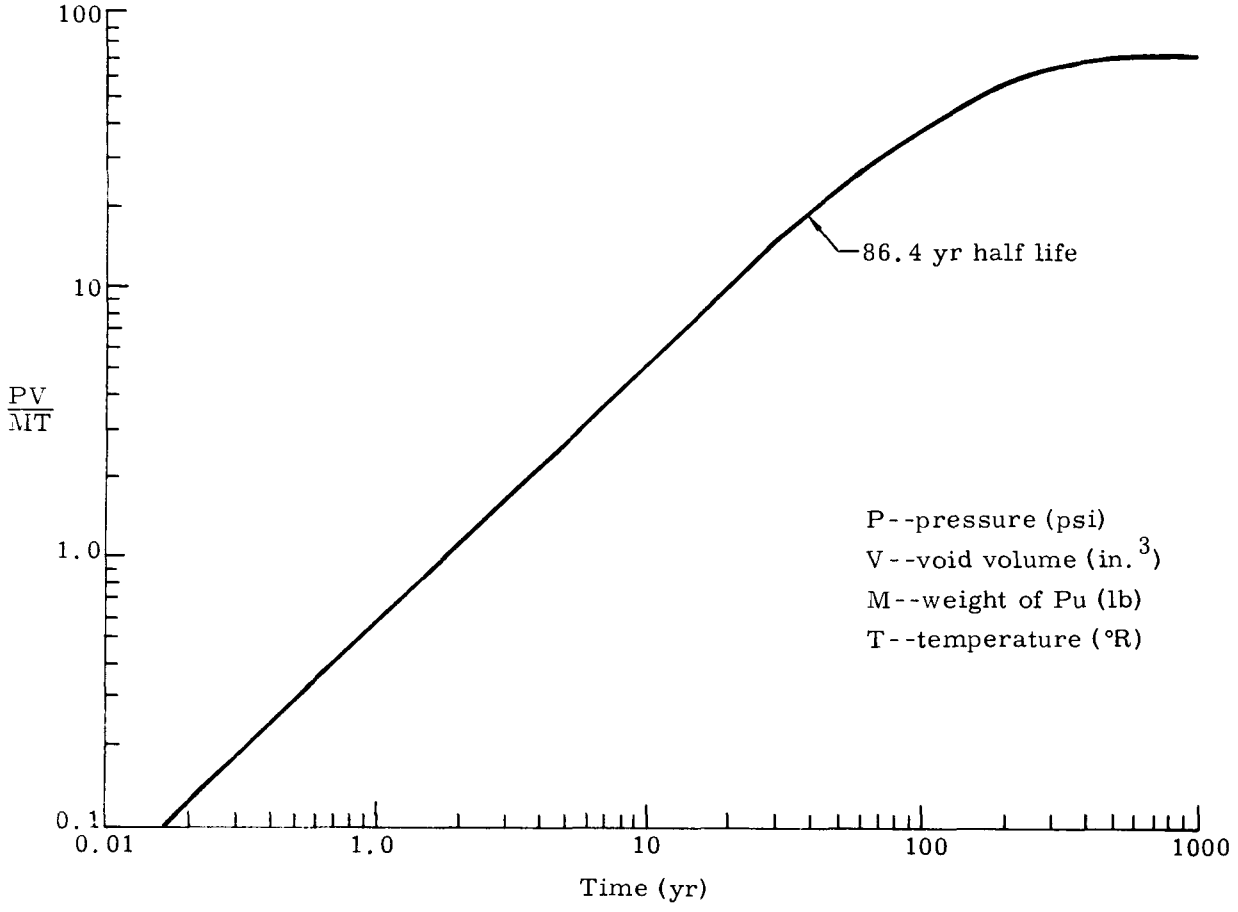

Fig. T-1. Plutonium-238 Pressure Buildup as Function of Time

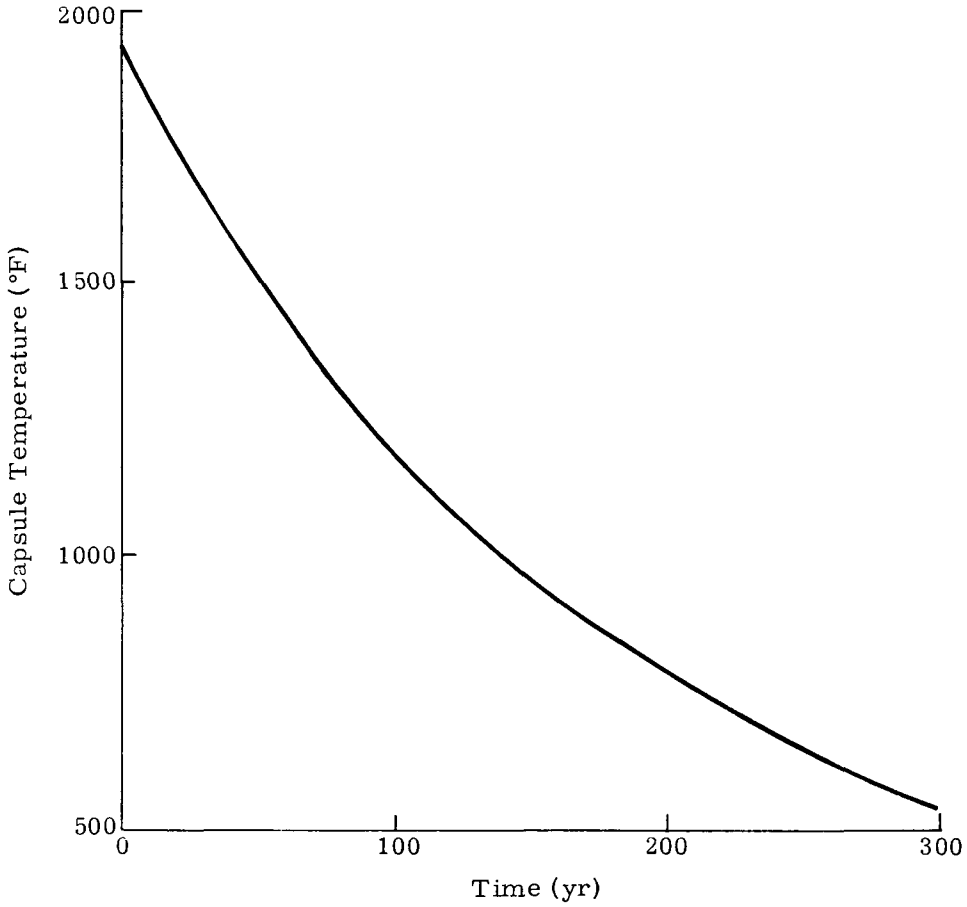

Fig. T-2. Capsule Temperature as Function of Time for Open Circuit Condition

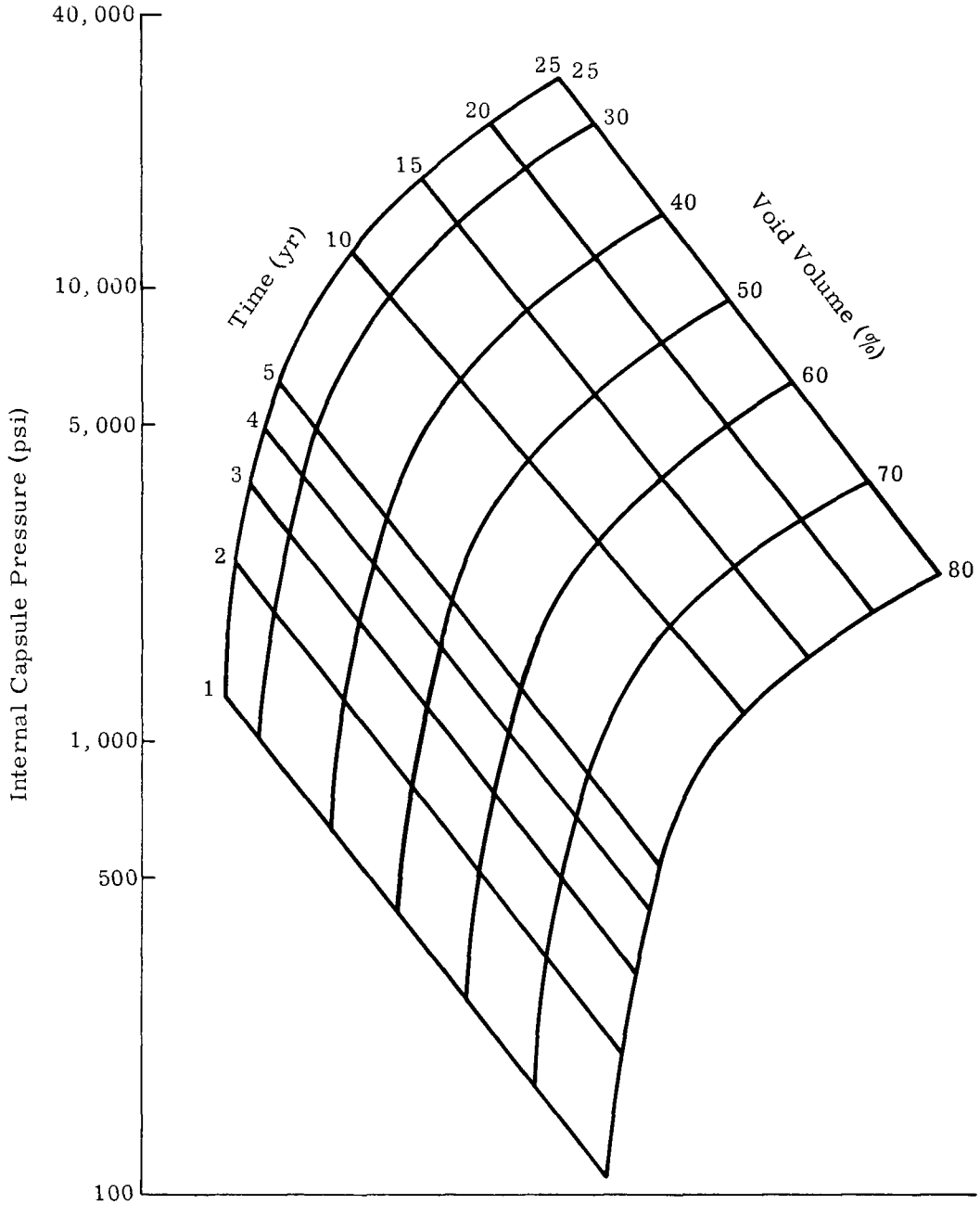

Fig. T-3. Internal Capsule Pressure as Function of Void Volume and Time

TABLE T-2

Void Volume ($in.^3$)	Plutonium ($lb/in.^3$)	M/V
0.25	0.243	0.970
0.40	0.194	0.485
0.50	0.162	0.324
0.60	0.130	0.217
0.80	0.065	0.081

Although Fig. T-3 shows the internal capsule pressure, it does not indicate the internal stress which is a function of the capsule dimensions. The stress at the inside diameter of a capsule is given by $\sigma = PD$, where σ is the stress, P is the internal pressure (Fig. T-3) and D is the dimension factor which is plotted in Fig. T-4 for radii of from one to three inches, and capsule thickness from 0.1 to 0.5 inch. Given a capsule size (right circular cylinders only) Figs. T-3 and T-4 can be used to establish the internal stress for any desired void volume at any period of time from 1 to 25 years.

For the 250-watt generator, the following calculation can be made to predict the characteristics of a capsule designed to contain the pressure for five years. Consider a 1.5-inch ID cylinder (length is immaterial) with a 0.2-inch wall thickness. This yields a dimension factor (D) of 4.6. The internal pressure, P, at five years for an 80% void is about 500 psi. Therefore, the stress is 2300 psi.

Rupture data for Haynes-25 bar is presented in Fig. T-5. For a stress of 2300 psi and an average capsule open circuit operating temperature of 1800° F, the time for capsule rupture is in excess of five years.

For accuracy, a Larson-Miller constant is needed to identify the real rupture time and this can be done in Phase I.

These preliminary calculations show that a capsule can be designed to contain helium pressure for a five-year period while the generator is in orbit. However, it is still recommended that use of a porous plug for helium venting be pursued in the design of the PuO_2 capsule because of the weight savings incurred. (SNAP 19 personnel are currently investigating these plugs for application in that generator.)

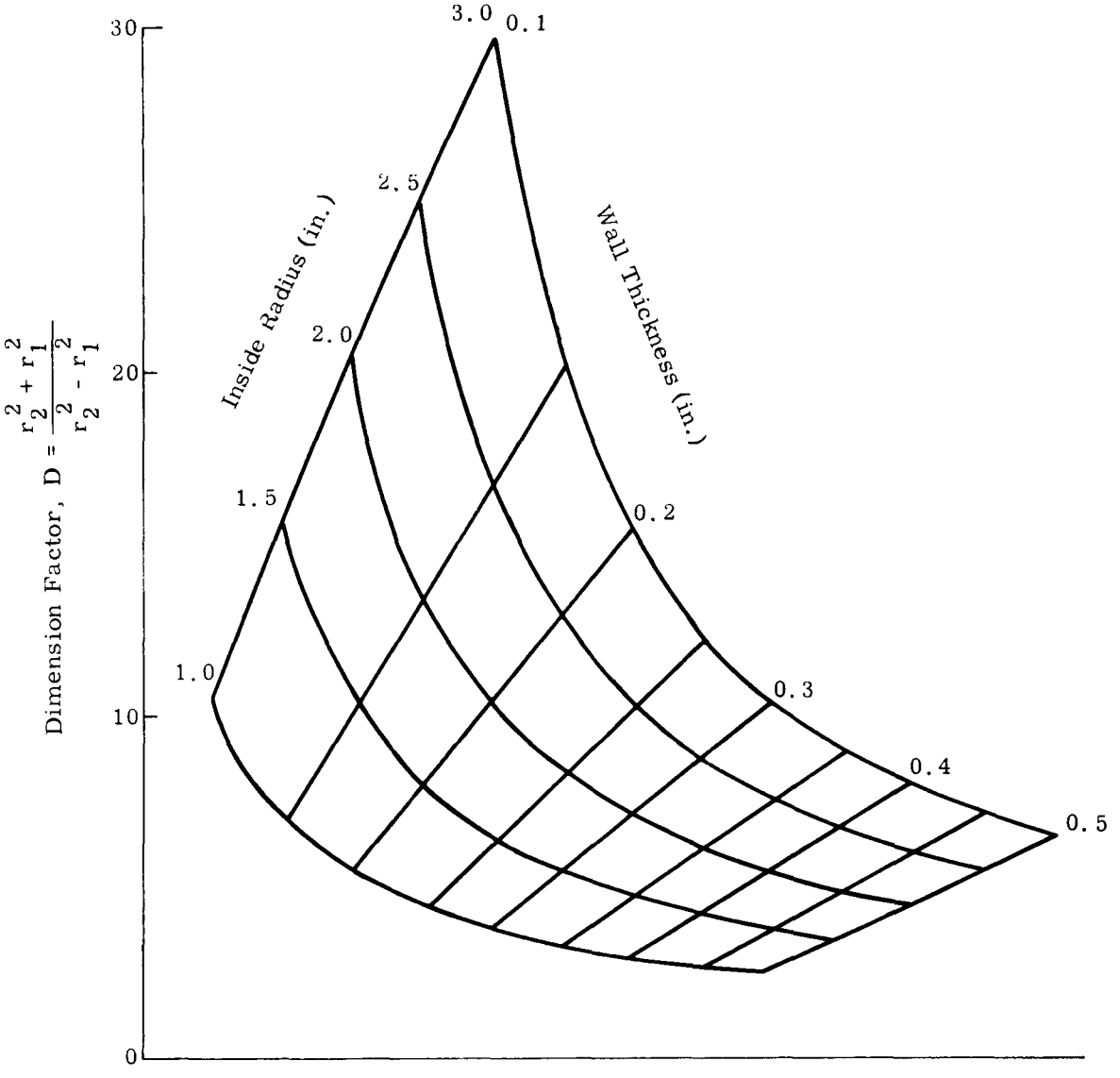

Fig. T-4. Dimension Factor D as Function of Inside Radius and Encapsulation Thickness

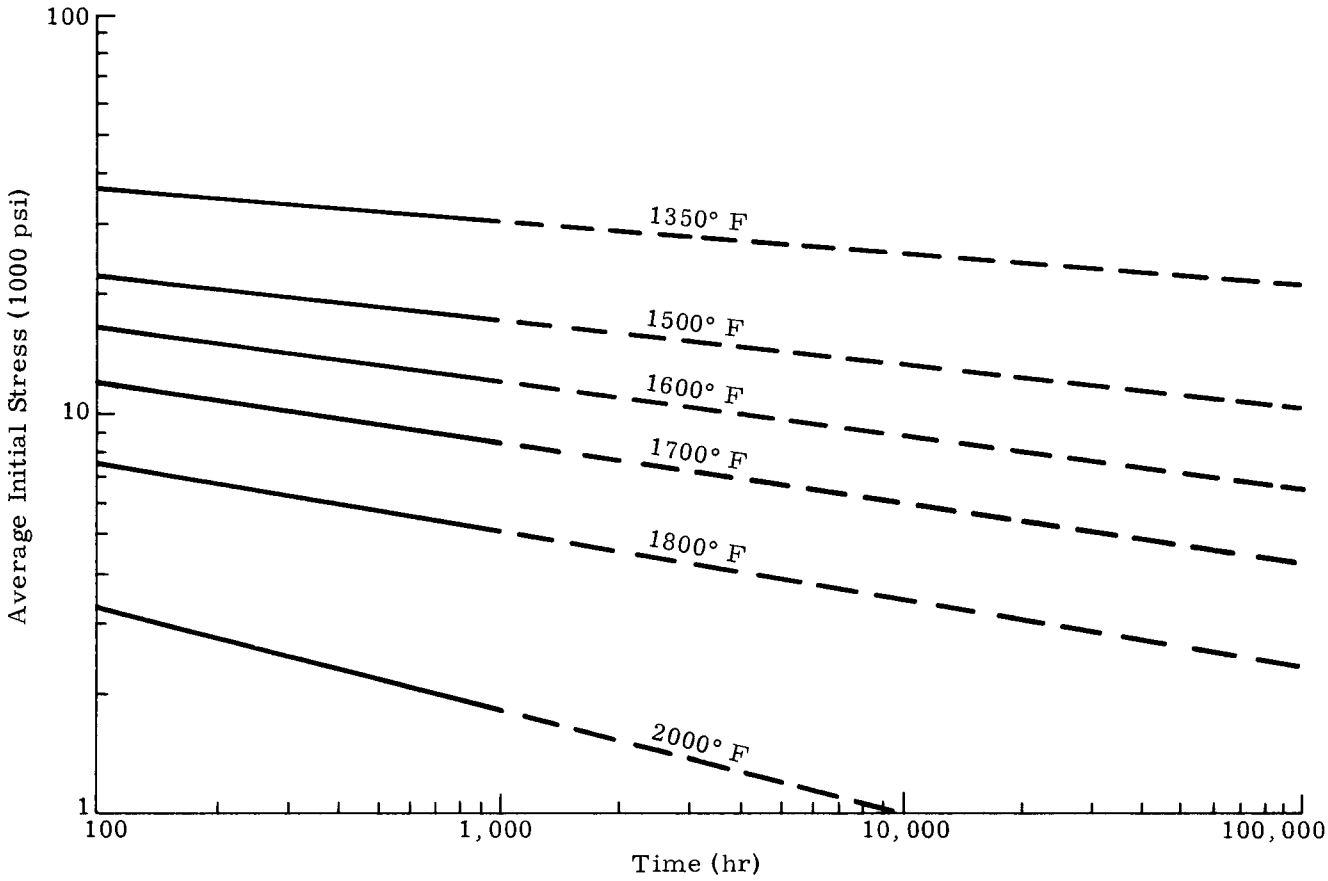

Fig. T-5. Rupture Range for Haynes-25 Bar

Also by the Larson-Miller approach, without a porous plug, the effect of the capsule being spiked to open circuit conditions prior to descent (and higher during descent) will have to be examined in Phase I. It may not be practical to design for pressure containment under these conditions. One possible alternative other than the porous plug is to incorporate a shorting device on the T/E module that does not allow open circuit conditions to occur at time of separation. This shorting plug would also reduce capsule temperatures during reentry.

APPENDIX U

CASCADED THERMOELECTRIC SYSTEM

The 250-watt reference concept employs SiGe thermoelectrics operating between 1450° and 550° F at the end of life with the following approximate parameters:

$\eta_{T/E}$ = 5.43%

$\eta_{thermal}$ ≈ 89%

η_{I^2R} ≈ $\frac{\text{net power to regulator}}{\text{gross power}}$

$\eta_{regulator}$ ≈ 99.5%

$\eta_{o/a}$ ≈ 4.4%

N = 396 couples (series parallel)

V = 30.5 volts (gross)

= 28 volts (net).

The purpose of this study was to determine the attractiveness of a cascaded system utilizing a SiGe topper rejecting heat to a PbTe (2N-3P) package. For this study, the cold junction temperature for the PbTe module was selected as 500° F. As with the SiGe noncascaded system (where the cold junction was 550° F), this cold junction temperature is not necessarily optimum. Furthermore, as shown in the analysis, these two cold junction temperatures permit direct substitution of the cascaded for the noncascaded system with little change in the radiator. This may be an advantage once the reference configuration is fully tested and proven although the 500° F cold junction may not be optimum for weight. (As with the SiGe module, cold junction optimization on the system will have to be done in Phase I.)

The incentive for considering a cascaded SiGe-PbTe system is best understood by reference to figure-of-merit curves for SiGe and PbTe where

$$\text{Figure of merit} = \frac{(\text{Seebeck coefficient})^2}{(\text{electrical resistivity})\,(\text{thermal conductivity})}$$

These are presented in Figs. U-1 and U-2 as a function of temperature for the N- and P-type materials, respectively. Indirectly, the figure

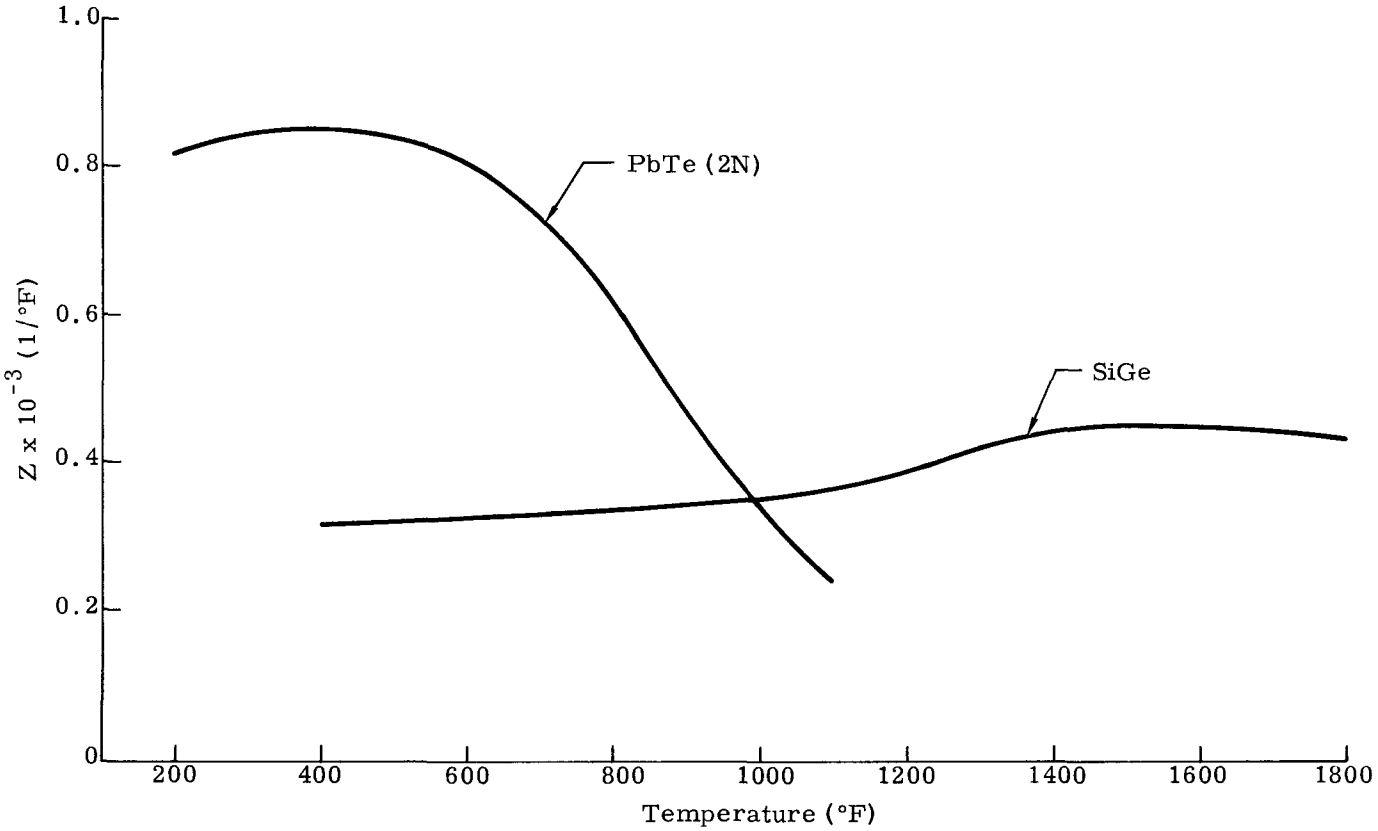

Fig. U-1. Figure of Merit for N Materials

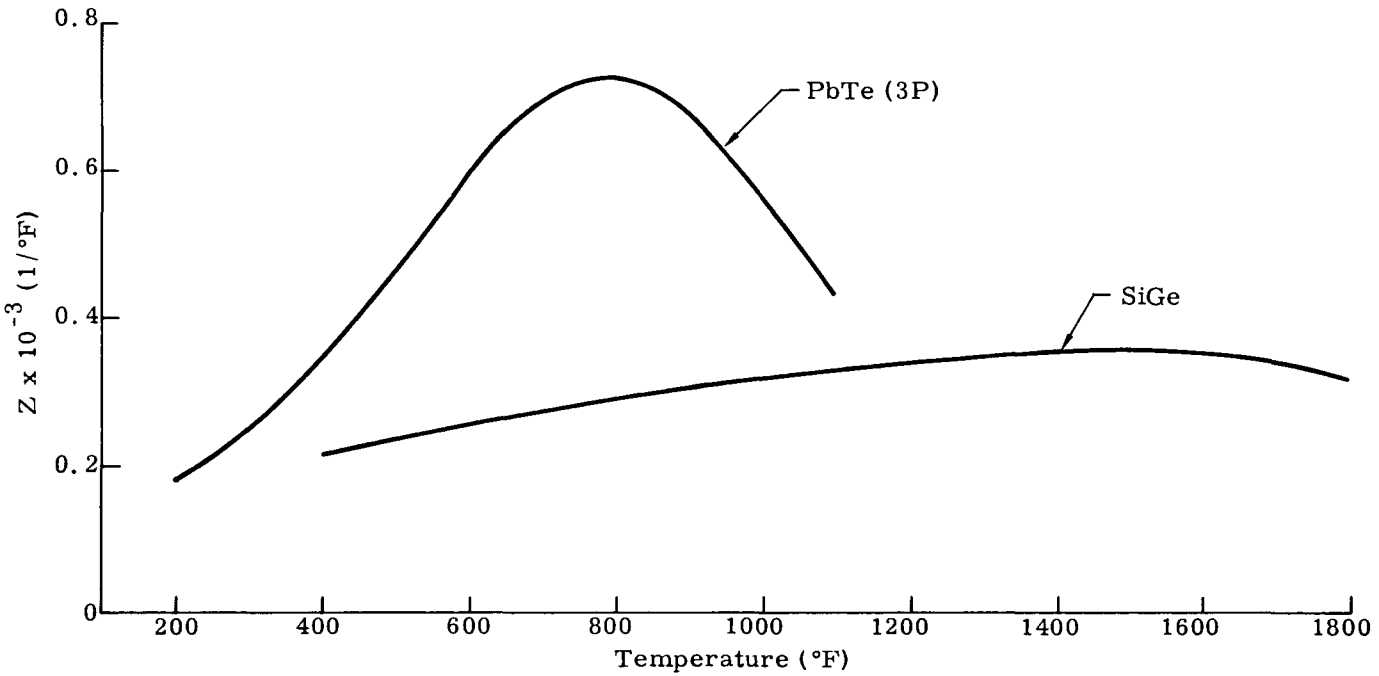

Fig. U-2. Figure of Merit for P Materials

of merit can be related to efficiency and thus an increase in efficiency is expected for a cascaded system.

A. ANALYSIS

1. Cascaded Performance

With the Martin digital code for thermoelectric (T/E) computations, T/E parameters were determined for SiGe for hot junction temperatures of 1300°, 1400° and 1500° F, cold junction temperatures of 900°, 1000° and 1100° F, a RCA recommended contact resistivity of 1800 $\mu\Omega$-cm^2, an element length of 0.75 inch and a gross voltage of 30.5 volts. The results are presented in Figs. U-3, U-4 and U-5. Similarly, results are presented for 2N and 3P type PbTe (Martin designation TEDN-0034/TEDP-0059) in Figs. U-6, U-7 and U-8 for hot junction temperatures of 900°, 1000° and 1100° F, cold junction temperatures of 300°, 400° and 500° F, an experimentally extrapolated contact resistivity of 3000 $\mu\Omega$-cm^2, an element length of 0.50 inch and a gross voltage of 30.5 volts.

For the cascaded system, it is assumed, by appropriate design, that a temperature drop of 100° F can be held between the SiGe cold junction and the PbTe hot junction at end of life (the design point).

In Table U-1 the SiGe efficiencies (from Fig. U-3) for cold junction temperatures of 1000°, 1050° and 1100° F are given. Also shown for later comparison are the noncascaded efficiencies for cold junctions of 350° to 600° F. In all cases, a hot junction temperature of 1450° F is used.

TABLE U-1

SiGe T/E Efficiency at End of Life for Hot Junction Temperature of 1450° F

Cold Junction Temperature (°F)	η T/E (%)
350	6.44
400	6.18
500	5.68
550	5.43
600	5.17
1000	2.88
1050	2.59
1100	2.29

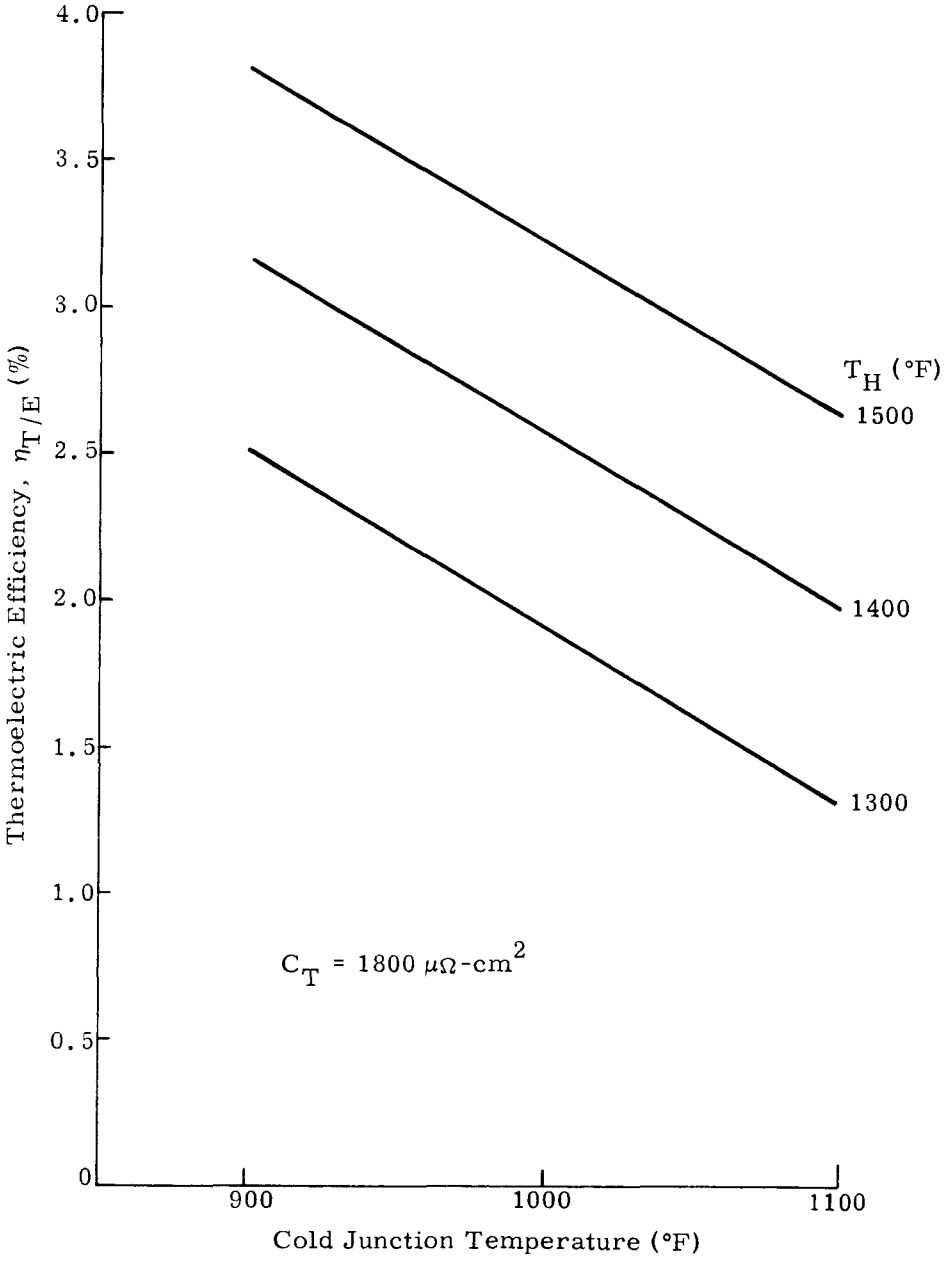

Fig. U-3. Thermoelectric Efficiency Versus Cold Junction Temperature

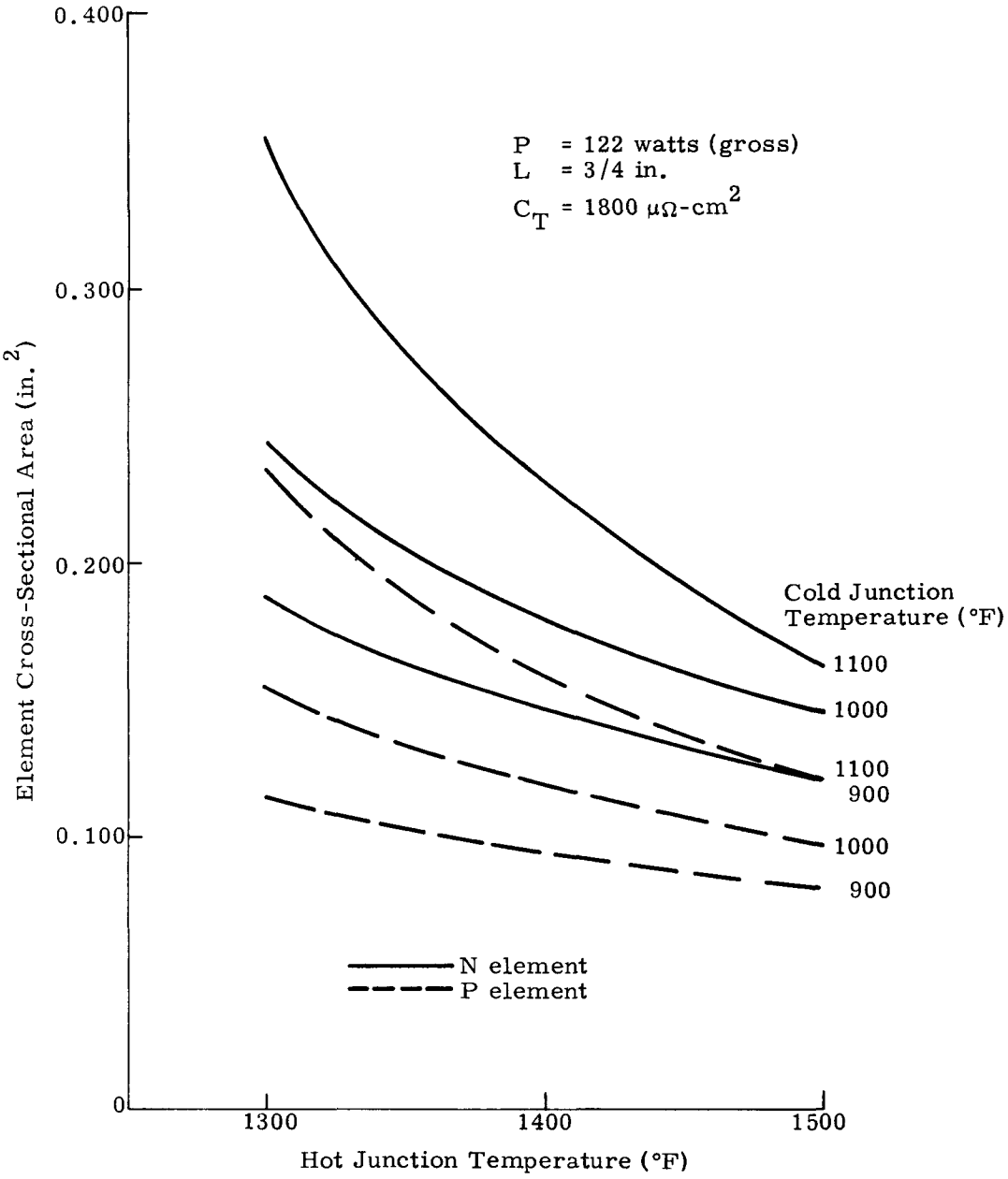

Fig. U-4. Single Element Area for SiGe Series - Connected

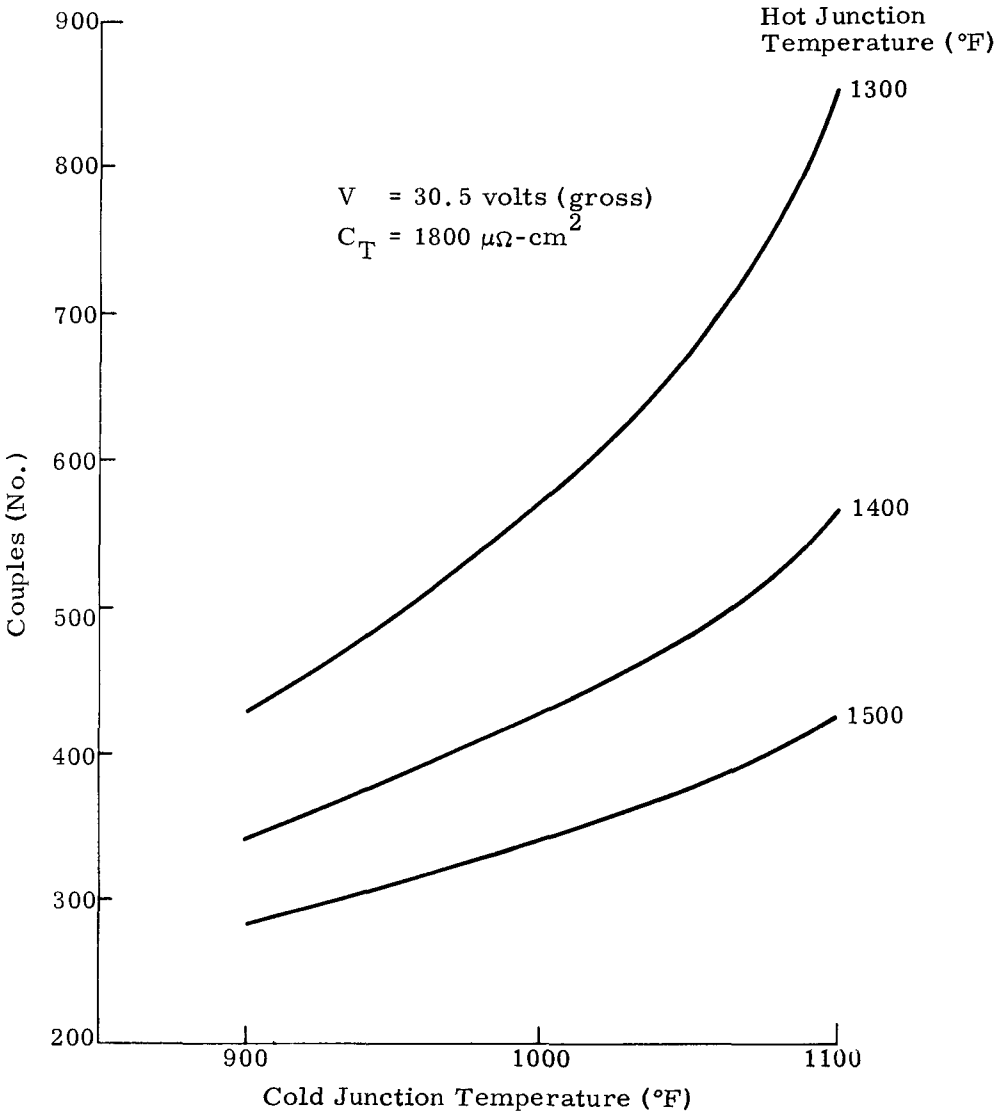

Fig. U-5. Number of Couples for SiGe Series - Connected

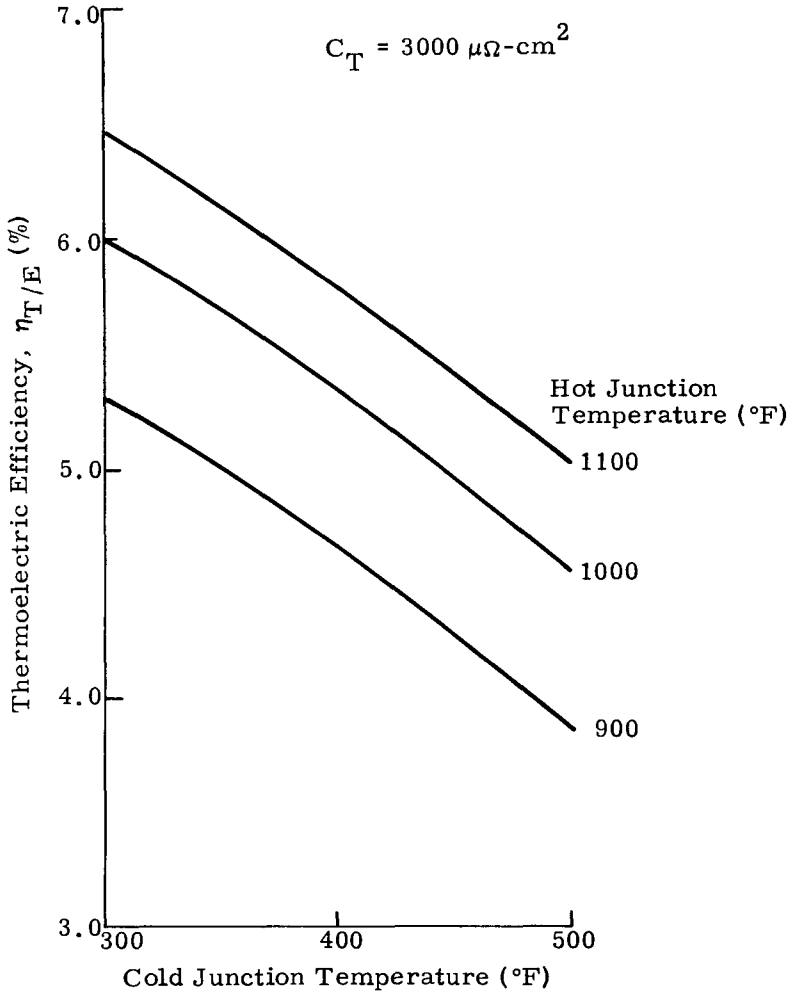

Fig. U-6. Thermoelectric Efficiency Versus Cold Junction Temperature for PbTe, 2N and 3P

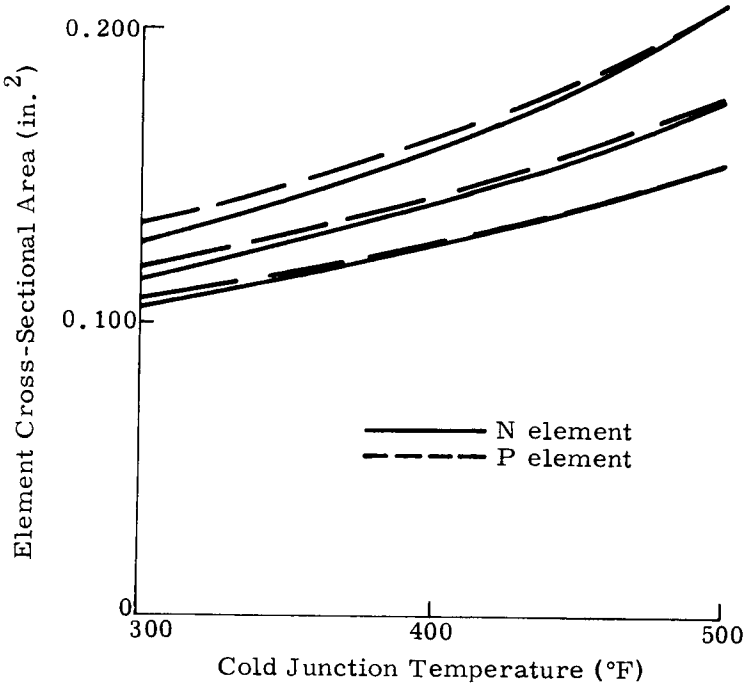

Fig. U-7. Single Element Area for PbTe, 2N and 3P Series - Connected

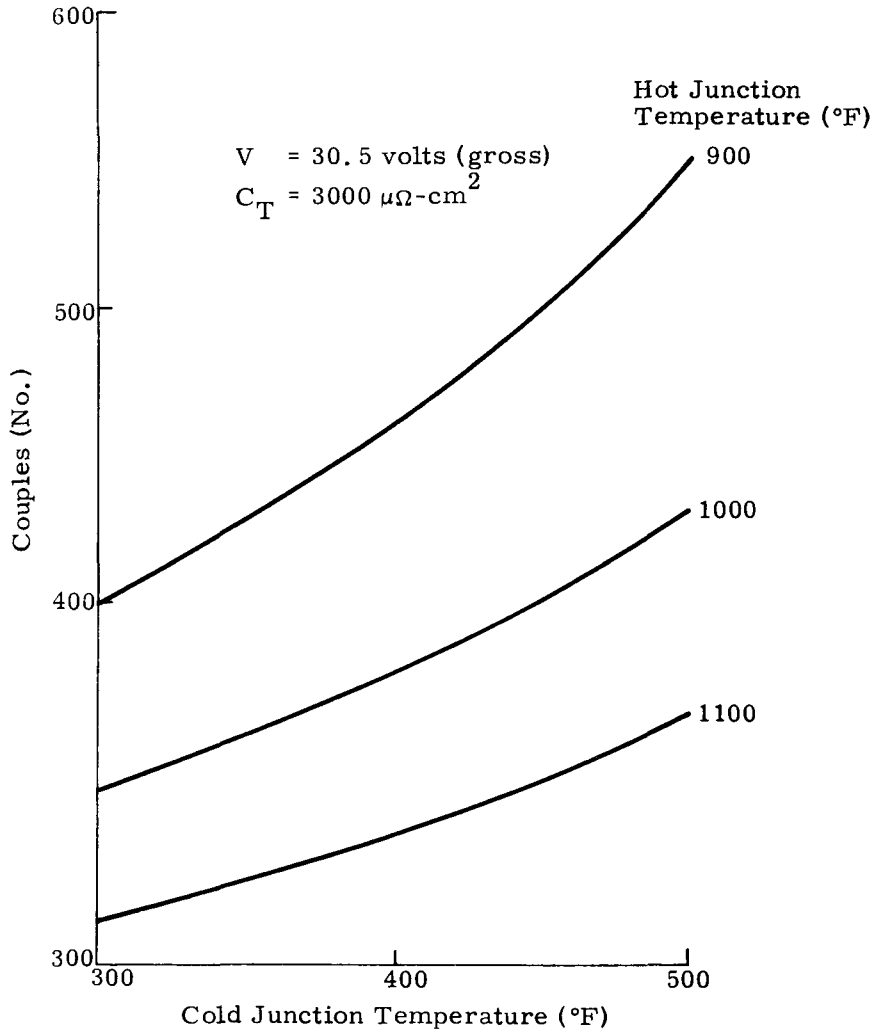

Fig. U-8. Number of Couples for PbTe, 2N and 3P Series Connection

In Table U-2 the PbTe efficiencies (from Fig. U-6) for cold junction temperatures of 350° to 550° F and hot junction temperatures of 900°, 950° and 1000° F are tabulated.

TABLE U-2

PbTe Thermoelectric Efficiency at End of Life

Cold Junction Temperature (°F)	$\eta_{T/E}$* (%)	$\eta_{T/E}$** (%)	$\eta_{T/E}$*** (%)
350	5.68	5.35	5.00
400	5.33	5.04	4.65
500	4.55	4.25	3.85
550	4.15	3.85	3.40

*T_H = 1000° F
**T_H = 950° F
***T_H = 900° F

Table U-3 provides the cascaded efficiencies for various temperature combinations as computed from the approximate formula

$$(\eta_{T/E})_{CASC} \approx (\eta_{T/E})_{SiGe} + (\eta_{T/E})_{PbTe} - (\eta_{T/E})_{SiGe}\,(\eta_{T/E})_{PbTe}$$

This formula, along with several other related equations, is derived in Appendix W.

From the data in Table U-3, it appears desirable to select an end-of-life PbTe hot junction temperature of 900° F (rather than 950° or 1000° F) since the slight loss in efficiency offsets the disadvantage of higher PbTe and cold end ‡SiGe temperatures. For the 500° F cold junction temperature, the cascaded thermoelectric efficiency is 6.62%.

‡With the present SiGe cold end stack, cold end temperatures are limited to ~475° F in air and ~930° F in vacuum. Thus, a new cold end stack would have to be developed but RCA thinks this is feasible.

TABLE U-3

Cascaded Thermoelectric Efficiency at End of Life for SiGe Hot Junction Temperature of 1450° F

Cold Junction Temperature (°F)	$\eta_{T/E}$, CASC* (%)	$\eta_{T/E}$, CASC** (%)	$\eta_{T/E}$, CASC*** (%)
350	7.84	7.80	7.73
400	7.50	7.50	7.39
500	6.73	6.73	6.62
550	6.34	6.34	6.18

*$T_{cold,\ SiGe}$ = 1100° F; $T_{hot,\ PbTe}$ = 1000° F

**$T_{cold,\ SiGe}$ = 1050° F; $T_{hot\ PbTe}$ = 950° F

***$T_{cold,\ SiGe}$ = 1000° F; $T_{hot,\ PbTe}$ = 900° F

The individual module efficiencies are:

$$\eta_{SiGe} = \eta_{T/E}\ \eta_{therm}\ \eta_{I^2R}\ \eta_{reg} = 2.88 \times 0.89 \times 0.92 \times 0.995 = 2.34\%$$

$$\eta_{PbTe} = \eta_{T/E}\ \eta_{therm}\ \eta_{I^2R}\ \eta_{reg} = 3.85 \times 0.90 \times 0.92 \times 0.995 = 3.17\%$$

The overall efficiency (see Appendix W) is:

$$\eta_{o/a} \approx \eta_{SiGe} + \eta_{PbTe} - \eta_{SiGe}\ \eta_{PbTe} - \frac{\eta_{PbTe}\ Q_{P1}}{Q_1}$$

$$= 0.0234 + 0.0317 - (0.0234)(0.0317) - 0.0317\ (0.05)$$

$$= 5.27\%$$

The fuel inventory (EOL) is

$$Q_1 = \frac{(P_1 + P_2)_{net}}{\eta_{o/a}} = \frac{250 \text{ watts}}{0.0527} = 4750 \text{ watts}$$

Once the operating temperatures on the two cascaded packages are selected, the individual output power of each module is uniquely determined, that is,

$$P_1 = Q_1 \, \eta_{SiGe} = 4750 \, (0.0234) = 111 \text{ watts (net)}$$

$$P_2 = P_{tot} - P_1 = 250 - 111 = 139 \text{ watts (net)}$$

On a gross basis, the SiGe module will produce

$$P_1 \text{ (gross)} = \frac{P_1}{\eta_{I^2R} \, \eta_{reg}} = \frac{111}{(0.92)\,(0.995)} = 122 \text{ watts (gross)}$$

while the PbTe module will produce

$$P_2 \text{ (gross)} = \frac{P_2}{\eta_{I^2R} \, \eta_{reg}} = \frac{139}{(0.92)\,(0.995)} = 152 \text{ watts (gross)}$$

2. Modules Connected in Parallel

Figures U-4 and U-5 show that for the SiGe module (1450° F hot junction, 1000° F cold junction) to produce 30.5 volts (gross) and 122 watts (gross), the following couples and couple sizes are needed:

	Series	Series parallel
Number of couples	380	760
Area per couple (in.^{2})		
N element	0.1630	0.0815
P element	0.1050	0.0525

Figures U-7 and U-8 show that for the PbTe module (900° F hot junction, 500° F cold junction) to produce 30.5 volts (gross) and 152 watts (gross), the following couples and couple sizes are needed:

	Series	Series parallel
Number of couples	547	1094
Area per couple (in.^{2})		
N element	0.2115	0.1058
P element	0.2125	0.1062

3. Modules Connected in Series

Consider the modules connected to one another in series (but each internally wired in series parallel). Design to 10 amperes for each module. Then,

$$V_{SiGe,\ net} = \frac{P_{SiGe,\ net}}{I} = \frac{111 \text{ watts}}{10 \text{ amperes}} = 11.1 \text{ volts}$$

$$V_{PbTe,\ net} = \frac{P_{SiGe,\ net}}{I} = \frac{139 \text{ watts}}{10 \text{ amperes}} = 13.9 \text{ volts}$$

and

$$\left(V_{SiGe} + V_{PbTe}\right)_{net} = 11.1 + 13.9 = 25 \text{ volts}$$

On a gross basis,

$$V_{SiGe,\ gross} = \frac{P_{SiGe,\ gross}}{I} = \frac{122 \text{ watts}}{10 \text{ amperes}} = 12.2 \text{ volts}$$

$$V_{PbTe,\ gross} = \frac{P_{PbTe,\ gross}}{I} = \frac{152 \text{ watts}}{10 \text{ amperes}} = 15.2 \text{ volts}$$

and

$$\left(V_{SiGe} + V_{PbTe}\right)_{gross} = 12.2 + 15.2 = 27.4 \text{ volts}$$

The number of couples and element sizes may be determined by a direct ratioing of the values previously presented for the modules in parallel. Then for SiGe (series parallel)

N_{SiGe} = 304 couples

N/couple = 0.2040 $in.^2$

P/couple = 0.1310 $in.^2$

while for PbTe (series parallel)

N_{PbTe} = 546 couples

N/couple = 0.2120 $in.^2$

P/couple = 0.2135 $in.^2$

4. Radiator Temperature

For the noncascaded system, the end-of-life radiator temperature is 505° F = 965° R. With the cascaded system, the radiator temperature would be (with the same area):

$$T_{rad} = 965 \left(\frac{q_{reject,\ cascaded}}{q_{reject,\ noncascaded}} \right)^{1/4}$$

$$965 \left(\frac{4750-250}{5660-250} \right)^{1/4} = 920° R = 460° F$$

Assume with this radiator temperature, cold junction temperature at end of life of 500° F can be designed. (If not, the radiator will have to be enlarged.)

5. Layout and Weight Statement

A layout of the cascaded system (modules connected to one another in series since this connection results in fewer couples and lighter weight) is shown in Fig. U-9. A weight statement is given in Table U-4.

B. CONCLUSIONS

The cascaded and SiGe noncascaded systems are compared in Table U-5 on items other than weight. On a weight basis, the cascaded RTG is significantly heavier at 479 pounds as compared to 345 pounds for the noncascaded system. The only possible advantage of the cascaded system will be one of efficiency (5.27%, overall, versus 4.42%). At beginning of life these efficiency differences correspond to thermal wattage differences of 1040 watts. If the price of PuO_2 of $1000/watt(t) is valid, the cascaded system would offer fuel savings of approximately one million dollars per system. This savings would have to be offset by the additional costs of launching the heavier cascaded system. The theoretical efficiency advantage may also be important because of availability limitations on PuO_2.

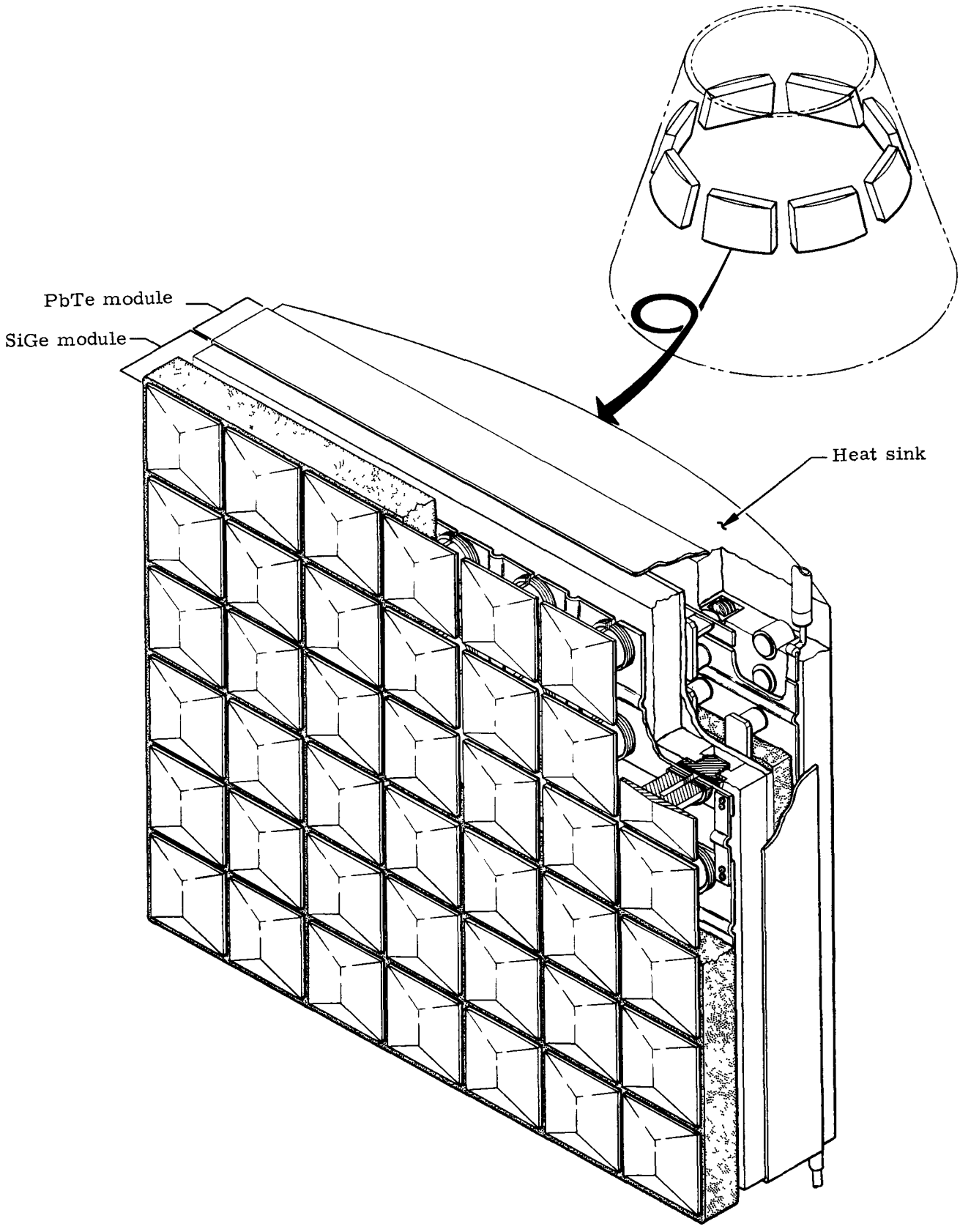

Fig. U-9. Cascaded System Layout (Modules Wired Together in Series)

TABLE U-4

Cascaded Module Weight

	Weight per Cascaded Module (lb)		Weight per Eight Cascaded Modules (lb)	
SiGe module		5.61		44.9*
Hot shoes	0.76		6.1	
Thermoelectric elements	1.35		10.8	
Cold shoes	1.11		8.9	
Flexi-Mod cold end hardware	1.60		12.8	
Thermal insulation	0.79		6.3	
PbTe module and canister		15.13		121.1
Hot plate	3.70		29.6	
Hot shoes	0.92		7.4	
Thermoelectric elements	4.38		35.0	
Cold end hardware (lumped with transfer plate)	--		--	
Thermal insulation	0.30		2.4	
Support membrane	0.32		2.6	
Transfer plate	5.51		44.1	
Total cascaded system		20.74		166.0
Total selected system (non-cascaded, SiGe based on using 33 12-couple modules).				(-) 32.0
Net savings with selected system (lb)				134.0

*Note that the SiGe portion of the cascaded system weighs more than the entire selected system using SiGe only, even though it supplies less than half the power output. This may be explained by the larger elements in the cascaded SiGe module since they operate over a much smaller ΔT.

TABLE U-5

EOL Performance Characteristics

	Noncascaded	Cascaded	
		SiGe to PbTe in Series	SiGe to PbTe in Parallel
Temperatures (°F)			
SiGe hot junction	1450	1450	
SiGe cold junction	550	1000	
PbTe hot junction	--	900	
PbTe cold junction	--	500	
Radiator	505	460	
Efficiencies (%)			
SiGe thermal	89	89	
PbTe thermal	--	90	
SiGe T/E	5.43	2.88	
PbTe T/E	--	3.85	
Cascaded T/E	--	6.62	
Joule (for each module)	92	92	
Regulator (for each module)	99.5	99.5	
Overall	4.42	5.27	
Fuel inventory (watts)			
EOL	5660	4750	
BOL	6420	5380	
Power (watts)			
Net	250	111 SiGe 139 PbTe	
Gross	273	122 SiGe 152 PbTe	
Current (amp)	~9	10 SiGe 10 PbTe	4 SiGe 5 PbTe
Voltage (volts)			
Net	~28	11.1 SiGe 13.9 PbTe	28 SiGe 28 PbTe
Gross	30.5	12.2 SiGe 15.2 PbTe	30.5 SiGe 30.5 PbTe
Number of couples			
Series parallel	396	304 SiGe 546 PbTe	760 SiGe 1094 PbTe
N-element area per couple ($in.^2$)			
Series parallel	0.0905	0.2040 SiGe 0.2120 PbTe	0.0815 SiGe 0.1058 PbTe
P-element area per couple ($in.^2$)			
Series parallel	0.0560	0.1310 SiGe 0.2135	0.0525 SiGe 0.1062 PbTe

APPENDIX V

POWER CONDITIONING FOR PEAK LOADS

Energy storage is necessary when the power demanded by a spacecraft load exceeds the capability of the onboard generator. Since storage devices generally are charged at potenials higher than their discharge potential, the voltage during peak load periods will be lower than during minimum load periods. The depth of voltage suppression when peak loads are applied is dependent on the type of storage device, the severity of the discharge rate relative to its capacity, its state of charge, how it is connected to the system, and whether supplementary power conditioning equipment is employed. Thus, given performance requirements may be met or exceeded by various system configurations, each having its own advantageous features. A series of configurations will be developed in the succeeding paragraphs, performance characteristics and weight will be enumerated and the relative probability of mission success of each will be indicated. The components of the configuration selected will be described.

A. REQUIREMENTS

1. General

Energy storage and power conditioning equipment shall be considered as a separate supplemental subsystem to the RTG/CIR system. An estimate of the weight of such a subsystem shall be provided.

2. Electrical

The energy storage and power conditioning (ES/PC) subsystem shall provide an output voltage of 28 volts dc ± 10% when subjected to the Nimbus B load profile for a period of five years (24,500 orbits). The load profile for each 107-minute orbit, shown in Fig. V-1, includes the following highlights:

Average load	235 watts
Minimum load	213 watts
Maximum load	390 watts, 30 seconds
Followed by	290 watts, 5 seconds
Secondary peak load	337 watts, 3 seconds

Although the impedance characteristics of the Nimbus B loads are not known, it has been conservatively assumed that they are constant wattage loads. Since the minimum output from the RTG is 250 watts (at EOL) and the average load requirement is 235 watts, at least 15 watts average are available for inefficiencies in battery charging.

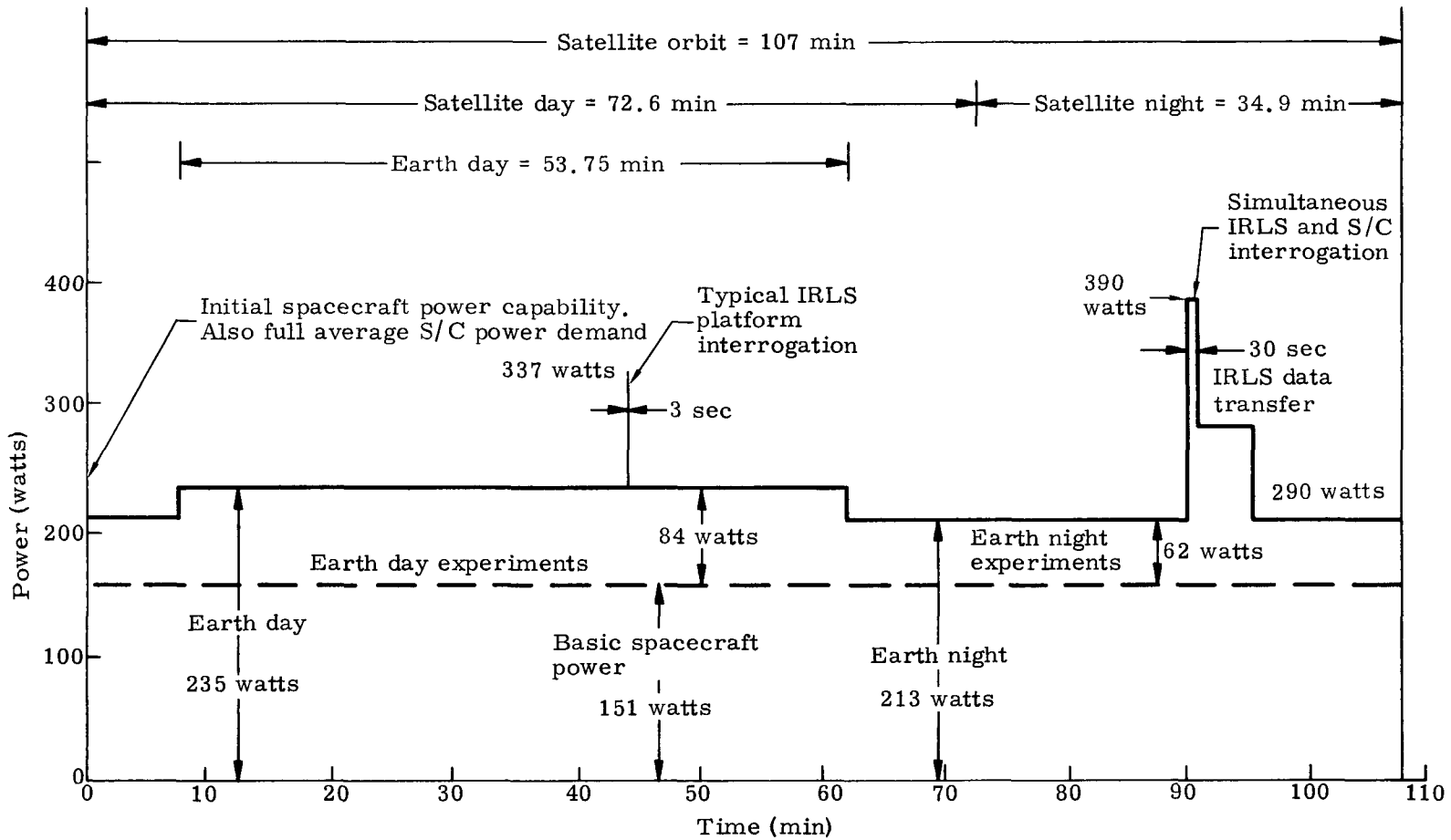

Fig. V-1. Nimbus B Load Power Profile

3. Environmental

The electronic equipment used in the ES/PC subsystem shall operate over the temperature ranges normally experienced by the other electronic equipment aboard the Nimbus B. Because of the orbit shade period duration variation and vehicle attitude changes, it is assumed that the batteries used in the ES/PC subsystem can be thermally located on the vehicle so as to experience a temperature range of 40° to 90° F.

B. SYSTEM DESIGN

1. Design Approach

Evaluation of the load profile together with the RTG capacity from beginning to end of life will reveal the continually changing battery discharge requirements. Since the battery will experience upward of 24,500 cycles of discharge, a shallow depth of discharge must be selected to provide the required cycle life. The various types of batteries available have differing cycle life capabilities, total stand life, space adaptability, and space experience. From the aforementioned requirements, the most suitable type of battery and the minimum required capacity will be selected.

Analysis of charge-discharge, voltage-current characteristics at both temperature extremes, using a minimum of battery capacity, should reveal the performance of the simplest system. Further study should reveal the opportunity to improve performance by increasing installed capacity and/or the use of ancillary regulation techniques. The analysis of the resultant alternative configurations should reveal the most appropriate energy storage/power conditioning subsystem.

2. Energy Storage Requirements and Type

Typical of thermoelectric elements, the voltage for maximum power at the beginning of RTG life (BOL) is greater than the voltage for maximum power at the end of RTG life (EOL). The 250-watt generator will be capable of supplying 360 watts at BOL; however, the 360 watts are available only at a voltage 20% higher than the EOL maximum power voltage. Thus, if power is taken at the BOL at the EOL voltage, less than 360 watts will be available. At the BOL only the 390-watt, 1/2-minute load exceeds the RTG capacity. Therefore, slightly more than 30 watts for 1/2 minute (0.25 watt-hr) will be supplied by the battery. At the EOL, the 390-, 290- and 337-watt loads (Section A.2) exceed the 250-watt RTG capability. The battery must supply the difference, which amounts to 275 watt-minutes or 4.6 watt-hours. In determining battery cycle life, it may be assumed that the average discharge over the five-year period is the average of the BOL and EOL discharges. Thus, during 24,500 orbits or discharge cycles, an average discharge will be 2.4 watt-hours.

To enhance the assurance of adequate battery cycle life, a life of 37,000 cycles (150% life) has been selected. According to Gulton Industries data, hermetically sealed nickel-cadmium batteries at 90° F should last 37,000 cycles if during each cycle they discharge at an average of less than 4-1/2% of their rated capacity; at 40° F, less than 2-1/2%. In five years, the batteries will be spending most of their time at 50° to 90° F (slightly more than 4-1/2% depth permitted) and will spend the least time at 40° F (2-1/2% depth). Therefore, the minimum rated battery capacity should be approximately 22 times the previously determined 2.4 watt-hours average discharge or 53 watt-hours. At an average discharge voltage of 28 volts, a single 53-watt-hour battery would be composed of two-ampere-hour cells (53/28 = 1.9 amp-hr).

Silver-cadmium cells have been considered for this application since they generally offer more watt-hours per pound. Unfortunately, considerably less is known about the cycle life of these cells, especially above 10,000 cycles. From scattered data, it appears that shallower depths of discharge would be required, thus requiring a greater minimum capacity and nullifying the watt-hr/lb advantage. The nonmagnetic qualities of silver-cadmium cells, if required by the spacecraft instrumentation, would be one possible reason for their use.

3. Evolution of Alternative Configurations

a. Configuration I

The simplest method of adapting storage devices to a generator system consists of floating batteries in parallel with the generator and load as shown in Fig. V-2, Configuration I. Analysis will reveal that the vehicle load will receive the maximum voltage at the BOL when the load is minimum and the batteries at 40° F are being overcharged. The lowest voltage will occur at the EOL when the load exceeds RTG capacity and the batteries at 40° F are experiencing their greatest discharge.

b. Configuration II

A minimum of battery capacity will cause a large definable voltage spread under these load extremes when the battery is at its minimum temperature (40° F). Tripling the battery capacity results in discharging the battery effectively at a much slower rate, resulting in a higher discharge voltage. Similarly, under charge, the effectively slower charge rate is accomplished at a slightly lower voltage. Thus, when the vehicle load changes from minimum to maximum, the voltage spread experienced is reduced considerably by increasing the installed battery capacity. The oversized battery configuration (II of Fig. V-2) is the same as Configuration I.

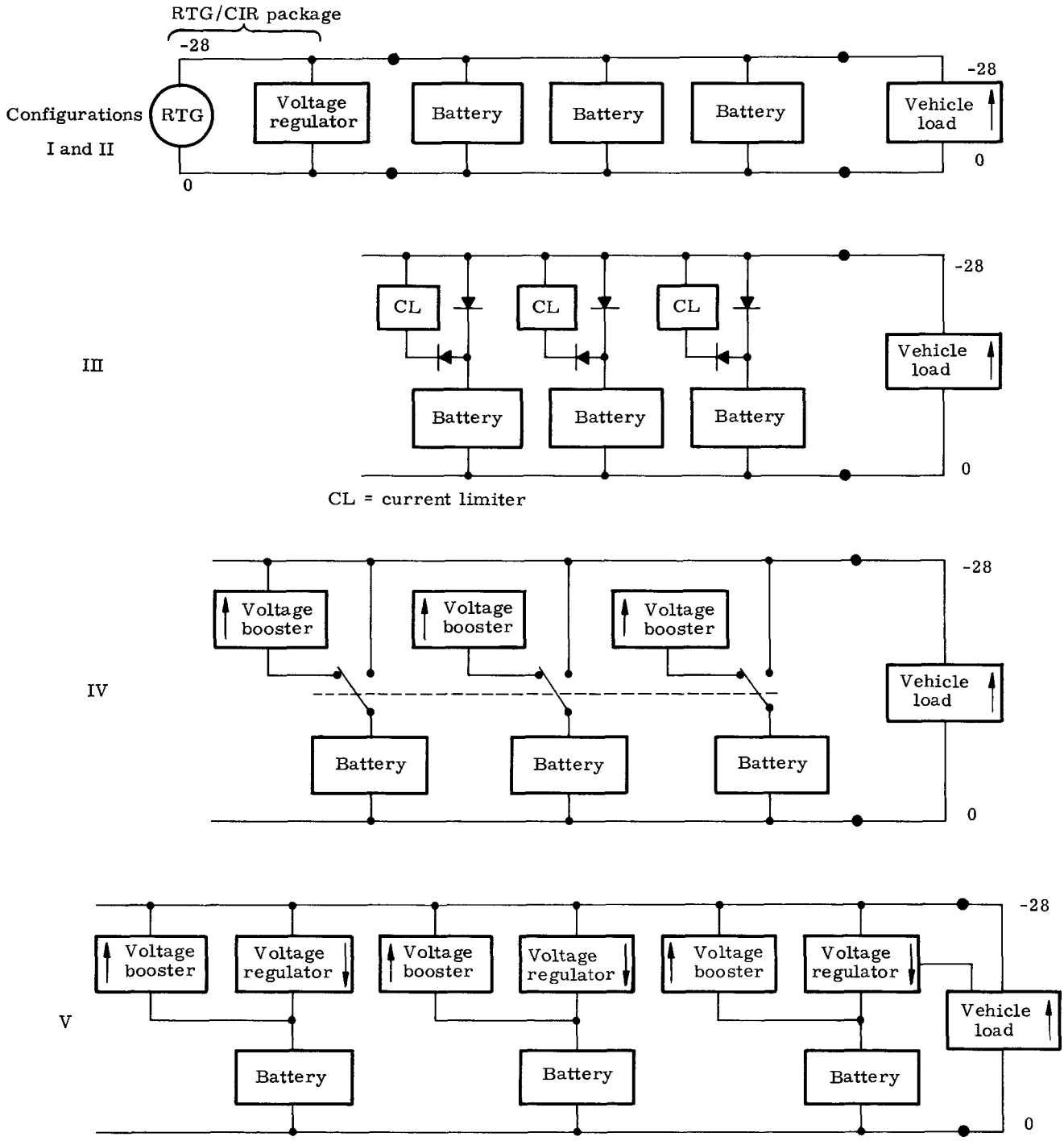

Fig. V-2. Power System Configurations

The voltage spread can also be reduced by maintaining a higher state of battery charge. At high charge states, the incremental ampere-hour charging efficiency is very low, thus requiring considerably more charging power. Because of charging power limitations and the potential of cell gassing at overcharge, charge states commensurate with these restrictions must be used.

c. Configuration III

If any one of the directly connected floating batteries of Configurations I and II shorts, the voltage across each of the remaining cells would increase 5%. Cells at 90° F, 90% charged, will charge at the nine-hour rate at 1.42 volts per cell. At a 5% higher voltage, they will charge at the 1.5-hour rate. This sixfold increase in charge current (and power) will cause the cells to gas at overcharge, ultimately resulting in an explosion. Thus, charge control is required. Configuration III (Fig. V-2) shows a method of isolating multiple batteries so that the shorting of any one battery will not impair the performance of the remaining batteries and a shorted cell will not draw excessive charging power nor gas.

d. Configuration IV

The isolation devices of Configuration III (discharge diodes and current limiting transistors) unfortunately introduce an additional voltage drop during both charge and discharge, further increasing the vehicle load voltage spread. To reduce the voltage spread and at the same time retain the battery isolation feature, the batteries could be isolated from the vehicle load when they are being charged, and connected to the load only when the load exceeds the present RTG capacity. Configuration IV (Fig. V-2) shows individual voltage boosters for battery charging and a three-pole switch for discharge control. Each pole would close only if its battery were at proper voltage and if the load voltage revealed the need for battery support. The number of cells in each battery would be selected such that at least 28 volts would be available under the heaviest discharge. At light discharges, the battery voltage normally would be higher. Since the batteries and load are in parallel with the RTG shunt voltage regulator, the shunt regulator will load the battery temperatures and states of charge; the battery discharge rate will be the same regardless of the actual load requirement. The shunt regulator loading alters to absorb any excess energy withdrawn from the battery. This configuration, therefore, overworks the battery, decreases its cycle life, and causes the battery to consume more than three times the charging power actually required.

e. Configuration V

The unnecessary battery discharges of Configuration IV can be overcome by providing a better voltage match between the battery and the bus

under the variable discharge conditions encountered. Configuration V includes a voltage regulator in the discharge circuit of each battery. When the bus voltage is above 27.9 volts, each regulator will have an infinite series resistance. When the vehicle lowers toward 27.7 volts, each battery series regulator will lower its resistance to a minimum value. The shunt regulator below 28 volts will be at an infinite shunt resistance. Current flow from the bus to a battery is precluded by the design of the series regulator. The voltage boosters, in this configuration, would have to be current-limited to preclude them from being overloaded when they are effectively shorted by the series voltage regulator during low bus voltage conditions (27.7 to 27.9 volts).

4. Configuration Performance

In order to evaluate these five configurations quantitatively, system characteristics for each have been determined. Figure V-3 presents the load voltage-current characteristics specifically for Configuration III and is somewhat representative of Configurations I and II. The resultant system characteristic is a composite of the characteristics of the RTG (at BOL and EOL), the batteries under discharge (at charge state and temperature extremes), and the batteries under charge (at temperature extremes) as controlled by the charge limiter.

On Fig. V-3, the space between the intersection of the RTG line with the battery charge and discharge characteristics is caused primarily by the sum of the voltage drops across the discharge diodes and the charge limiters when the latter are at minimum resistance. Configuration II excludes this drop; consequently, Fig. V-3 represents Configuration II if the battery charge and shunt regulator characteristics are translated downward 0.8 volt and the discharge characteristics similarly translated upward.

Configuration IV and V include a minimum capacity battery, one-third the capacity used in Fig. V-3. Consequently, the battery discharge curves of Fig. V-4 are three times as steep. Since Configurations IV and V furnish no less than 27.7 volts, the discharge curves are located at higher voltage levels on this figure. On Configuration IV, at BOL and a battery temperature of 90° F, the application of the maximum load (390 watts) causes the RTG to supply 12.6 amperes at 27.7 volts and the battery to supply 17 amperes at 27.7 volts, a total of 29.6 amperes. The load absorbs 14.2 amperes and the shunt regulator absorbs the difference, 15.4 amperes. Actually, the battery only needed to supply 14.2 - 12.6 = 1.6 amperes.

Configuration V overcomes this problem by supplying 1.6 amperes from the battery at 35.3 volts. The dotted line of Fig. V-4 shows the voltage across the series regulators to be 35.3 - 27.85 = 7.45 volts. This voltage drop, although wasting 12 watts to supply 30, is better than wasting (15.4) (27.7) = 426 watts, as was done in Configuration IV.

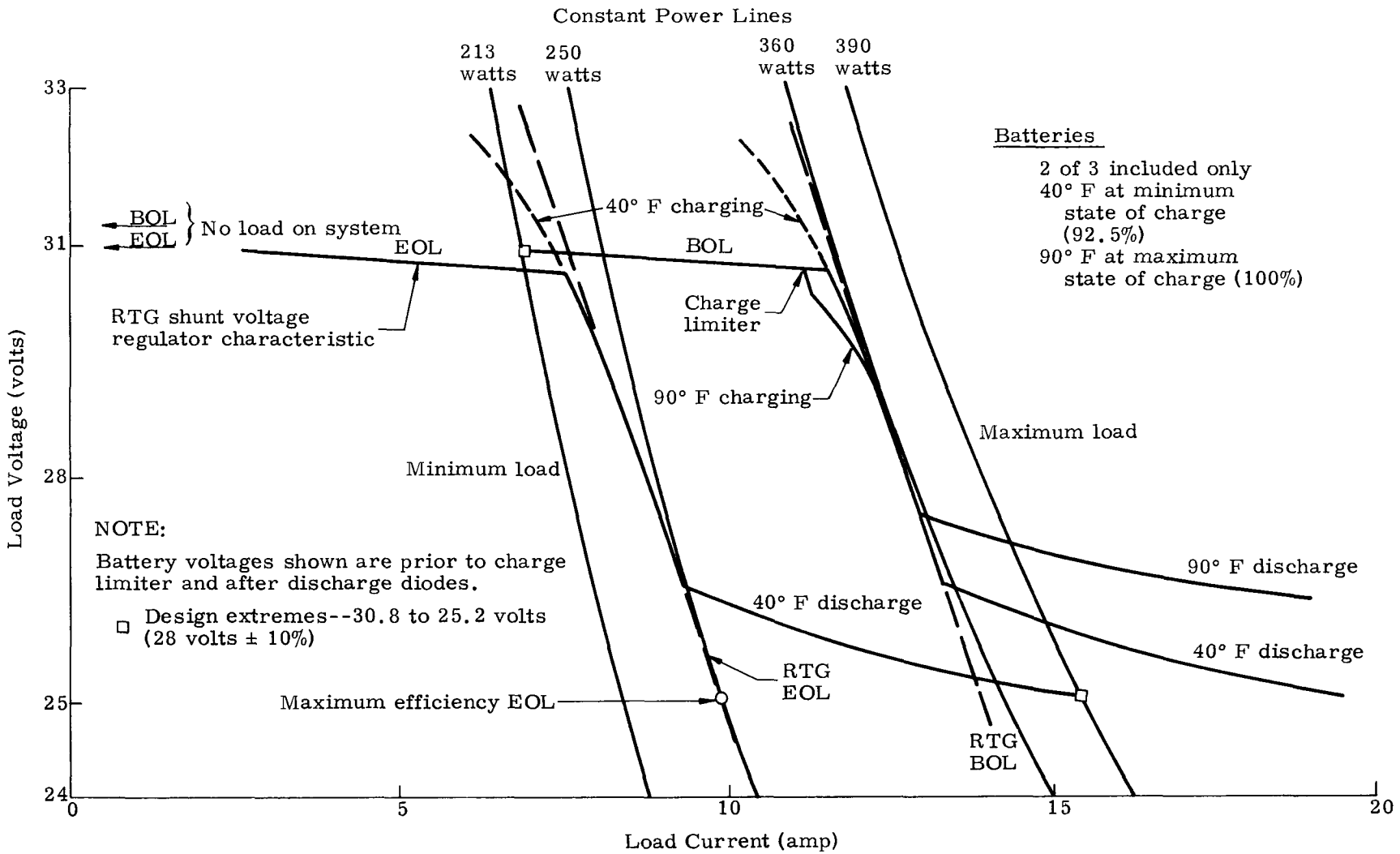

Fig. V-3. Electric Power System Characteristics for Configuration III

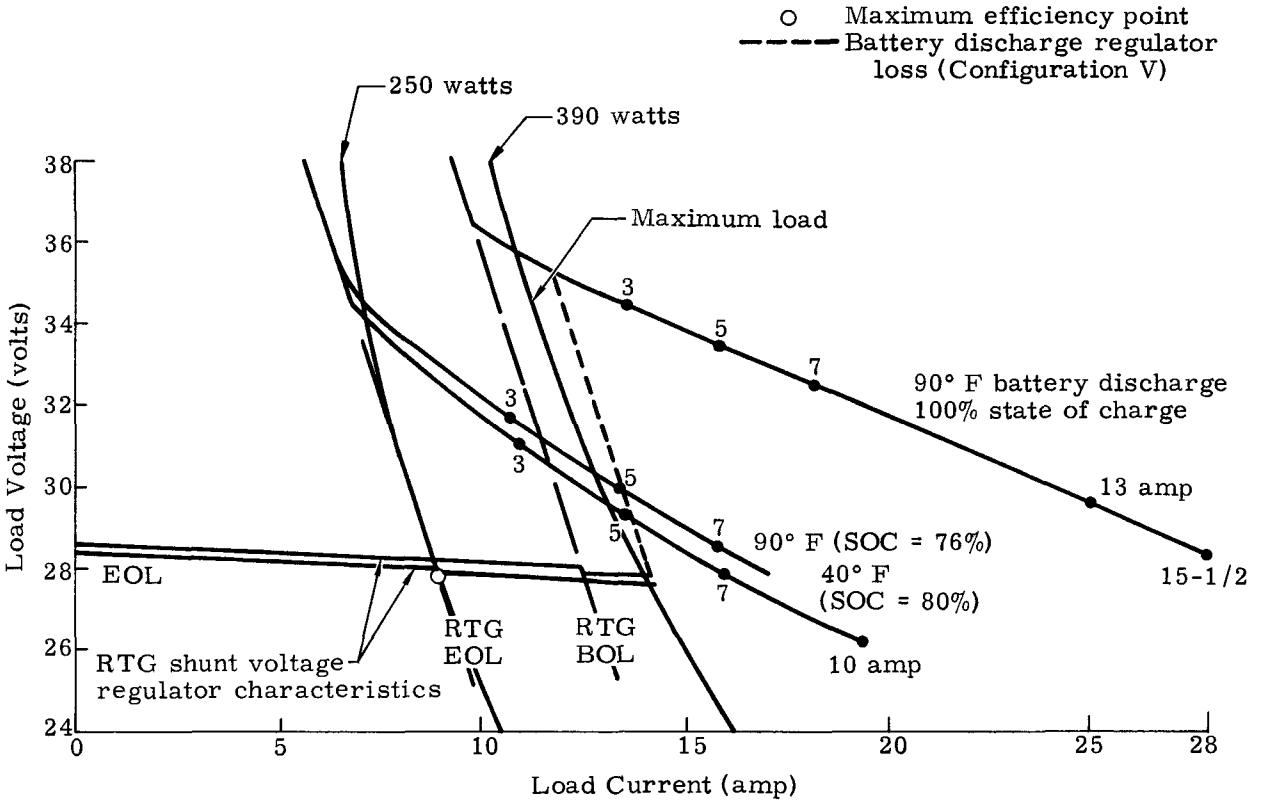

Fig. V-4. Isolated Charge Configuration Applicable to Configurations IV and V

5. Configuration Comparison

Characteristics and features of the five configurations previously discussed are summarized in Table V-1. The first five items describe the major constituents of each configuration. The next four items enumerate the respective features incorporated which have a direct bearing on the probability of mission success. Only Configurations III and V offer the greatest protection against various types of battery failure, excluding lack of capacity. A review of their respective voltage regulation qualities shows that all configurations except I meet the ± 10% requirement. Configurations IV and V far surpass this requirement, thus allowing the regulation to be eliminated locally at most vehicle loads. The different settings for the RTG shunt regulator for each configuration are caused by the differing battery discharge control methods and/or the top limits of the bus voltage tolerance of each of the configurations.

The efficiency of the energy storage and power conditioning subsystem is revealed by the charging losses (voltage booster), the charging power required and the extent of losses experienced during battery discharge. Since the batteries of Configurations I and II are charged directly at the RTG voltage, voltage boosters are not required and charging power is a minimum. The slight increase in charging power required by Configuration III reflects the loss through the charge limiter, a small cost for this advantageous feature. The disproportionately higher charging power required by Configuration IV is caused by the very inefficient discharge features of this configuration described in Section B. The voltage booster loss is therefore greater than for Configuration V. Quantitative examples of battery energy waste are shown for the 390-watt vehicle load condition. Configuration V, although a great improvement over IV, is considerably less efficient on discharge than III. This discharge inefficiency of Configuration V is not wholly reflected in the comparison of charge power required for III versus V since V is operated at a lower state of charge, thus having a higher incremental charge efficiency. Both Configurations III and V require considerably less charging power than the amount available from the RTG at EOL (15 watts).

The battery weights shown for the minimum battery capacity configurations (I, IV and V) differ since the batteries are composed of a differing quantity of cells in series. Configuration IV battery weight must be much greater than 14 pounds (minimum capacity weight) since minimum capacity will not provide adequate five-year cycle life due to the excessive discharges experienced by this configuration. Tripling the battery capacity (28-1/2 lb) reduces the battery discharge from 17 to 11 amperes but still provides only 16,000 cycles of operation. Therefore, Configuration IV becomes the heaviest and most inefficient configuration.

TABLE V-1

Power System Configuration Comparison

	I	II	III	IV	V
Battery charge--method --connection	Float Direct	Float Direct	Float Current limiters	Isolated boosters	Isolated boosters Current limited
Discharge through	Direct	Direct	Diodes	Switch	Voltage regulator switch
Battery capacity, excluding redundancy --total/vehicle (a-h)	Minimum 3	Oversized 9	Oversized 9	Minimum 3	Minimum 3
Protection against: Shorted battery Open cell Overcharge--all cells good --one cell shorted	 No Yes Yes No	 No Yes Yes No	 Yes Yes Yes Yes	 Yes Yes Yes No	 Yes Yes Yes Yes
Bus voltage tolerance (%) -90° F -40° F	 ±11-1/2 +14 -15.3	 ±5 ±7.2	 +10 -5.7 +10 -10	 +1.1 -1.0 ±1.0	 ±1 ±1
RTG shunt voltage regulator setting (volts)	31.8 to 32.4	29.8 to 30.4	30.6 to 31.2	27.75 to 28.3	27.75 to 28.3
Voltage booster power loss (watts)	--	--	--	2.0	0.41
Charging power at 40° F, EOL (watts)	4.	4.	6.4	>34	7.
390-watt system load, 90° F battery (watts) At BOL, should supply Supplies At EOL, should supply Supplies	 30 30 140 140	 30 30 140 140	 30 31 140 144	 30 426 140 225	 30 42 140 150
Battery weight (including 50% redundancy) (lb) ES/PC subsystem total weight (lb)	11 11	26 26	26 26-1/2	Much greater than 14 Much greater than 15	14 15
Mission success probability due to: Power conditioning equipment RTG*--first 3 years --4th and 5th year Battery shorts, overcharge Battery cycle life	 Out of tolerance Very good Poorest Poorest Good	 Best Very good Good Poorest Best	 Very good Very good Fair Best Best	 Good Best Best Best Failure	 Good Best Best Best Good

*Least thermal cycling (least Peltier current variation)

The total weights of the five ES/PC subsystems consist primarily of the weight of their respective batteries. Their respective charge/discharge devices, if employed, are also included. The higher battery weights for Configurations II and III are required to produce the bus voltage tolerances shown and do not infer the availability of this overcapacity. The oversizing, however, does provide greater assurance of being able to obtain the required cycle life.

The mission success probability comments on the last five lines of Table V-1 are generally self-explanatory or have been discussed previously, with the exception of the RTG thermal cycling. Systems which operate over a wide bus voltage tolerance, such Configurations I, II and III, cause a large change in RTG current when loads vary periodically. As a consequence, the changing Peltier effect within the thermoelectric elements causes temperature excursions which could result in thermal fatigue. During the first three years, overloads resulting in RTG current changes do not exceed 30 seconds duration and, hence, are thermally insignificant. During the fourth and fifth year the temperature excursions become more significant, as revealed in the table.

6. Configuration Selection

Configuration I does not meet the bus voltage tolerance limits required. Configuration II does not provide protection against shorted cells or shorted batteries. Configuration IV is grossly inefficient and fails to provide a five-year life. Configurations III and V have the most to offer, either being very acceptable and each having its own unique features. The close bus voltage tolerance of Configuration V could permit the elimination of most of the voltage regulation within its payload. A comparison of the overall power conditioning equipment would then show Configuration V to be almost comparable to Configuration III in regard to mission success probability. The RTG life and the weight advantage of Configuration V versus the battery cycle life of III remain as the principal differing features. In view of the adequate battery life of V, its close voltage tolerance, improved RTG life and low weight, Configuration V is recommended, provided subsequent general voltage regulation within the payload is eliminated.

C. DESCRIPTION OF SELECTED SYSTEM

1. Batteries

Three one-ampere-hour batteries are recommended, any two of the three batteries being capable of supplying an average of 2.42 watt-hours and a maximum of 4.6 watt-hours at not less than 28.55 volts for 24,500 discharge cycles in a five-year period. Each 4.7-pound, 75-cubic inch battery will be composed of 27 hermetically sealed nickel-cadmium cells in series.

2. Voltage Boosters

Each battery will be charged individually by a current-limited voltage booster. Each of the three boosters will produce 39 volts at 0.05 ampere from a 28-volt input at a 95% overall efficiency (85% boost efficiency). At 0.06 ampere the output will be 38 volts, and a maximum of 0.11 ampere at 28 volts. The three boosters should weigh less than one-half pound.

3. Discharge Voltage Regulators

Each battery will be discharged individually through a unidirectional series regulator. The resistance characteristics of the discharge route will be as follows:

Output--Bus Side (volts)	Route Resistance (ohms)	Input (volts)
>27.9	>2,200	39.0
27.7	<0.32	28.5

When the voltage on the bus side of the regulator attempts to fall below 27.9 volts, the route resistance will adjust to produce between 27.7 and 27.9 volts on the bus side of the regulator. These characteristics must be coordinated with the current limiting feature of the voltage boosters. The three discharge regulators should weigh less than one-half pound.

BLANK

APPENDIX W

DERIVATION OF CASCADED EFFICIENCY EXPRESSION

In the following derivation, the parameters for the SiGe module will be designated by the subscript 1 while those for the PbTe module will be designated by the subscript 2. The following schematic is a model of the energy balance on the system:

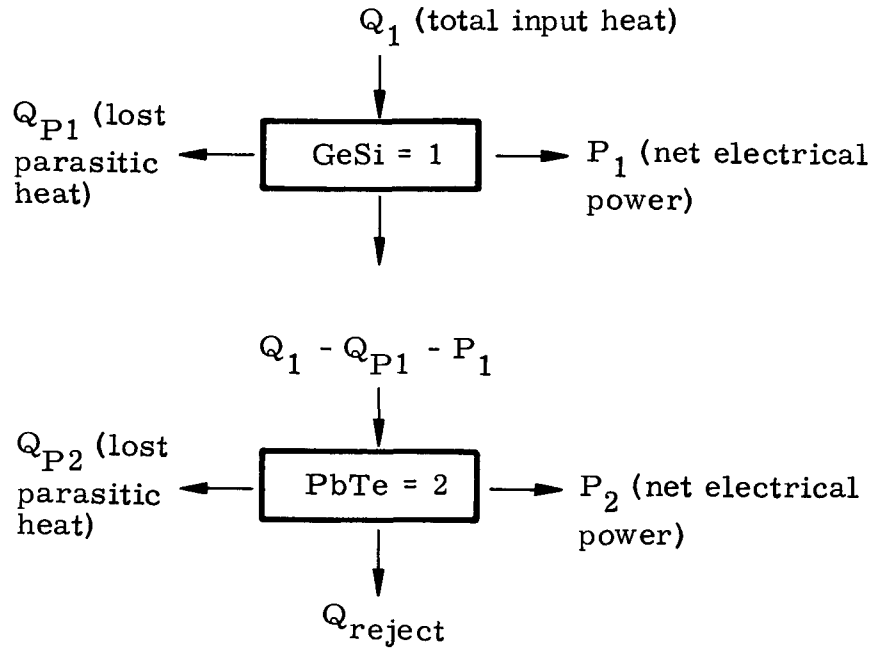

The overall efficiency of the SiGe module is given by

$$\eta_1 = \frac{P_1}{Q_1} \qquad \text{(W-1)}$$

where

P_1 = net electrical output power (i.e., power already corrected for joule losses) from the SiGe module

Q_1 = heat input to the SiGe module.

The overall efficiency of the PbTe module is given by

$$\eta_2 = \frac{P_2}{Q_1 - P_1 - Q_{P1}} \qquad \text{(W-2)}$$

where

P_2 = net electrical output power from the PbTe module

Q_{P1} = parasitic heat loss from the SiGe module that is not available for use in the PbTe module.

The overall efficiency of both modules is defined by

$$\eta_{0/A} = \frac{P_1 + P_2}{Q_1} \tag{W-3}$$

Substituting Eqs (W-1) and (W-2) into Eq (W-3) for P_1 and P_2, respectively,

$$\eta_{0/A} = \eta_1 + \eta_2 - \eta_1 \eta_2 - \frac{\eta_2 Q_{P1}}{Q_1} \tag{W-4}$$

Now η_1 may be written as

$$\eta_1 = \frac{P_1}{Q_1} = \frac{P_1}{P_{gross_1}} \times \frac{P_{gross_1}}{Q_{ele_1}} \times \frac{Q_{ele_1}}{Q_1} \tag{W-5}$$

$$= \left(\eta_{I^2R}\right)_1 \left(\eta_{T/E}\right)_1 \left(\eta_{th}\right)_1$$

where

η_{I^2R} = joule (strap) efficiency, to account for I^2R losses in the hot and cold shoes and wiring

η_{th} = thermal efficiency

$\eta_{T/E}$ = thermoelectric efficiency.

Similarly,

$$\eta_2 = \left(\eta_{I^2R}\right)_2 \left(\eta_{T/E}\right)_2 \left(\eta_{th}\right)_2 \tag{W-6}$$

Substituting Eqs (W-6) and (W-5) into Eq (W-4),

$$\eta_{0/A} = \left(\eta_{I^2R}\right)\left(\eta_{T/E}\right)_1\left(\eta_{th}\right)_1 + \left(\eta_{I^2R}\right)_2\left(\eta_{T/E}\right)_2\left(\eta_{th}\right)_2$$

$$- \left(\eta_{I^2R}\right)_1\left(\eta_{I^2R}\right)_2\left(\eta_{T/E}\right)_1\left(\eta_{T/E}\right)_2\left(\eta_{th}\right)_1\left(\eta_{th}\right)_2$$

$$- \frac{\left(\eta_{T/E}\right)_2 Q_{P1}\left(\eta_{th}\right)_2\left(\eta_{I^2R}\right)_2}{Q_1} \qquad \text{(W-7)}$$

This equation is the rigorous expression for overall cascaded system efficiency.

The definition of $\eta_{0/A}$ is

$$\eta_{0/A} = \frac{P_1 + P_2}{Q_1} = \frac{P_{gross_1}\left(\eta_{I^2R}\right)_1 + P_{gross_2}\left(\eta_{I^2R}\right)_2}{Q_1} \qquad \text{(W-8)}$$

where

$$Q_1 = Q_{ele_1}\left(\frac{Q_1}{Q_{ele_1}}\right) = \frac{Q_{ele_1}}{\eta_{th\ 1}} \qquad \text{(W-9)}$$

Substituting Eqs (W-8) and (W-9) into Eq (W-7), and dividing both sides of the resulting equation by $\left(\eta_{I^2R}\right)_1\left(\eta_{th}\right)_1$ yields

$$\frac{P_{gross_1} + P_{gross_2}\dfrac{\left(\eta_{I^2R}\right)_2}{\left(\eta_{I^2R}\right)_1}}{Q_{ele_1}} = \left(\eta_{T/E}\right)_1 + \left(\eta_{T/E}\right)_2\frac{\left(\eta_{I^2R}\right)_2}{\left(\eta_{I^2R}\right)_1}\frac{\left(\eta_{th}\right)_2}{\left(\eta_{th}\right)_1} \qquad \text{(W-10)}$$

$$- \left(\eta_{T/E}\right)_1\left(\eta_{T/E}\right)_2\left(\eta_{I^2R}\right)_2\left(\eta_{th}\right)_2$$

$$- \left(\eta_{T/E}\right)_2\frac{Q_{P1}}{Q_1}\frac{\left(\eta_{I^2R}\right)_2}{\left(\eta_{I^2R}\right)_1}\frac{\left(\eta_{th}\right)_1}{\left(\eta_{th}\right)_1}$$

For the limiting case of zero thermal and electrical losses (i.e., $\eta_{I^2R} = \eta_{th} = 100\%$, $Q_{P1} = 0$), Eq (W-10) becomes

$$\frac{P_{gross_1} + P_{gross_2}}{Q_{ele_1}} = (\eta_{T/E})_1 + (\eta_{T/E})_2 - (\eta_{T/E})_1 (\eta_{T/E})_2 \qquad (W-11)$$

or

$$(\eta_{T/E})_{casc} = (\eta_{T/E})_1 + (\eta_{T/E})_2 - (\eta_{T/E})_1 (\eta_{T/E})_2 \qquad (W-12)$$

where the cascaded thermoelectric efficiency is defined as gross power per heat to the elements.

This equation is useful in that the cascaded thermoelectric efficiency can be expressed in terms of known quantities, viz., output from the thermoelectric digital computer code described elsewhere, without recourse to thermal or joule efficiencies. Use of these latter terms would require information on a specific design.

The departure of the "ideal," Eq (W-12), from the "real," Eq (W-10), can be further investigated as follows: If

$$\frac{(\eta_{I^2R})_2}{(\eta_{I^2R})_1} \sim 1 \text{ and } \frac{(\eta_{th})_2}{(\eta_{th})_1} \sim 1,$$

then

$$(\eta_{T/E})_{casc} \approx (\eta_{T/E})_1 + (\eta_{T/E})_2 - (\eta_{T/E})_1 (\eta_{T/E})_2 (\eta_{I^2R})_1 (\eta_{I^2R})_2 - (\eta_{T/E})_2 \frac{Q_{P1}}{Q_1} \qquad (W-13)$$

The last two terms in Eq (W-13) are negligible for any practical design since

$$(\eta_{T/E})_1 + (\eta_{T/E})_2 >> (\eta_{T/E})_1 (\eta_{T/E})_2 (\eta_{I^2R})_1 (\eta_{I^2R})_2 + (\eta_{T/E})_2 \frac{Q_{P1}}{Q_1} \qquad (W-14)$$

$$\therefore \left(\eta_{T/E}\right)_{casc} \approx \left(\eta_{T/E}\right)_1 + \left(\eta_{T/E}\right)_2 \qquad \text{(W-15)}$$

Thus, subject to the constraint,

$$\frac{\left(\eta_{I^2R}\right)_2}{\left(\eta_{I^2R}\right)_1} \sim 1 \text{ and } \frac{\left(\eta_{th}\right)_2}{\left(\eta_{th}\right)_1} \sim 1$$

Equation (W-12) is a conservative formulation. Actually, the difference in Eqs (W-12) and (W-15) is very small.

~~CONFIDENTIAL~~

BLANK

~~CONFIDENTIAL~~

APPENDIX X

CAPSULE TEMPERATURE-TIME HISTORY FOR Pu-238

To design a capsule as a pressure vessel for the containment of helium (resulting from decay of an alpha-emitter), a knowledge of the capsule temperature history over several half-lives is necessary. To assume the beginning-of-life temperature to hold for long periods of time (relative to the fuel half life) is an ultra conservative assumption that unnecessarily penalizes capsule weight.

The correct expression for the capsule temperature history is the one derived by developing and manipulating the various heat balance equations within the generator. This method was previously used in developing the definitive equation for SNAP 9A--a conduction-type generator. In that case, the capsule temperature, while the capsule is in the generator, was given by:*

$$T_{cap} = \left(T_R\right)_o e^{-\lambda t/4} + \left(T_{cap} - T_R\right)_o e^{-\lambda t}$$

It is emphasized that this equation applies only to the conduction-type RTG.

For a different model RTG (e.g., a 250-watt SiGe generator or any other employing a major radiation gap internally), a different equation describes capsule temperature history. This latter equation is developed for three cases:

(1) Most general case where generator material properties are expressed as a function of temperature (and hence time), and generator is operating normally.

(2) Same as Item (1) but generator is open circuited.

(3) Case where beginning-of-life material properties may be used for the time period of interest. The result is a simpler expression for capsule temperature.

* Nomenclature is at the end of this appendix.

A. ANALYSIS AND RESULTS

1. Case I--General Equation

The approximate equation describing heat rejected by radiation from the generator to space is:

$$q = q_o e^{-\lambda t} = \sigma \epsilon A_s T_r^4 + \sigma \epsilon (A_{circ} - A_s) T_r^4 \eta_{fin} \qquad (X\text{-}1)$$

The cold junction temperature is related to the surface temperature by:

$$T_c = T_r + \frac{q_o e^{-\lambda t}}{K_{cold}} \qquad (X\text{-}2)$$

The hot junction temperature is related to the cold junction temperature by a heat balance including thermoelement heat conduction, Peltier effect and parasitic losses, viz.,

$$q = \left[\frac{\bar{k}_n A_n}{l_n} + \frac{\bar{k}_p A_p}{l_p}\right](T_h - T_c) N + \alpha_h I T_h + K_{par}(T_h - T_c) \qquad (X\text{-}3)$$

$$I = \frac{E_{oc}}{R_I + R_L} = \frac{(T_h - T_c) N \bar{\alpha}}{R_I + R_L} \qquad (X\text{-}4)$$

$$R_I = \left[\frac{\bar{\rho}_p l_p}{A_p} + \frac{\bar{\rho}_n l_n}{A_n} + \frac{C_n}{A_n} + \frac{C_p}{A_p}\right] N + R_{misc} \qquad (X\text{-}5)$$

The temperature drop by conduction through the hot shoe itself should be considered for the case of SiGe. Then, the maximum shoe temperature is related to the hot junction temperature by:

$$T_{shoe} = T_h + \frac{q_o e^{-\lambda t}}{K_{shoe}} \qquad (X\text{-}6)$$

The capsule surface temperature is related to the hot shoe temperature by the equation for radiation heat transfer,

$$T_{cap} = \left[\frac{q_o e^{-\lambda t}}{\sigma \bar{\epsilon} A_{env}} + T_{shoe}^4\right]^{1/4} \qquad (X\text{-}7)$$

The final expression for capsule temperature is obtained by the following procedure:

(1) Solve Eq (X-1) for T_r and substitute in Eq (X-2).

(2) Substitute this result for T_c into Eq (X-3). Solve for T_h.

(3) Substitute the resulting equation into Eq (X-6). Take the result and substitute it into Eq (X-7) for T_{shoe}.

The net result is the following expression for capsule surface temperature as a function of time (see Eq (X-8)), where the current, I, is itself temperature dependent and is given by Eq (X-4).

$$T_{cap} = \left\{ \left\{ \frac{q_o e^{-\lambda t}}{\sigma \bar{\epsilon} A_{env}} + \left\{ \frac{q_o e^{-\lambda t} + \left[\left(\frac{q_o e^{-\lambda t}}{\sigma \epsilon A_s + \sigma \epsilon (A_{circ} - A_s) \eta_{fin}} \right)^{1/4} + \frac{q_o e^{-\lambda t}}{K_{cold}} \right] \left[\left(\frac{\bar{k}_n A_n}{l_n} + \frac{\bar{k}_p A_p}{l_p} \right) N + K_{par} \right]}{N \left(\frac{\bar{k}_n A_n}{l_n} + \frac{\bar{k}_p A_p}{l_p} \right) + K_{par} + \alpha_h I} + \frac{q_o e^{-\lambda t}}{K_{shoe}} \right\}^4 \right\}^{1/4} \quad \text{(X-8)}$$

2. Case II--General Equation with Open Circuit

For the condition of an electrical open circuit, the Peltier cooling term vanishes and Eq (X-8) reduces to

$$T_{cap} = \left\{ \left\{ \frac{q_o e^{-\lambda t}}{\sigma \bar{\epsilon} A_{env}} + \left\{ \frac{q_o e^{-\lambda t}}{N \left(\frac{\bar{k}_n A_n}{l_n} + \frac{\bar{k}_p A_p}{l_p} \right) + K_{par}} + \left(\frac{q_o e^{-\lambda t}}{\sigma \epsilon A_s + \sigma \epsilon (A_{circ} - A_s) \eta_{fin}} \right)^{1/4} + \frac{q_o e^{-\lambda t}}{K_{cold}} \right\}^4 + \frac{q_o e^{-\lambda t}}{K_{shoe}} \right\}^{1/4} \quad \text{(X-9)}$$

3. Case III--Open Circuit--Initial Properties

For the case where the properties are not strong functions of temperature or alternately where long-time periods are not involved (hence, large temperature changes do not occur), initial material properties (emissivities, conductivities) may be used.

Then, Eq (X-1) may be written as:

$$q = q_o e^{-\lambda t} = K_1 T_r^4 \tag{X-10}$$

Evaluating K_1 at $t = 0$,

$$K_1 = \frac{q_o}{T_{r,o}^4} \tag{X-11}$$

Substitution into Eq (X-10) gives

$$T_r = T_{r,o} e^{-\lambda t/4} \tag{X-12}$$

Similarly, it may be shown that Eq (X-2) becomes:

$$T_c = T_{r,o} e^{-\lambda t/4} + \left(T_c - T_r\right)_o e^{-\lambda t} \tag{X-13}$$

For an open circuit condition, Eq (X-3) may be written as:

$$q_o e^{-\lambda t} = K_2 \left(T_h - T_c\right) + K_{par} \left(T_h - T_c\right) \tag{X-14}$$

Evaluating $K_2 + K_{par}$ at $t = 0$,

$$K_2 + K_{par} = \frac{q_o}{\left(T_h - T_c\right)_o} \tag{X-15}$$

Substitution into Eq (X-14) gives, after solving for T_h and further substituting for T_c from Eq (X-13),

$$T_h = \left(T_h - T_c\right)_o e^{-\lambda t} + T_{r,o} e^{-\lambda t/4} + \left(T_c - T_r\right)_o e^{-\lambda t} \tag{X-16}$$

Equation (X-6) is treated similarly to Eq (X-2). Then:

$$T_{shoe} = T_h + \left(T_{shoe} - T_h\right)_o e^{-\lambda t} \tag{X-17}$$

Equation (X-7) may be written as:

$$T_{cap} = \left(\frac{q_o e^{-\lambda t}}{K_3} + T_{shoe}^4\right)^{1/4} \tag{X-18}$$

Evaluation of K_3 at t = 0 and substitution back into Eq (X-18) gives:

$$T_{cap} = \left[\left(T_{cap} - T_{shoe}^4\right)_o e^{-\lambda t} + T_{shoe}^4\right]^{1/4} \tag{X-19}$$

Final substitution of Eqs (X-16) and (X-17) into Eq (X-19) gives:

$$T_{cap} = \left\{\left(T_{cap}^4 - T_{shoe}^4\right)_o e^{-\lambda t} + \left[\left(T_h - T_c\right)_o e^{-\lambda t} + T_{r,o} e^{-\lambda t/4} + \left(T_c - T_r\right)_o e^{-\lambda t} + \left(T_{shoe} - T_h\right)_o e^{-\lambda t}\right]^4\right\}^{1/4} \tag{X-20}$$

where the subscript o indicates that particular temperature is the value at t = 0. It should be noted that $T_{h,o}$, $T_{shoe,o}$ and $T_{cap,o}$ are not the initial normal operating temperatures, but rather are the initial open circuit temperatures which are typically 100° to 200° F above the normal operation values.

Also, note that because of the presence of radiation, all temperatures must be on the absolute scale.

B. CONCLUSIONS AND DISCUSSION

Capsule temperature as a function of time is most accurately described by Eqs (X-8) or (X-9), depending on whether a normally operating or open circuited generator is assumed.

Equation (X-20) (developed for open circuit generator) may be applied, however, with the assumption that the material properties (emissivities and conductivities) do not change as the temperatures change. This is a reasonable assumption and, in fact, conservative since thermoelement conductivity increases at lower temperature (increased conductivity will cause capsule temperature to be lower than predicted by use of beginning-of-life values).

As an example of the use of Eq (X-20), capsule temperature was computed as a function of time for the following initial conditions (open circuit) for Pu-238 ($t_{1/2}$ = 86.4 years):

$T_{cap,o}$ = 1950° F = 2410° R

$T_{h,o}$ = 1750° F = 2210° R

$T_{shoe,o}$ = 1765° F = 2225° R

$T_{c,o}$ = 550° F = 1010° R

$T_{r,o}$ = 520° F = 980° R

The resultant capsule temperature history is plotted in Fig. X-1. It is of interest to note that if the first equation cited was used (i.e., the equation used for SNAP 9A), lower (and hence optimistic) temperatures would result. (At the 200-year point, the SNAP 9A equation would give 483° F; and at the 300-year point, 206° F as contrasted with the more accurate values of 800° and 540° F, respectively.)

For pressure buildup calculations, it is recommended that normal operating temperatures be used for the time period during which the generator is not likely to open circuit. This time period is dependent on generator reliability. After that period, it is recommended that open circuit temperatures be used.

Finally, note that since absolute temperatures are used in the ideal gas law, small errors in capsule temperature will produce small errors in pressure buildup. Capsule material properties (yield strength, ultimate tensile strength, etc.) are quite sensitive to the temperatures used, particularly in the range 1600° to 2000° F.

C. NOMENCLATURE

A	Area
C	Element contact resistivity

Open circuit
Pu-238

$$T_{cap} = \left\{ (T_{cap} - T_{shoe})_o e^{-\lambda t} + \left[(T_h - T_c)_o e^{-\lambda t} + T_{r,o} e^{-\lambda t/4} + (T_c - T_r)_o e^{-\lambda t} + (T_{shoe} - T_h)_o e^{-\lambda t} \right] 4 \right\}^{1/4}$$

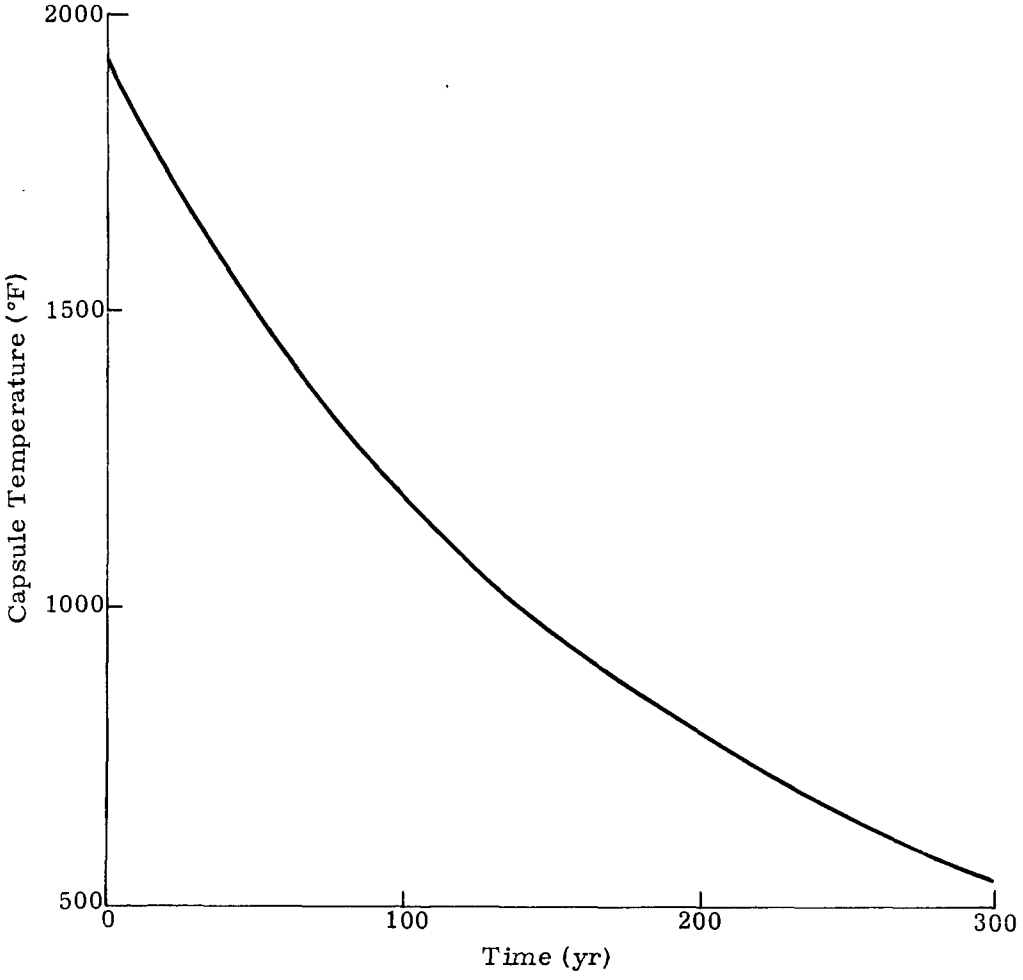

Fig. X-1. Capsule Temperature Versus Time

E	Voltage
I	Current
K	Thermal conductance
k	Thermal conductivity
$\overline{k}$	Integrated average thermal conductivity
l	Element length
N	Number of couples
q	Heat rate
R	Electrical resistance
T	Temperature
t	Time
$t_{1/2}$	Isotope half-life
α	Seebeck coefficient
ϵ	Emissivity of radiator
$\overline{\epsilon}$	Effective emissivity between capsule and hot shoe
η_{fin}	Radiator fin efficiency
λ	Isotope decay constant = $0.693/t_{1/2}$
ρ	Thermoelement electrical resistivity
σ	Stefan-Boltzmann constant

Subscripts

circ	Circumscribed (refers to area envelope about the radiator fins)
c	Cold junction
cap	Capsule
cold	Refers to cold end hardware on thermoelements

env	Envelope (area of heat source)
h	Hot junction
I	Refers to total internal resistance
L	Load (resistance)
misc	Miscellaneous
N	N element
o	initial value
oc	Open circuit
P	P element
par	Parasitic
S	Refers to area of shell (or casing) of generator (i.e., without fins)
shoe	Thermocouple hot shoe

BLANK

APPENDIX Y

AERODYNAMIC COEFFICIENTS AND PRESSURE DISTRIBUTIONS

The aerodynamic coefficients for the RTG/RB which were obtained by analytical techniques are discussed first. Later, the pressure distributions which were obtained from experimental data for this configuration will be discussed.

A. AERODYNAMIC COEFFICIENTS

The hypersonic aerodynamic coefficients for the RTG/RB were determined by a digital code which utilized modified Newtonian impact theory. For these calculations a maximum pressure coefficient ($C_{P_{max}}$) of 1.833 was used. These coefficients are:

Coefficients

(1) C_x--axial force

(2) C_z--normal force

(3) C_y--side force

(4) C_ℓ--rolling moment

(5) C_m--pitching moment

(6) C_n--yawing moment

and are referenced to a body-axis system.

Figure Y-1 presents the positive directions for the force and moment coefficients and angles. These coefficients are presented in Figs. Y-2 through Y-6 as a function of total angle of attack, η, and roll angle, ξ. Because the pressure always acts perpendicular to the surface, the rolling moment for this vehicle was zero. The moments were determined about a point 19.3 inches (42% of maximum diameter) aft of the spherical nose on the axis of revolution. Reference area and length used in these calculations were based on the maximum diameter. Figure Y-7 shows the pertinent dimensions for the RTG/RB and the orientation of the fixed body axis system.

It can be concluded from these figures that the RTG/RB is stable about zero η (blunt end first) and unstable about η = 180 degrees (conical afterbody first) if the center of gravity is located at x/D = 0.42.

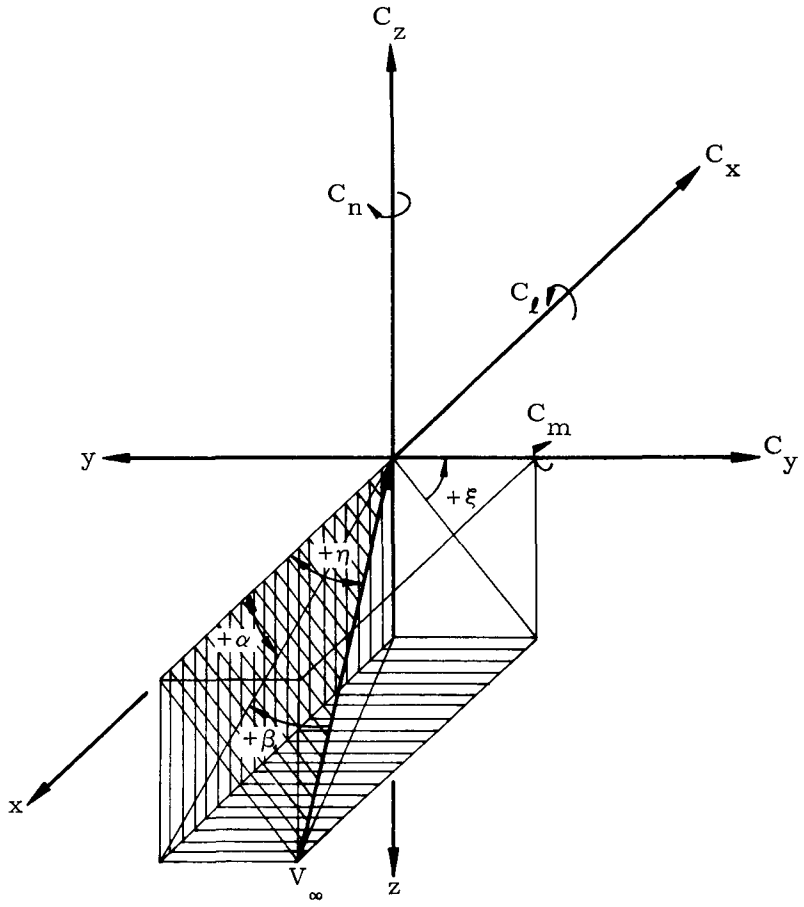

Fig. Y-1. Relationship Between Velocity Vector and Body Axes Showing Positive Directions for Force and Moment Coefficients

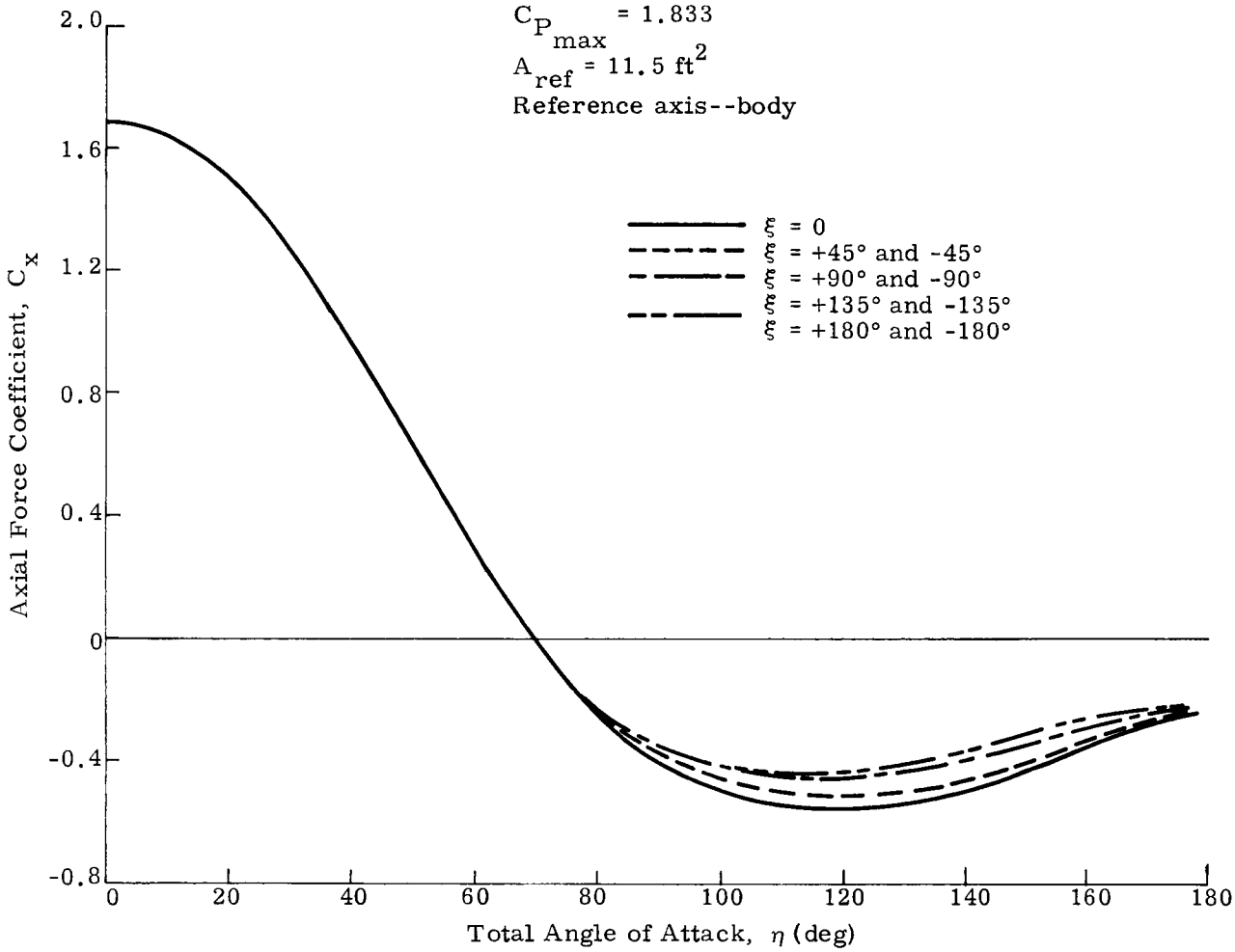

Fig. Y-2. Hypersonic Axial Force Coefficient for the CRONUS RB

$C_{P_{max}} = 1.833$
$A_{ref} = 11.5\ ft^2$
Reference axis--body

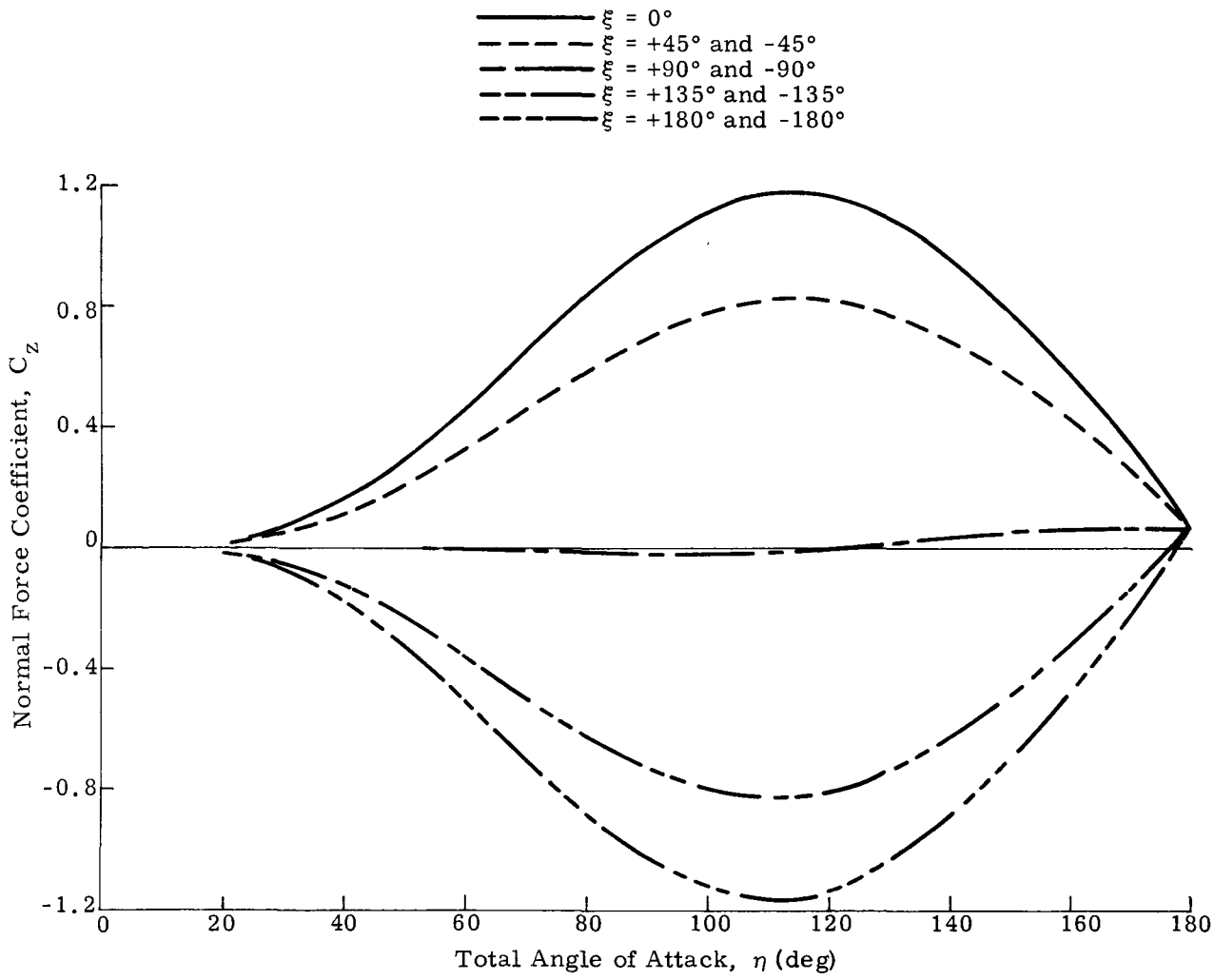

Fig. Y-3. Hypersonic Normal Force Coefficient for the CRONUS RB

$C_{P_{max}}$ = 1.833
A_{ref} = 11.5 ft^2
Reference axis--body

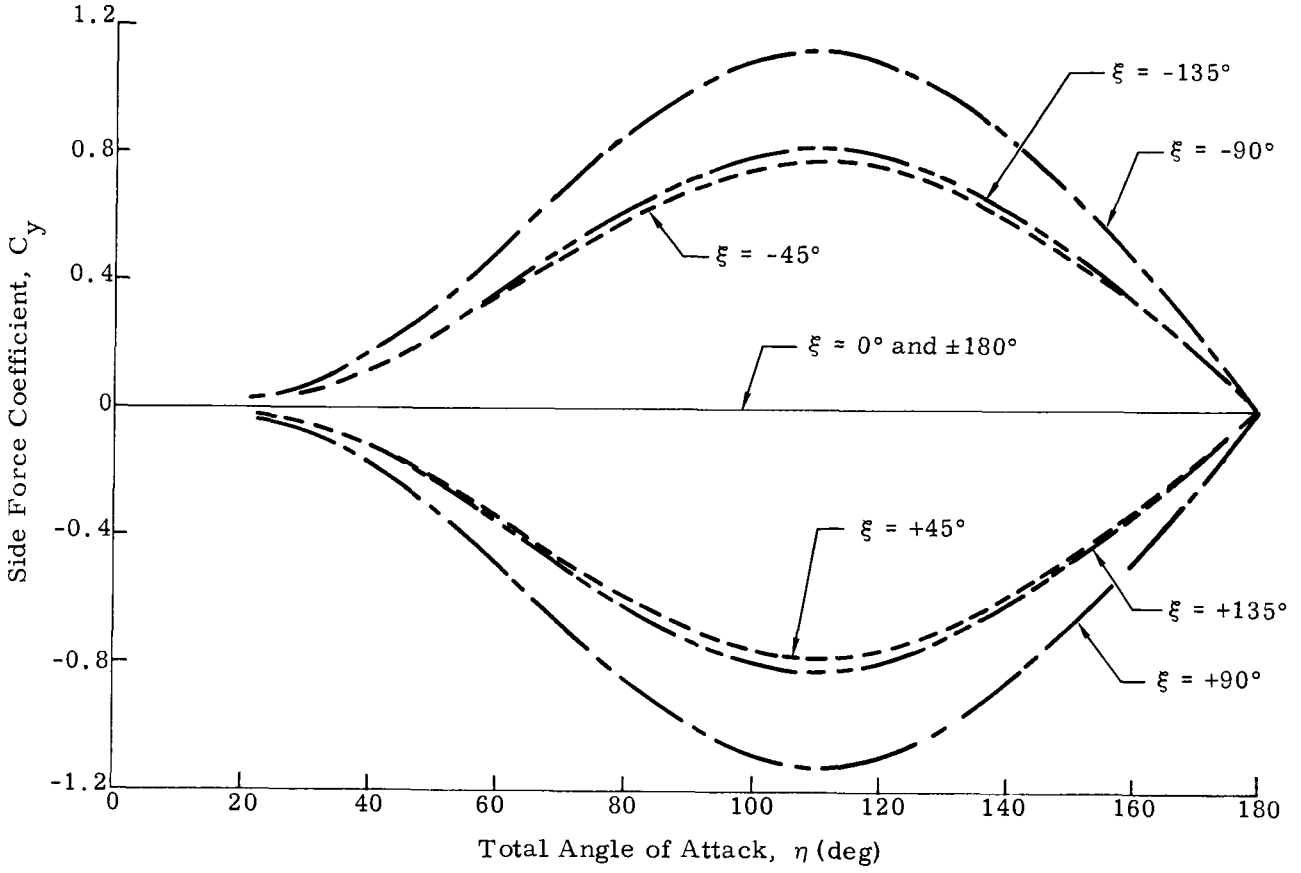

Fig. Y-4. Hypersonic Side Force Coefficient for the CRONUS RB

$C_{P_{max}}$ = 1.833
A_{ref} = 11.5 ft^2
Reference length: D = 3.83 ft (max dia)
Moment center at 0.42 D from spherical nose on $\mathcal{L}$
Reference axis--body

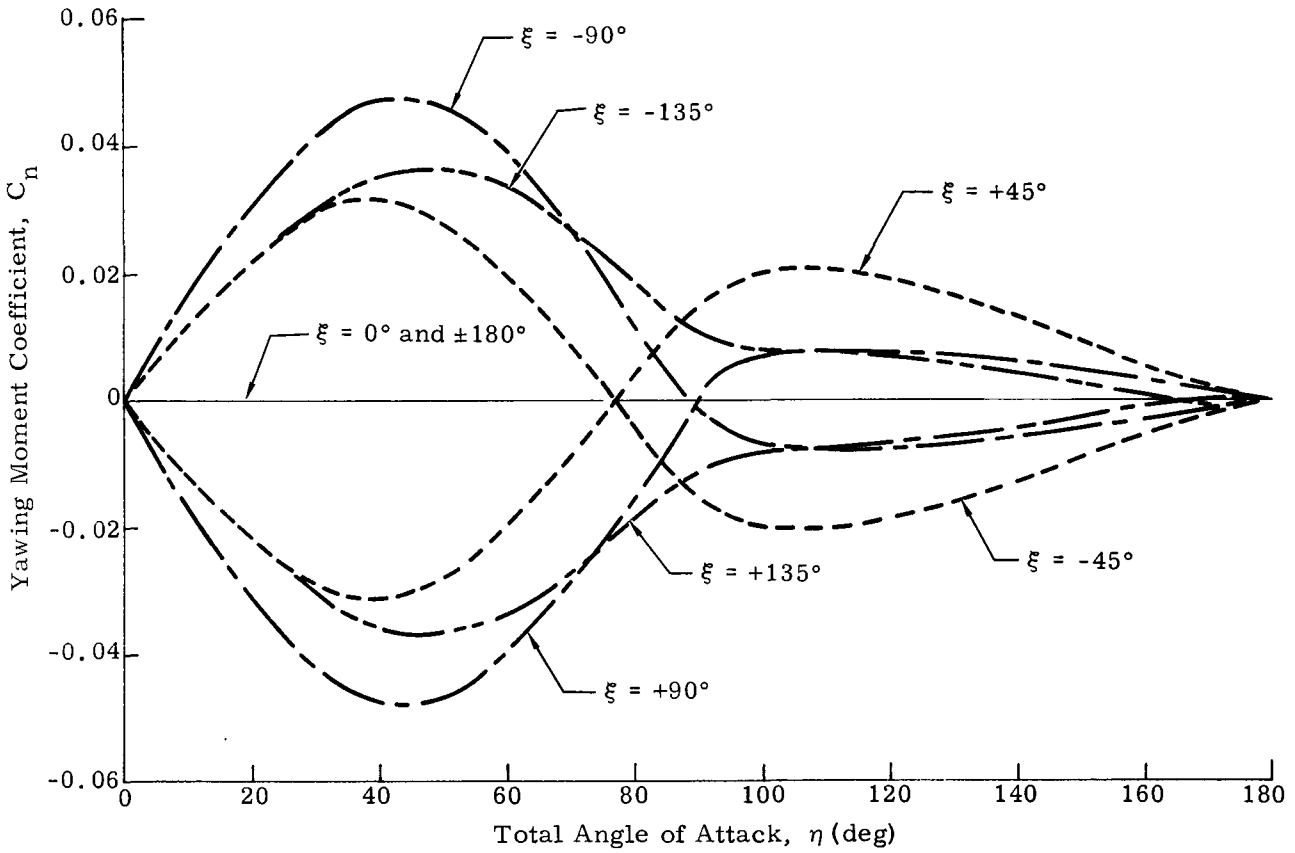

Fig. Y-5. Hypersonic Yawing Moment Coefficient for the CRONUS RB

$C_{P_{max}}$ = 1.833
A_{ref} = 11.5 ft^2
Reference length: D = 3.83 ft (max dia)
Moment center at 0.42 D from spherical nose on ℄
Reference axis--body

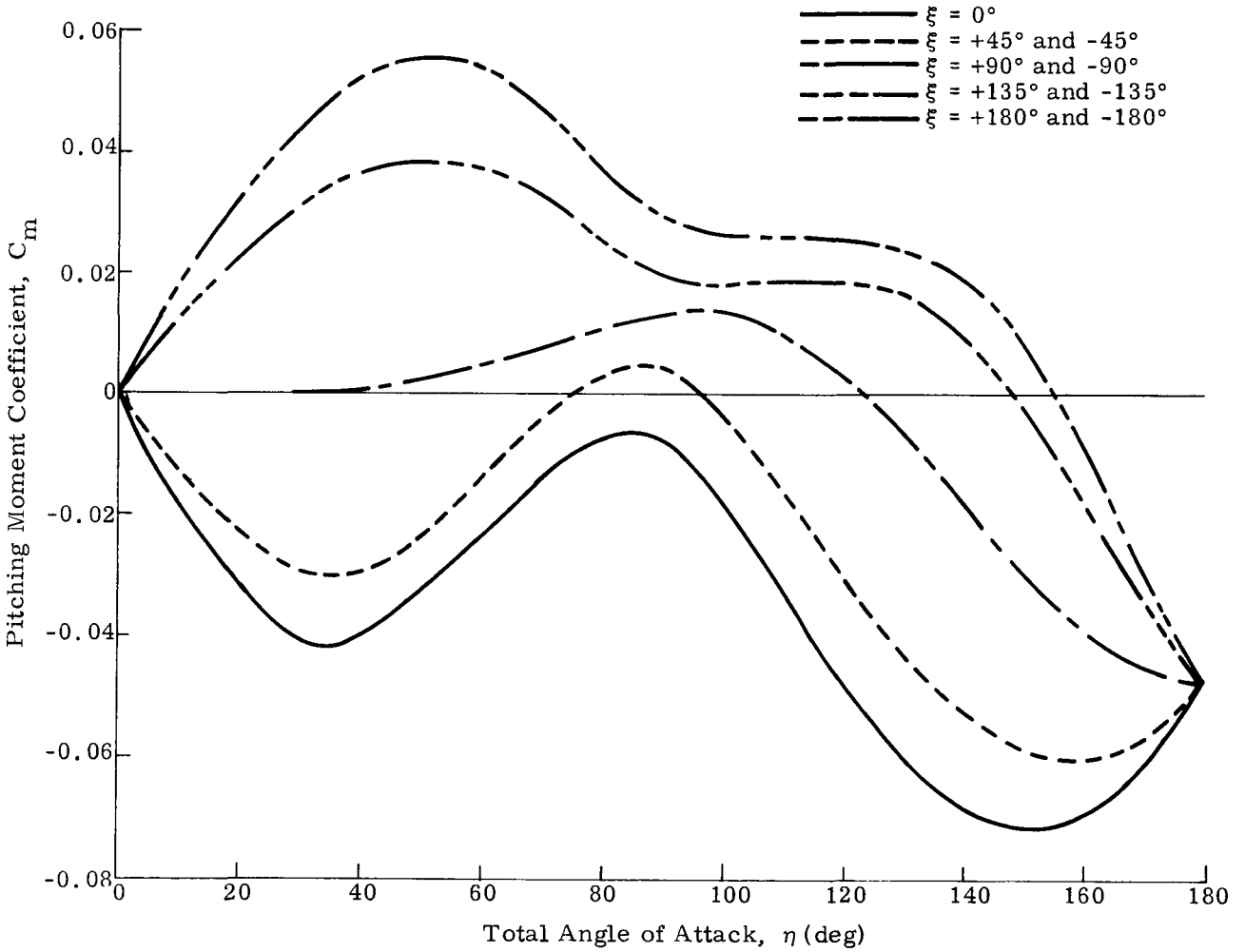

Fig. Y-6. Hypersonic Pitching Moment Coefficient for the CRONUS RB

D = 46 inches = aerodynamic reference length
$A_{ref} = \pi D^2/4$ = aerodynamic reference area
Moment center at 0.42 D aft of spherical nose
$\alpha = \eta$, $\beta = 0°$, $\xi = 0°$

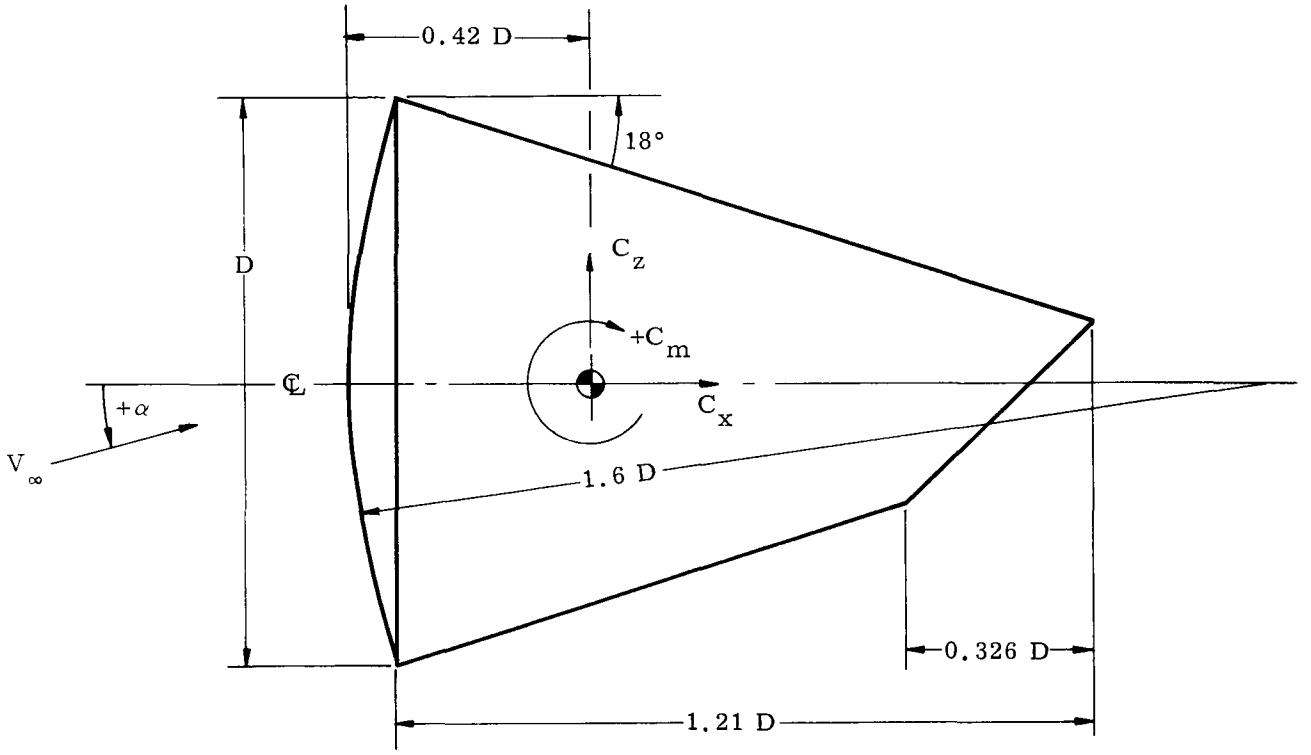

Fig. Y-7. Dimensions for the CRONUS Blunt Cone

These coefficients were used in an analog computer program to determine the dynamics of the RTG/RB for various initial angular rates and displacement along three different reentry trajectories. This will be discussed in Chapter VII.

B. PRESSURE DISTRIBUTION

The pressure distributions were approximated from the experimental data presented in Ref. Y-1. Figure Y-8 presents the dimensions of the reference body, Gemini reentry vehicle, used in this reference as a function of maximum body diameter. From a comparison of Fig. Y-7 with Fig. Y-8, it can be seen that these two vehicles are geometrically similar over the blunt nose and the front portion of the conical afterbody. Figure Y-9 presents the pressure orifice locations as a function of meridian angle (ϕ). $\phi = 180°$ was defined as the windward meridian and $\phi = 0°$ was the leeward meridian. The pressure distributions in terms of C_P for angles of attack from 0 to 40 degrees are presented in Figs. Y-10 through Y-13 as a function of the nondimensional surface distance for $\phi = 0$, 90, 135 and 180 degrees, respectively. This nondimensional surface distance (s/s') is defined in Fig. Y-9. In Fig. Y-10, the pressure coefficient ($C_P = -0.05$) over the conical afterbody at $\phi = 0°$ was independent of angle of attack over the range tested. The same was approximately true for $\phi = 90°$ meridian (Fig. Y-11). In Figs. Y-12 and Y-13 ($\phi = 135$ and 180 degrees, respectively), the pressure coefficient is increasing over the aft portion of the conical afterbody. This was due to the cylindrical portion of the Gemini vehicle just aft of its conical afterbody. This phenomenon would not be present on the RTG/RB because of the absence of this cylindrical section. Therefore, the RTG/RB C_P curve could be drawn ignoring these points.

REFERENCES

Y-1. Price, E. A., Jr., Stallings, R. L., Jr. and Howard, P. W., "Pressure and Heat-Transfer Distributions of 0.1 Scale Gemini Exit and Re-entry Models at Mach Numbers of 3.51 and 4.44," NASA TM X-1149, September 1965. CONFIDENTIAL.

Ref. NASA TM X-1149

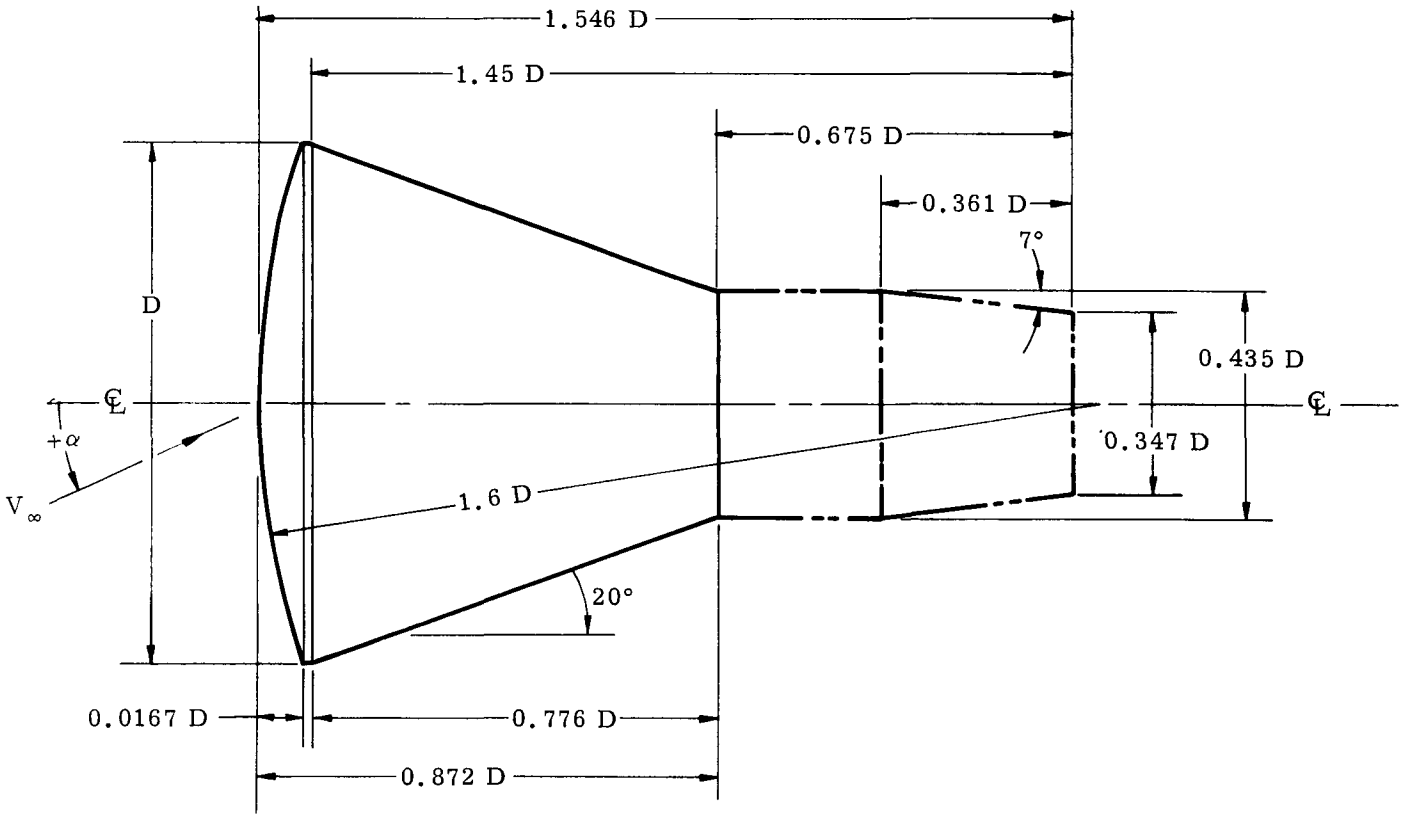

Fig. Y-8. Gemini Dimensions

Ref. NASA TM X-1149

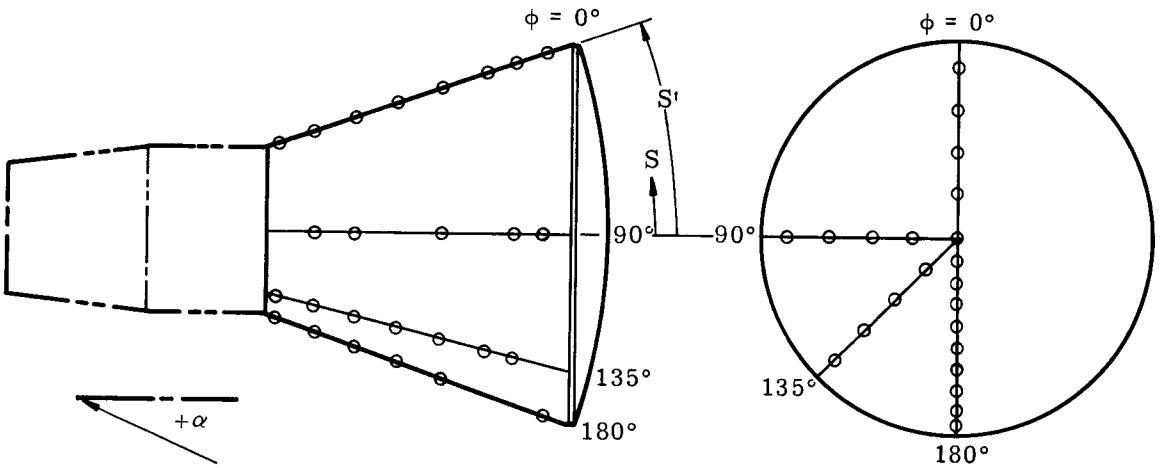

Fig. Y-9. Pressure Orifice Locations on Gemini Spacecraft in Reentry Orientation

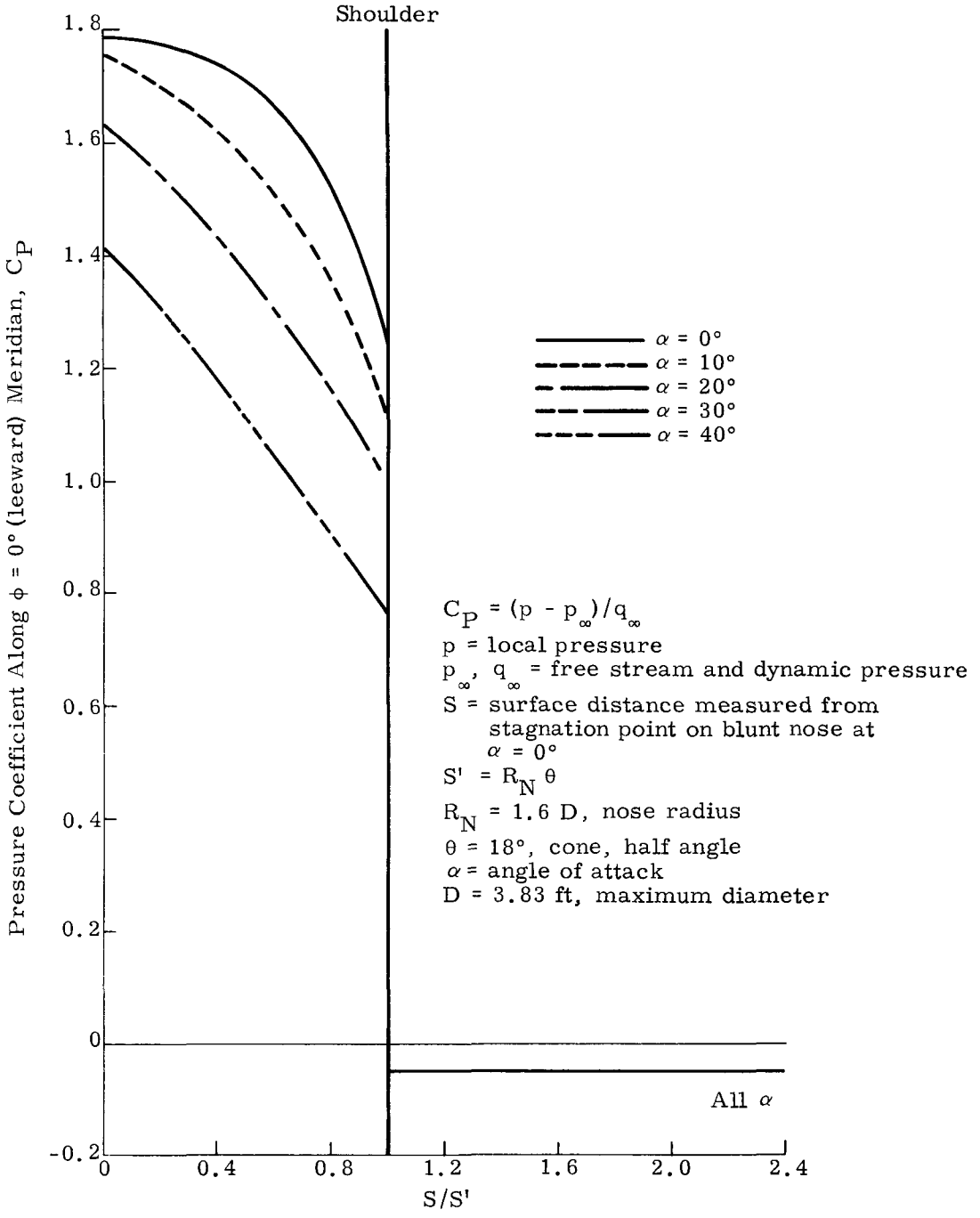

Fig. Y-10. Pressure Distribution Along ϕ = 0° (leeward) Meridian for the CRONUS RB

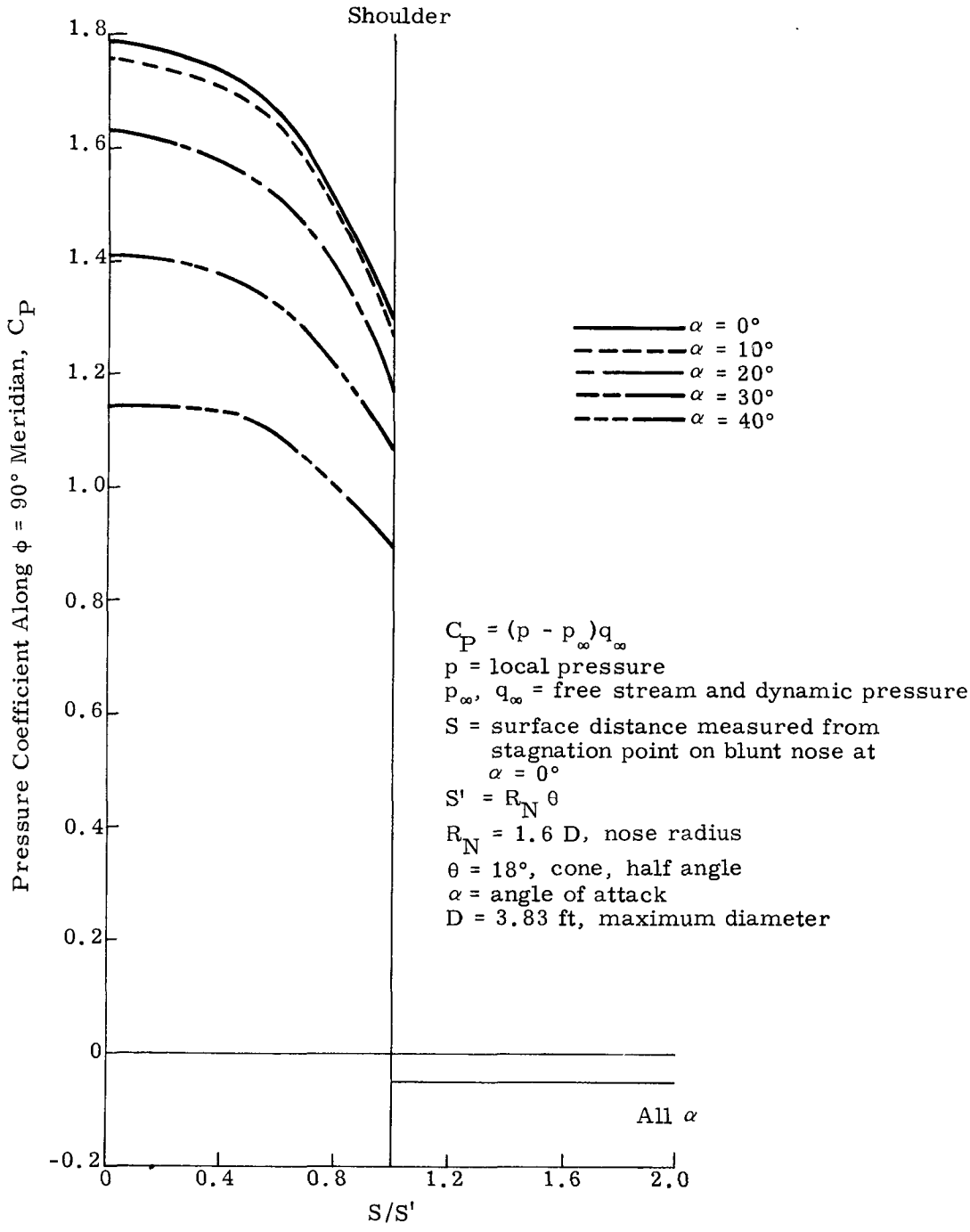

Fig. Y-11. Pressure Distribution Along ϕ = 90° Meridian for the CRONUS RB

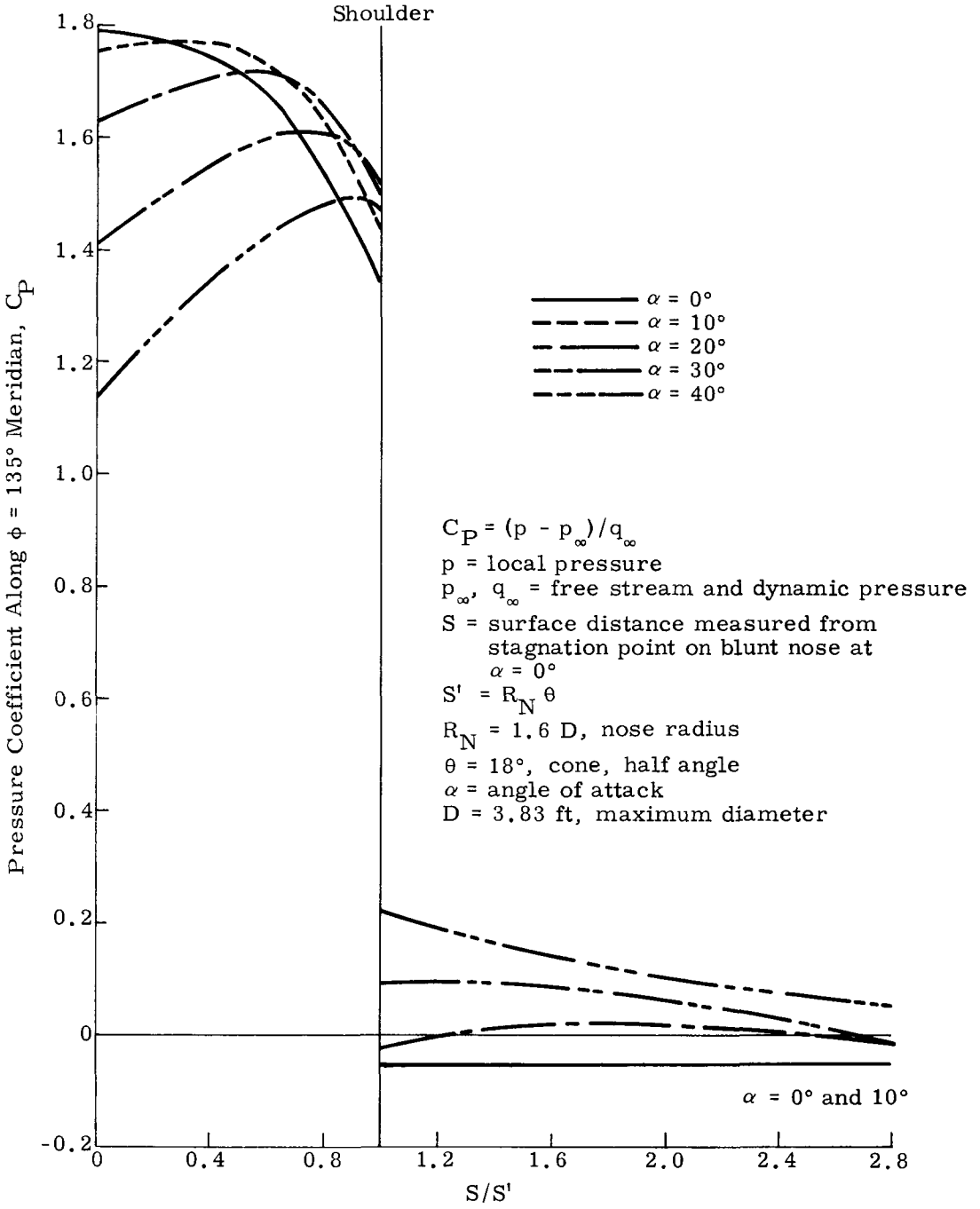

Fig. Y-12. Pressure Distribution Along ϕ = 135° Meridian for the CRONUS RB

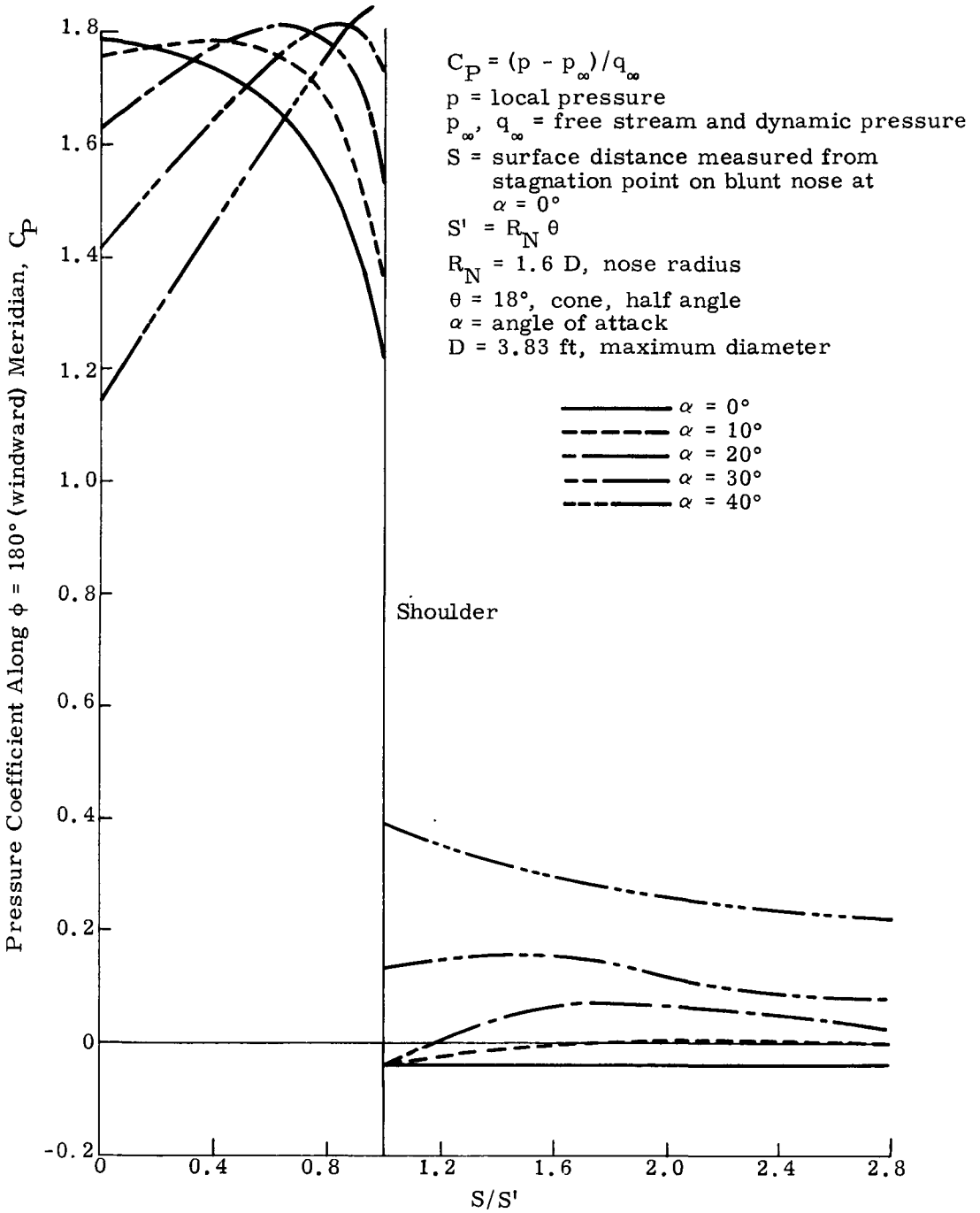

Fig. Y-13. Pressure Distribution Along ϕ = 180° (windward) Meridian for the CRONUS RB

BLANK

APPENDIX Z

LAUNCH PAD FIREBALL DATA

A. FIREBALL GROWTH

During a fireball growth period, the propellants intermix rapidly as the fireball forms a hemispheric dome. After the fireball reaches its maximum diameter (nominally between two and three seconds after ignition), it starts to rise in the typical mushroom shape pattern. Luminosity of the flames within the fireball lasts for about five or six seconds. Random vapor explosions have been known to occur in the wake of the rising fireball, creating additional luminous flames. Compared to a powder charge detonation, the deflagration phenomenon is relatively slow. Particle velocities (propellants, fragments or flame gases) can reach velocities up to 8 to 900 fps during the first 0.005 second of the explosion.

Figure Z-1 illustrates sequentially the growth of the half scale Titan II destruct test fireball which reached a maximum diameter of about 140 feet. Ground fires which are quite long in duration are less intense than the fireball and can be cooled rapidly by launch pad flood water systems. Figure Z-2 shows fireball diameter as a function of time from destruct for the Titan II, Tests 1 and 2. The total propellant inventories for the two tests were 15,800 and 32,700 pounds, respectively.

Figures Z-3 and Z-4 (Ref. Z-1) present fireball duration and diameter as a function of total propellant weight for many types of fuel used in launch vehicles. Approximately 65 to 70 data points have been obtained for each curve, either from designed tests or actual launch pad accidents. The results of the half scale Titan II tests have also been plotted on these curves and agree quite well.

The following empirical expressions can be used to predict the two fireball characteristics within the obvious band of error.

$$D = 9.3\,W^{1/3} \text{ and} \qquad (Z\text{-}1)$$

$$T = 0.23\,W^{1/3} \qquad (Z\text{-}2)$$

where D = diameter in feet, T = time in seconds, and W = total propellant weight in pounds.

Unfortunately, very little data are available for in-flight explosions other than photographic documentation, which in itself is not always of good quality. However, a few generalizations can be made based on the photographic analysis. The size of the in-flight fireball is smaller than

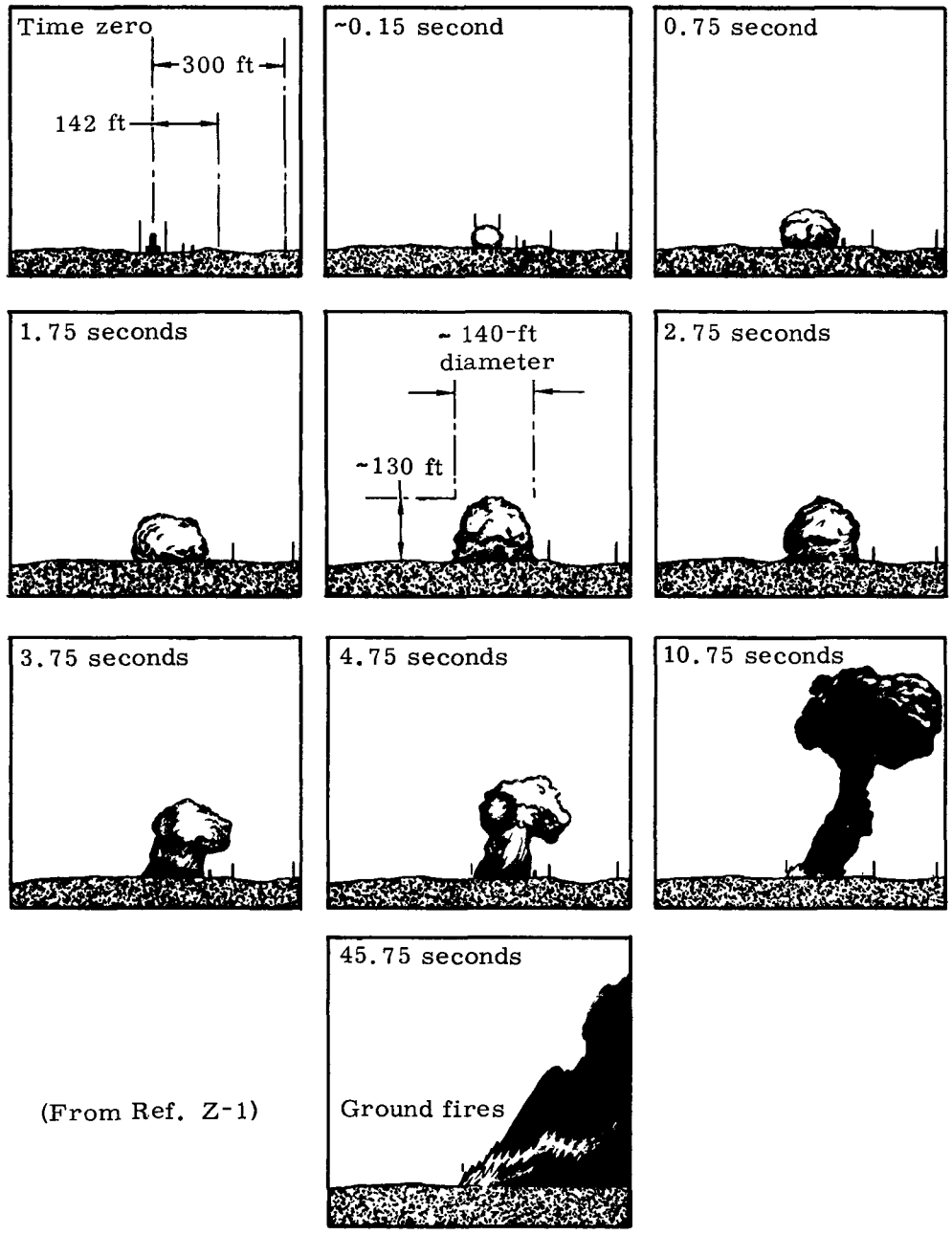

(From Ref. Z-1)

Fig. Z-1. Titan II Half-Scale Destruct Test

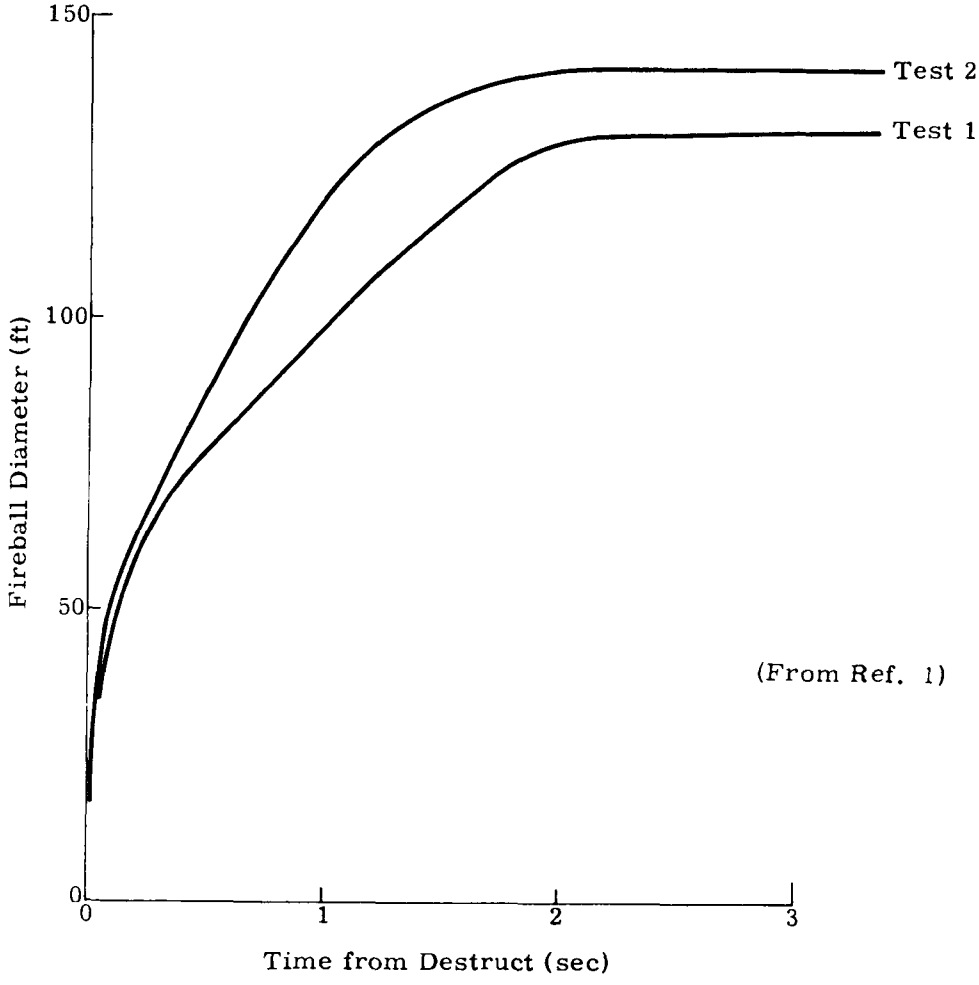

Fig. Z-2. Titan II Half-Scale Destruct Test

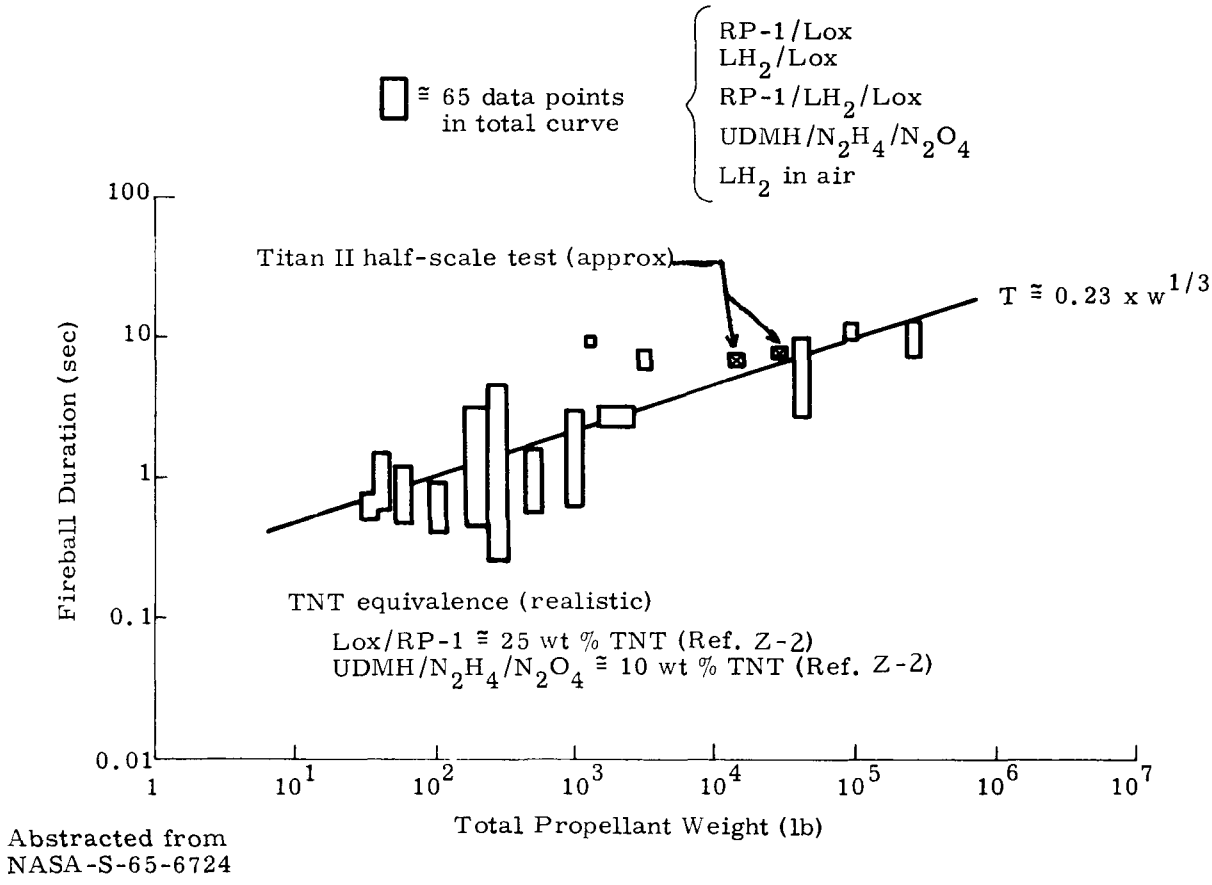

Abstracted from
NASA-S-65-6724

Fig. Z-3. Fireball Duration

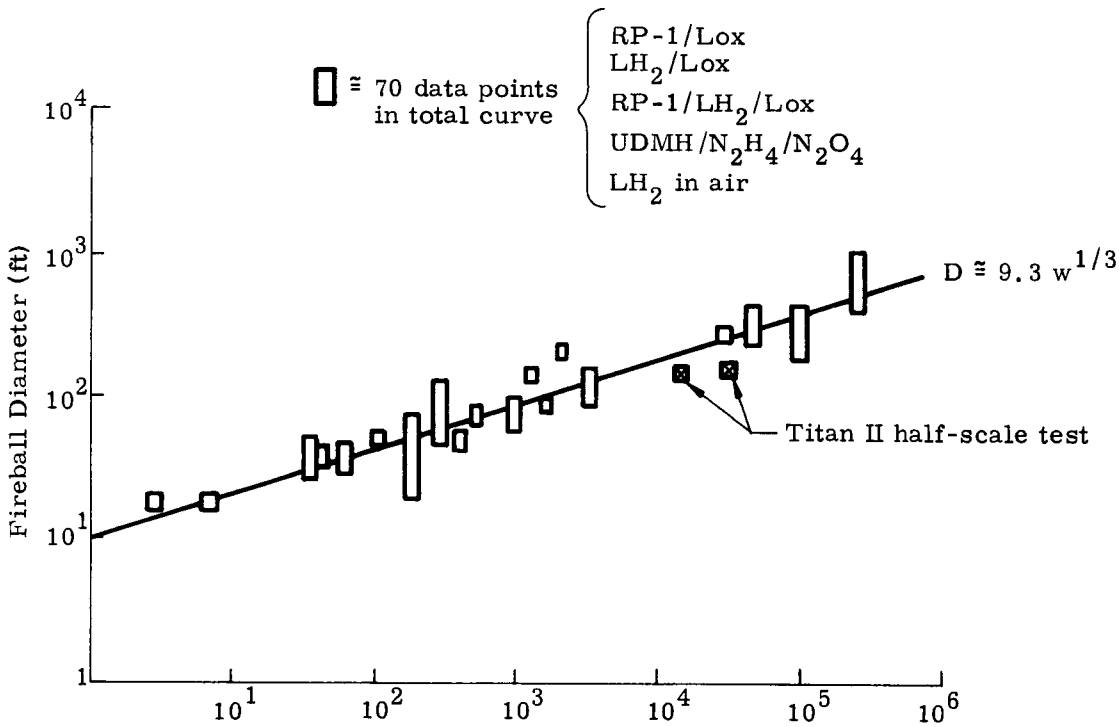

Abstracted from
NASA-S-65-6723

Fig. Z-4. Fireball Diameter

the launch pad fireball, yet, for certain geometries of vehicle orientation and flight path, mixing of propellants could be optimized to yield explosions equivalent to the launch pad situations.

A most significant statement with respect to isotopic generator nuclear safety was made in Ref. Z-1, "Throughout the duration of the major reactions . . . (for an in-flight accident). . . the missile nose cone remained visible." Hopefully then, one might expect quick separation between fireball and generator due to the difference in drag between the two. For the remainder of this discussion, the consequence of an in-flight explosion will be assumed the same as a launch pad explosion, with respect to generator or fuel encapsulation integrity.

B. THERMAL ENVIRONMENTS

In general, it appears that the temperatures and heat flux associated with fireballs are somewhat independent of the total propellant inventories and propellant combinations (Ref. Z-2). For any specific system, the fireball duration is the predominant parameter. Emissivities of luminous fireballs vary from 0.9 to 1.0 (Ref. Z-1) and it is suggested that the value of 1.0 be used for conservatism (nonluminous gas may have emissivities as low as 0.45). Fireball temperature profiles as a function of specific propellant, Lox/RP, UDMH/IRFNA, etc., have not been adequately measured or documented, but it is anticipated that Project PYRO (Refs. Z-2 and Z-3) will ultimately fill in the required information gaps for fireball thermal environments.

Figure Z-5 shows typical temperature traces as a function of time for three selected thermocouple positions also illustrated in relation to the half scale Titan II test vehicle. The wide fluctuations of temperature indicate the inhomogeneity within the turbulent fireball. Incomplete temperature-time history for some thermocouples is due to either electrical power failure or thermocouple failure during the tests. It is estimated from the data that a mean fireball temperature of between 2000° and 2500° F might be applicable over the entire fireball duration period. However, this may be a significant underestimation, since temperatures of an Atlas-Centaur (Ref. Z-2) remained above 3000° F for about five seconds with fluctuating peak temperatures greater than 5000° F. Even 200-pound propellant tests (Ref. Z-2) have yielded 3000° F temperatures for as long as 0.5 second. Additional information (Ref. Z-4) indicates maximum temperatures of about 3400° F for Lox/RP systems and 3100° F for hypergolics; the latter corresponds to the maximum temperatures predicted as a result of the half scale Titan II tests. The higher fireball temperatures (Ref. Z-2) appear to be the most recent data, and for that reason, plus a measure of conservatism, the temperature suggested as a standard for generator-capsule heat transfer calculations is 3000° F over the entire duration of the fireball as determined by Eq (Z-2), $T = 0.23\,W^{1/3}$.

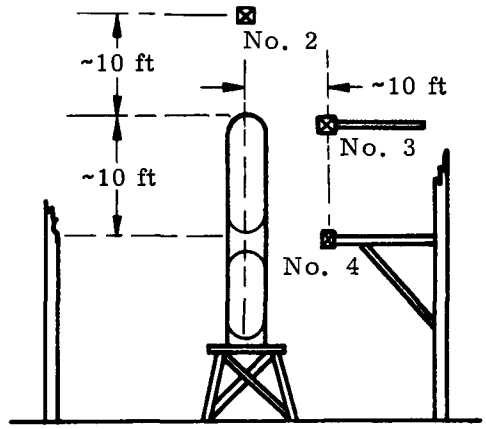

Test stand and thermocouples

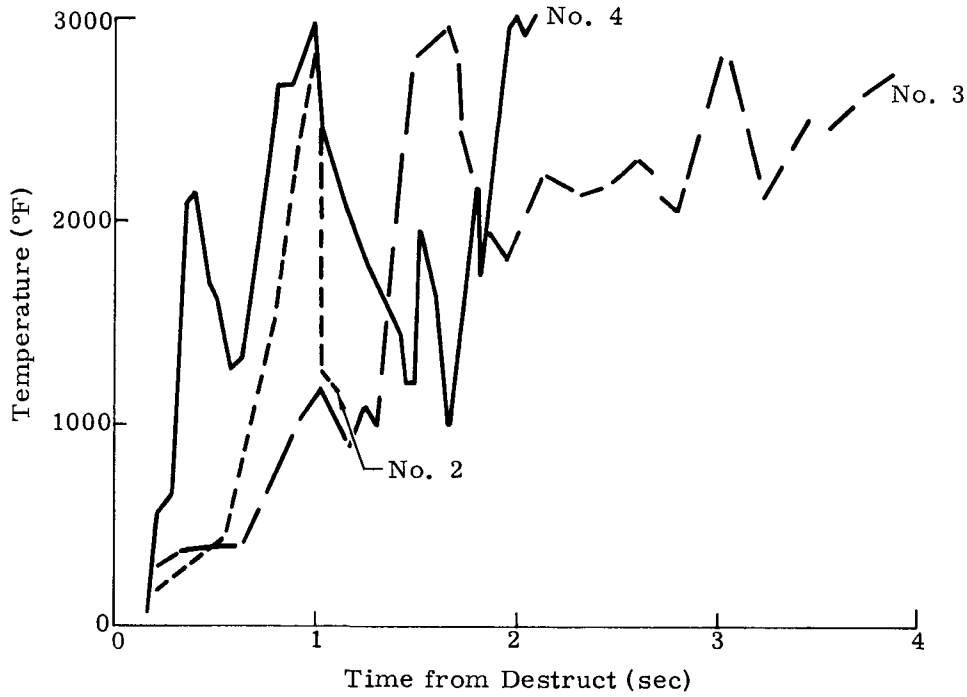

Fig. Z-5. Titan II Half-Scale Destruct Test

Heat flux traces from the Titan tests are shown in Fig. Z-6. The fluctuations are typical of the temperature plots and further indicate the inhomogeneity of the fireball's thermal characteristics. Maximum heat flux within the fireball reaches ~400 Btu/ft^2-sec, while the average is between 50 to 200 Btu/ft^2-sec. Average heat flux predicted from a Saturn IB or V (Ref. Z-1) at a temperature of 3000° F is about 80 Btu/ft^2-sec (emissivity of 1.0, fireball diameter of 844 to 1408 feet). Although it would be desirable to describe a functional relationship between heat flux and time, the data, as in the case of temperature, simply do not describe a coherent relationship.

Table Z-1 summarizes the recommended thermal parameters to be used for the fireball safety analysis of an isotopic generator system.

TABLE Z-1

Thermal Parameters

Time Duration of Environment	$T = 0.23\,W^{1/3}$ (Eq (Z-2))
Temperature of Fireball During Time, T	3000° F
Heat Flux of Fireball During Time, T	80 Btu/ft^2-sec
Fireball Emissivity	1.0

Many questions of a practical nature immediately arise when one attempts to set criteria for such an erratic phenomenon as a launch pad accident, e.g.: How long will the generator-capsules remain in the environment, or what about multiple fireballs from more than a one-stage ignition? And, of course, how reliable are the criteria?

Table Z-1 allows the system to be in the environment for the total duration of the luminous fireball. (We have acknowledged that an in-flight accident will probably see separation between payload and fireball.) Table Z-1 does not consider repetitive fireballs. Afterfire heating has also been neglected. As to reliability of criteria (and associated accident philosophy), it is adequately representative of the situation for the purpose of a nuclear hazard accident analysis and represents the best data available at this time.

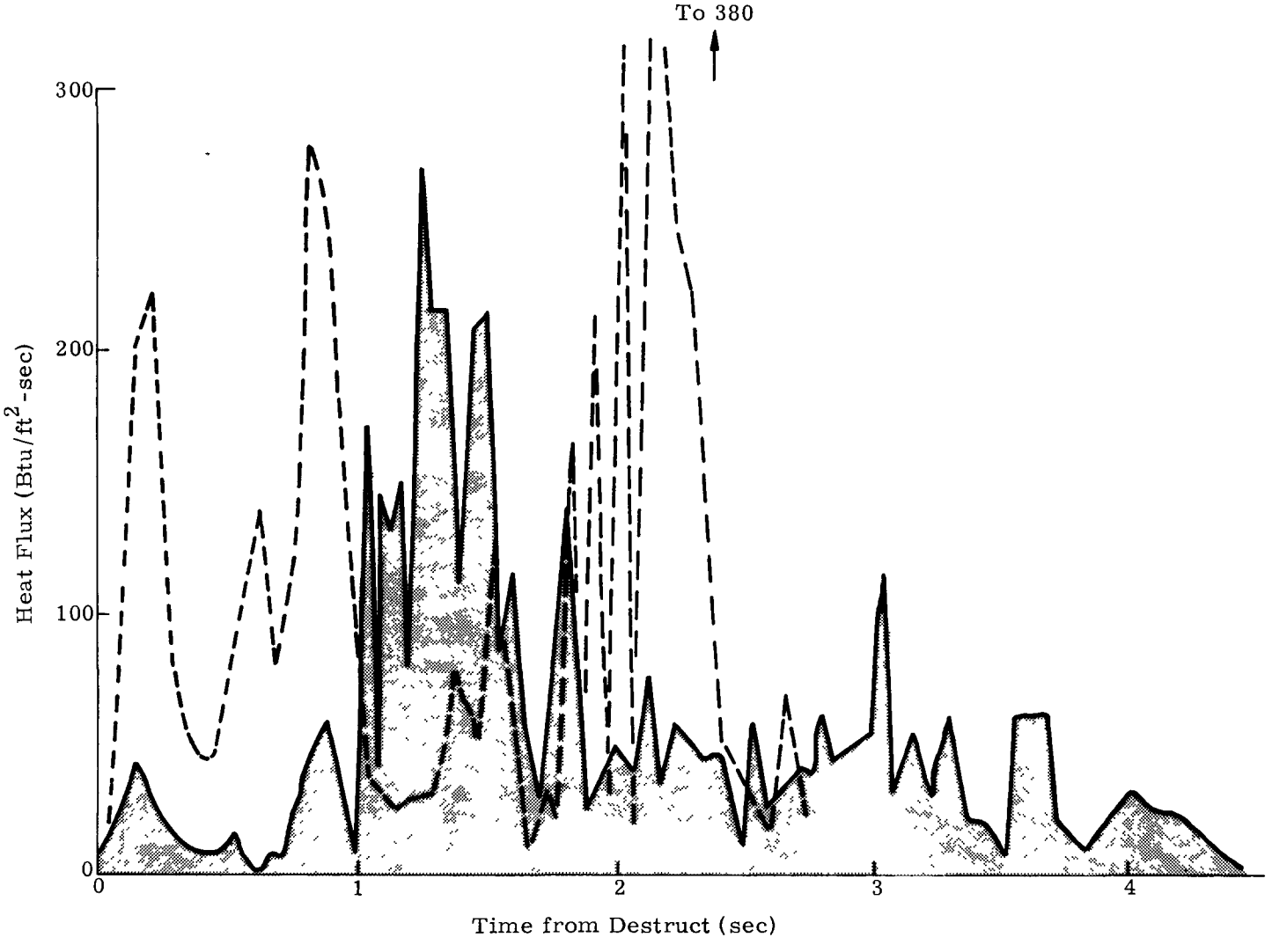

Fig. Z-6. Titan II Half-Scale Destruct Test

CONFIDENTIAL

C. SHOCK OVERPRESSURE AND IMPACT

At present, there are insufficient data and analyses to adequately predict overpressures generated during a fuel explosion. Figure Z-7 represents some of the more reasonable data (Ref. Z-5) obtained during various overpressure tests. Although it appears that a major correlation between the overpressure and the fuel contact area exists, fuel ignition delays, fuel tank geometry, fuel mixing and total fuel inventory can yield large differences in the overpressures generated by any given vehicle. However, one conclusion is obvious: overpressures of 100 psi or greater have been measured and can be expected, but inherently do not offer a serious restriction to the design of an intact fuel encapsulation. Only when these overpressures result in high fragmentation velocities is the integrity of the fuel encapsulation jeopardized.

Fragmentation velocities can initially reach 800 fps, although it is apparent (Ref. Z-2) that velocities in the region of 300 to 400 fps are more realistic for the pad accident as shown in Fig. Z-8. The maximum recorded debris trajectory time was measured at 48.6 seconds, with an average time of 0.2 to 0.25 second spent within the fireball. In-flight fragment velocities are about the same with a possible maximum of 500 fps. Contrast this to the expanded propellant vapor velocity of around 2000 fps.

Figure Z-9 (Ref. Z-2) illustrates the radial impact distribution as a function of size for an actual accident. The extremely large fragments at great distances from the source are somewhat misleading because equipment pods were located in the immediate vicinity of the point of ignition. However, the figure does illustrate the potential for debris scatter. It is quite conceivable that 1- to 10-pound capsules could easily be projected thousands of feet at initial velocities of 400+ fps, thus search areas for fuel capsules can be quite large because of the geometry between payload and point of ignition. The probability for such a situation is low.

REFERENCES

Z-1. High, R. W. and Fletcher, R. F., "Estimation of Fireball from Saturn Vehicles Following Failure on Launch Pad," NASA Program, Apollo Working Paper No. 1181, Houston, Texas, August 1965.

Z-2. Letter from V. E. Blake, Manager, Aerospace Nuclear Safety, Sandia, to A. W. Finelly, NASA-Goddard; entitled "Launch Abort Hazards Assessment for SNAP 19/Nimbus Assembly," February 1966.

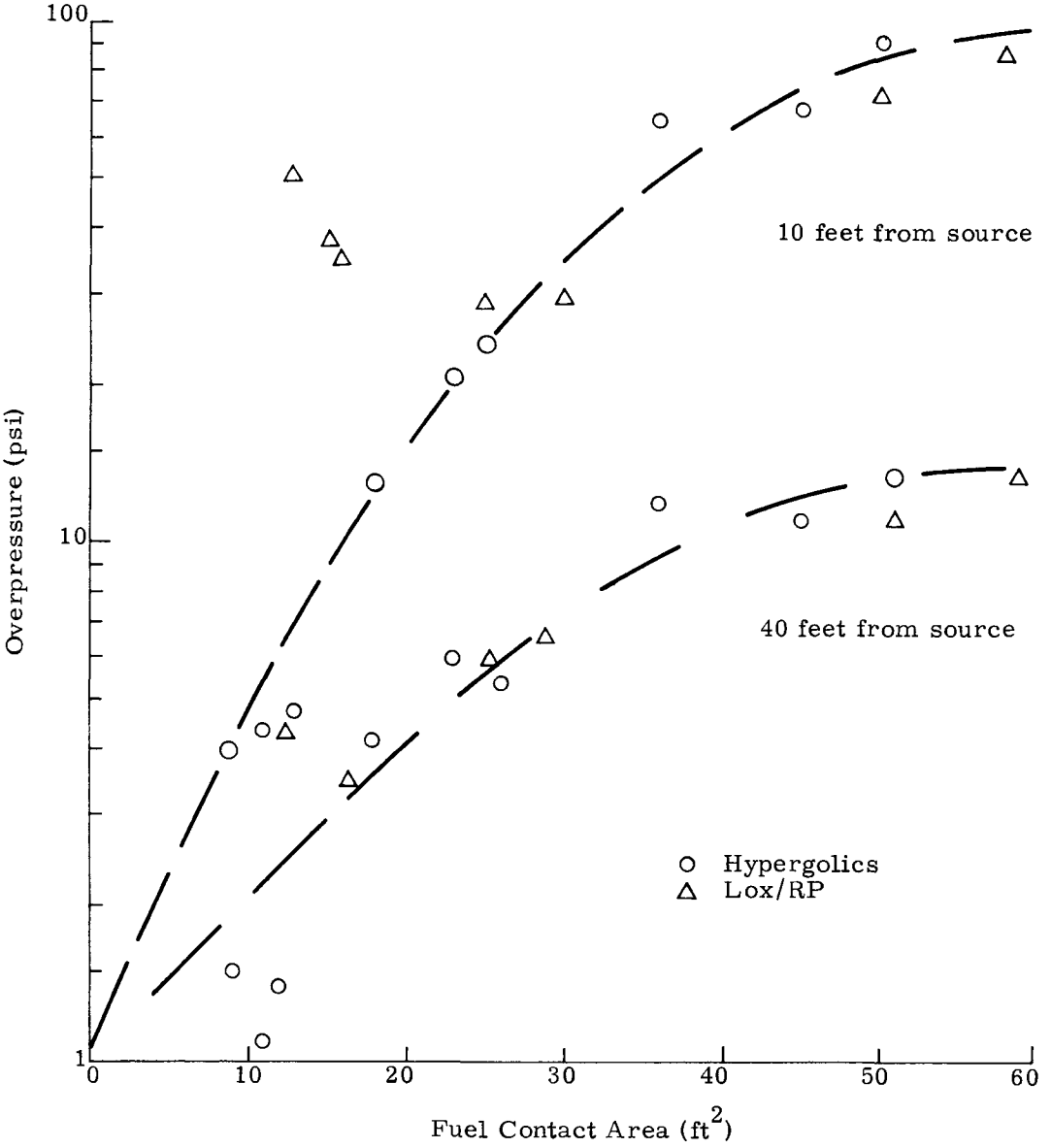

Fig. Z-7. Overpressures as a Function of Fuel Contact Area

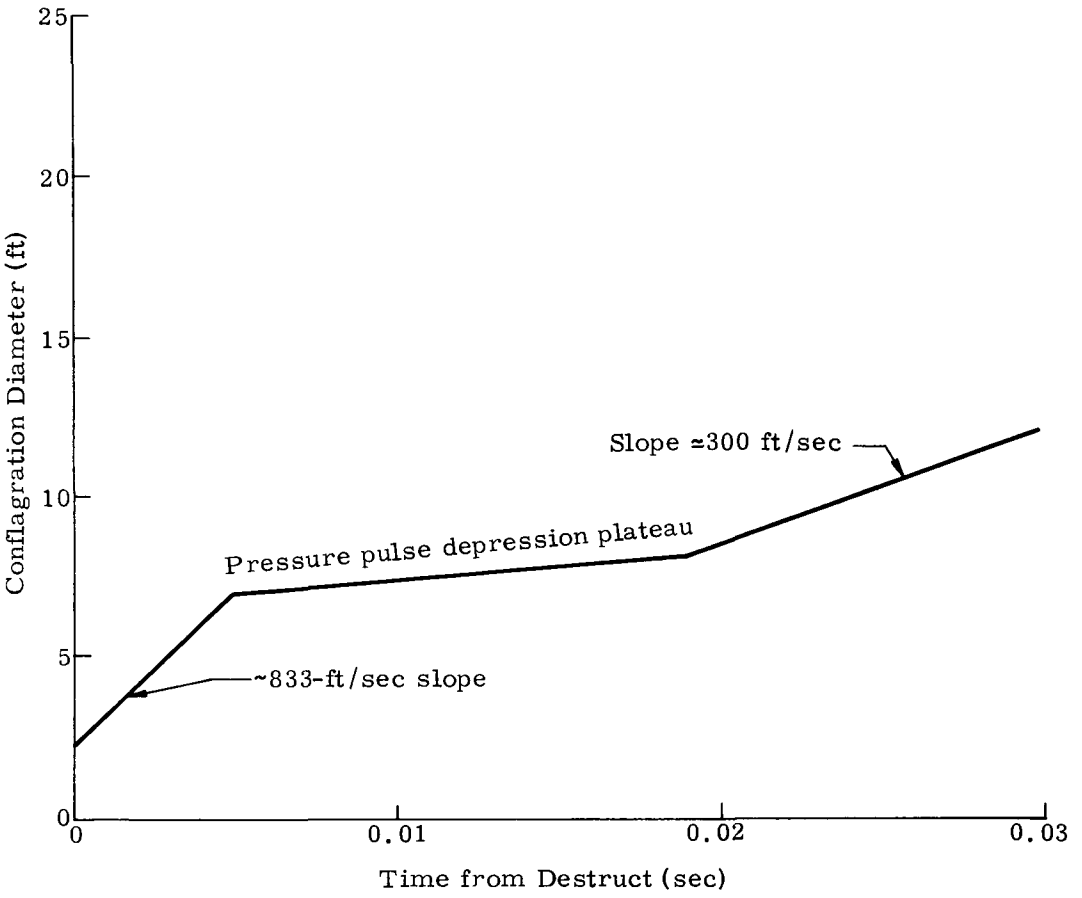

Fig. Z-8. Fragmentation Velocities

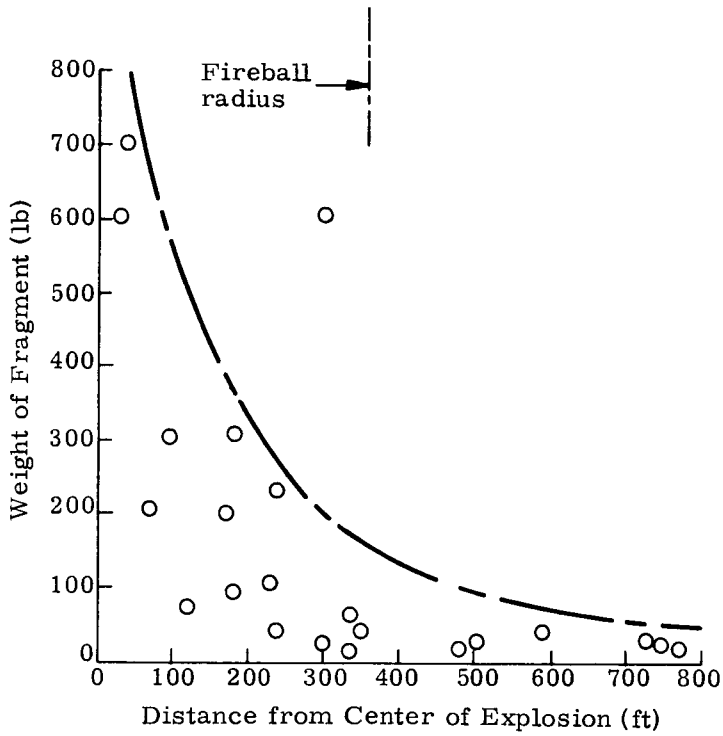

Fig. Z-9. Lox/RP Booster Explosion Fragmentation

Z-3. Cooke, C. R., "NASA/USAF Liquid Propellants Hazards Program (PYRO)," Bulletin of the 6th Liquid Propulsion Symposium, September 1964, Vol. 1, pp 601 to 626.

Z-4. "Blast and Fireball Comparison of Cryogenic and Hypergolic Propellants," Final Report, Aerojet General Corporation, Downey Plant Report No. 0822-01(01)FP, June 1964, Contract 9-2055.

Z-5. Final Report, "Blast and Fireball Comparison of Cryogenic and Hypergolic Propellants," Houston Research Institute, Contract No. NAS9-3506, August 1964 (also see Ref. Z-4).

APPENDIX AA

ANALYTICAL ESTIMATES OF TUMBLING AND OSCILLATORY MOTIONS OF CRONUS REENTRY BODY

The design of a reentry body requires an evaluation of the dynamic behavior of the body during its descent through the atmosphere. The most elementary requirement of such a design is to provide static stability by locating the center of gravity so that one obtains a negative value for the slope of the moment coefficient curve as a function of angle of attack in the vicinity of the trim point. The provision of static stability is, however, not sufficient to assure satisfactory dynamic behavior of a reentry body. During entry it is possible for a body to have an angle-of-attack behavior which is oscillatory but with an amplitude that is excessive during periods of maximum heating and maximum loads.

Some of the salient features of the oscillatory motion of a reentry body were obtained by Allen (Ref. AA-1) whose analysis was based upon the formulation of Friedrich and Dore (Ref. AA-2). The analytical results of Allen, while quite useful, are restricted to the case of a reentry body which enters the atmosphere with no angular velocity and whose oscillations are limited to small angles of attack. The effect of an initial spin rate upon the angle of attack convergence, also for small angles of attack, was investigated by Leon (Ref. AA-3) who obtained a correction to Allen's results. Recently, two papers by Tobak and Peterson have considered the inherently nonlinear problems of tumbling bodies entering planetary atmospheres (Ref. AA-4) and of spinning bodies entering planetary atmospheres at large initial angles of attack (Ref. AA-5). In the present note, the results of Refs. AA-4 and AA-5 are applied to the case of the CRONUS reentry body to estimate some of the dynamic characteristics of this body.

A. DISCUSSION AND RESULTS

To reduce the problem to manageable proportions, several simplifying assumptions and approximations were made in Refs. AA-4 and AA-5. The significant assumptions and approximations are as follows: rotation of the planet and atmosphere are neglected; aerodynamic damping terms are neglected; the flight path angle, γ, and velocity, V, remain constant at their initial values γ_i and V_i; the density, ρ, of the atmosphere varies exponentially with altitude; the motions of the non-spinning cases are planar; the variation of moment coefficient, C_m, with the magnitude of the angle of attack, η, is sinusoidal and may be written in the form

$$C_m(\eta) = C_{m_{max}} \sin \eta \qquad \text{(AA-1)}$$

and for the spinning case, the body is axisymmetric both inertially and aerodynamically. It should be noted that in Refs. AA-4 and AA-5 sample calculations were made to assess the accuracy of the methods presented with results in which no approximations were made either to the equations of motion or to the aerodynamic forces and moments. For the tumbling motion (Ref. AA-4), it was found that the agreement between the exact results and the theory was within 10% throughout; for the spinning case (Ref. AA-5), satisfactory agreement was also obtained (within approximately 15%). The characteristics of the body and the atmosphere used in the application of the methods of Refs. AA-4 and AA-5 are summarized in Table AA-1. The value of the maximum moment coefficient, $C_{m_{max}}$, was evaluated so that the area under a half-cycle of the approximating sine curve equaled the area under a representative pitching moment variation for the CRONUS reentry body. A comparison of the two curves is shown in Fig. AA-1.

TABLE AA-1

Properties of Vehicle and Atmosphere Used in Estimating Dynamic Characteristics

Moment of inertia in pitch, I	14 slug-ft^2
Ratio of pitch moment of inertia to roll moment of inertia, I/I_z	1.0
Reference area, A	11.5 ft^2
Reference length, d	3.83 ft
Flight velocity, V	25,690 fps
Maximum moment coefficient, $C_{m_{max}}$	-0.0498
Ballistic coefficient, $W/C_D A$	25 lb/ft^2
Density parameter β for exponential atmosphere ($\rho = \rho_0 e^{-\beta y}$)	(21,138 ft)$^{-1}$

The variation of the envelope of the angle-of-attack oscillations with dynamic pressure is shown in Fig. AA-2 for an entry angle of -8 degrees and for several values of initial angle of attack and zero initial angular velocity. These results show that the envelopes converge very rapidly at low values of dynamic pressure and reach a minimum at maximum dynamic pressure. The same envelopes are also

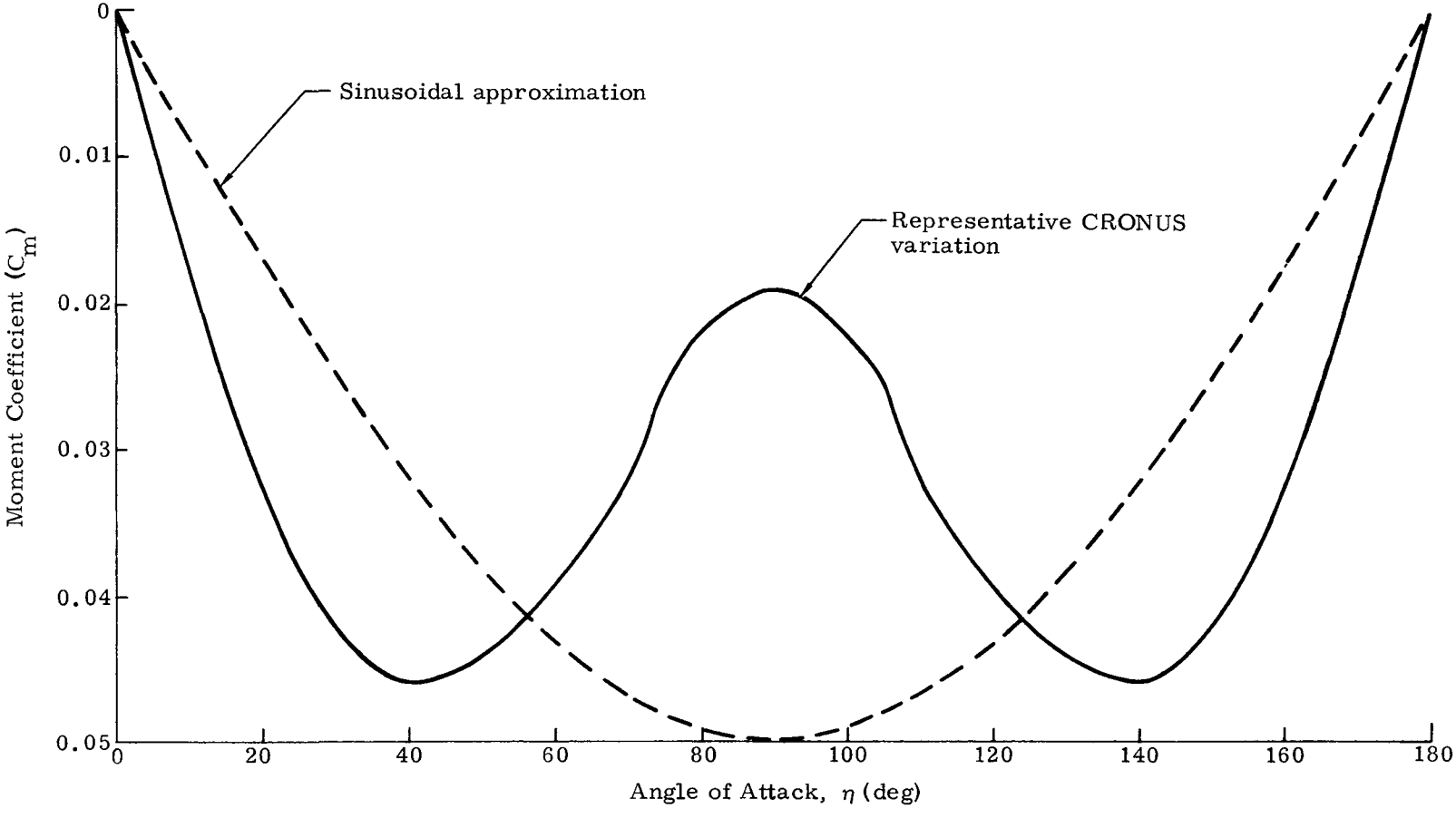

Fig. AA-1. Comparison of Moment Coefficient of CRONUS Vehicle with Sinusoidal Approximation Assumed in Analytical Methods

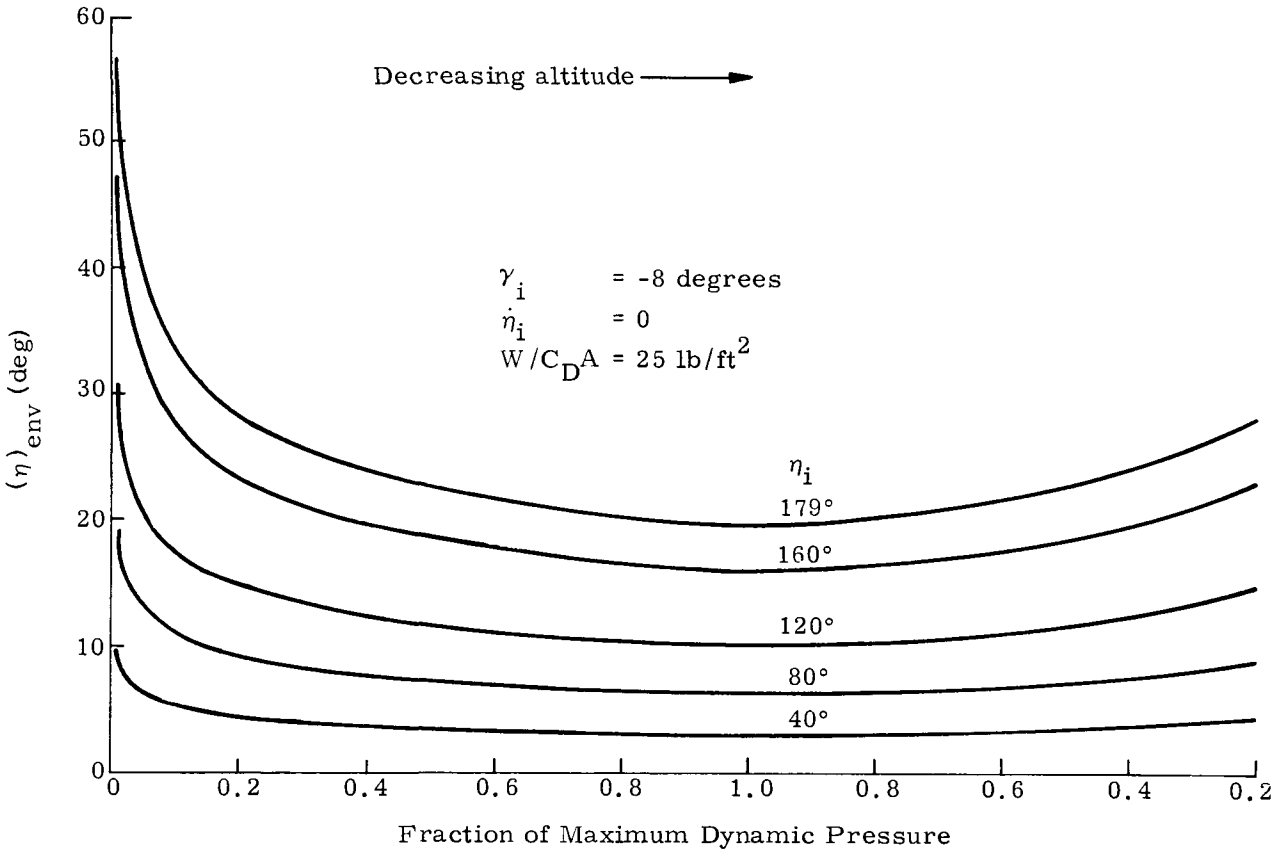

Fig. AA-2. Variation of Envelope at Angle of Attack Oscillations with Dynamic Pressure. Zero Initial Angular Velocity

shown as functions of the fraction of maximum stagnation point heating rate in Fig. AA-3. It will be noted that for the largest initial angle of attack considered (η_i = 179 deg), the envelope converges to approximately 20 degrees at maximum dynamic pressure and at peak stagnation point heating, the angle of attack is less than 25 degrees. For smaller initial values, smaller minimum values are obtained. The effect of flight path angles upon the minimum value of the angle-of-attack envelope (at peak dynamic pressure) is shown in Fig. AA-4. Increasing the flight path angle results in an increase in the minimum value of the envelope. For entry angles less than 30 degrees, however, the envelopes converge to an angle of attack of less than 30 degrees even for the largest initial angle of attack (179 deg) considered here.

When a body enters the atmosphere, it will not, in general, do so with zero angular velocity. In most cases, the body will have some angular momentum and will enter the atmosphere with a tumbling rate about its center of gravity. As it enters the atmosphere, the aerodynamic moments will come into play and, if some measure of aerodynamic stability exists, the tumbling motion will generally be arrested and the body will undergo an oscillatory motion. This oscillatory motion will be of diminishing amplitude, at least during the period of increasing dynamic pressure, but may be of large amplitude. It is of interest, therefore, to estimate the dynamic pressure at which the tumbling motion ceases as well as the magnitude of the subsequent angle-of-attack envelopes.

In Fig. AA-5 the variations of dynamic pressure, q, at which the tumbling motion ceases as a function of initial tumbling rate, η_i, for two values of entry angle, γ_i, are presented. The initial altitude for these results was taken to be 400,000 feet. The lowest curves on this figure show the minimum values of dynamic pressure at which tumbling can cease, i.e., the initial tumbling motion will persist at least to these values of dynamic pressure. The uppermost curves on this figure represent the values of dynamic pressure whose probability of being exceeded is 0.01 when tumbling ceases. Thus, tumbling will cease at dynamic pressures between the uppermost and the lowest curves for 99% of the tumbling reentries. The reason for using a probabilistic criterion for the upper curve is that, for a given initial tumbling rate, there exists one value of initial angle of attack (out of a total of 360 deg) at which the body will not oscillate, but will come to rest at the unstable trim point (η = 180 deg for the sinusoidal variation of moment coefficient with angle of attack). The probability of this occurrence is, however, negligible and the use of a finite probability criterion is more meaningful. It should be noted that in Ref. AA-4 it was found that there exists a nonzero minimum value for the first peak of the variation of angle of attack during reentry. This minimum

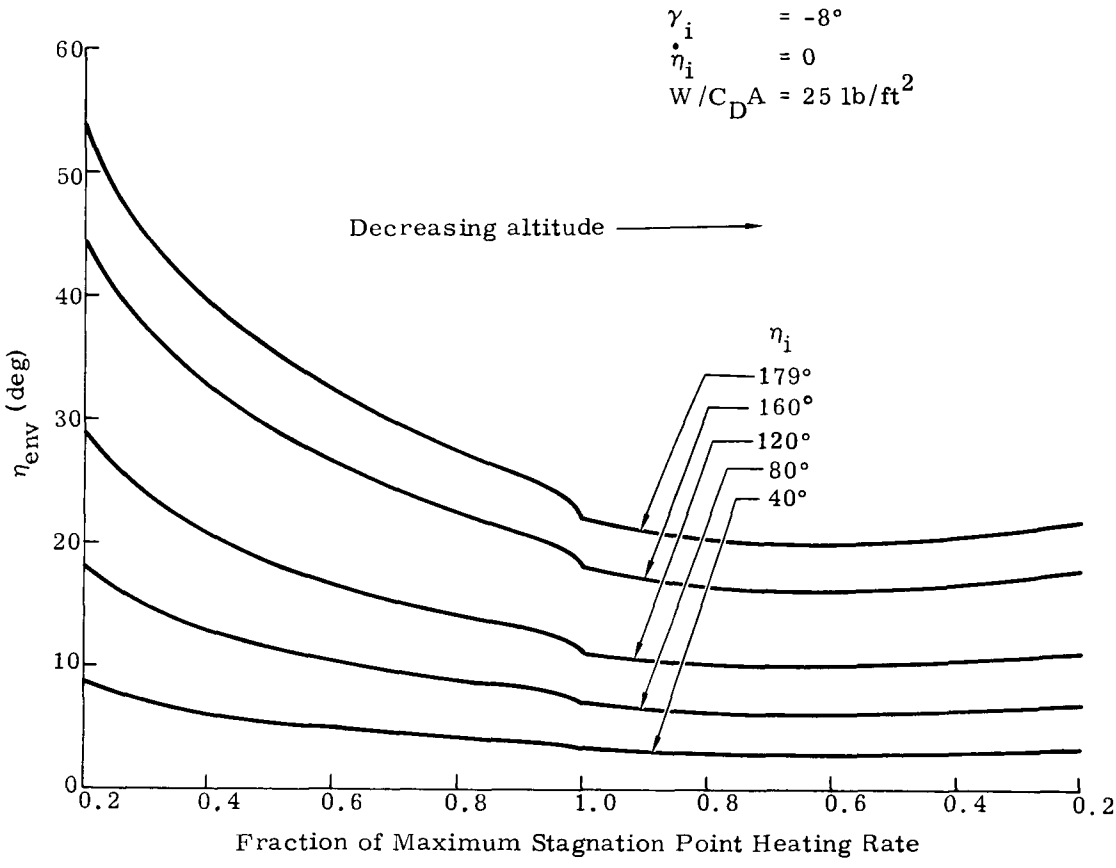

Fig. AA-3. Variation of Envelope of Angle of Attack Oscillations with Fraction of Maximum Stagnation Point Heating Rate. Zero Initial Angular Velocity

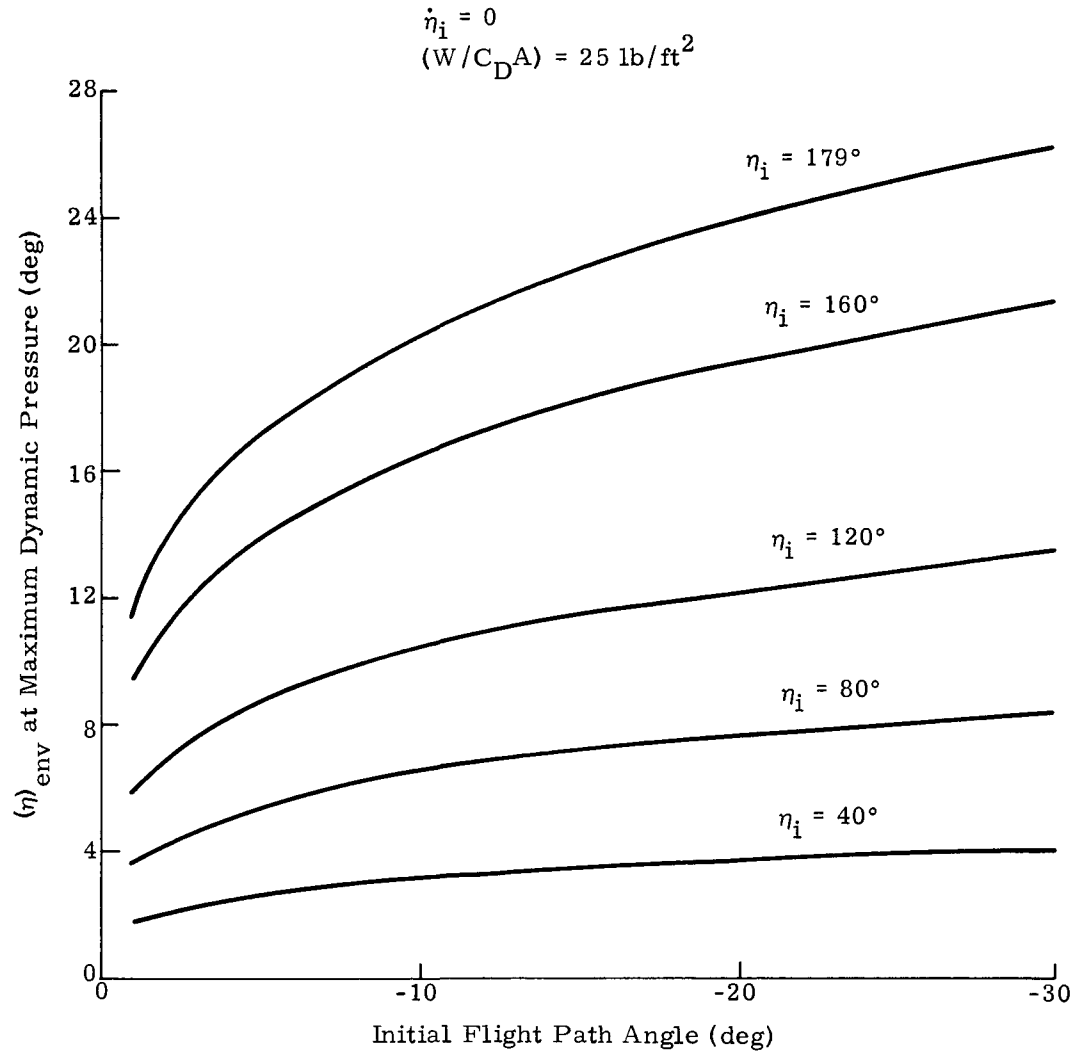

Fig. AA-4. Effect of Initial Flight Path Angle upon Value of Angle of Attack Envelope at Peak Dynamic Pressure. Zero Initial Angular Velocity

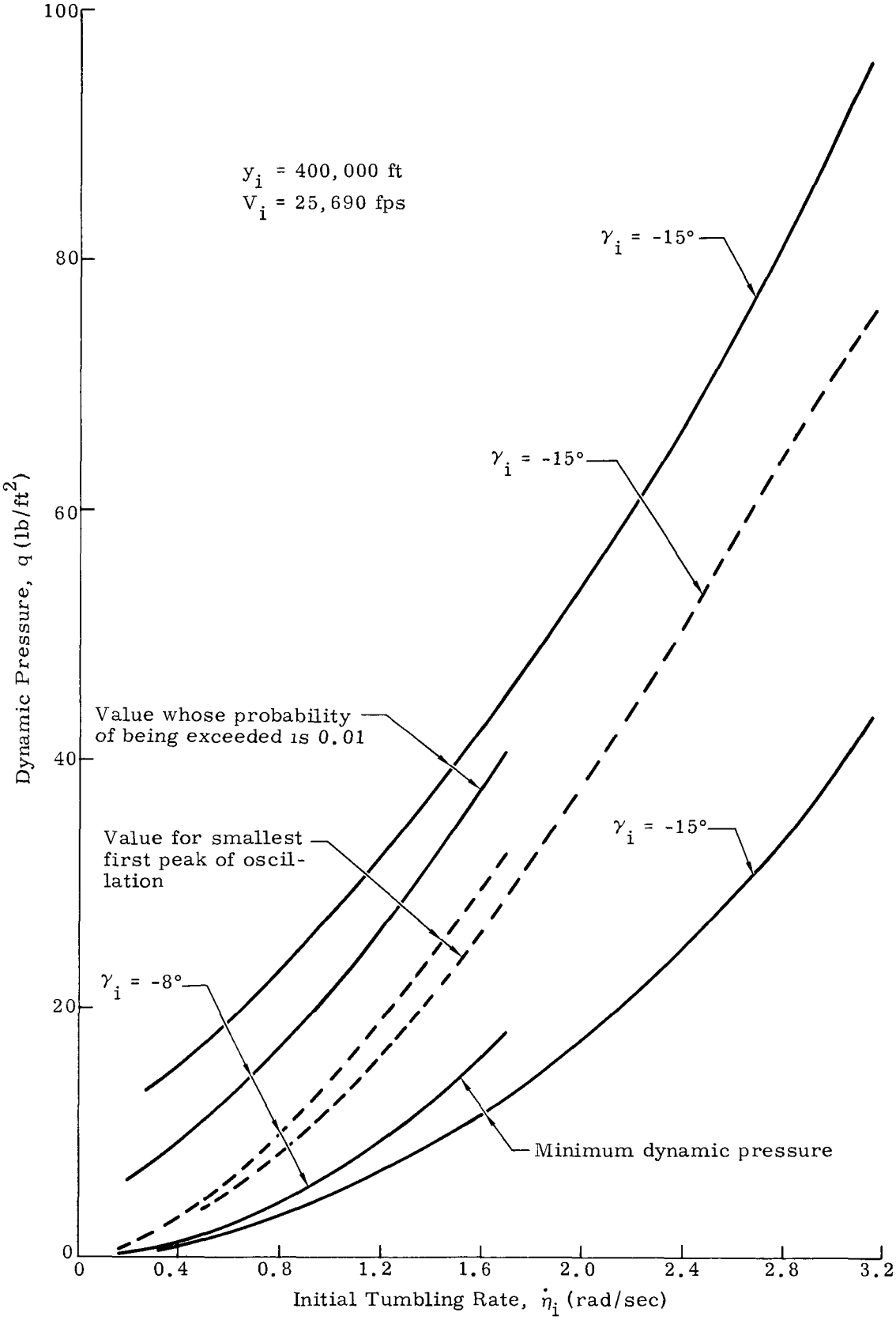

Fig. AA-5. Dynamic Pressure at Which Tumbling Ceases as Function of Initial Tumbling Rate. Zero Spin Rate

value of the first peak of the angle of attack results in the minimum value of the angle of attack envelope at peak dynamic pressure. The values of the dynamic pressure at which this minimum value of the first peak of oscillation occurs are also shown in Fig. AA-5. The variation of the angle-of-attack envelopes with a fraction of maximum stagnation point heating rate is presented in Fig. AA-6 for a tumble rate of 0.85 radian/sec. The lower curve in this figure corresponds to the envelope resulting from the minimum value of the first peak of oscillation, the upper curve is the envelope whose probability of being exceeded is 0.01. Thus, 99% of the entries with an initial tumble rate of 0.85 radian/sec will have angle-of-attack envelopes between these two curves. The effect of entry angle γ_i upon the minimum values of angle-of-attack envelope, i.e., at maximum dynamic pressure, is shown in Fig. AA-7 for an initial tumble rate of 0.85 radian/sec. Again, the upper curve corresponds to the envelope whose probability of being exceeded is 0.01 and the lower curve corresponds to the minimum value of the first peak of oscillation. It will be noted that both curves decrease with steepening entry angles.

To obtain a controlled reentry of an orbiting body, it is often desirable to spin stabilize the reentry body prior to the application of the deorbit retrorockets. In such cases, the reentry body will enter the atmosphere with an initial spin rate. Thus, it is desirable to estimate the effects of such an initial spin rate upon the angle-of-attack envelopes of a reentry body. The methods developed in Ref. AA-5 provide a means for estimating the effects of such an initial spin rate for a body which enters the atmosphere with a given initial angle of attack and zero initial pitch (or yaw) rate. For the case of an initially spinning body, the motion is no longer planar as was obtained for the bodies that enter the atmosphere with an initial angle of attack and zero pitch rate as well as for the body that enters the atmosphere with an initial tumbling rate. As soon as a spinning body enters the atmosphere at a non-zero angle of attack, the aerodynamic pitching moment will generate a pitching rate which then couples with the gyroscopic moments of the spinning body to induce a yawing rate and the motion is, in general, nonplanar. Qualitatively, this nonplanar motion of a spinning body may be described as a precessional motion of the body axis about the velocity vector upon which is superposed a nutational oscillation. Such a motion generally is bounded between two envelopes corresponding to the maximum and minimum values of the magnitude of the angle of attack. This type of motion differs from the planar case in which the minimum value of the magnitude of the attack is equal to zero.

For a spinning reentry body, the variation of the maximum and minimum envelopes with dynamic pressure and with heating rate is similar to those shown in Figs. AA-2 and AA-3 for the nonspinning body. The minimum value of these envelopes, which occurs at peak dynamic

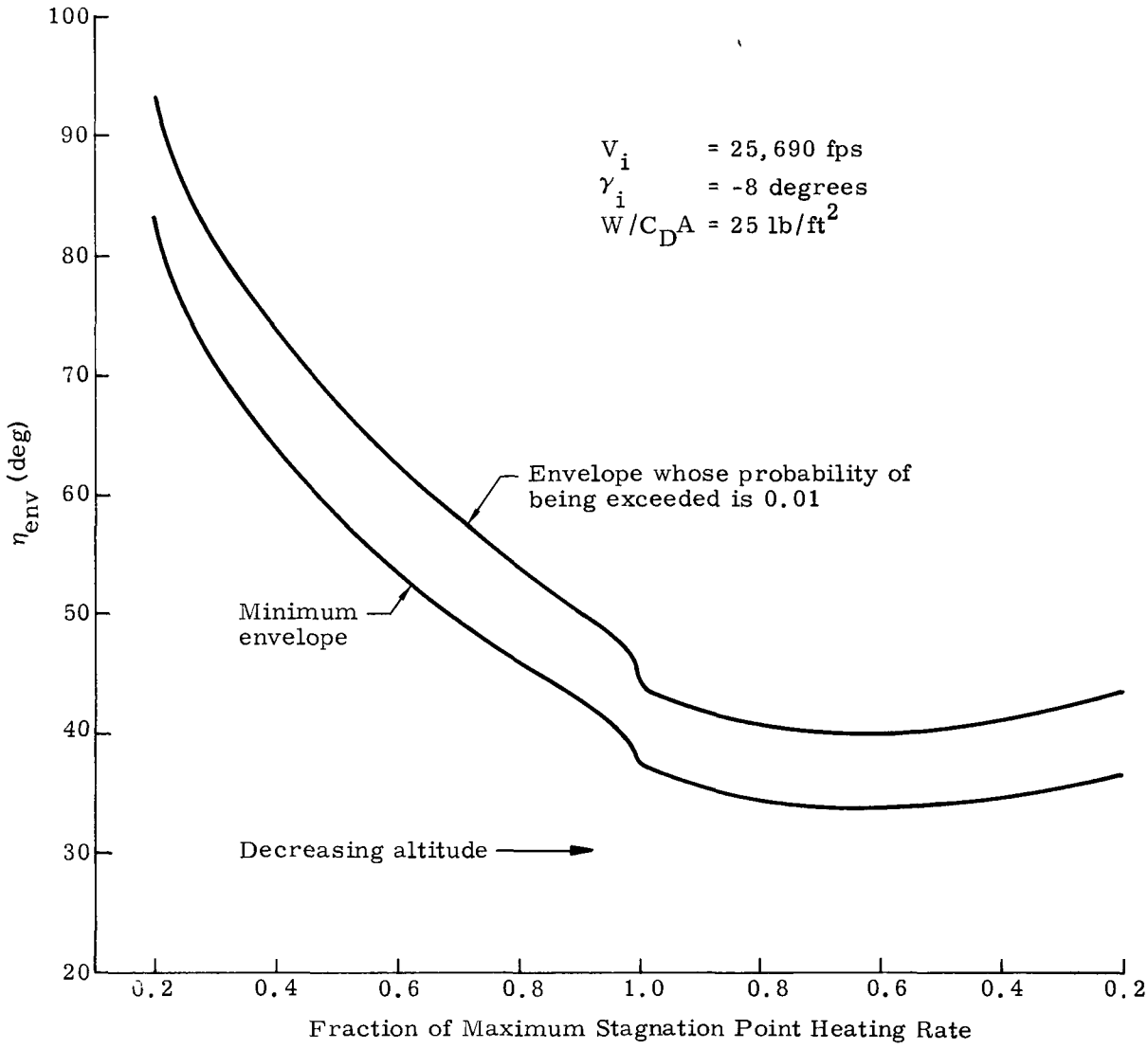

Fig. AA-6. Variation of Envelope of Angle of Attack Oscillations with Fraction of Maximum Stagnation Point Heating Rate. Initial Tumbling Rate $\dot{\eta}_i$ = 0.85 rad/sec. Zero Initial Spin Rate

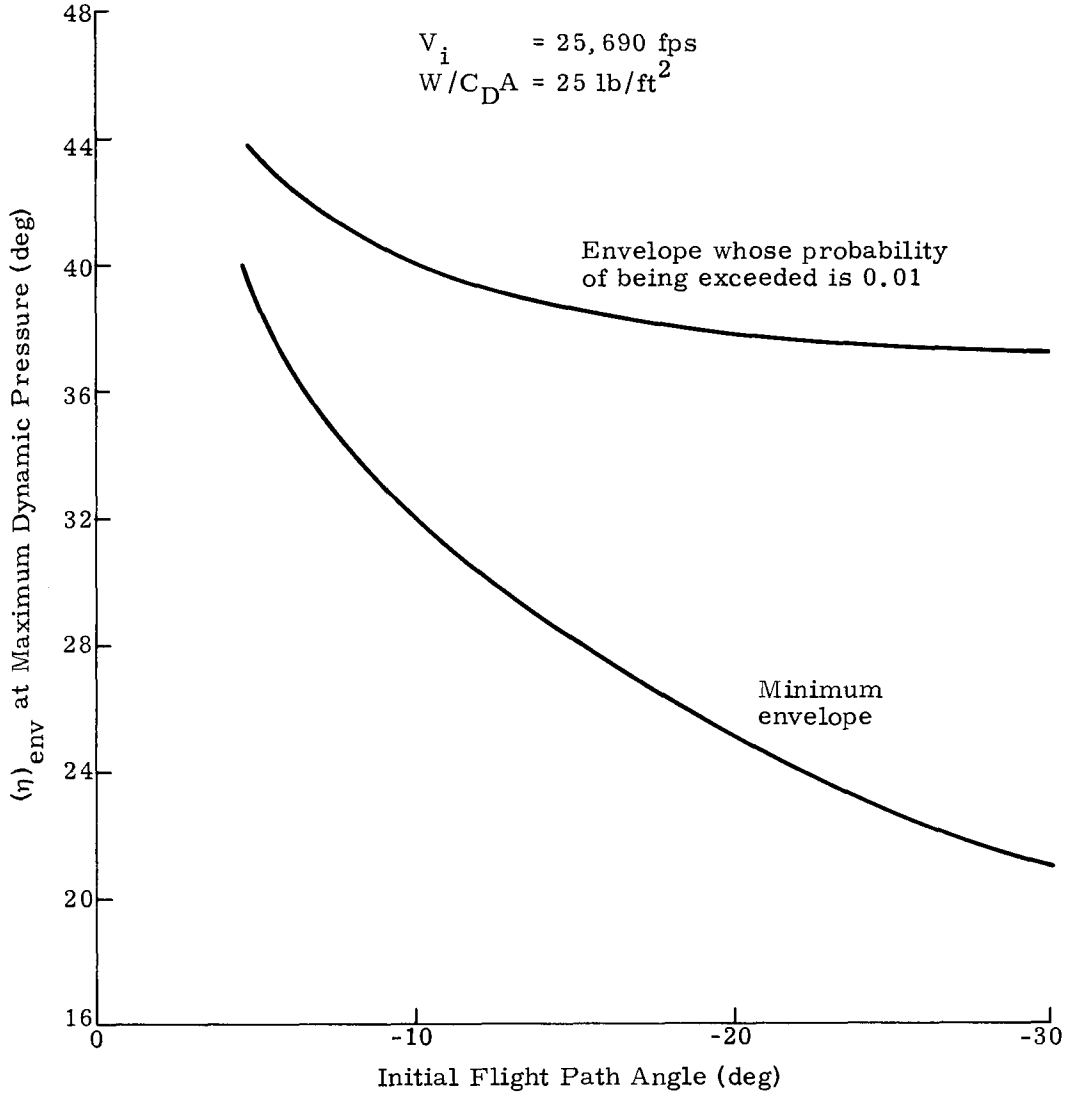

Fig. AA-7. Effect of Initial Flight Path Angle upon Value of Angle of Attack Envelope at Peak Dynamic Pressure. Initial Tumbling Rate $\dot{\eta}_i$ = 0.85 rad/sec. Zero Initial Spin Rate

pressure, does change with spin rate. The effect of spin rate upon the value of the two envelopes at peak dynamic pressure is presented in Fig. AA-8 for an entry angle of -8 degrees and two values of initial angle of attack. It will be noted that the envelope values at peak dynamic pressure increase with increasing spin rate. In addition, as the spin rate increases, the difference between the maximum envelope and the minimum envelope decreases, i.e., the nutational oscillations become smaller and the precession of the body axis about the velocity vector increases and becomes the dominant part of the motion.

B. CONCLUDING REMARKS

The present study indicates that a significant amount of information concerning the dynamic behavior of reentry bodies can be obtained from existing analytical methods. For the range of conditions covered in this investigation, it appears that there is a rather low probability that the angle of attack at maximum dynamic pressure will exceed 50 degrees. Inasmuch as the results obtained here depend upon several simplifying approximations, they should be used as a guide to the expected behavior of such a body in the preliminary design stages. For the evaluation of the dynamic behavior of a final design, it would be desirable to obtain the solution of the exact equations and aerodynamic forces and moments utilizing modern computing machines.

REFERENCES

AA-1. Allen, H. Julian, "Motion of a Ballistic Missile Angularly Misaligned with the Flight Path Upon Entering the Atmosphere and Its Effect Upon Aerodynamic Heating, Aerodynamic Loads, and Miss Distance. NACA TN 4048, October, 1957.

AA-2. Friedrich, Hans R. and Dore, Frank J., "The Dynamic Motion of a Missile Descending Through the Atmosphere." Jour. Aero. Sci., Vol. 22, No. 9, September, 1955, pp 628 to 632; 638.

AA-3. Leon, Herman I., "Angle of Attack Convergence of a Spinning Missile Descending Through the Atmosphere." Jour. Aero/ Space Sci., Vol. 25, No. 8, August, 1958, pp 480 to 484.

AA-4. Tobak, Murray and Peterson, Victor L., "Theory of Tumbling Bodies Entering Planetary Atmospheres with Application to Probe Vehicles and the Australia Tektites." NASA TR R-203, July, 1964.

AA-5. Tobak, Murray and Peterson, Victor L., "Angle of Attack Convergence of Spinning Bodies Entering Planetary Atmospheres at Large Inclinations to the Flight Path." NASA TR R-210, October, 1964.

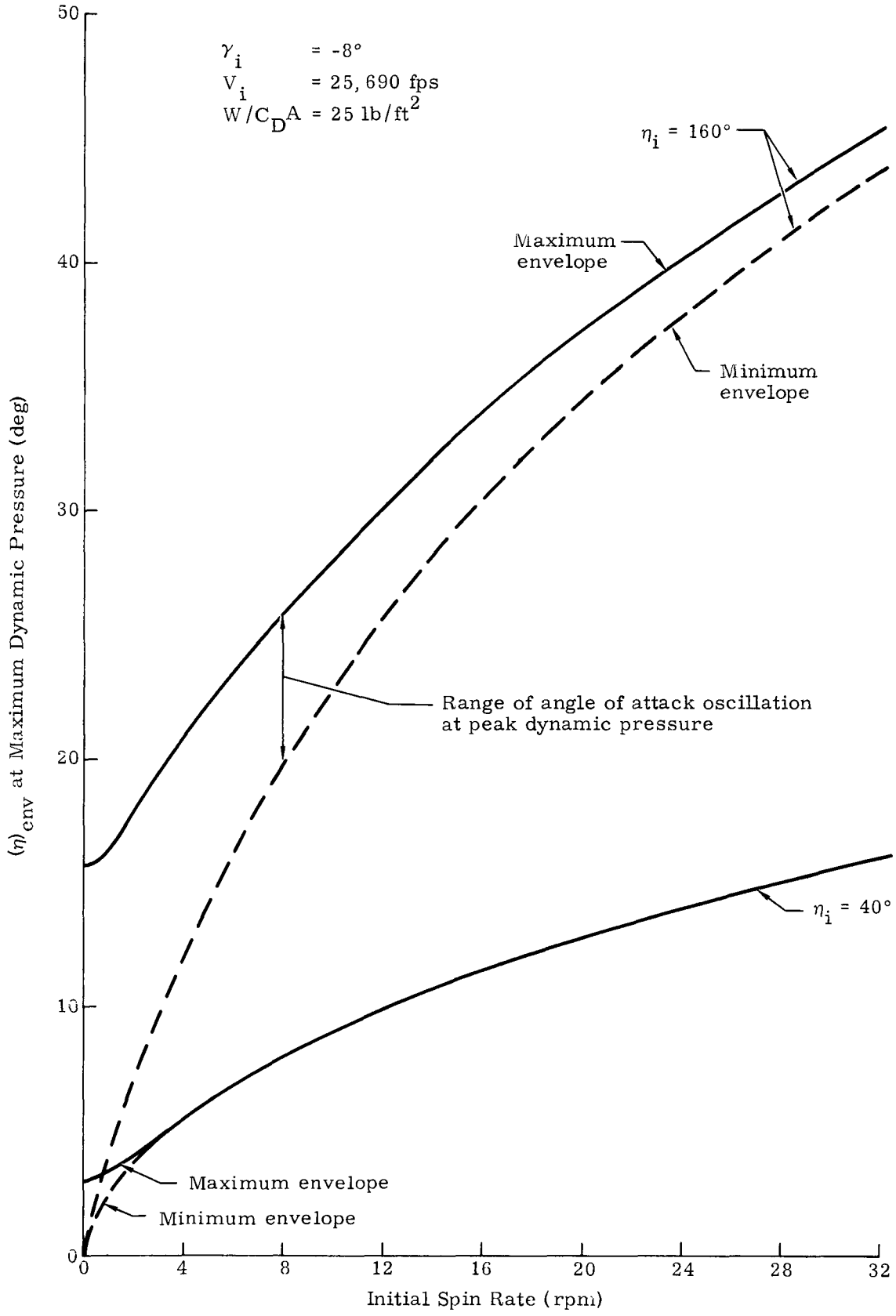

Fig. AA-8. Effect of Initial Spin Rate upon Values of Angle of Attack Envelopes at Peak Dynamic Pressure. Zero Initial Tumbling Rate

BLANK

APPENDIX BB

GUIDANCE/CONTROL CHARACTERISTICS

The RTG/RB is designed to abort under controlled orientation conditions and to maintain this orientation by spin stabilization. Therefore, the CIR-RTG/RB must be separated from the spacecraft, and subsequently deorbited, whenever there is an indication that a disastrous malfunction is developing or if loss of spacecraft (or launch vehicle) orientation beyond relatively narrow limits is imminent. These precautions could have the following effects:

(1) A mission could be unnecessarily voided.

(2) Intentional reentry and retrieval of the RTG/RB from the planned spacecraft orbit would be dependent upon the ability to ground command the spacecraft to the proper attitude for RTG/RB separation.

(3) Achievement of partial or secondary missions would be prevented if a satisfactory long-life circular orbit cannot be attained.

Incorporation of an attitude control system in the CIR could alleviate these conditions. However, the advantages to be gained do not appear to overcome the disadvantages of increased complexity and weight. Let us examine the realities of the potential advantages.

The first effect, voiding a mission unnecessarily, does not appear significant since automatic MDS functions cannot be overridden, and aborts based on telemetry and/or tracking data, which indicate deviations in the boost trajectory, excessive angular rates, etc., are subject to ground command. In the case of this latter point, the decision to separate the RTG/RB is no more critical than the decision to abort (destruct) the launch vehicle by ground command. Thus the only way in which a normally successful mission could be voided unnecessarily would be for Ground Control to receive a false signal from the injection stage after injection into the elliptical orbit, indicating that a nondestructive malfunction is about to occur which will prevent proper orientation of the RTG/RB for deorbit.

The second effect relates only to the planned return of a fueled power supply which has been placed in its planned circular orbit.

The third effect simplifies to the probability that a malfunction occurs which prevents the injection stage from injecting the spacecraft into the planned circular orbit yet permits attainment of a satisfactory elliptical orbit (100/600 naut mi) from which secondary or partial

mission objectives can be achieved; the planned use of a spacecraft with a nuclear power supply in a short duration elliptical orbit is not considered.

Since no mission objectives that can be accomplished in a short duration elliptical orbit can be identified at this time and the probability of a desirable elliptical orbit after failure to achieve the desired circular orbit appears low, there seems to be no way of justifying the added cost, complexity and weight of an attitude control system for added mission success possibilities. Consequently, the only real basis for providing an attitude control system in RTG/RB is to assure return of a fueled RTG/RB from the planned circular orbit if the spacecraft attitude control system malfunctions. On this basis, the RTG/RB attitude control system would simply act as a redundant system to the spacecraft ACS.

Incorporation of an attitude control for the latter purpose will eliminate the need for spinning the RTG/RB if it can be shown that the probability of a deorbit rocket motor-out condition is so remote that it does not impose a design requirement. Chapter VI shows that a motor-out condition is not sufficiently probable to serve as a design condition. The spin-despin system must be retained in any event, since the attitude control system has no reference during the boost ascent phase of the mission (unless a completely independent inertial platform is also included). Since there would be insufficient time after abort during boost flight to search for a reference and orient the deorbit rocket thrust vector, the capability for spin stability must be retained.

An RTG/RB attitude control system for intentional recovery from the planned orbit or from the 100/600 naut mi elliptical orbit will:

(1) Recover from a tumbling condition introduced by a gyrating spacecraft at separation of the RTG/RB

(2) Provide guidance reference point (sun) search and orientation for deorbit under limit cycle conditions

(3) Overcome the effects of small misalignments in the deorbit rocket thrust vectors.

Since the total impulse requirements are low (1000 to 4000 lb-sec), a nitrogen cold gas system has been compared with a monopropellant hydrazine system. While the bipropellant (hydrazine, nitrogen tetroxide) system is competitive with the monopropellant at this impulse level, only the monopropellant system with its inherently higher reliability was evaluated against the nitrogen system. The nitrogen system offers high inherent reliability and an extensive background of experience and application. However, the low specific impulse of the cold gas system results in heavy propellant and inert weight penalties which must ultimately be traded against reliability.

The thrust level for the attitude control system and the bulk of the propellant weight are dependent upon the requirement to overcome tumbling of the RTG/RB immediately after separation from the spacecraft. For this reason, system weight has been plotted as a function of tumbling rate (Fig. BB-1). The graph shows that if the RTG/RB can be separated from the spacecraft before a tumbling rate in excess of one revolution per second is imposed on the RTG/RB, the cold gas system weight disadvantage may be acceptable in order to reap the benefits of simplicity and reliability. Selection of the type of attitude control system will depend upon the characteristics of the spacecraft and the magnitude of the rates it can impose on the RTG/RB prior to separation.

Assumptions and design requirements for analysis of the ACS systems follow.

1. Basis for Analysis

This analysis provides a system's definition for independent operation of the present reference configuration. The analysis is limited to the cost in terms of equipment weight, volume and power requirements for finding a relative orientation with respect to sun and earth, communicating this orientation to a central command facility, determining attitude and time for deorbit execution, communicating these parameters to the RTG/RB and executing controlled deorbit and reentry. The weight penalty, excluding those functions common to the spin-stabilized version, is found to be 91.7 pounds.

2. Assumptions

The RTG/RB will consist of the RTG, structure and associated operational components shown in Fig. BB-2. A vehicle mass table is given (Table BB-1), and the inertia matrix computed from this data in the six-degree-of-freedom stability program is given in Table BB-2.

The equipment complement required for independent orientation is:

(1) Four wide-angle sun sensors placed about periphery of equipment module

(2) Two horizon sensors placed at opposite sides of equipment module

(3) Rate-switch controlled reaction jet system with six nozzles and associated fuel tanks

(4) One single-degree-of-freedom rate integrating gyro with associated electronics for gyro compassing to orbital angular momentum vector during the dark-side portion of orbit; this will maintain vehicle azimuth reference

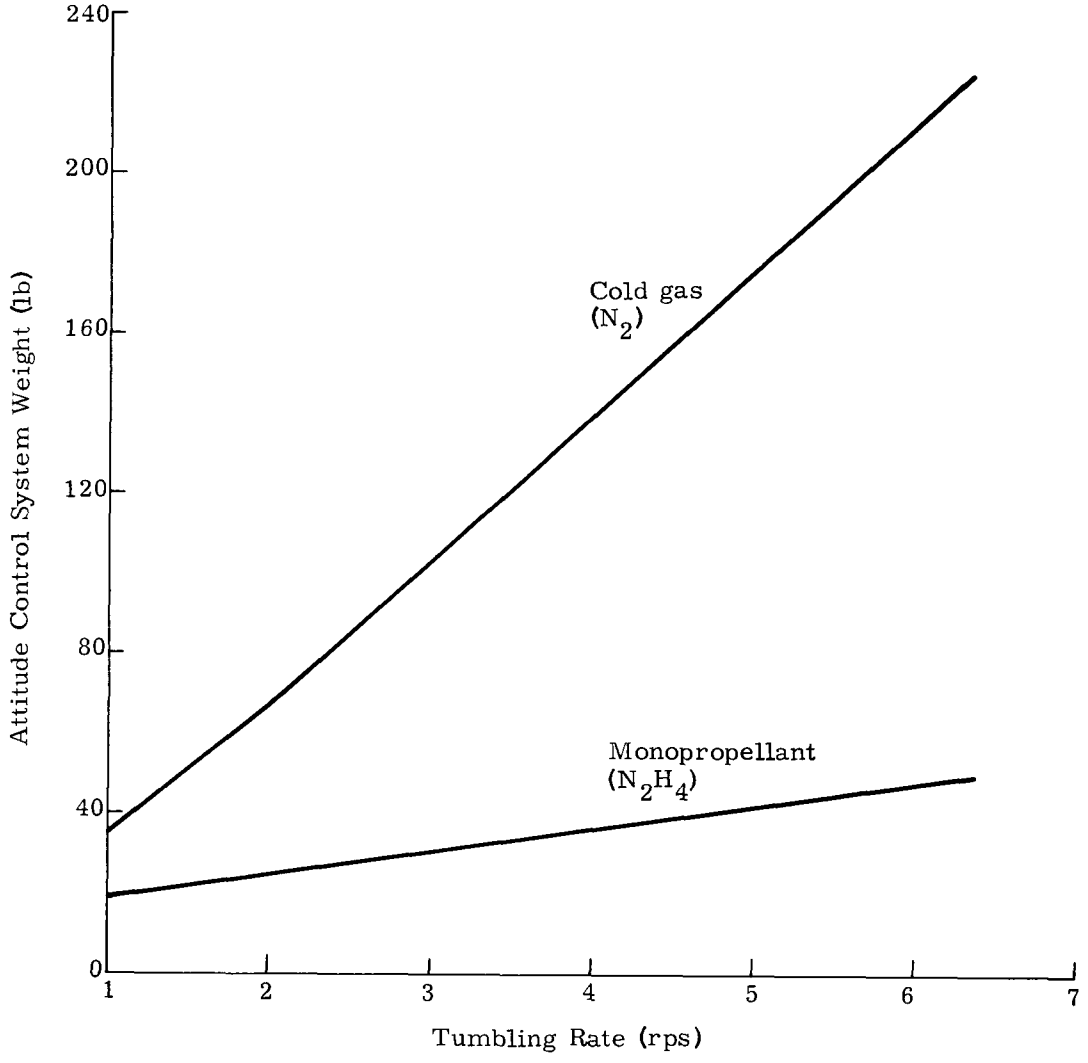

Fig. BB-1. System Weight as a Function of Tumbling Rate

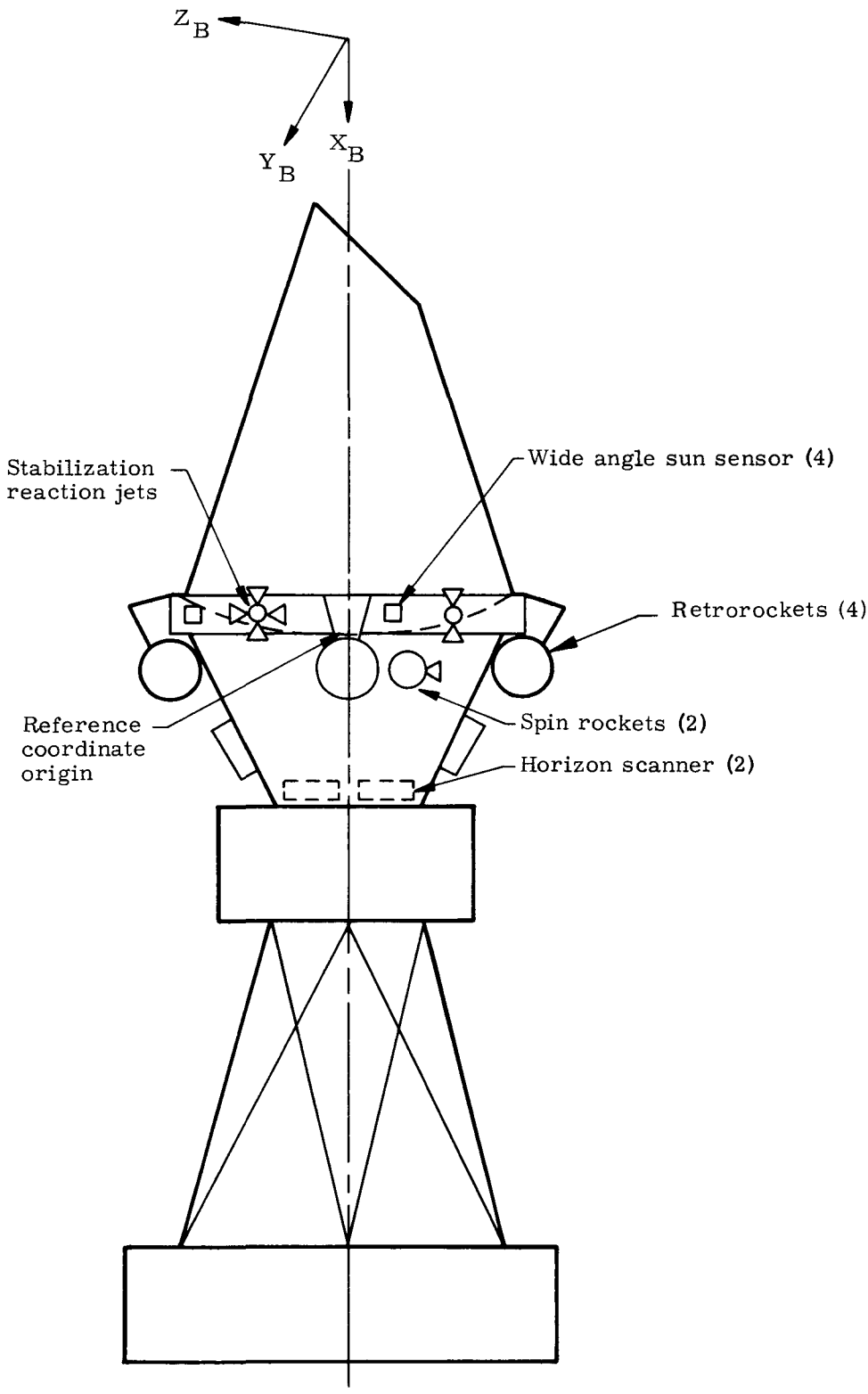

Fig. BB-2. Reentry Body, Configuration "D"

TABLE BB-1

Vehicle Masses

Item	Part Description	Weight (lb)	Location of Center of Gravity of Incremental Weights		
			X	Y	Z
1	RTG thermoelectrics	12	-21	-12	12
2	RTG thermoelectrics	12	-21	-12	-12
3	RTG thermoelectrics	12	-21	12	-12
4	RTG thermoelectrics	12	-21	12	12
5	RTG fuel block	49	-21	-6	6
6	RTG fuel block	49	-21	-6	-6
7	RTG fuel block	49	-21	6	-6
8	RTG fuel block	49	-21	6	6
9	RTG radiator shell	27	-21	-11	11
10	RTG radiator shell	27	-21	-11	-11
11	RTG radiator shell	27	-21	11	-11
12	RTG radiator shell	27	-21	11	11
13	Retrorockets	8.6-34	6	0	25
14	Retrorockets	8.6-34	6	-25	0
15	Retrorockets	8.6-34	6	0	-25
16	Retrorockets	8.6-34	6	25	0
17	Spin rockets	3.8-15	6	-21	8
18	Spin rockets	3.8-15	6	21	-8
19	Heat shield	12.5	-3	-11	11
20	Heat shield	12.5	-3	-11	-11
21	Heat shield	12.5	-3	11	-11
22	Heat shield	12.5	-3	11	11
23	Tracking beacon system	15	-48	0	-5
24	Aft skirt	4	-49	0	-1
25	Subsystems electronics and power	15.5	10	-8	8
26	Subsystems electronics and power	15.5	10	-8	-8
27	Subsystems electronics and power	15.5	10	8	-8
28	Subsystems electronics and power	15.5	10	8	8
29	Subsystems housing and mounting	7.5	6	-9	9
30	Subsystems housing and mounting	7.5	6	9	-9
31	Subsystems housing and mounting	7.5	6	9	-9
32	Subsystems housing and mounting	7.5	6	9	9

TABLE BB-2

Vehicle Physical Characteristics

Inertia Matrix with Respect to Center of Gravity

$$\begin{vmatrix} I_{XX} & I_{XY} & I_{XZ} \\ I_{YX} & I_{YY} & I_{YZ} \\ I_{ZX} & I_{ZY} & I_{ZZ} \end{vmatrix} = \begin{vmatrix} 38.7056 & 0.1994 & -1.5704 \\ 0.1994 & 63.6072 & 1.8532 \\ -1.5704 & 1.8532 & 65.8587 \end{vmatrix} \text{ slug ft}^2$$

Center of Gravity Location with Respect to Reference Coordinates (ft)

X	0.12224
Y	-0.07731
Z	0.02945

Total Mass

21.10397 slugs

(5) Programmer, beacon and communications electronics

(6) Independent battery power supply system capable of operation for up to five orbits after separation.

The RTG/RB is assumed attached to Nimbus or another satellite which may have lost its attitude reference and be tumbling. The vehicle is in a determined orbit,and power and command communications are available within the RTG/RB system. Ground command has made limited functional verification of RTG/RB systems. Therefore, the sequence of events is:

(1) The RTG/RB is separated from the Nimbus on ground command as a result of decision to recover or dispose of the RTG. The spin rockets are not used for this case.

(2) Tip-off rates are reduced to zero as a result of reaction jet system operation under rate switch sensing.

(3) The RTG/RB begins to search about its roll axis for sun line.

(4) Upon acquisition with any one sensor, the RTG/RB searches about the cross axis (either Y_B or Z_B) for the horizon.

(5) Upon acquisition and orientation, the RTG/RB searches about its roll axis (X_B) to establish a minimum (null) rate upon the gyro oriented along $+Z_B$; this axis is then established in the orbital plane and parallel to the velocity vector. The vehicle is stabilized to the horizontal and pitching about Y_B at the orbital rate.

(6) The RTG/RB communicates its locked-on condition to ground.

(7) Ground facilities will have determined orbit and predicted position and azimuth of sun as a function of time. Time for deorbit is determined, if required, and an incremental roll command is computed. The pitch command required will be a function of desired deorbit ΔV application angle.

(8) The RTG/RB is given a deorbit program consisting of:

(a) Time to commence orientation for deorbit

(b) Incremental roll command to place Y axis perpendicular to orbital plane, if required

(c) Incremental pitch command to position rockets for deorbit ΔV

(d) Update of RTG/RB clock.

(9) The RTG/RB executes reorientation on time and in position for reentry to the desired target impact area.

(10) At this point, two options are available:

(a) Programmer ignites the deorbit rockets which apply deorbit thrust. The reaction control system counteracts the disturbing torques resulting from deorbit rocket thrust vector misalignment and from variations in thrust level between rockets.

(b) Programmer ignites spin rockets for spin stabilization. The programmer then ignites the deorbit rockets. The reaction control system counteracts tumbling rates produced by deorbit rocket misalignments. The programmer initiates reduction of spin rate utilizing the reaction control system, after the deorbit impulse delivery is completed.

(11) The time available to complete either of these options is 26.58 minutes, based on an initial altitude of 600 naut mi, an application angle of -135 and a nominal ΔV of 1500 fps. It is assumed for this analysis that each function--tumble correction and despin--will require 90 seconds to achieve.

(12) The RTG/RB is then separated from auxiliary systems by release of the retention band and permitted to reenter in its aerodynamic configuration with arbitrary attitude and residual tumbling rates from the last separation.

(13) Upon atmospheric reentry, the RTG/RB is stabilized rapidly to normal reentry aspect through aerodynamic moments caused by the asymmetric aft body.

The choice of Option (10b) is only pertinent if the possibility of a single-deorbit-rocket-out condition is used as the design criterion. It can be shown that the propellant expended to overcome anticipated thrust misalignments for a system in which all deorbit rockets are functioning is quite small. On the other hand, a single rocket-out condition would generate angular accelerations on the order of 30 rad/sec^2. At this angular acceleration, the vehicle would be set tumbling, and deorbit would fail. Any practical increase in reaction jet thrust would fail to account for this situation, hence spin stabilization. However, even spin stabilization will not completely prevent the vehicle from tumbling in the rocket-out condition. Rather, it will tend to distribute the angular momentum between two axes, providing a longer period of time in which the thrust vector application is near nominal.

In view of the extremely low probability of encountering a single-deorbit-rocket-out condition and because spin stabilization is not a guaranteed solution to the motor-out condition, this approach has not been used. Evaluation of reaction control system requirements and comparison of reaction jet propulsion systems are made on the basis of Option (10a).

3. Reaction Control Propulsion System

A reaction jet system incorporated in the deorbit system associated with the reference vehicle must provide sufficient thrust and total impulse to enable the RTG/RB to recover from a tumbling condition at separation from the spacecraft, accomplish a sun reference seeking maneuver and compromise any pitch, yaw and roll torques generated by misalignment of the deorbit rocket thrust vectors.

The ACS thrustors are located radially two feet from the reference vehicle centerline, approximately six inches aft of the center of gravity. The time for rate stabilization should be within possible communications contact time; a time of 90 seconds is assumed. Since:

$$\dot{\theta} = \ddot{\theta}\,(\Delta t)$$

where

$\dot{\theta}$ = tumbling rate

$\ddot{\theta}$ = angular acceleration required to null the tumbling rate in 90 seconds

and

$$\ddot{\theta} = \dot{\theta}/90$$

also

$$FR = I\,\ddot{\theta}$$

where

F = thrust level for one axis

R = thrust moment-arm (2.0 ft)

I = moment of inertia of vehicle in axis of interest: 66 slug-ft^2 in pitch and 39 slugs in roll

Thus, the thrust level required in the pitch and yaw axes is

$F_{PY} = 33\ (\dot{\theta}/90) = 0.367\ (\dot{\theta})$ pitch and yaw

$F_R = 19.5\ (\dot{\theta}/90) = 0.217\ (\dot{\theta})$ roll

Although the high level of thrust required for correction of tumbling is not efficient for fuel economy during the limit cycle operation required to accomplish sun reference, a pulsed system of variable repetition rate can be used to minimize the impulse bit. It is possible to operate in a control mode such that "on" pulses are so rapid that the valve never closes. Thus, constant operation can be achieved while the capability to return to a minimum impulse bit limit cycle is retained. Reaction jets of the size required (5 to 15 pounds of thrust) can have "on" times of 0.020 second and repetition rates of 50 pulses per second. Propellant consumption during the limit cycle is derived as follows:

f = pulsing frequency

$\Delta\dot{\theta}$ = angular velocity change due to torque impulse of applied thrust

J = polar moment of inertia

r = radius arm of thrust motor

I_t = impulse bit (Fot)

$J\Delta\dot{\theta} = rI_t$

$$\Delta\dot{\theta} = \frac{rI_t}{J}$$

Assume the angular velocity of the vehicle between

$t_0 \leq t \leq t_1$ is $\dot{\theta}_1$

$$t_1 - t_0 = \frac{-2\Delta\theta}{-\dot{\theta}_1} = \frac{2\Delta\theta}{\dot{\theta}_1}$$

This is shown in Fig. BB-3.

If, at $t = t_1$ a velocity change, $\Delta\dot{\theta}$, is given to the vehicle,

$\dot{\theta}_2 = -\dot{\theta}_1 + \Delta\dot{\theta}$

where,

$\dot{\theta} = \dot{\theta}_2$, $t_1 \leq t \leq t_2$

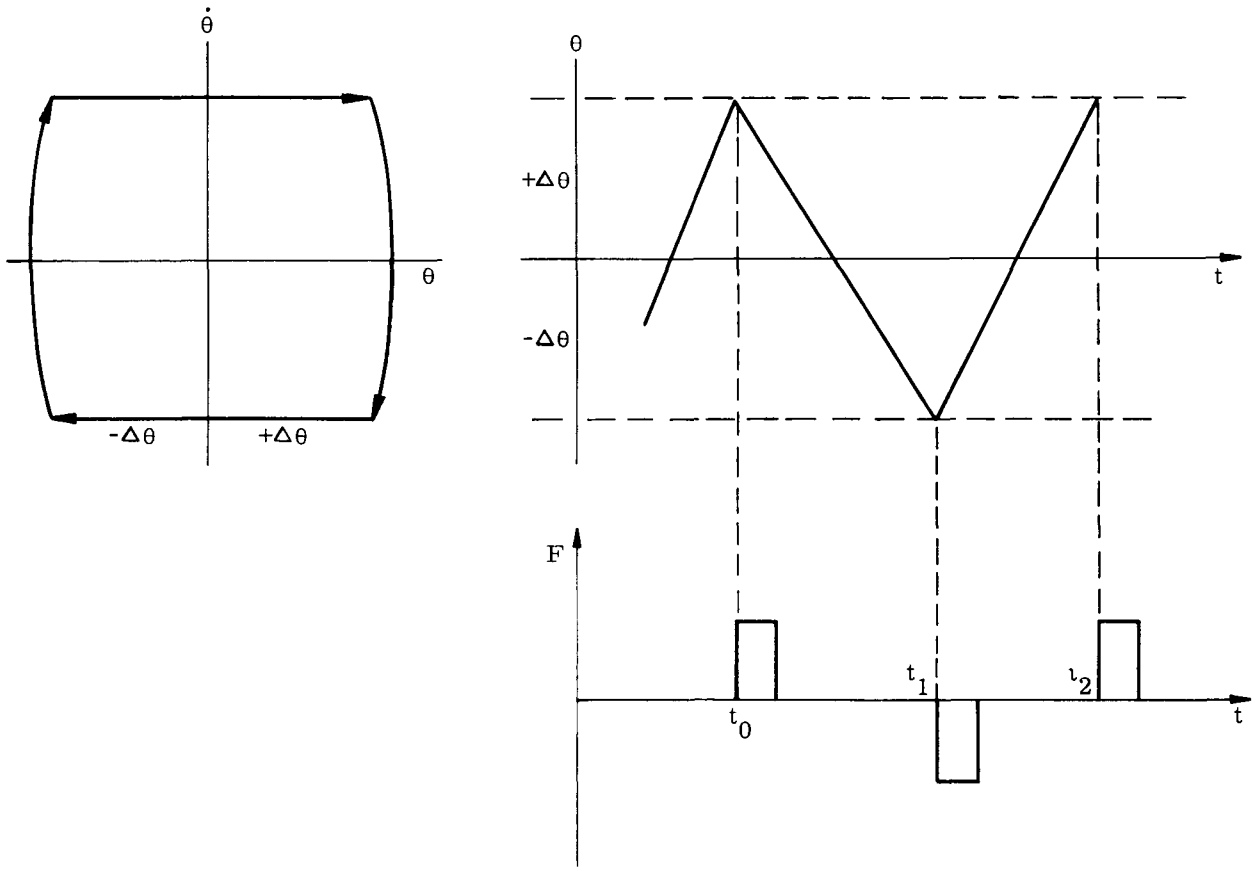

Fig. BB-3. Reaction Jet Limit Cycle

we find,

$$t_2 - t_1 = \frac{2\Delta\theta}{\Delta\dot{\theta} - \dot{\theta}_1}$$

Then, for τ = period, $f = \frac{1}{\tau}$

$$\tau - t_2 - t_0 = (t_2 - t_1) + (t_1 - t_0)$$

$$\tau = \frac{2\Delta\theta}{\dot{\theta}_1} + \frac{2\Delta\theta}{\Delta\dot{\theta} - \dot{\theta}_1} = 2\Delta\theta\left(\frac{1}{\dot{\theta}_1} + \frac{1}{(\Delta\dot{\theta} - \dot{\theta}_1)}\right)$$

$$\tau = 2\Delta\theta\left(\frac{\Delta\dot{\theta}}{\dot{\theta}_1\,(\Delta\dot{\theta} - \dot{\theta}_1)}\right)$$

$$f = \frac{\dot{\theta}_1\,(\Delta\dot{\theta} - \dot{\theta}_1)}{2\,\Delta\theta\,\Delta\dot{\theta}} \text{ where } 0 \leq \dot{\theta}_1 \leq \Delta\dot{\theta}$$

Then, a time averaged frequency over an initial rate spectrum $(0 - \Delta\dot{\theta})$ is

$$f_{ave} = \frac{1}{\Delta\dot{\theta}} \int_0^{\Delta\dot{\theta}} \frac{\dot{\theta}_1\,(\Delta\dot{\theta} - \dot{\theta}_1)}{2\,\Delta\theta\,\Delta\dot{\theta}}\, d\dot{\theta}$$

$$= \frac{\Delta\dot{\theta}}{12\,\Delta\theta}$$

and since the reaction jet is pulsed twice per cycle,

$$f'_{ave} = 2f = \frac{\Delta\dot{\theta}}{6\Delta\theta}$$

where f'_{ave} is the average frequency of the pulses. Let I be the time rate of impulse expenditure,

$$\dot{I} = I_t\, f'_{ave} = I_t\, \frac{\Delta\dot{\theta}}{6\Delta\theta}$$

$$\dot{I} = I_t\, \frac{(r\, I_t)}{6J\Delta\theta} = \frac{r\, I_t^{\,2}}{6J\,\Delta\theta}$$

If $\dot{W}_p$ = weight flow rate,

$$\dot{W}_p = \frac{\dot{I}}{I_{sp}}$$

where I_{sp} = specific impulse,

we have,

$$\dot{W}_p = \frac{rI_t^2}{6JI_{sp}\Delta\theta} \qquad \text{(BB-1)}$$

The minimum impulse bit is the average thrust over the pulse width. We define here an impulse bit which is the product of the peak thrust and an effective pulse width (Δt_ϵ). Thus

$$I_{t_{PY}} = F_{PY}(\Delta t) = 0.367\ \dot{\theta}\ (\Delta t_\epsilon) = 0.00724\ \dot{\theta}\ \text{lb-sec}$$

where

$$\Delta t_\epsilon = 0.02 \text{ second}$$

and the propellant flow rate for one axis from Eq (BB-1) is

$$W_{P_{PY}} = 0.366 \times 10^{-3} \left(\frac{\dot{\theta}}{I_{sp}}\right) \frac{\text{lb}}{\text{sec}}$$

where

$$\Delta\theta = 0.1 \text{ rad}$$

I_{sp} = specific impulse of the propellant used in the attitude control system

If we assume that a maximum of five orbits is required to assure acquisition of the sun reference and attainment of proper RTG/RB orientation, the total propellant expended for the pitch or yaw axis during this period is

$$W_{P_{PY}} = 9.88 \left(\frac{\dot{\theta}}{I_{sp}}\right) \text{ lb}$$

Propellant consumed in reducing the tumbling rate is based on an impulse bit (steady state) of

$$I_t = F_{PY}\,(\Delta t)$$

where

Δt = 90 seconds

The weight of propellant expended per axis is

$$W_{P_{PY}}' = \frac{I_t}{I_{sp}} = 90\left(\frac{F_{PY}}{I_{sp}}\right) \text{ pitch or yaw axis}$$

Since the attitude control system must counteract the effects of deorbit thrust misalignments, the maximum torque which must be provided by the ACS is:

$$L = F_{rockets}\,(\gamma)\,R' \cong 3 \text{ ft-lb}$$

where

F = total thrust of the deorbit rockets = 3280 lb

γ = angular misalignment = 0.10°

R' = deorbit rocket thrust vector moment arm = 0.5 ft

Torque provided by the ACS should be at least 1-1/2 times the torque generated by the deorbit rocket thrust. Expenditure of propellant per axis during burning of the deorbit rockets is:

$$W_{P_{PY}}'' = \frac{I_t}{I_{sp}} = \frac{F_{PY}\,(\Delta t)'}{I_{sp}} = 3.67\,\frac{\dot{\theta}}{I_{sp}}$$

where

$(\Delta t)'$ = deorbit rocket burning time (10 seconds).

The total weight of propellant consumed during RTG/RB abort is:

$$W_{P_T} = 2\left(W_{P_{PY}}\right) + W_{P_R} + 2\,W_{P_{PY}}' + W_{P_R}' + 2\,W_{P_{PY}}'' + W_{P_R}''$$

The total weight of propellant, W_{P_T}, is plotted against RTG/RB tumbling rate $\dot{\theta}$ (Fig. BB-1), since $\dot{\theta}$ has the greatest effect on propellant weight required. Pressure tanks were assumed to be titanium spheres and the monopropellant tank was assumed to have a minimum thickness of 0.06 inch. Redundant thrustors are utilized for a total of 16 units. Valves and control components for the cold gas and monopropellant systems are one and two pounds, respectively. Table BB-3 provides the detail data for the two systems, and Fig. BB-1 is a graph of system weight as a function of tumbling rate. If a tip-off tumbling rate of 40 rad/sec is assumed, the monopropellant reaction control propulsion system weight is 50 pounds.

4. Control System

The reaction jet control loop for a single axis is given in Fig. BB-4. The rate switch is an on-off device set to the desired limit cycle rate. Its output is analog integrated to provide a signal which commands an increasing pulse repetition rate with time up to the limit of the steady-state on condition for the reaction jet valves. The integrator is reset when the rate switch goes off. A limit cycle condition is thus established wherein minimum pulse rate is generated. Such systems are generally referred to as hysteresis switch control. The sensors illustrated are for the Z_B axis. The sun sensor is used only in the acquisition phase when it is desired to orient the vehicle normal to the sun line. Thereafter its output is switched off, and only the horizon scanner controls attitude about Z_B, with rate limiting provided by the rate switches. The output of the gyro is added to the X_B axis control signal with alternative utilization of the sun sensor signals as backup. The programmer provides control sequencing by gating sensor signals in proper combination for the particular phase of the reentry process. The final despin control is achieved by nulling the X_B axis rate switch. The Y_B axis mechanization is identical to Z_B except for the absence of the gyro.

5. Component Selection

Components must be chosen for availability, high reliability, long shelf life under orbital conditions and resistance to the nuclear and space radiation environments. Typical of components which can meet these requirements is the Barnes Radiometric Balance Horizon Sensor which has sensitive elements composed of arrays of evaporated thermopile detectors and provides accuracy of about one degree with direct digital output. Characteristics of the horizon sensor, together with those of the Ball Brothers coarse eye sun sensors, are given in Table BB-4. The sun sensors are simple bolometer units which may be placed about the periphery of the vehicle. The field for the coarse

TABLE BB-3

Attitude Control System Characteristics

Type of System	Cold Gas	Monopropellant	Cold Gas	Monopropellant	Cold Gas	Monopropellant	Cold Gas	Monopropellant
Tumbling rate (rad/sec)	6.3	6.3	12.6	12.6	25	25	40	40
Specific impulse	70	205	70	205	70	205	70	205
Pitch/yaw thrust total (lb)	2.5	2.5	5	5	10	10	15	15
Roll thrust total (lb)	1.5	1.5	3	3	6	6	10	10
Minimum impulse bit (lb-sec)								
Pitch and yaw	0.05	0.05	0.10	0.10	0.20	0.20	0.30	0.30
Roll	0.03	0.03	0.06	0.06	0.12	0.12	0.20	0.20
Propellant weight (lb)								
Limit cycle (5 orbits)	0.126	0.043	0.50	0.17	2.02	0.69	4.78	1.63
Tumble correction	8.370	2.86	16.74	5.7	33.48	11.40	51.45	17.50
Thrust misalignment correction	0.928	0.316	1.86	0.634	3.71	1.27	5.71	1.95
Total (includes 10% margin)	10.37	3.52	21.00	7.16	43.1	14.7	68.1	73.2
Total impulse (lb-sec)	725	725	1340	1340	2740	2740	4760	4760
Number of thrustors*	16	16	16	16	16	16	16	16
Stored gas weight (lb)	16		32.5		66.5		105	
Tankage volume (cu ft)	1.142	0.065	2.32	0.1325	4.75	0.272	7.5	0.43
Tankage weight (lb)	13.6	0.56	27.5	0.90	56	1.46	89.3	1.98
Pressurant weight (lb)		0.228		0.47		0.94		1.5
Pressure tank volume (cu in.)		28.1		58		116		185
Pressure tank weight (lb)		0.393		0.63		1.07		1.87
Weight of thrustors (lb)	3.0	7.6	4.5	9.4	15.5	11.8	28.0	14.2
Miscellaneous weight (lb)	1.0	2.0	1.0	2.0	1.0	2.0	1.0	2.0
Plumbing weight (lb)	2.0	5.0	2.0	5.0	2.0	5.0	2.0	5.0
Total system weight (lb)	35.6	19.3	67.5	25.6	141	36.9	225.3	49.8
Pulse width (min) (sec)	0.02							
Deorbit thrust (lb)	3300							
Deorbit thrust misalignment (deg)	0.10	Common to analysis						
Misalignment torque (ft-lb)	3.0							
ACS moment arm (ft)	2.0							

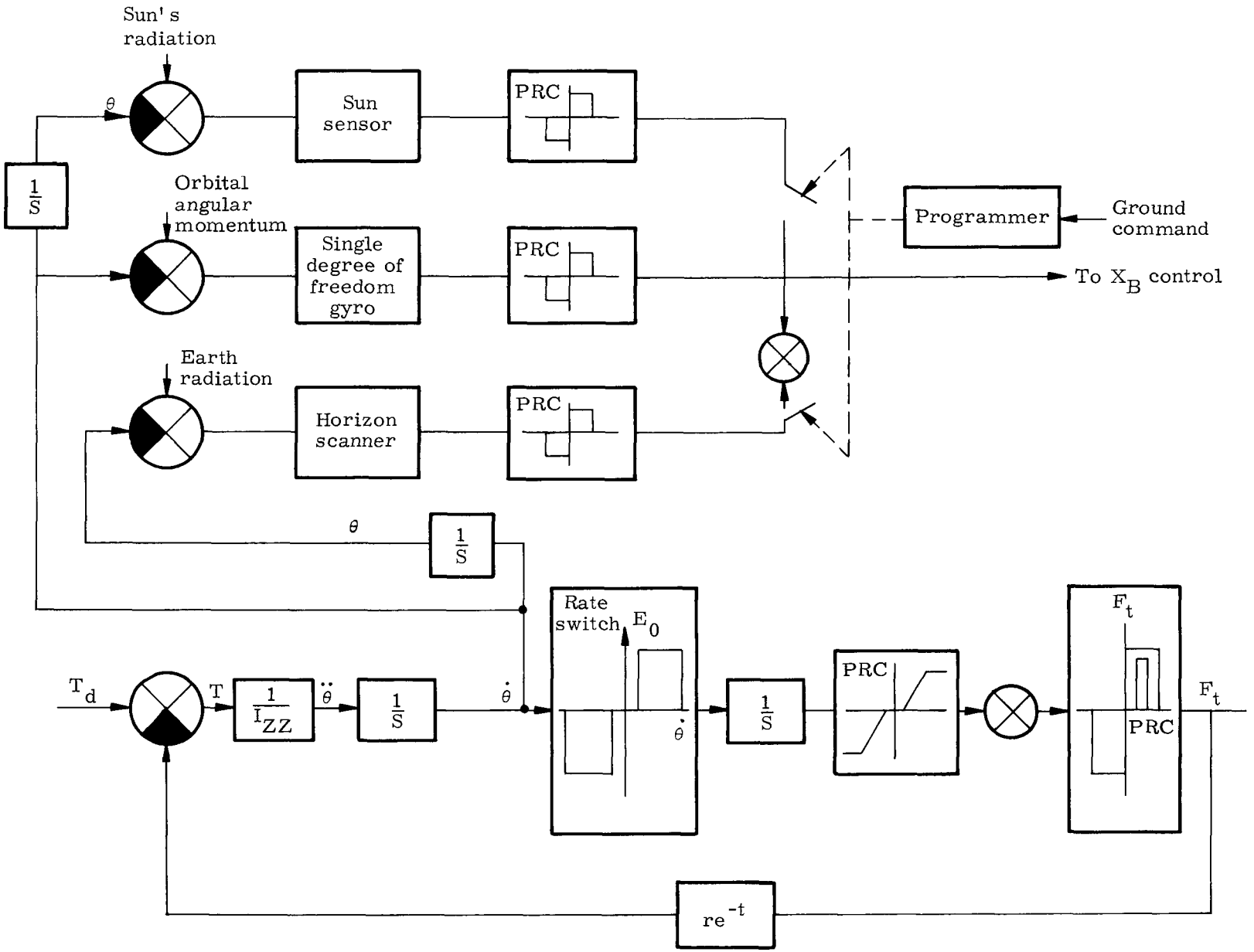

Fig. BB-4. Z_B Axis Control System

TABLE BB-4

Horizon and Sun Sensor Characteristics

	Horizon Sensor	Sun Sensor
Type	Radiometric balance, thermopile array	Bolometer (knife edge) coarse eye
Accuracy	± 1°	± 5°
Reliability	250,000 hr	200,000 hr
Field of view	180° to 100°	± 90°
Power consumption	1.5 watts	1.5
Weight	1 lb	0.8
Volume	22 cu in.	10 cu in.
Company	Barnes	Ball Brothers

eye is 90 degrees and four are sufficient to cover the entire sphere. The signal falls off rapidly at the extremes, however, and more may be required with but small penalty in weight and complexity. These components have been utilized in various planetary probes and are space proven.

Integrating and rate gyro components present the greatest hazard from the reliability point of view. The characteristics of two of these units are given in Table BB-5. They are selected on the basis of resistance to nuclear environment as well as satisfaction of system requirements. In particular, the rate gyro threshold is selected on the basis of the limit cycle rate:

$$\ddot{\theta} = \frac{T}{I_{ZZ}} = \frac{30}{66}\ 0.454\ \text{rad/sec}^2$$

Since the pulse must reverse the motion, the limit cycle will become half of this angular acceleration times the pulse width:

$$\dot{\theta}_2 = \frac{0.454}{2}\ (0.020) = 4.54 \times 10^{-3}\ \text{rad/sec}$$

$$= 0.26\ \text{deg/sec}$$

Since dynamic range is about 100/1 for these units, we expect the gyro to limit at about 26 deg/sec. For the integrating gyro, its drift rate is required to be significantly lower than the orbital rate of

$$\dot{\theta}_0 = \frac{6.28}{90 \times 60} = 1.162 \times 10^{-3}\ \text{rad/sec}$$

TABLE BB-5

Design Goal Performance Specification Values

a. Kearfott Gas Bearing King II Gyro (C70 2590)

	Units	Proposed Specification
Weight	lb	1 (maximum)
Angular momentum at 24,000 rpm	gm-sq cm/sec	$0.350 \times 10^6 \times 4\%$
Gyro gain		12 x 20%
Transfer function	mv/deg input	2500 ± 25%
Pickoff output per degree of float trend (9-volt, 19.2-kc excitation)	mv/deg output	620 ± 10%
Characteristic time	second	Not yet determined
Output axis freedom	degrees	± 2 ± 25%
Operating temperature	°F	154° F nominal
Torquer scale factor	deg/hr/ms	40 ± 5%
Maximum torquing rate	deg/hr	12,000
Torquer linearity to 25°/hr	%	0.01
Motor excitation	3 phase	800 cps, 26 v
Starting power	watts	15 (maximum)
Starting current	millisecond	600 (maximum)
Running power	watts	8 (maximum)
Running current	millisecond	450 (maximum)
Synchronization time	second	25 (maximum)
Vibration		Not yet determined
Shock		Not yet determined
Operating life	hours	40,000 (minimum)
Stops and starts		500 (minimum)
Warmup heater	watts	80 nominal
Maintenance heater	watts	25 nominal
Temperature sensor	ohms	780
Mass unbalance (maximum each axis)	deg/hr/g	0.15
Fixed torque (maximum)	deg/hr	1.0

TABLE BB-5 (continued)

	Units	Proposed Specification
Mass unbalance shift (maximum) spread (based on 5 six position run with CD)	deg/hr/g	0.15 spread 0.05ℓ
Fixed torque spread (maximum)	deg/hr	0.10 spread 0.03ℓ
Random drift vertical (10 hr)	deg/hr	0.001ℓ
Random drift azimuth (10 hr)	deg/hr	0.001ℓ
Maximum anisoelasticity under vibration	deg/hr/g^2	0.02 maximum to 500 cps
Cross axis compliance	deg/hr/g^2	0.01 maximum to 500 cps

b. Nortronics SMT-1 Body Rate Characteristics

Outside dimensions	0.936 ± 0.001-in. dia by 2.015 in. long max
Weight	4.5 oz
Input range	$400^{+40°}_{-0°}$/sec
Sensitivity, full scale	8 volts (20 mv/deg/sec)
Over temperature range	Add + tolerance
Voltage supply variation	Voltage supply variations result in equivalent sensitivity variations; linearity is affected accordingly when voltage varies during test run. (See "Linearity under normal conditions.")
Excitation frequency variation	Sensitivity will vary in direct proportion to excitation frequency variation due to wheel speed change. Effect on pickoff will be negligible if voltage remains constant with choke excitation.
Angular momentum (spin motor)	13,500 gm-cm^2/sec
Gimbal moment of inertia	19 gm-cm^2
Gimbal displacement	1.46 typical

TABLE BB-5 (continued)

Natural frequency range (undamped)	70 ± cps
Damping ratio over operative temperature range	0.6 ± 0.15
Temperature range, operative	+ 40 to + 125° F
Null, AC RMS	25 mv
Zero set (in-phase component)	± 0.5° /sec
Zero drift with temperature (in-phase component)	± 0.4° /sec
Zero drift with vibration (in-phase component)	± 0.3° /sec
Hysteresis	0.1° /sec
Resolution and threshold	0.1° /sec
Linearity under normal conditions	Independent 10%
Linear acceleration sensitivity	0.1° /sec/g
Angular acceleration sensitivity (about OA)	0.08° /sec/rad/sec^2
Spin motor synchronization time	1 sec
Spin motor excitation	26-volt, 800 cps, 2-phase start 13-volt, 800 cps run
Pickoff excitation	20-volt, 800 cps
V_{in}/V_{out} phase angle	15° with 10K secondary load and 800 cps
Environmental Capability Tested	
Vibration	10 g, 20 cps, 2000 cps
Shock	50 g, 1/msec; 250 g 2 msec
General	MIL-E-5272, MIL-T-5400
Radio frequency interference	MIL-I-26600
Storage temperature	-65° F to 160° F
Service life	Instrument is warranted against defects in workmanship and material for 1000 hours of operation or one year, whichever occurs first.

Accuracy of 1° will then require

$$\Delta\theta = 1°, \quad \Delta\theta = \frac{\dot{\theta}_\epsilon}{\dot{\theta}_0}, \quad \dot{\theta}_\epsilon = \frac{1}{57.3}\,(1.162 \times 10^{-3})$$

$$= 2.03 \times 10^{-5} \text{ rad/sec}$$

$$= 4 \text{ deg/hr}$$

This order of accuracy is difficult to achieve after long storage. However, the gyro is backed up by sun sensor information,and stabilization may still be achieved via the rate gyros if their free drift is minimal. Integrating gyros may also be used in place of the rate gyros for stabilization in the event that additional backup is required. The gyros described in Table BB-5 are both proposed for missile systems in which nuclear environment is expected.

Total sensor and electronics requirements are given in Table BB-6. Command communications and the programmer are common to any system for deorbit and hence are not included here. The power supply, however, will require batteries as backup to the RTG which may be inoperative. If we design for 8.5 hours operation (5 orbits plus deorbit time), we will require a capacity of about 467 watt-hour. Nickel-cadmium batteries have been the standard for rechargeable space power systems because of their high cycle life. However, they cannot be stored easily in an inactivated condition. Silver/zinc batteries have a very low cycle life but may be stored in charged condition and provide a power-to-weight ratio of 80 watt-hr/lb at an eight-hour discharge rate. For a one-shot operation such as we have, the Ag/Zn battery is a natural selection; these batteries are supplied by Eagle-Picher. The weight of the activation system must also be included as well as relaying and control circuitry.

Reaction jet systems are highly reliable except for the failure mode in which valves may stick in the "on" position, depleting the fuel supply. Reliability may be assured by programmer controlled shutoff valves which limit the time that an "on" signal may be present.

6. Summary

This analysis was undertaken to determine the cost of independent attitude control and stabilization for the RB. Environmental considerations, safety and the as yet uncertain sequence of operations were used to size a complete control system. The results are summarized in Table BB-6 which shows a total weight of 91.7 pounds attributable to independent attitude control. It is possible to depend on the host vehicle for these functions and impose the cost of safety on the vehicle manufacturer. The system design given is quite capable of space operation with the RTG operational and the vehicle tumbling for an indefinite period of time. This may be advantageous if independent orbital test is part of the development program.

TABLE BB-6

Attitude Stabilization and Control System Characteristics

Item	Quantity	Weight Each (lb)	Power (watts, avg)	Reliability (MTBF in hr)	Weight (lb)	Volume
Sun sensor	4	0.8	1.5	200,000	3.2	10 cu in.
Horizon sensor	2	1.0	1.5	250,000	2.0	22.0 cu in.
Rate gyro	3	0.5	12	10,000	1.5	10.0 cu in.
Integrating gyro	1	3.0	10	10,000	3.0	23 cu in.
Control electronics	2	10.0	20	20,000	10.0	300 cu in.
Propellant, tankage, valves, nozzles	1		10	20,000	50.0	2.0 cu ft
			55		69.7	2.21 cu ft
Power supply	1				22.0	1.0 cu ft
(55 watts at 90% for 8.5 hours)					91.7	3.21 cu ft

APPENDIX CC

SIX-DEGREE-OF-FREEDOM STABILITY PROGRAM

The Six-Degree-of-Freedom Stability Program is designed for the investigation of detailed motion of spinning and thrusting bodies with variable masses and inertias. The bodies may be acted upon by aerodynamic forces, and control forces may be added if required. The program is written for the IBM 1130 computer in FORTRAN IV programming language. Requirement for the capability of handling high spin rates has led to the use of integrating algorithms rather than simply the standard Runge-Kutta or other integration schemes for the inertial matrix. Therefore, some loss in accuracy is to be expected, but capability for obtaining amplitude and frequency of spin and precessional motion at reasonable computation times has been achieved.

Presented in the following sections are the program philosophy, problems for which it is intended, and a summary of the derivations of the equations mechanized with more detailed sources referenced. The program has been applied to the determination of separation and spin dynamics of the Controlled Intact Reentry (CIR) system under various trajectory conditions representative of Titan III launch trajectories.

A. PROGRAM PHILOSOPHY

Most six-degree-of-freedom programs are complex systems with many options and differing input formats. We have attempted here to write a simple program with matrix operations, such that those functions not required may simply be removed from execution by modification of the executive program. The program was mechanized for the IBM 1130 primarily because machine time for a larger computer was not available and because of its experimental nature.

Programming philosophy with regard to mechanization of the equations of motion is that force magnitudes will change less rapidly than their resolution into body axes of a spinning or tumbling vehicle. Hence, external forces (gravity, aerodynamic) are transformed into body axes once per computation cycle. Thrust forces are similarly evaluated once per cycle and the summation of forces is integrated in body axes. The body axes to inertial space transformation matrix is updated by a DDA-type algorithm eight times per cycle, however, and inertial velocities are transformed from body axes to inertial space via this matrix. This technique permits small angular steps and, actually, the number of times per cycle of matrix updating may be varied to ensure validity of the small angle approximation. The integration interval must be only small enough to prevent rapid change in the forces.

Mass and inertia properties are calculated once per cycle and their rate effects are included in the equations of motion. Provision is also made for inclusion of jet damping (the damping moment generated within a rocket chamber under constant angular rate). These effects become appreciable in deorbit of small vehicles having as much as 50% of their mass in expendable fuel.

The program includes both an atmosphere and calculation of arguments for the usual aerodynamic forces. This process is made difficult in that all angles may go through 0 to 2π and because no unique inverse of the standard Euler angle transformation is possible unless the quadrant of at least one angle is known. For this purpose, we establish the roll angle about the body axes with respect to the horizontal and compute angle-of-attack and sideslip angle as a function of relative velocities in body axes and the roll. Though ambiguities remain (i.e., $\alpha = 180°$), they are transient and, in any case, do not affect the essential integration.

Finally, the program is pointed to design analysis of separation, spin stabilization and deorbit. For this reason, we calculate relative trajectory parameters as well as inertial quantities useful for impact dispersion studies with point mass trajectory programs. The origin of the inertial coordinates is placed at the initial vehicle position so that roundoff due to large numbers will not affect separation time histories.

B. PROBLEMS FOR APPLICATION

The reference configuration for the present problem (Fig. CC-1) includes a blunted cone with an equipment module attached including four solid deorbit rockets about the periphery. The vehicle is attached to a spin bearing which rides in a track. Separation is effected by a separation motor while the vehicle is simultaneously spun up by peripherally mounted spin rockets. The problem to be solved is the spin rate necessary to stabilize the deorbit thrust vector and determination of the motion after burnout. This motion will represent inertial conditions for atmospheric reentry. At this point the vehicle is required to aerodynamically stabilize itself to present its ablative shield to the air stream. Aerodynamic moments generated by the clipped section of the cone must be sufficiently large for this purpose and we would like to determine a feasible design. Thus, we would expect to produce requirements for spin rockets, deorbit propulsion alignment and aerodynamic design.

Other problems to which the program may be applied are:

(1) Short term stability of aircraft and lifting body vehicles.

(2) Evaluation of kinematic effects on inertial guidance systems of the strapped down configuration.

(3) Separation problems, including those of ejection seats such as the P6M.

C. SUMMARY OF EQUATIONS OF MOTION COORDINATE SYSTEMS AND TRANSFORMATIONS

1. Earth Centered Inertial

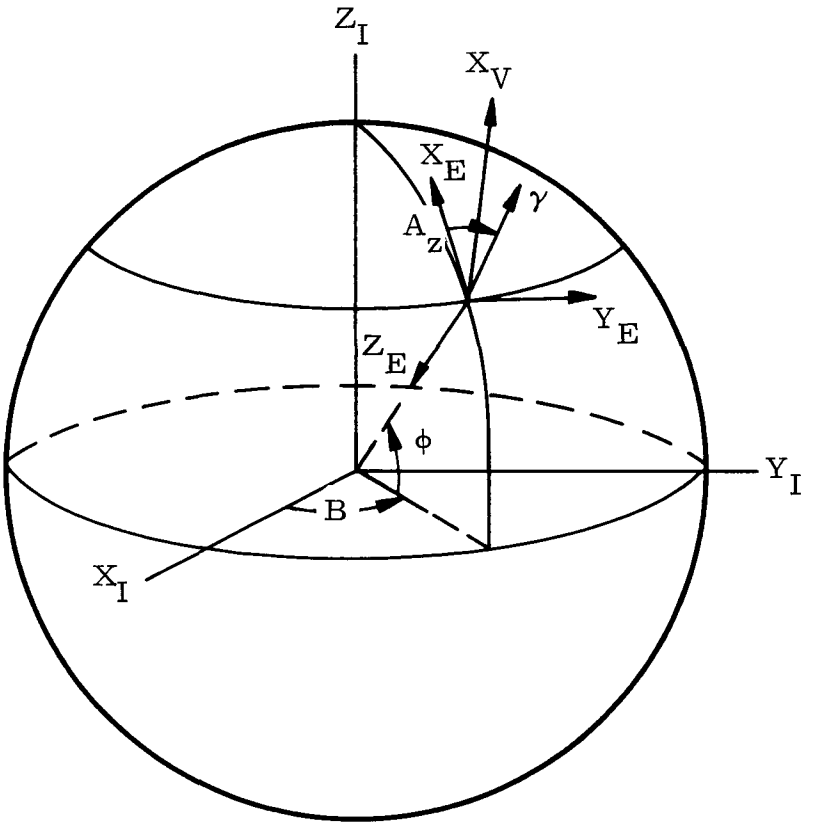

X_I, Y_I, Z_I ⟷ ECI

X_E, Y_E, Z_E ⟷ earth fixed at vehicle, EVR

$B = \lambda_v + w_e t$

λ_v = vehicle longitude

w_e = earth rate

t = elapsed time

ϕ = geocentric latitude

TEI ≙ Transformation from Earth Fixed to Inertial

$$\underset{\text{TEI}}{\begin{vmatrix} X_I \\ Y_I \\ Z_I \end{vmatrix}} = \begin{vmatrix} -S\phi CB & -SB & -C\phi CB \\ -S\phi SB & CB & -C\phi SB \\ C\phi & 0 & -S\phi \end{vmatrix} \begin{vmatrix} X_E \\ Y_E \\ Z_E \end{vmatrix}$$

TIE

$$\begin{vmatrix} X_E \\ Y_E \\ Z_E \end{vmatrix} = \begin{vmatrix} -S\phi CB & -S\phi SB & C\phi \\ -SB & CB & 0 \\ -C\phi CB & -C\phi SB & -S\phi \end{vmatrix} \begin{vmatrix} X_I \\ Y_I \\ Z_I \end{vmatrix}$$

2. Vehicle Centered, Velocity Oriented

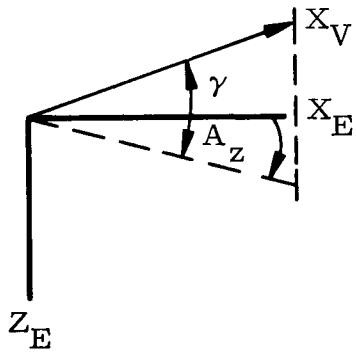

Az $\triangleq$ azimuth from north of vehicle velocity vector projection in tangent plane to sphere at subvehicle point.

γ $\triangleq$ flight path angle between velocity vector and its projection in tangent plane.

TEV

$$\begin{vmatrix} X_V \\ Y_V \\ Z_V \end{vmatrix} = \begin{vmatrix} C\gamma CAz & C\gamma SAz & -S\gamma \\ -SAz & CAz & 0 \\ S\gamma CAz & S\gamma SAz & C\gamma \end{vmatrix} \begin{vmatrix} X_E \\ Y_E \\ Z_E \end{vmatrix}$$

TVE

$$\begin{vmatrix} X_E \\ Y_E \\ Z_E \end{vmatrix} = \begin{vmatrix} C\gamma CAz & -SAz & S\gamma CAz \\ C\gamma SAz & CAz & S\gamma SAz \\ -S\gamma & 0 & C\gamma \end{vmatrix} \begin{vmatrix} X_V \\ Y_V \\ Z_V \end{vmatrix}$$

3. Transform from Body Axes to Relative Velocity Axes

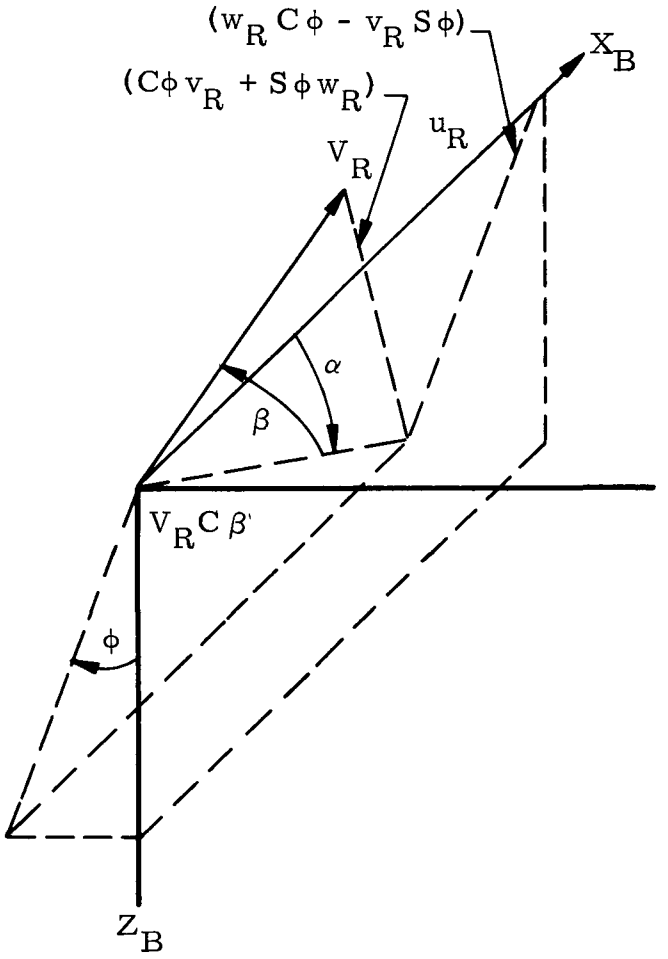

Order ϕ, α, β

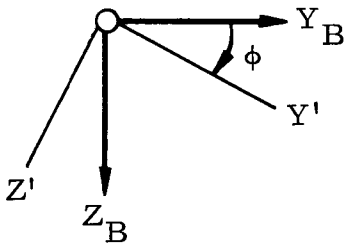

$$\begin{vmatrix} X' \\ Y' \\ Z' \end{vmatrix} = \begin{vmatrix} 1 & 0 & 0 \\ 0 & C\phi & S\phi \\ 0 & -S\phi & C\phi \end{vmatrix} \begin{vmatrix} X_B \\ Y_B \\ Z_B \end{vmatrix}$$

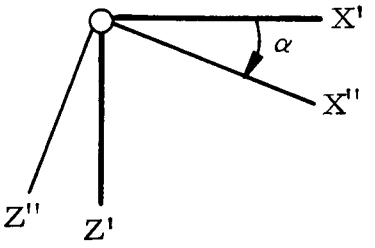

$$\begin{vmatrix} X'' \\ Y'' \\ Z'' \end{vmatrix} = \begin{vmatrix} C\alpha & 0 & S\alpha \\ 0 & 1 & 0 \\ -S\alpha & 0 & C\alpha \end{vmatrix} \begin{vmatrix} X' \\ Y' \\ Z' \end{vmatrix}$$

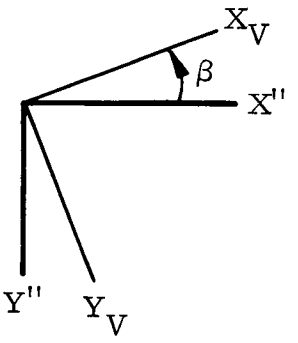

$$\begin{vmatrix} X_V \\ Y_V \\ Z_V \end{vmatrix} = \begin{vmatrix} C\beta & -S\beta & 0 \\ S\beta & C\beta & 0 \\ 0 & 0 & 1 \end{vmatrix} \begin{vmatrix} X'' \\ Y'' \\ Z'' \end{vmatrix}$$

TBV

$$\begin{vmatrix} X_V \\ Y_V \\ Z_V \end{vmatrix} = \begin{vmatrix} C\beta C\alpha & -(C\beta S\alpha S\phi + S\beta C\phi) & (C\beta S\alpha C\phi - S\beta S\phi) \\ S\beta C\alpha & (-S\beta S\alpha S\phi + C\beta C\phi) & (S\beta S\alpha C\phi + C\beta S\phi) \\ -S\alpha & -C\alpha S\phi & C\alpha C\phi \end{vmatrix} \begin{vmatrix} X_B \\ Y_B \\ Z_B \end{vmatrix}$$

4. Solution of TBV for $\alpha(\phi)$, $\beta(\phi)$

TVB

$$\begin{vmatrix} u_R \\ v_R \\ w_r \end{vmatrix} = \begin{vmatrix} C\beta C\alpha & S\beta C\alpha & -S\alpha \\ -(C\beta S\alpha S\phi + S\beta C\phi) & (-S\beta S\alpha S\phi + C\beta C\phi) & -C\alpha S\phi \\ (C\beta S\alpha C\phi - S\beta S\phi) & (S\beta S\alpha C\phi + C\beta S\phi) & C\alpha C\phi \end{vmatrix} \begin{vmatrix} V_R \\ 0 \\ 0 \end{vmatrix}$$

$$u_R = C\beta C\alpha V_R$$

$$v_R = -(C\beta S\alpha S\phi + S\beta C\phi) V_R \rightarrow S\beta C\phi + C\beta S\alpha S\phi = -v_R / V_R$$

$$w_R = (C\beta S\alpha C\phi - S\beta S\phi) V_R \rightarrow S\beta S\phi - C\beta S\alpha C\phi = -w_R / V_R$$

The last two equations give

$$S\alpha = \frac{w_R C\phi - v_R S\phi}{V_R C\beta}$$

or, from the diagram,

$$S\alpha = \frac{w_R C\phi - v_R S\phi}{\left[u_R^2 + (w_R C\phi - v_R S\phi)^2\right]^{1/2}}$$

$$C\alpha = \frac{u_R}{\left[u_R^2 + (w_R C\phi - v_R S\phi^2\right]^{1/2}}$$

Using the first two equations of TBV

$$V_R = C\beta C\alpha u_R - (C\beta S\alpha S\phi + S\beta C\phi)\, v_R + (C\beta S\alpha C\phi - S\beta S\phi)\, w_R$$

$$0 = S\beta C\alpha u_R + (-S\beta S\alpha S\phi + C\beta C\phi)\, v_R + (S\beta S\alpha C\phi + C\beta S\phi)\, w_R$$

Multiplying these equations by $S\beta$ and $C\beta$, and subtracting,

$$S\beta = \frac{-(C\phi v_R + S\phi w_R)}{V_R}$$

Then,

$$C\beta = \frac{u_R C\alpha}{V_R}$$

These equations give sines and cosines of the angles unambiguously and, hence, permit definition of the proper quadrant. They are used in determination of the aerodynamic forces with an arbitrarily defined roll angle.

5. Initialization

Present initialization is based on the following input variables.

h = altitude

V_R = relative velocity

γ = relative flight path angle

ψ = relative azimuth

ϕ_L = geocentric latitude

λ_L = longitude w/r Greenwich

α = angle of attack

β = sideslip angle

ϕ = roll angle

p, q, r = initial body rates.

The initialization procedure computes

$$X_I,\ Y_I,\ Z_I,\ \dot{X}_I,\ \dot{Y}_I,\ \dot{Z}_I$$

and sets up the initial matrices:

TEI (ϕ_L, β)

TVE (γ, ψ)

TBV (α, β, ϕ)

These matrices are multiplied to obtain the initial transformation (TBI) from body to inertial axes:

TBI = (TEI) (TVE) (TBV)

Initial values of u, v, w (components of inertial velocity in body axes) are found by transforming V_R to inertial axes and then through TIB = $(TBI)^{-1}$ to body axes.

$$\begin{vmatrix} \dot{X}_I \\ \dot{Y}_I \\ \dot{Z}_I \end{vmatrix} = (TEI)\,(TVE) \begin{vmatrix} V_R \\ 0 \\ 0 \end{vmatrix}$$

$$\begin{vmatrix} u \\ v \\ w \end{vmatrix} = (TIB) \begin{vmatrix} \dot{X}_I \\ \dot{Y}_I \\ \dot{Z}_I \end{vmatrix}$$

Inertial coordinates are found from the radius vector: R = Re + h

$$\begin{vmatrix} X_I \\ Y_I \\ Z_I \end{vmatrix} = (TEI) \begin{vmatrix} 0 \\ 0 \\ -R \end{vmatrix}$$

6. Thrust Characteristics

Thrust characteristics are computed as follows:

BEGAN

(1) Read thrust table for five thrustors:

Time, T(1), T(2), T(3), T(4), T(5)

(2) Read error in thrust level (%), nozzle exit area (sq in.), specific impulse.

EPSTH(J), J = 1, 5
HEXIT(J), J = 1, 5
SPIMP(J), J = 1, 5

(3) Read thrust alignment matrix (TABA (I, J))
Read thrust alignment matrix (TABB (I, J))
The thrust alignment matrices become

TMK (I, J) = TABA (I, J) XTABB (I, J), K = 1, 5

These matrices are retained in common for use in determining thrust forces.

THMAS

(4) For each thrustor, the thrust force FTHRUS (J), J = 1, 5 is derived from the thrust table as a function of time. This nominal thrust (vacuum) is modified by the atmospheric back pressure:

FTHRUS (J) = TVAC - APRES * AEXIT

where AEXIT is the nozzle exit area. FTHRUS (J), J = 1, 5 is retained in common.

FØRMØ

(5) Each thrust vector is multiplied by its alignment matrix and the results are summed to obtain total force along body axes.

(6) Components of each thrust vector are multiplied by their displacement component about center of gravity reference axes and summed to obtain torques about center of gravity reference axes.

7. Mass Properties

The program allows for five variable masses and 25 fixed masses. The sequence of computation of center of gravity and inertias is:

BEGAN

(1) Read mass table consisting of mass, m_i and reference axes coordinates $X_R Y_R Z_R$

m_i, X_{Ri}, Y_{Ri}, Z_{Ri}

(2) Compute CGREF (reference center of mass)

$$CGREF\ (J) = \Sigma \frac{m_i\ X\ (j)}{m}$$

(3) Compute CGFR (reference center of mass for fixed masses)

(4) Compute moments of inertia about reference axes:

$$I_{xx} = \int (y^2 + Z^2)\ dm \cong \Sigma\ (y_i^2 + Z_i^2)\ m_i$$

$$I_{yy} \cong \Sigma\ (Z_i^2 + X_i^2)\ m_i$$

$$I_{ZZ} \cong \Sigma\ (X_i^2 + y_i^2)\ m_i$$

$$I_{xy} = I_{yx} = \Sigma\ X_i y_i m_i$$

$$I_{yZ} = I_{Zy} = \Sigma\ y_i Z_i m_i$$

$$I_{Zx} = I_{xZ} = \Sigma\ X_i Z_i m_i$$

(5) Compute moments of inertia about reference axes for fixed masses only (as in (4)).

THMAS

(6) We have the sum of fixed masses and the fixed mass moments of inertia. The thrust and mass flow are computed as a function of time for the variable masses. Compute the center of gravity of variable mass as in (3).

(7) Compute variable inertia about reference axes as in (4).

(8) Sum fixed and variable inertias about reference axes.

(9) Transform total inertia to center of gravity reference using parallel axes theorem:

$$I_{xx}\Big]_{CG} = I_{xx}\Big]_{ref} - \Sigma\,(\Delta Y_{CG}^2 + \Delta Z_{CG}^2)\, m_i$$

At this point we have XIN (i, j), a 3 x 3 inertia matrix representing the time varying inertia as a function of thrust time history. We compute the rate of change of XIN (i, j) by saving back values, subtracting from the current value and dividing by the time interval.

8. Equations of Motion

a. Force equations

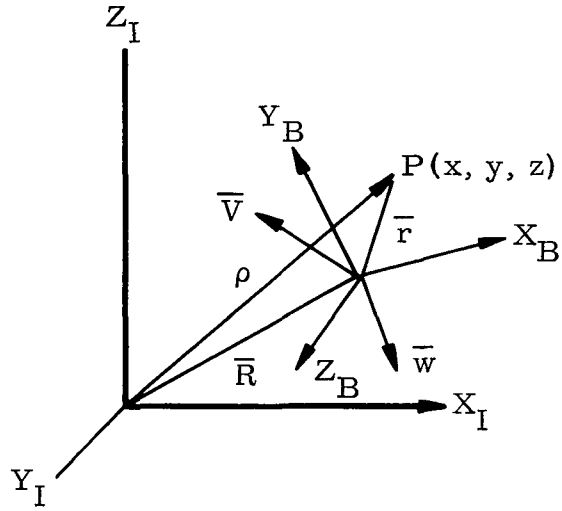

$$\overline{F} = \frac{d}{dt}(m\overline{V})$$

$$\overline{M} = \frac{d}{dt}(\overline{H})$$

$$\overline{r} = x\overline{X}_{Bu} + y\overline{Y}_{Bu} + z\,Z_{Bu}$$

$$\overline{R} = X\overline{X}_{Iu} + Y\overline{Y}_{Iu} + ZZ_{Iu}$$

$$\overline{w} = w_x\overline{X}_{Bu} + w_y\overline{Y}_{Bu} + w_z\overline{Z}_{Bu}$$

where u → unit vector

The total velocity of P is given by:

$$\dot{\bar{\rho}} = \dot{\bar{R}} + \dot{\bar{r}} = \dot{X}\bar{X}_{Iu} + \dot{Y}\bar{Y}_{Iu} + \dot{Z}\bar{Z}_{Iu}$$
$$+ (\dot{x}_P - y_P w_z + z_P w_y)\,\bar{X}_{Bu}$$
$$+ (\dot{y}_P + x_P w_z - z_P w_x)\,\bar{Y}_{Bu}$$
$$+ (\dot{z}_P - x_P w_y + y_P w_x)\,\bar{Z}_{Bu}$$

Writing $\dot{\bar{R}} = \bar{V}$ in body coordinates,

$$\dot{\bar{R}} = \dot{X}\bar{X}_{Iu} + \dot{Y}\bar{Y}_{Iu} + \dot{Z}\bar{Z}_{Iu} = \dot{x}_0\bar{X}_{Bu} + \dot{y}_0\bar{Y}_{Bu} + \dot{y}_0\bar{Z}_{Bu}$$

where x_0, y_0, z_0 represent velocity of the origin.

$$\dot{\bar{\rho}} = (\dot{x}_i + \dot{x}_P - y_P w_z + z_P w_y)\,\bar{X}_{Bu}$$
$$+ (\dot{y}_0 + \dot{y}_P + x_P w_z - z_P w_x)\,\bar{Y}_{Bu}$$
$$+ (\dot{z}_0 + \dot{z}_P - x_P w_y + y_P w_x)\,\bar{Z}_{Bu}$$

Differentiating,

$$\ddot{\bar{\rho}} = (\ddot{x}_0 - \dot{y}_0 w_z + \dot{z}_0 w_y)\,\bar{X}_{Bu}$$
$$+ (\ddot{y}_0 + \dot{x}_0 w_z - \dot{z}_0 w_x)\,\bar{Y}_{Bu}$$
$$+ (\ddot{z}_0 - \dot{x}_0 w_y + \dot{y}_0 w_x)\,Z_{Bu}$$
$$+\left[\ddot{x}_P - 2\dot{y}_P + 2\dot{z}_P - x_P(w_Z^2 + w_y^2) + y_P(w_x w_y - \dot{w}_z + z_P(\dot{w}_y + w_x w_z)\right]\bar{X}_{Bu}$$
$$+\left[\ddot{y}_P + 2\dot{x}_P w_z - 2\dot{z}_P w_x - y_P(w_x^2 + w_z^2) + z_P(w_x w_y - \dot{w}_z) + z_P(\dot{w}_y + w_x w_z)\right]\bar{Y}_{Bu}$$
$$+\left[\ddot{z}_P + 2\dot{x}_P w_y + 2\dot{z}_P w_x - z_P(w_y^2 + w_x^2) + x_P(w_Z w_x - \dot{w}_y) + y_P(\dot{w}_x + w_y w_z)\right]\bar{Z}_{Bu}$$

Then, if P (x_P, y_P, z_P) is the center of gravity, assume

$$x_P = z_P = 0,\ \dot{y}_P = \dot{z}_P = \ddot{y}_P = \ddot{z}_P = 0$$

i.e., the CG travel is restricted to X_B. Change notation:

$$\dot{x}_0 = u \qquad w_x = p$$

$$\dot{y}_0 = v \qquad w_y = q$$

$$\dot{z}_0 = w \qquad w_z = r$$

$$F_x = m\left[\dot{u} - vr + wq + \ddot{x}_P = x_P (r^2 + q^2)\right]$$

$$F_y = m\left[\dot{v} + ur - wp + 2\dot{x}_P r + x_P (\dot{r} + pq)\right]$$

$$F_z = m\left[\dot{w} - uq + vp - 2\dot{x}_P q + x_P (rp - \dot{q})\right]$$

Then if the center of gravity is made the reference point and we may assume its velocity and acceleration to be negligible, the matrix form of the force equations becomes:

$$\begin{vmatrix} F_x \\ F_y \\ F_z \end{vmatrix} = m \left| \begin{vmatrix} \dot{u} \\ \dot{v} \\ \dot{w} \end{vmatrix} + \begin{vmatrix} 0 & -r & q \\ r & 0 & -p \\ -q & p & 0 \end{vmatrix} \begin{vmatrix} u \\ v \\ w \end{vmatrix} \right|$$

The momentum exchange of the thrusting body with the expelled gas is given by the term

$$\bar{F} = \frac{dm}{dt}\,\bar{C}$$

where $\bar{C}$ is the relative velocity between gas and vehicle. This term is included in external forces. The jet damping contributions due to reaction of the gas velocity vector with chamber walls become

$$F_{yj} = -2\dot{m}r\ell_y$$

$$F_{zj} = 2\dot{m}q\ell_z$$

where ℓ_y and ℓ_z are moment arms of the thrustors.

$$\begin{vmatrix} F_x \\ F_y \\ F_z \end{vmatrix} = m \left| \begin{vmatrix} \dot{u} \\ \dot{v} \\ \dot{w} \end{vmatrix} + \begin{vmatrix} 0 & -r & q \\ r & 0 & -p \\ -q & p & 0 \end{vmatrix} \begin{vmatrix} u \\ v \\ w \end{vmatrix} \right| + \begin{vmatrix} o \\ -2\dot{m}r\ell_y \\ 2\dot{m}q\ell_y \end{vmatrix} \qquad \text{(CC-1)}$$

(b) Moment equations

$$\overline{H} = |I| \overline{w}$$

$$\begin{aligned}\overline{H} = &(I_{XX}p - I_{xy}q - I_{xz}r)\,\overline{X}_{Bu} \\ &+ (-I_{xy}p + I_{yy}q - I_{yz}r)\,\overline{Y}_{Bu} \\ &+ (-I_{xz}p - I_{yz}q + I_{zz}r)\,\overline{Z}_{Bu}\end{aligned}$$

Differentiating,

$$\begin{aligned}\dot{\overline{H}} = &\Big[I_{xx}\dot{p} + \dot{I}_{xx}p + (I_{zz} - I_{yy})\,qr - I_{yz}\,(q^2 - r^2) \\ &- I_{xz}\,(\dot{r} + pq) - I_{xy}\,(\dot{q} - pr) - \dot{I}_{xz}r - \dot{I}_{xy}q\Big]\,\overline{X}_{Bu} \\ &+ \Big[I_{yy}\dot{q} + \dot{I}_{yy}q + (I_{xx} - I_{zz})\,pr - I_{xz}\,(r^2 - p^2) \\ &- I_{xy}\,(\dot{p} + qr) - I_{yz}\,(\dot{r} - pq) - \dot{I}_{xy}p - \dot{I}_{yz}r\Big]\,\overline{Y}_{Bu} \\ &+ \Big[I_{zz}\dot{r} + \dot{I}_{zz}r + (I_{yy} - I_{xx})\,pq - I_{xy}\,(p^2 - q^2) \\ &- I_{yz}\,(\dot{q} + pr) - I_{xz}\,(\dot{p} - qr) - \dot{I}_{xz}p - \dot{I}_{yz}q\Big]\,\overline{X}_{Bu}\end{aligned}$$

The jet damping contribution is:

$$\Delta M_J = - p\dot{m}\ell_\ell^2\,\overline{X}_{Bu} - q\dot{m}\ell_m^2\,\overline{Y}_{Bu} - r\dot{m}\ell_n^2\,\overline{Z}_{Bu}$$

The matrix form of the moment equations is:

$$\begin{vmatrix} L \\ M \\ N \end{vmatrix} = \begin{vmatrix} I_{xx} & -I_{xy} & -I_{xz} \\ -I_{yx} & I_{yy} & -I_{yz} \\ -I_{zx} & -I_{yz} & I_{zz} \end{vmatrix} \begin{vmatrix} \dot{p} \\ \dot{q} \\ \dot{r} \end{vmatrix} + \begin{vmatrix} \dot{I}_{xx} - \dot{m}\ell_\ell^2 & -\dot{I}_{xy} & -\dot{I}_{xz} \\ -\dot{I}_{yx} & \dot{I}_{yy} - \dot{m}\ell_m^2 & -\dot{I}_{yz} \\ -\dot{I}_{zx} & -\dot{I}_{zy} & \dot{I}_{zz} - \dot{m}\ell_n^2 \end{vmatrix} \begin{vmatrix} p \\ q \\ r \end{vmatrix}$$

$$+ \begin{vmatrix} 0 & -r & q \\ r & 0 & -p \\ -q & p & 0 \end{vmatrix} \begin{vmatrix} I_{xx} & -I_{xy} & -I_{xz} \\ -I_{yx} & I_{yy} & -I_{yz} \\ -I_{xz} & -I_{yz} & I_{zz} \end{vmatrix} \begin{vmatrix} p \\ q \\ r \end{vmatrix} \qquad \text{(CC-2)}$$

Equations (CC-1) and (CC-2) are mechanized in XINTF. They are integrated to produce u, v, w, p, q, r.

9. Direction Cosine Equations

The matrix TBI is given by

$$TBI = (TEI)(TVE)(TBV) = \begin{vmatrix} \ell_1 & \ell_2 & \ell_3 \\ m_1 & m_2 & m_3 \\ n_1 & n_2 & n_3 \end{vmatrix}$$

Then,

$$\begin{vmatrix} X_B \\ Y_B \\ Z_B \end{vmatrix} = \begin{vmatrix} \ell_1 & m_1 & n_1 \\ \ell_2 & m_2 & n_2 \\ \ell_3 & m_3 & n_3 \end{vmatrix} \begin{vmatrix} X_I \\ Y_I \\ Z_I \end{vmatrix}$$

Differentiating the unit vectors (X_{Bu}),

$$\begin{vmatrix} \dot{X}_{Bu} \\ \dot{Y}_{Bu} \\ \dot{X}_{Bu} \end{vmatrix} = \begin{vmatrix} \dot{\ell}_1 & \dot{m}_1 & \dot{n}_1 \\ \dot{\ell}_2 & \dot{m}_2 & \dot{n}_2 \\ \dot{\ell}_3 & \dot{m}_3 & \dot{n}_3 \end{vmatrix} \begin{vmatrix} X_{Iu} \\ Y_{Iu} \\ Z_{Iu} \end{vmatrix} = \begin{vmatrix} p \\ q \\ r \end{vmatrix} \times \begin{vmatrix} X_{Bu} \\ Y_{Bu} \\ Z_{Bu} \end{vmatrix}$$

The cross product of the last expression arises from the fact that the unit vectors change by rotation only and only the $\bar{w} \times \bar{r}$ terms remain. As a result, we have

$$\dot{X}_{Bu} = rY_{Bu} - qZ_{Bu}$$

$$\dot{Y}_{Bu} = pZ_{Bu} - rX_{Bu}$$

$$\dot{Z}_{Bu} = qX_{Bu} - pY_{Bu}$$

$$\bar{w} = pX_{Bu} + qY_{Bu} + rZ_{Bu}$$

Then,

$$\begin{aligned}\dot{X}_{Bu} &= \dot{\ell}_1 X_{Iu} + \dot{m}_1 Y_{Iu} + \dot{n}_1 Z_{Iu} \\ &= r\left[\ell_2 X_{Iu} + m_2 Y_{Iu} + n_2 Z_{Iu}\right] \\ &\quad -q\left[\ell_3 X_{Iu} + m_3 Y_{Iu} + n_3 Z_{Iu}\right]\end{aligned}$$

Equating components along each axis,

$$\dot{\ell}_1 = r\ell_2 - q\ell_3$$

$$\dot{m}_1 = rm_2 - qm_3$$

$$\dot{n}_1 = rn_2 - qn_3$$

Applying this process to $\dot{Y}_{Bu}$ and $\dot{Z}_{Bu}$, we obtain nine differential equations for the time rate of change of the direction cosines (elements of TBI):

$$\begin{aligned}\dot{\ell}_1 &= r\ell_2 - q\ell_3 \\ \dot{\ell}_2 &= p\ell_3 - r\ell_1 \\ \dot{\ell}_3 &= q\ell_1 - p\ell_2 \\ \dot{m}_1 &= rm_2 - qm_3 \\ \dot{m}_2 &= pm_3 - rm_1 \\ \dot{m}_3 &= qm_1 - pm_2 \\ \dot{n}_1 &= rn_2 - qn_3 \\ \dot{n}_2 &= pn_3 - rn_1 \\ \dot{n}_3 &= qn_1 - pn_2\end{aligned}$$

and fully written out,

$$\dot{TBI} = \begin{vmatrix} r\ell_2 - q\ell_3 & p\ell_3 - r\ell_1 & q\ell_1 - p\ell_2 \\ rm_2 - qm_3 & pm_3 - rm_1 & qm_1 - pm_2 \\ rn_2 - qn_3 & pn_3 - rn_1 & qn_1 - pn_2 \end{vmatrix}$$

The off-diagonal terms of this set depend on both off-diagonal cosines and diagonal cosines while diagonal terms depend only on off-diagonal cosines. The integration procedure is as follows:

Assume the off-diagonal terms will change more slowly than the diagonal and they are updated first. This enables current updating of diagonal elements directly without repetitive iteration. Thus,

$$(\Delta \ell_2)_n = \left[p\,(\ell_3)_{n-1} - r\,(\ell_1)_{n-1}\right]\Delta t$$

$$(\Delta \ell_3)_n = \left[q\,(\ell_1)_{n-1} - p\,(\ell_2)_{n-1}\right]\Delta t$$

$$(\Delta m_1) = \left[r\,(m_2)_{n-1} - q\,(m_3)_{n-1}\right]\Delta t$$

$$(\Delta m_3)_n = \left[q\,(m_1)_{n-1} - p\,(m_2)_{n-1}\right]\Delta t$$

$$(\Delta n_1)_n = \left[r(n_2)_{n-1} - q\,(n_3)_{n-1}\right]\Delta t$$

$$(\Delta n_2)_n = \left[p(n_3)_{n-1} - r\,(n_1)_{n-1}\right]\Delta t$$

We now update the off-diagonal elements

$$(\ell_i)_n = (\ell_i)_{n-1} + (\Delta \ell_i)_n\,,\quad i = 2,\ 3$$

$$(m_i)_n = (m_i)_{n-1} + (\Delta m_i)_n\,,\quad i = 1,\ 3$$

$$(n_i)_n = (n_i)_{n-1} + (\Delta n_i)_n,\quad i = 1,\ 2$$

It is now possible to compute the changes in diagonal elements with updated off-diagonal terms:

$$(\Delta \ell_1)_n = r\,(\ell_2)_n - q\,(\ell_3)_n$$

$$(\Delta m_2)_n = p\,(m_3)_n - r\,(m_1)_n$$

$$(\Delta n_3)_n = q\,(n_1)_n - p\,(n_2)_n$$

The diagonal terms are then updated as for the off-diagonals and the updated matrix is complete. This process has demonstrated an error of 0.03% after nine seconds when subjected to sinusoids at one radian per second with integration interval not permitted to exceed small angle increments, i.e., $(\Delta\theta/\text{interval}) \leq 5°$. The matrix is updated eight times per integration interval of the main program, each time being orthogonalized as follows.

Let the updated matrix be given by:

$$A_C = \begin{vmatrix} \ell_{1C} & m_{1C} & n_{1C} \\ \ell_{2C} & m_{2C} & n_{2C} \\ \ell_{3C} & m_{3C} & n_{3C} \end{vmatrix}$$

Let the true matrix of direction cosines be given by:

$$A = \begin{vmatrix} \ell_1 & m_1 & n_1 \\ \ell_2 & m_2 & n_2 \\ \ell_3 & m_3 & n_3 \end{vmatrix}$$

Now, A is orthogonal, its determinant is one and each element is equal to its cofactor. Assume a constant error, α, is introduced at each time step:

$$A_C = (1 + \alpha)A$$

The inverse of A_C is then

$$A_C^{-1} = \frac{1}{1+\alpha} A^T$$

where T indicates the transpose ($A^T = A^{-1}$)

For $\alpha << 1$, the Maclawin expansion

$$\frac{1}{1+\alpha} = (1 - \alpha) + \alpha^2 - \alpha^3$$

converges rapidly and we retain only the terms in parentheses.

Substituting,

$$A_C^{-1} = (1 - \alpha) A_T$$

The average of corresponding terms in $(A_C^{-1})^T$ and A_C eliminates the assumed error for

$$\frac{1}{2}\left[(A_C^{-1})^T + A_C\right] = A\left[\frac{1-\alpha}{2} + \frac{1+\alpha}{2}\right] = A$$

The orthogonalization is mechanized in XINTF by the following equations:

(1) Determinant of A_c

$$\Delta = \ell_1 m_2 n_3 + \ell_3 m_1 n_2 + \ell_2 m_3 n_1 - \ell_3 m_2 n_1 - \ell_2 m_1 n_3 - \ell_1 m_3 n_2$$

(2) The elements of the transpose of the inverse $(A_c^{-1})^T$

$$\ell_1' = m_2 n_3 - n_2 m_3$$

$$\ell_2' = n_1 m_3 - m_1 n_3$$

$$\ell_3' = m_1 n_2 - n_1 m_2$$

$$m_1' = n_2 \ell_3 - \ell_2 n_3$$

$$m_2' = \ell_1 n_3 - n_1 \ell_3$$

$$m_3' = n_1 \ell_2 - n_2 \ell_1$$

$$n_1' = \ell_2 m_3 - m_2 \ell_3$$

$$n_2' = m_1 \ell_3 - \ell_1 m_3$$

$$n_3' = \ell_1 m_2 - m_1 \ell_2$$

and to return to the original notation, the updated matrix becomes:

$$(TBI)_n = \frac{1}{2} \left[\left(A_C^{-1} \right)^T + A_C \right]_n$$

10. Gravitational Accelerations

Expansion of the gravitational potential in terms of Legendre functions of geocentric latitude, $P_n(\phi)$

$$U = \frac{\mu}{R} \left[1 + \frac{J}{3} \left(\frac{Re}{R} \right)^2 P_2 + \frac{H}{5} \left(\frac{Re}{R} \right)^3 P_3 + \frac{K}{30} \left(\frac{Re}{R} \right)^4 P_4 + \ldots . \right]$$

The radial component:

$$g Z_e = -\frac{\partial U}{\partial R} = -\frac{\mu}{R}\left[-\frac{2J}{3}\left(\frac{Re^2}{R^3}\right)P_2 - \frac{3H}{5}\left(\frac{Re^3}{R^4}\right)P_3 - \frac{4K}{30}\left(\frac{Re^4}{R^5}\right)P^4\right]$$

$$+\frac{\mu}{R^2}\left[1 + \frac{J}{3}\left(\frac{Re}{R}\right)^2 P_2 + \left(\frac{Re}{R}\right)^3 P_3 + \frac{K}{30}\left(\frac{Re}{R}\right)^4 P_4\right]$$

The horizontal component:

$$g X_e = \frac{1}{R}\frac{\partial U}{\partial \phi} = \frac{\mu}{R^2}\left[\frac{J}{3}\left(\frac{Re}{R}\right)^2 (-6 \sin\phi \cos\phi)\right.$$

$$+\frac{H}{5}\left(\frac{Re}{R}\right)^3 (3\cos\phi - 15\sin^2\phi\cos\phi)$$

$$\left.+\frac{K}{30}\left(\frac{Re}{R}\right)^4 (-60\sin\phi\cos\phi + 140\sin^3\phi\cos\phi)\right]$$

Collecting terms:

$$g Z_e = \frac{\mu}{R^2}\left[1 + J\left(\frac{Re}{R}\right)^2 P_2 + \frac{4H}{5}\left(\frac{Re}{R}\right)^3 P_3 + \frac{K}{6}\left(\frac{Re}{R}\right)^4 P_4\right]$$

$$g X_e = \frac{\mu}{R^2}\left[-2J\left(\frac{Re}{R}\right)^2 P_5 + \frac{3H}{5}\left(\frac{Re}{R}\right)^3 P_6 + \frac{2K}{3}\left(\frac{Re}{R}\right)^4 P_7\right]$$

$P_2 = 1 - 3\sin^2\phi$

$P_3 = 3\sin\phi - 5\sin^3\phi$

$P_4 = 3 - 30\sin^2\phi + 35\sin^4\phi$

$P_5 = \sin\phi\cos\phi$

$P_6 = \cos\phi\,(1 - 5\sin^2\phi)$

$P_7 = \sin\phi\cos\phi\,(-3 + 7\sin^2\phi)$

$\mu = 1.407698 \times 10^{16}$ cu ft/sec^2

$Re = 20,925,631$ ft

$J = 1623.41 \times 10^{-6}$

$H = 6.04 \times 10^{-6}$

$K = 6.37 \times 10^{-6}$

These equations are mechanized in CΦGRV, the results transformed to body axes and integrated in XINTF.

11. Aerodynamic Forces and Moments

Aerodynamic forces and moments are computed in MAERΦ. This subroutine is presently a skeleton program which computes α, β, ϕ, M as arguments for tables which will provide aerodynamic coefficients as functions of these quantities. Since the particular form of the coefficients seems as variable as the number of artists engaged in their production, table storage and calling statements for DISCT are left for the individual problem. Present plans include the following coefficients:

C_ℓ, C_m, C_n (roll, pitch, yaw moments)

C_X, C_Y, C_Z (body axes force coefficients)

The arguments will be:

$$\alpha_T = \tan^{-1}\left(\frac{\sqrt{(w - w_w)^2 + (v - v_w)^2}}{(u - u_w)}\right), \quad S\alpha_T = \frac{\sqrt{v_R^2 + w_R^2}}{V_R}, \quad C\alpha_T = \frac{u_R}{V_R}$$

$$\phi_T = \tan^{-1}\left(\frac{w - w_w}{v - v_w}\right), \quad S\phi_T = w_R\Big/\sqrt{v_R^2 + w_R^2}, \quad C\phi_T = v_R\Big/\sqrt{v_R^2 + w_R^2}$$

$0 \leq \alpha_T \leq 180$

$0 \leq \phi_T \leq 360$

These are the so-called aerodynamic roll angle and angle of attack and must be mechanized either from 0 to 360° or 0 to ±180°. They are not sufficient, however, to initiate body attitude. For this purpose, and for purposes of evaluating abort from booster trajectories, we compute the more usual values of α, β, ϕ. The roll angle, ϕ, is arbitrarily defined with reference to the Z_V velocity axis. We transform Z_{Vu} to body axes.

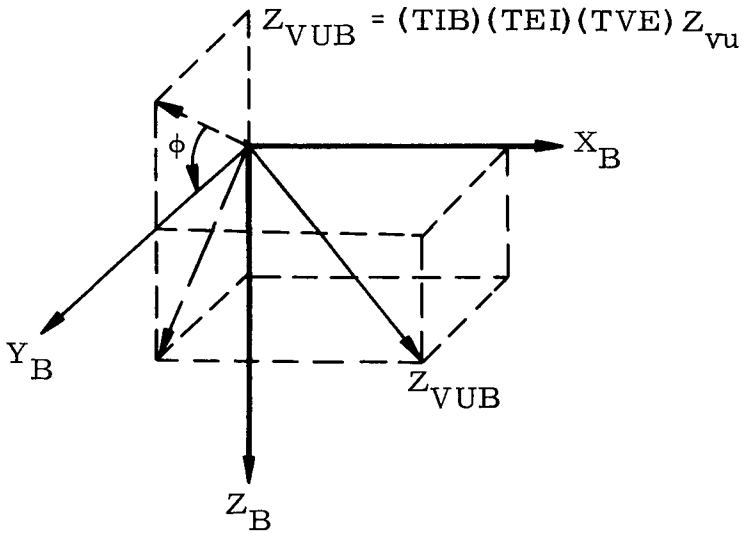

The roll angle is defined as the complement of the angle between the V_B - Z_B projection of Z_{Vu} and Y_B taken positive about X_B. We have

$$C\phi = \frac{ZVUYB}{\left[ZVUYB^2 + ZVUBZ^2\right]^{1/2}}$$

$$S\phi = \frac{ZEUZB}{\left[ZVUYB^2 + ZVUBZ^2\right]^{1/2}}$$

We may then solve the transformation between body and relative wind axes as follows:

$$S\alpha = \frac{-S\phi\, v_w + C\phi\, w_w}{\left[u_w^2 + (-S\phi\, v_w + C\phi\, w_w)^2\right]^{1/2}}$$

$$T\alpha = \frac{-S\phi\, v_w + C\phi\, w_w}{u_w}$$

$$C\alpha = S\alpha / T\alpha$$

$$S\beta = \frac{v_w C\phi + w_w S\phi}{V_w}$$

$$C\beta = u_w / (V_w C\alpha)$$

where

$$V_w = \sqrt{u_w^2 + v_w^2 + w_w^2}$$

$$u_w = u - u_R$$

$$v_w = v - v_R$$

$$w_w = w - w_R$$

u_R, v_R, w_R = components of wind in body axes.

Of these functions, only the tangent is likely to go to infinity and cause overflow problems. The signs of all are uniquely determined and, hence, the quadrant may be determined without ambiguity.

REFERENCES

CC-1. "Six-Degree-of-Freedom Flight-Path Study, Generalized Computer Program, Part I, Problem Formulation," AF FDL TDR-64-1, Part I, Volume I.

CC-2. Byrne, B., Murphy, W. and Lanzkron, R. W., "Gimballess Inertial Reference System," IRE Convention Record, 1963.

CC-3. "System/360 Scientific Subroutine Package (360A-CM-03X), Programmer's Manual," IBM Publication H20-0Z05-0.

CC-4. Ried, R. C. Jr. and Mayo, E. E., "Equations for the Newtonian Static and Dynamic Aerodynamic Coefficients for a Body of Revolution with an Offset Center of Gravity Location," NASA TND-1085.

APPENDIX DD

PROPULSION ANALYSIS

The reference configuration requires propulsion for spin-up, separation of the CIR-RTG/RB from the launch vehicle, deorbit and despin prior to initial reentry. In all cases, performance requirements were compared with existing rocket motors to minimize the necessity for new rocket programs.

A. SEPARATION

The particular mode of operation selected for separation of the CIR-RTG/RB from the launch vehicle makes it desirable, if not mandatory, that the ejection velocity be achieved by the time the CIR-RTG/RB leaves the launch rails which are 2.31 feet in length. To achieve this ejection velocity without excessive accelerations (hence extremely short burning durations), an ejection velocity of 20 fps was assumed. On this basis, a rocket burning duration of about 0.23 second is required. The average mass to be accelerated in 0.231 second is approximately 23.9 slugs (770 pounds); therefore, the thrust required is 2070 pounds.

In summary, the separation rocket motor must provide:

(1)	Thrust	2070 pounds
(2)	Duration	0.231 second
(3)	Total Impulse	478 lb-sec

An existing rocket motor, the MARC 17D1 manufactured by Atlantic Research, meets the burning time requirements with a 0.2317-second duration, but generates approximately 2.5 times the required thrust level. The proven design concept, which utilizes a number of propellant "sticks" with circular perforations, is recommended for the reference vehicle separation motor. A new motor has been designed which is a scaled version of the MARC 17D1. The number of propellant sticks has been reduced to 10 and the length of the sticks has been reduced proportionately to yield the desired performance. The design details are presented later in this appendix. Table DD-1 lists the major parameters for the new unit. The configuration is shown on the inboard profile (Fig. III-1).

TABLE DD-1

Rocket Parameters

	Atlantic Research MARC 17D1	New Development
Total impulse (lb-sec)	1155	476
Thrust (lb)	4823	2070
Duration (sec)	0.2317	0.2317
Specific impulse (sec)	238.8	238.8
Number of propellant grains	19	10
Propellant grain OD (in.)	1.102	1.102
Propellant grain ID (in.)	0.448	0.448
Propellant grain length (in.)	5.25	4.13
Chamber volume (in.)	219	90
Chamber diameter (in.)	6	4.5
Chamber length (in.)	6	4.73
Overall rocket length (8 in.)	9.7	7 to 7.5
Nozzle throat diameter (in.)*	0.783	0.468
Nozzle exit diameter (in.)*	1.76	1.016
Nozzle expansion ratio	5.1	5.1
Number of nozzles	3	3
Propellant weight (lb)	4.83	2.0
Gross weight (lb)	12.85	7.2
Mass fraction	0.376	0.28
Propellant loading density (%)	43.5	43.5
Cross-sectional loading (%)	64	64

*Per nozzle

B. SPIN-DESPIN

Since the reference configuration utilizes four separate rockets for deorbit impulse, the RB must be spin stabilized sufficiently to overcome destabilizing moments introduced by thrust misalignments, center of gravity displacement error, etc. A spin rate of 60 rpm has been used to compensate for any combination of these destabilizing conditions.

Atlantic Research also provides a rocket motor, two of which will generate the necessary spin rate. The angular acceleration is 1.872 rev/sec^2, where the moment arm (d) = 23 inches and single rocket thrust (f) = 119 pounds. The spin rate at the end of rocket burning is 62.5 rpm. In 0.23 second, the RB leaves the separation track and the spin rate is 27 rpm--43% of its final value. The final spin rate of 62.5 rpm is achieved 0.325 second after the RB leaves the separation tracks. The same basic rocket will be used to despin the RB after delivery of the deorbit impulse.

Design characteristics of this rocket are given in Table DD-2, and the rocket is shown in Fig. III-1. The rocket designation is MARC 5A1.

C. DEORBIT

The ΔV required to assure reentry will vary between 1200 and 1500 fps, depending upon the retro firing angle and accuracy requirements.

A rocket manufactured by Thiokol Chemical Company (SARV RETRO MK I) will satisfy the minimum ΔV requirement of 1200 fps.

$$\Delta V = gI_s \ln \frac{W_{PL} + W_R}{W_{PL} + W_R - W_P}$$

where

W_{PL} = weight retroed less retrorocket weight
I_s = propellant specific impulse
W_R = retrorocket weight
W_P = retrorocket propellant weight

$$\Delta V = 32.2 \times 253 \ln \frac{571 + 4\,(38.56)}{571 + 4\,(38.56) - 4\,(26.3)}\ 0.94 = 1200 \text{ fps}$$

TABLE DD-2

Rocket Motor Design Characteristics

Function	Separation	Spin-Despin		Deorbit		
Rocket designation		MARC 5A1		SARV MK I		SARV MK IV
Manufacturer	Atlantic Research	Atlantic Research	--	Thiokol	--	Thiokol
Performance requirement	20 fps	60 rpm	60 rpm	1200 fps	1500 fps	1500 fps
Average thrust (vac) (lb)	2070	119	275	755	3300	820
Duration (sec)	0.231	0.556	0.23	9	10	10.9
Total impulse (vac) (lb-sec)	476	66	66	6660	33,000	8900
Specific impulse (vac) (sec)	238.8	238	238	253	260	255
Chamber pressure (psi)	2380	1150	1150	1175	1000	700
Loaded weight (lb)	7.2	1.45	1.60	38.56	153 (est)	55.2
Weight expended (lb)	5.2	1.15	1.30	12.09	36 (est)	20.7
Mass fraction	0.28	0.190	0.175	0.676	0.83	0.636
Loading density (%)	0.23	84.5	84.5	84.8	85	80
Throat diameter (in.)	0.468	0.30	0.455	0.716	1.10	0.97
Exit cone diameter (in.)	1.016	1.70	2.58	3.29	6.0	4.40
Expansion ratio	5.1	32.0	32	21.2	30	20.6
Number of nozzles	3	1	1	1	2	1
Motor diameter (in.)	4.5	2	2.6 (est)	10	16.5	12
Motor length (in.)	7.5	8.3	5.5 (est)	12	Sphere	12.76
Temperature limits (°F)	+20 to 125	-35 to +160	-35 to 160	40 to 110	40 to 110	40 to 110
Number required	1	4	4	4	1	4
Status	Requirement for CRONUS	Production	Requirement for CRONUS	PFRT	Requirement for CRONUS	Production
Remarks	Recommended for reference configuration (scale version of ARC's MARC 17D1)	Selected for reference configuration		Selected for reference configuration	Alternative approach to MK I	Must be modified

The factor 0.94 accounts for the rocket cant angle and nozzle skew. The characteristics of this rocket are given in Table DD-2.

Design and performance characteristics of a rocket developed to provide a 1500-fps ΔV to the RB are discussed in Chapter IX. This new rocket at 1500 fps would be equivalent in weight to and slightly larger than the SARV MK I at 1200 fps. The characteristics of a suitably modified, off-the-shelf rocket motor (Thiokol SARV RETRO MK IV) which will generate a 1500-fps ΔV and is being manufactured in large numbers at this time are also discussed, for comparison, in Chapter IX. The characteristics of both these 1500-fps rocket motors also are listed in Table DD-2.

D. SCALE DESIGN OF MARC 17D1 (Atlantic Research Motor)

Separation of the airborne system from the spacecraft requires that the propulsion function be completed in a short period of time (about 0.23 second). The Atlantic Research MARC 17D1 rocket motor offers a proven design concept which will provide the 2000 pounds of thrust for this brief duration. While the current method of bonding the propellant "sticks" or rods to a head end spider truss may make it difficult for the otherwise unsupported propellant to withstand the longitudinal loads during the boost period (the separation rocket is mounted perpendicular to the launch vehicle centerline), it is believed that additional propellant support can be provided without interfering with the basic rocket design approach.

Calculations performed to estimate the characteristics of a scaled-down version of the MARC 17D1, suitable for the RB-CIR-to-spacecraft separation function are provided herein.

1. Grain Characteristics

The total surface area for 19 propellant "sticks" was calculated to be 345.34 sq in. Since the diameters of the "sticks" are maintained, the total impulse per unit area was determined as 3.35 lb-sec/sq in. We assume that 10 "sticks" of propellant will be used in the new rocket design; therefore, since the new motor must provide 478 lb-sec of total impulse, the total "stick" area required is $\left(\frac{478}{3.35}\right)$ 143 sq in. or 14.3 sq in. per "stick." The length of the new sticks will be proportional to the current motor "sticks" in the ratio of stick surface area or

$$X_L = \frac{14.3 \text{ sq in.}}{18.176 \text{ sq in.}} \times 5.25 \text{ in.} = 4.13 \text{ in.}$$

2. Motor Dimensions

The existing motor has a total propellant enclosed volume of $V_P = \pi r^2 1$ (19 sticks) = 95 cu in.

The total chamber volume is approximately

$$V_c = \pi(3)^2 (7.75) = 219 \text{ cu in.}$$

Thus, the volumetric loading density is approximately 43.5%. The new rocket propellant volume is 39.4 cu in. By maintaining the same volumetric loading density, the new rocket chamber volume must be 90.0 cu in. The length-to-diameter ratio is determined by maintaining the same cross-sectional loading. The current rocket's is

$$\frac{19 \times \pi(0.551)^2}{\pi(3)} = 0.64$$

The chamber diameter of the new rocket will be

$$D_c = 2\sqrt{\frac{10(0.551)^2}{0.64}} = 4.36 \text{ in. } (\approx 4.5 \text{ in. OD})$$

The length of the chamber, based on a volume of 90 cu in. is

$$L_c = \frac{V}{\pi R_c^2} = \frac{90}{\pi(2.18)^2} = 6.0 \text{ in.}$$

The length of the cylindrical portion of the chamber is approximately 4.73 inches. The overall length of the rocket will be 7 to 7.5 inches.

3. Nozzle Parameters

Since the ratio of propellant grain surface area (A_s) to the nozzle throat area (A_t) must be constant for a given propellant and chamber pressure, the nozzle total throat area required is

$$A_t = A_s/K_N = \frac{143 \text{ sq in.}}{300} = 0.476 \text{ sq in.}$$

The total exit area (A_E) for the same nozzle expansion ratio (ϵ) is

$$A_E = A_t \epsilon = 0.476 \times 5.1 = 2.43 \text{ sq in.}$$

The three-nozzle system is retained to minimize nozzle length. Each nozzle will have throat and exit diameters of 0.468 inch and 1.016 inches, respectively.

4. Motor Weight Estimate

The chamber is by far the heaviest inert component of the rocket. The chamber weight has been scaled with respect to surface area and chamber radius. Using a cylindrical case and 2:1 elliptical end domes, the total surface area of each rocket was calculated to be

$$S_{A_{\text{existing motor}}} = \pi D L_c + \left(2\pi R_c^2 + \frac{(R_c/2)^2}{e} \ln \frac{1+e}{1-e}\right)$$

$$= 176.5 \text{ sq in.}$$

$$S_{A_{\text{new motor}}} = \pi(4.5)(4.73) + \left(2\pi(2.25)^2 + \pi \frac{(1.12)^2}{e} \ln \frac{1+e}{1-e}\right)$$

$$= 100.0 \text{ sq in.}$$

The wall thickness will be reduced by 20% based on the closest higher standard sheet thickness of steel to the calculated thickness required.

The surface area ratio is then $\frac{0.100}{176.5} \times 0.8 = 0.453$ and the chamber weight for the new motor will be approximately 2.35 lb (0.453 x 5.18 lb).

The propellant weight is

$$W_{P_{\text{new rocket}}} = \frac{N_{\text{new}} \times L_{\text{new}}}{N_{\text{exist}} \times L_{\text{exist}}} \left(W_{P_{\text{exist}}}\right)$$

$$= \frac{10 \times 4.13}{19 \times 5.25} (4.83)$$

$$= 2.0 \text{ lb}$$

where N is the number of propellant "sticks" and L is the length of the propellant "stick." The estimated gross weight is:

Chamber	-2.35
Nozzle inserts	-0.30
Head closure and igniter	-1.95
Nozzle closure	-0.40
Propellant	-2.0
	7.00 lb

The mass fraction is 0.28.

BLANK

APPENDIX EE

MICROMETEOROID PENETRATION PROBABILITY

A quick computation has been performed to estimate the probability that a portion of CRONUS will be penetrated by a micrometeoroid. As usual in this type of analysis, it is assumed that the probability of penetration is a function of the type of meteoroid bumper and the product of exposed area times time. This implies that we can express:

$$t_s = f(P, AT)$$

where

t_s = effective thickness of aluminum (inches)

P = probability of no penetration

= 1 - probability of at least one penetration

A = exposed surface area (sq ft)

T = time in orbit (days).

This function is illustrated in Fig. EE-1. Pertinent assumptions made in generating Fig. EE-1 are:

(1) Meteoroid flux. The flux model as supplied by NASA Headquarters for Contract NASw-1053 was used. In particular, the flux equations, in the vicinity of the earth, are:

$$\text{Cometary}--\log_{10} N_C = -1.34 \log_{10} M_C - 10.27$$

$$\text{Asteroidal}--\log_{10} N_A = -1.0 \log_{10} M_A - 10.3$$

where

N_C, N_A = flux of cometary, asteroidal particles (no. / sq ft day)

M_C, M_A = mass of cometary, asteroidal particles (gm)

No earth shielding is assumed.

(2) Penetration equation. The Langley penetration model was used, the equation of which is:

$$t = K(MV)^{1/3}$$

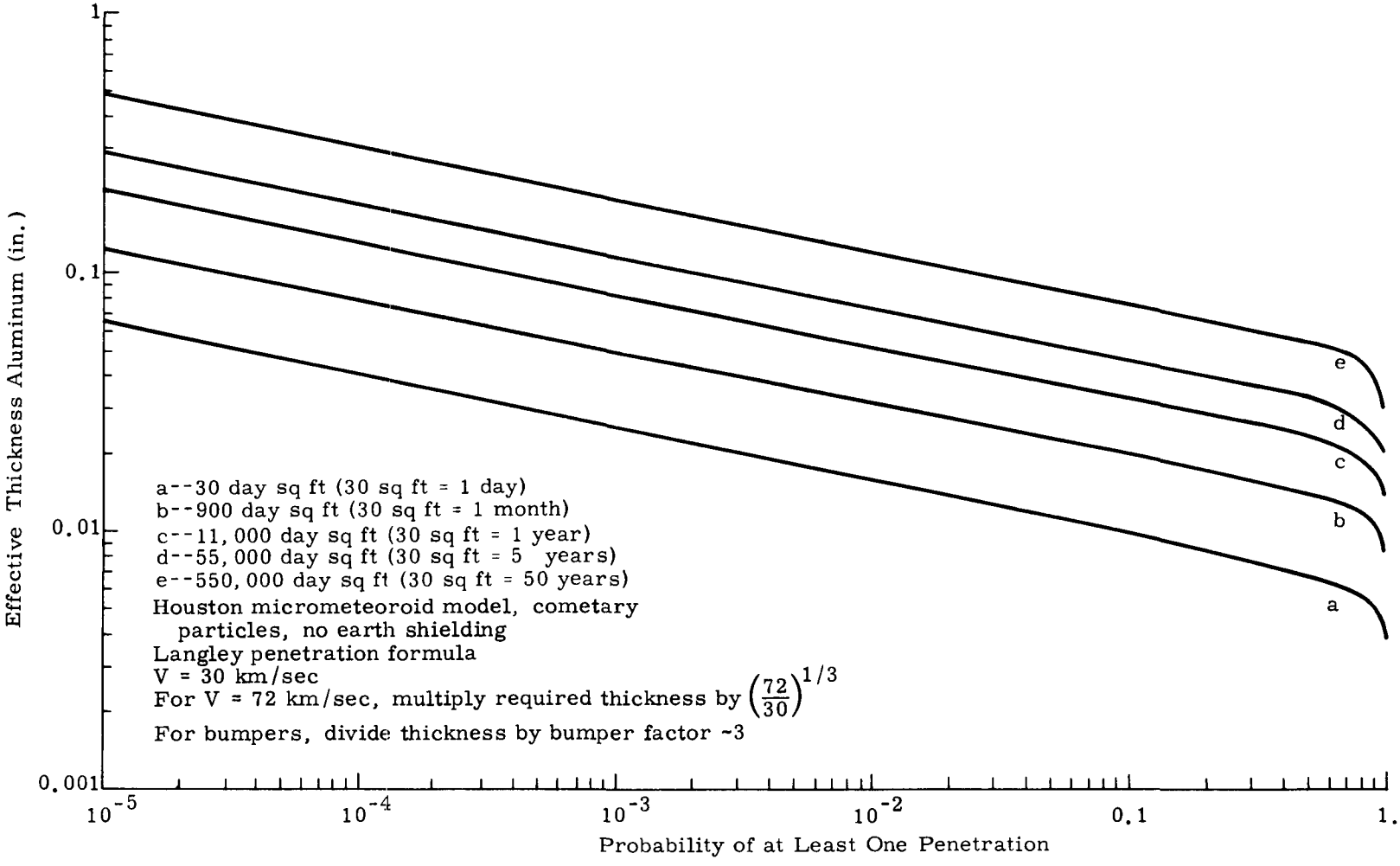

Fig. EE-1. Micrometeoroid Penetration Probability: Low Earth Orbit

where

t = thickness of thin sheet that will just be penetrated (inches)

V = particle velocity (km/sec)

M = particle mass (gm)

K = target material constant.

For aluminum single skin construction, K = 0.154.

(3) Particle velocity. A velocity of 30 km/sec is used in Fig. EE-1. Particles may travel as fast as 72 km/sec in the near vicinity of the earth. For this velocity or any other velocity, the required thickness can be scaled by $\left(\frac{V}{30}\right)^{1/3}$.

It is important to mention that there is considerable uncertainty in the actual meteoroidal flux. There is even more uncertainty in the actual effects of meteoroids on thin, metal skins. Consequently, penetration probability estimates can easily vary by one order of magnitude, depending upon the explicit assumptions.

Using these equations, it can be shown that, for short recall periods, no micrometeoroid protection is needed for any component, since the presently provided structure is sufficient. For long term missions (five years), the retro motors must be provided with some shielding, since a puncture of the motor may cause an explosion at ignition. The heat shield, if it is an ablator, would also have to be protected if reentry after five years is desired. Provided the beryllium coating survives the continuous bombardment by very fine particles, no protection seems needed for the power generation subsystems, since the probability of a sizable particle impacting the RTG/RB is rather low.

BLANK

APPENDIX FF

SGLS DESCRIPTION

The SGLS configuration selected for the CIR is shown in Fig. FF-1. Its functions include range and range rate tracking, angle tracking, ground-to-vehicle command, and PCM and FM/FM telemetry. Performance curves for both the spacecraft-to-ground and ground-to-spacecraft links are shown in Figs. FF-2 and FF-3, on which threshold signal power required is plotted as a function of communications range. The horizontal lines indicate signal power required for the combination of services desired and their intersection with the threshold signal power gives the maximum functional range available. Therefore, the two-watt transmitter will provide 64K bit PCM, 20-kc telemetry, ranging, range rate and 1K baud command to synchronous altitudes.

The vehicle flight unit for the functional configuration selected is shown in Fig. FF-4. Its physical characteristics are given in Table FF-1. A small programmer has been added to this unit to effect the time program. SGLS vehicle equipment uses a coherent phase-lock receiver with a 205/8 receiver-to-transmitter drive ratio. The receiver is capable of receiving any fixed frequency signal in the 1762- to 1842-range through selection of the VCO frequency. This receiving band covers the entire allocation by translation into a 2200- to 2300-mc transmitting band. The signal conditioner provides the reconstructed, ternary bit stream and bit synchronization signals to be fed to the vehicle command decoder and programmer. Squelch information is available when the signal-to-noise ratio drops to a level where sync and command data cannot be maintained at a low error rate. The squelch signal is used to reset the digital process after signal dropout. The decoder to be used for SGLS demonstration can accept signals from one of four different types of inputs (Fig. FF-5). The data lines consist of serial bit streams which the decoder transforms into 39 discrete commands. It is planned that this decoder interface directly with the programmer for time sequencing of the operation during ascent. The decoder authenticates the data by performing the following checks:

(1) Address confirmation

(2) Parity verification

(3) Message length check.

This process provides some degree of communications security against random noise or tampering, but will not prevent interference with the system through repetition of recorded messages.

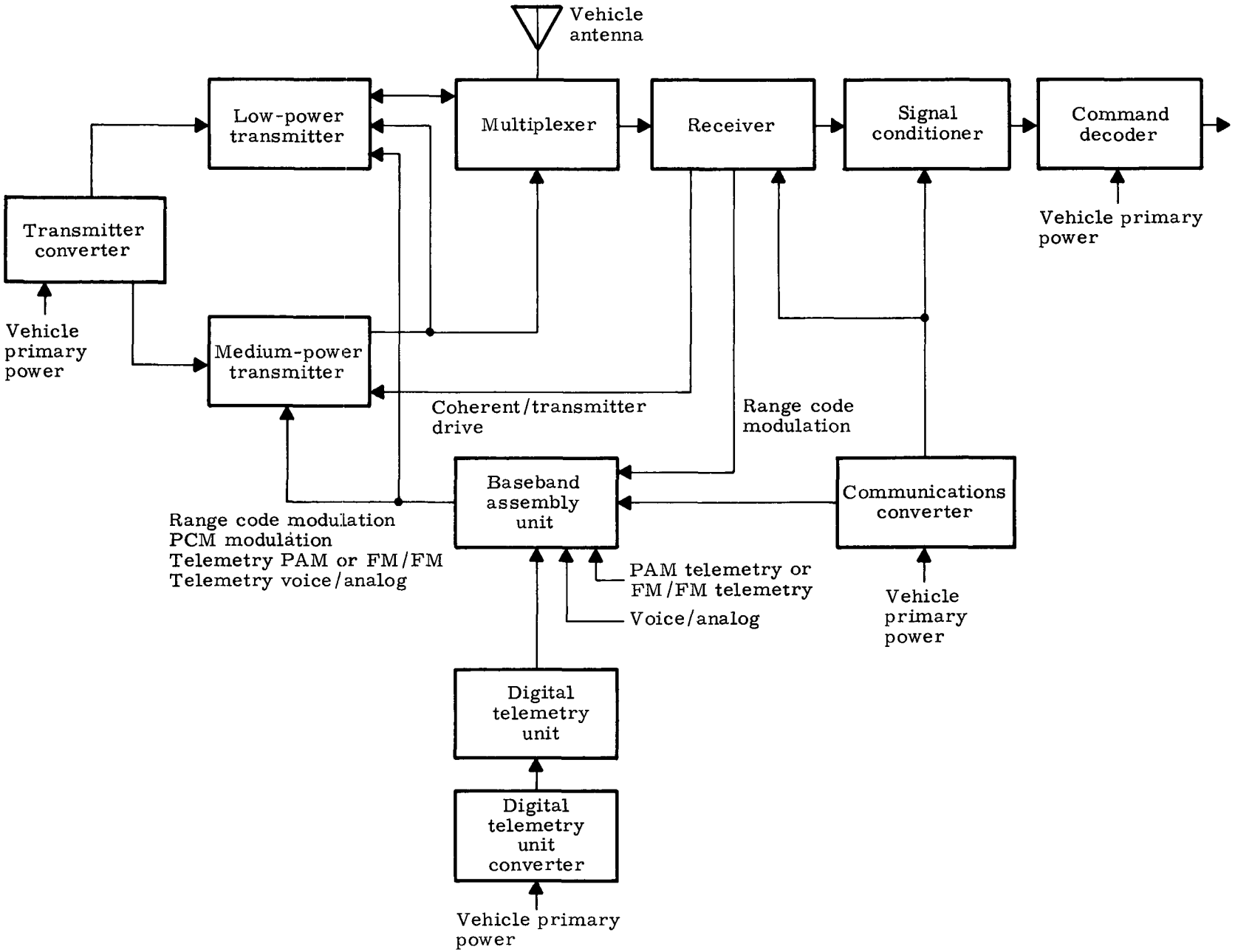

Fig. FF-1. SGLS Vehicle Equipment Configuration

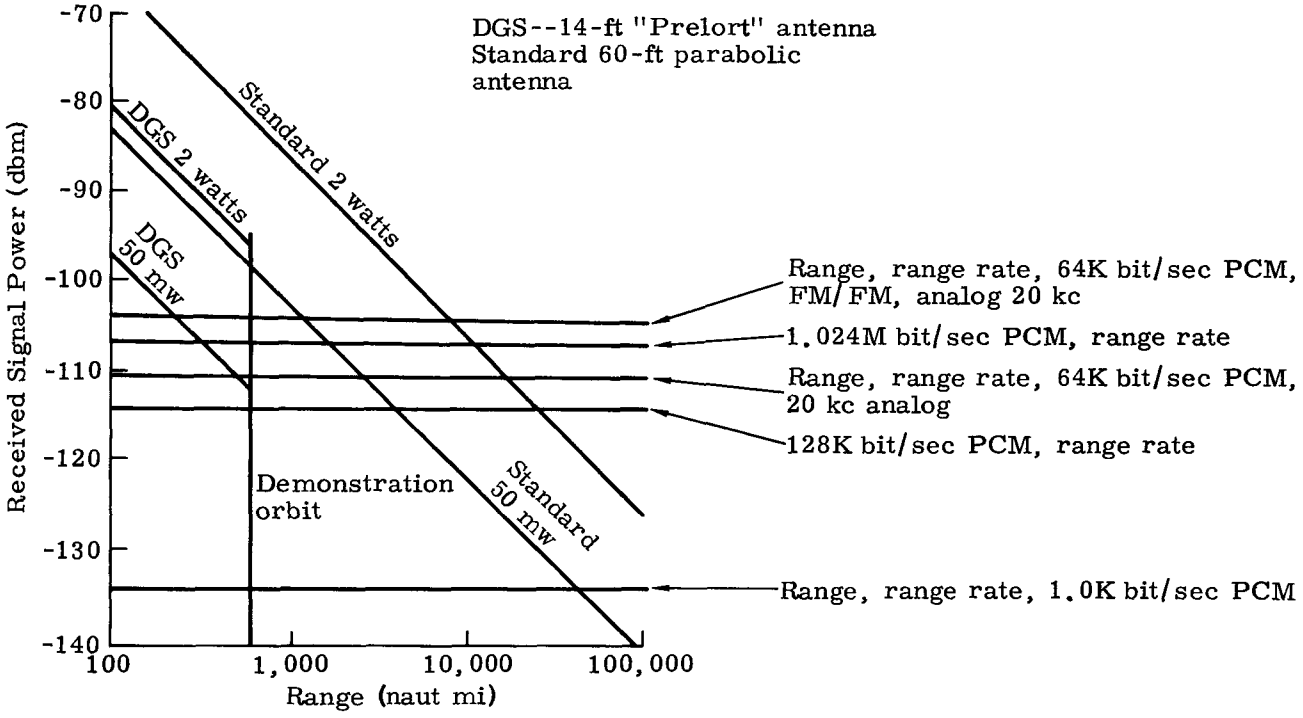

Fig. FF-2. Spacecraft-to-Ground Link Performance, Standard and Demonstration Ground Station

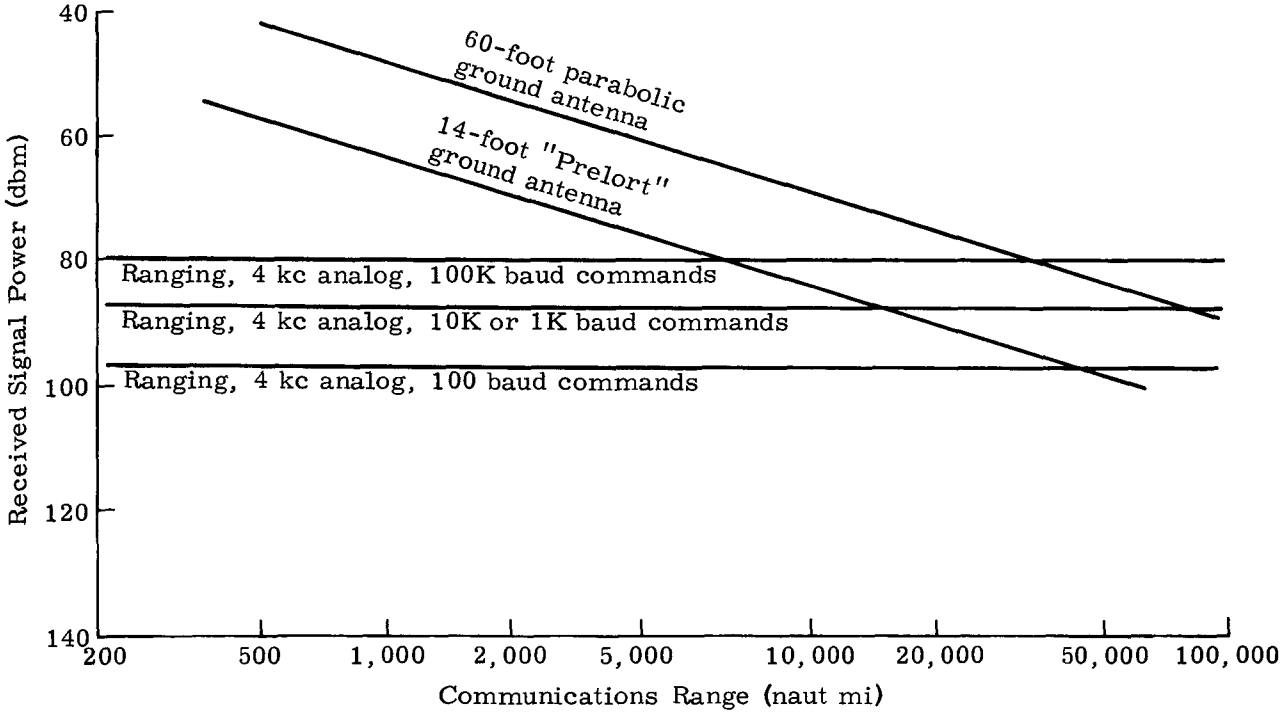

Fig. FF-3. Ground-to-Spacecraft Link Performance, Standard and Demonstration Ground Station

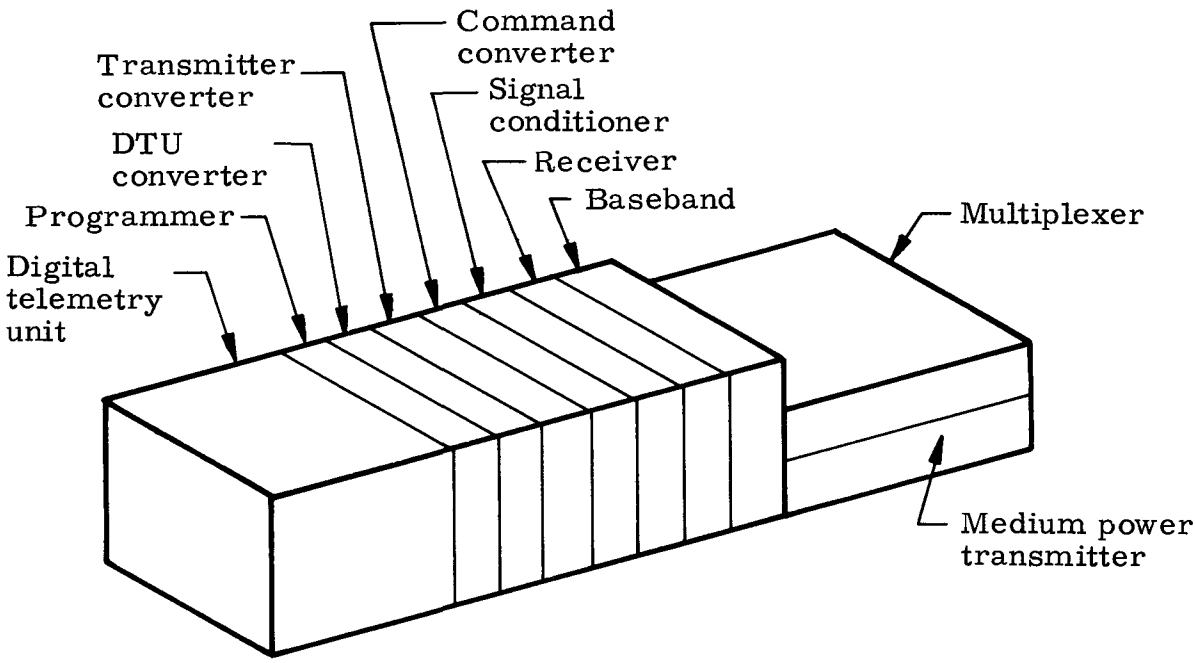

Fig. FF-4. SGLS Vehicle Flight Unit

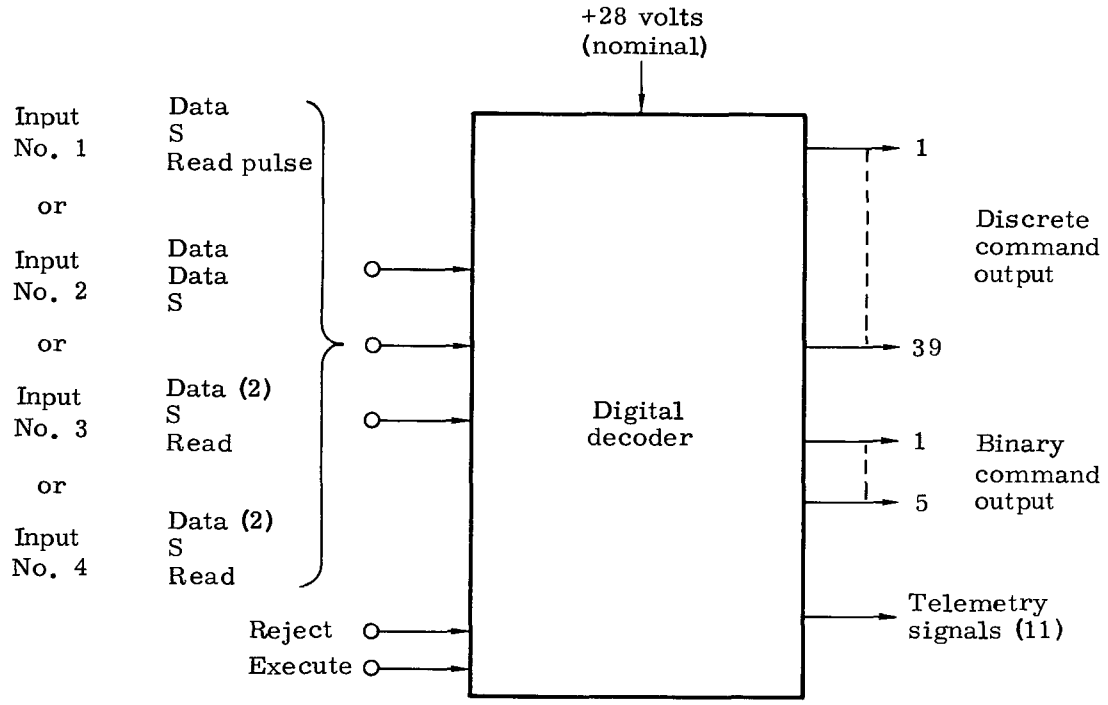

Fig. FF-5. Interface Signals

TABLE FF-1

Vehicle Equipment

Item	Weight (lb)	Power (watts)	Volume ($in.^3$)
Multiplexer	2.0	--	122
Receiver	3.4	1.44	109
Medium Power Transmitter (2 watts)	2.6	24.78	59
Power Converter (communication)	1.45	1.79	41
Power Converter (transmitter)	2.1	3.7	59
Power Converter (DTU)	1.3	0.2	72.5
Baseband Assembly Unit	1.3	0.2	72.5
256 Inputs	8.0	11.0	219
Signal Conditioner	1.5	0.5	63
Command Decoder	2.25	2.5	44
Programmer	6.0	9.0	130
	32.0	68.1	992

Dimensions: 7.25 by 5.0 by 27.36 inches

The vehicle transmitter selected for the CTR will be the two-watt, medium power, version. The transmitter is preset to work on any one of 10 channels in the 2200- to 2300-mc range, and is capable of being driven from either a coherent source provided by the receiver or an internal crystal oscillator in accordance with a signal present logic voltage generated in the receiver. The coherent drive provides the range/range rate tracking link.

The multiplexer is a four-terminal pair network with terminals for the antenna, receiver and two transmitters. The unit consists of two bandpass filter networks, a low-pass filter, a four-part ferrite port circulator, a three-decibel hybrid network and associated resistive networks. The hybrid network permits combining two transmitters to a single input to the antennas, with isolation between the antennas. The ferrite circulator provides receiver-transmitter isolation, while the bandpass filter gives a narrow 30-mc pass band centered at the transmitter frequency, which is tunable over the frequency range of 2200 to 2300 mc. The receiver channel contains a bandpass filter with a 20-mc pass band tunable over a frequency range of 1750 to 1850 mc.

The digital telemetry unit processes analog, digital or discrete input signals into a time multiplexed PCM format. Analog signals are quantized to either four or eight bits, depending upon requirements. Digital words and discretes bypass analog-to-digital conversion, and are directly combined with its output together with synchronization and identification words. The digital words are integral multiples of four bits. The format consists of a 1024-bit main frame, with 256 words available. A programmer and clock provide time sequencing and synchronization which are available to other units of vehicle equipment. The baseband assembly unit generates the down-link subcarriers, which are modulated with their respective telemetry signals. These modulated subcarriers are summed with the ranging signal to form the baseband structure applied to the modulator of the transmitters.

Three power converters are used for the SGLS system:

(1) Transmitter converter

(2) Communications converter

(3) Digital telemetry unit (DTU) converter.

The converters are separated into functional units because of differences in tolerances required. Pulse width-controlled switching regulators are used with high-power handling transistors and diodes mounted on separate heat sinks. Environmental specifications for SGLS are given in Table FF-2.

BLANK

TABLE FF-2

SGLS Environmental Specifications

Shock:	100 g nonoperating, 30 g operating
Vibration:	
Sine wave:	5 g from 5 to 2000 cps
Random:	0.16 g^2/cps from 300 to 1200 cps
Acceleration:	25 g
Temperature:	-30° to 165° F
Humidity:	90%
Pressure:	10^{-7} torr
RF interference:	MIL-I-26600
Radiation resistance integrated dose:	10 rad gamma 10^{14}-1 Mev electrons/sq cm
Reliability:	Minimum acceptance MTBF = 6750 hr (9 mo) Goal = 18 mo

BLANK

APPENDIX GG

HYDROSTATIC GAS BEARING ANALYSIS

A. OPERATION

In operation the hydrostatic gas bearing surfaces are separated by a film of gas; there is no metal-to-metal contact between bearing surfaces. When the operating supply pressure is discontinued, the bearing surfaces come into contact in accordance with the direction of the applied load. A balanced spring system is incorporated to cause the compliance mechanism to automatically center when pneumatic operating pressure is supplied to the bearings, and there is no external force acting on the system other than gravity.

Figures GG-1 and GG-2 show typical hydrostatic bearing configurations. The succeeding calculations specify the physical dimensions for each of the bearings used in the system. The operating gas supply is fed to the system through a flexible line leading from the launch site facilities to the bearing internal manifolds shown in Figs. GG-1 and GG-2. Routing of the gas to each bearing is handled by external, flexible lines.

In a typical hydrostatic bearing, the gas is admitted under pressure to the bearing clearance space, and control of admission is a critical design parameter. The flow control device, or restrictor (usually an orifice) and the transition space or recess are the most important items in this control. The transition space is used to introduce the gas to the clearance with a minimum of shock and pressure drop. Figure GG-3 shows a schematic of a typical bearing feeder section. System pressurization gas is introduced into the supply manifold, flows through the restrictor (orifice) and into the transition space (recess). From this point it flows through the bearing film to the exit region of ambient pressure. When eccentric bearing loading occurs, or the load value changes, the bearing clearance tends to close down in the direction of the applied load. This causes the restriction of gas flow to vary across the bearing in a direction which will resist the load displacement or change. The bearing is thus self-compensating.

B. FEASIBILITY ANALYSIS (REF. GG-1)*

1. Primary Cylindrical Bearings

Assume: Maximum suspended load on bearing system is 500 pounds
Maximum eccentricity loading due to three-inch excursion
Maximum load on single bearing

*Ref. GG-1. Rieger, N. F. and Peterson, M. B., "Hydrostatic Gas Bearings," Machine Design, March 31, 1966, pp 106 to 115.

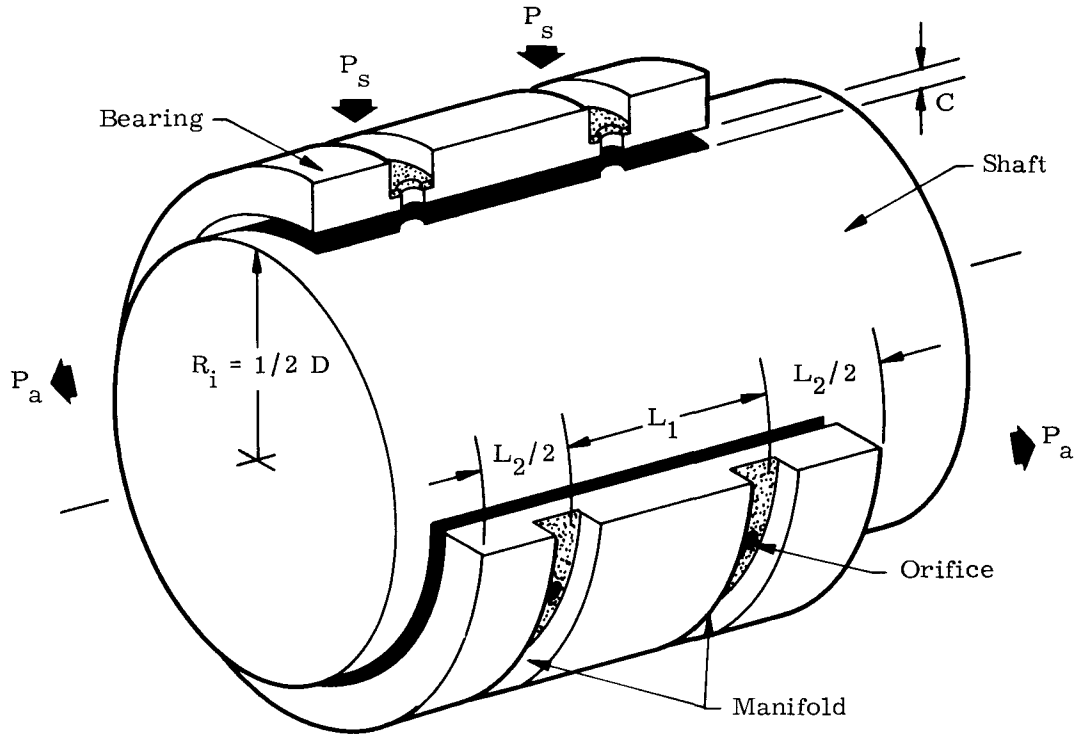

Fig. GG-1. Cylindrical Bearing

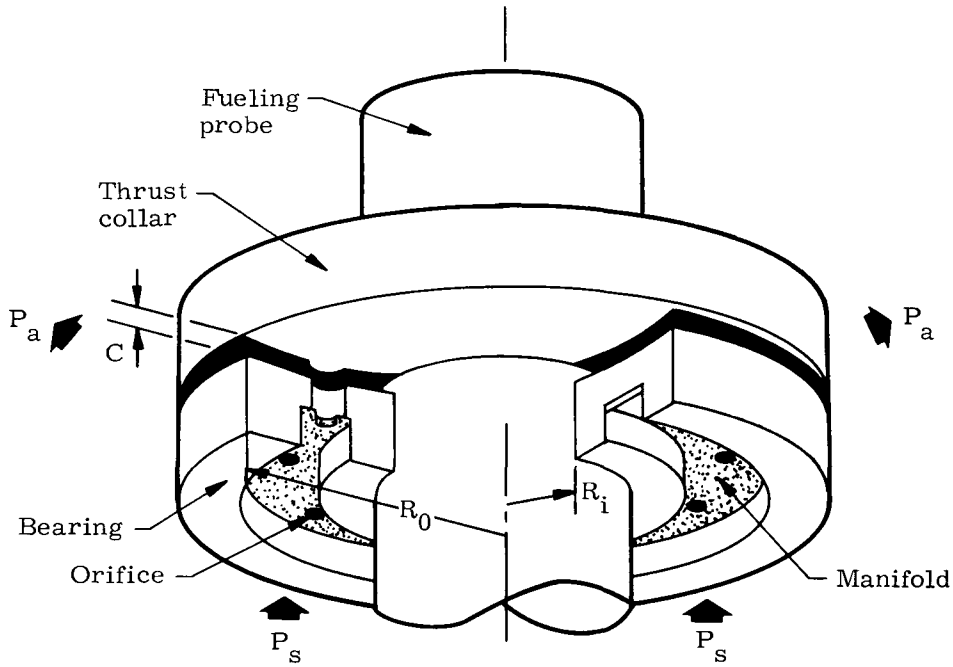

Fig. GG-2. Spherical Bearing

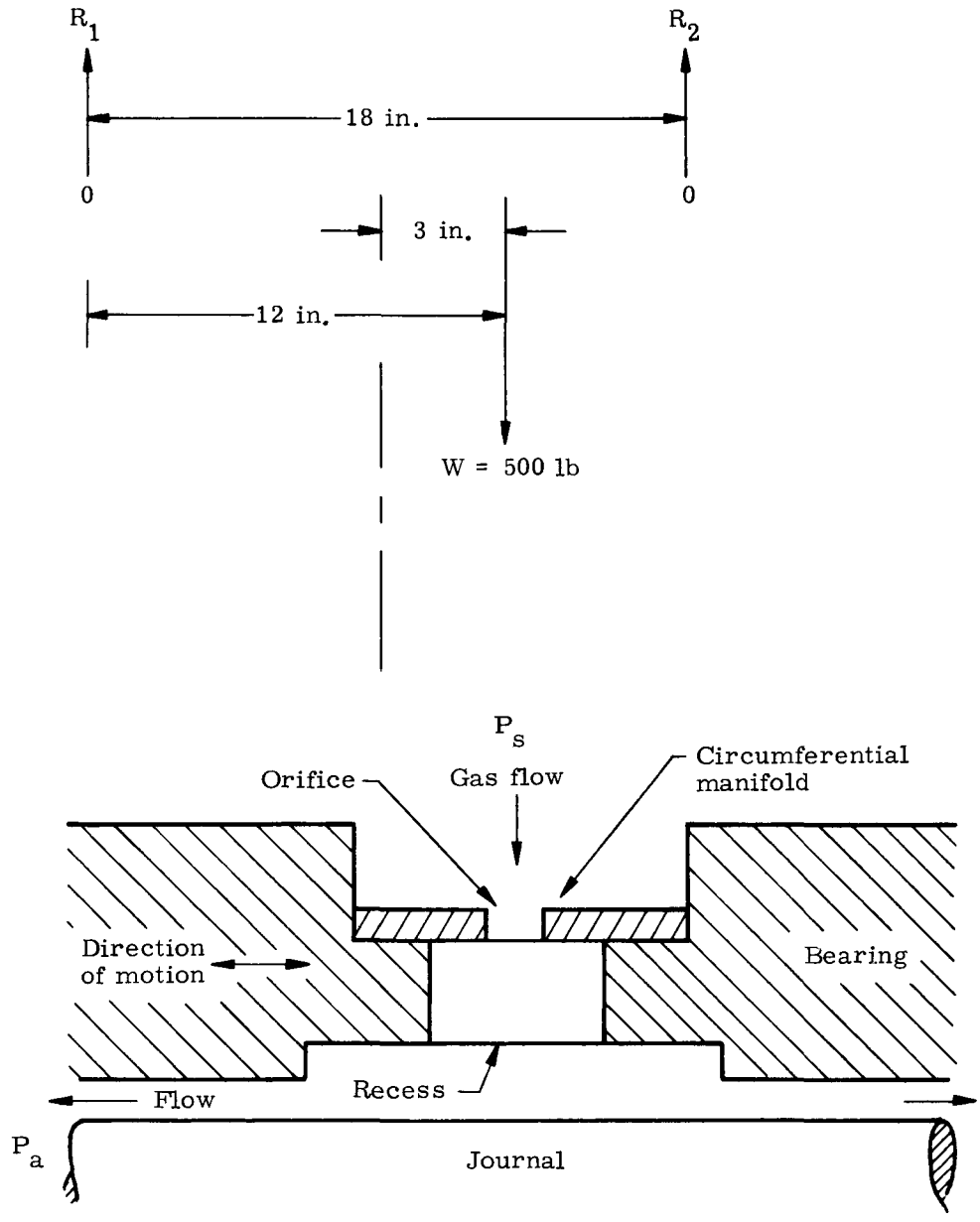

Fig. GG-3. Geometry of Feeder Nozzle

$$\left.\begin{aligned} \Sigma M_{R_1} &= 0 = 12 \times 500 - 18\ R_2 \\ R_2 &= \frac{12 \times 500}{18} = 333 \text{ lb} \end{aligned}\right\} \quad \text{Ref. Fig. GG-3}$$

Assume that one-half the total pressure drop occurs across the restrictor and one-half across the bearing, and that the average pressure in the bearing is one-half the transition pressure

$$P_s = P_a + \frac{4W}{A}$$

where

P_s = supply pressure (psi)

P_a = ambient pressure ≈ 14.7 psi

W = bearing load = 333 lb

A = projected bearing area normal to load = L x D

= 7 x 2.5 (from layouts)

$$P_s = 14.7 + \frac{4(333)}{7 \times 2.5} = 14.7 + 76.1 \approx 91 \text{ psi}$$

This indicates that the supply pressure required (<100 psig) is consistent with available standard equipment, components and technology.

Assume restrictor coefficient $\Lambda_s = 0.42$ (median value in Fig. 11 of Ref. GG-1)

$$\frac{L}{D} = \frac{7}{2.5} = 2.8$$

$$\frac{L_2}{D} = \frac{3.5}{2.5} = 1.4$$

$$\frac{P_s}{P_a} = \frac{91}{14.7} = 6.2$$

Q' = dimensionless flow

From Fig. 11a of Ref. GG-1,

$Q' = 0.32$

Q = gas flow through bearing

$$= \frac{\pi P_s^2 C^3}{6\mu RT} Q'$$

using air at 120° F

where

C = film thickness (bearing clearance) = 0.001 in.

μ = gas viscosity = 2.8×10^{-9} lb-sec/sq in.

R = gas constant = 2.472×10^5 lb^2/sec^2 °R

T = gas temperature = 580° R

RT = 1.434×10^8 lb^2/sec^2

$$Q = \frac{\pi(91)^2 (1 \times 10^{-3})^3 \ 0.32}{6(2.8 \times 10^{-9}) \ 2.472 \times 10^5 \ (580)}$$

$$= \frac{\pi \times 82.81 \times 10^2 \times 10^{-9} \times 0.32}{16.8 \times 10^{-9} \times 1.434 \times 10^8}$$

$= 3.46 \times 10^{-6}$ lb-sec/in.

(3.46×10^{-6}) 386 in./sec^2 = 1337×10^{-6}

Q = 0.001337 lb/sec

For double plane admission

Q_{tot} = 2 x 0.001337 = 0.002674 lb/sec/bearing

Total gas flow for primary bearing

2 x 0.002674 = 0.005348 lb/sec

2. Secondary Cylindrical Bearings

Assume: Maximum load = 400 pounds
No eccentric loading
∴ W = 200 pounds/bearing

$$P_s = P_a + \frac{4W}{A}$$

$$A = LD = 4 \times 2.5 = 10 \text{ sq in.}$$

$$P_s = 14.7 + \frac{4(200)}{10} = 14.7 + 80 = 94.7 \text{ psi}$$

Assume:

$$P_s = 91 \text{ psi}$$

$$A = \frac{4W}{P_s - P_a} = \frac{4(200)}{91 - 14.7} = 10.5 \text{ sq in.}$$

This indicates an increase to 4.2-inch calculated bearing length is required, which is within reason.

$$\frac{L}{D} = \frac{4.2}{2.5} = 1.68$$

Assume:

$\Lambda_s = 0.42$ (the median value in Fig. 11 of Ref. GG-1)

$Q'_s = 0.32$

Since $Q = \frac{\pi P_s^2 C^3}{6\mu RT} Q'$ and all parameters may be made equal between bearings by the sizing and the number of orifices between the supply manifold and the transition space, the flow through each journal bearing may be made essentially equal. Therefore, the total Q through secondary journal bearings is 0.005348 lb/sec. By sizing the system for equal flows, the line sizes may be held constant.

3. Spherical Bearing; Thrust Type (Fig. GG-2)

Assume: Bearing load = 300 pounds

From design layouts

$R_i = 2.25$ inch

$R_0 = 3.375$ inch

$$A = \pi\left(R_0^2 - R_1^2\right) = \pi(3.375^2 - 2.25^2)$$

$$= 19.85 \text{ sq in.}$$

$$P_s = P_a + \frac{4W}{A} \text{ (applies for thrust-type bearing)}$$

$$= 14.7 + \frac{4(300)}{19.85} = 14.7 + 60.5 = 75.2 \text{ psi}$$

Assume $P_s = 91$ psi

$$A = \frac{4W}{P_s - P_a} = \frac{4(300)}{91 - 14.7} = 15.7 \text{ sq in.}$$

R_i is fixed to provide clearance with the fuel block attachment mechanism to achieve minimum area,

$$R_0 = \left(\frac{A}{\pi} + R_1^2\right)^{1/2} = \left(\frac{15.7}{\pi} + 5.06\right)^{1/2} = (5.0 + 5.06)^{1/2}$$

$$= 317 \text{ inches}$$

This indicates leeway in design to parameters to achieve optimum size and performance considering the proposed configuration.

$$\frac{R_0}{R_i} = \frac{3.17}{2.25} = 1.41$$

W' = dimensionless bearing load

$$= \frac{W}{A_c (P_s - P_a)}$$

where

A_c = calculated bearing area

$$W' = \frac{300}{15.7 (91 - 14.7)} = 0.25$$

$$\frac{P_s}{P_a} = \frac{91}{14.7} = 6.2$$

Λ_s = restrictor coefficient = 1.8 (from Fig. 7 of Ref. GG-1).

$Q' = 1.2$

Assume:

C = bearing clearance = 0.001

$$Q = \frac{\pi P_s^2 \, C^3}{6\mu \, RT} \, Q'$$

$$= \frac{\pi(9.1 \times 10)^2 \, (1 \times 10^{-3})^3 \, 1.2}{6(2.8 \times 10^{-9}) \, 1.434 \times 10^8}$$

$$= \frac{\pi 82.81 \times 10^2 \times 1 \times 10^{-9} \times 1.2}{16.8 \times 10^{-9} \times 1.434 \times 10^8}$$

$$= \frac{\pi 82.81 \times 1.2}{24.1 \times 10^6} = 12.94 \times 10^{-6} \text{ lb-sec/in.}$$

$$12.94 \times 10^{-6} \times 386 = 0.00500 \text{ lb/sec}$$

Total air flow for system

$$Q_{tot} = 0.00535 + 0.00535 + 0.00500 = 0.0157 \text{ lb/sec}$$

This shows that the flow required is within the capability of the existing facility and with small adjustment to these figures, due to the difference in gas viscosity and gas constant, may be made to apply to nitrogen. Both air and nitrogen are available at the launch pad and are suitable for use.

APPENDIX HH

REENTRY TRAJECTORIES

In evolving a rational design, reentry environment is probably the strongest factor involved since overall weight and shape are decidedly influenced. Environmental factors under consideration include the highest g load, peak aerodynamic heating rate and total heat absorbed. It is well known that steep and fast entries result in maximum loads and heating rates while shallow entries at high speed produce long heating pulses.

This section extricates those entry conditions that result in design trajectories for the RB.

1. Ascent Trajectory Implications

In the booster family under study (Titan IIIA, IIIB and IIIC), it becomes necessary to examine the relative importance as to their contribution to the design. The object is to logically reduce, if possible, the number of launch vehicles to be studied. To begin with, it is pointed out in Chapter IV that the Titan IIIC configuration exhibits the longest liftoff-to-injection range of the three vehicles. This fact alone must be heavily weighed since, in essence, it has dictated the abort impulse requirement of 1500 fps. However, in Fig. HH-1 it is observed that altitude differences between ascent profiles are quite large. Part of the difference can be directly attributed to the fact that Titan IIIA and Titan IIIB, as presented here, do not have the same uprated core as the Titan IIIC. It is expected that, with the same core element, these differences would be reduced, but trajectories with the uprated core were not available during this study. Even though it is anticipated that the inputs that generated the results of Fig. HH-1 will be improved, it will be shown subsequently that the Titan IIIA and Titan IIIB ascent profiles, as shown here, do not significantly alter the design inputs.

This is demonstrated in Fig. HH-2 which takes the Titan IIIA and compares the entry conditions as influenced by the abort application angle, δ, with Titan IIIC. The major difference in entry occurs below a velocity of 22,000 fps when $\delta = 180°$. Once the vehicle is injected into the transfer orbit, launch vehicle dependency no longer exists. Note that for the entire spectrum of δ ($90° \leq \delta \leq 180°$) as applied at perigee, γ_{max} of the transfer trajectory, and at the apogee point of transfer, the case of $\delta = 180°$ at the apogee point is by far the most critical steep entry. It is further noted that regardless of the application angle during the Titan IIIA trajectory, the aforementioned critical point remains as such. The maximum g load indicated for this design point is on the order of 25 g, which signifies that the maximum heating rate will also be experienced for this entry.

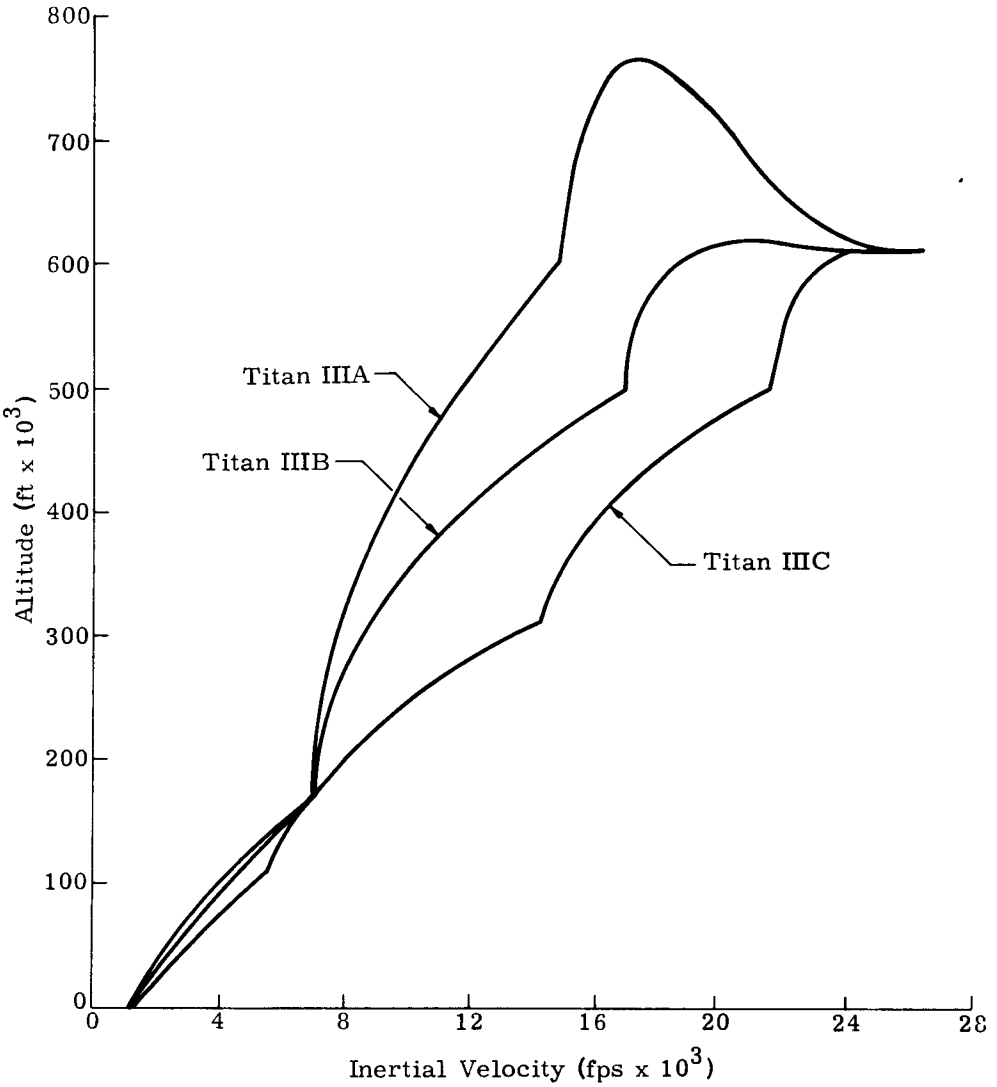

Fig. HH-1. Launch Vehicle Trajectory Comparison

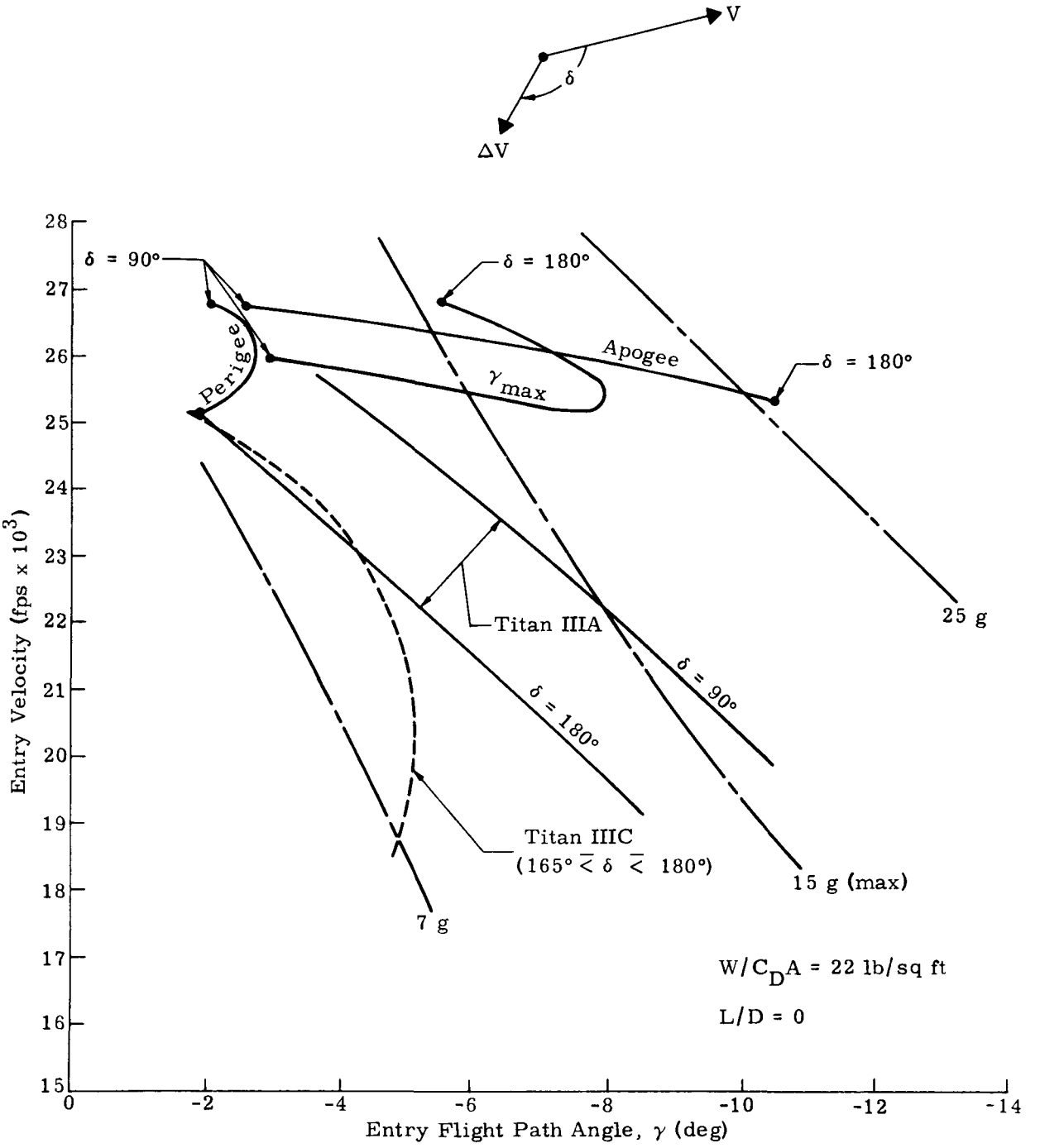

Fig. HH-2. Comparison of Entry Design Criteria

The criterion establishing this abort case rests on the design philosophy that call-down capability will exist at any point in the profile. For this case, apogee call-down can be initiated, with subsequent impact being in the Pacific and Arctic Oceans, respectively.

Thus far, no mention has been made of the difference in the local pitch attitude of the launch vehicles and the significance that this might make with regard to range control. Figure HH-3 has been prepared to specifically illustrate this consideration. This figure, first of all, shows that the local flight path angles for all launch vehicles are within 5° of each other above a flight speed of 10,000 fps. Secondly, the offset angle (α) measured between the velocity vector and booster centerline is within three degrees for speeds up to 15,000 fps. For speeds above 15,000 fps, up to 13° difference is noticeable. However, range control is not a problem for speeds less than 24,000 fps (Ref. Appendix LL) and, consequently, the differences that do exist up to this speed are of no concern. More important is the variation of α as injection is approached. Observe that δ = 180° as Titan IIIC approaches injection, but that δ = 173° for Titan IIIB and 165° for Titan IIIA at injection. From Fig. HH-2 it was shown that δ's less than 180° at injection provide a somewhat greater range control and, therefore, the remainder of this discussion will concentrate on aborts from the Titan IIIC vehicle as a satisfactory origin for design criteria.

2. Ballistic Entry Trajectory Summary

Using the Titan IIIC ascent trajectory, aborts were performed which directed their thrust along the launch vehicle's centerline in the aft direction ($165° \leq \delta \leq 180°$). The abort pulse magnitude is 1500 fps and the RB aerodynamic characteristics are:

$L/D = 0$

$W/C_D A = 22$ lb/sq ft

Nose radius = 6.1 ft.

Figure HH-4 presents a summary chart that shows the maximum load factor, g, encountered for an abort along the boost and transfer orbit as a function of time into the flight phase. All trajectories are point-mass and do not include dynamic effects. The figure also indicates the case of $\Delta V = 0$, which is nothing more than a separation from the launch vehicle. This case is shown up to a speed of 25,000 fps since impact points are acceptable up to this point, and ΔV application does not become necessary.

Actually, the design philosophy chooses to abort with ΔV = 1500 fps at all times because of the inherent simplicity in mechanizing the sequence of events. However, all physically realizable conditions are covered in the environmental criteria.

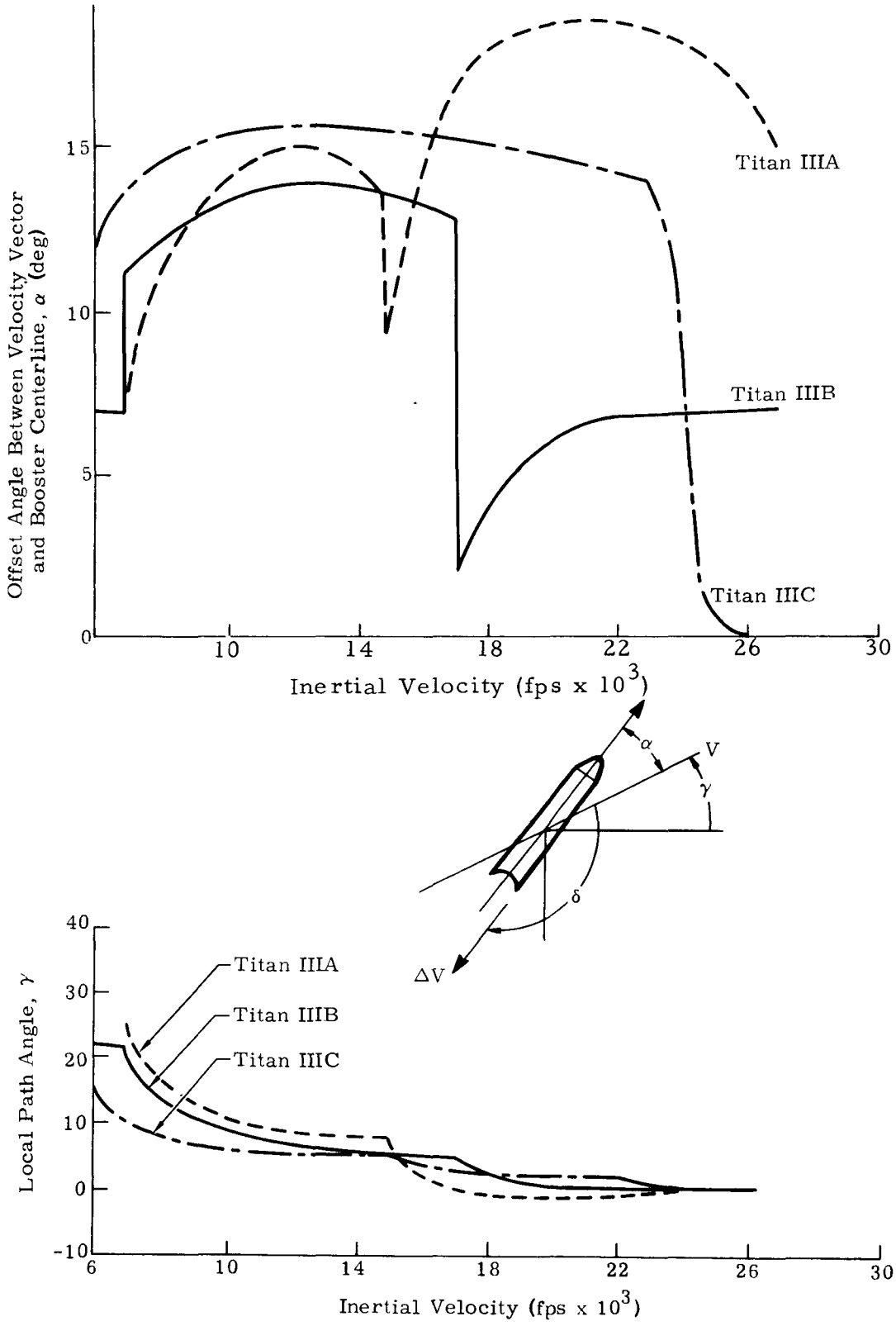

Fig. HH-3. Attitude and Trajectory Characteristics of Launch Vehicles

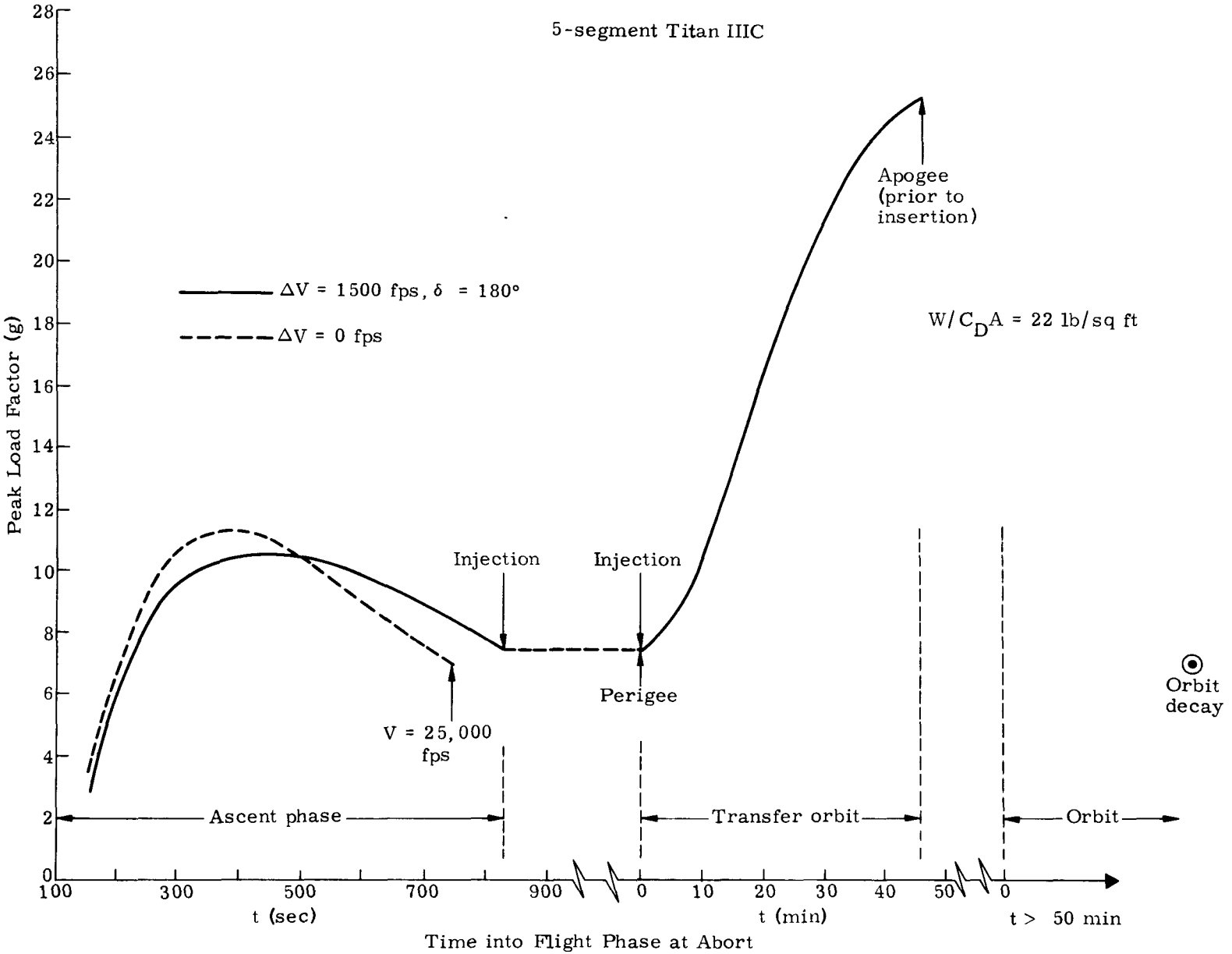

Fig. HH-4. Maximum Abort Load Factor Encountered in Flight Profile

The peak load factor encountered during the ascent phase is 10.7 g and occurs at an abort flight time of 460 seconds. Of more significance is the transfer phase, wherein the maximum load factor continually increases until the apogee point is reached. Abort from this point results in a g_{max} of 25.5, and the abort flight time occurs 45.6 minutes after injection. Call-down from a 600 by 600 nautical mile orbit or an orbit that has decayed because of drag results in peak gs of 17.3 and 7, respectively.

Figure HH-5 shows the maximum heating rate of 95 Btu/sq ft-sec and, as expected, the critical abort point is again the apogee point.

In Fig. HH-6 for the ascent phase, a maximum heat load of 4800 Btu/sq ft is experienced when the abort is made at perigee. For a normal call-down this heat load decreases to 3333 Btu/sq ft. But in the event a failure occurs in the CIR system (e.g., insufficient thrust) the RB may enter an orbit that decays within the half lifetime of the fuel element; then the RB will experience extremely shallow entry angles. For this situation, the maximum heat load is 10,680 Btu/sq ft and becomes the design entry condition.

Table HH-1 summarizes the initial conditions and the resulting entry conditions for aborts with ΔV = 1500 fps from a Titan IIIC trajectory.

The initial angle of attack that the vehicle would have upon entering the atmosphere is α_R. Appendix MM discusses the implications of RB dynamics as influenced by α_R and initial axes rates and demonstrates the effectiveness of the RB's inherent stability to control these offsets and rates.

Figures HH-7 through HH-10 present detail time histories for the critical design entry trajectories of q_{max}, g_{max} and Q_{max}. Additional trajectories (Figs. HH-11 through HH-16) represent cases of abort at perigee, normal call-down, and abort during the boost phase for a ΔV = 0 fps.

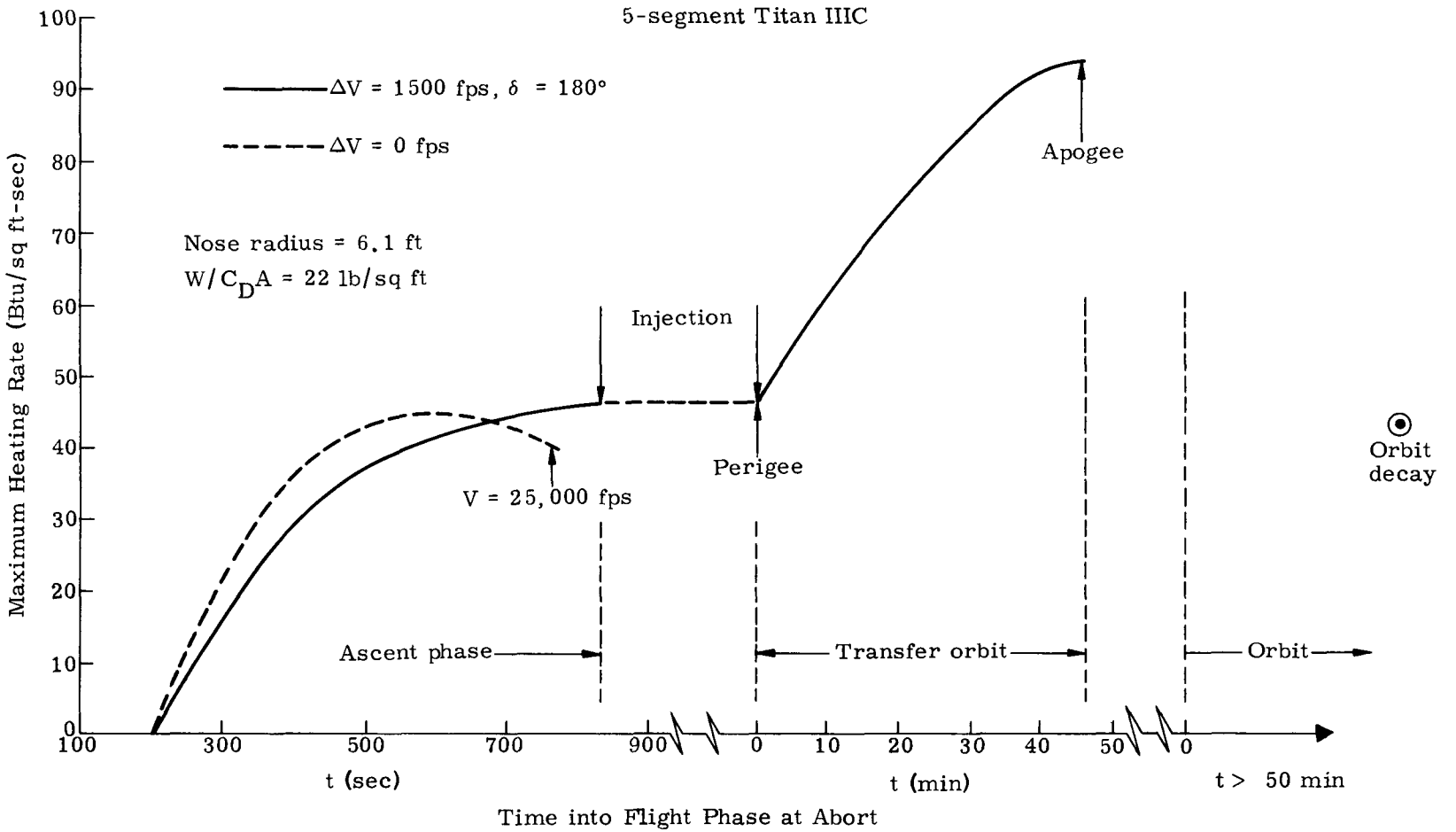

Fig. HH-5. Maximum Abort Heat Rate Encountered in Flight Profile

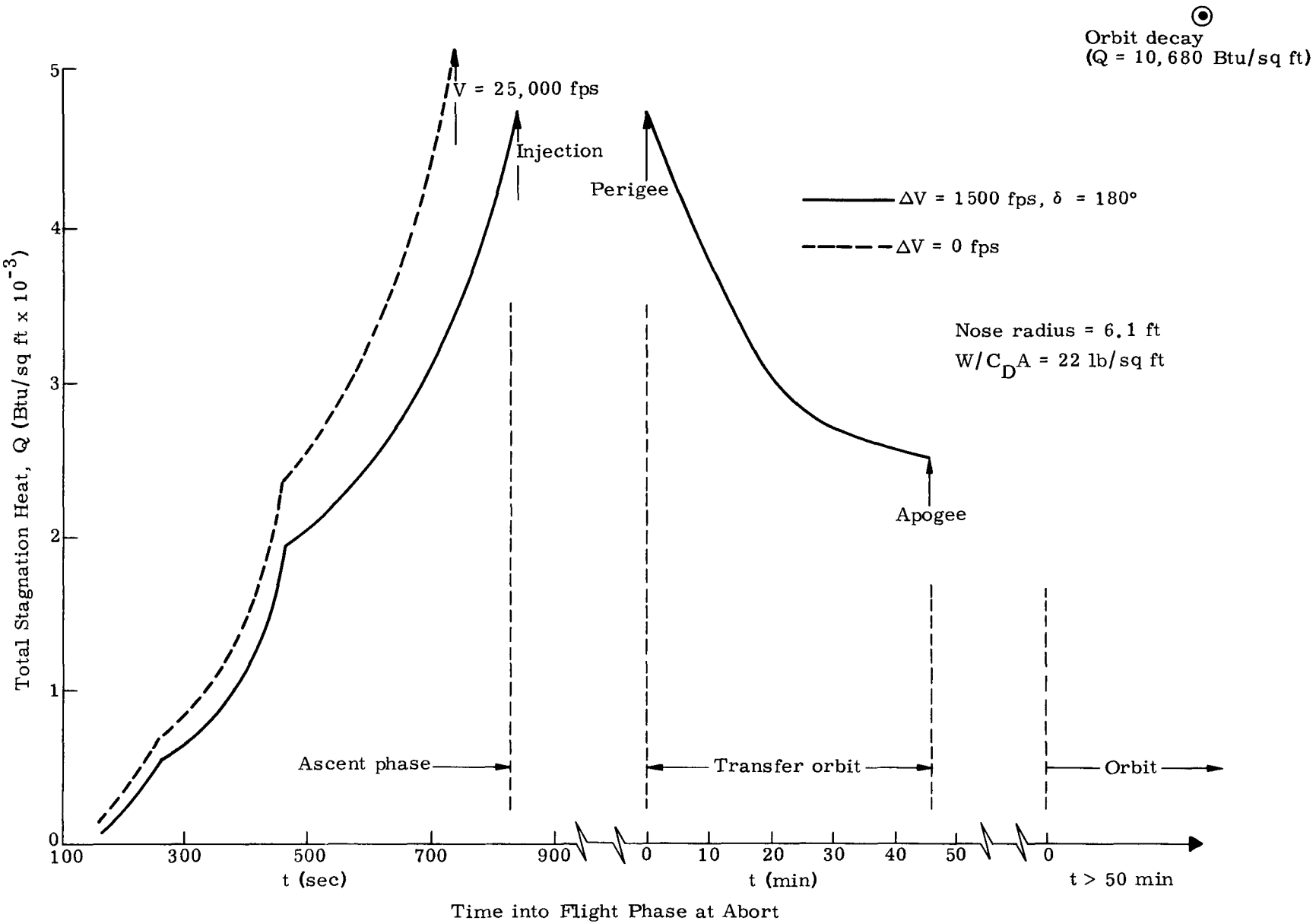

Fig. HH-6. Abort Heat Load Encountered in Flight Profile

The curves for g (acceleration) and q (dynamic pressure) are nearly identical except at the peaks.

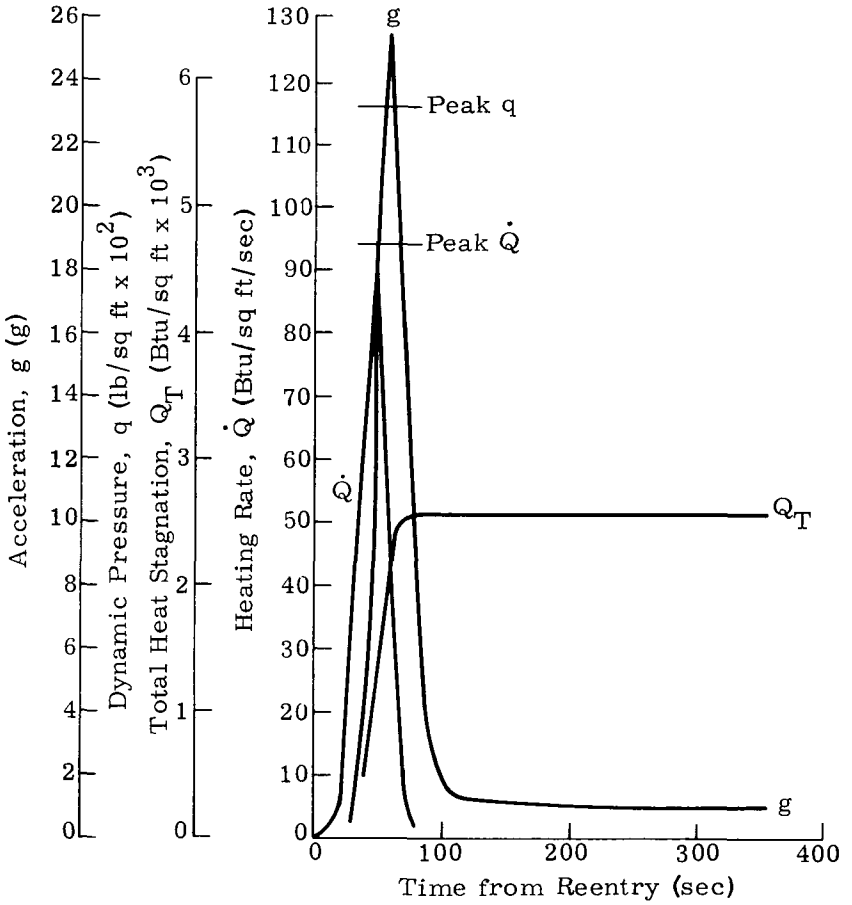

Fig. HH-7. Acceleration, Pressure, Stagnation Heat and Heating Rate Time Histories: Deorbit from Apogee = 600 Nautical Miles; ΔV = 1500 fps

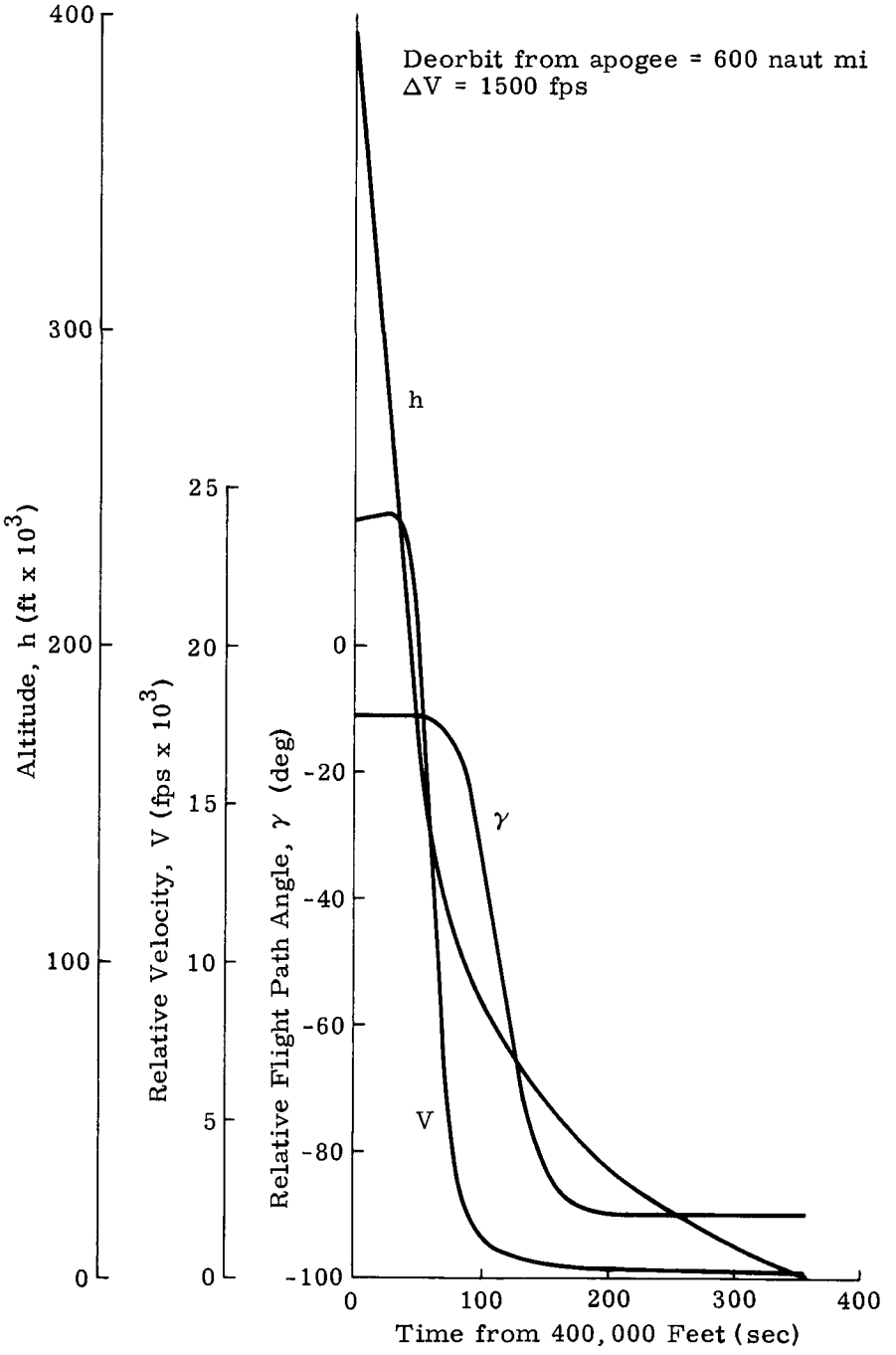

Fig. HH-8. Altitude, Velocity and Flight Path Angle Time Histories:

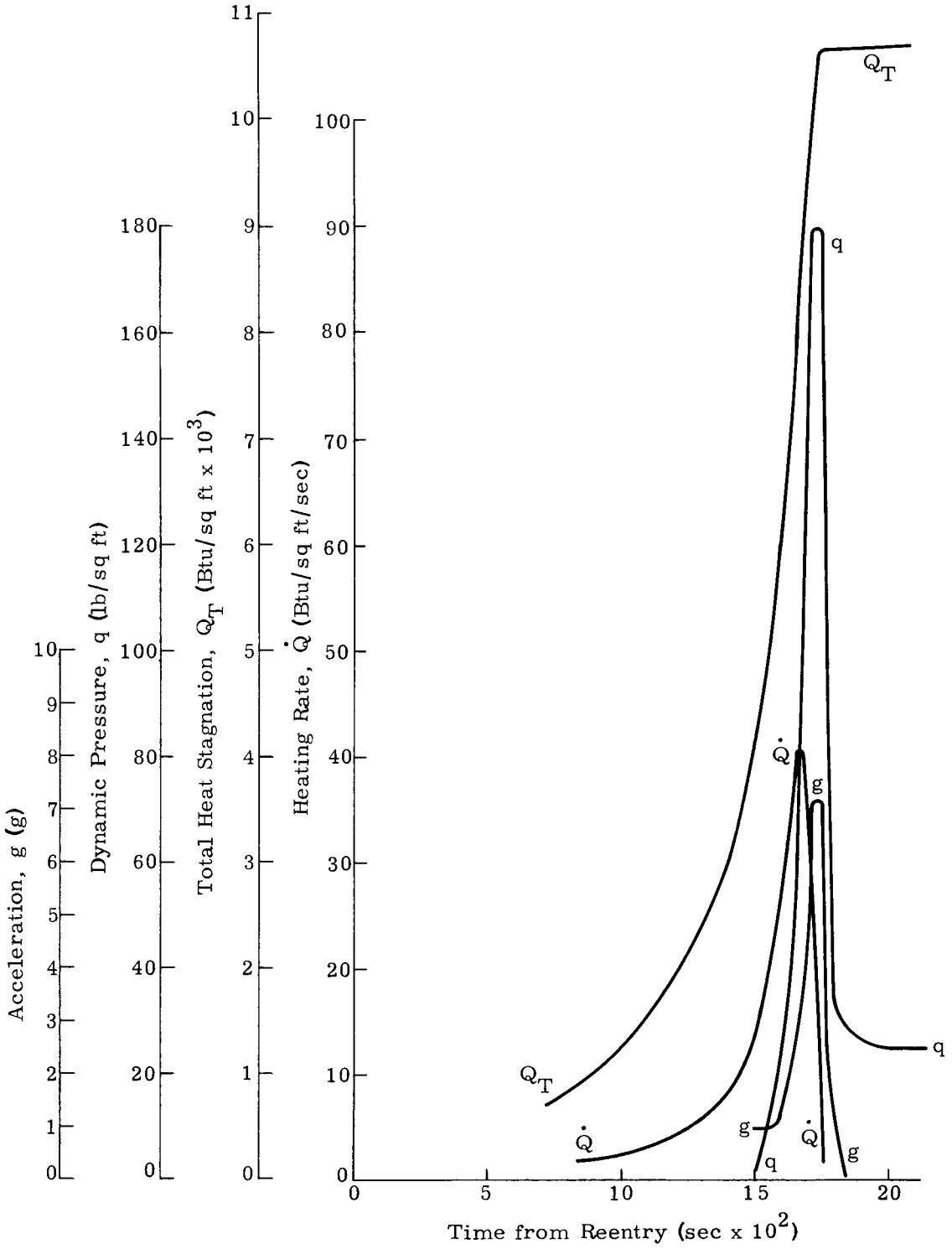

Fig. HH-9. Acceleration, Pressure, Stagnation Heat and Heating Rate Time Histories: Shallow Flight Path Angle ($\gamma = 0.1°$); Near Circular Velocity (V = 25,640 fps)

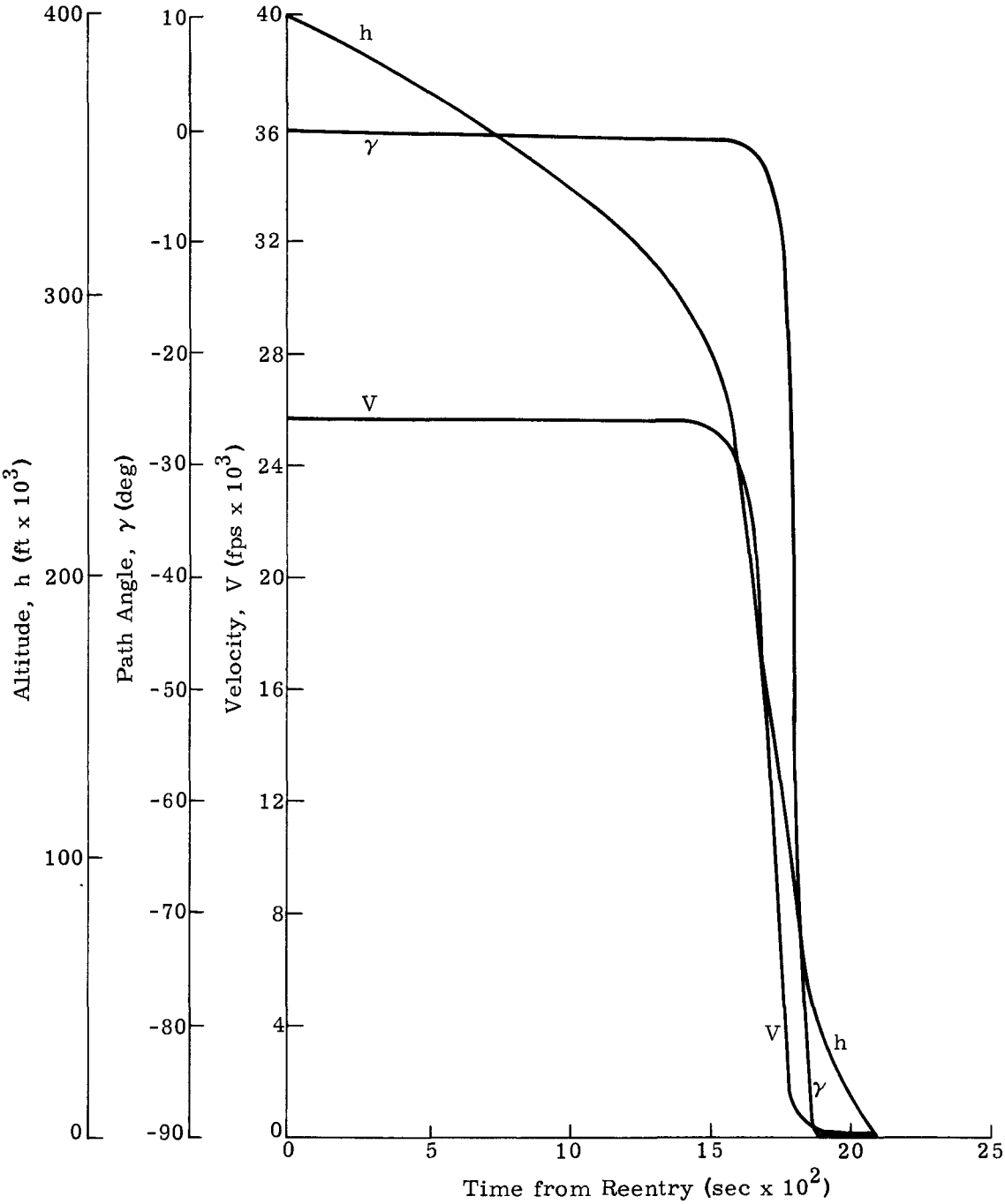

Fig. HH-10. Altitude, Path Angle and Velocity Time Histories: Shallow Flight Path Angle (γ = -0.1°); Near Circular Velocity (V = 25,640 fps)

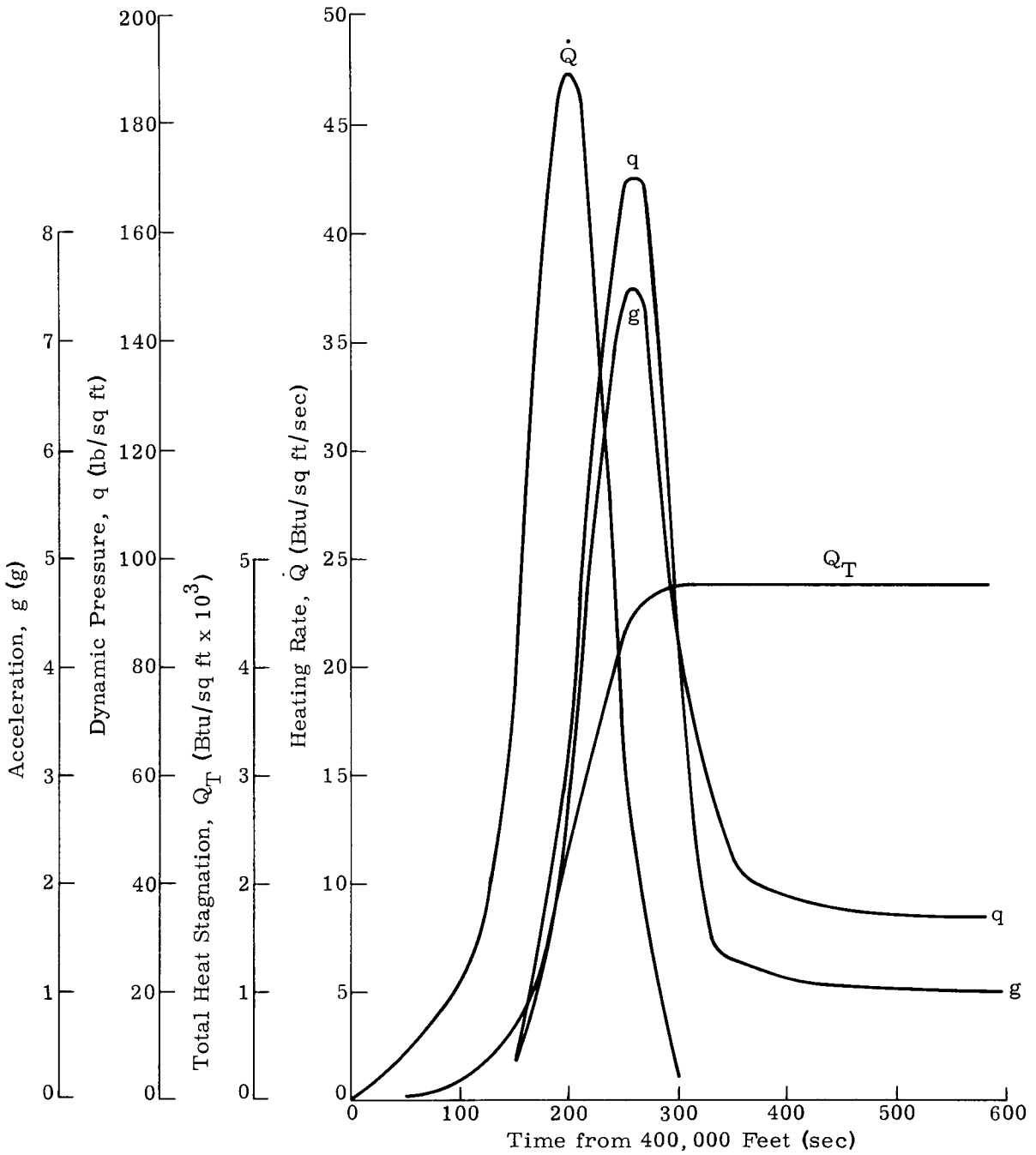

Fig. HH-11. Acceleration, Pressure, Stagnation Heat and Heating Rate Time Histories: Deorbit from Perigee = 100 Nautical Miles; ΔV = 1500 fps

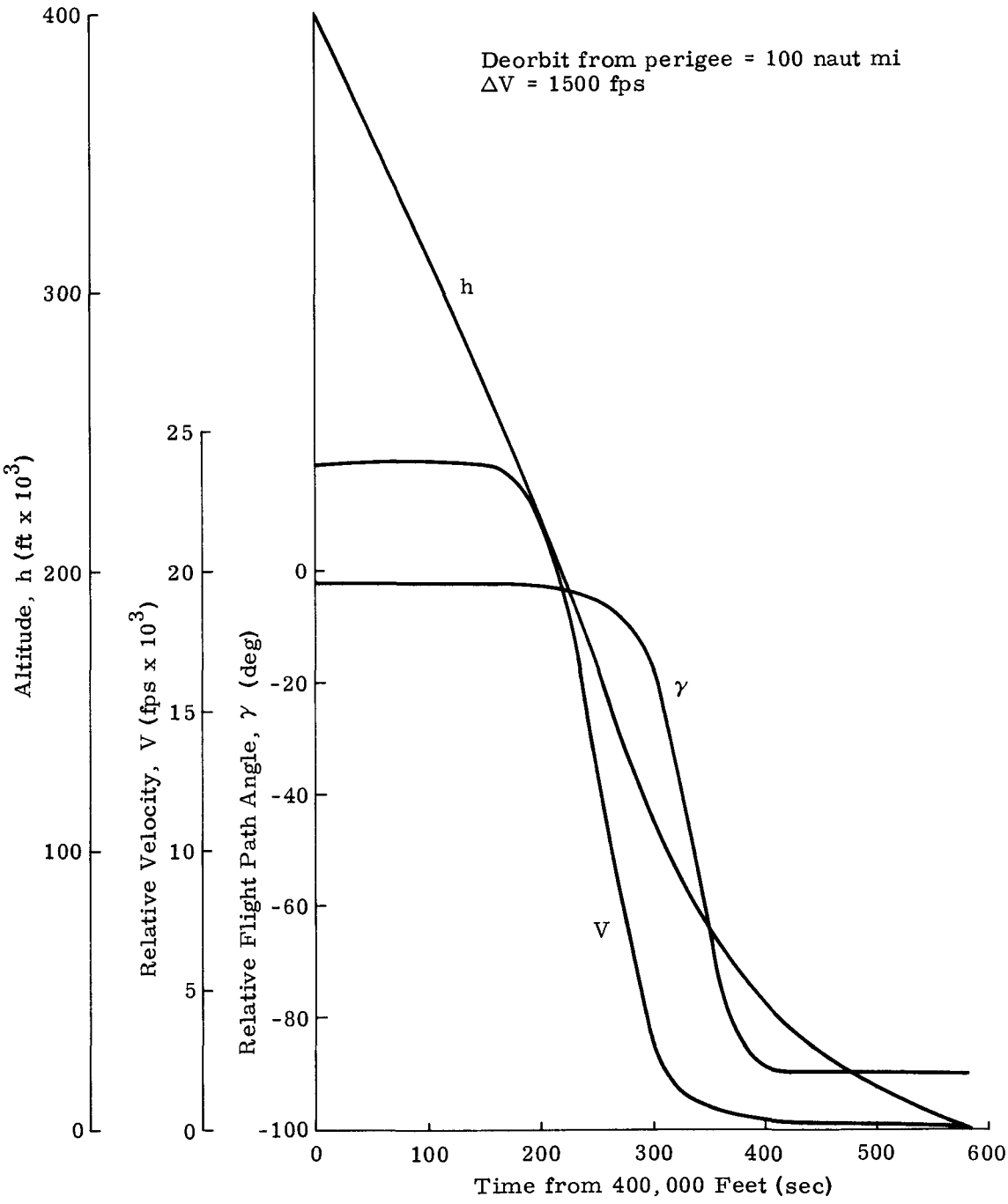

Fig. HH-12. Altitude, Velocity and Flight Path Angle Time Histories

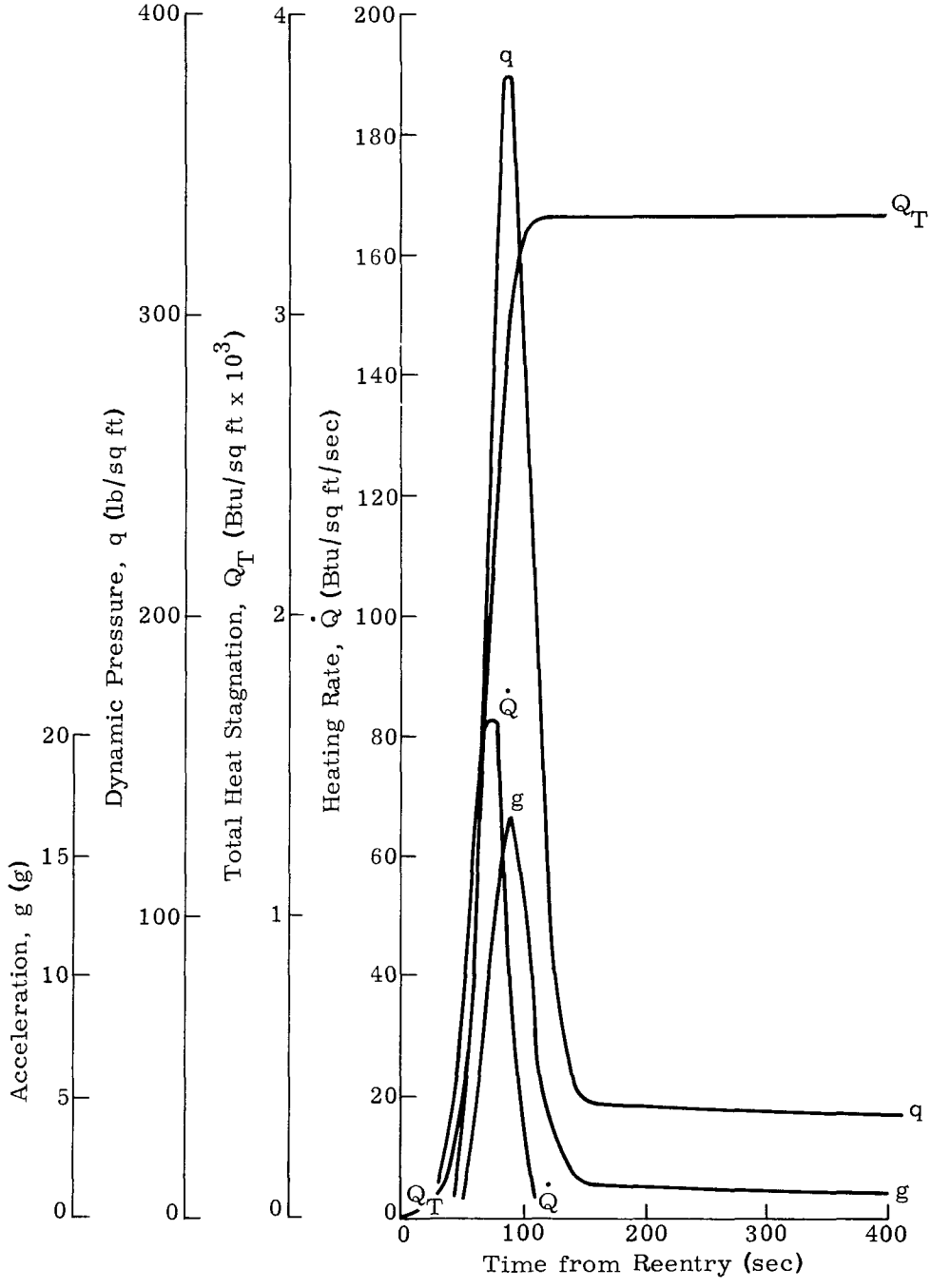

Fig. HH-13. Acceleration, Pressure, Stagnation Heat and Heating Rate Time Histories: Deorbit from 600-Nautical Mile Circular Orbit; ΔV = 1500 fps

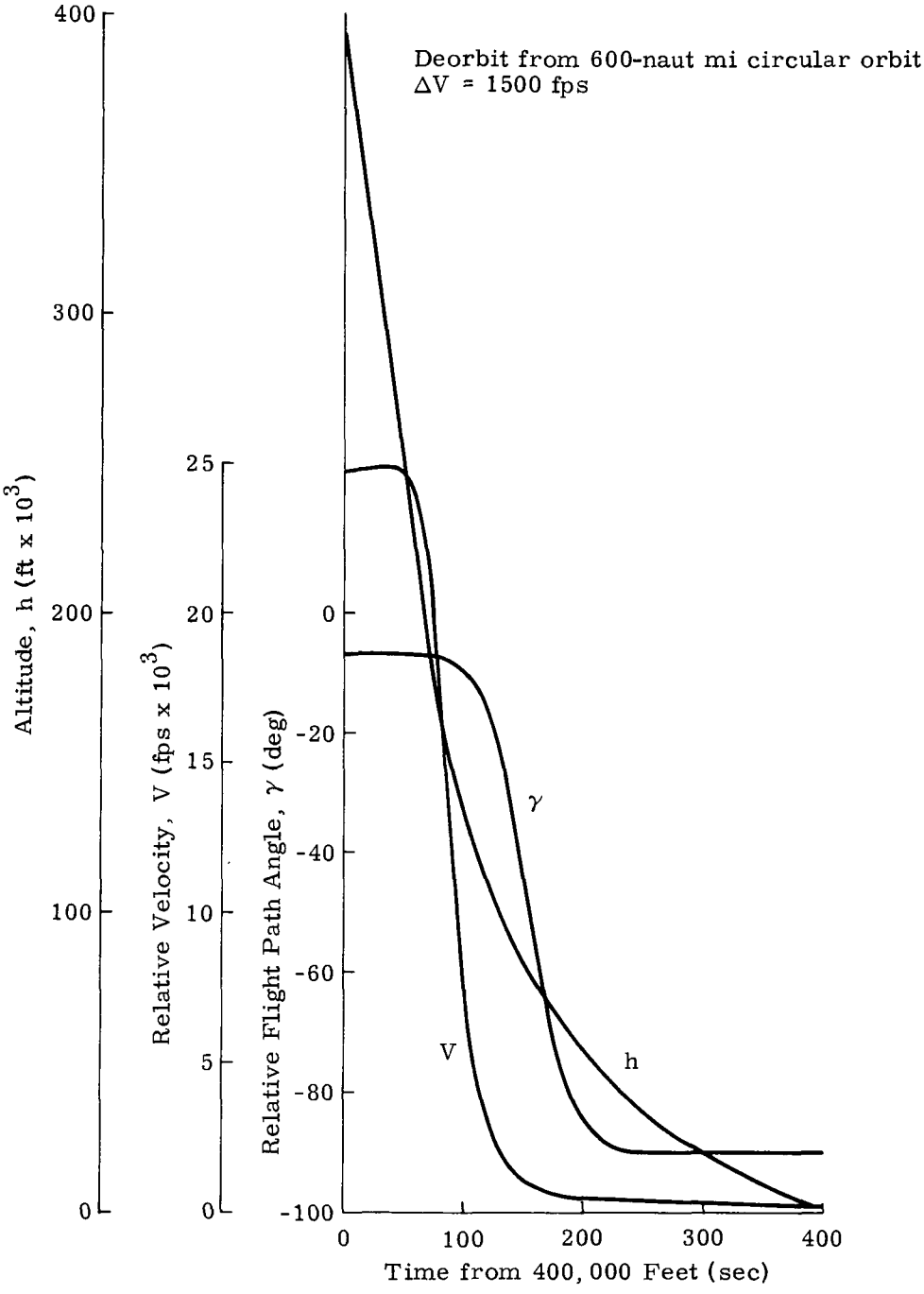

Fig. HH-14. Altitude, Velocity and Flight Path Angle Time Histories

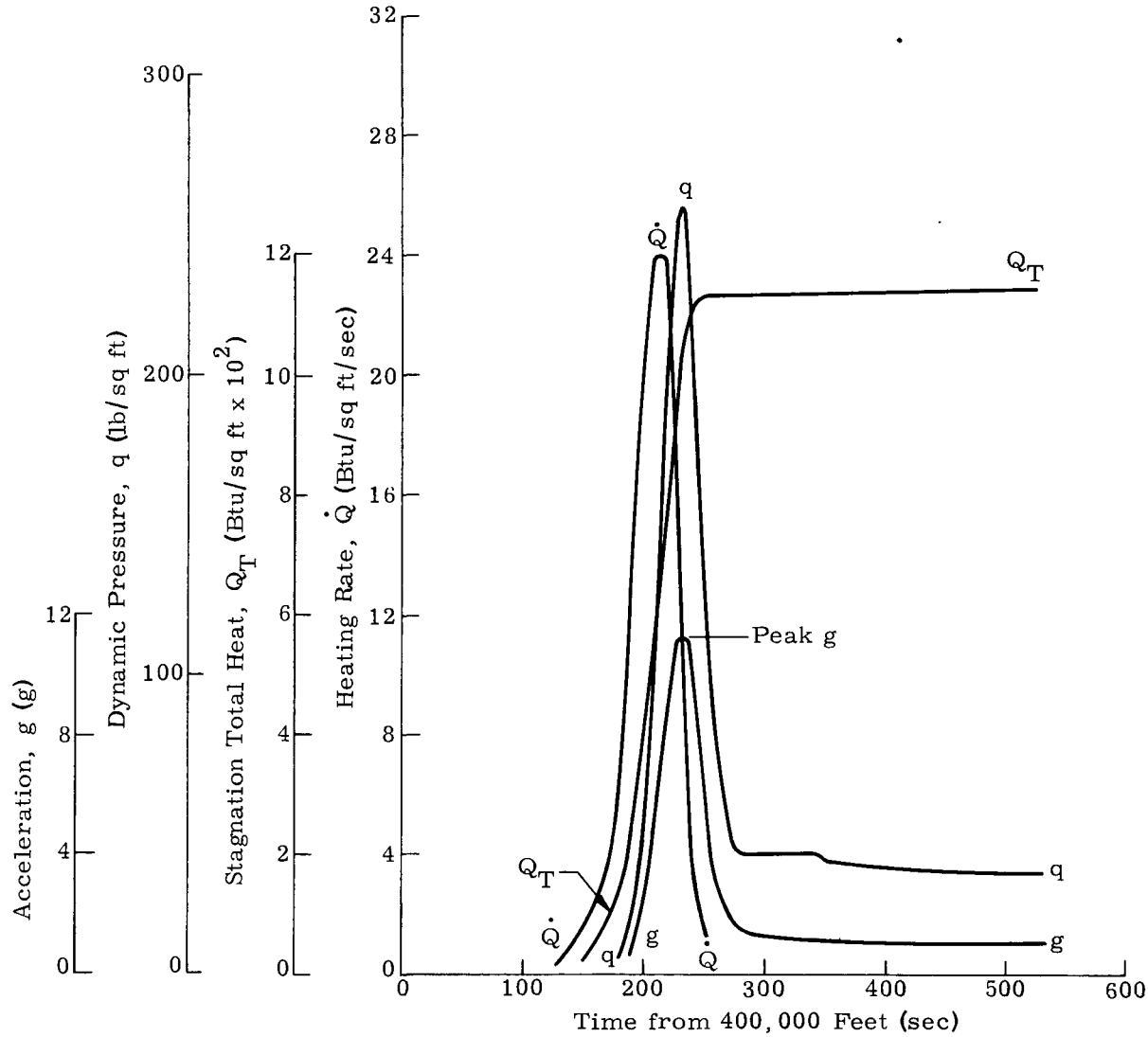

Fig. HH-15. Acceleration, Pressure, Stagnation Heat and Heating Rate Time Histories: · Abort During Boost; t = 360 sec; ΔV = 0

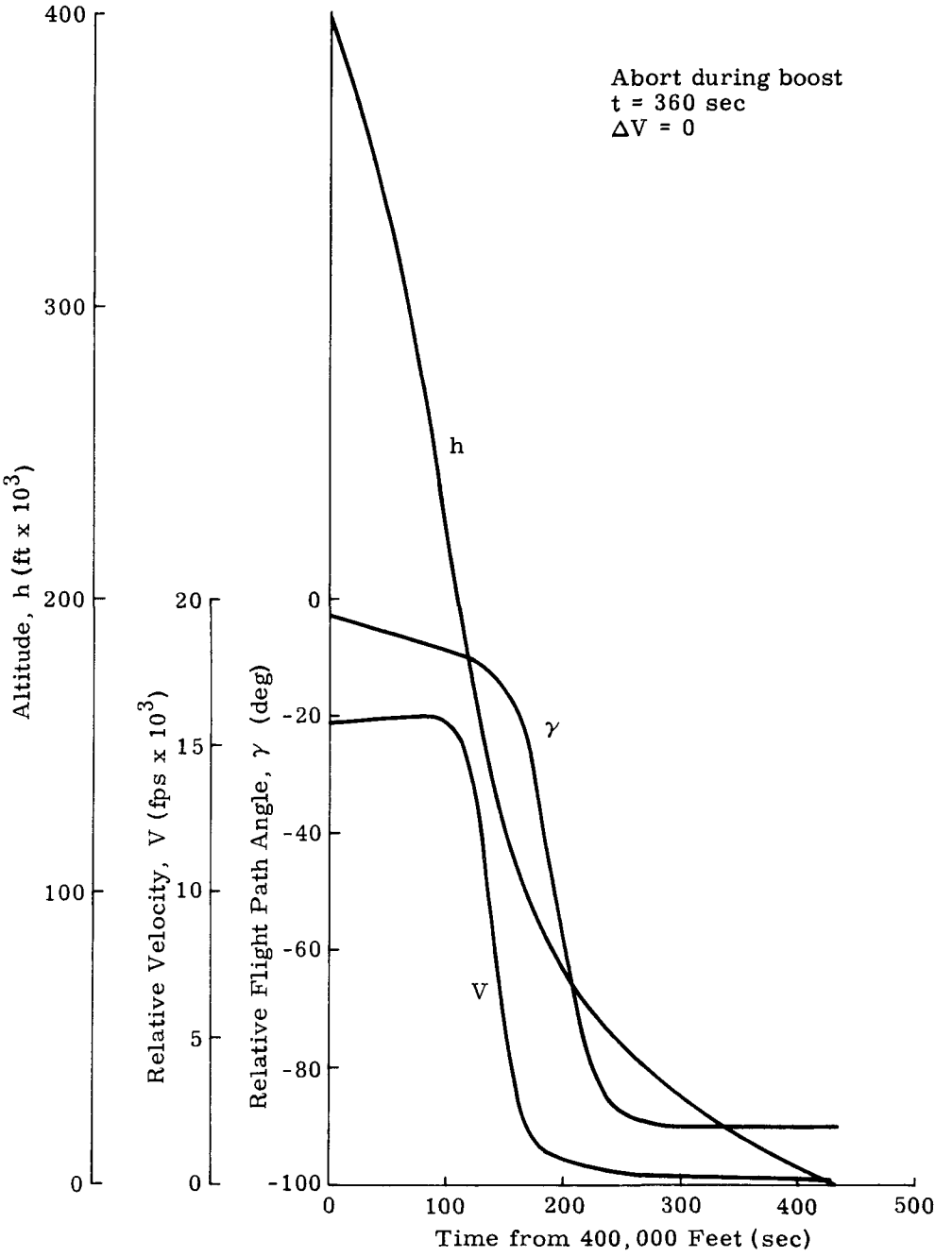

Fig. HH-16. Altitude, Velocity and Flight Path Angle Time Histories

TABLE HH-1

Abort Conditions

ΔV = 1500 fps
Titan IIIC, 5-Segment Ascent

Design Condition		Time into Phase	h_0 (ft)	V_0 (fps)	γ_0 (deg)	h_r (ft)	V_R (fps)	γ_R (deg)	α_R (deg)
		160 sec	191,099	7,561	9.74	191,099	6,127	+6.02	-164
	B	260	313,811	14,270	6.38	313,811	12,833	+4.56	-164
	O	360	424,605	17,126	2.61	400,000	15,753	-3.67	-214
	O	460	501,615	21,553	2.78	400,000	20,273	-4.65	-22.3
	S	560	607,887	23,709	0.422	400,000	22,504	-4.47	-18.5
	T	760	613,178	25,171	0.018	400,000	23,945	-3.22	-18.3
Yes		832	614,459	26,388	0.097	400,000	25,151	-1.8	-28.7
	T								
	R	7.6 min	787,448	26,190	1.785	400,000	25,163	-3.07	-72
	A	15.2	1,294,444	25,619	3.162	400,000	25,197	-5.24	-87.8
	N	22.8	2,026,540	24,818	3.77	400,000	25,244	-7.257	-85.7
	S	30.4	2,808,521	23,990	3.38	400,000	25,293	-8.94	-79
	F	38	3,415,613	23,365	2.00	400,000	25,330	-10.048	-70
Yes	E	45.6	3,645,665	23,132	0	400,000	25,344	-10.44	-60.5
	R								
Yes		Orbit	3,645,665	23,952	--	400,000	26,047	-6.71	-89.3

APPENDIX II

ABORT AND IMPACT AREA CONTROL

COMMUNICATION FACILITIES AND OPERATIONS

The launch vehicle assumed is Titan IIIC and two typical missions, one of 32° inclination launched from ETR and one with polar inclination launched from WTR, are described. The inclination of 32.2° was used for the ETR analysis since that was the only inclination for which Titan IIIC trajectory data were available. However, the impact points shown in the following sections use the 30° orbit inclination. The results for that orbit were extrapolated from the presented data. Range facilities utilized include tracking, telemetry and command from both ships and ground stations. The transtage of the Titan IIIC will contain a Malfunction Detection System mechanized such that it can effect the separation and spin stabilization of the CIR at any time after fairing separation. Application of the ΔV impulse will, however, occur only upon ground command via the S-band command system. The orbits assumed are both 600 naut mi circular orbits with injection directly into a transfer orbit of 100 naut mi altitude perigee. The critical phases of each ascent trajectory correspond to engine burning times. These periods are indicated in the sequence of events given in Table II-1 (timing is approximate).

Continuous range safety determination of the trajectory is required during this time such that quick reaction to failure may be obtained. During coast periods after injection into the transfer orbit the MDS may initiate abort but the CIR will not require continuous coverage and, in fact, controlled delay in deorbit becomes desirable to avoid impact on the various land masses over which the vehicle may be passing. A deorbit impulse from the transfer orbit is, however, mandatory since with perigee at 100 naut mi its lifetime is about one week and the descent trajectory difficult to predict.

The transtage will contain C-band tracking, UHF command and either VHF or S-band telemetry while CIR will contain a C-band beacon and S-band telemetry and command. The C-band system aboard the RB will be activated only at separation while the S-band system operates from launch. It is planned to pulse code modulate the RB C-band beacon signal to enable tracking facilities to immediately determine whether an abort separation has occurred. Range facilities required will include tracking and communications in the frequency bands mentioned and maximum utilization will be made of present or planned systems on the ranges, the Apollo Net and the Satellite Control Facility Net. The single exception is removal of the CIR command frequency from the range UHF net. This was

TABLE II-1

Nominal Sequence of Events (ETR Launch, 600-Naut Mi Circular Oribit)

Time (sec)	Altitude (ft)	Event
0	22.35	Lift-off
60	39,252	q_{max} = 875 lb/ft^2
106.5	109,848	Begin decay of solids (Stage O cutoff)
109.02	114,229	Stage I ignition
119.168	131,816	Separate solids
210.0	249,016	Jettison fairing (q = 3.23) lb/ft^2
259.125	312,431	Stage I burnout and separation Stage II ignition
461.11	502,769	Stage II burnout and separation
474.11	515,580	Stage III ignition (Transtage)
832	612,436	Cutoff transtage. Injection into 100/600-naut mi transfer orbit. Begin coast from perigee.
3832	3,645,600	Apogee of transfer orbit. Transtage ignition. Circularize orbit to 600 naut mi.
3900	3,645,600	Circularization complete. Begin attitude maneuver to separate payload.
4100	3,645,600	Separate payload. Mission complete.

specified in the interest of economy of equipment aboard the RB and because it is emphatically a reentry rather than a destruct system. Range safety requirements are still satisfied in that a destruct signal to the transtage over the redundant UHF link will cause abort of the CIR for controlled reentry.

Table II-2 indicates the availability of equipment on both the WTR and ETR. For the tabulation, SGLS and USBS equipment are considered equivalent since modification to either to accommodate the other's uplink frequency and command code are feasible. Compatibility of the present project with scheduled usage of these equipments must be investigated. It will be noted that extensive use is made of the Apollo ships for coverage of the polar launch. This is because continuous coverage is required for orbit prediction in the initial launch phase and because command must be provided for deorbit in the South Atlantic. Figure II-1 shows the coverage, timing and impact areas from selected abort situations. In each case, at least part of the descent trajectory of an aborted RB is covered by tracking adequate to establish impact within close tolerances. Coverage of all possible cases would necessarily be continuous and would, in any case, be difficult in the last 500 naut mi because of ionization.

IMPACT AREAS SELECTION

1. ETR Launch

The ground track for the ETR launch (Fig. II-1) is adequately covered by the facilities indicated in Table II-2. Both UHF and S-band command are available. The impact area for an abort at 660 seconds is indicated by A of Fig. II-1; this is controlled by Antigua. Injection into the transfer orbit at 832 seconds is covered by an additional range tracking ship with command capability--the impact area resulting from controlled abort at this point is shown at B--just short of the African coastline. The additional range tracking ship will also provide the first data for orbit prediction which is relayed via radio-link to Ascension. From this point to Ascension, coverage is not required since the impact point would cross the land mass of Africa and because the vehicle will have successfully achieved coast. If automatic separation of the CIR, due to booster system malfunction, occurs between 660 and 832 seconds (completion of the transfer orbit injection phase), the separation is detected by Ascension and deorbit is commanded by that station to coincide with impact areas at C. Continued coverage of the coast phase is given by Pretoria (tracking time of 11 minutes), the Apollo Indian Ocean Ship and Carnavon. Deorbit execution in this area must, however, be carefully controlled because of possible impact in Indonesia. As it nears apogee, it will come within range of Carnavon 11 minutes before the circularization maneuver and

TABLE II-2

Equipment Availability

Station	C-band Tracking	S-band Tracking	UHF Command	S-band Command USBS or SGLS
ETR (32° inclination)				
1. Cape Kennedy	X	X	X	X
2. Grand Bahama	X	L	X	
3. Bermuda	X	X		X
4. Grand Turk	X	L	X	L
5. Antigua	X	X	X	X
6. USNS Twin Falls (TAGM 11)	X	X	X	X
7. Ascension	X	X	X	X
8. Pretoria	X			
9. Apollo Indian Ocean Ship	X	X	X	X
10. Carnavon	X	X	X	X
11. Guam (USBS)	X	X		X
12. Kwajalein	X	X	X	X
13. Hawaii	X	X	X	X
14. Pt. Arguello (Vandenberg)	X	X	X	X
WTR (Polar Inclination)				
1. Point Arguello	X	X	X	X
2. Point Mugu	X	X	X	
3. San Nicholas	X	X	X	X
4. Range Tracker (WTR Ship)	X		X	
5. Watertown (Apollo Ship 4)	X	X	X	X
6. Huntsville (Apollo Ship 5)	X	X	X	X
7. Johnstown (Apollo Ship 2)	X	X	X	X
8. Mahe	X	X	X	X
9. Anchorage	X	X	X	X
10. Hawaii	X	X	X	X

X = availability; L = limited availability

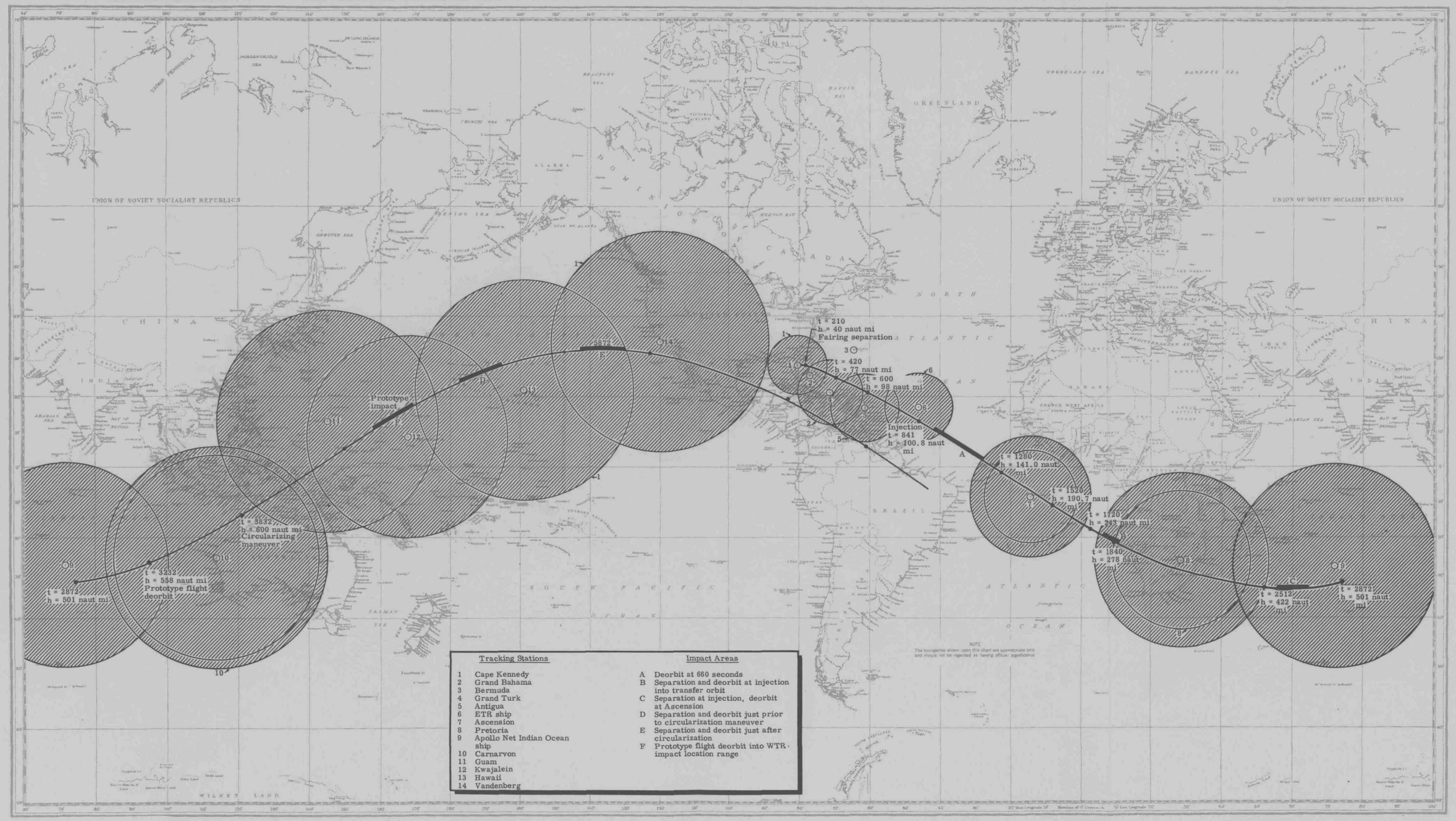

Tracking Stations		Impact Areas	
1	Cape Kennedy	A	Deorbit at 660 seconds
2	Grand Bahama	B	Separation and deorbit at injection into transfer orbit
3	Bermuda	C	Separation at injection, deorbit at Ascension
4	Grand Turk	D	Separation and deorbit just prior to circularization maneuver
5	Antigua	E	Separation and deorbit just after circularization
6	ETR ship	F	Prototype flight deorbit into WTR impact location range
7	Ascension		
8	Pretoria		
9	Apollo Net Indian Ocean ship		
10	Carnarvon		
11	Guam		
12	Kwajalein		
13	Hawaii		
14	Vandenberg		

Fig. II-1. Coverage, Timing and Impact Areas for Selected Abort Situations

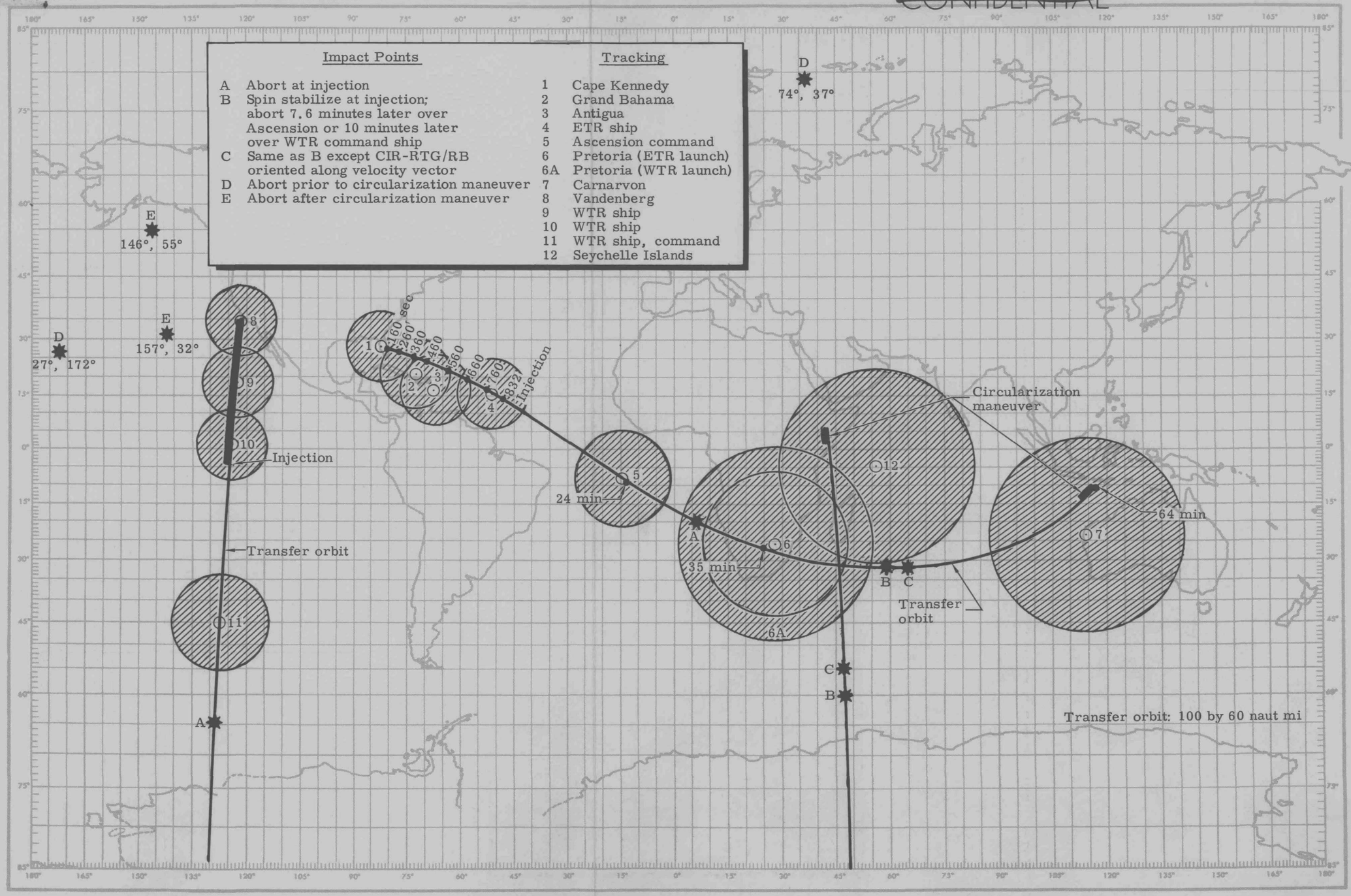

Fig. II-2. Titan IIIC Flight Profiles

will remain in range for five minutes after the maneuver. Carnavon may control abort and deorbit after the circularization maneuver with impact areas at D if initiation is conducted before circularization and E for post-circularization abort. Additional coverage for the latter case is provided by Guam. The proximity of D to the Hawaiian chain indicates the limit of the inhibited deorbit occasioned by the Indonesian archipelago and the island chains to the northeast. The vehicle has now achieved a 600-naut mi circular orbit and the transtage conducts an attitude maneuver and separates from its payload. Thereafter, it is not planned to attempt recovery of the Sr-90 fueled RTG. For the plutonium system, recovery may be accomplished from a stable vehicle for an indefinite period with nearly continuous tracking and command coverage from stations of the Apollo Net.

Several points may be made in favor of an ETR launch for development purposes. The proximity of the ground track to Kwajalein and Wake Island permits a test operation in which deorbit is initiated by the Indian Ocean ship and the descent trajectory is covered by the Press radar at Kwajalein, with impact location provided by installations at Eniwetok and Wake. Almost the full ascent trajectory is executed and complete test facilities are available in the impact area (F) for recovery if this is planned. In addition, the orbit passes over only Africa and is therefore optimum from the safety viewpoint.

2. WTR Launch

A similar treatment is given to a WTR launch which results in a polar orbit. It is evident that three tracking ships might be required for launch operations. The first two are required to augment Vandenberg during the ascent phase, while the third is essentially equivalent to Ascension. This last ship is located further downrange (45° S, 126.5° W) than Ascension because the Antarctic Ice Cap extends a greater distance than South Africa. For all abort conditions below injection speed, the retro pulse must be applied immediately after the abort signal is generated. It may be possible to alleviate this condition somewhat by locating the third tracking ship a little further downrange (50° to 55° S latitude). This will result in a minimum speed of 26,140 fps for delayed aborts but with impact points C and B approaching the coast of Madagascar. All impact points have been designated identically to their ETR counterparts on Fig. II-2.

From Fig. II-2, it is also shown that the tracking station located on the Seychelle Islands will monitor pre-injection and post-injection into the nominal 600-naut mi circular orbit. For an abort occurring prior to the circularization maneuver, the corresponding impact point (Point D), will be in the Arctic Ocean 74° N lat, 37° E long). Abort just after the circularization maneuver would result in an impact on Alaska, requiring a four-minute delay in applying the retro pulse to move impact to Point E (55° N lat, 146.5° W long).

IMPACT AREA DISPERSION CONTOURS

Abort pulse requirements for this analysis were assumed sufficient to produce a 1500-fps velocity differential; hence, controlled intact reentry of the RTG/RB. Appendix P presents the analysis techniques used to generate impact dispersions and their corresponding probabilities. Results of the dispersion analysis are summarized in this section. Dispersion patterns presented herein only represent a proper functioning of the CIR/RB within its tolerances and in no way reflect malfunctions in the abort system (e.g., failure of the deorbit retrorockets to operate).

Dispersion contours have been determined for each of the aforementioned impact points (A, B, C, D and E) by the analytic techniques reported in Appendix P. Additional contours have been computed for the various boost time points noted in Fig. II-2, for aborts from the transfer trajectory and, finally, for a normal call-down situation from the 600-naut mi circular oribit.

State vector covariance matrices and tracking covariance matrices associated with these points are given in Appendix P and are not repeated here. The $3\sigma\Delta V$ cutoff error is 1% of ΔV magnitude. A 3σ coning error of five degrees was assumed. These errors, taken with the state errors, were used to produce impact confidence ellipses by statistically propagating the errors.

1. Boost Phase

Figures II-3 through II-8 present the impact dispersions for aborts occurring at 160, 260, 360, 460, 660 and 832 seconds (injection). Each figure, except Fig. II-8, shows comparative impact zones with the application of ΔV= 1500 fps and with ΔV = 0 fps. The impact zone is bounded by an ellipse which denotes that the probability that impact will occur within the zone is 99%. Observe that the crossrange error is one to two orders of magnitude less than the downrange dispersion. An interesting observation is the increase in downrange dispersion from ± 40 maut mi at 160 seconds to ± 400 naut mi at 460 or 660 seconds, decreasing to ± 300 naut mi at injection. This expansion and contraction is attributed to the 3σ dispersion of the launch vehicle during ascent, and reflects the influence of the guidance system to reduce accrued errors prior to injection. All crossrange errors are on the order of ± 20 naut mi.

Noteworthy is Fig. II-8, which depicts the impact zone for an abort at the injection point. As predicted in Appendix LL, the maximum downrange dispersion is limited to ± 330 naut mi but to a greater confidence level (99% rather than 95%). Impact occurs before the western extremity of Africa, with sufficient allowance for dispersions; thus confirming the abort pulse requirement of 1500 fps.*

*1500 fps is sufficiently high. A lower ΔV might also suffice.

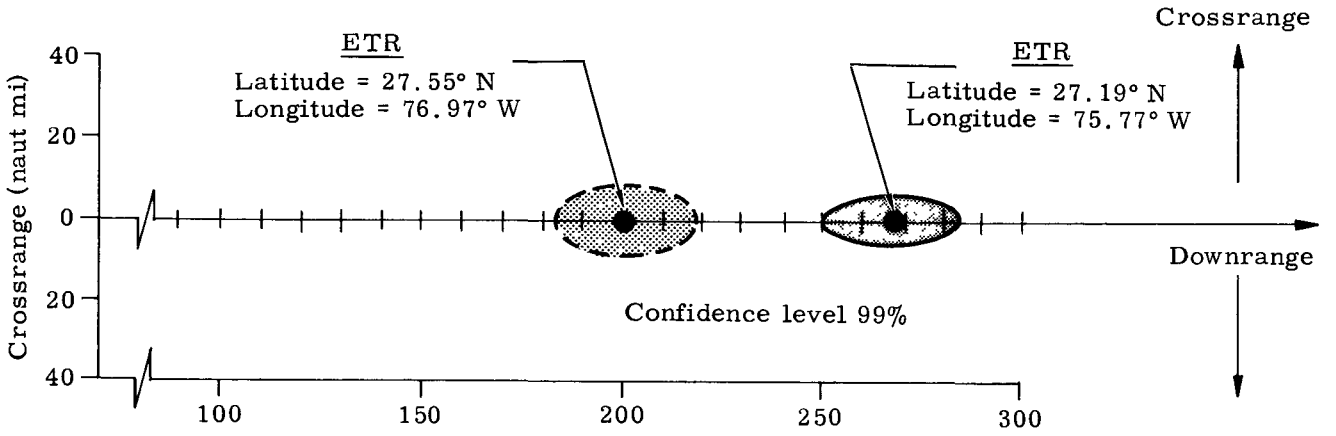

Fig. II-3. Impact Dispersion Boundaries (3σ): Five-Segment Titan IIIC; Launch Azimuth 106°; Abort Time = 160 Seconds

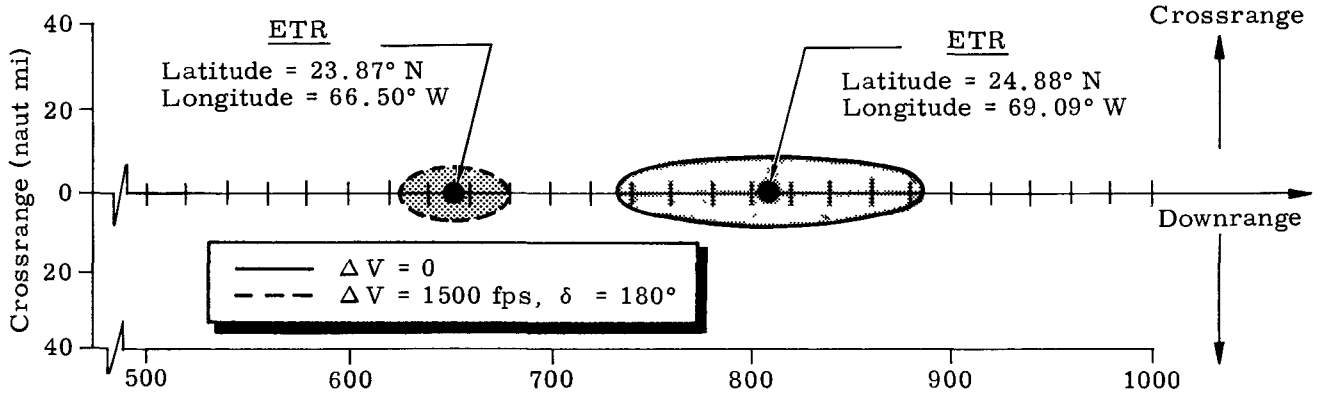

Fig. II-4. Impact Dispersion Boundaries (3σ): Five-Segment Titan IIIC; Launch Azimuth 106°; Abort Time = 260 Seconds

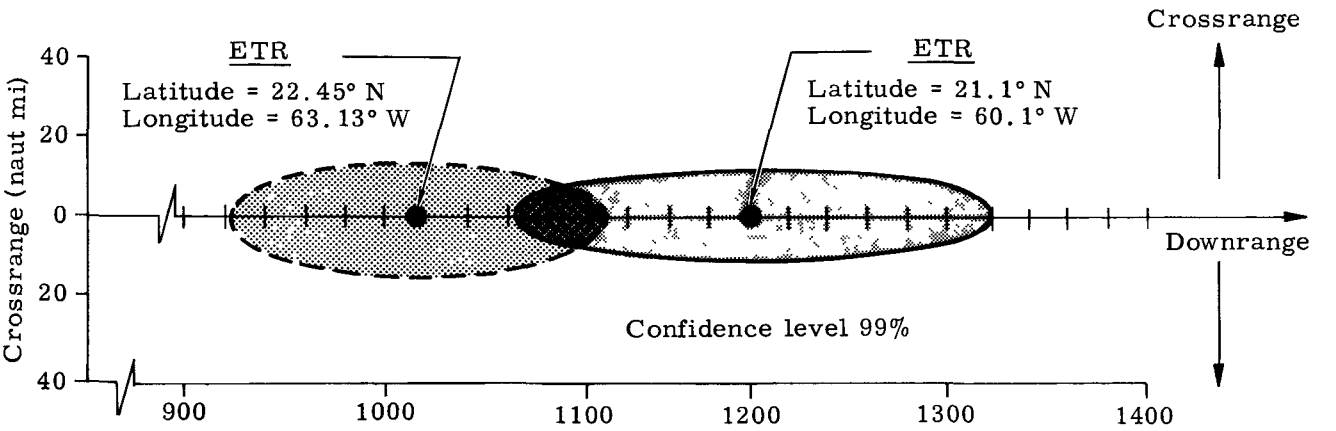

Fig. II-5. Impact Dispersion Boundaries (3σ): Five-Segment Titan IIIC; Launch Azimuth 106°; Abort Time = 360 Seconds

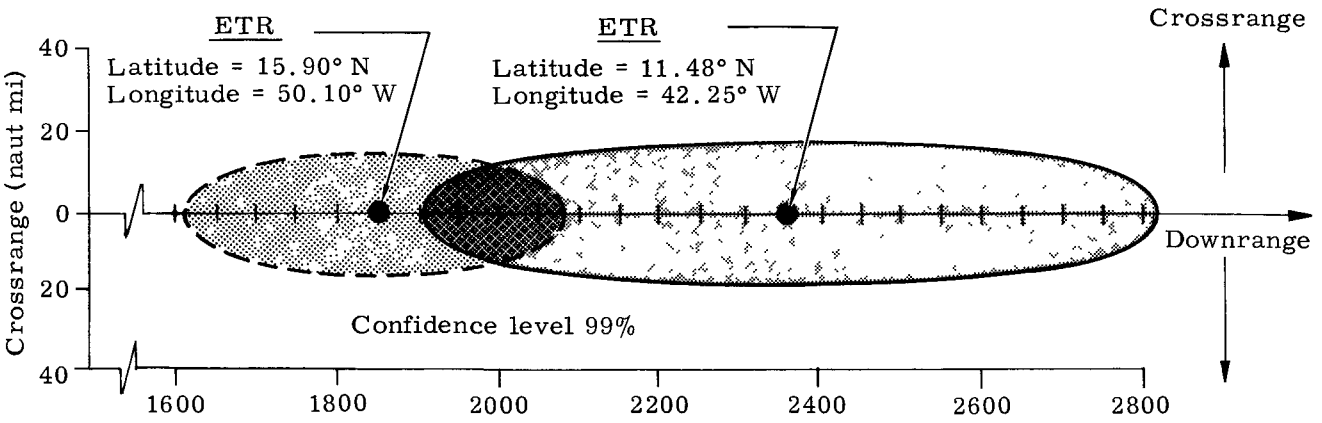

Fig. II-6. Impact Dispersion Boundaries (3σ): Five-Segment Titan IIIC; Launch Azimuth 106°; Abort Time = 460 Seconds

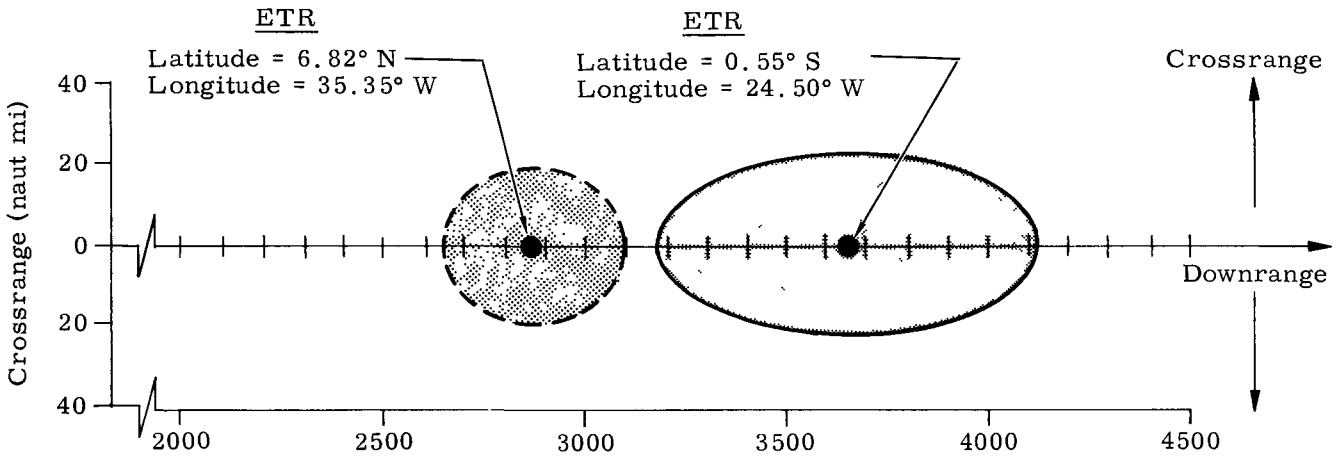

Fig. II-7. Impact Dispersion Boundaries (3σ): Five-Segment Titan IIIC; Launch Azimuth 106°; Abort Time = 660 Seconds

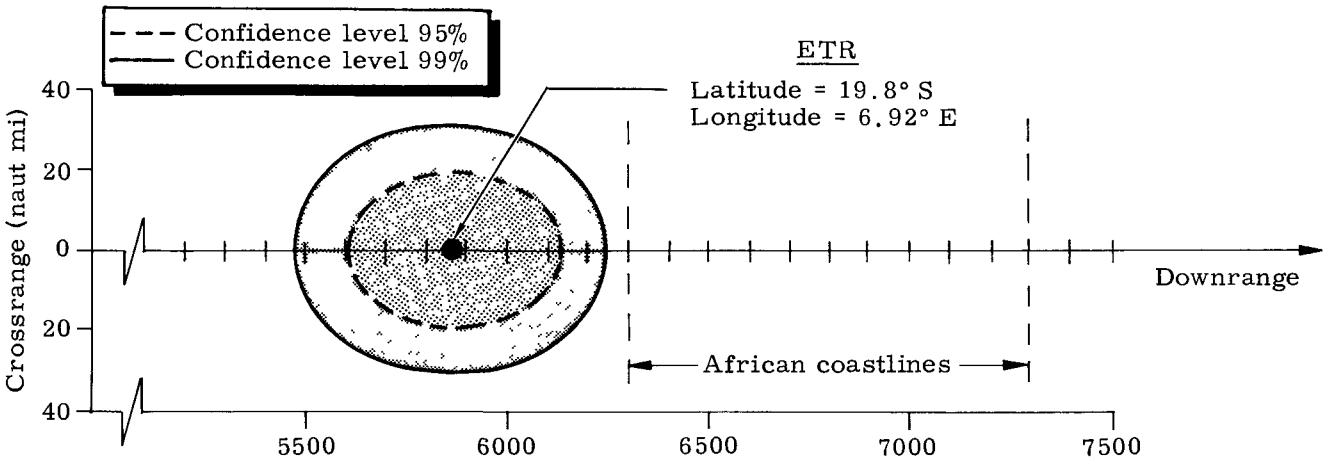

Fig. II-8. Impact Dispersion Boundaries (3σ): Five-Segment Titan IIIC; Launch Azimuth 106°; Abort Time = Perigee-Transfer Orbit

2. Transfer Orbit Phase

For this phase, although the guidance system may sense the injection errors and steer to a biased injection condition in an effort to compensate for these errors, injection differences are still treated as random errors. In other words, although a correlation may exist, injection errors are still considered random in nature. This approach will result in conservative estimates of the impact dispersions.

Figure II-9 presents the dispersions for abort pulses delayed 7.6 and 15.2 minutes after injection. These times correspond to 30° and 60° arc (Points B and C on Fig. II-2) travel in the transfer orbit. Two cases are shown, one for an RB spin-stabilized immediately after injection; and the other for an RB aligned with the velocity vector at the time of the abort pulse. Figure II-9 verifies that, for a vehicle spin-stabilized immediately after injection, the range to impact will be shorter because of the "automatic" drift of the ΔV vector to a more optimum application angle. However, the trend reverses itself as the coast continues beyond 30° because of two reasons. First, and most prominent, the altitude begins to increase rapidly and the abort pulse tends to deflect the flight path only rather than decreasing the orbital energy level. Figure II-9 indicates that delayed aborts, with spin stabilization, appear feasible only up to a coasting arc length of 60 degrees (15 minutes).

For spin-stabilized vehicles, the downrange dispersions grow from ±450 to ±800 naut mi but remain the same (±450 naut mi) for retro pulses aligned with the velocity vector. Aborts for this latter case, up to the point of injection, result in impacts less than ±400 naut mi.

Figure II-10 shows the impact dispersion corresponding to an abort executed just prior to injection into the circular 600-naut mi mission orbit (Point D in Fig. II-2). The 3σ downrange dispersion is ±380 naut mi and the crossrange is ±25 naut mi.

Figure II-10 also shows the impact dispersion for an abort occurring immediately after the circularization maneuver. Downrange dispersion is ±575 naut mi, and the crossrange dispersion is ±15 naut mi. This particular case can also be interpreted as the calldown accuracy for a normal deorbit situation.

For all practical purposes, the dispersions presented in Figs. II-3 through II-10 can be applied to the WTR launch profile as well. For convenience, the dispersions are numerically recorded in Table II-3, and the vehicle position and velocity errors are given by Table II-4.

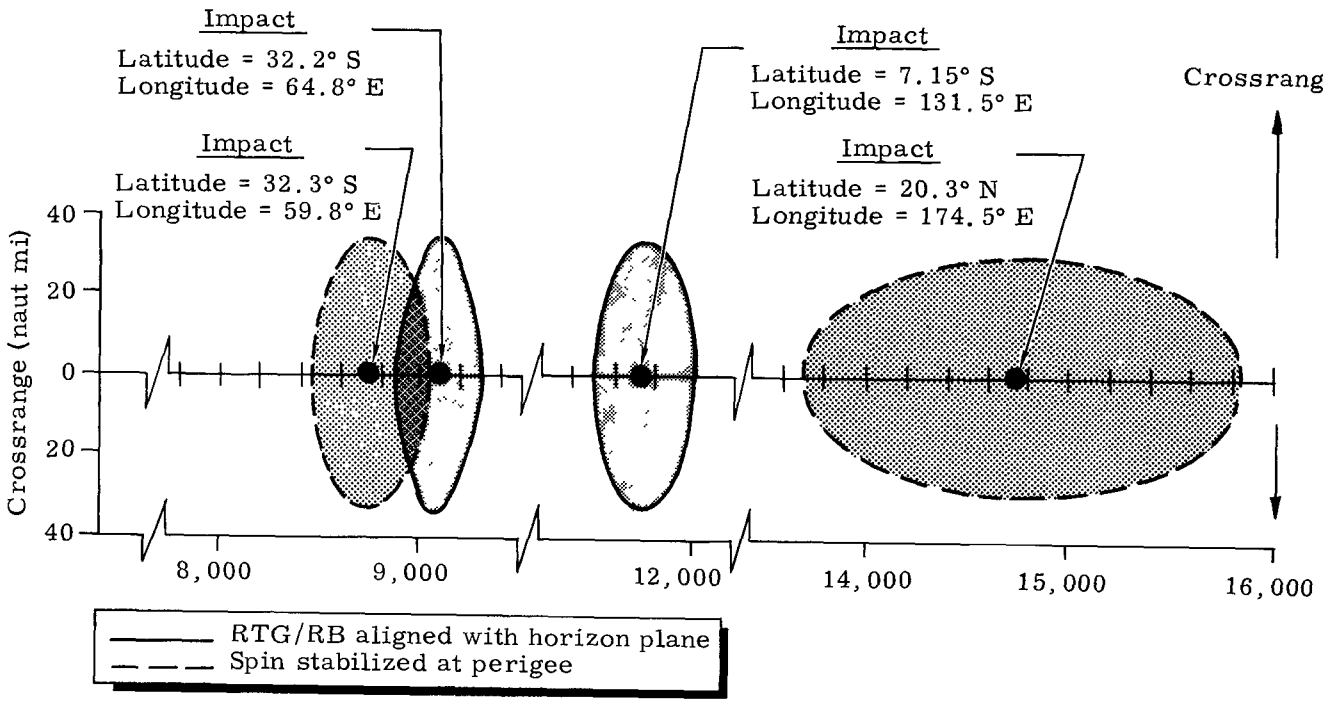

Fig. II-9. Impact Dispersion Boundaries (3σ): Five-Segment Titan IIIC; Launch Azimuth 106°; Abort at 30° and 60° from Injection

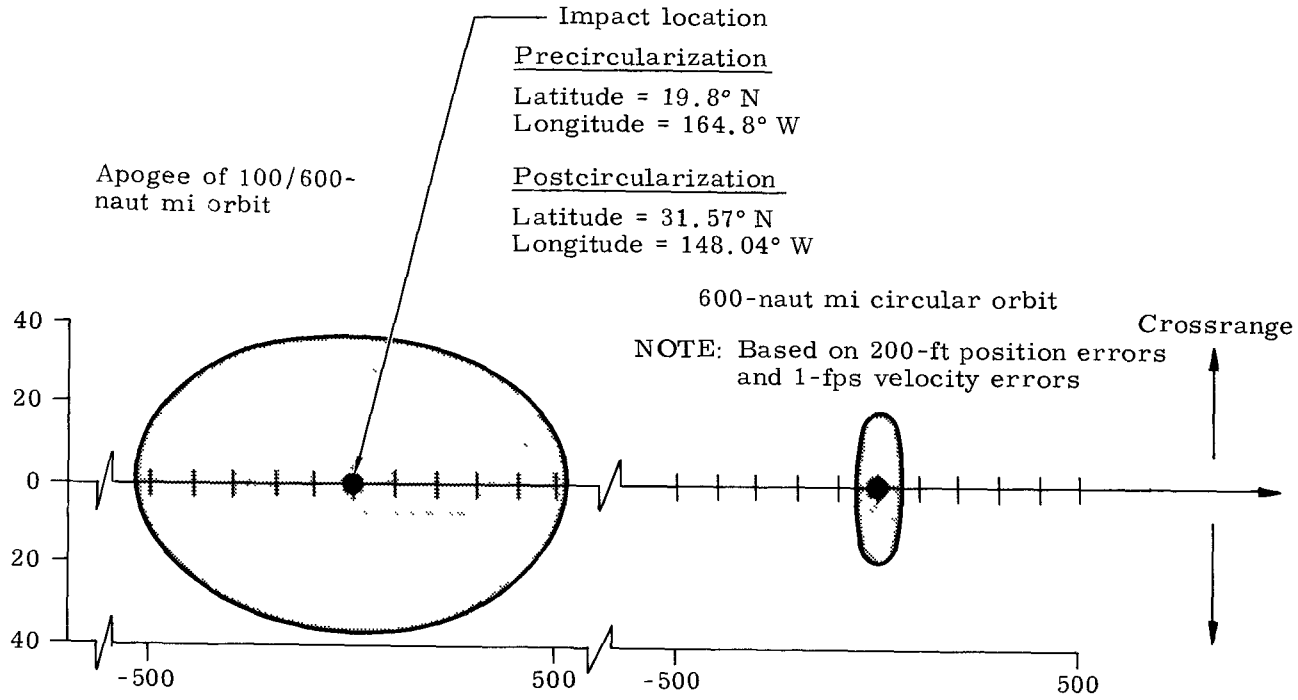

Fig. II-10. Impact Dispersion Boundaries (3σ): Five-Segment Titan IIIC; Launch Azimuth 106°; Calldown from 600 Nautical Miles

TABLE II-3

Three Sigma Dispersions in Impact Position
(0- and 1500-fps deorbit velocity)

Launch Phase

Deorbit Velocity, ΔV (fps)	Phase Time (sec)	Downrange Dispersion, ΔR_D (naut mi)	Crossrange Dispersion, ΔR_C (naut mi)	Reentry Time, t_R (min)
0	160	16	4	2.7
0	260	78	8	4.3
0	360	119	12	4.5
0	460	454	18	7.8
0	660	504	21	9.0
1500	160	18	8	2.3
1500	260	32	7	3.5
1500	360	94	14	3.7
1500	460	239	17	5.7
1500	660	225	19	6.7
1500	Injection 832	384	31	15.3

Transfer Orbit and 600-Nautical Mile Circular Orbit

Range Angle (deg)	Downrange Dispersion, ΔR_D (naut mi)	Crossrange Dispersion, ΔR_C (naut mi)	Reentry Time, t_R (min)
30	314	34	17.0
30 (spin stabilized)	208	34	12.0
60	237	34	18.6
60 (spin stabilized)	1060	31	20.6
90	218	36	22.2
120	217	37	23.5
150	285	39	23.6
180	526	38	23.0
Circular orbit *	50	19	30.0

* Assumes essentially no initial position or velocity error.

TABLE II-4

Three Sigma Dispersions for Launch, Transfer Orbit and Circular Orbit

Boost Time or Range Angle	$3\sigma_x$ (ft x 10^3)	$3\sigma_y$ (ft x 10^3)	$3\sigma_z$ (ft x 10^3)	$3\sigma_{\dot{x}}$ (fps)	$3\sigma_{\dot{y}}$ (fps)	$3\sigma_{\dot{z}}$ (fps)
160 sec	37	14	23	400	100	70
260 sec	106	29	19	1100	200	110
360 sec	221	47	17	1300	200	160
460 sec	351	67	2	1400	200	130
660 sec	732	78	2	700	200	60
Injection	1060	88	1	10	200	0.4
30 deg	1080	12	0	12	200	6
60 deg	1110	16	0	12	200	13
90 deg	1180	18	0	13	200	22
120 deg	1320	17	0	13	200	4
150 deg	1830	12	0	14	200	9
180 deg	3750	10	0	14	200	22
Circular orbit	0.2	0.2	0.2	1	1	1

APPENDIX JJ

REENTRY HEATING ANALYSES

The aerodynamic reentry heating analyses consist of the heating distribution over the conical afterbody (radiator) as a function of angle of attack, three typical reentry trajectories, and a discussion of results from the heat transfer analysis of the radiator for each trajectory.

AERODYNAMIC HEATING DISTRIBUTION

The aerodynamic heating distribution over the conical afterbody of the RTG/RB was obtained from Ref. JJ-1 for an angle of attack (α) range of 0 to 40 degrees. At higher angles of attack ($70° < \alpha < 140°$) these distributions were calculated by considering this conical afterbody as a yawed cylinder and correcting this distribution factor for the change in characteristic radius. Reference JJ-2 was used to obtain these results. Figure JJ-1 presents the heating distribution over the conical afterbody as a function of surface distance (s/s') and angle of attack ($0° \leq \alpha \leq 140°$). This nondimensional surface distance was defined as the ratio of local surface distance measured from the stagnation point on the blunt nose at zero angle of attack to the distance from this stagnation point to the shoulder of the blunt nose. These curves were averaged over the complete radiator at a constant angle of attack and the results are shown in Fig. JJ-2. Between 40° and 70°, this curve was faired with the existing data. The curve was then averaged over the angle of attack range to determine the heating distribution over the radiator if the RTG/RB is oscillating during reentry. Figure JJ-3 presents these results as a function of the peak angle of oscillation or attack (α_p) during reentry. This curve will be used in the next section to determine the amount of heat available as a function of α_p and trajectory.

REENTRY TRAJECTORIES

Histories of various trajectory parameters are shown in Figs. JJ-4 through JJ-6 for three typical reentry trajectories. Orbital velocity (25,690 fps) was used initially at 400,000 feet, with initial flight path angles of -0.1, -2 and -8 degrees, respectively. These are constant ballistic coefficient (W/C_DA = 25 lb/sq ft) trajectories. The total cold wall stagnation heat (q_s) for each trajectory was:

$\dot{q}$ = average local heating rate at s/s'

$\dot{q}_{s_{\alpha=0°}}$ = stagnation heating rate on blunt nose at α = 0°

α = angle of attack

s = local surface distance measured from stagnation point at α = 0°

s' = 1.95 feet

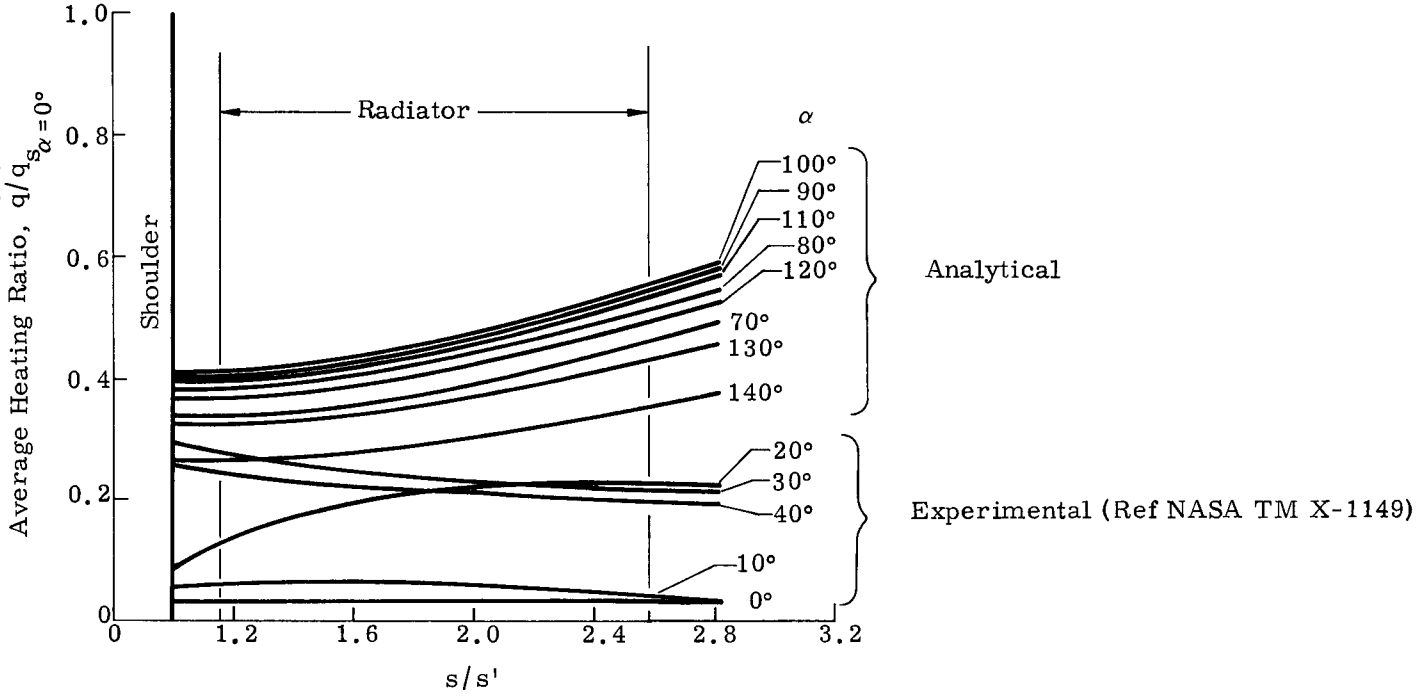

Fig. JJ-1. Average Heating Distribution over the Radiator Portion of CRONUS RB for Various Angles of Attack

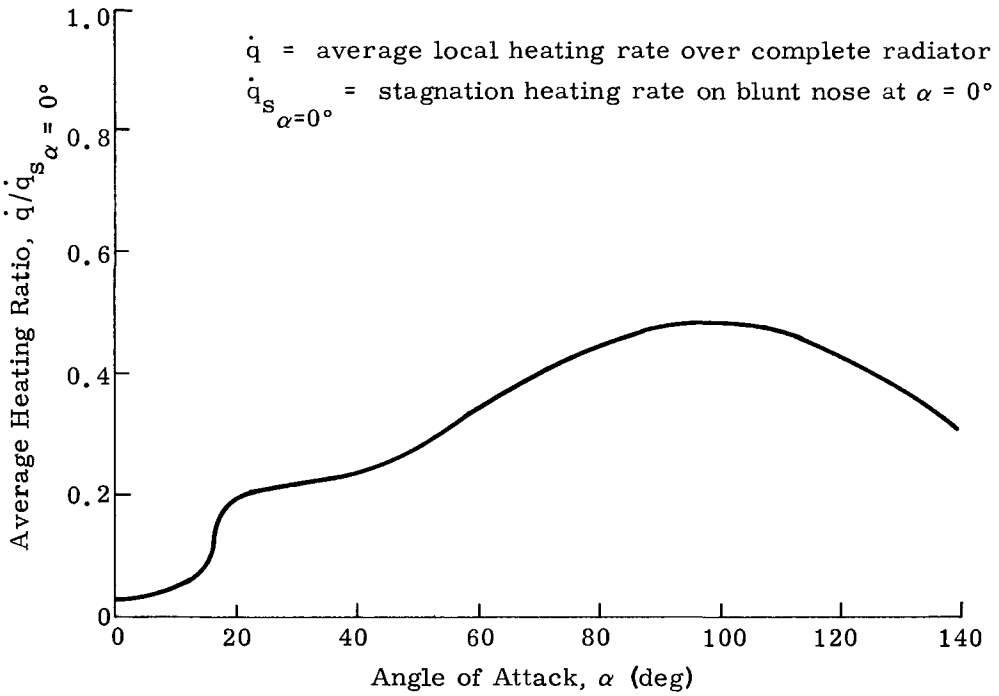

Fig. JJ-2. Average Heating Distribution over the Complete Radiator of CRONUS RB at Constant Angles of Attack

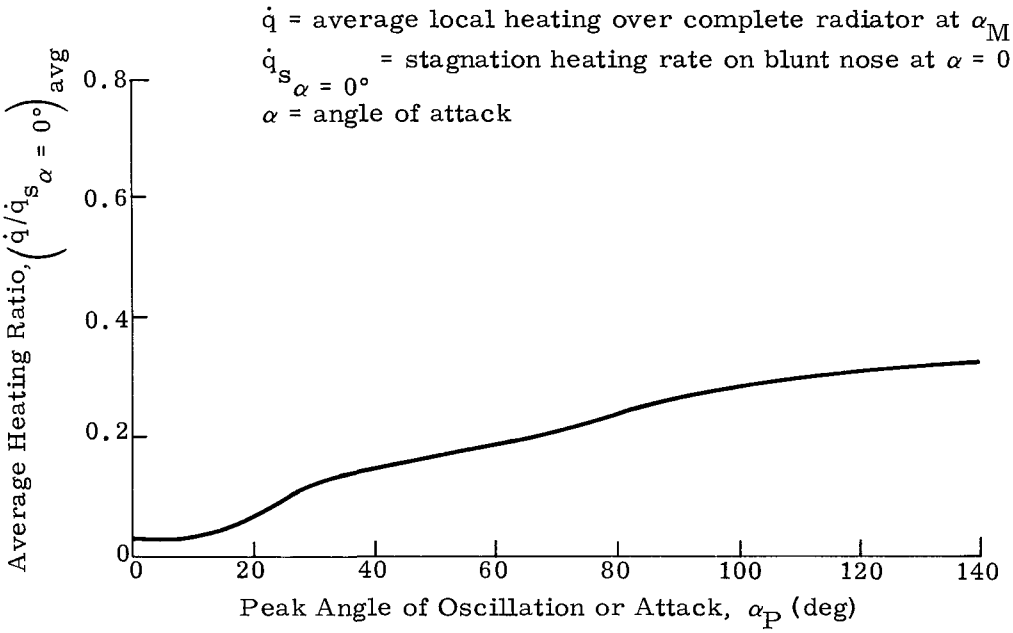

Fig. JJ-3. Average Heating Distribution over the Complete Radiator of CRONUS RB as a Function of Peak Angle of Attack or Oscillation

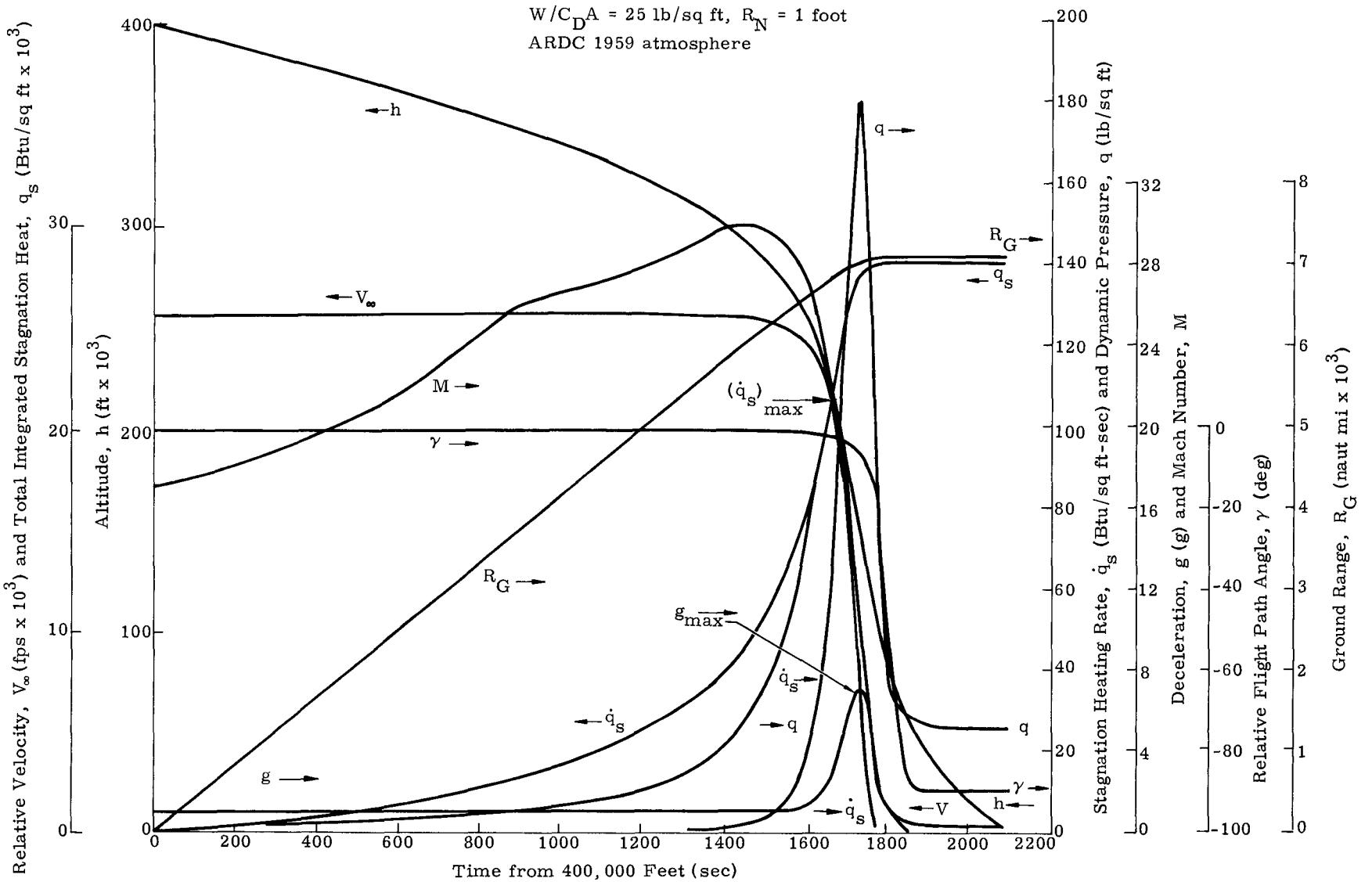

Fig. JJ-4. Trajectory Parameters for a Reentry Trajectory with $V_E = V_C = 25{,}690$ fps and $\gamma_E = -0.1°$

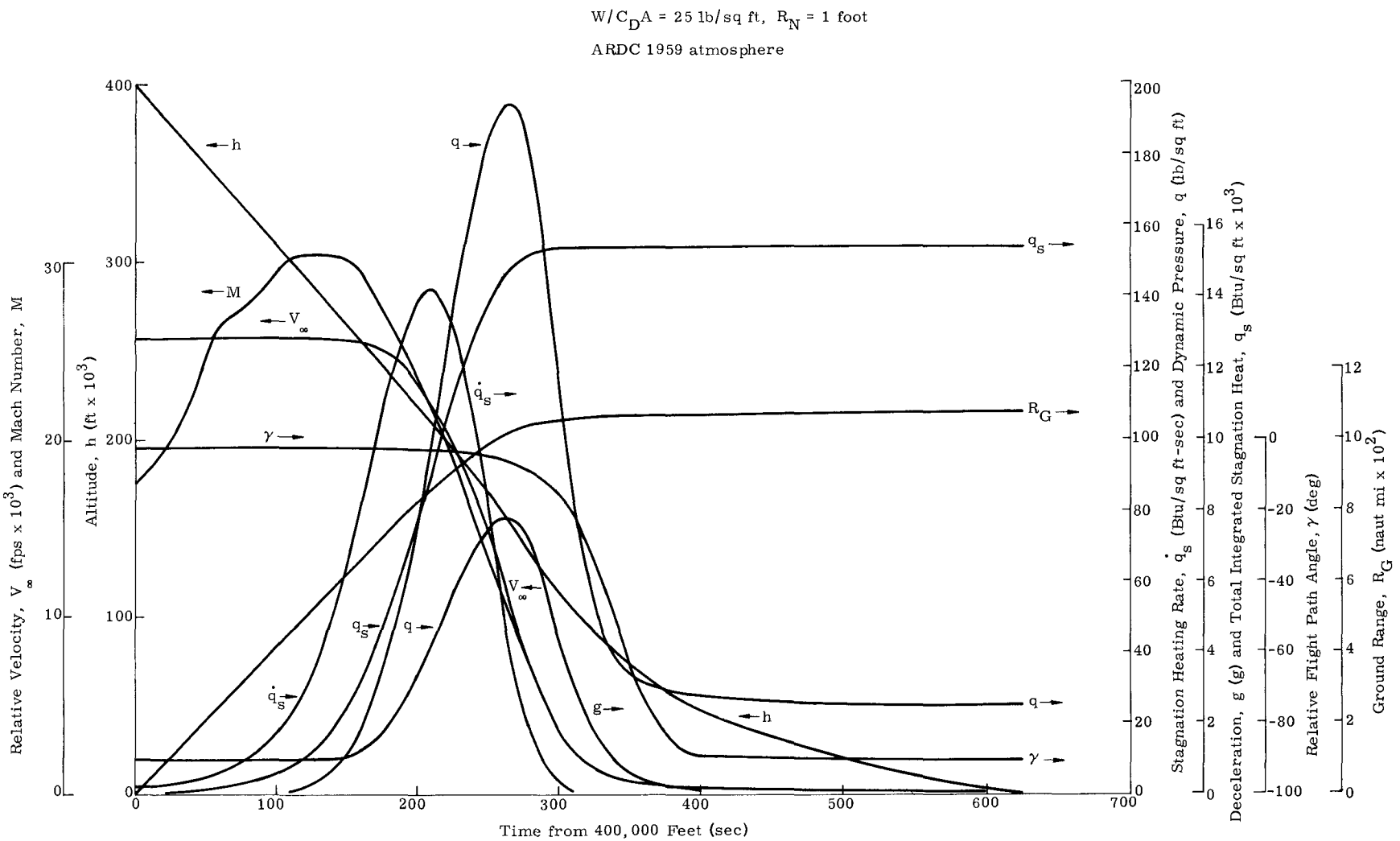

Fig. JJ-5. Trajectory Parameters for a Reentry Trajectory with $V_E = V_C = 25{,}690$ fps and $\gamma_E = -2°$

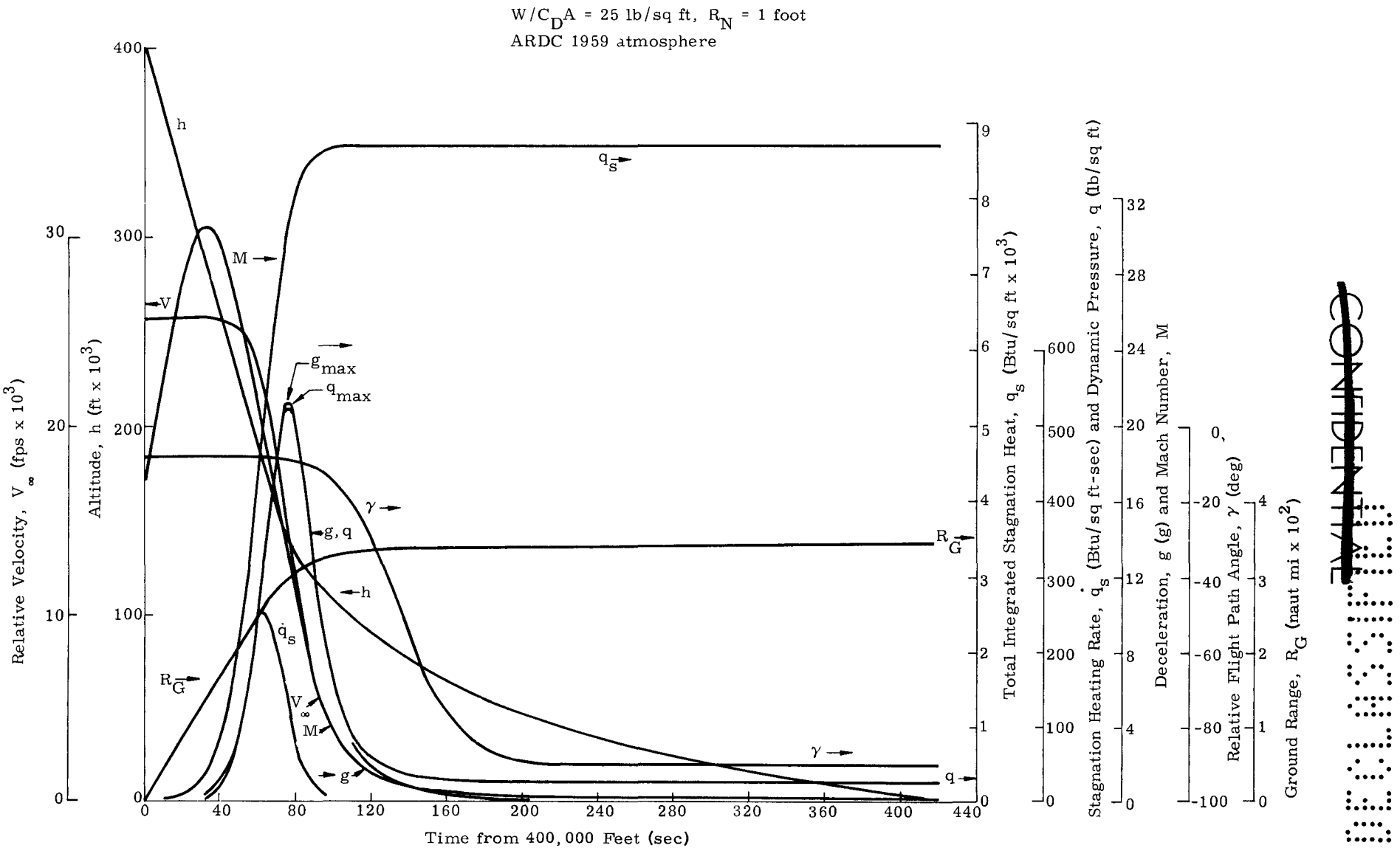

Fig. JJ-6. Trajectory Parameters for a Reentry Trajectory with $V_E = V_C =$ 25,690 fps and $\gamma_E = -8°$

$\gamma_E = -0.1°$ $q_s = 28,100 \frac{3.6}{25} = 10,680$ Btu/sq ft

$\gamma_E = -2.0°$ $q_s = 5860$ Btu/sq ft

$\gamma_E = -8°$ $q_s = 3310$ Btu/sq ft

} Based on $W/C_D A = 22$ lb/ft, $R_N = 6$ ft

These three quantities are now used in conjunction with the curve in Fig. JJ-3 to generate the three curves in Fig. JJ-7. The latter figure presents the total heat available to the complete radiator as a function of peak angle of oscillation for each of these three trajectories. This figure will be used to determine if the heating factors used in the heat transfer analysis were reasonable.

The heating distribution for the radiator in the heat transfer analysis (Appendix C) was averaged over the trajectory heating time for each node. Figure JJ-8 presents the results of this calculation. These curves were then integrated to determine the average heating factors used in the heat transfer analysis of the radiator for the three trajectories. The factors were:

$$\gamma_E = -0.1°, \left(\dot{q}/\dot{q}_{s_{\alpha = 0°}}\right)\text{avg} = 0.253$$

$$\gamma_E = -2°, \left(\dot{q}/\dot{q}_{s_{\alpha = 0°}}\right)\text{avg} = 0.234$$

$$\gamma_E = -8°, \left(\dot{q}/\dot{q}_{s_{\alpha = 0°}}\right)\text{avg} = 0.217$$

Multiplying the factors by the total cold wall stagnation heat (calculated previously), the total heat seen by the radiator (q_{rad}) during the trajectories of the RTG/RB was:

$$\gamma_E = -0.1°, \dot{q}_{rad} = 10,680 \times 0.253 = 2700 \text{ Btu/sq ft}$$

$$\gamma_E = -2°, \dot{q}_{rad} = 1370 \text{ Btu/sq ft}$$

$$\gamma_E = -8°, \dot{q}_{rad} = 718 \text{ Btu/sq ft}$$

Using these quantities and Fig. JJ-7, the peak angles of oscillation were:

$$\alpha_p = 87° \text{ for } \gamma_E = -0.1°$$

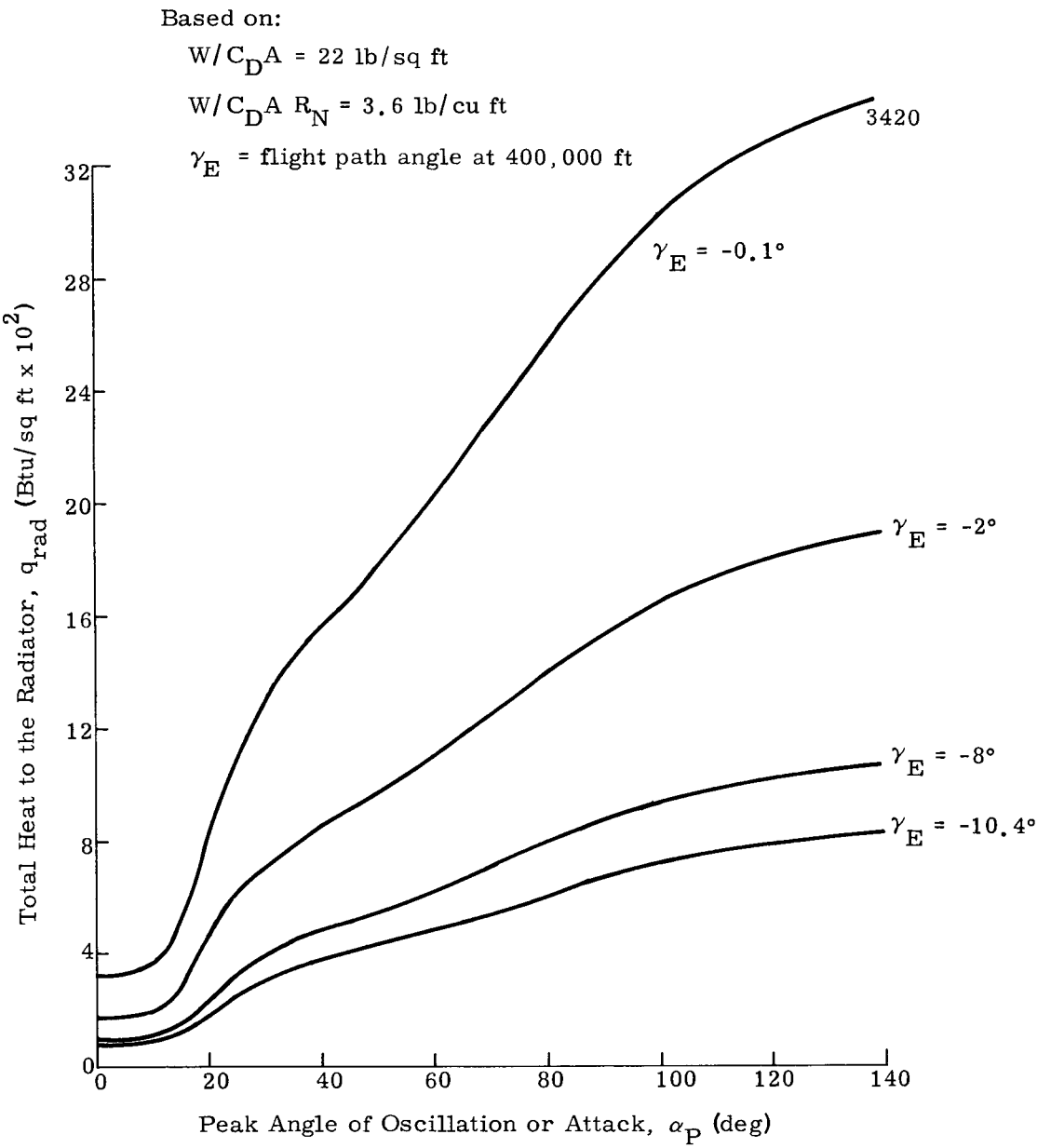

Fig. JJ-7. Total Heat Available to the Radiator of the CRONUS RB as a Function of Reentry Trajectory and Peak Angle of Oscillation or Attack

~~CONFIDENTIAL~~

$\left(\dot{q}/\dot{q}_{s_{\alpha = 0°}}\right)_{avg}$ = average heating ratio around radiator at s/s'

$\dot{q}$ = local heating rate

$\dot{q}_{s_{\alpha = 0°}}$ = stagnation heating rate on blunt nose at $\alpha = 0°$

α = angle of attack

s = local surface distance measured from stagnation point at $\alpha = 0°$

s' = 1.95 feet

γ_E = flight path angle at 400,000 ft

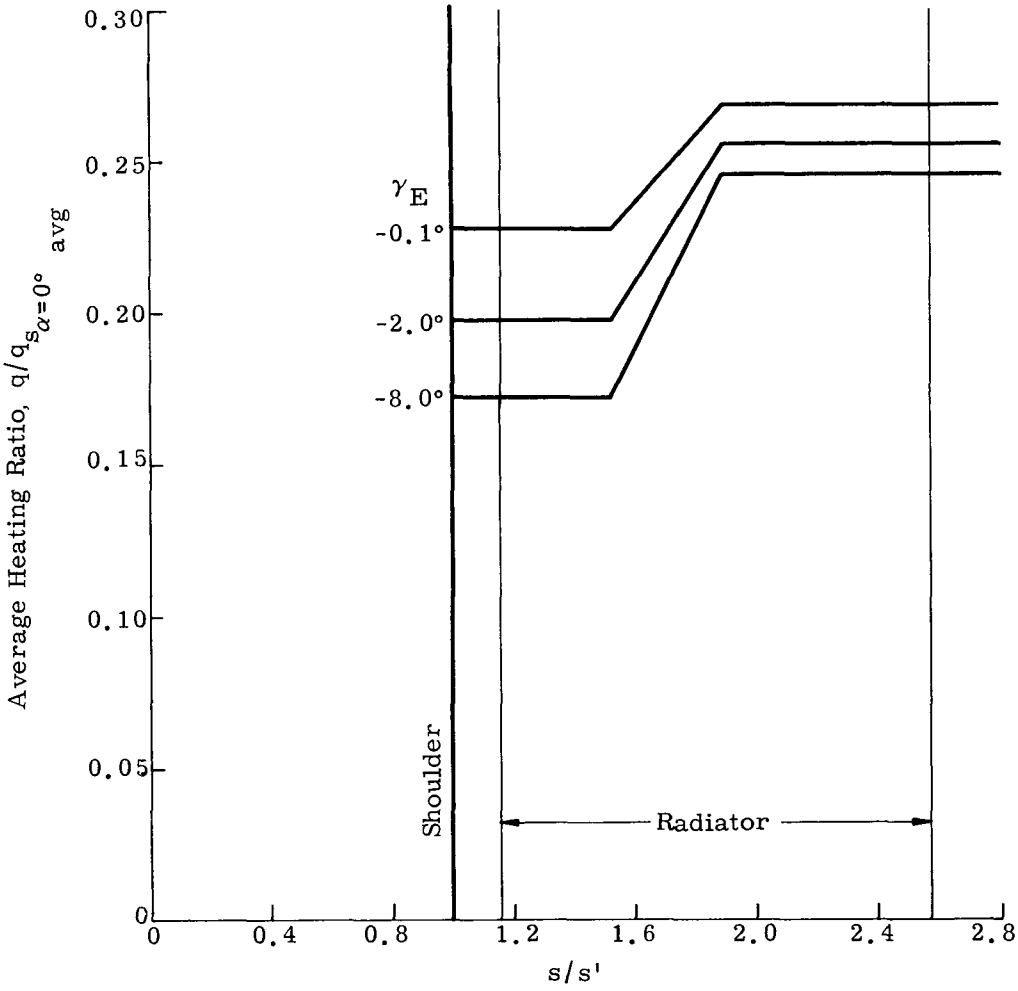

Fig. JJ-8. Average Heating Distribution over the Radiator for Three Reentry Trajectories used in Heat Transfer Analysis

~~CONFIDENTIAL~~

$\alpha_p = 79°$ for $\gamma_E = -2°$

$\alpha_p = 72°$ for $\gamma_E = -8°$

The results state that for the heating distribution used in the heat transfer analysis of the radiator, the RTG/RB can have these average angles of oscillation without damaging the integrity of the radiator.

Using the information in Appendix MM in conjunction with the results from the heat transfer analysis presented in Fig. JJ-7, the radiator will not be damaged under all normal reentry trajectories, orbital decay and abort. The word normal is used here without respect to the angular rates that the RTG/RB could experience during the ascent trajectory and operation in space. For these reentry conditions, we have a safety factor of nine for decaying orbits, and a safety factor of about 14 for normal (-2°) entry angles insofar as the radiator heat absorption is concerned.

It can be concluded, from the results in this appendix, Appendix MM and Appendix C (heat transfer analysis), that the RTG/RB's radiator will not be damaged for all normal and most abnormal reentry conditions.

REFERENCES

JJ-1. Price, E. A. Jr., Stallings, R. L. Jr., and Howard, P. W., "Pressure and Heat Transfer Distribution of 0.1-Scale Gemini Exit and Re-entry Models at Mach Numbers of 3.51 and 4.44," NASA TM X-1140, September 1965, CONFIDENTIAL.

JJ-2. Hagis, W., "SNAP Programs - Upper Atmosphere Experimental Re-entry Study Final Summary Report," MND-P-2953, Martin Company, April 1963.

BLANK

APPENDIX KK

SEPARATION AND DEORBIT STABILIZATION

The reference RB must be capable of separation from its booster or space vehicle carrier and deorbit under controlled conditions. To achieve this capability most simply and reliably, spin stabilization to an attitude reference provided by the carrier is utilized. The CIR-RTG/RB is propelled down a track by the separation rocket and simultaneously spun up to 30 rpm by the spin rockets. At this point (~0.24 second) separation is achieved but the spin rockets continue to burn to about 0.5 second to bring the spin velocity up to 60 rpm or higher for stabilization of the deorbit thrust vector. Deorbit thrust may be applied at this point or within a reasonable number of orbits thereafter in accordance with a time program established by ground command. To establish specifications for the various components required in this sequence of events, the problem is separated into three phases:

(1) Specification of spin velocity required to stabilize the deorbit thrust vector

(2) Specification of separation parameters (tip-off rates and linear velocity required to assure vehicle separation)

(3) Mechanical specification of track device required to provide constraints during initial spin.

The first two of these problems have been solved utilizing the six-degree-of-freedom stability program (Appendix CC) to define the trajectories resulting from thrust misalignments and asymmetry. The third problem is primarily mechanical and is pertinent to the motion only in its contribution to tip-off rates.

Constraints imposed on the configuration by spin stabilization are far reaching. Careful balance of the moments of inertia is necessary and, in particular, the roll moment of inertia should be maximum consistent with the aerodynamic requirements. This is achieved in part by peripheral location of the thrustors. In addition, the most effective minimization of the thrust misalignment effects will be at the largest possible spin rates (maximum number of revolutions during the thrust application). The full six-degree-of-freedom equations of motion are developed in Appendix CC. However, a glance at the simplified form of the moment equations may aid in understanding the motion to be expected.

$$L = I_{xx}\dot{p} - I_{yy}rq + I_{zz}qr$$

$$M = I_{xx} rp + I_{yy} \dot{q} - I_{zz} pr$$

$$N = - I_{xx} qp + I_{yy} pq + I_{zz} r$$

where

L, M, N = moments about body axes

I_{xx}, I_{yy}, I_{zz} = moments of inertia

p, q, r = body angular rates about X_B, Y_B, Z_B.

Given an initial spin rate, p, and finite moments of inertia about all three axes, it is evident that application of torque about Y_B or Z_B will cause precession about the orthogonal axis which is in turn reflected back. This gives rise to an angular coning motion in which angular momentum is exchanged between Y and Z in a fashion determined by the values of the inertias and the unbalanced torque. It is the objective of spin stabilization to minimize the amplitude of the coning motion and to average out the error in the thrust application angle over thrustor burning time with least waste of deorbit energy. The precessional rates will become the residual rates after burning but may be minimized by despin devices. The frequency of the precessional motion is determined by the inertia ratios:

$$(I_{xx} - I_{zz})/I_{yy}$$

and

$$(I_{yy} - I_{xx})/I_{zz}$$

Hence, a rotationally symmetric cone demands $I_{yy} = I_{zz}$. However, this requirement is of lesser importance than a large I_{xx} and maximum frequency of the coning motion. The results presented in the following represent a configuration in which $I_{yy} \neq I_{zz}$. It is to be expected that the frequency of the precessional motion will increase with decreasing inertia and the spin rate will increase for the same reason. An approximate analysis of these effects may be found in Ref. KK-1* which contains parametric studies of an Apollo shaped capsule similar in shape to the RB. The problem is approached here numerically since more exact solution seems required because of the critical safety considerations.

*Ref. KK-1. "Errors Associated with Spinning-Up and Thrusting Symmetric Rigid Bodies," JPL Technical Report No. 32-644.

The spin velocity required to stabilize deorbit thrust is dependent on results of thrust application under the following error conditions:

Thrust misalignment	± 0.1 degree
Thrust level error	± 2%
Center of gravity location error	± 0.1 inch
Initial angular error	± 5 degrees

The first three of these errors have a common effect in resultant torques about the body axis, and by far the most serious of these is the thrust level error which is the result of difference in thrust between two opposing deorbit engines. The RB configuration may be well balanced, but a comparatively large percentage of its mass is composed of expendable propellant at a large radius. This fact demands analysis including time varying moments of inertia, mass and center of gravity location. The critical trajectory parameter is the flight path angle error ($\delta\gamma$) found after application of deorbit thrust. Residual rates are also of importance since the vehicle must be despun to permit aerodynamic stabilization upon reentry; i.e., restoring torque available from aero moments is required to overcome residual rates prior to peak heating. This last requirement stems from the relatively low capability of the beryllium skin to protect the RB from thermal heating at high angles of attack or in a tumbling reentry mode, as well as the increase in the potential impact area caused by spinning reentry bodies. In analysis of these effects, inertial attitude angles are of little value and, for this reason, roll angle about the body axis (ϕ) referred to the horizontal is used as one angular coordinate. The total angle of attack α_T (angle between the X_B axis and the velocity vector) may then be uniquely determined. The motion of X_B is essentially coning about the velocity with a reentrant spiral path (Fig. KK-1). With non-zero initial rates about all three axes, X_B will generally deviate from the velocity to some angular amplitude as a function of spin rate, and then converge slowly to a minimum amplitude established by initial deviation and mass flow rate effects. The spiral is asymmetric about the velocity vector since flight path angle is slowly changing.

Spin velocity requirements may be established with the aid of Fig. KK-2, which indicates the maximum angular deviation of body axes with respect to the velocity vector as a function of spin rate and the resultant $\delta\gamma$ at completion of the deorbit thrust. Residual rates about body axes are also given. The data shown are for the thrust level error case which produces an unbalanced torque as a function of the thrust/time curve of maximum amplitude at about 77 ft-lb. Evidently, spin

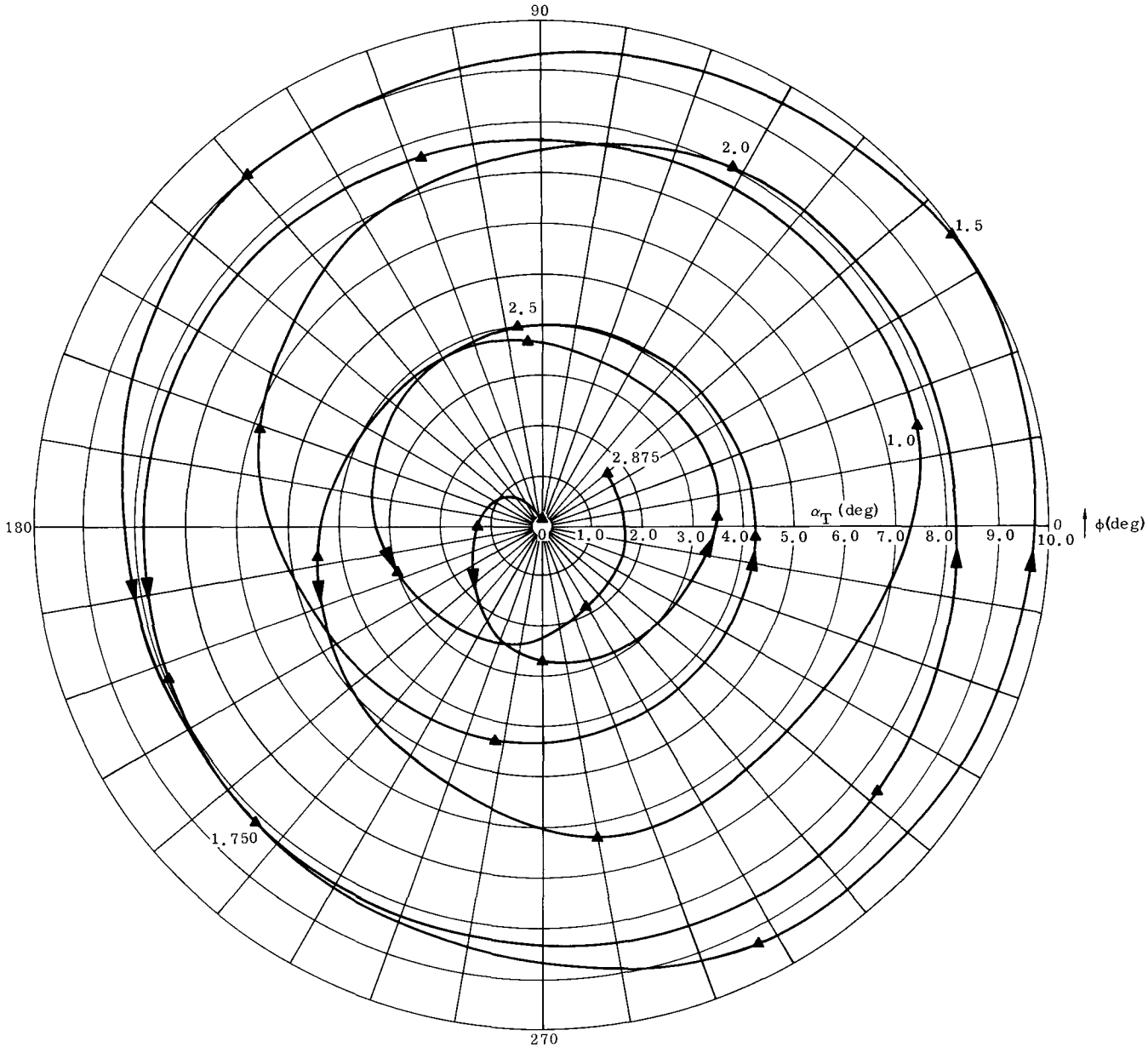

Fig. KK-1. Spin Stability--ϵ_T = ±2%, ϕ = 12.56 rad/sec

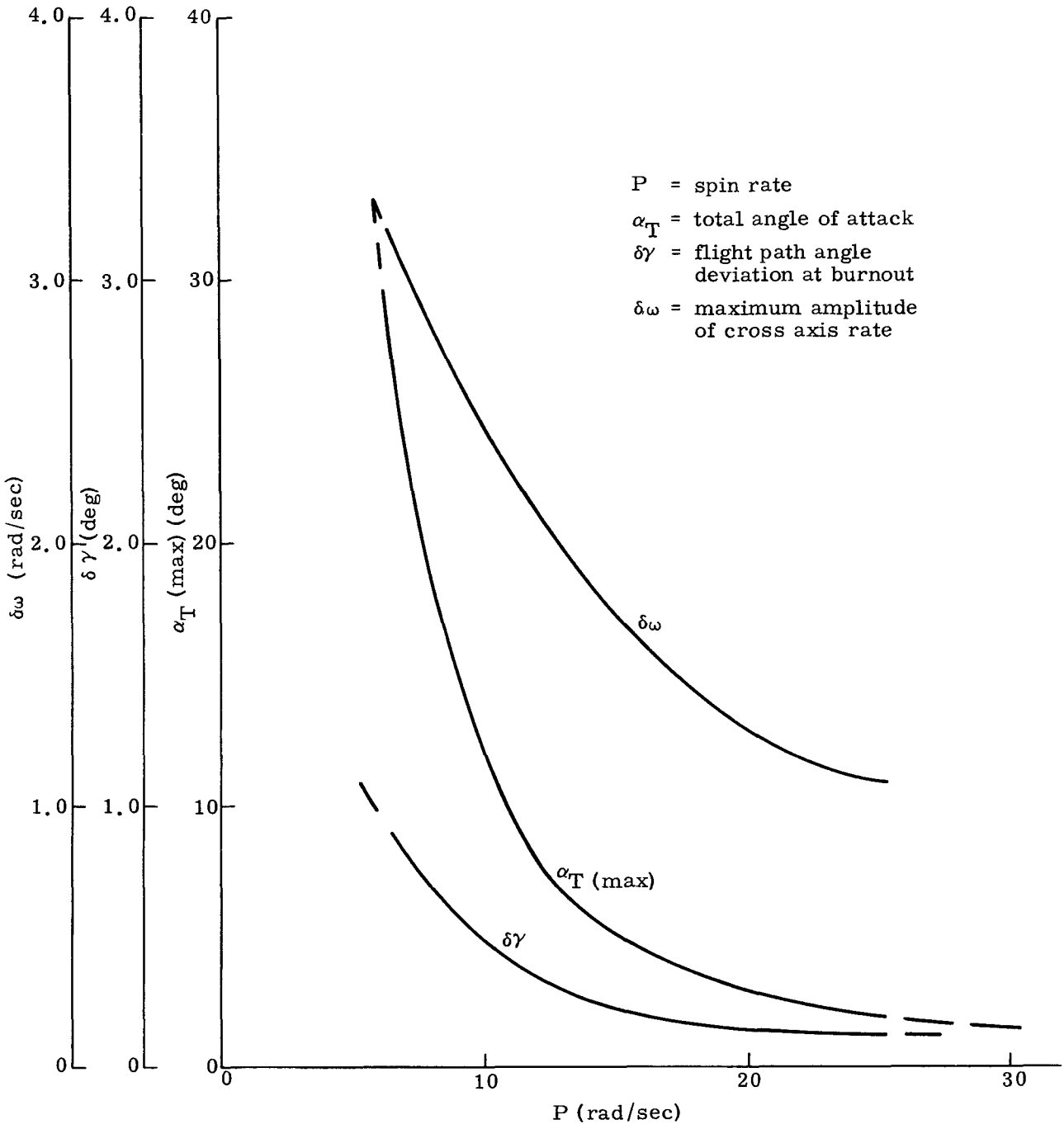

Fig. KK-2. Spin Stabilization Parameters

rates of two to three rps will provide minimal errors in $\delta\gamma$ and residual rates less than 1 rad/sec. It may be noted that a limitation is placed on the usable rate by component performance. At high spin rates, centrifugal forces become excessive and may require structural beefup, with attendant weight penalties. Rocket motors may fail to burn evenly and jet damping moments may become appreciable factors in the motion; the last effect may be favorable.

The time history of the physical parameters for a spin rate of 25 rad/sec is shown in Fig. KK-3. It will be noted that as mass (and hence inertia) decrease, the vehicle spin velocity increases by an appreciable factor and a cross moment of inertia is developed as a result of unequal mass flow rate in opposing rocket motors. The body rates in Y_B and Z_B oscillate as previously explained at frequencies increasing with decreasing inertia.

Another trajectory parameter of interest is the inertial thrust application angle. The actual trajectory of the vehicle is a spiral in space and hence the ΔV resultant obtained is an oscillating quantity (Fig. KK-4). The steady-state value is a function of initial conditions and only the amplitude of the oscillation is of interest in perturbation analyses of impact sensitivity. An uncertainty in this parameter of about one degree results from application of thrust level unbalance of $\pm$ 2% for a spin rate of 12.56 rad/sec. This, together with the data of Fig. KK-2, leads to selection of minimum spin rates of the order of 12 rad/sec for the CIR, if the simultaneous occurrence of a +2% and a -2% thrust error in opposite motors is considered a reasonable event. However, since present indications are that a 3σ value at the thrust difference is about 2%, the selected 6.3 rad/sec spin rate is adequate for the current performance limits.

The time required for the selected RB configuration to aerodynamically stabilize itself at reentry increases with increasing spin rate. It is for this reason that the RB is despun after the deorbit impulse has been delivered. Therefore, magnitude of the residual spin rate can affect design. The magnitude of this residual spin rate is dependent upon the net magnitude and direction of the multiple thrust vector misalignments.

Multiple, fixed-nozzle rockets tend to generate roll moments about the vehicle velocity vector due to misalignment of the rocket thrust vectors. The induced roll can either add to or subtract from the spin rate of the RB during burning of the deorbit rockets so that there will be a residual spin rate following completion of the despin function.

When operational conditions warrant the expense, solid propellant rockets of the size required for the deorbit system can be balanced and aligned (nozzle thrust axis to rocket principal axis) to an accuracy

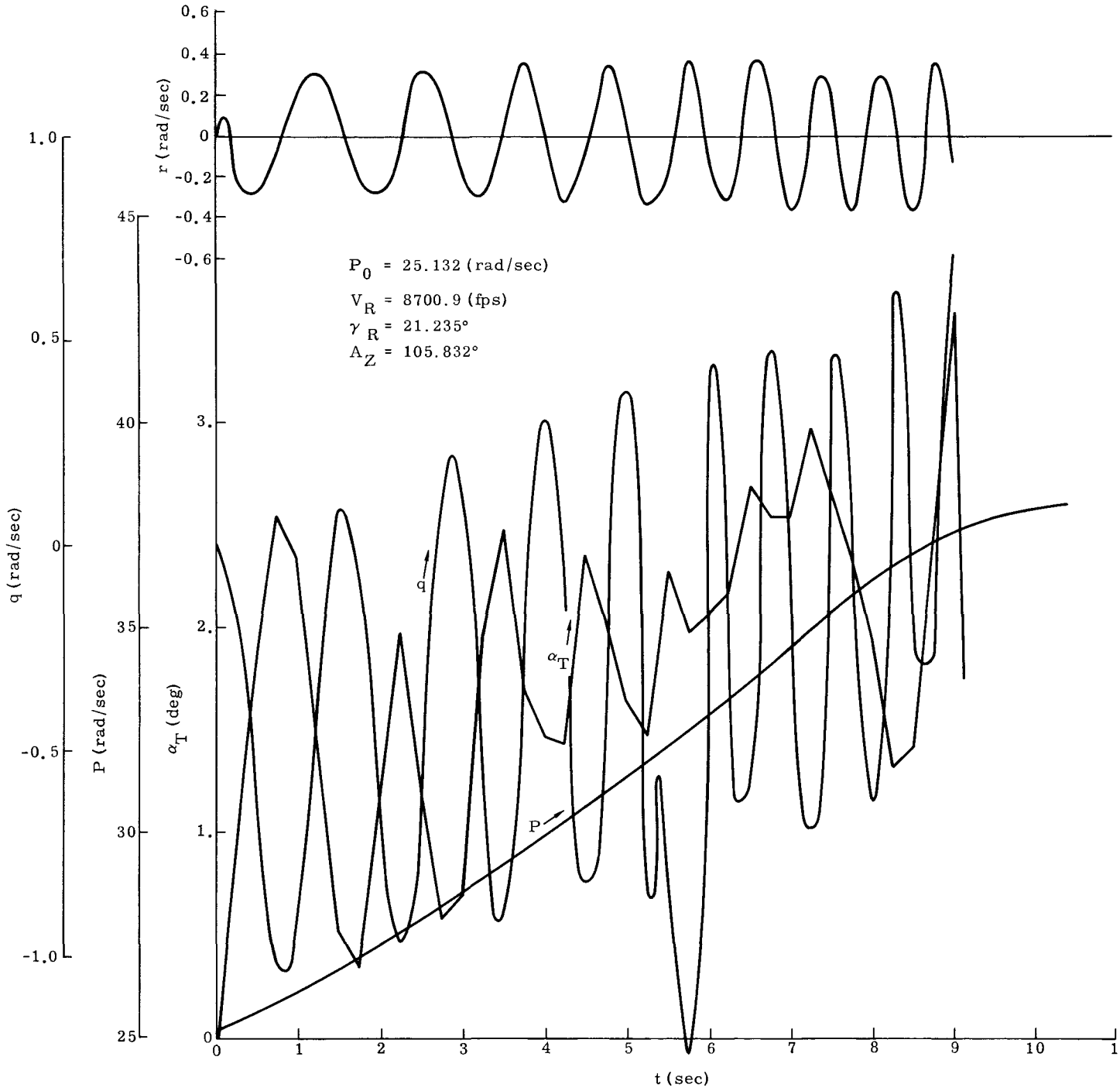

Fig. KK-3. Spin Stabilization Variables

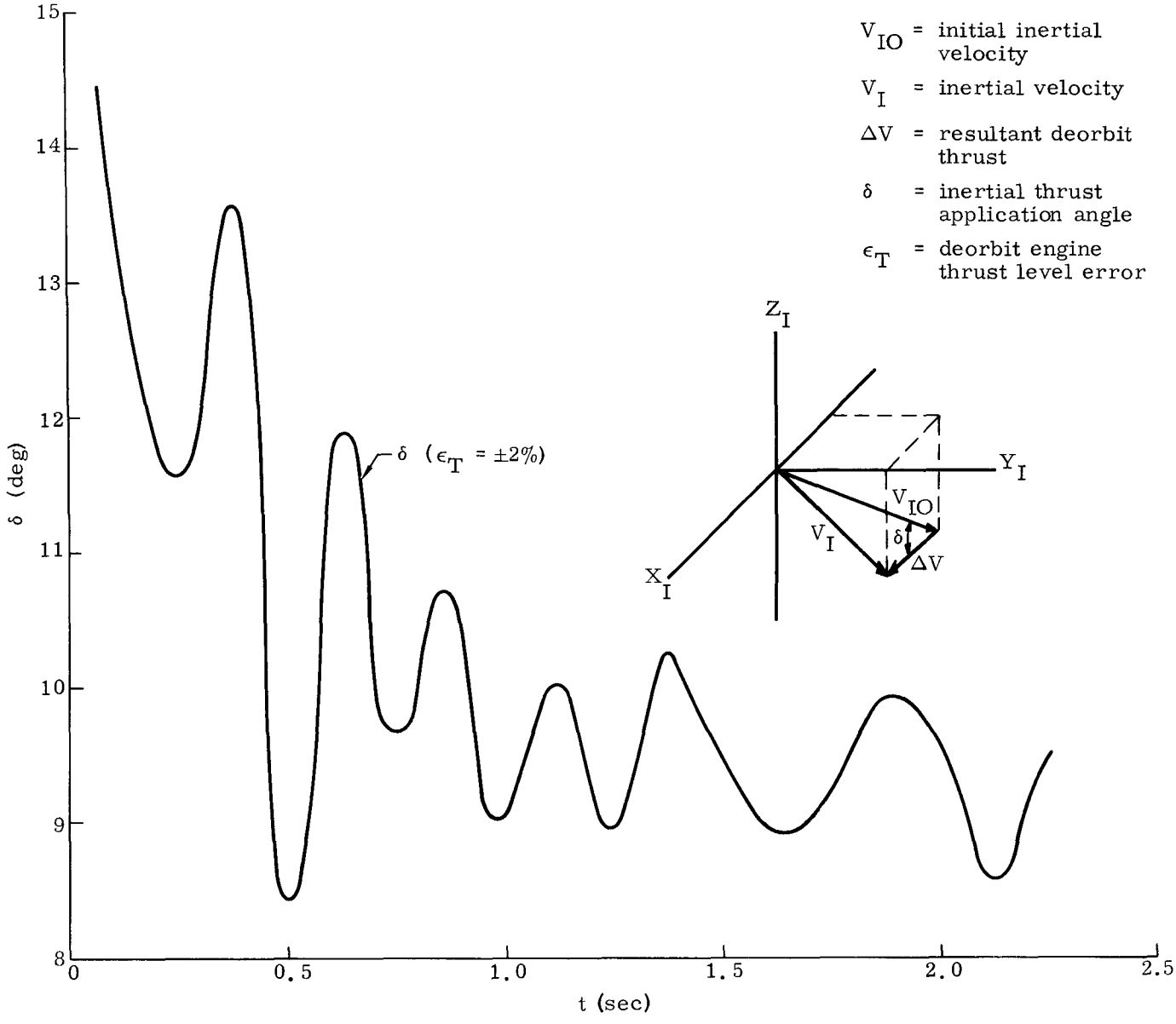

Fig. KK-4. Inertial Thrust Application Angle

of 0.003 radian or better. The third stage of Vanguard was so balanced. Data on eight Scout vehicle flights (Ref. KK-1) show third stage misalignments on the average of about 0.001 radian (0.06°) with only one of the normal flight records exceeding 0.002 radian (0.10°). These Scout misalignments include the rocket itself, installation inaccuracies, vehicle center of mass variations, vehicle bending, etc. Recent data on the Surveyor indicate installed misalignment of the Surveyor descent deceleration solid motor as 0.0002 radian (0.015°) before firing and 0.0006 radian (0.045°) after firing. Preliminary analysis of telemetered data on Surveyor I tends to substantiate these small misalignments. In the face of this evidence, an effective misalignment of any one deorbit rocket is assumed to be less than 0.10 degrees (3σ). On this basis, the maximum residual roll rate generated by the total effect of all four deorbit rocket misalignments should be less than

$$\Delta W = \frac{F_T R \theta_\epsilon \ (\Delta t)}{I_{M_{Roll}}} = \frac{3280 \text{ lb} \times 2 \text{ ft} \times 0.1 \text{ deg} \times 10 \text{ sec} \times 60 \text{ sec}}{35 \text{ slugs ft}^2 \times 57.3 \text{ deg/rad} \times 2\pi \text{ min}} = 31 \text{ rpm}$$

where:

ΔW = residual spin rate

F_T = total deorbit rocket thrust

R = moment arm (roll)

θ_ϵ = misalignment error (all errors produce a roll rate in the same direction for this example)

Δt = deorbit rocket burning time

I_M = average roll moment of inertia of RB during deorbit rocket burn period

The probability that all four rockets will be at their 3σ value and aligned additively in either the positive or negative roll direction is extremely remote. Design conditions should account for less than 10 rpm residual roll rate.

BLANK

APPENDIX LL

VELOCITY IMPULSE REQUIREMENTS

To arrive at a selection of velocity impulse (ΔV) for the RTG/RB, the three phases of flight (ascent, transfer orbit and orbit) must be investigated with the following objectives in mind. First, the range from deorbit to atmospheric entry and impact should be such that small errors in ΔV will not produce drastic changes in impact range. Secondly, the magnitude of ΔV should be sufficiently large for adequate impact range control in an ascent abort situation. Finally, the selected ΔV pulse must not be oversized because of design economics. A velocity impulse of 1500 fps was selected because it satisfies these considerations and because it can be suitably obtained by existing, proven rocket engines.

This velocity increment is conservative in that a lower velocity increment (e.g., 1200 fps) would also satisfy the basic mission requirements. The optimum ΔV selection, which would balance the excess velocity increment against the added safety, smaller depressions and greater operational flexibilities, will be conducted in the subsequent phase of study. The reason for the final choice of 1500 fps is that the worst cases of entry conditions, misalignment, weight, etc., will have been examined in the feasibility portions of the study.

The approach used to arrive at this ΔV choice first investigates the deorbit or calldown case with the perigee-apogee conditions of the elliptical transfer orbit. Since these flight conditions represent the extreme energy levels encountered, it can be reasoned that, during the transfer itself, quite acceptable entry control will be available. Next, the ascent abort case is studied and the respective requirements compared.

DE-ORBIT ΔV REQUIREMENTS

After an overspeed injection at 100 nautical miles, the vehicle will coast to an altitude of 600 nautical miles where a circularization maneuver is performed. Once in this circular orbit an option exists to either leave the RB in orbit or retrieve the power unit. In the latter case, the design must concern itself with providing positive entry after the ΔV is applied. To ensure this absolute entry without oversizing the ΔV magnitude, consideration must be given to such items as skip-out conditions, ΔV application angle, ΔV magnitude, impact range sensitivity and severe entry conditions.

A skipout boundary is defined as that combination of velocity (V), flight path angle (γ), lift-to-drag ratio (L/D) and ballistic coefficient (W/C_DA) which just allows a vehicle to reenter the earth's atmosphere and impact in a single pass. In Ref. LL-1* Chapman shows skipout boundaries for various entry velocities with L/D versus a perigee parameter F_p. This parameter is a function of entry altitude, ballistic coefficient and entry path angle. These data have been interpreted for this design mission where it is anticipated that entry velocities will be between 24,000 and 27,000 fps, entry path angles will be between -2° and -12° and, ballistic coefficients will be on the order of 10 to 50 lb/sq ft. The results are shown in Fig. LL-1 for an L/D of zero, which represents the aerodynamics of the selected ballistic shape. More specifically, for a 600 by 600 nautical mile orbit calldown, it is expected that the entry velocity will be between 26,000 and 26,500 fps. Figure LL-1 indicates that the minimum acceptable γ must be greater than (negative sense) -0.75° to -1.3° if impact is to be certain within one pass. Although Fig. LL-1 is based on Chapman's analytic analysis, the results are quite valid for preliminary design purposes.

The skipout boundary just mentioned is reflected in Fig. LL-2 which shows the 600 by 600 nautical mile deorbit requirements. It is immediately apparent that the minimum ΔV requirement is 1000 fps. However, the manner in which it is applied (i.e., the application angle and ΔV magnitude) can produce serious impact dispersions. Figure LL-2 shows the impulse requirement and resulting impact range for two deorbit techniques, the first of which applies the ΔV at the optimum application angle that minimizes the magnitude of the pulse. The second technique, of interest to the present design, applies the pulse opposite to the velocity direction. Only small differences exist between the two methods in the 1000 to 1500 fps ΔV regime. Included in the subject figure are sensitivity coefficients of range-to-impulse error and range-to-application angle error ($\partial R/\partial \Delta V$, $\partial R/\partial \delta$). To arrive at a practical ΔV requirement, a preliminary goal in the restriction of dispersions must be assumed. Before setting the goal for this design, it should be mentioned first that downrange dispersions are normally an order of magnitude greater than crossrange dispersions. This fact allows consideration of one random variable (downrange error), rather than two, as the criterion for establishing the dispersion restriction. To this end, it is highly desirable and very reasonable to request a downrange dispersion control of ±300 nautical miles with a 95% confidence of achieving this control. This confidence level is tantamount to a 2σ dispersion for one random variable.

*Ref. LL-1. Chapman, D. R., "Analysis of the Corridor and Guidance Requirements for Supercircular Reentry into Planetary Atmospheres," NASA TR-55, 1959

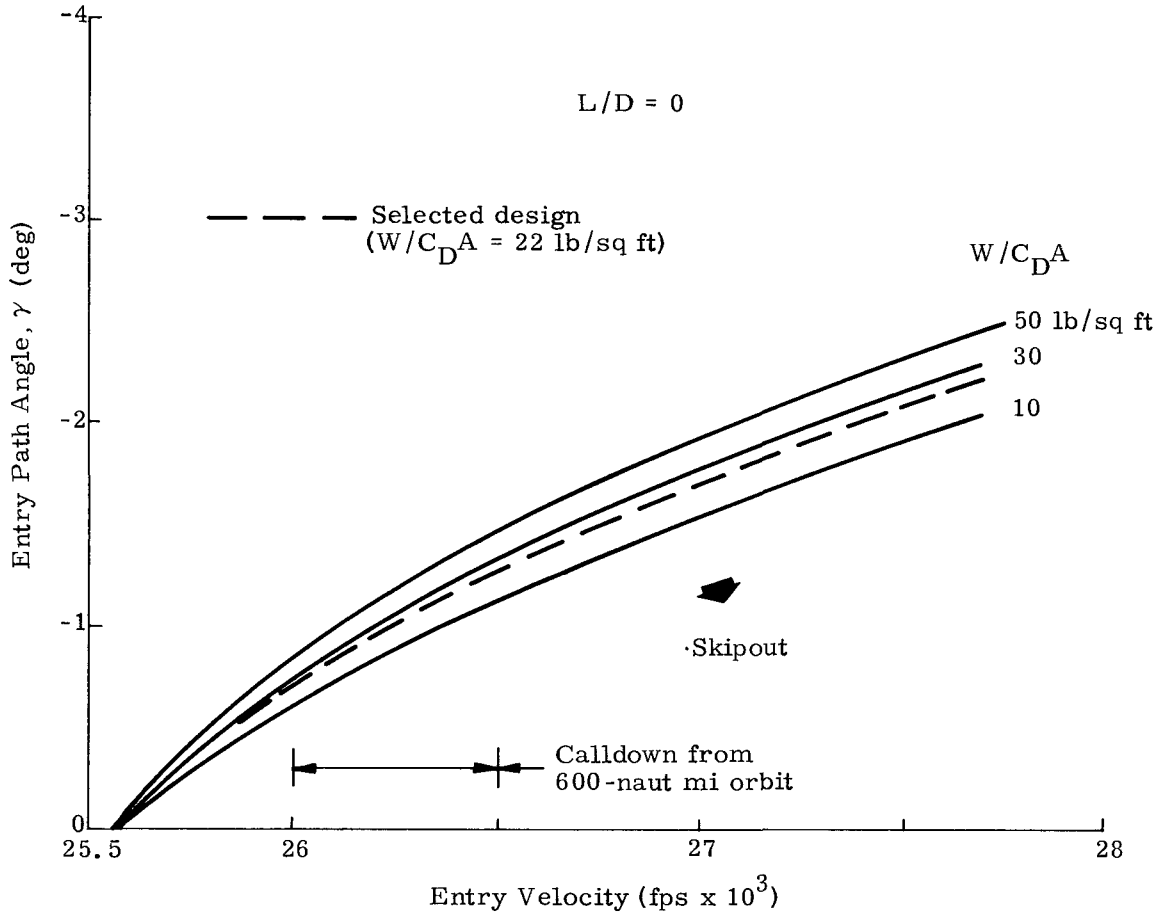

Fig. LL-1. Skipout Boundaries

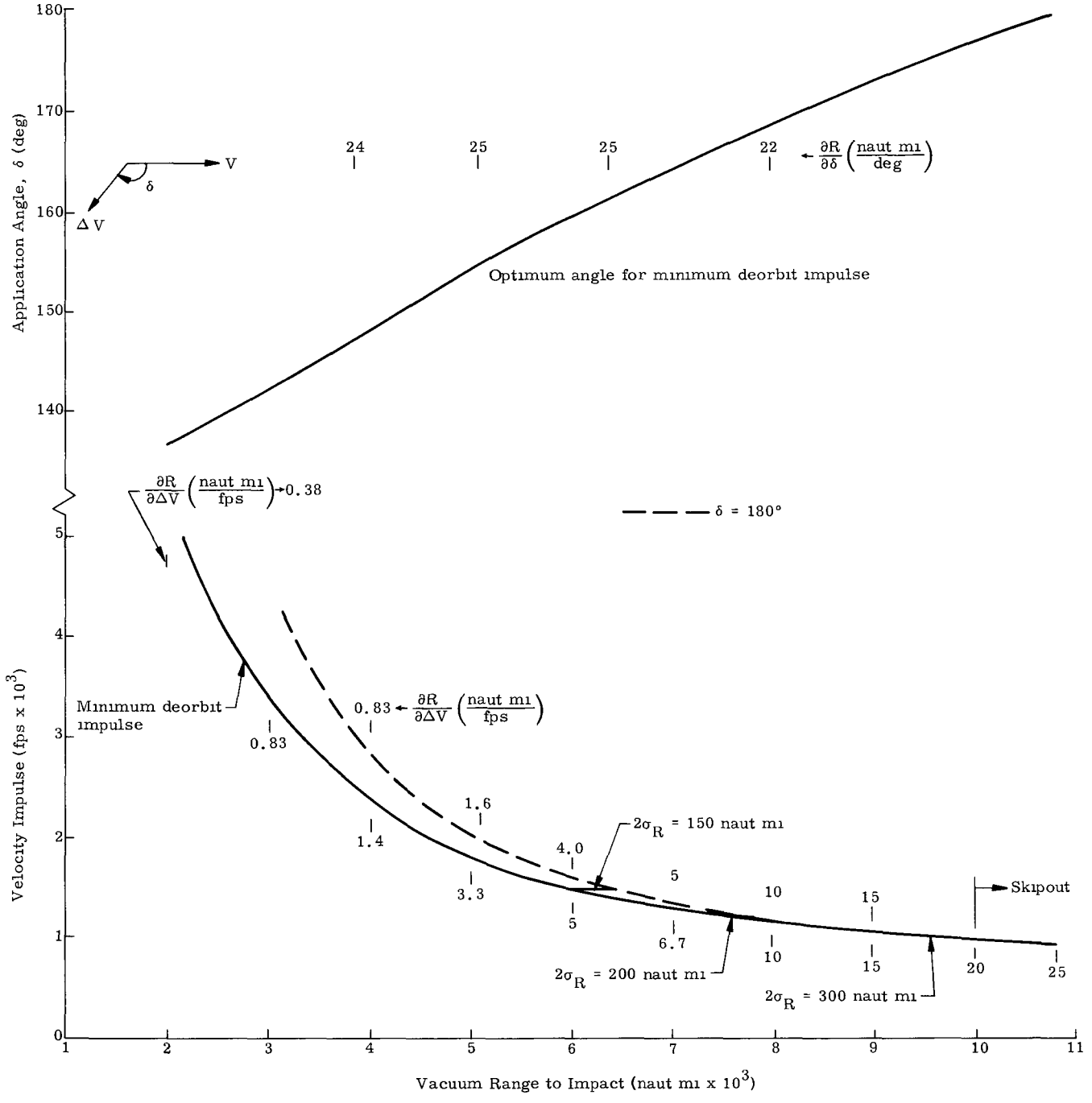

Fig. LL-2. Deorbit Requirements for a 600-Nautical Mile Circular Orbit

The effect of this dispersion goal on deorbit requirements depends on the expected system and state vector uncertainties. For the contemplated design, it is estimated that the 2σ variance in ΔV application will be 10 fps. The 2σ variance in application angle, δ, is 3.4°. Additional errors will be realized because of the uncertainty in the vehicle state vector as deduced from tracking data and are computed to be 2 fps in velocity and 0.6° in attitude. This can be summarized as:

$$2\sigma_{\Delta V} = 12 \text{ fps and } 2\sigma_{\delta} = 4°$$

Although it is improbable that these maximum errors will be experienced simultaneously, the following analysis assumes the additive (conservative) approach rather than RMS approach. With the data given in Fig. LL-2, the dispersion restriction requirement can now be computed and is so indicated in the figure. A minimum ΔV of 1100 fps must be selected to realize the 95% confidence in limiting impact dispersions to ± 300 nautical miles.

TRANSFER ORBIT REQUIREMENTS

The minimum ΔV of 1100 fps required for the calldown or normal deorbit situation must now be compared to the minimum transfer orbit requirement. Because of the speed and sensitivity of δ upon impact points, the perigee of the transfer orbit becomes the crucial point of study. Figure LL-3 depicts the variation of range control with δ for various ΔV's. Note the high sensitivity of impact range to errors in thrust application angle $(\frac{\partial R}{\partial \delta})$ and how the ΔV = 1000 fps level is automatically eliminated except for $\delta < 130°$.

Figure LL-4 presents the same data except in a different fashion in order to show the sensitivity of range-to-thrust magnitude errors $(\partial R/\partial \Delta V)$. Table LL-1 has been prepared to provide an insight to the minimum acceptable ΔV and uses the injection variances of $2\sigma_{\Delta V}$ = 20 fps and $2\sigma_{\delta}$ = 4° again in an additive manner.

It is obvious that if a thrust application angle of 130° is used, the minimum requirement would be a little greater than 1000 fps. However, in considering some of the design problems associated at this point in flight (injection)--namely the mounting of the CIR-RTG/RB, catapult and spinup mechanisms--and the desire to maintain absolute simplicity, a pulse application angle of 180° would both simplify the design and remove launch vehicle roll induced errors. With this tactic, an abort impulse of approximately 1500 fps is necessary. The need to examine the apogee case can be eliminated since this particular flight point would require less than 1000 fps in light of the 600 by 600 nautical miles deorbit requirements.

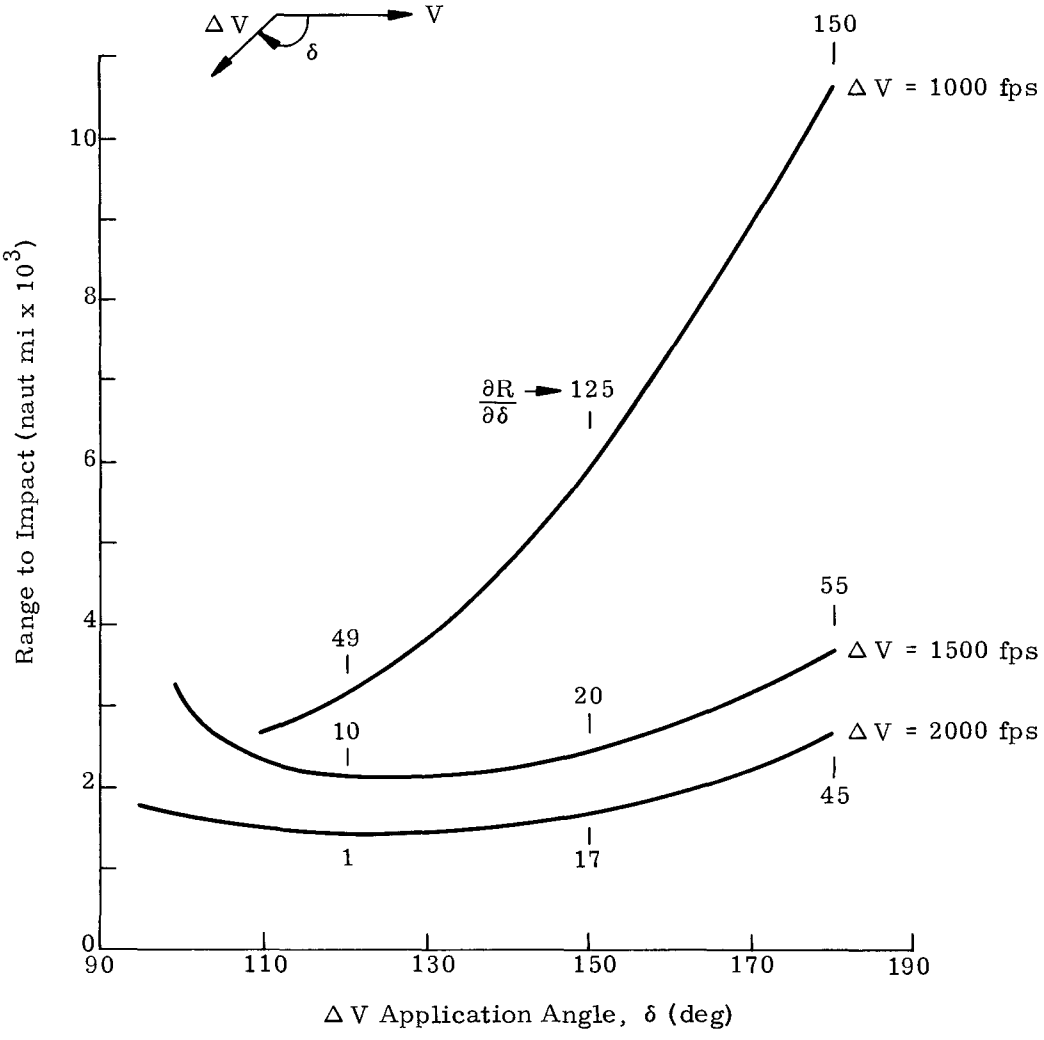

Fig. LL-3. Abort from Perigee Off 600-Nautical Mile Circular Orbit

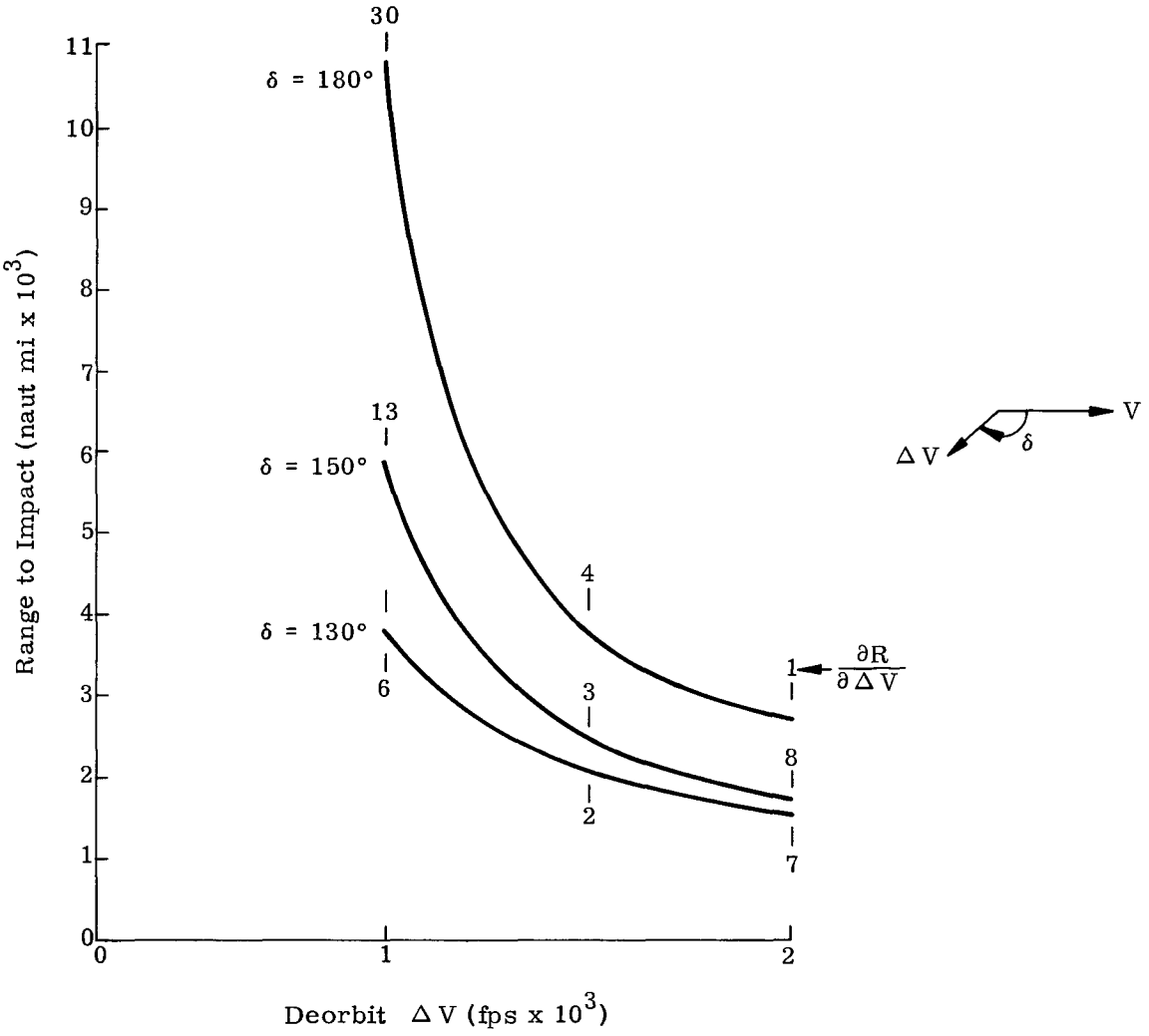

Fig. LL-4. Abort from Perigee of Transfer 100- by 600-Nautical Mile Orbit

TABLE LL-1

Dispersions: Perigee Abort (100 by 600 nautical miles)

ΔV (fps)	δ (deg)	$2\sigma_{\Delta R}$ (naut mi)
1000	180	1200
	150	760
	130	340
1500	180	298
	150	140
	130	80
2000	180	200
	150	84
	130	42

ASCENT ABORT REQUIREMENTS

Thus far it has been shown that an impulse level of 1500 fps would adequately allow a successful abort or deorbit from the injection point and any other point in subsequent flight. Furthermore, downrange impact dispersions can be limited to ±300 nautical miles to a high probability. However, the impulse derived thus far must be checked as to the overall range control requirements. This requirement actually stems from the ascent or boost phase of flight since the locus of instantaneous impact points will intersect land masses before injection. For example, an ETR launch will fly over the southern tip of Africa and a polar launch from WTR will fly over Antarctica. It is extremely desirable to have a design that is capable of limiting the impact point to location offshore from these land masses. The most stringent range control requirement will be realized for that launch vehicle whose boost trajectory exhibits the longest downrange-to-injection trait. For the launch vehicles considered, the Titan IIIC configuration has the longest range, approximately 2000 nautical miles from liftoff to injection (Fig. LL-5).

On examining the Eastern and Western Test Ranges it is noticed that the same downrange arc angle to the first land encounter exists for both ranges. This is depicted in Fig. LL-6 which shows the instantaneous impact points for a Titan IIIC launch. The figure also indicates that it is unnecessary to apply an abort pulse for ascent speeds less than 25,000 fps. Therefore, the most critical phase of boost is

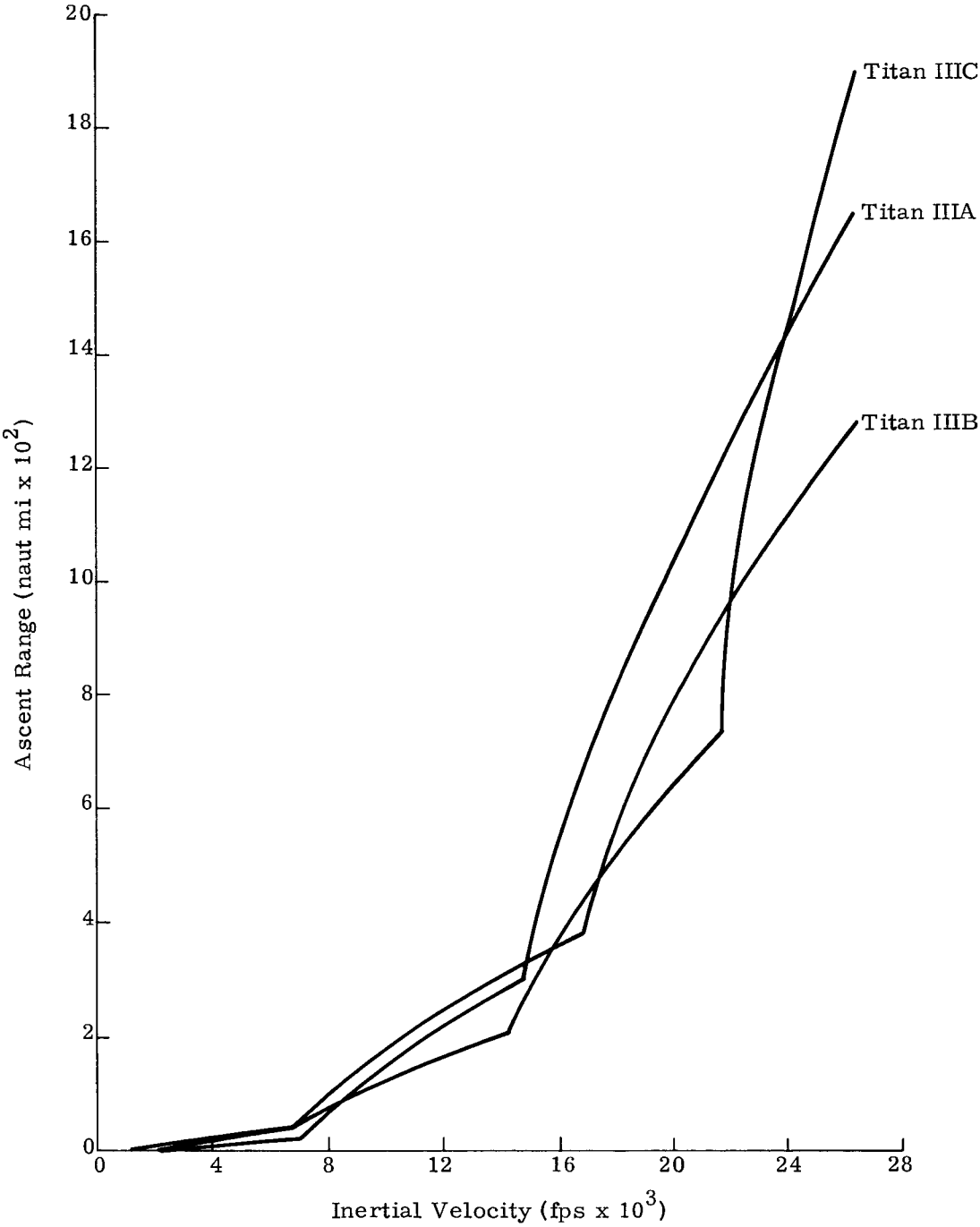

Fig. LL-5. Ascent Ground Range Comparison

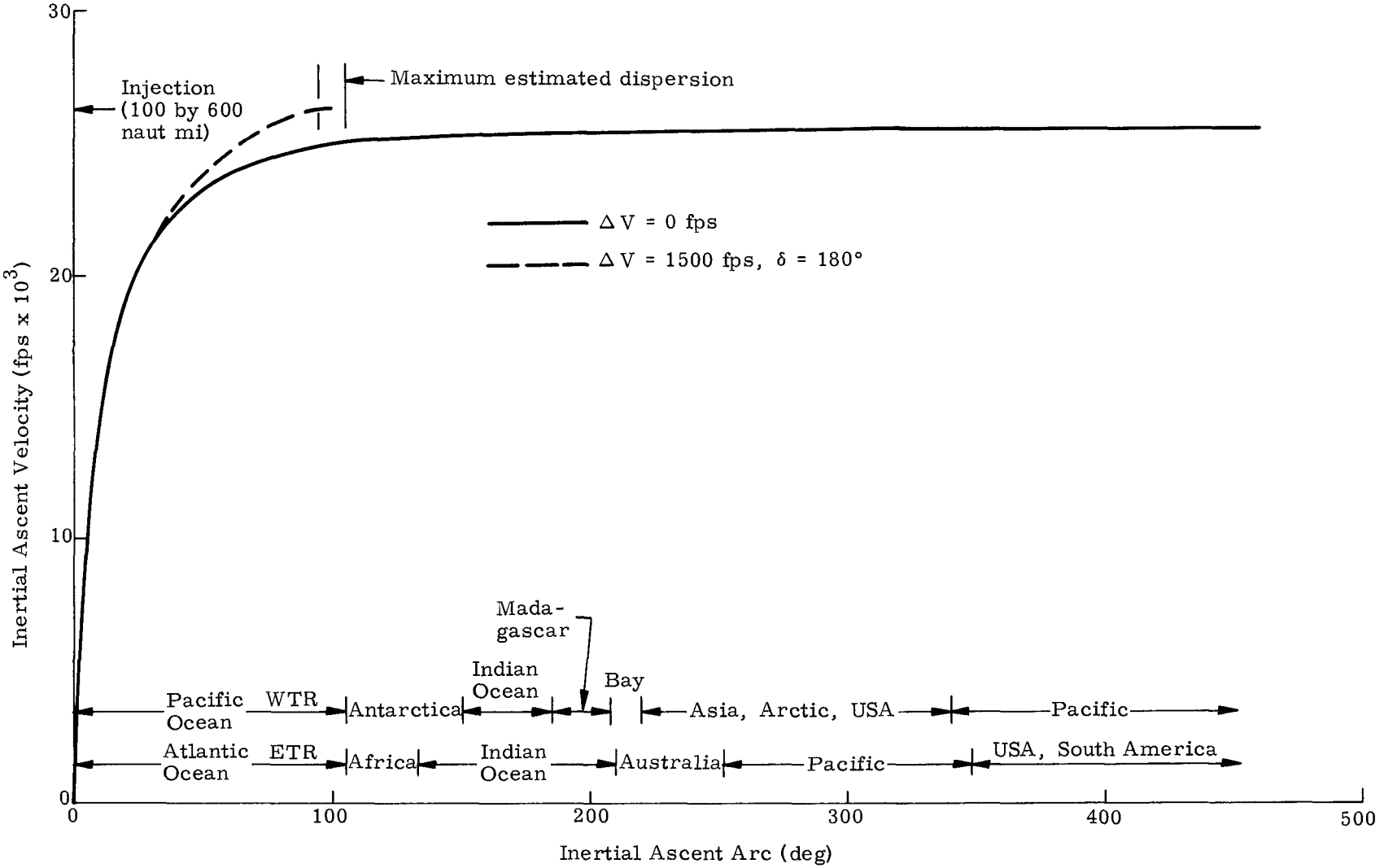

Fig. LL-6. Instantaneous Impact Points for a Titan IIIC Launch

the approach to injection where impacts cannot be contained to acceptable repository areas. The question that must be answered is whether the previously derived abort pulse of 1500 fps is sufficient for the exercise of range control in this area. With this intent, the instantaneous impact points are also shown for the case where the abort impulse 1500 fps is applied in a retrograde direction ($\delta = 180°$). As can be seen, the magnitude of the pulse is adequate, even in the presence of the maximum expected dispersion. There remains only to conduct a more detailed dispersion analysis to validate these findings. The results of the dispersion analysis are reported in Appendix II and confirm the findings to a even greater degree of confidence.

Nominal entry conditions resulting from a retrograde application of 1500 fps are summarized in Table LL-2.

TABLE LL-2

Entry Conditions at 400,000 Feet

ΔV (fps)	δ (deg)	Deorbit Condition	Entry Velocity (fps)	Entry Path Angle (deg)
1500	180	Perigee } Transfer orbit	25,150	-1.77
		Apogee } Transfer orbit	25,345	-10.44
		600 by 600 nautical miles orbit	26,044	-6.73

The most severe entry conditions are experienced when the retropulse is applied at apogee of the transfer orbit. It is shown in Appendix JJ that although entry is quite steep it does not pose formidable design problems for the configuration selected.

KINEMATIC REQUIREMENTS

The minimum ΔV requirement for the RB to just skin the atmosphere (400,000 ft) is shown in Fig. LL-7 as a function of the application angle and the explicit orbital conditions. It is of considerable interest to see that the 1500-fps velocity increment, selected on the basis of range and range sensitivity, will also permit a considerable variation in the application angle if we are only concerned with deorbiting the system, and not with the exact location of impact. For example, we can survive a 60° error in the application angle, starting from a 600-nautical mile circular orbit. Therefore, we can have a high confidence in deorbiting the RTG/RB, even if there are severe errors in the initial attitude of the airborne system.

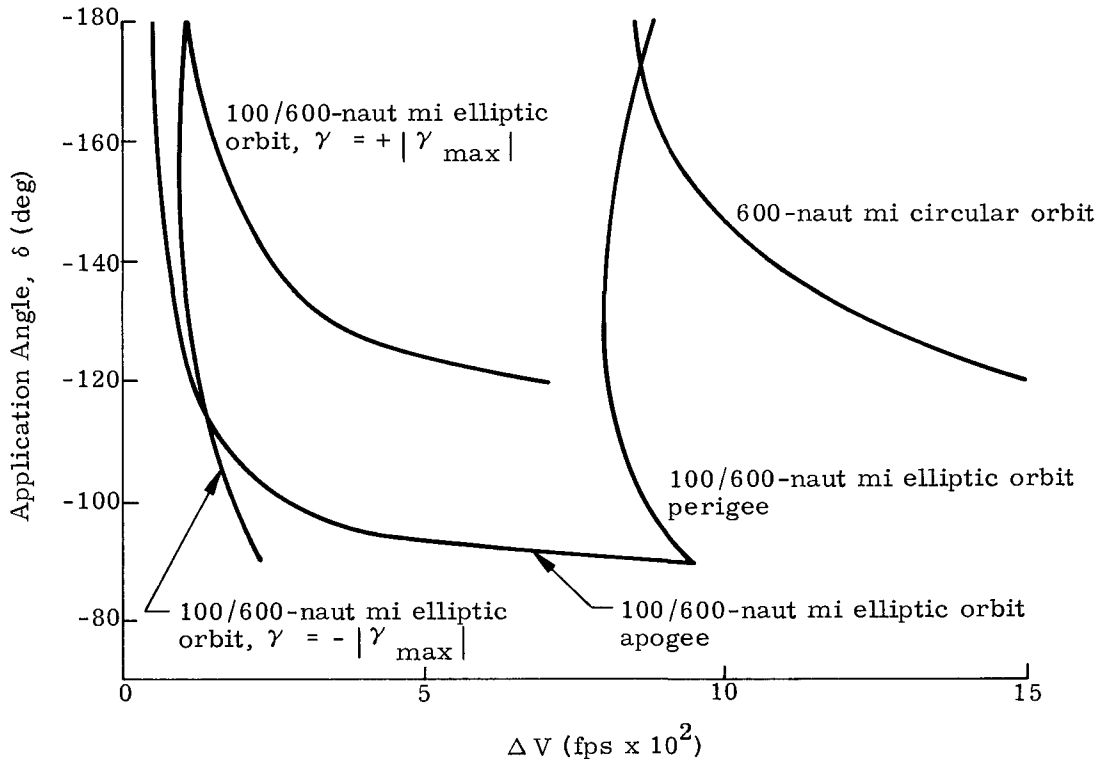

Fig. LL-7. Minimum ΔV Requirements for Reentry at 400,000 Feet

APPENDIX MM

DYNAMIC REENTRY ANALYSIS

An analog simulation was conducted to determine the dynamic, six-degree-of-freedom, reentry characteristics of the RTG/RB. This study was conducted in order to: (1) assess some of the (minor) differences between the standard, ballistic trajectories analysis and the real world; (2) investigate the aerodynamic stability of the configuration; and (3) determine the rate at which the configuration turns toward the stable attitude, as a function of the initial roll and pitch rates, and initial attitude.

Although ballistic trajectories have been acceptable for safety analysis (which, after all, is the main motivation of these reentry trajectories), we were interested in this type of trajectory simulation in order to gain an understanding of malfunctioning reentries.

These investigations were conducted for orbital entry conditions. Primary emphasis was placed upon malfunction conditions such as entry at very shallow entry angles (i.e., a decaying orbit). This orbital entry condition results in the lowest maximum dynamic pressures. Consequently, if a vehicle can survive a set of initial conditions for shallow entry, it will stabilize quicker for steeper entry angles. This theoretical result (Ref. MM-1*) has been verified in this study.

The aerodynamic characteristics of the referenced vehicle used in this analysis are presented in Appendix Y. The vehicle center of gravity was assumed to be at $\frac{X}{D} = 0.42$ (19.3 inches aft of the heat shield). The actual center of gravity location is at $\frac{X}{D} = 0.39$ (18 inches aft).

This center of gravity location increases the stability of the system. To conserve running time and increase accuracy, the atmospheric entry conditions for the analog were assumed to be at 300,000 feet (as compared to 400,000 feet for the digital programs). The velocity and flight path angle correspond to the digital results, based upon -0.1°, -2°, and -8° entry angles. A total of 41 different reentry trajectories were run. Of course, not all results are exposed in the report. Only a few of the trajectories and some parametric cross plots are presented.

---

*Ref. MM-1. Tobak and Peterson, "Theory of Tumbling Bodies Entering Planetary Atmospheres with Application to Probe Vehicles and the Australian Tektites," NASA TR R-203, 1964.

The reentry trajectory for a normal (-2°) entry condition is shown in Fig. MM-1. The initial pitch and roll rates were 6°/sec, and the initial attitude was vertical with a 90° initial angle of attack. To clearly present the results, the envelopes of the maximum and minimum angles of attack are presented rather than the highly oscillatory η versus t history.

The reentry trajectory for a steep (-8°) reentry is shown in Fig. MM-2 for the same initial conditions as above, and a shallow entry (-0.1°) is shown in Fig. MM-3. These results are quite interesting, as they show that the initial roll rate causes the reentry body to cone. This causes the minimum angle of attack to remain at about 10°. The maximum excursion, however, is clearly damped by the action of the increasing dynamic pressure acting on C_M.

It is interesting to see that the dynamic effects in the shallow entry had the tendency to increase the maximum dynamic pressure above the same value for the ballistic (η=0) trajectory. It is suspected that this effect is due to the lower drag coefficient at angles of attack than at α = 0, as well as to the oscillatory in the trajectory arising from an effective (but almost random) L/D ratio due to a finite η. This latter condition is most likely a contributor, since there was some scatter in the results of trajectory with almost identical initial conditions.

It is clear from these trajectories that a steep entry increases the effective damping of the initial rates. A parametric study was conducted for the shallow entry angle to determine the effect of initial pitch rate on the maximum angle of attack in the high aerodynamic heating region. The results of this are shown in Fig. MM-4. The contour is a function of the initial orientation. However, this dependency is quickly eliminated as the initial rates become large. The maximum pitch rate at which the reentry body will stop tumbling is approximately 600 deg/sec (Fig. MM-4). When the center of gravity of the vehicle is moved to the actual location (as compared to reference aerodynamic coefficients), the maximum allowable initial pitch rate is calculated to be about 1200 deg/sec. For steeper entry angles, higher maximum pitch rates can be tolerated.

A similar parametric study was made to determine the effect of initial roll rate on the maximum angle of attack in the high heating regime (Fig. MM-5). One rather strange feature of these reentry trajectories was the tendency of the reentry body to act like a lifting body at high (600 deg/sec) spin rates. The net effect of the oscillatory motion is to increase downrange at impact, to decrease the maximum dynamic pressure and, apparently, to decrease the maximum angle of attack. It is not as yet known whether the results at high spin rates are the result of peculiarities in the analog equipment. In any case, these results confirm the decision to despin the RTG/RB prior to reentry.

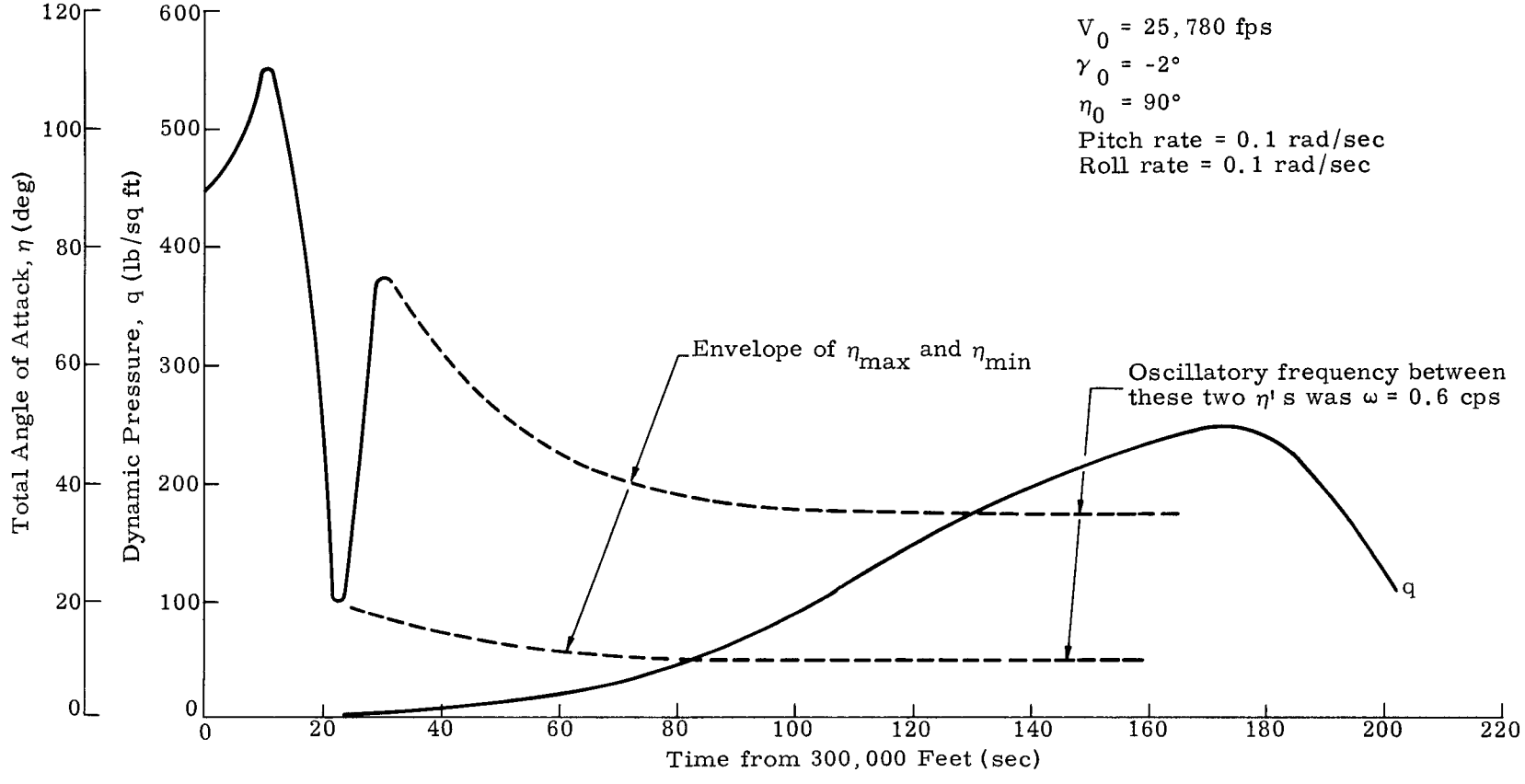

Fig. MM-1. Dynamic Trajectory for CRONUS RTG/RB

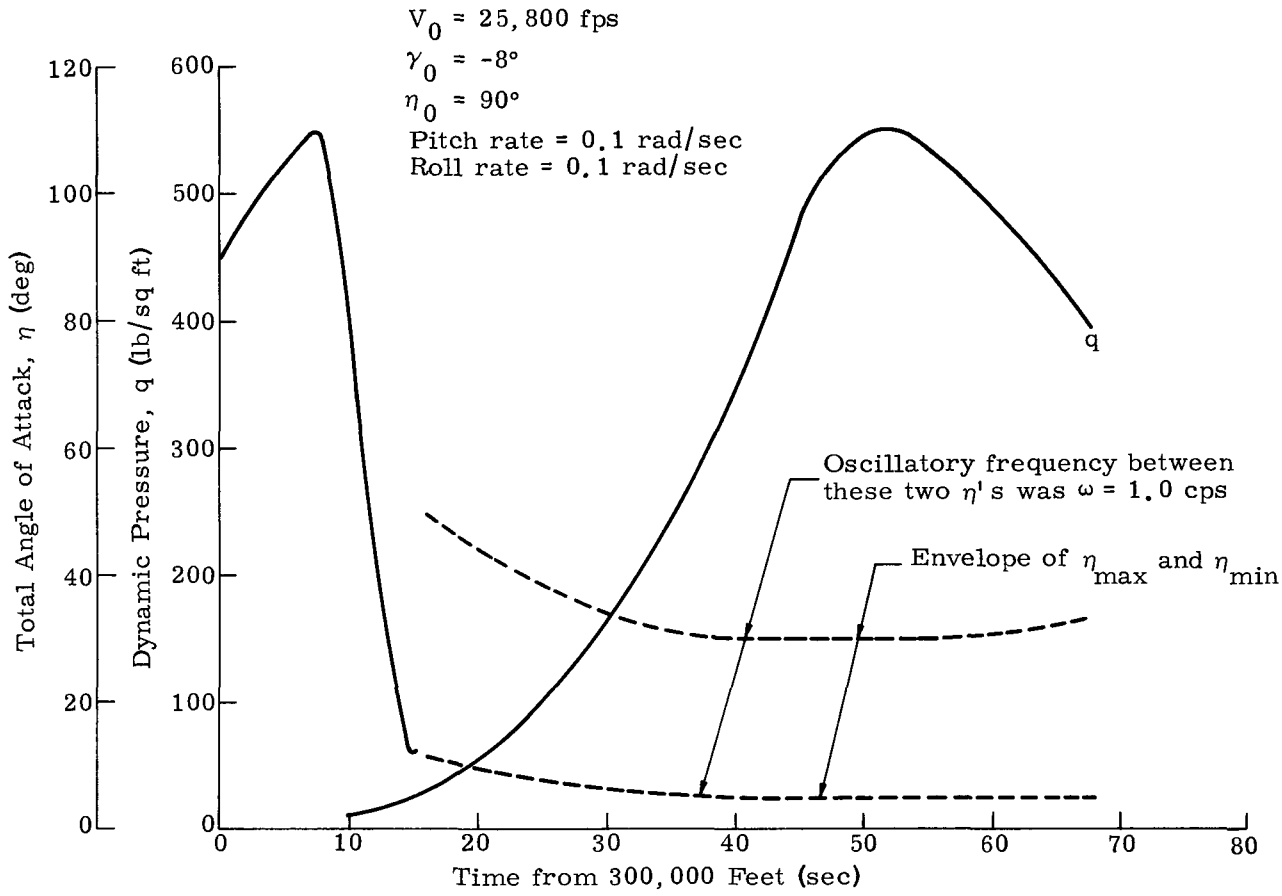

Fig. MM-2. Dynamic Trajectory for the CRONUS RTG/RB

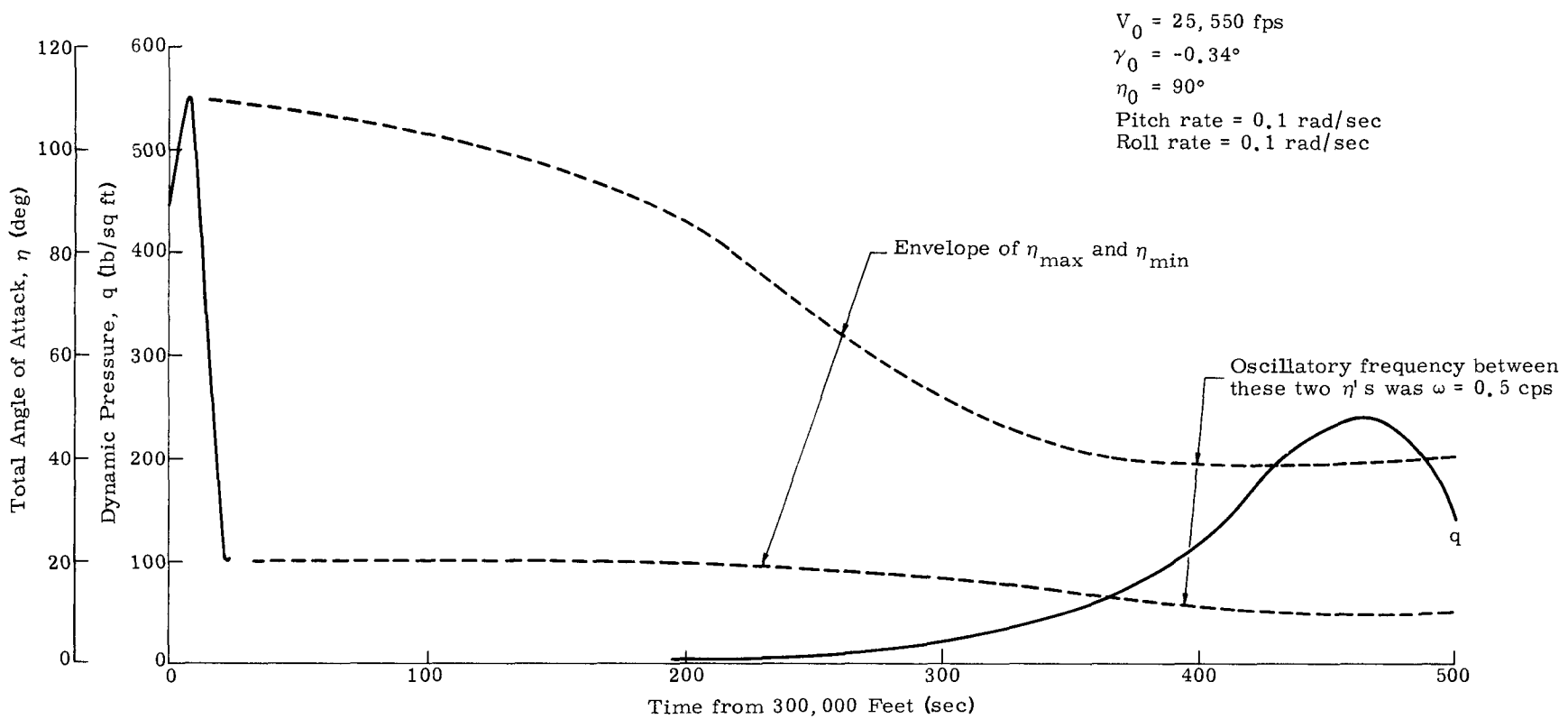

Fig. MM-3. Dynamic Trajectory for CRONUS RTG/RB

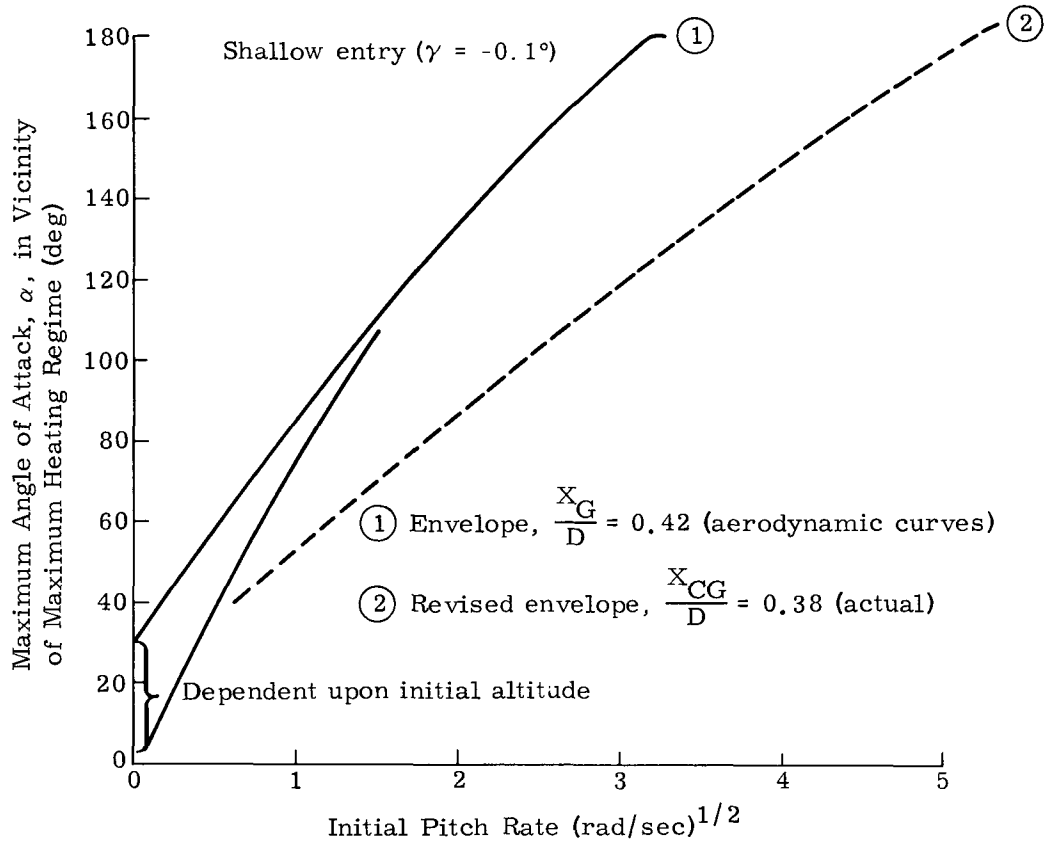

Fig. MM-4. Effect of Initial Pitch Rate on Maximum Angle of Attack, Shallow Orbital Entry

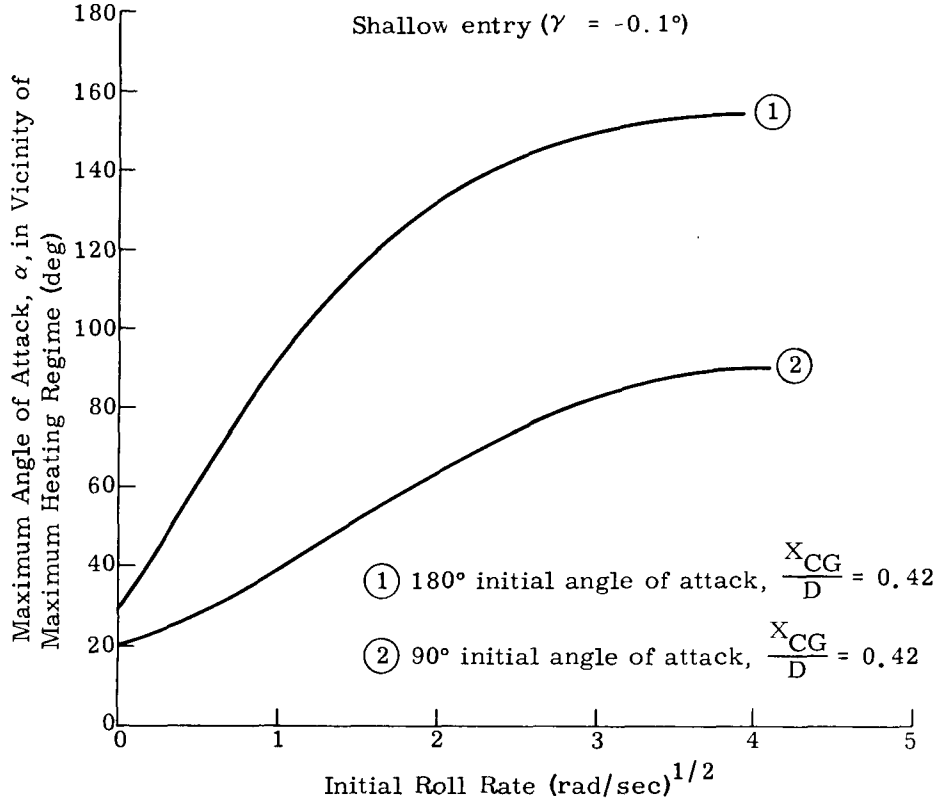

Fig. MM-5. Effect of Initial Roll Rate on Maximum Angle of Attack, Shallow Orbital Entry

APPENDIX NN

TERMINAL VELOCITIES

Terminal velocities at sea level for the several RB's possible are presented in this section. Bodies considered were:

(1) Thermoelectric generator reentry body without the deorbit package (RTG/RB).

(2) Thermoelectric generator reentry body with the deorbit package (CIR-RTG/RB).

(3) Heat source, including 36 fuel capsules

(4) Fuel capsule.

Terminal velocities were determined for the normal sea level atmospheric conditions (the air density, $\rho_{sl} = 2.38 \times 10^{-3}$ slugs/cu ft) with the various bodies in different attitudes (end-on, side-on and tumbling). Since some of the reentry shapes (numbers two, three and four) have never been tested (in free flight and tunnels), it was necessary to estimate the drag coefficients by comparing the reentry bodies to conventional (or tested) shapes.

Terminal velocity is the condition when the weight and the drag are equal in magnitude but opposite in direction. Therefore, the following expression was used:

$$W = D = C_D \frac{\rho}{2} A_{ref} V_T^2 \qquad \text{(NN-1)}$$

or

$$V_T^2 = \frac{2}{\rho} \frac{W}{C_D A}$$

Inserting the air density at sea level and taking the square root of both sides of Eq (NN-1), the terminal velocity at sea level is:

$$(V_T)_{sl} = 29 \, (W/C_D A_{ref})^{1/2} \qquad \text{(NN-2)}$$

where

W = weight of body at impact (lb)

D = drag force (lb)

C_D = drag coefficient at terminal velocity

ρ = air density at prescribed altitude (slugs/cu ft)

A_{ref} = aerodynamic reference area (sq ft)

V_T = terminal velocity (fps)

and the subscript

sl = sea level conditions

The drag coefficients for the RTG/RB were obtained from Ref. NN-1. For the end-on orientation (blunt end first), the drag coefficient was 1.1. In the tumbling attitude, its average coefficient was 0.77. The CIR-RTG/RB's drag coefficient for the end-on case was assumed to be 0.5. An average coefficient of 0.6 was assumed for the CIR-RTG/RB in the tumbling reentry mode. Terminal velocities for the RTG/RB and CIR-RTG/RB at sea level are presented in Table NN-1 for the end-on and tumbling attitudes.

The subsonic drag coefficients for the heat source and the fuel capsule were estimated by assuming both configurations to be right circular cylinders. These coefficients for the end-on (small end first) and side-on (flow perpendicular to the axis of revolution) cases were obtained from Ref. NN-2 for laminar flow (below the critical Reynolds number of approximately 3×10^5). These coefficients were determined from the following expressions:

End-on case: $C_D = 0.8$ (NN-3)

Side-on case: $C_D = 1.465\ \ell/D$ (NN-4)

and were based on the cross sectional area. The factors ℓ and D were defined as the length and diameter of the cylinder, respectively. For the tumbling case, this equation was integrated

$$C_D = \frac{1}{\pi/2} \int_0^{90^\circ} \left[1.465 \frac{\ell}{D} \sin^3\alpha + 0.8 \cos^3\alpha\right] d\alpha \quad \text{(NN-5)}$$

to obtain

Tumbling case:

$$C_D = 0.621\ (\ell/D) + 0.339 \quad \text{(NN-6)}$$

TABLE NN-1

Terminal Velocities

Configuration	Weight (lb)	Area (sq ft)	Attitude	C_D (subsonic)	W/C_DA (lb/ft)	$V_{T_{sl}}$ (fps)
Reentry body without deorbit package	430	11.5	Blunt end first	1.1	34	170
	430	11.5	Tumbling	0.77	49	202
Rentry body with deorbit package with rocket motors empty	631	11.5	Blunt end first	0.50	109	310
	631	11.5	Tumbling	0.60	91	277
Reentry body with deorbit package with rocket motors fueled	755	11.5	Blunt end first	0.50	131	332
	755	11.5	Tumbling	0.60	109	310
Heat source	182	2.52	End-on	0.8	90	276
	182	2.52	Side-on	1.44	50	205
	182	2.52	Tumbling	0.95	76	253
Fuel capsule	4.02	1.23×10^{-2}	End-on	0.8	409	585
	4.02	1.23×10^{-2}	Side-on	12.8	26	147
	4.02	1.23×10^{-2}	Tumbling	5.77	57	218

The angle α was defined as the angle of attack. This coefficient was also based on the cylinder's cross sectional area. Terminal velocities for the heat source and fuel capsule are presented in Table NN-1 for the different orientations. The heat source will probably be tumbling at impact, while the capsule will be oscillating about the side-on attitude at impact.

REFERENCES

NN-1. Bradley, E. P., "Aerodynamic Information Note No. 20-Gemini Mission Aerodynamics," McDonnell Aircraft Corporation, December 27, 1962.

NN-2. Hoerner, S. F., "Fluid-Dynamic Drag," 1965.

APPENDIX OO

RELATIVE MOTION OF THE UMBILIBAL TOWER AND LAUNCH VEHICLE

Three parameters are identified contributing to the deviation of the L/V longitudinal centerline of the Titan IIIC from its theoretical structural centerline. These are:

a. structural misalignments including stage mismatch, tooling tolerances and other asymmetry

b. wind drag

c. wind induced oscillation (WIO) perpendicular to the drag component and wind direction.

From experimental data on the Titan IIIC at ETR, it was found that at launch vehicle station +106, static deflection due to structural misalignments is a maximum of 1.2 inches (Ref. OO-1). The structural misalignment is a constant for an individual launch vehicle and, for purposes of this study, the misalignment will not be considered in the determination of the total excursion of the launch vehicle relative to the umbilical tower.

Using the NASA 99.9% Ground Wind Profile, the Titan IIIC AGE design wind criteria is 46 mph at 30 feet above ground. Per Ref. OO-1, the wind drag deflection of the Titan IIIC and the simultaneous wind induced oscillation (WIO) is approximately 2.0 and ± 1.2 inches respectively at a reference elevation 130 ft above ground (approximately VS-135) in the design criteria wind condition. See sketch I. The drag is a constant direction deflection in the + x wind direction as shown. The WIO varies between + y and -y direction perpendicular to the wind drag.

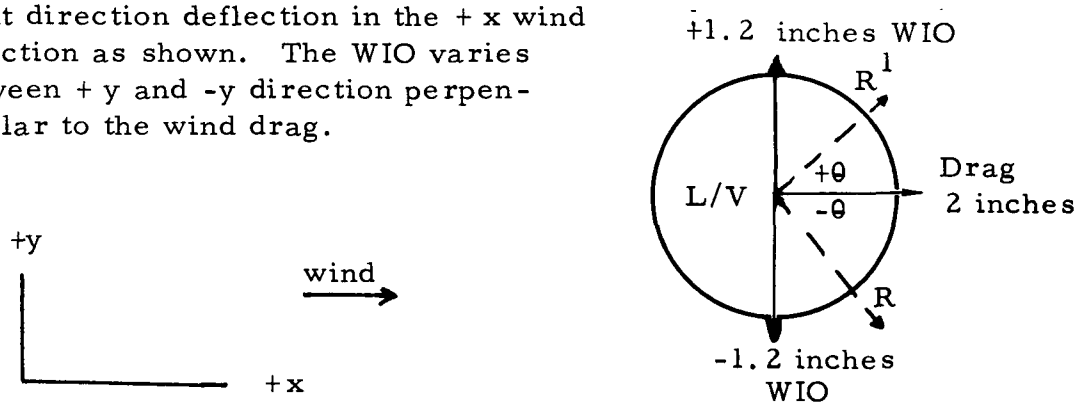

Sketch I

The resultant total deflection of the launch vehicle is

$$= \sqrt{2^2 + (\pm 1.2)^2} = \pm 2.33 \text{ inches}$$

at an angle, $\pm\theta = \sin^{-1} \pm \frac{1.2}{2.33} = \pm 31^{\circ}$ with the direction of the wind.

Per the facility criteria (Ref. OO-2), the maximum drag deflection of the umbilical tower in a 60 mph wind, including gusts, is less than 6 inches at a 170 foot elevation. Proportioning this deflection to the 130 foot elevation and 46 mph (assuming a conservative straight line relation):

$\frac{6 \text{ in.}}{170 \text{ ft}} = \frac{x}{130}$ at 60 mph

$x_{60} = 4.6$ inches

$x_{46} = \frac{46}{60} \times 4.6 = 3.5$ inches

Reference Sketch II

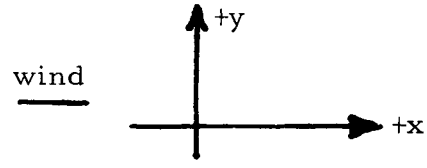

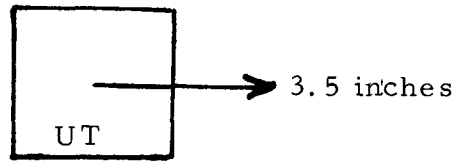

Sketch II

The system of UT and L/V is indicated in Sketch III. The relative displacement of the UT to the L/V in the direction of the wind is simply the difference between the two drag deflections, i.e. 3.5 - 2.0 = 1.5 inch assuming both structures deflect in the same direction in similarily directed winds. An estimation of the relative deflection of the system in a direction perpendicular to the wind is indicated in Sketch III. With the wind direction as shown, the oscillating deflection of the L/V is the WIO of $\pm$ 1.2 inches. For purposes of estimating the maximum relative deflection, the UT drag deflection is arbitrarily rotated perpendicular to the wind direction and assumed oscillatory of magnitude $\pm \frac{3.5}{2} = \pm 1.75$ inches.

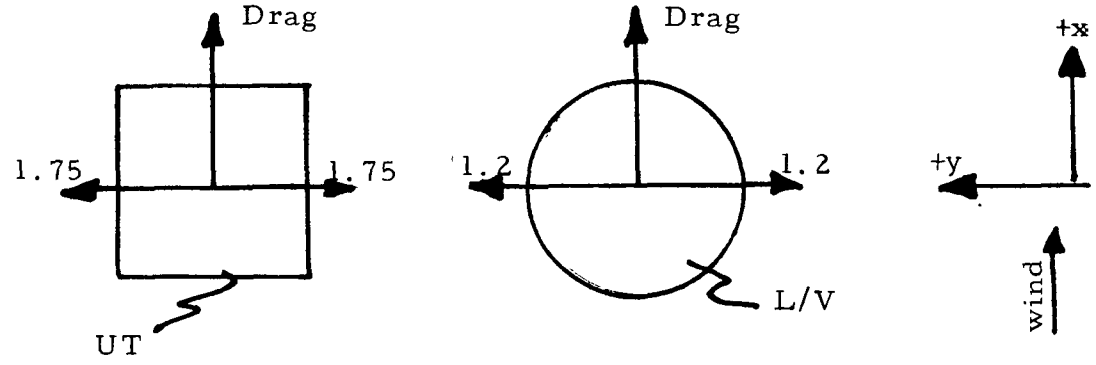

Sketch III

Per Ref OO-1, the natural frequency of the Titan IIIC in a fueled condition is .46 cps. The motion of the Titan IIIC is illustrated graphically in Sketch IV in a direction perpendicular to the wind direction.

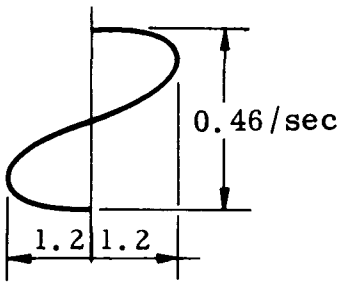

Sketch IV

The natural frequency of the UT is not defined, but as a limiting case is assumed the same as the launch vehicle. A graph of the UT deflection versus frequency is shown in Sketch V.

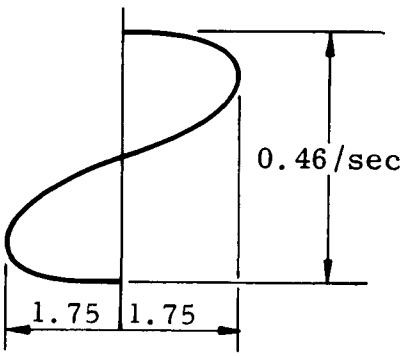

Sketch V

For purposes of obtaining the maximum relative deflection, the two structures are shown in phase in Sketch VI.

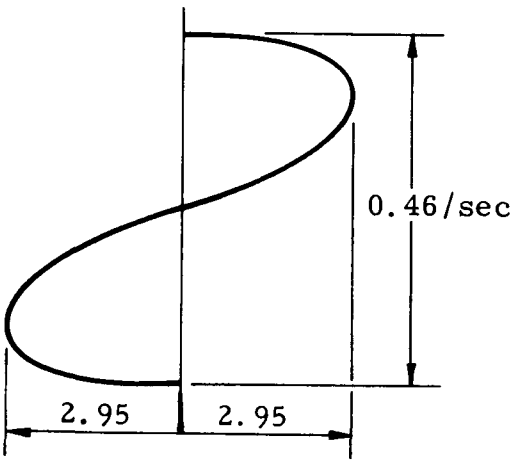

Sketch VI.

Stated in other words, the UT and L/V move in an oscillatory motion relative to each other of magnitudes $\pm$ 1.75 and $\pm$ 1.2, respectively, perpendicular to the wind, providing the following possible relative deflections.

+ 1.75 + 1.2	=	2.95 inches
- 1.75 - 1.2	=	-2.95 inches
+ 1.75 - 1.2	=	.55 inches
- 1.75 + 1.2	=	-.55 inches

based on whether the structures are in phase or out of phase.

Therefore, the maximum relative motion between the launch vehicle and umbilical tower is approximately 6 inches ($\pm$ 2.95 inches) at .5 cps (.46 cps).

To determine the influence of the FHM on the launch vehicle under the frequencies and amplitudes cited, a diagram of the system is shown in the following sketch where the umbilical tower is assumed static and all motion of the system is allowed in the launch vehicle. Therefore the launch vehicle oscillates at .46 cps and a 5.90 inch excursion. The FHM on a frictionless support and rigidly connected to the launch vehicle follows, in phase, the vehicle's motion. It is assumed that this motion is approximated by a sinusoidal function:

$$x = A \sin \omega t$$

$$\dot{x} = \frac{dx}{dt} = \omega A \cos \omega t$$

$$\ddot{x} = \frac{d^2x}{dt^2} = -\omega^2 A \sin \omega t$$

and

$$F = \frac{W}{g} \ddot{x}$$

$$F = -\frac{W}{g} \omega^2 A \sin \omega t$$

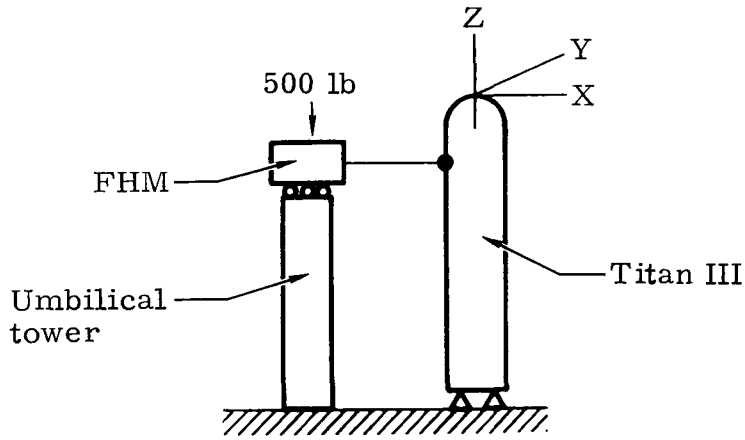

F is max when $\sin \omega t = 1$

$$F = -\frac{W}{g} \omega^2 A$$

$$\omega = 2\pi f$$

$$= 2\pi \times 0.46$$

$$\omega = 0.92\pi \text{ radian/sec.}$$

$$= -\frac{500}{32.2} (0.92\pi)^2 \left(\frac{5.90}{12}\right)$$

$$F = -63.8 \text{ lb.}$$

The above indicates that the resultant load in the launch vehicle due to relative motion of the umbilical tower and launch vehicle and a zero friction suspension of the FHM is approximately 64 pounds.

REFERENCES

OO-1. Analytical data based on wind tunnel tests with 7.5% model, Telecon with Robert Morra M/D x 2131 per M. Krietz.

OO-2. CR-62-1000, Erratas, "Criteria and Concepts, SLV(5) ITL System (Titan III), Technical Launch Facilities," CCMTA.

APPENDIX PP

IDEALIZED GHE CONCEPTS

A. FIXED TOWER, FOLDING BOOM, FUEL BLOCK LOADING

This concept is a modification of the SNAP 29 fueling concept in the following areas:

(1) The loading device uses a lighter weight cask than the ICC cask in which the fuel block is shipped.

(2) A heater block compartment is located beside the transfer cask.

(3) A separate ram rod is used for the fuel block and the heater block. The ram rods have a gripper mechanism on the end to engage a knob on the fuel and heater blocks.

(4) A guide tunnel or duct with rollers in the bottom is used to transfer the fuel and heater blocks to the RTG.

This proposed concept differs from the SNAP 29 fuel loading device in the following manner:

(1) The length of the tunnel or duct connecting the RTG to the loading cask is approximately 20 feet compared to a few feet for SNAP 29.

(2) The ram rods are proportionally increased in length.

(3) The cask is mounted on a fixed platform rather than the three-way carriage of SNAP 29.

(4) The transfer tunnel is connected to the space vehicle manually under a cold environment rather than remotely connected. It will remain connected to the space vehicle up to liftoff.

(5) The loading device is mounted on the umbilical tower rather than the MST.

(6) The ram rods are motor-driven and remotely controlled rather than manually controlled by an operator located at the loading device.

1. Equipment List

The equipment list that is required for fuel block loading on the fixed tower folding boom is as follows:

(1) Transportation cask (ICC regulations)

(2) Transfer cask (for use in loading device)

(3) Fuel block loading device

  (a) Cask support structure

  (b) Folding tunnel boom with actuator and support structure

  (c) Fuel block ram rod with gripper, latch release and support structure

  (d) Heater block container and ram rod

  (e) Pneumatic system

  (f) Hydraulic system

  (g) Cooling air system

(4) ICC cask skid

(5) Transfer device to transfer fuel block from ICC cask to transfer cask

(6) Transfer cask dolly or trailer

(7) Slings and special tools.

2. Launch Complex Modifications

Modifications to the launch complex will be minor. Point Arguello Launch Complex 2 (PALC 2) Pad 3, a Titan IIIB Agena complex, is shown in the loading configuration drawing but other Titan III complexes would be similarly adaptable to this loading configuration (Fig. PP-1).

The loading device will be installed on top of the existing umbilical tower and modifications to the tower will be minimal. Preliminary analysis shows that the tower will support the 5000-pound transfer cask without tower reinforcement. A support stand will be added to the umbilical tower to support the transfer cask and heater container. The transfer tunnel boom will also be supported from the stand. Attachment of the boom actuator and ram rod support structure will be made to the top platform. (Elevation: 130-1/2 ft)

A modification to the MST curtain door will have to be made to allow tunnel boom penetration. Modifications or additions to existing hydraulic,

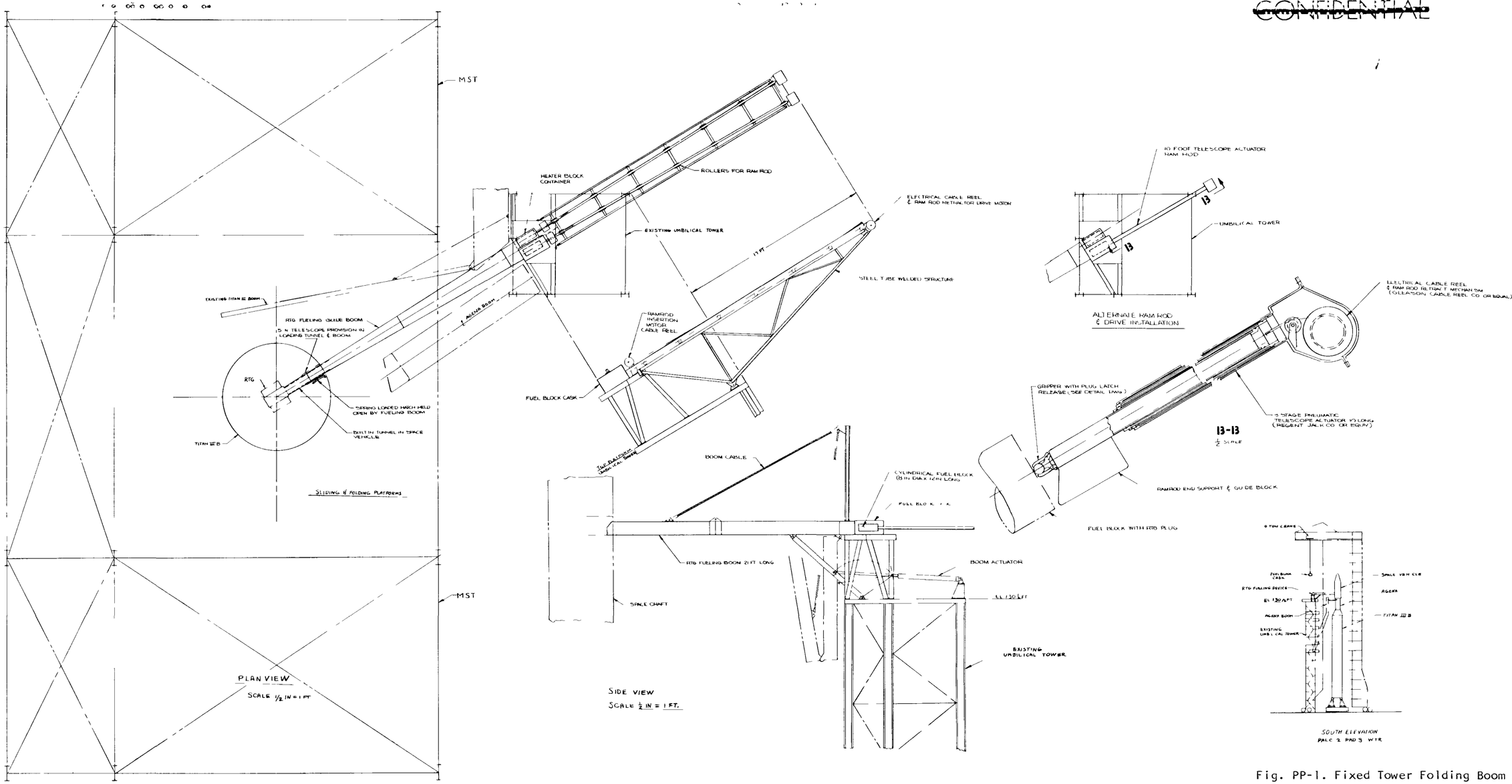

Fig. PP-1. Fixed Tower Folding Boom

pneumatic and air conditioning systems will be required for RTG GSE requirements.

3. Description and Operation

a. Fuel block shipment

The fuel block will be shipped to the launch site in a cask designed to ICC regulations. The cask will be mounted on a skid which will distribute the load to permit air, rail or truck transportation. Provisions will be made on the cask for attachment to the transfer cask and a push rod transfer system will be provided.

b. RTG shipment

The RTG will not be fueled when shipped to the launch site. Shipping will be in a normal shipping manner.

c. Launch site preparations

Nonradiation environment condition. The RTG will be installed in the space vehicle on the ground. The space vehicle will then be erected and installed on the Titan III in the normal manner. The tunnel boom will be erected to a horizontal position by the actuator. The outer section of the boom, which was not connected to the inner boom, will be inserted manually into the space vehicle, then connected to the inner boom. The support cable will be attached and adjusted with a turnbuckle. The heater block will be installed in the transfer container on the umbilical tower and the transfer ram rod connected. Electrical contact is made through the ram rod. The fuel block transfer rod is positioned on the tower support rollers in readiness for the transfer cask installation.

Radiation environment condition. The ICC shipping cask will be connected to the transfer cask and the fuel block will be pushed into the transfer cask with a push rod. The transfer cask will be transported to the launch pad on a flat-bed trailer and positioned under the MST 10-ton crane. The crane hook will be connected to the cask sling and will lift the cask to the fuel transfer device located on top of the umbilical tower. Guide ways will assist in positioning the cask in the loading device. The cask will be positioned on the umbilical tower on R-1 day. Loading the fuel block into the RTG will occur late in the countdown on launch day. After propellant loading has been completed, the heater block will be remotely inserted into the RTG by actuating the ram rod. The RTG temperature will be gradually brought up to the operating range. As soon as the temperature stabilizes, the heater block will be withdrawn by the ram rod which remains connected to the heater block at all times. The fuel block ram rod will be actuated and will insert the fuel block, with the RTG plug attached, into the RTG.

A torque-limiting clutch will maintain a maximum predetermined ram force on the RTG even under differential motion of the space vehicle and loading device. Door latch mechanisms on the RTG or fuel block plug will lock the fuel block in place. The ram rod retractor motor will be actuated and it will be determined if the fuel block is securely locked in the RTG as the ram rod will not retract. If the fuel block is determined to be secured in the RTG, then the grippers on the end of the ram rod will be disengaged and the ram rod fully retracted. The tunnel boom connecting the cask to the space vehicle will remain connected through liftoff. Liftoff switches, located on the Titan thrust mount, will send a signal to the tunnel boom actuator to retract. The outer section of the boom is hinged so that the first motion of the spacecraft will cause the boom to fold upward and this motion can be used for redundant switches to signal actuator motion. Redundancy will also be built into the actuator and hydraulic valving system. The L/V hatch will be spring-loaded closed as the boom is withdrawn from the loading hatch.

In the event liftoff does not occur after engine start, the boom and fuel block retracting devices will be ready so the fuel block can be removed immediately. The ram rod will travel through the boom tunnel guided by a runner on the end of the boom which rolls on rollers in the bottom of the tunnel boom. Engagement is made as soon as the gripper contacts the knob on the fuel block plug. Trip fingers in the gripper mechanism release the latch, allowing the fuel block to be retracted into the cask.

B. TOWER-MOUNTED, CABLE TRANSFER, BLOCK LOADING

This concept is similar to Concept A in the following respects:

(1) The loading device uses a lighter weight cask than the ICC cask in which the fuel block is shipped.

(2) The loading device is mounted on the fixed umbilical tower.

(3) The fuel block transfer system is connected to the RTG manually under a radiation cold environment.

(4) The fuel block transfer is conducted remotely from the block house.

(5) The transfer system remains connected to the RTG until liftoff.

The major differences between this concept and Concept A are as follows:

(1) No internal provisions in the fuel loading device are made for a heater block to preheat the RTG, although, a heater block system could be provided.

(2) A cable is used to guide the fuel block rather than a tunnel boom.

(3) A motor-driven cable is used instead of ram rods.

(4) Remotely operated cable cutters or cable release devices are used to disengage the fuel block rather than grippers on a ram rod.

1. Equipment List

The equipment list for this concept is:

(1) Transportation cask (ICC regulation)

(2) Transfer cask for use in loading device

(3) Fuel block loading device

  (a) Cask support structure

  (b) Cable transfer system with motor or winches and remotely operated cable cutters or cable release devices

  (c) Cable slack takeup device

(4) ICC cask skid

(5) Cooling air system

(6) Transfer device to transfer fuel block from ICC cask to transfer cask

(7) Transfer cask dolly or trailer

(8) Slings and special tools.

2. Launch Complex Modifications

Modifications to the launch complex will be minor. Titan III, Complex 40 at ETR is shown in the loading configuration drawing but other

Titan III complexes would be similarly adaptable to this loading configuration (Fig. PP-2).

The loading device will be located between Platforms 10 and 11 on the existing umbilical tower. Modifications to the tower will be minimal. Preliminary analysis shows that the tower will support the 5000-pound transfer cask without tower reinforcement. A structure will be added above Platform 10 to support the cask and transfer device. The structure will be tied directly into four vertical H beams.

3. Description and Operation

a. Fuel block shipment

The fuel block will be shipped to the launch site in a cask designed to ICC regulations. The cask will be mounted on a skid which will distribute the load to permit air, rail or truck transportation. Provisions will be made on the ICC cask for attachment to the transfer cask and a push rod transfer system will be provided.

b. RTG shipment

The RTG will not be fueled when it is shipped to the launch site. Shipping will be in a normal shipping manner.

c. Launch site preparation

Nonradiation environment condition. The RTG will be installed in the space vehicle on the ground. The space vehicle will then be erected and installed on the Titan III in the normal manner. The transfer cable will be installed through the RTG and the free ends coiled in preparation for the transfer cask installation on the umbilical tower. Installation will be made on the cask support platform of the cask takeup device which is used to maintain cable tension during wind sway of the launch vehicle. The transfer drive motor or winch will also be installed on the transfer cask platform.

Radiation environment condition. The ICC shipping cask will be connected to the transfer cask and the fuel block will be pushed into the transfer cask with a push rod. The transfer cask will be transported to the launch pad on a flat-bed trailer and positioned under the MST crane. The crane hook will be connected to the cask sling and the cask will be lifted up the umbilical tower and positioned into the fuel transfer device with the aid of tag lines. The transfer cable, with quick release fittings on each end, will be inserted through each end of the transfer cask and connected to the fuel block plug. The closed loop cable will be connected to the spring-loaded takeup mechanism and the transfer drive

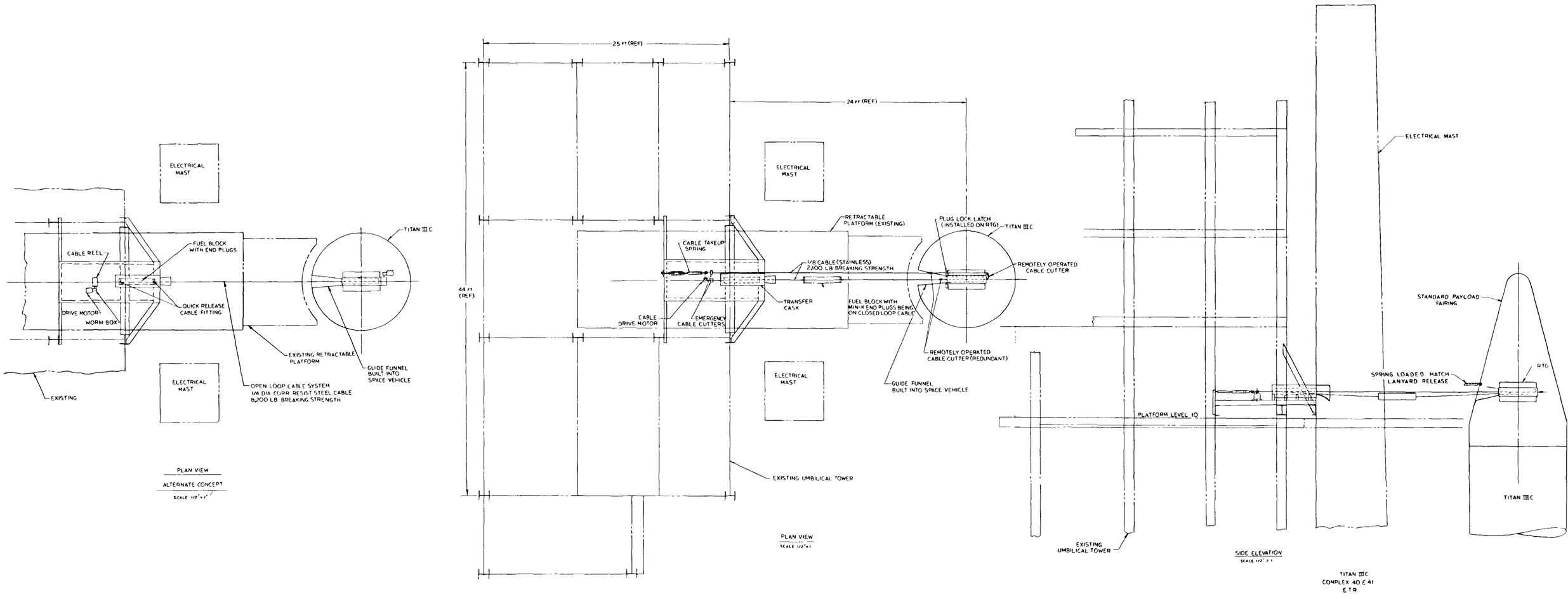

Fig. PP-2. Fixed Tower--Cable Transfer

motor will be hooked to the cable. Transfer of the fuel block from the cask will be conducted remotely late in the countdown on launch day.

The transfer operation begins with opening the cask plug and actuating the transfer motor. With the closed loop cable system the cable acts as guide, support and means of transfer. The transfer is accomplished by driving the cable with an electric motor. With the open loop cable system, a cable winch is located behind the RTG in the launch vehicle and another is located on the other end of the cable on the umbilical tower. Transfer of the fuel block is accomplished by actuating the cable winch on the RTG. The winch on the umbilical tower will be braked to maintain tension in the cable. A funnel-shaped duct in the launch vehicle will assist in guiding the fuel block into the RTG and will prevent loss of air conditioned air in the space vehicle. The winch will continue to pull the fuel block into the RTG until a specified preload has been achieved, at which point wedge-shaped latches will be released to maintain preload. The winch will be designed to stall when the preload value is reached. The cable to the umbilical tower winch will remain connected until liftoff has been achieved, at which time a mechanically actuated cable release will disconnect the cable from the fuel block plug in the RTG. The cable will be reeled in as the launch vehicle rises. The launch vehicle hatch, which is spring-loaded closed, will be remotely latched. In the event liftoff does not occur after engine start, the fuel block can be immediately removed as the guide cable remains attached. Removal would consist of retracting the fuel block latches in the RTG and actuating the umbilical tower cable winch. The winch on the RTG will act as a drag brake to maintain tension in the cable. The fuel block will be retracted into the cask and the cask plug remotely closed.

d. Heater block installation

The heater block will not be an integral part of the fuel block loading device and the need for a fuel block is questionable at this time. If a heater block is required, it will be installed from a UT retractable platform which will be retracted before the fuel block is transferred.

C. GUIDE RAILS AND TROLLEY, FUEL BLOCK LOADING

This concept proposes a guide rail and remotely operated trolley to transfer the fuel block from the transport cask, located at ground level, to the RTG which is installed on the launch vehicle. This system will permit fueling late in the countdown and will remain intact until liftoff in event that defueling of the RTG is required before launch (Fig. PP-3).

1. Equipment List

The following equipment will be furnished for the complete system:

~~CONFIDENTIAL~~

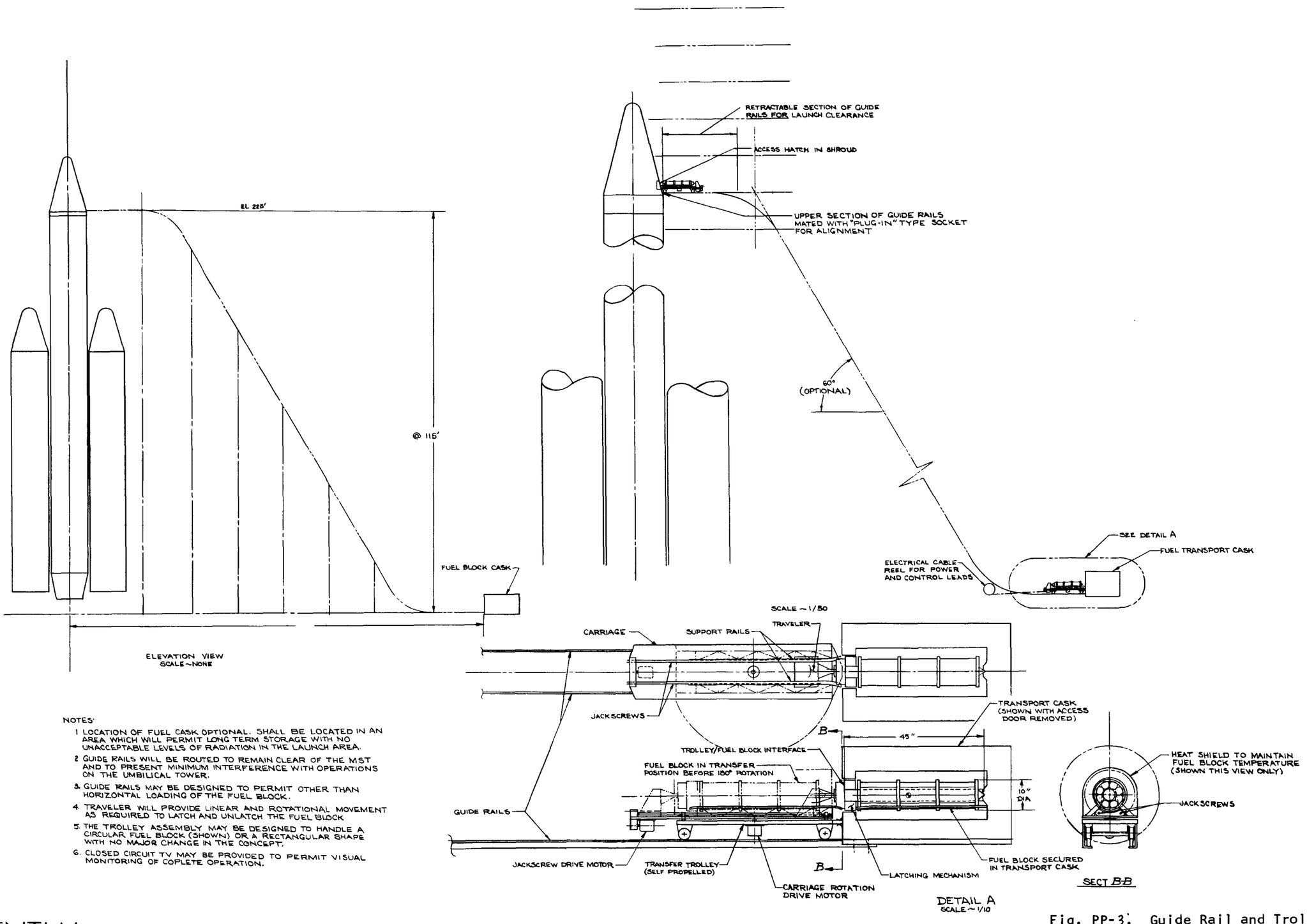

NOTES:

1. LOCATION OF FUEL CASK OPTIONAL. SHALL BE LOCATED IN AN AREA WHICH WILL PERMIT LONG TERM STORAGE WITH NO UNACCEPTABLE LEVELS OF RADIATION IN THE LAUNCH AREA.
2. GUIDE RAILS WILL BE ROUTED TO REMAIN CLEAR OF THE MST AND TO PRESENT MINIMUM INTERFERENCE WITH OPERATIONS ON THE UMBILICAL TOWER.
3. GUIDE RAILS MAY BE DESIGNED TO PERMIT OTHER THAN HORIZONTAL LOADING OF THE FUEL BLOCK.
4. TRAVELER WILL PROVIDE LINEAR AND ROTATIONAL MOVEMENT AS REQUIRED TO LATCH AND UNLATCH THE FUEL BLOCK
5. THE TROLLEY ASSEMBLY MAY BE DESIGNED TO HANDLE A CIRCULAR FUEL BLOCK (SHOWN) OR A RECTANGULAR SHAPE WITH NO MAJOR CHANGE IN THE CONCEPT.
6. CLOSED CIRCUIT TV MAY BE PROVIDED TO PERMIT VISUAL MONITORING OF COPLETE OPERATION.

Fig. PP-3. Guide Rail and Trolley

~~CONFIDENTIAL~~

(1) Transportation cask (ICC regulations)

(2) Cask cooling system

(3) Guide rail assembly

(4) Cask support structure at launch site

(5) Hoist to remove cask cover

(6) Trolley assembly

(7) Power and control cable reel assembly

(8) Closed circuit TV installation

(9) Retract mechanism for upper section of rails

(10) Remote control panel and instrumentation.

2. Launch Complex Modifications

The following additions or modifications to the launch complex will be required to accommodate this concept:

(1) Installation of a pad and structure to support the fuel block transport cask for long-term storage. Location will be in an area which will not interfere with normal launch preparations.

(2) Installation of a rail system leading from the cask support structure to the RTG in its position on the launch vehicle. The upper section of the rail will be movable to provide vehicle clearance at launch. The rails will be routed to remain clear of the MST. The upper end of the rails will be supported by the umbilical tower where a flexible section will be employed to accomplish compliance with the RTG.

(3) A retract mechanism will be installed on either the umbilical mast or the umbilical tower. The mechanism will be triggered immediately prior to ignition of Stage 0 to cause the section of rail adjacent to the payload to be retracted.

(4) A control and instrumentation console will be added to the launch control center for remote operation and monitoring of the system. The system will be interconnected by landline.

3. Description and Operation

a. Fuel block shipment

The fuel block will be shipped to the launch site in a cask designed to ICC regulations. The cask will incorporate cooling provisions and instrumentation as required to condition and monitor the fuel block.

b. RTG shipment

The RTG will be shipped to the launch site in the unfueled condition, using standard shipping containers and methods.

c. Launch site preparation

Nonradiation environment condition. The RTG, with an electrically heated simulated fuel block, will be installed on the spacecraft by manual procedures. The RTG will be brought up to equilibrium temperature and the complete spacecraft electrical system will be checked out. During this period, the isotope fuel block will remain in the closed shipping cask.

Radiation environment condition. When the countdown and checkout reaches the point where installation of the fuel into the RTG is to be accomplished, the fuel cask cover will be unbolted by manual operation. At the same time, the electrically heated fuel block will be removed from the RTG. At this point, the launch pad will be cleared of personnel and all operations will be remotely controlled. The fuel block cask will be opened by remotely controlling the crane installed at the shipping cask location. The cask will be designed so that with the cover removed, the fuel block will be exposed in a manner that will make it accessible to the trolley. The trolley will be moved up into a position adjacent to the cask and the traveler extended to contact and latch onto the fuel block. Next the traveler will be retracted by actuation of the jack screws to draw the fuel block onto the trolley. With the fuel secured in place, the trolley will be self-propelled through a switch assembly in the guide rails and up into contact with the RTG mounted on the space vehicle. By actuation of the jack screws, the traveler will be moved forward to insert the fuel block into the RTG. Rotation of the traveler fuel support interface will cause the fuel block to lock into the generator. The trolley will then be moved back clear of the retractable section of the rail system. The rails will remain in contact with the RTG until the moment of liftoff in case defueling is required. To defuel the RTG, the reverse of this procedure will be followed to return the fuel to the fuel cask. The cask will be closed by remote control which will return the launch site to a radiation free environment.

d. Heater block installation

At any time after initial heatup at the launch site, the RTG will remain at temperature by means of electrical heaters when the fuel block is not installed. The electrical heaters will be manually installed and removed as required.

D. ERECTABLE TOWER, SITE INDEPENDENT, FUEL BLOCK LOADING

This concept utilizes a transportable tower with the fuel block transfer device mounted on top. The tower which includes an elevator and erecting winches was adapted from the Bucyrus-Erie Mark 1-50 tower crane (Fig. PP-4).

1. Equipment List

The following is the equipment list required for this concept:

(1) Movable tower

(2) Shipping cask

(3) Fuel block loading device

(4) Cooling air system

(5) Cask dolly

(6) Slings and special tools.

2. Launch Complex Modifications

No modifications are required at the launch complex assuming that sufficient access is available on the launch pad to accommodate the erectable tower.

3. Description and Operation

a. Fuel block shipment

The fuel block will be shipped to the launch site in a cask which has a removable top plug. The cask will be designed for ICC regulations and will also serve as the transfer cask in the loading device.

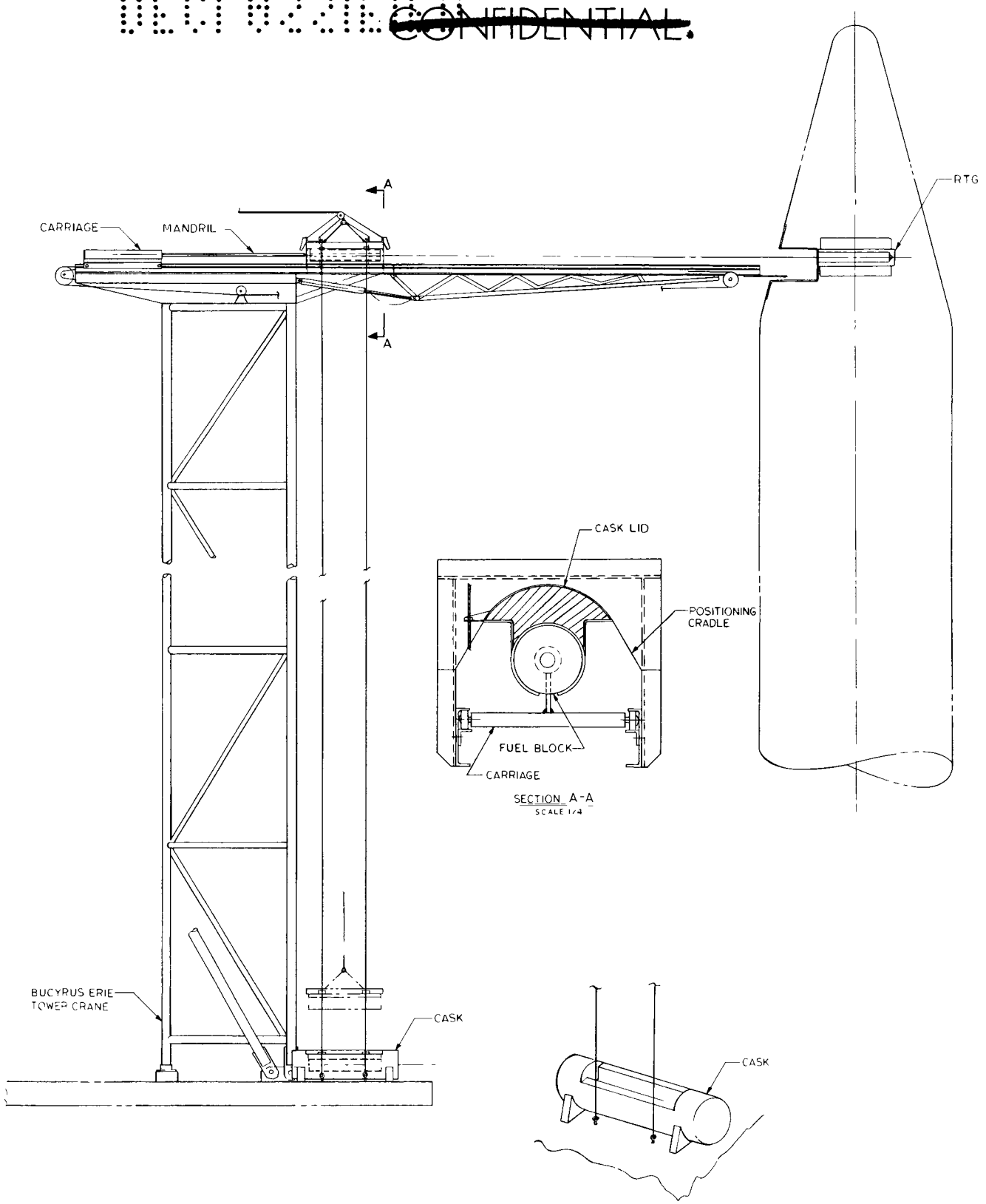

Fig. PP-4. Erectable Tower--Site Independent

b. RTG shipment

The RTG will be shipped to the launch site in a normal shipping manner.

c. Launch site preparation and operation

The fuel loading preparation will begin with rolling the tower up to the launch pad and erecting it to a vertical position using its built-in winch system. The cask will be installed on the tower platform at the base of the tower. The transfer boom will be erected with the actuator and manually aligned with the space vehicle. Positioning fingers will be inserted into the space vehicle opening and will serve to maintain alignment between the space vehicle and the loading boom. An inverted cradle is mounted on the transfer boom and guide cables pass from the cradle to the cask. The cables pass through guide blocks on the cask lid. A hoist cable is attached to the cask lid which raises the lid and fuel block up the guide cables and into the inverted cradle at the end of the transfer boom. A track-mounted carriage with a mandrel attached to the forward end is positioned behind the fuel block cradle. The carriage moves the mandrel into the fuel block, picks it up and carries it to the RTG. A door latch mechanism locks the fuel block into the RTG by applying pressure until the door-type latches on the RTG lock in place. The carriage is retracted to the stowed position. The positioning fingers at the end of the boom are remotely retracted and the boom folded to a down position.

Fuel unloading can be accomplished in the event of an aborted launch. The boom is erected to a horizontal position by the actuator. The positioning fingers are inserted remotely into the space vehicle to align the boom with the RTG. The carriage is moved along the track until the mandrel is inserted into the fuel block. Fingers on the mandrel lock onto the fuel block while other fingers on the mandrel unlatch the fuel block. The carriage is reversed and moves the fuel block back to the cask lid. The fuel block is unlatched from the mandrel and the carriage continues back to a stowed position. A hoist lowers the cask lid with the fuel block along the guide cables to the cask at the base of the tower.

During launch the only nuclear ground handling equipment attached to the space vehicle might be a lanyard attached to the loading hatch. The hatch will be spring loaded and will be closed by the liftoff motion, pulling a pin which holds the hatch open. Another method which would eliminate the lanyard would be an over center spring which would rely on wind load during liftoff to close the hatch. This method is similar to that used to close the air conditioning hatch on the Gemini launch vehicle during liftoff.

E. SPLIT CASK, TOWER-MOUNTED, FUEL BLOCK LOADING

This concept, shown in Fig. PP-5, is similar to the loading device used on top of the movable tower, Concept D. It differs in the fact that the cask is split in half and each half is mounted on the tracks which move the cask sideways. This permits the carriage to pick up the fuel block and pass through the cask for installation in the RTG. Boom alignment is achieved by actuating a rod into a guide cone which is mounted on the exterior of the S/V. The cone is jettisoned by lanyard at liftoff. (See Section D for other procedural details.)

F. CAPSULE BELT, FUEL BLOCK LOADING, TOROIDAL RTG

The loading device, which consists of the transfer cask, transfer tunnel boom, boom actuator, transfer drive motor, cask door actuators and transfer belt takeup device, is mounted on a pallet which can be readily installed on existing tower structures or a mobile tower.

1. Equipment List

The equipment required for this approach is:

(1) Transportation/transfer cask

(2) Fuel block loading device

  (a) Cask support structure

  (b) Transfer tunnel boom

  (c) Cask door actuators

  (d) Transfer belt takeup device

  (e) Boom actuator and support structure

  (f) Fuel block lock actuator

  (g) Transfer belt

  (h) Transfer belt remote disconnect

(3) Cask shipping skid

(4) Cask protective screen

(5) Slings and special tools.

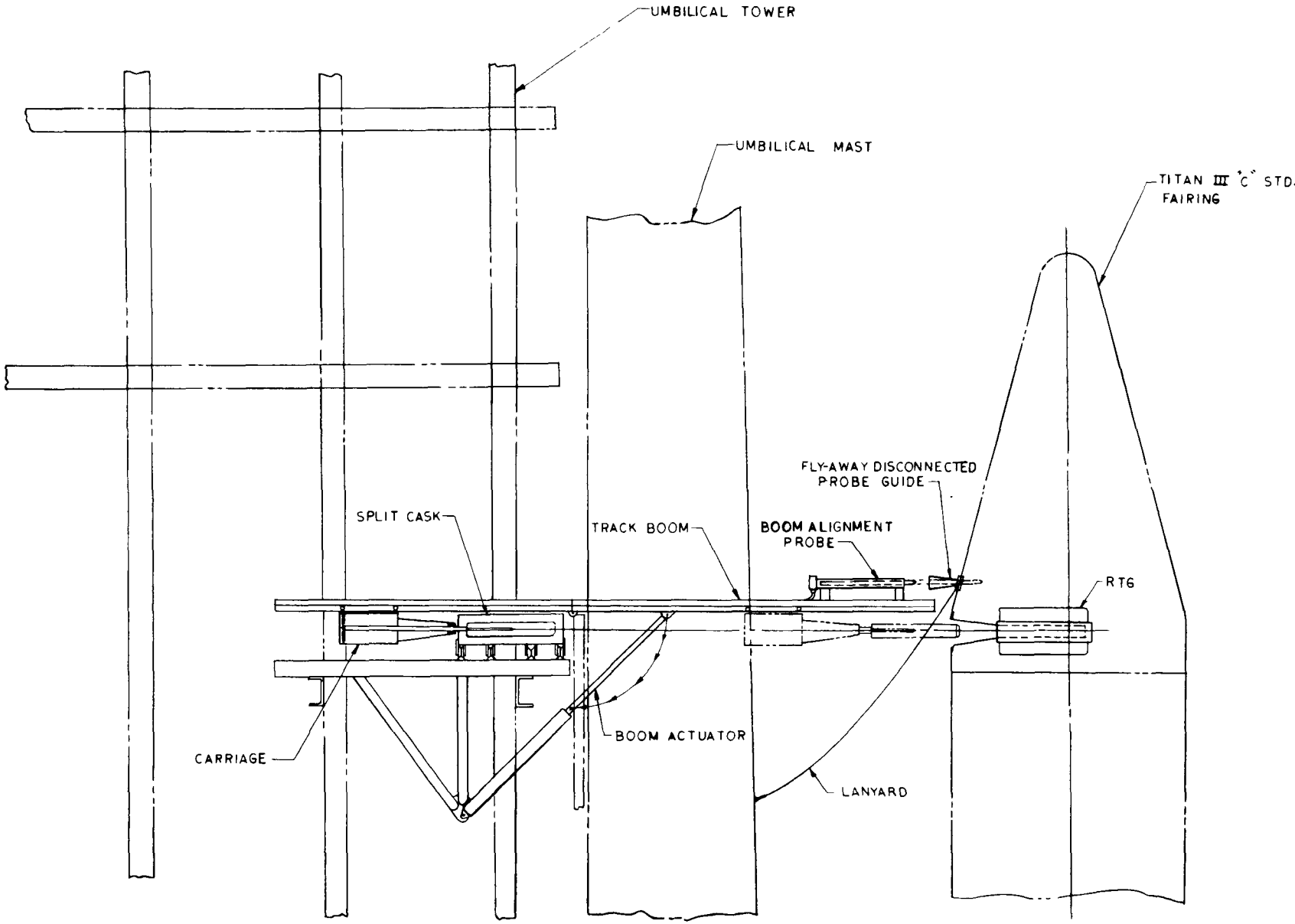

Fig. PP-5. Tower Mounted Split Cask

2. Launch Complex Modifications

Modifications to the launch complex will be minor. Titan III, Complex 40 at ETR is shown in the loading configuration drawing but other Titan III complexes would be similarly adaptable to this loading configuration (Figs. PP-6 and PP-7).

The loading device is installed between the uprights of the electrical umbilical mast and between Platforms 9 and 10 of the umbilical tower. Installation on the umbilical tower is also feasible. Structural steel members must be added horizontally and tied into existing vertical beams to support the loading device pallet.

3. Description and Operation

a. Fuel block shipment

The fuel capsules will be shipped in the same cask that is used for RTG loading. Little weight would be saved by reducing shield thickness and increasing dose rate due to the long length of the cask.

b. RTG shipment

The RTG will be shipped to the launch site unfueled and in a normal shipping manner.

c. Launch site preparation

Nonradiation environment condition. The RTG will be installed in the launch vehicle on the ground and the space vehicle will be erected and installed on the Titan III in the normal manner. The palletized fuel transfer device will be installed on the tower and the tunnel boom connected to the launch vehicle. The transfer belt will be inserted in and around the donut shaped RTG and down through the tunnel boom. A fuel block latching actuator will be connected to the RTG latch mechanism. All electrical power and control wiring will be connected as will the fuel block cooling lines.

Radiation environment condition. The transfer cask will be transported to the base of the umbilical tower and hoisted to the transfer device pallet by the MST crane. Tabs extending from the ends of the fuel capsule belt and through the cask doors will be connected to the transfer belt which passes up through the tunnel boom. The belt will also be passed through the drive motor drum which is mounted on the belt slack takeup device. Transfer of the fuel block from the cask to the RTG is accomplished, after remotely opening the cask doors, by actuating the belt-driven motor. The capsule belt moves from the cask, rolling over a drum inside the cask, and continues up the tunnel

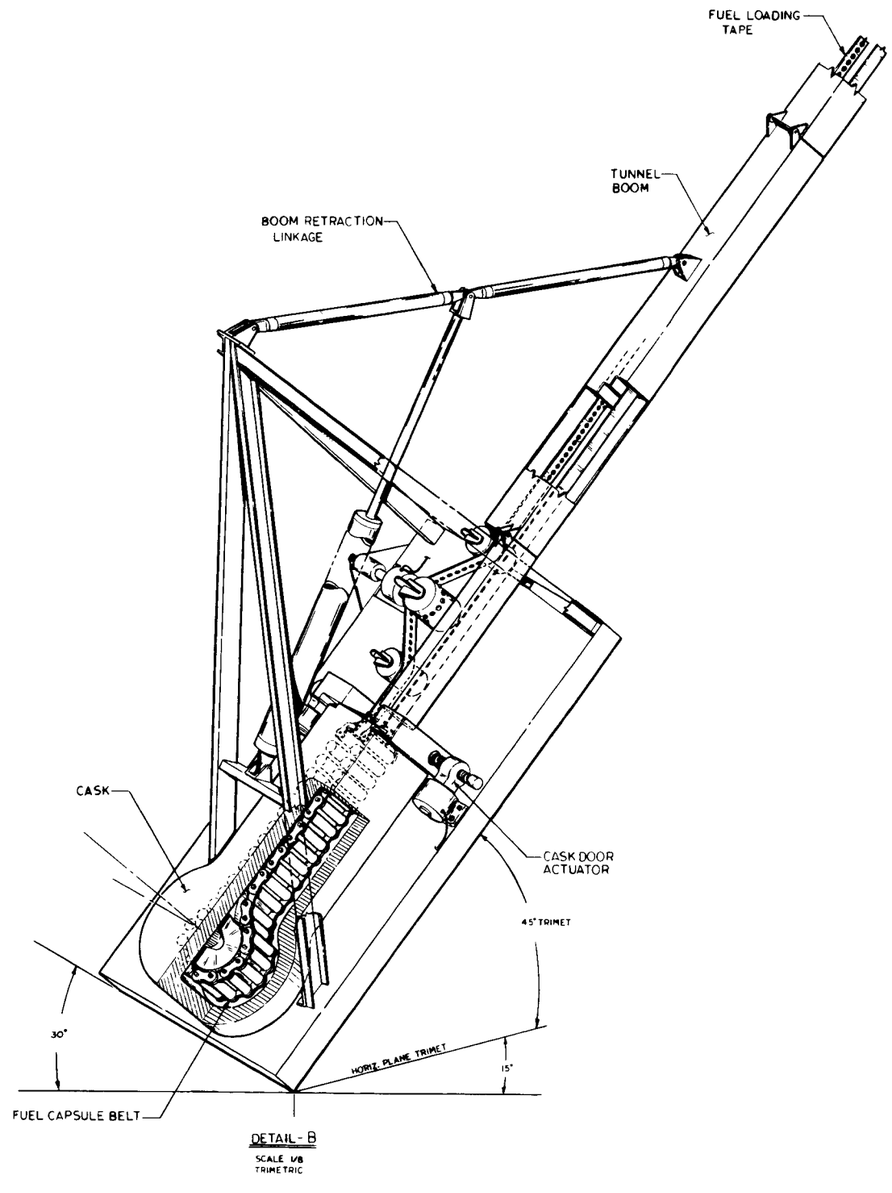

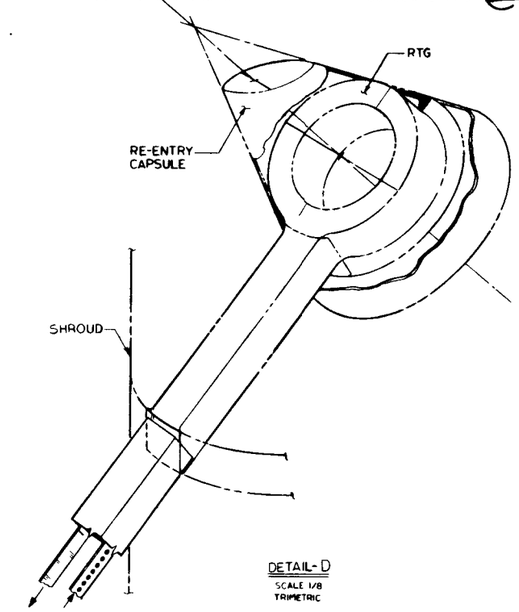

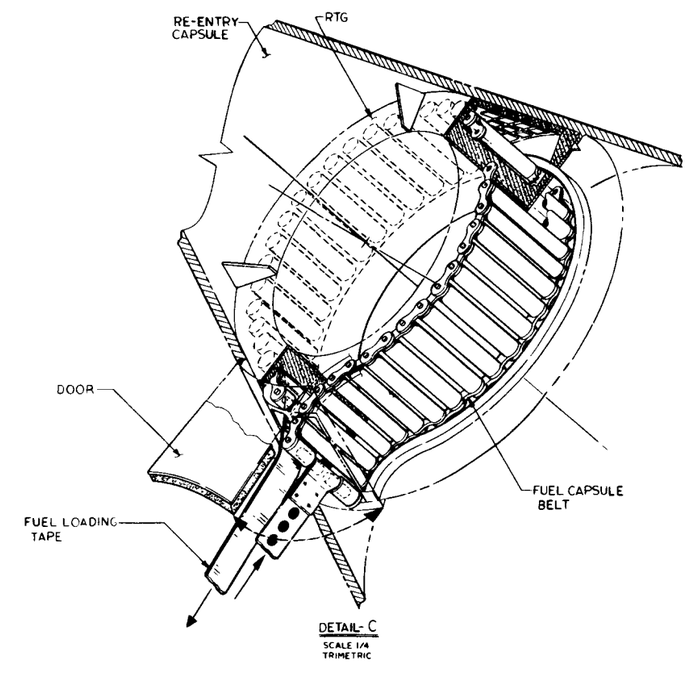

Fig. PP-6. Capsule Belt--Toroidal RTG

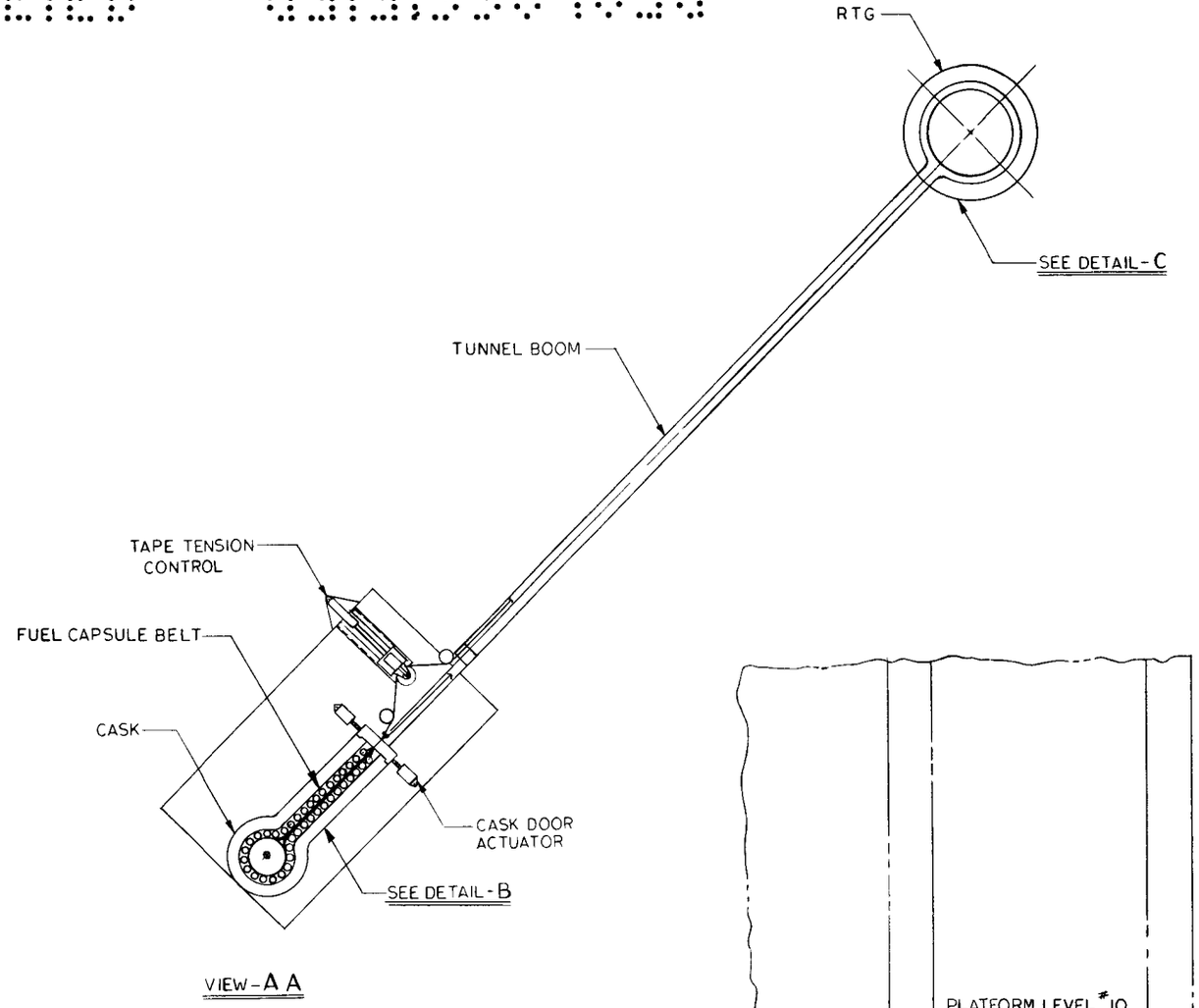

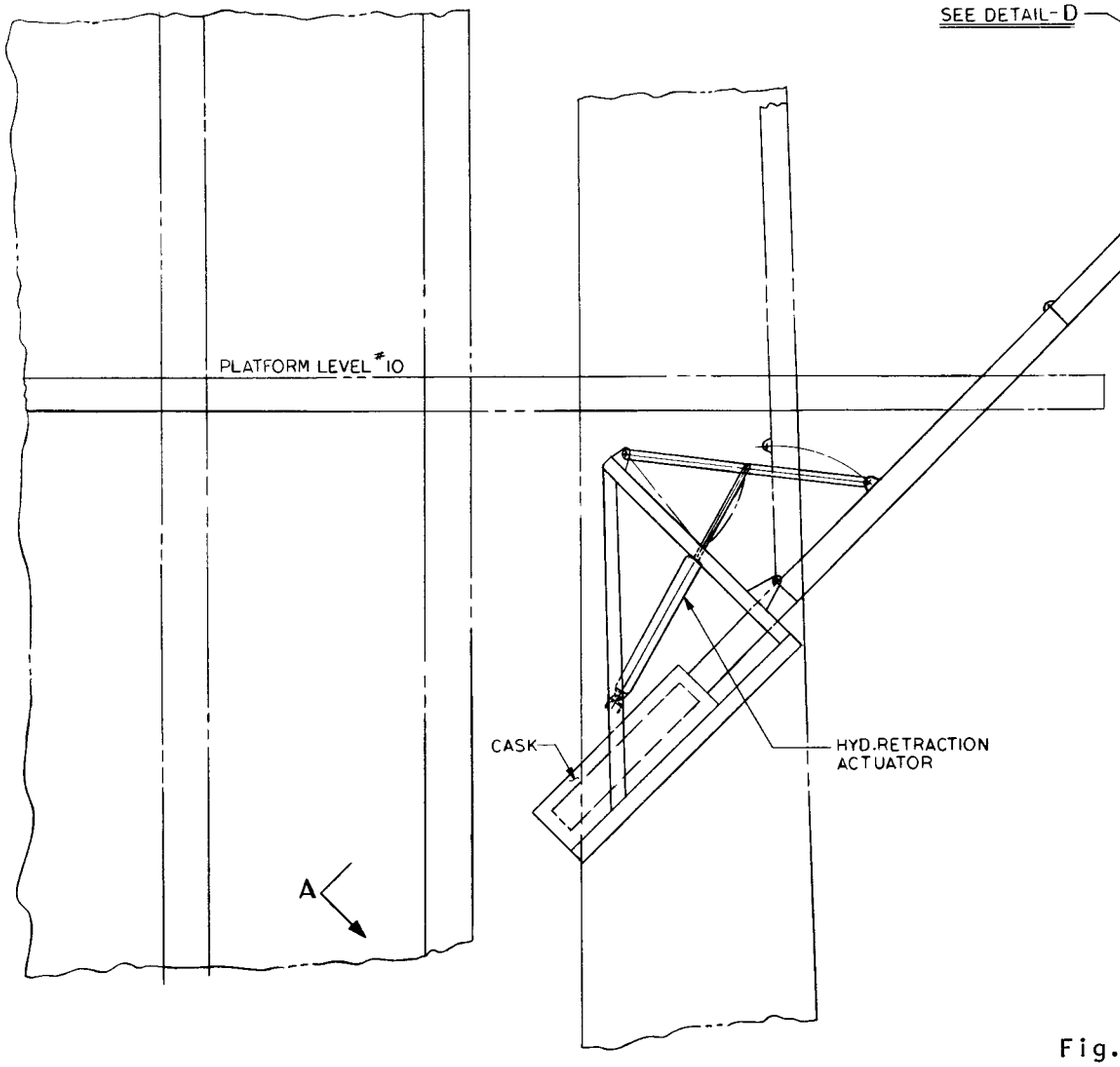

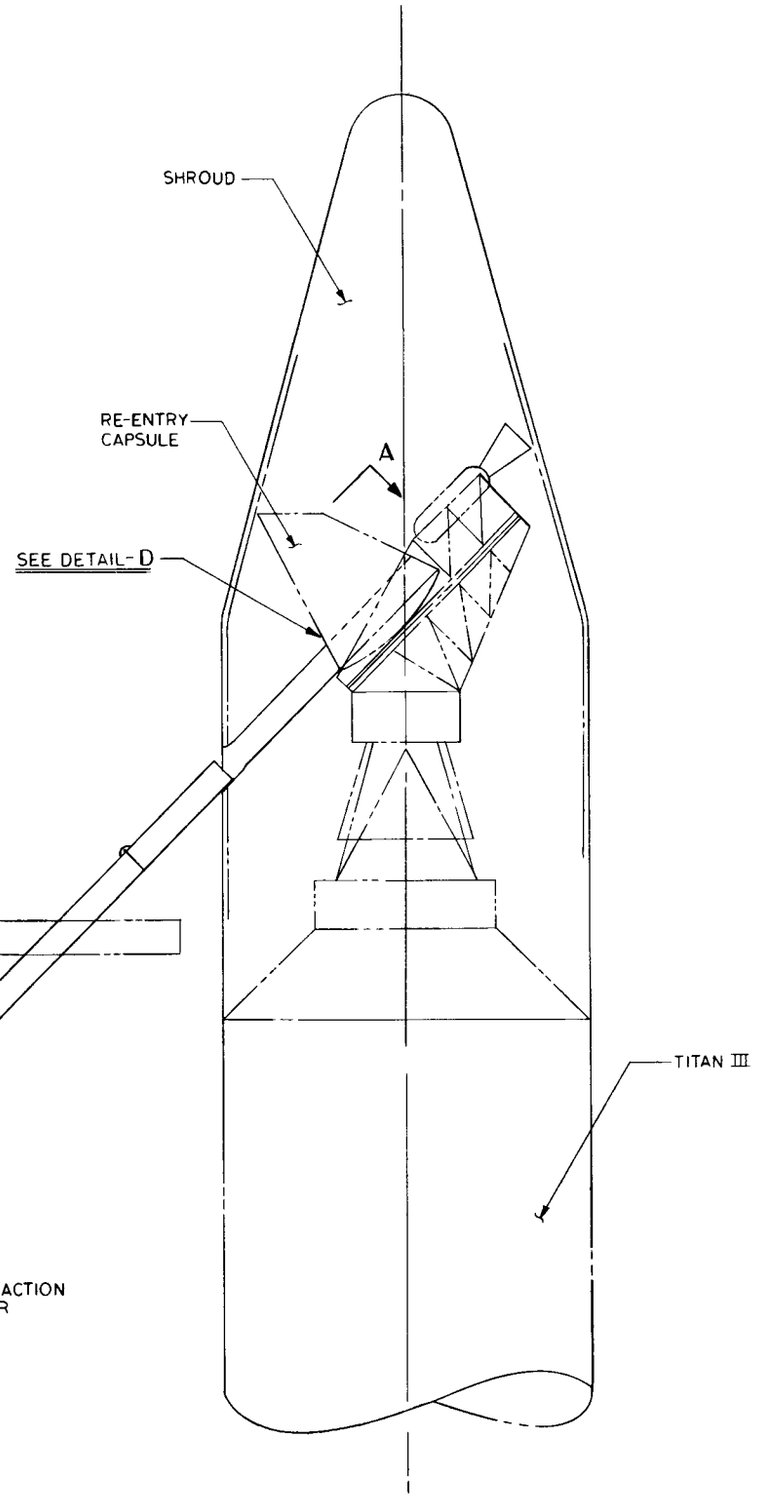

Fig. PP-7. Capsule Belt--Toroidal RTG

boom to the RTG. The continuous loop belt rolls or slides around the inner diameter of the donut-shaped RTG and moves down the tunnel boom as the capsule belt is pulled around inside the RTG. A latch mechanism at the loading opening in the RTG has a pair of arms which rotate and grab fittings at each end of the capsule belt.

Launch operation. The tunnel boom remains connected to the space vehicle and the transfer belt remains connected to the fuel block capsule belt until liftoff. At liftoff a signal is sent by the liftoff switches in the thrust mount to the transfer belt disconnect and the latch control disconnect. An explosive charge cable cutter is provided in the boom as a redundant feature and shear plugs are provided as a third redundant disconnect feature. The tunnel boom is also actuated and retracts to a vertical position at liftoff, controlled by the liftoff switches. A redundant retraction feature is provided. Hatches on the reentry vehicle and the spacecraft are spring-loaded closed and are held open by a pin through the hinge fitting. Lanyards connected on one end to the umbilical tower and the other end connected to the pins pull the pins by vertical motion of the launch vehicle. This feature is similar to the eight-inch air conditioning duct door on Gemini.

In the event launch does not occur, the fuel block can be immediately removed by remotely unlatching the fuel capsule belt and running the belt driven motor in the reverse direction until it is inside the cask.

4. Remote Controls and Instrumentation in Blockhouse

The following controls and instrumentation will be required in the blockhouse for this concept:

(1) Transfer motor control switch

(2) Limit switches to stop the transfer motor when the fuel block is properly positioned

(3) Position indicator lights to indicate position of fuel block

(4) Cask door actuator control.

G. ROTATING EXTENSION INSERTER

With this concept (Fig. PP-8), the fuel block will be loaded into the RTG by an extension arm which is mounted on the umbilical mast. The arm will rotate to align with the fuel cask and the RTG as required. Insertion of the fuel block into the RTG may be accomplished at any altitude between approximately 45 degrees above and below the horizontal. The fuel cask will be mounted on the umbilical mast at an elevation within reach of the arm when it is in the extended position.

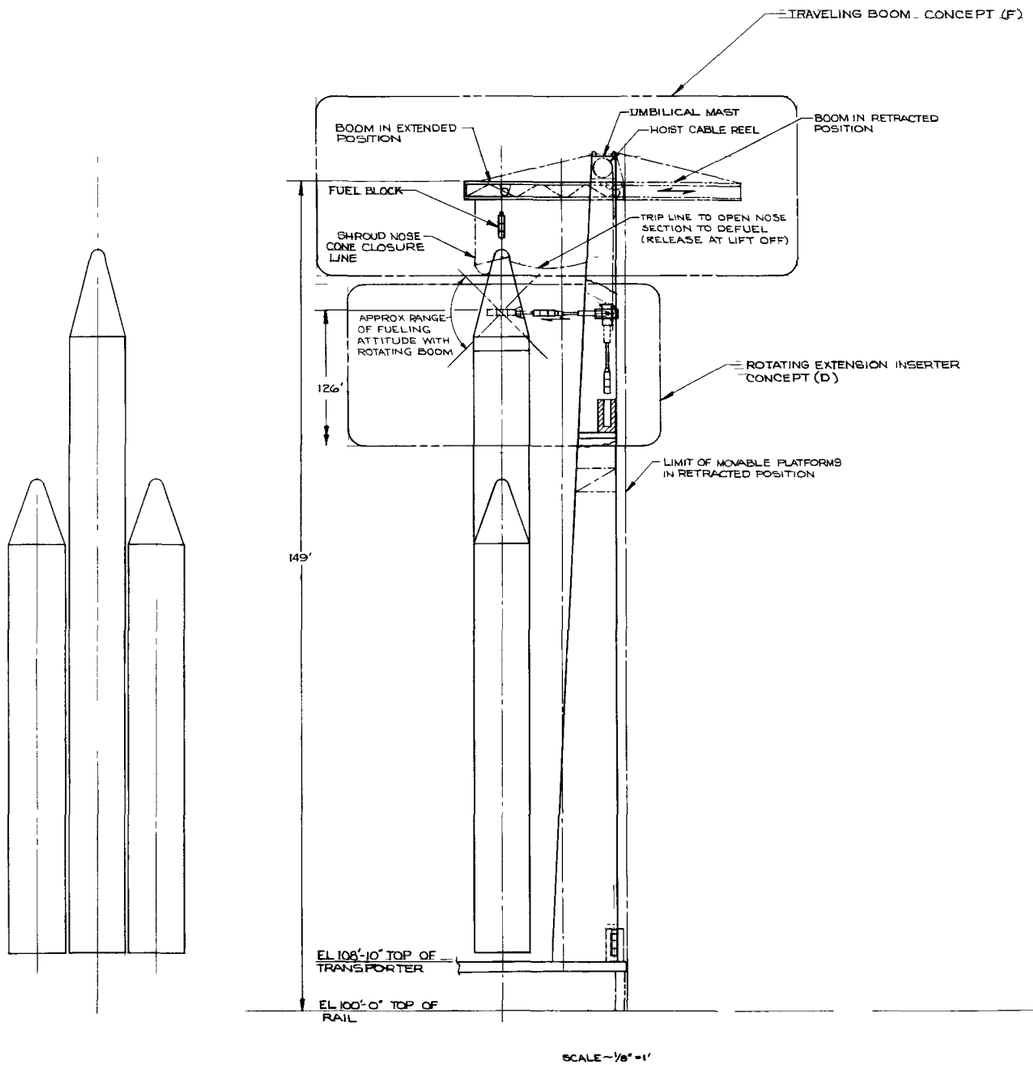

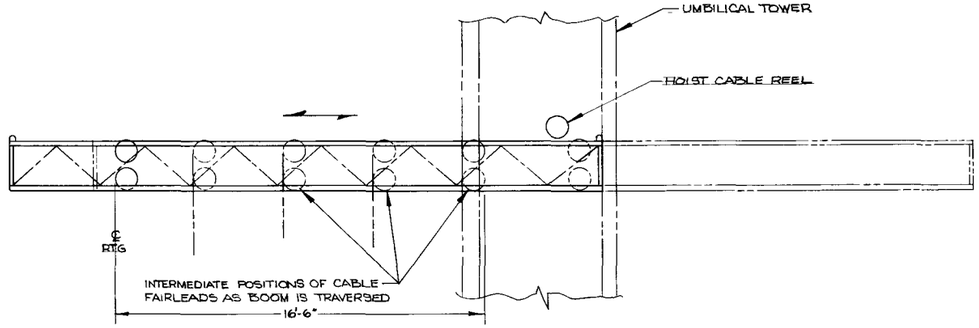

DETAIL OF BOOM- TRAVELING BOOM CONCEPT (F)
SCALE - 1/2" = 1'

NOTES:
1 THESE CONCEPTS ARE EQUALLY ADAPTABLE TO HANDLING RECTANGULAR OR CYLINDRICAL FUEL BLOCKS.

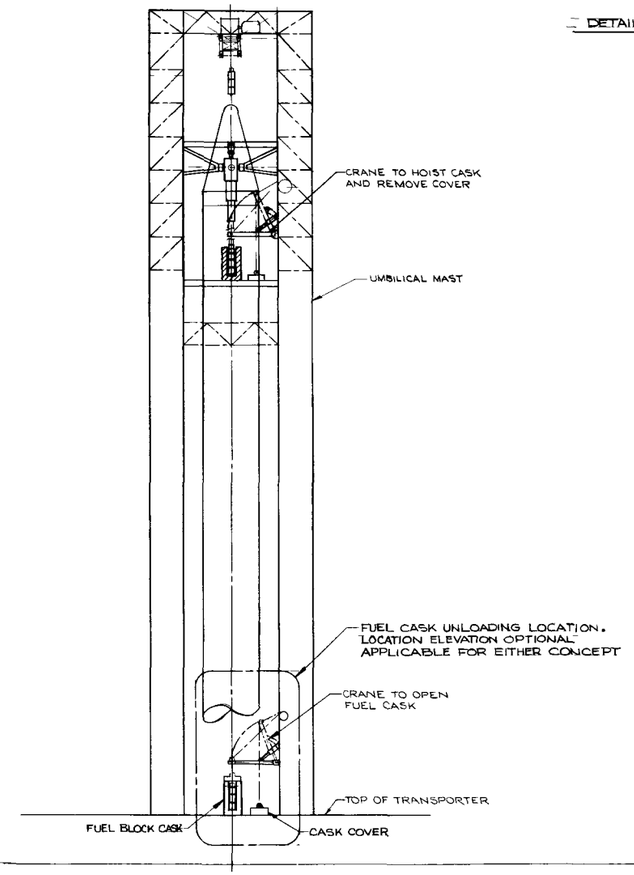

Fig. PP-8. Rotating Extension Inserter--Traveling Boom

1. Equipment List

Included in the equipment that will be needed for this concept are:

(1) Transportation cask (ICC regulations)

(2) Cask support structure installed on the umbilical mast

(3) Cask cover removal crane

(4) Rotating extension inserter

(5) Shroud access door opening mechanism

(6) Fuel cask handling sling

(7) Rotating extension inserter support structure

(8) Control and instrumentation console

(9) Closed circuit TV installation

(10) Fuel block shipping cask cooling system.

2. Launch Complex Modification

A support structure for the fuel block shipping cask will be installed between the uprights of the electrical umbilical mast. The structure will be at an elevation which will place the fuel block within reach of the inserter arm.

A remotely operated cask cover removal crane will be installed on the umbilical mast. Also, a suitable cover storage support will be installed as required.

A fuel block inserter arm, drive mechanism and support structure will be installed between the umbilical mast uprights at an elevation suitable to permit alignment of the fuel block with the RTG.

A control console and instrumentation will be installed in the launch control center for remote operation of the fueling concept equipment. Connecting power and instrumentation lines shall be installed between the control console and remote equipments of the system.

3. Description and Operation

a. Fuel block shipment and storage

The fuel block will be shipped to the launch complex in its shipping cask, using commercial transportation methods. The required conditioning and monitoring equipment will be designed as an integral part of the cask assembly. The cask will also be used to store the fuel at the launch site.

b. RTG shipment

The RTG, in the unfueled condition, will be shipped to the launch site using commercial transportation methods.

c. Launch site preparation

Nonradiation environment. The RTG will be installed on the spacecraft and erected on the launch vehicle. All systems will be checked out using power from the electrically heated RTG. The fuel block and cask will be hoisted to the support structure on the umbilical mast at any convenient time in the countdown. The cask shall be designed to maintain the radiation level to within tolerable limits in the inhabited regions of the launch pad so that restrictions on exposure time will not be required. When launch preparations reach the point where fueling of the RTG is to be accomplished, the electrical heaters will be removed from the RTG, the fuel cask cover manually unfastened from the cask, and the pad evacuated.

Radiation environment. The cover of the cask will be removed and set aside by use of the remotely operated crane installed on the umbilical mast. The inserter arm will be rotated to align with the fuel block and then extended to contact and latch onto the fuel block. Both linear and rotational motion may be transmitted by the attaching mechanism to ensure a positive lock with the fuel. The inserter will be retracted to withdraw the fuel block from the cask and then rotated to align the fuel with the RTG. A universal-type joint and actuator, combined with the extension and rotation of the inserter, will provide the compliance required between the fuel block and RTG during loading. The fuel will be inserted into the RTG and locked in place by the fuel handling mechanism. The inserter will remain in contact with the fuel block until the moment of ignition when a signal will be transmitted to retract. A lanyard will be used to close and latch the shroud access opening which in turn is linked to the RTG access opening which will cause it to close. The lanyard will fall away after completing its operation.

Defueling operation. In the event defueling is required, the fuel handling mechanism on the inserter, which is still in contact with the fuel block, will be actuated to lock onto the fuel block and cause it to

release from the RTG. The inserter arm will be retracted to withdraw the fuel block clear of the shroud, rotated to align with the fuel cask and extended to insert the fuel in the cask and latch it in place. Then, with the inserter retracted and rotated aside, the cask cover will be repositioned on the cask by the remotely operated crane, returning the launch site to a radiation-free condition.

H. TRAVELING BOOM, VERTICAL FUEL BLOCK LOADING

This concept proposes a traveling boom and hoist assembly to accomplish vertical loading of the fuel block through the nose section of the shroud. The fuel will remain in its shipping cask located on the transporter at the base of the umbilical mast until fueling operations begin. A remotely operated crane will be used to remove the shipping cask cover. The traversing boom will be retracted to align the hoist cable with the fuel block in the cask. A latching mechanism will be lowered into the cask to attach to the fuel block. The fuel will be hoisted to the boom elevation, and the boom will be extended to align the fuel block with the RTG. The fuel will be lowered into the RTG and the latching mechanism triggered to lock the fuel block in place. The boom will be retracted to provide clearance for launch.

1. Equipment List

The following equipment will be furnished for the complete system:

(1) Transportation cask (ICC regulations)

(2) Cask cooling system

(3) Remotely operated crane to remove cask cover

(4) Traversing boom assembly

(5) Electrically driven cable hoist

(6) Closed circuit TV installation mounted on boom for visual monitoring

(7) Remote control panel and instrumentation

(8) Umbilical cable to close shroud after fueling the RTG

(9) Umbilical cable to release shroud nose access opening by remote operation in event defueling is required.

2. Launch Complex Modifications

The following additions or modifications to the launch complex will be required to accommodate this concept.

(1) Installation of a boom and traversing drive at the upper end of the umbilical mast. The installation will include adjustable support cables and driven reels to maintain the boom attitude as it moves.

(2) A remotely controlled hoist will be installed within the upper cross member structure of the umbilical mast to raise and lower the fuel block.

(3) A support interface will be installed on the transporter to mount the fuel shipping cask and associated equipment.

(4) A control and instrumentation console will be added in the launch control center for remote operation and monitoring.

3. Description and Operation

a. Fuel block shipment

The fuel block will be shipped to the launch site in a shielded cask designed to ICC regulations. The cask will incorporate cooling provisions and instrumentation as required to condition and monitor the fuel block.

b. RTG shipment

The RTG will be shipped to the launch site in the unfueled condition, using standard shipping containers and methods.

c. Launch site preparation

Nonradiation environment condition. The RTG, with an electrically heated simulated fuel block, will be installed on the spacecraft. The RTG will be brought up to equilibrium temperature and the complete spacecraft electrical system checked out using RTG-supplied power. The isotope fuel block will remain closed in its shipping cask. The cask will be designed to limit the radiation field to within the tolerance acceptable for personnel to work in the area for unlimited periods of time.

Radiation environment condition. When the countdown and checkout reaches the point where installation of the fuel into the RTG is to be accomplished, the fuel cask cover will be unbolted by manual operation and the electrically heated fuel block will be removed from the RTG. The pad will be cleared of all personnel and all operations will be con-

trolled from the launch center from this point on. The fuel block cask cover will be removed by the remotely controlled crane mounted on the vertical support of the umbilical mast. With the traveling boom in the retracted position, the hoist cable will be in line with the fuel block. A mechanism which interfaces with the fuel block latching device will be attached to the end of the cable. By lowering the cable, the mechanism will lock onto the fuel block and at the same time cause it to release from the fuel cask. The fuel block will be hoisted to the required elevation to allow the boom to be extended to a position where the fuel block is in line with the RTG. By paying out the cable, the fuel will be lowered into the RTG where it will be latched into place. A cable attached to the shroud nose section will be used to pull the nose section to the closed position. A mechanical link between the shroud and the reentry body nose cap will cause the reentry body to be closed and latched by the same cable movement.

Defueling operation. To defuel the RTG, the shroud and reentry body are opened for access by actuation of a lanyard connected to an unlatching device on the shroud. This will also release a spring which will cause movement to the open position. The boom will be traversed to the extend position and the fuel block handling mechanism lowered into the RTG and attached to the fuel block. The fuel will be hoisted clear of the shroud, the boom retracted and the fuel lowered into the fuel cask. The cask cover will be replaced by remote operation.

I. SILO LAUNCH CONCEPT

Under this concept, either the fuel block may be loaded into the RTG or the fueled RTG may be loaded into the launch vehicle. It is also possible to accomplish horizontal or vertical loading. A hot cell which connects directly into the silo will be constructed under the crane hardstand. Alongside the hot cell, a control room will be constructed. Manipulators, instrumentation and monitoring equipment will be connected between the control room and hot cell. The hot cell will incorporate moving mechanisms to extend into the silo to accomplish the loading. The concept is shown in Fig. PP-9.

1. Equipment List

The equipment necessary to this type of operation is as follows:

(1) Transportation cask (ICC regulations)

(2) Fuel block conditioning equipment

(3) Overhead traveling crane

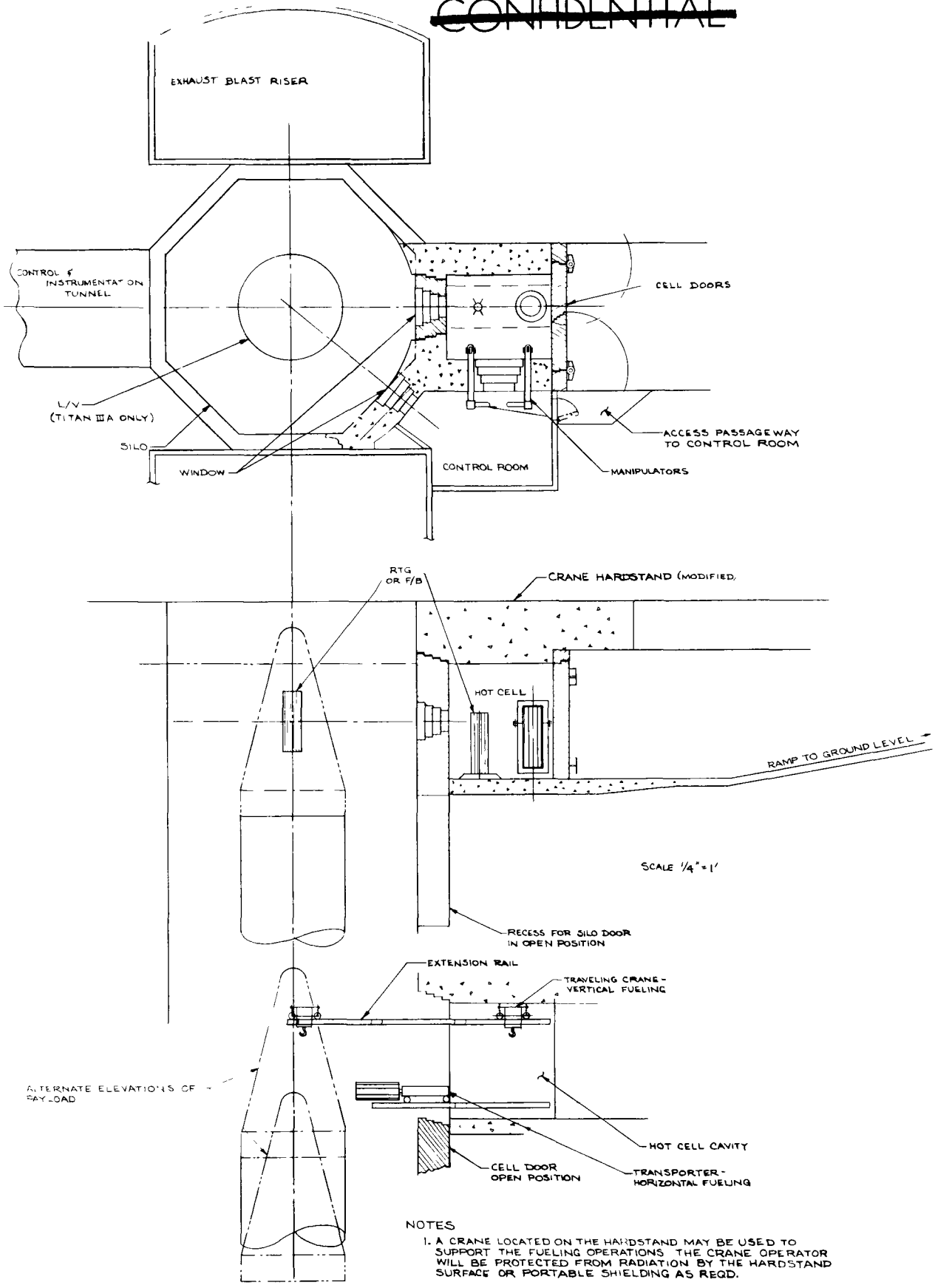

NOTES

1. A CRANE LOCATED ON THE HARDSTAND MAY BE USED TO SUPPORT THE FUELING OPERATIONS. THE CRANE OPERATOR WILL BE PROTECTED FROM RADIATION BY THE HARDSTAND SURFACE OR PORTABLE SHIELDING AS REQD.

Fig. PP-9. Silo Hot Cell--Fuel Block or RTG Loading

(4) Remotely operated manipulators

(5) Control console

(6) RTG checkout instrumentation

(7) Special handling fixtures and tools.

2. Launch Complex Modifications

Construction of a complete isotope handling hot cell adjacent to the silo which will include entrance doors on the roadway access side and a door entering into the silo will be required. An overhead traveling crane and/or vertical loading trolley and track at floor level, manipulators and other required accessories will be installed as a part of the hot cell.

Construction of a control room adjacent to the hot cell with visual access to the hot cell and the silo will have to be completed. Control console, instrumentation, checkout panel, environmental control equipment, and required safety features will be included in the control room installation.

An access road into the hot cell and access passageway to the control room will be provided.

Hardline connections between hot cell, control room, silo and the launch control center will be installed as required to monitor the complete fuel handling concept.

3. Description and Operation

a. Fuel block shipment

The fuel block will be shipped to the hot cell in its transportation cask. The design of the cask will permit use of commercial handling methods for shipment. The cask will also be suitable for storage of the fuel block outside of the hot cell at the launch site if this will aid in launch preparations.

b. RTG shipment

The unfueled RTG will be shipped using standard commercial containers and transportation methods necessary for this type of equipment.

c. Launch site preparation

(1) Fuel block loading

Nonradiation environment. The RTG will be installed on the spacecraft and the entire system checked out using electrical heaters to simulate the fuel loading. When the checkout is complete, the electric heaters will be removed from the RTG; the fuel cask will be delivered to the hot cell; the cover unfastened manually; the hot cell access door closed and the site prepared for remote operation.

Radiation environment. The fuel cask will be opened by use of the manipulators and overhead crane to expose the fuel block. Again, by use of manipulators and crane in conjunction with a fuel handling mechanism, the fuel block will be attached to the mechanism and removed from the cask. If vertical fuel loading is required, the crane will be moved on tracks that may be extended into the silo to position the fuel over the RTG. Next the fuel will be lowered into the RTG and locked in place. Alignment problems between the units will be at a minimum with this concept. For horizontal fueling, the fuel block will be transported by a trolley which will travel on tracks that are located across the hot cell floor and will extend into the silo to contact the RTG. Upon completion of fueling, all protrusions into the silo related to the RTG fueling operation will be retracted into the hot cell. The access openings in the RTG reentry body and the shroud will be closed by means of a lanyard that will fall away upon completing its function. The hot cell door connecting to the silo will be closed in preparation for liftoff.

RTG defueling. To defuel the RTG, the access openings in the shroud and reentry body will be opened by a lanyard action which remains attached to the launch vehicle until actual liftoff. The tracks used for travel by the fueling device, crane or trolley will be extended into the silo and aligned with the RTG. Due to the lack of uneven heating of the launch vehicle or windage, the alignment problem is at a minimum and the close proximity of the operator in the control room with visual contact with the operations makes remote manipulation of the alignment operation feasible. With the tracks extended and aligned, the fueling device will be moved into position to contact the fuel block lock and cause it to release from the RTG. The fuel will be returned to the hot cell, all extensions into the silo from the hot cell retracted and the cell door closed.

(2) Fueled RTG loading

Nonradiation environment. All checkout of the space vehicle will be completed using external power supplied by the site and matched to the RTG power output which is being monitored in the hot cell. The RTG will have been fueled in the hot cell and brought up to temperature without

creating a radiation hazard in the silo area. The external power will remain connected until the RTG is installed and connected in parallel to avoid power interruption to the spacecraft which may cause an unnecessary repeat of system checkouts. When the RTG is coupled in, the external power will be removed.

Radiation environment. When the spacecraft systems have been checked out on external power, the hot cell door to the silo will be opened and the appropriate tracks extended into the silo for overhead or side loading. The RTG will be picked up in the hot cell and transported to the spacecraft where it will be installed in the reentry body. Electrical connection between the RTG/RB will be accomplished by remote action, and instrumentation will be provided to check and ensure a zero resistance contact. The RTG/RB will be secured to the spacecraft by remote closing of the same system that will be used to release the reentry body in space. The shroud will be closed by lanyard action, remotely controlled, and all extension into the silo from the hot cell will be retracted and the cell door closed.

Defueling procedure. To remove the RTG/RB from the spacecraft, the access through the shroud will be reopened by action of a lanyard and spring system that remains intact until liftoff occurs. The hot cell door will be opened and the equipment used to install the RTG/RB will be repositioned and attached. The mechanism used to release the reentry body in space will be triggered; also a cable cutter to separate the power and instrumentation leads. The reentry body will be removed from the spacecraft, returned to the hot cell, the handling mechanisms retracted and the cell door closed to return the silo to a radiation-free condition. A certain amount of refurbishing of those systems actuated to release the reentry body will have to be accomplished to return the system to the configuration required to reinstall the RB.

J. PALLETIZED RETRACTABLE TOWER BOOM WITH FHM MOUNTED ON AIR BEARING DEVICE

Concept J is as shown in Fig. PP-10 for overall configuration and Fig. PP-11 for the details of a typical attachment method between the fuel block and the fuel handling machine.

1. Manufacturing Checks

The fuel block is loaded and verified, as applicable, in hot lab facility.

The RTG, after manufacture, is subjected to the necessary checks to verify conformity with the engineering drawings.

~~CONFIDENTIAL~~

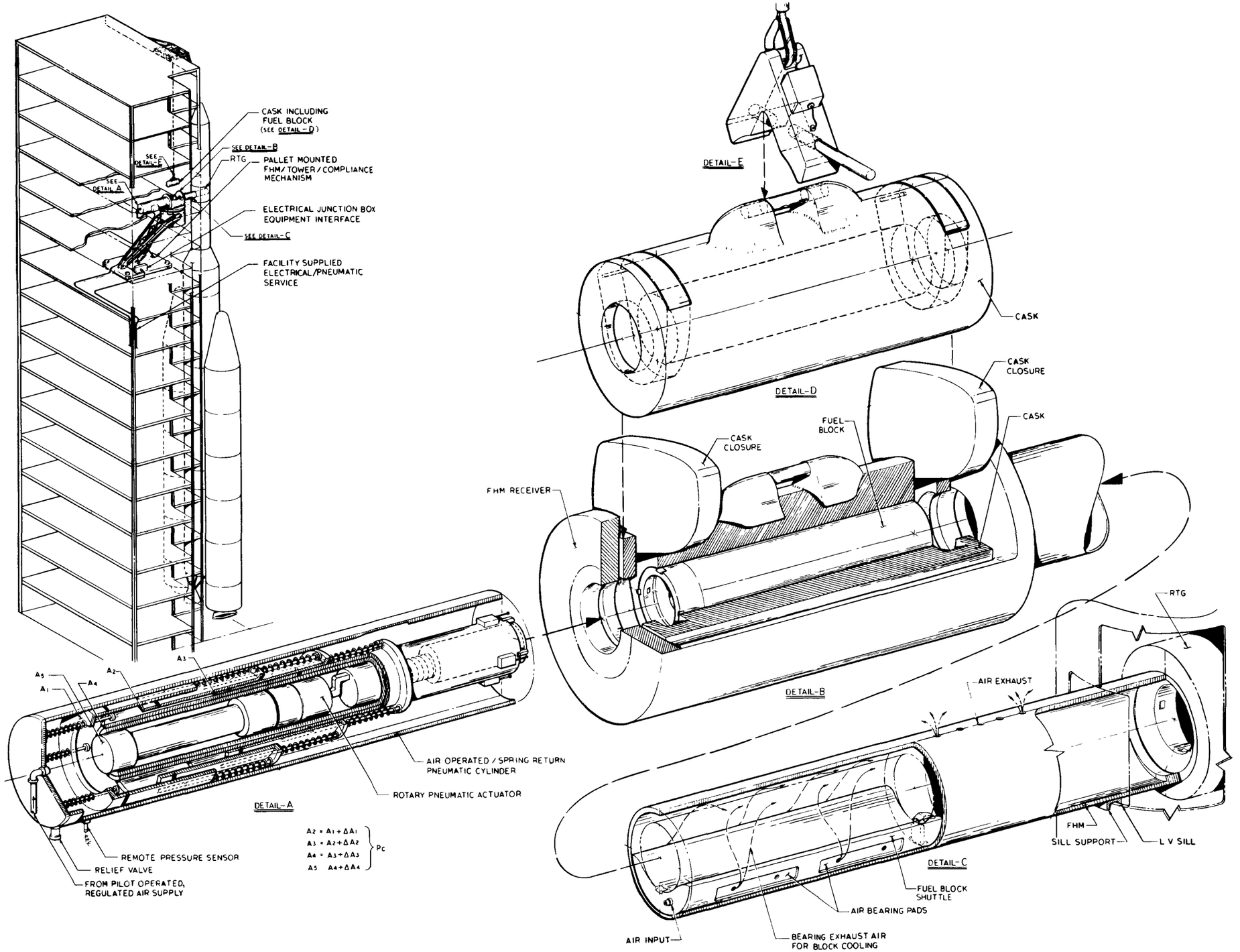

Fig. PP-10. Retractable Tower Air Bearing Compliance

~~CONFIDENTIAL~~

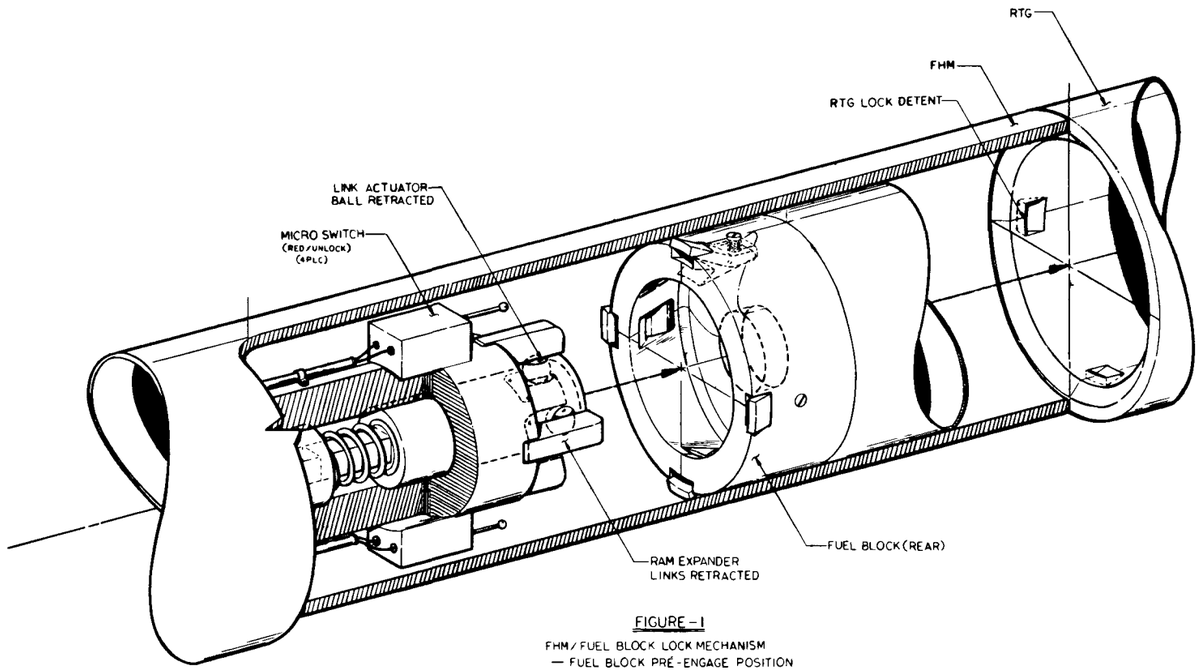

FIGURE-1
FHM/FUEL BLOCK LOCK MECHANISM
— FUEL BLOCK PRÉ-ENGAGE POSITION

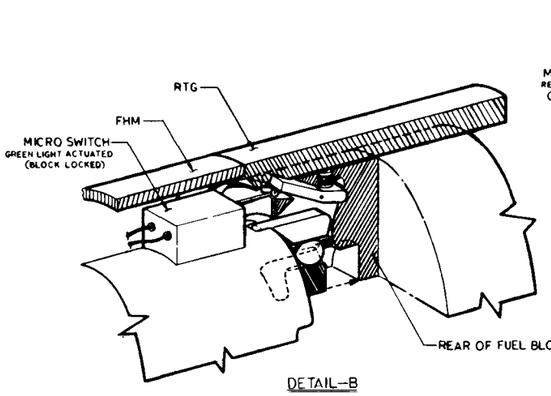

DETAIL-B
LOCKING OF FUEL BLOCK IN RTG

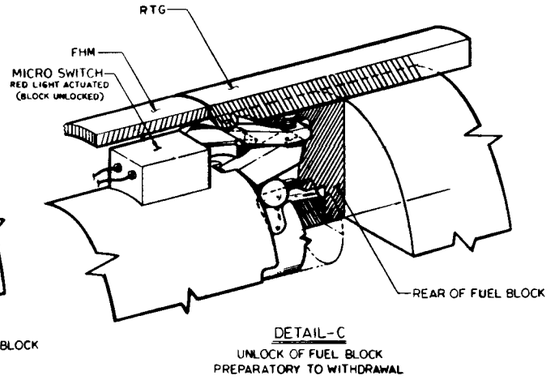

DETAIL-C
UNLOCK OF FUEL BLOCK PREPARATORY TO WITHDRAWAL

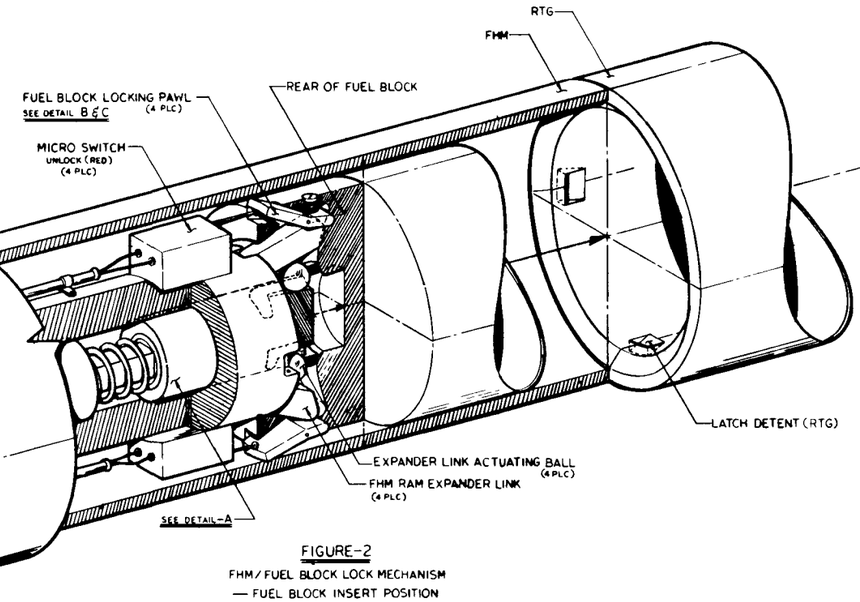

FIGURE-2
FHM/FUEL BLOCK LOCK MECHANISM
— FUEL BLOCK INSERT POSITION

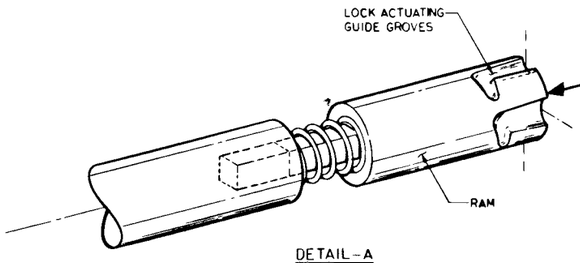

DETAIL-A
FHM RAM

Fig. PP-11. Retractable Tower Air Bearing Compliance

2. Transportation

The RTG is transported to the launch site hangar area or possibly to the spacecraft subcontractor' s facility where the RTG is installed in the spacecraft.

The fuel block is installed in the provided GSE cask including necessary thermal control means, and is transported, per applicable ICC regulations, to the launch site where it is stored until required.

3. Checkout

Checkout of the RTG installed in the S/C in the hangar area, or at the S/C contractor' s facility, is accomplished using an electrical heat source in the RTG. Proper functioning of the RTG is verified and operating parameters of RTG-operated systems are checked. An alternate check might be acceptable using an electric power source (≈28 volts at 9 amperes) duplicating the RTG output impressed on the system by the output of the RTG. Systems downstream of the RTG are checked in this manner. The RTG would have been acceptance tested at the factory prior to this test. Using the "impressed power mode" of testing may require the rerunning of the RTG acceptance tests after it is installed in the S/C.

4. Fueling/Defueling

After the launch vehicle is erected on the pad, the S/C, including the installed RTG, is interfaced with the launch vehicle. The pallet-mounted FHM/tower is manually positioned and connected to the spacecraft. The compliance mechanism within the FHM mount of air bearings providing five degrees of freedom compensates for the relative motion between the L/V and the umbilical tower. After the MST is removed, and after chemical fueling of the L/V, the fuel block including the cask is hoisted and installed in the receiver of the FHM. In this operation, the crane hook includes a hydroset and adapter device for mating with the cask (Fig. PP-10). When loading the fuel block into the RTG is to be accomplished, the cask closures are opened sequentially, the ram of the fueling machine connected to the fuel block, and the block pushed forward by pressurizing the pneumatic step-cylinder and the block locked up in the RTG (Figs. PP-10 and PP-11).

Defueling is accomplished, generally, in the reverse process except that before the block is unlocked from the RTG the shaft in the ram is rotated 45 degrees to unlock the over center lock mechanisms on the back end of the fuel block. Figure PP-11 provides a detail of this mechanism. After the locks are released, the block is withdrawn from the RTG to the cask in the receiver of the FHM. The cask closures are positioned to the closed position. The fuel block is now secure in the cask and if removal from the FHM is desired, the crane is positioned and the cask and fuel block removed.

K. FUELED RTG (UNSHIELDED AND SHIELDED)

This concept proposes to install a fueled and completely checked out RTG/RB using the MST crane. This will permit assembly of the RTG under the most favorable conditions in the laboratory and hot cell. The concept applies identically to either a shielded or unshielded RTG configuration.

1. Equipment Required

The equipment required to accomplish this phase of the mission is as follows:

(1) Shipping cask (ICC regulations) to transport the complete reentry body (less the deorbit package)

(2) Conditioning equipment to maintain the required environment in the shipping cask

(3) Instrumentation to monitor the health hazard at the RTG

(4) Control and instrumentation console

(5) Handling slings and special tools

(6) Trailer for transporting the shipping cask and reentry body at the launch site

(7) Crane installation for remote removal of the shipping cask cover.

2. Launch Complex Modifications

A storage area, with required power supply, for storage, conditioning, and monitoring of reentry body/cask/cart will be required. A shielded crane operator's booth on the MST to be used during the installation of the RTG/RB will be constructed.

3. Description and Operation

a. RTG/RB shipment

The fueled RTG/RB will be shipped to the launch site in a shipping cask designed to ICC regulations. The cask will incorporate cooling provisions and instrumentation as required to condition and monitor the RTG. Standard commercial means of transportation will be used to transport the cask.

b. Launch site preparation

Nonradiation environment. The launch site will remain in a radiation-free condition until the actual installation of the RTG/RB. The RTG will remain stored in its shipping cask until the last operation in the countdown before retraction of the missile service tower (MST). The MST crane will be used to hoist the RTG/RB into place. The last manual operations on the launch site will be to unfasten the cask cover in preparation for removal and attach the handling mechanism to the MST crane.

Radiation environment. With the cask cover unfastened, the remotely operated crane will be used to remove and set aside the cover to expose the reentry body. A handling mechanism attached to the MST crane will be lowered into place and latched onto the RB. The RB will be hoisted into position on the spacecraft. A mechanical centering and attaching clamp will be employed to fasten the RB in place on its deorbit package. An electrical connection between the RB and L/V will be accomplished by an electrically energized fused-type connection. Instrumentation will be provided to check that a zero resistance contact has been accomplished. The shroud will be installed by remote operation and latched into place. The MST will then be rolled back and the countdown and launch completed.

Defueling procedure. To defuel (remove the RB) will require that the MST be moved back into place, surrounding the launch vehicle. The system used to eject the shroud in space will be actuated to expose the reentry body. The MST crane, with the handling mechanism attached, will be used to attach to the RB. The system used to separate the RB from the deorbit package will be triggered to release the RB. When the RB is released, it will be picked up by the MST crane and returned to the shipping cask. The cask will be closed by the remotely operated crane to return the site to a radiation-free condition. Refurbishing of the systems actuated to release the reentry body will have to be accomplished to return the system to the configuration required to reinstall the RB.

L. TOROIDAL FUEL BLOCK LOADING, SPLIT RTG, TOWER-MOUNTED

The loading device consists of a standard boom which can be mobile or mounted on the umbilical tower. A shipping cask carried on a dolly would remain at ground level on the launch pad during the loading or unloading operation. This is shown in Fig. PP-12.

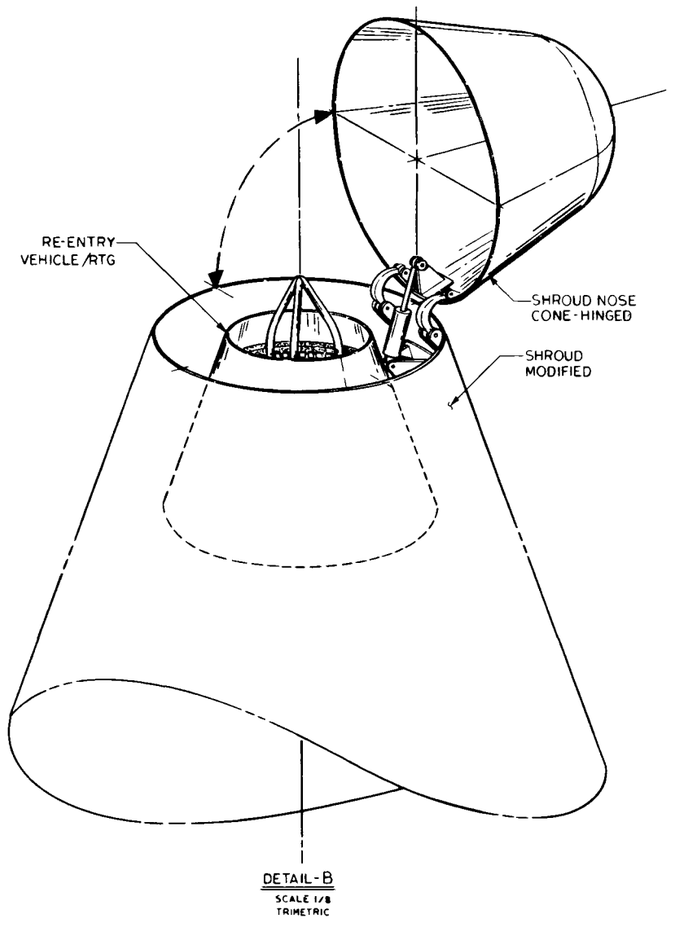

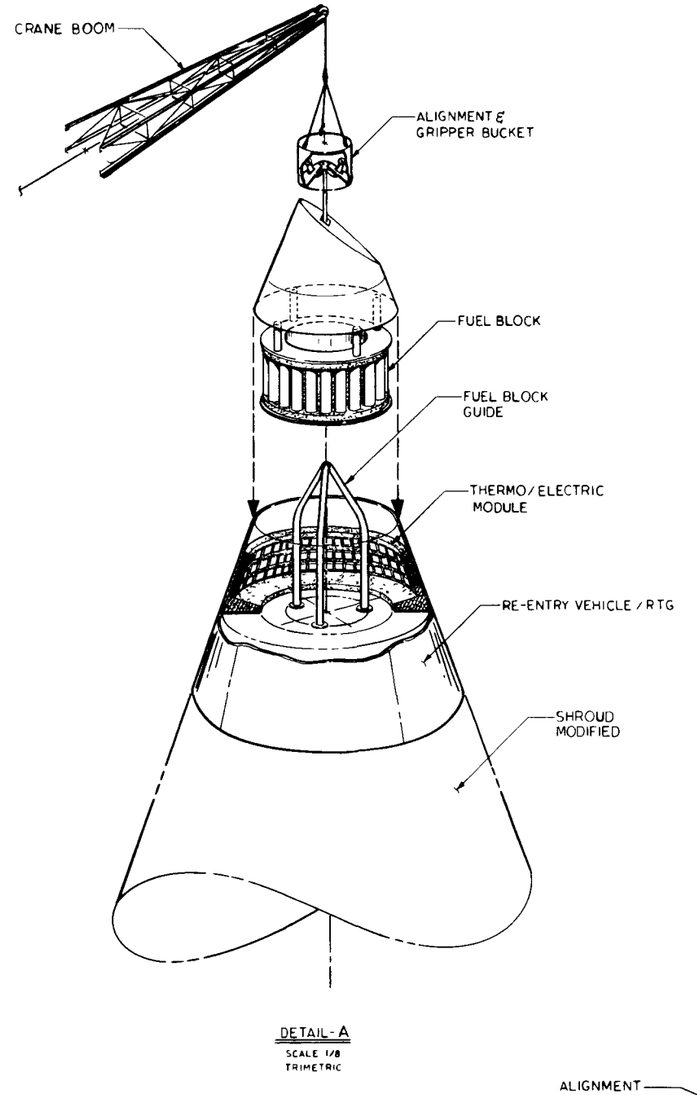

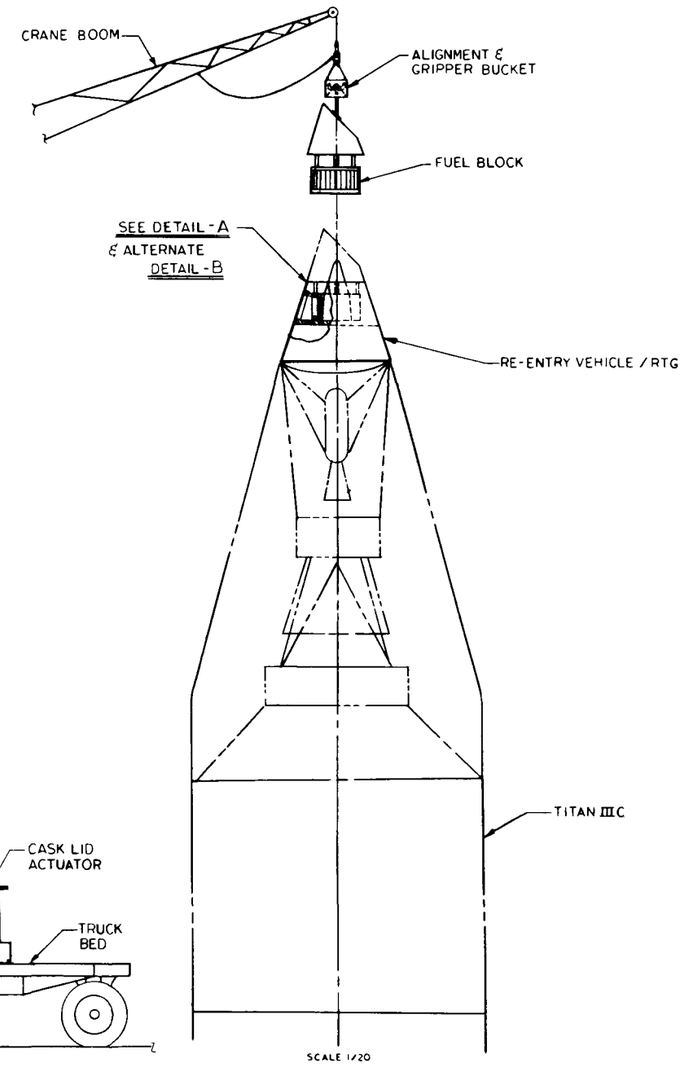

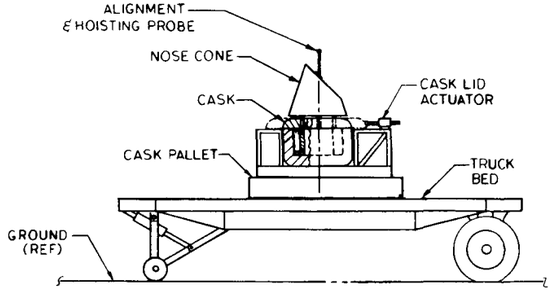

Fig. PP-12. Tower-Mounted Loading Boom--Split RTG

1. Equipment List

The equipment required for this operation is:

(1) Transportation cask

(2) Standard boom crane

(3) Crane hook centering and gripper device

(4) Cask dolly with cask door actuators.

2. Launch Complex Modifications

No modifications would be required if a mobile crane is used.

Minor modifications would be required if a boom crane is mounted on the umbilical tower. Remote controls in the blockhouse and wiring on the umbilical tower will have to be installed.

3. Description and Operation

a. Fuel block shipment

The fuel block will be shipped in a cask to the launch site in a toroidal shape completely assembled with the inner structure of the generator and with Min-K insulation. The cask will have a remotely actuated lid remover and four manually removable plugs. The plugs will be removed to insert studs for attaching the nose cone.

b. RTG shipment

The RTG, which will be an integral part of the reentry body, will be shipped, unfueled, in a normal shipping manner.

c. Launch site preparation

Nonradiation environment condition. The lower section of the reentry body which includes the thermoelectric elements of the RTG will be installed on top of the payload with the cone pointing up, similar to the Gemini installation. All wiring will be connected and the RTG checked out with an electric element. The upper portion of the cone will not be installed at this time.

Radiation environment RTG loading. The four shield plugs in the lid of the cask will be removed manually and four studs will be screwed into fittings in the fuel block support structure inside of the cask. The upper cone section of the RTG/RB will be placed on top of the four studs

and attached with nuts. The crane gripper bucket will be positioned and attached to the probe on the top of the RTG/RB cone. All workmen with the exception of the crane operator who is a minimum of 100 feet away from the cask will leave the area. The loading operation will begin by remotely sliding the segmented lid of the cask open. The crane operator will operate the winch and lift the nose cone with the fuel block attached out of the cask and raise it to the top of the space vehicle. With the aid of a TV camera mounted on the crane boom, the fuel block package will be positioned over the lower half of the RTG/RB. It will be lowered onto a guide cone which will compensate for relative motion sway and the two halves of the RTG/RB will be joined. Latches in the lower section will be actuated and will lock the upper section in place. The gripper bucket latches will be released from the probe and the crane swung to the side.

Radiation environment, RTG unloading. In the event of an aborted launch, provisions are made to unload the RTG. The crane with the gripper bucket attached is swung over the space vehicle and, aided by TV, is aligned with the probe on the top of the RTG/RB. The gripper bucket is lowered onto the probe and the internal cone centers the bucket. The grippers are actuated as soon as the probe presses the switch at the apex of the cone or the grippers can be controlled manually. Latch fingers in the RTG are released by solenoids. In the event the solenoids fail, the system would be designed so that shear pins would shear in the latches when the upper RTG/RB section is hoisted by the crane.

Radiation environment, cask loading. The crane operator swings the boom with the fuel block package over the cask which is located at ground level. Vertical guides attached to the cask assist the crane operator to lower the fuel block into the cask. The grippers are released and the remotely actuated cask lid is closed. The nose cone remains attached to the fuel block while the block is in the cask. Workmen return to the cask area and remove the nose cone and studs and replace the cask plugs.

M. SPLIT RTG, TOP LOADING SLIDING BOOM

The loading device (Fig. PP-13) consists of a pallet-mounted sliding boom which is installed on the umbilical tower. Alignment and fuel block pickup actuators are mounted at the end of the boom. A fuel block cask is mounted on the fueling machine pallet.

1. Equipment List

The equipment required for this operation is as follows:

(1) Transportation cask

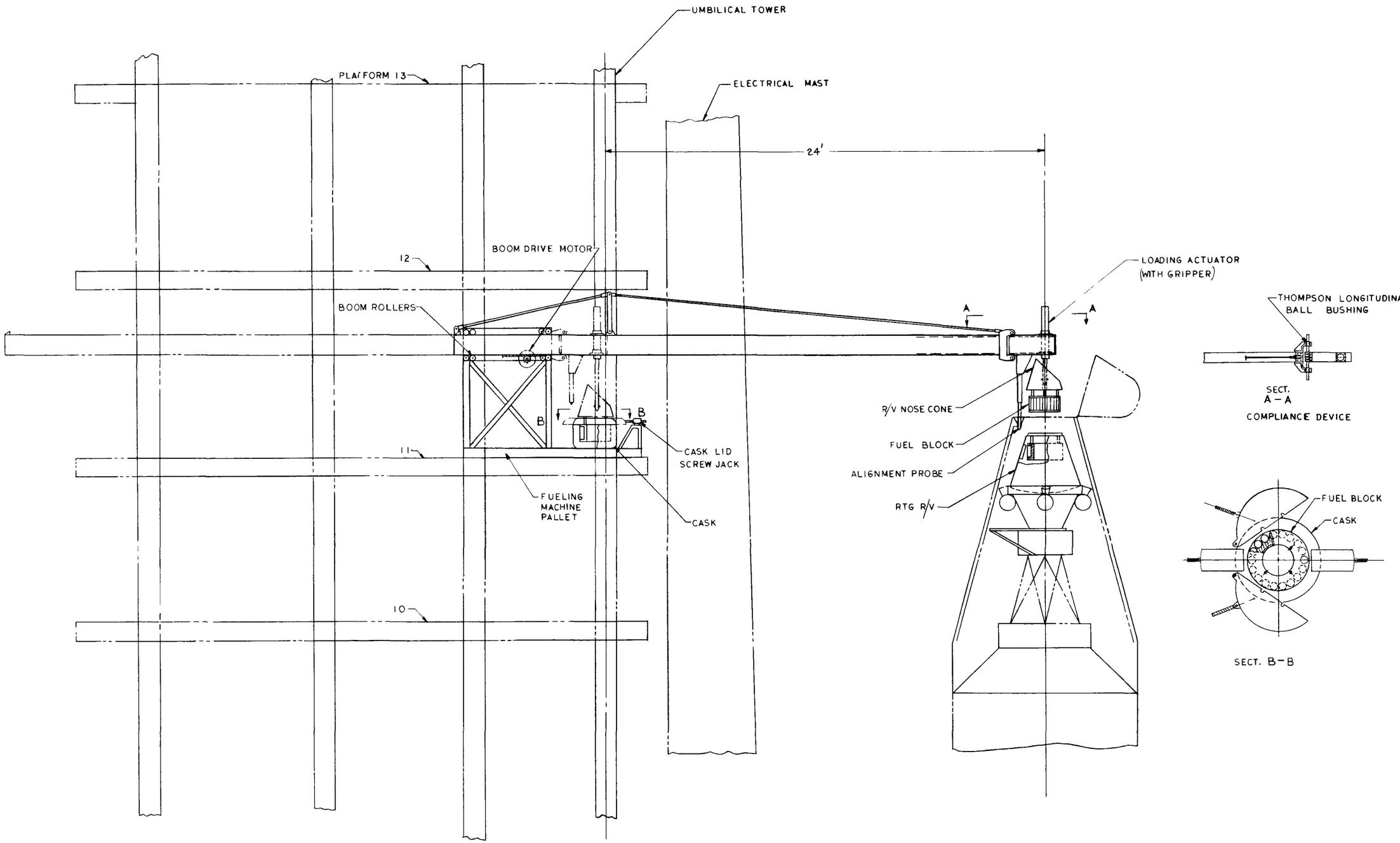

Fig. PP-13. Top Loading Sliding Boom--Split RTG

(2) Palletized loading boom

(3) Cask sling

(4) Cask skid

(5) Loading device sling

(6) Remote control console

(7) TV camera, monitor and controls.

2. Launch Complex Modifications

Minor modifications will be required to install the system at a Titan III launch complex. Tiedowns for the loading device pallet will be required on the umbilical tower. Power, control and cooling lines will be installed on the umbilical tower. A control panel and TV monitors will be installed in the blockhouse or could be installed in a portable van.

3. Description and Operation

a. Fuel block assembly

The fuel block, consisting of a series of cylindrical capsules arranged in a toroidal shape, will be assembled in a laboratory hot cell. The capsules will be installed securely into a spool structure with a Min-K insulation liner. Preload will be applied at this time. The entire assembly, which forms the inner portion of the RTG, will be installed vertically into the shipping cask. Four threaded bosses in the spool structure will be oriented with four holes in the shipping cask lid. The threaded bosses will be used later for RB nose cone installation. Shield plugs will be installed into the four open holes in the cask lid after the segmented cask lid has been closed. The cask will be shipped to the launch site on a skid.

b. RTG shipment

The RTG, an integral part of the reentry body, will be shipped to the launch site unfueled in a normal shipping manner.

c. Launch site preparation

Nonradiation environment condition. The lower section of the reentry body which includes the thermoelectric elements of the RTG will be installed on top of the payload with the cone pointing up, similar to the Gemini installation. All wiring will be connected and the RTG will be checked out with an electric heater element. The upper portion of the RB cone will not be installed at this time.

The fuel loading device will be installed on the umbilical tower and the shipping cask positioned in the loading device.

Radiation environment, RTG loading. The four shield plugs in the lid of the cask will be removed manually and four studs will be screwed into the fuel block support structure inside the cask. The upper cone section of the RTG/RB will be placed on top of the studs and attached with nuts. The fuel loading boom loading actuator will be aligned with the nose cone coupling and positioning stops on the loading boom manually adjusted to suit. All personnel will clear the launch stand area in preparation for the remote portion of the loading operation. The loading operation will begin by remotely opening the cask lid. The fuel block with the nose cone attached is lifted from the cask by raising the loading actuator. The boom drive motor is operated to extend the boom until the fuel block is approximately positioned over the RTG. Limit switches stop the drive motor. An alignment probe actuator is lowered from the boom and contacts a socket on the payload fairing. A lead-in cone provides for a transition between the coarse and fine alignments. A compliance device on the end of the boom permits a 10-inch lateral motion while the boom, mounted on rollers, provides ample motion in the direction of the umbilical tower. A close tolerance can be held between the centers of the loading actuator and the alignment actuator. Likewise, a close tolerance can be maintained between the centerline of the RTG and the alignment funnel in the fairing. Precision and controlled insertion of the fuel block into the RTG can be accomplished even during the differential motion of 10 inches between the launch vehicle and the umbilical tower. The loading actuator is extended until the fuel block latch in the base of the RTG springs closed and locks the fuel block in place. The loading actuator gripper is released and the actuator withdrawn from the nose cone. The alignment probe is withdrawn and the boom retracted to the stowed position inside the umbilical tower.

Radiation environment, RTG unloading. In the event of an aborted launch, provisions are made to unload the RTG. The boom is extended over the launch vehicle and is stopped by the action of a limit switch in a course alignment position. The alignment probe is extended and engages the funnel alignment socket in the payload fairing. The loading actuator is now aligned with the lifting socket in the nose cone. Alignment will be maintained even with differential motion between the launch vehicle and umbilical tower as the lateral compliance device and the sliding boom provide two axes of motion freedom. The lifting probe actuator is extended into the nose cone and is latched. An inner extension of the probe is extended and releases the fuel block latch. The fuel block with nose cone attached is raised and returned to the cask.

APPENDIX QQ

STRUCTURAL DESIGN STUDIES--AIRBORNE SYSTEMS

Studies have been performed on the major structural components of the RTG/RB-CIR reference configuration in order to define specific problem areas and develop practical concepts from which to generate realistic preliminary structural weight data. Significant structural environmental criteria imposed upon the reference configuration are discussed below:

1. Airloads

Since during ascent the payload is shrouded in the standard Titan III fairing, the only airloads experienced occur during an abort or normal reentry. The maximum airload on the blunt forebody heat shield occurs during an abort reentry ($\gamma_E = -8.0°$), 860 psf at the stagnation point. At the shoulder (heat shield edge) the airload decreases to 638 psf. By way of comparison, the stagnation airload for orbital decay reentry is 298 psf.

2. Inertia Loads

Figure QQ-1 defines the coordinate system and sign convention selected to define the inertia load factors. The inertia load factors defined in Table QQ-1 are peak values and, for a given condition, the vector quantities are not necessarily concurrent.

TABLE QQ-1

Summary of Peak Structural Load Factors

Condition	N_X	N_Y	N_Z	$N_{\dot{\theta}}/R$ (per ft)	$N_{\ddot{\theta}}/R$ (per ft)
Ascent	+4.16	0.40	0.40	NA	NA
Spacecraft separation	NA	-2.95	NA	1.33	0.367
Deorbit (retro)	-5.06	NA	NA	NA	NA
Reentry	+25.5	12	12	0.084	0.16

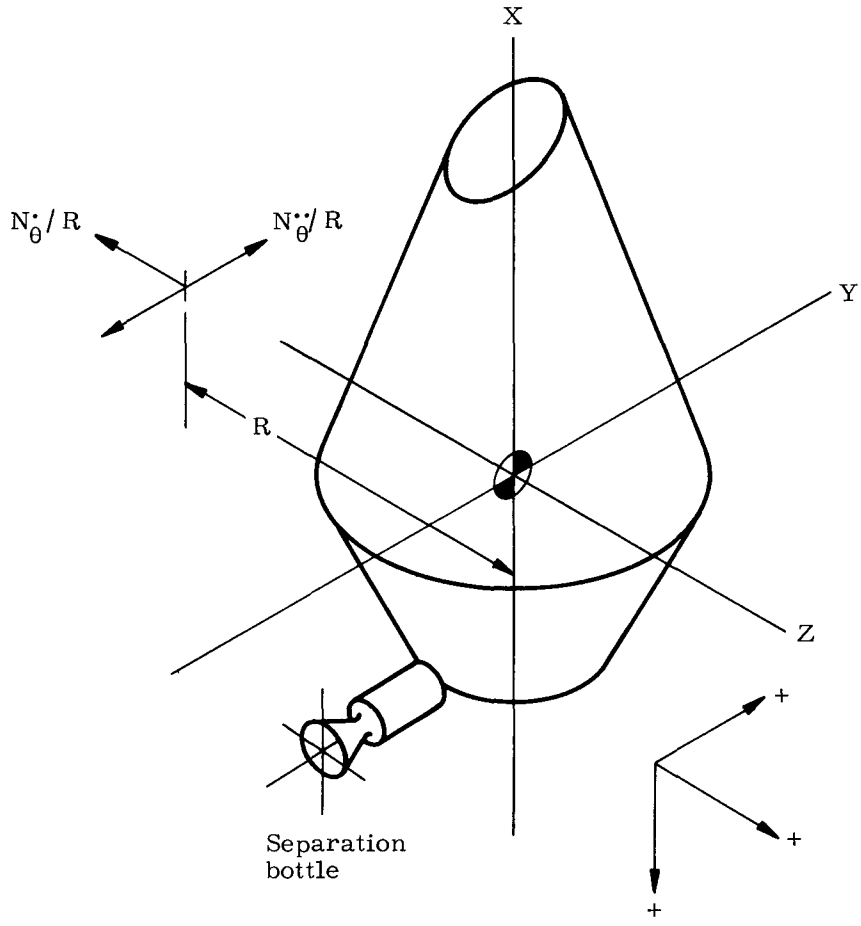

Fig. QQ-1. Load Factor Sign Convention

3. Blast Overpressures

The current estimates of blast overpressures resulting from a fireball environment are 100 psi. Reference QQ-1* defines some pertinent acoustic, shock and vibration design criteria for the reference configuration. These data are primarily significant for equipment and equipment support requirements and, for the preliminary studies defined herein, were not considered influential to the overall structure sizing.

In developing preliminary structural concepts and sizes for the reference configuration, the following structural factors of safety were applied to the appropriate load factors and/or airloads.

Safety Factor	Structural Integrity Criterion
1.10	Yield stress
1.25	Ultimate stress
1.25	Stability

For loading conditions occurring at elevated temperatures, no factors have been applied to the structural temperatures.

Critical environmental factors for the major structural subsystems of the RTG/RB-CIR reference configuration are:

Component	Critical Structural Design Parameter
Heat shield subassembly	Reentry (airload)
Beryllium aft cone (radiator)	RTG thermal design critical
CIR shell structure	Blast overpressure (fireball)
R/B to CIR attachment	Deorbit or abort
Separation structure (tracks)	Spacecraft separation

4. Heat Shield Substructure Studies

Under the airloads imposed upon the heat shield of the reference configuration during reentry, the supporting structure for the heat shield must remain stable and transmit the airload to its peripheral attachment

*Ref. QQ-1. "Titan IIIA and IIIC Standard Space Launch System (SSLS) Definition for Payload Contractors," SSD-CR-65-18 (Rev. 2), June 1966.

with the beryllium radiator shell where it is reacted by inertia loads. A spherical honeycomb panel offers an efficient structural concept with minimal fabrication problems.

A phenolic-glass honeycomb core of 5.5 lb/cu ft was chosen for light weight and low thermal conductance. Comparative studies were performed on face sheets of beryllium and phenolic-glass laminate which were bonded to the core with HT-424 adhesive. Both the beryllium and phenolic-glass honeycomb substructures were analyzed for the orbital decay and abort reentry airloads. From a fabrication and/or material availability standpoint, a group of minimum acceptable dimensions were imposed upon the designs. Thus, the minimum acceptable core depth was set at 0.188 inch, and the minimum face thicknesses for the phenolic/glass and beryllium were 0.02 and 0.01 inch, respectively. Calculated substrate temperatures coincident with peak airloads were employed in the analysis. Calculated unit weight requirements for each of the cases are tabulated in Table QQ-2.

TABLE QQ-2

Heat Shield Substructure Design Comparisons

Condition	Material	Weight (psf)
Orbital decay	Beryllium	0.694
Abort	Beryllium	0.694
Orbital decay	Phenolic/glass	0.860
Abort	Phenolic/glass	0.960

Minimum gages dictate the design weights for both beryllium cases and the phenolic/glass honeycomb panel under the orbital decay airloads. In all cases the heat shield substructures are critical in the buckling mode. The weights in Table QQ-2 include the weight of three adhesive bond layers (two for the panel assembly, one for the ablator attachment). Although the beryllium concept offers a three-pound weight saving, the phenolic/glass concept was selected based on lower cost and fewer fabrication problems.

The heat shield substructure is joined to the aft beryllium cone (RTG radiator) by a short transition structure which:

(1) Transmits loads between the RTG and heat shield.

(2) Reacts membrane stresses at the heat shield substructure periphery by hoop tension.

(3) Provides a flexible structural link between the heat shield and the radiator which minimizes the structural interactions between these two components due to temperature differentials during steady-state operation and reentry.

Analysis revealed that Item (1) is not critical for design. Analysis for Item (2) resulted in the selection of 6Al-4V titanium for this application. Although slightly heavier than beryllium, the slight weight penalty more than offsets the cost and fabrication problems associated with beryllium. Stainless steel and Haynes 25 were also reviewed and were found to be heavier. Analysis related to Item (3) indicated that, during reentry, the differential radial thermal expansion between the heat shield substructure and the RTG radiator will be ~0.20 inch. To minimize the introduction of high stress levels into the ablator and substructure due to structural interaction resulting from this differential thermal expansion, the titanium frame around the periphery of the heat shield substructure was integrated into a short conical transition shell structure between the heat shield substructure and beryllium radiator. Analysis performed on the transition piece (0.05 in. thick, 2.5 in. long) indicates that sufficient relief of the structure interactions is afforded by this approach and no failure is induced in the ablator or heat shield structure.

5. CIR Studies

The CIR structure shell must withstand the overpressure resulting from a fireball environment. The current estimate of fireball overpressure is 100 psi. Table QQ-3 summarizes the estimated weights of a shell structure which will withstand the fireball overpressure.

TABLE QQ-3

Comparison of Retro Structure Weights

Configuration	Frames	Material	Shell Weight (lb)
Monocoque	None	Aluminum	58.2
	None	Steel	110.0
	None	Beryllium	22.0
	One	Aluminum	44.1
	One	Beryllium	16.6
Honeycomb	None	Aluminum	22.9
	One	Aluminum	21
Skin-string-frame	Two	Aluminum	17.8*

*Stringer and frames portions will withstand the 100 psi overpressures, although the skin may be damaged locally.

Table QQ-3 indicates that, in order to withstand the fireball overpressure, the lightest practical configuration would be an aluminum honeycomb shell. The beryllium monocoque shell offers a five-pound weight reduction but the inherent fabrication problems and material costs discourage its use. Similarly, use of beryllium honeycomb has been dropped from consideration. The need for an access door and load distribution members for the propulsion units suggests that use of a honeycomb shell is undesirable. In fact, a conventional skin-stringer-frame construction would be a more practical concept if the fireball overpressure criteria were not critical. Since the overpressure criteria are only estimates and are subject to further verification, it has been elected to utilize a skin-stringer-frame concept for the CIR structure shell. This design will not withstand the 100 psi overpressure but does provide a more efficient solution to the other structural requirements (component support, access doors). Should review of the fireball overpressure reveal that it remains the dominant design criterion, the honeycomb concept can be adopted for the shell configuration. For an overpressure critical shell structure, the honeycomb concept will result in the lightest weight, but will require a more complex design to satisfy secondary requirements.